FACULDADE DE ENGENHARIA DA UNIVERSIDADE DO PORTO



EVALUATION OF SOIL LIQUEFACTION POTENTIAL BASED ON LABORATORY DATA
Major factors and limit boundaries

Sandra Marisa da Costa Soares

A dissertation submitted to the Faculty of Engineering of the University of Porto in accordance with the requirements of the degree of Doctor in Civil Engineering

Supervisor: Prof. Doutor António Joaquim Pereira Viana da Fonseca

January 30, 2015

© Sandra Soares, 2014

Abstract

Soil liquefaction remains as an unclarified geomechanical behaviour. Despite being extensively studied by several researchers, soil liquefaction is far from being accurately predicted, being worst on the case of cyclic liquefaction events. While proper constitutive models are being developed, semi-empirical frameworks, such as the "Simplified Procedure", which correlates the standard penetration tests results (SPT effective stress normalized values, $(N_1)_{60}$) with a cyclic resistance ratio ("CRR"), remains as the one and preferable way to assess liquefaction "risk" on sandy soils. Later this framework was adapted to normalized values of static cone penetration tests (CPT, q_{c1N}) and to shear/distortional seismic waves (V_{s1}), despite the later one not being contemplated on current standards for geotechnical engineer. Notwithstanding these approaches are exclusive addressed to field conditions under cyclic conditions, limiting the generalization of a proper interpretation under applied soil mechanics.

Aiming to perceive soil liquefaction, and the overall geomechanical behaviour of soils, an extensive laboratory program was carried out. The study involved six distinct materials, three sands, a silt and two silty sands, which were studied under monotonic loading conditions basing on CSSM theory. Plus, two of the six soils, Algeria and Coimbra sands, were also investigated under cyclic loading conditions, which allowed distinguishing flow liquefaction from cyclic mobility. Aware of triaxial stress conditions limitations, most of the research was developed on triaxial devices which, due to it easy performing, resulted on the collection of a large data set. Triaxial cells available in the Geotechnical Laboratory, of Faculty of Engineering of Porto University ("FEUP"), are equipped with bender-extender elements, which allowed the measurement of seismic waves, (both, primary or compression wave's velocities, V_p, and shear or distortional wave's velocities, V_s), during the tests performance. Plus in order to evaluate principal stress rotation during cyclic loading conditions, Algeria and Coimbra sands were also studied on a Direct Simple Shear ("DSS") device. During this research fundamental factors that influence liquefaction susceptibility, regardless the type of phenomenon (cyclic liquefaction or cyclic mobility), were considered to comprehend experimental results and make them valuable for practical applications. Therefore liquefaction potential was assessed under distinct initial state conditions by varying the void ratio, the confining stress, the induced anisotropic stress state condition (K_0), the sample preparation method and the degree of saturation. Furthermore instability was also investigated under distinct stress-paths which allowed to understand the distinct soil behaviour coupled to it ultimate states.

While under cyclic conditions a universal framework was difficult to delineate, the final results achieved under monotonic conditions granted the achievement of a general framework to assess soil liquefaction potential well captured by both state parameter and shear wave velocities. The different mechanics of liquefiable granular soils allowed delimiting clear borders which were found to be function of the uniformity coefficient (Cu).

Resumo

A liquefação é um dos fenómenos geomecânicos do solo que permanece incompreensível. Apesar de ter vindo extensivamente estudado por vários investigadores, a capacidade de previsão deste fenómeno está longe de ser precisa, sendo pior no caso de eventos cíclicos.

Na ausência de um modelo constitutivo capaz de prever a liquefação do solo, a sua avaliação continua a basear-se em ábacos, tais como o "Procedimento Simplificado" construídos a partir de dados semi-empíricos que correlacionam a resistência à penetração normalizada ($(N_{60})_{60}$) e a razão da resistência cíclica (CRR). Posteriormente estes foram adaptados à resistência de cone normalizada (CPT, q_{c1N}), e às ondas sísmicas distorcionais/ de corte (V_{s1}), apesar deste último ainda não ser contemplado nas normas convencionais de projeto. Estes ábacos, circunscritos a condições in situ sob condições de carregamento cíclico, limitam a sua compreensão à luz da mecânica dos solos.

Com o objetivo de perceber a liquefação do solo, bem como o comportamento geomecânico dos solos, foi elaborado um programa laboratorial extensivo. O estudo envolveu seis materiais distintos, três areias, um silte e dois solos silto-arenosos, que foram estudados sob condições de carregamento monotónico tendo por base a teoria da MSEC. A acrescer, dois dos seis solos, foram igualmente estudados sob carregamento cíclico. Apesar das limitações do estado triaxial de tensões, a maioria do estudo foi desenvolvido em câmaras triaxiais que, devido à sua facilidade de execução, permitiram a obtenção de um grande conjunto de dados. Estas câmaras triaxiais, alojadas no Laboratório de Geotecnia da FEUP, são equipadas com *bender-extender elements* que permitiram a medição das ondas sísmicas nos solos, (ondas P de compressão e ondas S de corte), no desenrolar dos testes. Ademais, a fim de avaliar o efeito da rotação das tensões principais sob carregamento cíclico, as areias da Argélia e de Coimbra foram igualmente estudadas num equipamento de corte direto simples.

Durante esta investigação deu-se primazia ao estudo dos fatores que têm um papel preponderante do desencadeamento da liquefação. Desta forma várias condições iniciais do solo foram recriadas, para tal fez-se variar fatores tais como o índice de vazios, a tensão efetiva inicial, a anisotropia induzida (K_0), o método de preparação e o grau de saturação. A instabilidade por liquefação foi igualmente investigada sob diferentes trajetórias de tensões que permitiram uma compreensão da sua influência acoplada ao seu estado último de tensão.

Apesar de não ter sido obtido um gráfico universal para condições de carregamento cíclico, os resultados obtidos pelos solos submetidos a carregamentos monotónicos resultaram na obtenção de resultados consistentes tendo o potencial de liquefação sido bem capturado por ambos o parâmetro de estado e a velocidade das ondas S. As distintas respostas dos solos granulares permitiram o estabelecimento de fronteiras entre comportamentos estáveis e instáveis que foram encontradas serem função do coeficiente de uniformidade dos solos (Cu).

Acknowledgments

For better expressing my acknowledgments I decided to use my native language, Portuguese, excepting for those entities and persons who do not share my language.

Em primeiro lugar gostaria de agradecer ao meu orientador e mentor Professor Dr. António Viana da Fonseca pela sabedoria, preocupação, confiança e credibilidade que deu à minha capacidade intelectual e criativa de prosseguir com este estudo. A ele agradeço a sua disponibilidade, quase que infinita, no acompanhamento ao longo destes quatro anos. Acredito até que a qualidade e quantidade de trabalho laboratorial em muito se deve à sua incessante exigência alimentada pela constante curiosidade. Sem ele não seria possível esta jornada. Sempre presente, um Professor e pessoa admirável, cuja convicção e paixão pela ciência que é a Geotecnia é de notável reconhecimento. Agradeço ainda pelas conferências e missões ao estrangeiro que me incumbiu, que certamente me abriram novos horizontes e permitiram conhecer outros "gurus" da Geotecnia.

I would also like to acknowledge to Professor Andy Fourie for his kindness, knowledge and obviously for his support and for allowing the possibility of carrying out part of my work at University of Western Australia (UWA). Many special thanks to Professor Fernando Schnaid, which cleared up the interpretation of my tests, and to Professors Luis Filipe Prada and Alfonso Ramos, which helped me out with the model calibration. I would also like to thank to these Professors for their hospitality, concern and availability during these missions to Australia, at UWA, to Brazil, at *Universidade Federal do Rio Grande do Sul* (UFRGS), and to Colombia, at Universidad Javeriana.

Agradeço ainda ao Sr. Armando Pinto, à Daniela e à Cláudia pela integração na equipa do LabGeo, pelo conhecimento e ajuda, que me possibilitaram atingir esta meta. Agradeço sobretudo pelo companheirismo e amizade. Sem dúvida que sem eles esta etapa não seria a mesma.

Parts of my acknowledgments are also directed to the amazing staff at UWA, mainly to Binaya Bhattarai and to Manuel Passos which helped me out with the equipment procedures. Special thanks to Behnaz Abdollahzadeh, Usha Mani and to Sharmin Farhana for their kindness and fellowship during my stay at UWA.

Um especial agradecimento ao meu amigo Fabrizio, meu amigo e colega, que em breve, também ele, será Doutorado por esta *muy* nobre Faculdade. Sem dúvida alguma que a uma pessoa brilhante como ele terá reservado um futuro próspero e promissor.

A estadia alargada desta pós-graduação permitiu-me ainda conhecer a Sara Rios, a Cristiana Ferreira e o Miguel Amaral, pessoas fantásticas, entusiastas, dinâmicas, disponíveis e acima de tudo que nutrem uma grande admiração e curiosidade pela área que une os nossos laços, a Geotecnia.

Obviamente que este percurso traçou uma proximidade maior com alguns colegas que com outros, mas não poderei deixar de agradecer a todos aqueles com quem travei conhecimentos, empatia e por vezes amizade, tais como o Anderson Fonini, o André Domingues, o Bérnat Csécs, o Eng. Cândido, a Eng. Elisabete Esteves, o Énio Abreu, o Francisco Miranda, ao João Travanca, a Eng. Mafalda Laranjo, o Márcio Floss, a Mariana Benessiuti, a Mariana Oliveira, e o Eng. Nuno Raposo. Agradeço ainda ao meu amigo Marco Fonseca que, para além da amizade, prestou ainda serviços no âmbito deste projeto de investigação.

Tenho ainda a agradecer a todos os Doutorados e Mestres colegas que me forneceram os ficheiros de dados, resultado das suas investigações. A eles, ao Marco Fonseca, André Pinheiro, José Rocha, Joana Silva, Eng. Ghili Tahar e nomeadamente à Eng. Jucélia Bedin, devo parte desta vasta base de dados.

Todo este percurso teria sido impossível sem a presença, física ou espiritual, dos meus amigos/as, em especial das minhas grandes amigas Ana Sofia Peixoto e Kátia Mota. O vosso entusiasmo contagiante e suporte integral tornaram esta etapa tranquila e objetiva, e muito mais fácil de ser atingida.

À minha família, em especial a meus pais, agradeço o amor incondicional, o incentivo, confiança e carinho.

À minha irmã Diana Soares, recente Mestre desta *muy* nobre Faculdade agradeço a persistência e sobretudo paciência, que já depois de ter entregue a sua tese prescindiu do descanso para me ajudar na formatação do presente documento. A ela, acima de tudo agradeço a amizade, o amor incondicional, a gentileza e bondade.

Por último, mas não menos, agradeço o suporte dado pela FCT através do projeto PTDC/ECM/103220/2008, e financiado pelo QREN, Programa Operacional Factores de Competitividade – COMPETE, sem o qual teria sido impossível a realização deste trabalho e investigação, incluindo todas as missões ao estrangeiro.

Marisa Soares

"Discovery consists of seeing what everybody has seen and thinking what nobody has thought"

Albert Szent-Györgyi

Contents

1 Introduction **1**
- 1.1 Prologue . . . 1
- 1.2 Scope and Objectives . . . 2
- 1.3 Structure of Presentation . . . 4

2 Soil Liquefaction – An Historical Overview **7**
- 2.1 Introduction . . . 7
- 2.2 Liquefaction – Lexical Disambiguation . . . 7
- 2.3 Past Soil Liquefaction Events . . . 9
  - 2.3.1 Remarkable Case Histories . . . 9
  - 2.3.2 Case Histories In Portugal . . . 18
  - 2.3.3 Liquefaction Hazard Mapping . . . 20

3 Liquefaction Susceptibility Criteria **23**
- 3.1 Specifications And Standards To Assess Liquefaction Susceptibility . . . 23
  - 3.1.1 Eurocode . . . 25
- 3.2 From Field-Based Procedures To Laboratory Studies . . . 27
  - 3.2.1 Empirical Criteria . . . 28
  - 3.2.2 Procedures Developed From Field/ In Situ Performance Studies . . . 31
  - 3.2.3 Theoretical Background On Stiffness At Very Small Strains . . . 46
  - 3.2.4 Procedures Developed From Laboratory Studies . . . 50

4 Mechanics Of Soil Liquefaction **69**
- 4.1 Introduction . . . 69
- 4.2 Static Liquefaction Of Sands Within The Context Of Critical State Soil Mechanics 71
  - 4.2.1 Drained Behavior . . . 71
  - 4.2.2 Undrained Behaviour . . . 73
- 4.3 Factors Affecting Static Liquefaction . . . 90
  - 4.3.1 Influence Of Initial Confining Stress Level And Relative Density . . . 90
  - 4.3.2 Influence Of Non Plastic Fines Content . . . 91
  - 4.3.3 Influence Of Anisotropy . . . 107
- 4.4 Factors Affecting Cyclic Liquefaction . . . 121
  - 4.4.1 Influence Of Earthquake Magnitude Scaling . . . 123
  - 4.4.2 Influence Of Initial Confining Stress Level And Relative Density . . . 124
  - 4.4.3 Influence Of Anisotropy . . . 127
  - 4.4.4 Undrained Cyclic Shear Strength Obtained From Distinct Laboratory Testing Devices . . . 134

5 Scope Of The Research And Characterization Of The Materials **141**
5.1 Introduction . . . 141
5.2 Algeria Sand . . . 141
5.2.1 Historical Overview - The Boumerdès Earthquake . . . 142
5.2.2 Past Research . . . 144
5.3 Coimbra Sand . . . 148
5.3.1 Historical Overview – Lisbon And Benavente Earthquakes . . . 148
5.3.2 Past Research . . . 152
5.4 Silt, Osorio Sand And Mixture . . . 159
5.4.1 Historical Overview – Liquefaction Of Tailings . . . 159
5.4.2 Past Research . . . 163
5.4.3 Present Research . . . 167

6 Equipments, Testing Procedures and Experimental Program **173**
6.1 Introduction . . . 173
6.2 Equipments and Test Procedures . . . 174
6.2.1 Oedometer . . . 174
6.2.2 Triaxial Cell . . . 176
6.2.3 Direct Simple Shear Device . . . 191
6.2.4 Piezoeletric Transducers . . . 195
6.3 Test Analysis . . . 197
6.3.1 Oedometer Tests . . . 197
6.3.2 Triaxial Tests . . . 198
6.3.3 Direct Simple Shear Tests . . . 202
6.4 Introduction to the Experimental Work Done . . . 203

7 Static Liquefaction **217**
7.1 Introduction . . . 217
7.2 Algeria Sand . . . 218
7.2.1 Basic Characterization . . . 218
7.2.2 Triaxial Tests . . . 218
7.2.3 Prediction of Liquefaction Resistance . . . 228
7.2.4 Partial Conclusions . . . 233
7.3 Coimbra Sand . . . 234
7.3.1 Basic Characterization . . . 234
7.3.2 Triaxial Tests . . . 235
7.3.3 Prediction of Liquefaction Resistance . . . 242
7.3.4 Partial Conclusions . . . 246
7.4 Coimbra Sand With 20% FC . . . 247
7.4.1 Basic Characterization . . . 247
7.4.2 Triaxial Tests – Soil Behavior Under Applied CSSM . . . 248
7.5 Coimbra Sand With 40% FC . . . 251
7.5.1 Basic Characterization . . . 251
7.5.2 Triaxial Tests – Soil Behavior Under Applied CSSM . . . 251
7.6 Osorio Sand . . . 254
7.6.1 Basic Characterization . . . 254
7.6.2 Triaxial Tests . . . 254
7.6.3 Prediction Of Liquefaction Resistance . . . 260
7.6.4 Partial Conclusions . . . 265

7.7 Silty Sand - Mixture . . . 266
7.7.1 Basic Characterization . . . 266
7.7.2 Triaxial Tests . . . 267
7.7.3 Prediction Of Liquefaction Resistance . . . 275
7.7.4 Partial Conclusions . . . 280
7.8 Silt . . . 281
7.8.1 Basic Characterization . . . 281
7.8.2 Triaxial Tests . . . 282
7.8.3 Prediction Of Liquefaction Resistance . . . 295
7.8.4 Partial Conclusions . . . 300
7.9 Silty Sand - Gold Tailings . . . 302
7.9.1 Basic Characterization . . . 302
7.9.2 Triaxial Tests . . . 303
7.9.3 Prediction Of Liquefaction Resistance . . . 311
7.9.4 Partial Conclusions . . . 315
7.10 Similarities And Differences Between Soils . . . 316
7.10.1 Comparison Of CSL Positioning . . . 317
7.10.2 Comparison Of Residual Or Constant Volume Friction Angle, ϕ'_{cv} . . . 324
7.10.3 Comparison Of Soil Liquefaction Potencial . . . 325

8 Cyclic Liquefaction **329**
8.1 Introduction . . . 329
8.2 Algeria Sand . . . 330
8.2.1 Cyclic Triaxial Tests . . . 330
8.2.2 Cyclic DSS Tests . . . 346
8.2.3 Comparison Of Liquefaction Resistance Of Algeria Sand Under Simple Shear And Triaxial Stress Conditions . . . 353
8.3 Coimbra Sand . . . 355
8.3.1 Cyclic Triaxial Tests . . . 355
8.3.2 Cyclic DSS Tests . . . 365
8.3.3 Comparison Of Liquefaction Resistance Of Coimbra Sand Under Simple Shear And Triaxial Stress Conditions . . . 371

9 Sanisand Model Description And Application **375**
9.1 Introduction . . . 375
9.2 Description Of The Constitutive Model SaniSand . . . 376
9.2.1 Description Of The Model . . . 376
9.2.2 Flow Liquefaction Criterion . . . 382
9.3 Parametrical Calibration For SANISAND Modelling . . . 384
9.3.1 Model Constants . . . 384
9.3.2 Calibration Of Osorio Sand . . . 386
9.3.3 Calibration Of Mixture . . . 392
9.4 Limitations Of The Model . . . 397

10 Conclusions **399**
10.1 Conclusions . . . 399
10.1.1 Static Liquefaction . . . 399
10.1.2 Cyclic Liquefaction . . . 401
10.1.3 SANISAND Model Application . . . 404

10.1.4 Implications for design practice 405
10.2 Future Developments 405

References **407**

Appendix A Initial Stiffness, Peak Strengths, Critical And Steady State Parameters **429**

Appendix B Degree of Saturation of Undrained Triaxial Tests Performed with Silt and Gold Tailings **447**

List of Figures

2.1 a) Dikes filled with sediments in the road to Falésia beach in Algarve, south of Portugal (ERSTA); b) Sand boils beneath elevated West Grand Avenue distribution structure adjacent to Interstate Highway 80 east of San Francisco-Oakland Bay Bridge Toll Plaza during Loma Prieta, California, Earthquake of October 17, 1989. 8
2.2 Oblique view of Fort Peck Dam Failure, in 1938. 9
2.3 Oblique view of Aberfan disaster. 10
2.4 Stava tailing dams before and after the collapse. 11
2.5 Liquefaction during the 1964 Good Friday earthquake in Alaska results in lateral spreading collapse of the coastline. 15
2.6 (a) Building build on sands tilted and (b) Bridges collapsed due to liquefaction, during Niigata Earthquake, 1964. 16
2.7 Sand boils and ground surface cracking caused by liquefaction at Wu-Feng during Chi- Chi earthquake. 17
2.8 (a) Liquefaction-induced damages in CBD; (b) and (c) Liquefaction on Kilmore St. 18
2.9 (a) Terreiro do Paço; (b) Scheme of the tunnel and piles location on Terreiro do Paço. 19
2.10 Liquefaction-scenario seismic-hazard map of the greater Oakland, California, area for a magnitude 7.1 earthquake on the Hayward Fault. Geologic units were geotechnically characterized with 210 cone-penetration-test (CPT) soundings. 21

3.1 Relationship between stress ratios causing liquefaction and $N_1(60)$ values for clean and silty sands for Mw = 7.5 earthquakes 27
3.2 Limits in the gradation curves separating liquefiable and nonliquefiable soils. . . 30
3.3 "Modified Chinese Criteria". 30
3.4 Curves relating CRR to $(N_1)_{60}$ published over the past 24 years for clean sands, including the one currently accepted for geotechnical design and the recommended curve for M=7.5 and $\sigma'_{v0} = 1$ atm. 34
3.5 Curves relating CRR to q_{c1N} proposed by various investigators for clean, including the one currently accepted for geotechnical design design and recommended curve for M=7.5 and $\sigma'_{v0} = 1$ atm. 37
3.6 Average correlation for deriving the in situ state parameter using the normalized dilatometer horizontal index K_D/K_0 obtained by the DMT tests. 38
3.7 Average correlation for deriving the in situ state parameter using the normalized dilatometer horizontal index K_D/K_0 obtained by the DMT tests. 39
3.8 Body waves propagation mode within a uniform, infinite medium. 42
3.9 Curve recommended for calculation of *CRR* from V_{s1} measurements. 43

3.10 Typical variation in compression wave velocity with degree of saturation changing from 99.4 to 100% for sand. . . . 46
3.11 V_s as function of the void ratio and confining pressure – Ottawa sand. . . . 47
3.12 (a) G_{vh} of 0 deg and 90 deg deposition angles measured for Toyoura sand; (b) Relationship between degree of anisotropy and axial stress. . . . 48
3.13 B parameter as function of the fines content. . . . 49
3.14 Comparison of liquefaction resistance of Ottawa sand in simple shear and triaxial compression. . . . 52
3.15 Early hypothesis of critical void ratio from direct simple shears. . . . 52
3.16 Dimensional Critical State Line. The balck dot is the CSL. The white dots represent the projections in the three planes. The black square dot is the starting point before undrained shearing. The white square dots are its projections. . . . 53
3.17 Behaviour of initially loose and dense specimens under drained and undrained and undrained conditions for (a) arithmetic and (b) logarithmic effective confining pressure. . . . 54
3.18 Use of CVR line as a boundary between initial states that are and are not susceptible to liquefaction. . . . 55
3.19 Concept of liquefaction reached through a strain controlled test. . . . 56
3.20 Britleness index of sands with a range of λ. . . . 57
3.21 (a) Variations of the Brittleness Index with ψ_{cs} in 3 sands tested in Triaxial (TxC, C for compression) and Ring Shear (RS) in damaged and undamaged conditions by the end of the tests; (b) Variations of I_B with $\sigma_c^{'}/\sigma_{cs}^{'}$ in OT, IR and MR sands). 57
3.22 *"Basic Berkeley School liquefaction assessment chart"* - Field history data representation. . . . 58
3.23 Liquefaction assessment charts based on V_{s1} proposed by Tokimatsu et al. (1991). 60
3.24 Method of first wave arrival; Stress waves measurement using bender-extender elements (LabGeo). . . . 61
3.25 Critical state parameter expressed as a function of normalized peak shear strength (q_1) and shear stiffness. . . . 62
3.26 Effects of mean stress, normalized peak shear strength (q_1), and stiffness. . . . 63
3.27 Relation between P-wave velocity and B for Toyoura sand. . . . 65
3.28 Comparison of demand energy imported by the soil and capacity energy predicted by GP-based model for various real sites and centrifuge tests. . . . 67

4.1 Inter-particle forces after and before liquefaction. . . . 69
4.2 Initiation of flow liquefaction by cyclic and monotonic loading. . . . 70
4.3 Three cases of cyclic mobility: (a) no stress reversal and no exceedance of the steady-state strength; (b) no stress reversal with momentary periods of steady-state strength exceedance; (c) stress reversal with no exceedance of the steady-state strength. Zones of susceptibility of cyclic mobility. . . . 71
4.4 (a) Dilation and contraction of dense and loose sand in a simple shear test; (b) Curved peak strength envelope on Mohr's circle plot. . . . 72
4.5 Normalized critical state and normal consolidation lines. . . . 73
4.6 Critical state lines of Fujian sand and Toyoura sand. . . . 75
4.7 Critical state line of Stava tailings; Suggested scheme of subdivision of the area of the area above the CSL intro three different regions connected to different behaviour. 75
4.8 Critical state lines of gold tailings. . . . 76
4.9 Steady State Diagram obtained from drained and undrained tests sheared from a single isotropic consolidation line on Nevada sand with 7% fines. . . . 76

4.10 Undrained compression tests on Nevada sand with 7% of fines between 25 and 200 kPa initial confining pressure: (a) Effective stress-path; (b) Stress-strain relationship. 77

4.11 (a) SSL for samples of various fines content (fc), tested under drained conditions and based on the void ratio; (b) Steady-state points from samples with fines content ranging from 0% to 30%, tested under drained and undrained conditions, being the connected points data obtained from the drained tests. 78

4.12 (a) Stress paths for three specimens of different initial densities consolidated at the same confining pressure (the white dots represent the initial states) and the position of the Steady States (black dots) on the Steady State Line; (b) Undrained strength of sands. 79

4.13 Four distinctly different general types of undrained effective stress paths for loose silty sands: Static liquefaction, temporary liquefaction; temporary instability, and instability shown in $p^{'}$-q diagram. 80

4.14 Monotonic undrained behaviour at constant relative density: (a) State diagram; (b) Stress path plot. 82

4.15 Definition of the elements of state boundary surface. The collapse line is below the state boundary in the undrained plane. 84

4.16 Stress ratio at peak undrained strength of loose sand expressed in terms of current state parameter ψ at onset of liquefaction. 85

4.17 Flow liquefaction due to: 1) increase of u due to water infiltration; 2) increase of q due to increasing material deposition. 87

4.18 (a) Instability or collapse curve at e = 0.809 and CSD test, i.e. triaxial tests with deviator stress and mean stress controlled, (q = 100 kPa) on Ottawa sand; (b) Definition of the state parameter ψ and the modified state parameter 88

4.19 Relationships between the effective stress ratio at instability and the modified state parameter for Changi sand in triaxial conditions. 88

4.20 Schematic diagram of locations of yield surfaces and instability lines for isotropically and K_0-consolidated soil elements. 89

4.21 Effective stress-paths in p'-q diagram for three triaxial compression tests on medium-dense Cambrian sand exposed to undrained creep initiated outside the instability region. Two tests eventually exhibited instability inside the instability region. . . 89

4.22 Steady state diagram from undrained tests on three densities of Nevada sand with 6% of fines showing non-uniquess of SSLs and QSSLs. 91

4.23 Schematic diagram showing silty sand deposited in a loose state with silt grains between large grains. Application of stresses causes silt grains to move into void spaces, resulting in large volumetric contraction in static liquefaction. 92

4.24 Three-dimensional diagram showing static liquefaction related to volumetric compressibility, which in turn is influenced by fines content and void ratio for specimens of fine Ottawa sand and Loch Raven fines. 93

4.25 Measured and adjusted one-dimensional compression curves shown on (a) arithmetic, and (b) log-log scales with best fitting lines for description by power functions. 94

4.26 CSL and SSL for sands and silts; Undrained shear strength of soils delimited in a diagram e-log p'; Measurement of liquefaction potential through the state parameter ψ. 95

4.27 (a) SSL for samples of various fines content; (b) Grain size distribution curves for the nonplastic host silt (Sil co sil No. 40) and the host sand (F55, Foundry Sand, U.S. Silica Company, Ottawa, Ill.); (c) SSL for static and dynamic triaxial tests (mixed under compaction) for Ardebil sand with fines; (d) Grain size distribution curves of Ardebil sand being the fines natural particles collected from the natural Ardebil sand. 96
4.28 (a) SSL for samples of various fines content, tested under drained conditions on the void ratio after consolidation; (b) Grain size distribution curves for mixtures obtained with an host silt (Chengbei nonplastic silt) and an host sand (clean Hokksund sand); (c) CSL for samples of various fines content; (d) Grain size distribution curves of sand and silt of Stava tailings. 97
4.29 (a) SSL for Kogyuk 350 sand with different silt content; (b) Grain size distribution curve of Kogyuk 350 sand with 2% silt; the fines content was varied by adding fines to previously washed Kogyuk 350 sand; (c) Iddealized effect of fines content on CSL determined statically for 42 different parent sands. 98
4.30 (a) Extreme void ratios for soils obtained for mixtures obtained between Hokksund and Chengbei non-plastic silt; (b) Variation of potential for static liquefaction with silt content for Stava tailings. 98
4.31 Correlation between CSL interception, Γ, and the maximum and minimum void ratio. 99
4.32 Effect of particle shape on extreme void ratios (natural sands with CU $\leq$ 2.5). . . 99
4.33 Effect of particle shape on critical state parameters. 100
4.34 Effect of particle roundness on constant volume friction angle. 101
4.35 (a) Particle size distribution curves of the reconstituted sands ;(b) Relationship between uniformity coefficient and normalized strength of loose specimens. . . . 101
4.36 (a) Stable undrained triaxial behaviour due to Large-to-Large grain contacts (L-L) – Behaviour predominantly governed by sand behaviour; (b) Unstable undrained triaxial behaviour due to Large-Small-Large grain contacts (L-L) – Behaviour predominantly governed by silt behaviour. 102
4.37 Variation of inclination of the phase transformation line and the instability line with fines content for fine Ottawa sand and Loch Raven fines. 104
4.38 (a) Intergranular soil mix classification; (b) Intergranular matrix diagram classification. 105
4.39 SSL data : (a) e vs p'_{SS}; (b) $(e_c)_{eq}$ vs p'_{SS}; (c) $(e_f)_{eq}$ vs p'_{SS} for granular mixes between F55, Foundry Sand, U.S. Silica Company, Ottawa, Ill. and nonplastic crushed silica fines (Sil co sil No. 40). 107
4.40 (a) Examples of grain shapes for each aspect ratio; (b) Distribution of contact orientations at the end of the dry pluviation process. 109
4.41 Stress-strain response comparing water pluviation (WP), air pluviation (AP): (a) and moist tamping (MT) for medium density Syncrude sand specimens tested under simple shear conditions; (b) for low density Fraser River sand specimens tested under triaxial conditions, both on compression and extension. 110
4.42 (a) Stress-strain and stress-path response of undrained triaxial test comparing water sedimentation (WS), tapped funnel deposition (TFD), and fast funnel deposition (FFD) for medium density Nevada sand specimens, with 11% of FC; (b) Stress-strain and stress-path response of undrained triaxial test comparing mixed dry de- position (MDD) with tapped funnel deposition (TFD) for low density Nevada sand specimens, with 10% of FC. 111

4.43 (a) Stress-strain and stress-path response of undrained triaxial test comparing water sedimentation (WS), tapped funnel deposition (TFD), and fast funnel deposition (FFD) for medium density Nevada sand specimens, with 18% of FC; (b) Stress-strain and stress-path response of undrained triaxial test comparing mixed dry deposition (MDD) with tapped funnel deposition (TFD) for low density Nevada sand specimens, with 20% of FC. 112
4.44 Comparison of simple shear, triaxial compression and extension behaviour for Fraser Delta sand. 114
4.45 Loading and stress conditions in HTC specimens. 115
4.46 Strain and stress-paths for Fraser River sand: (a) at b = 0; (b) at b = 0.5. 116
4.47 (a) Dependence of friction angle mobilized at peak deviator stress on α_σ for Fraser River sand; (b) Dependence of brittleness index IB on α_σ for Fraser River and Syncrude sand (Uthayakumar and Vaid,1998). 116
4.48 Examples of principal stress direction variation along potential failure surfaces: (a) Limiting equilibrium stress states beneath an embankment; (b) Limiting equilibrium stress states beneath a gravity platform; (c) Lateral spreading failure of level to mildly sloping ground. 118
4.49 Stress paths from undrained triaxial compression tests of loose tailings with 0% fines: (a) on isotropically consolidated specimens; (b) on K_0-consolidated specimens; (c) Variation of modified state parameter with stress ratio at initiation of liquefaction for isotropically and anisotropically consolidated specimens of loose Merriespruit gold tailings, with 0% fines. 119
4.50 Comparison of steady state lines derived from isotropically and K_0-consolidated specimens of loose Merriespruit gold tailings, with 0% fines. 120
4.51 Conditions at the instant of the trigger of strain softening: (a) effective stress states, and (b) dependence of mobilized friction angle ϕ_{CSR} on α_σ; (c) Modified brittleness index with static shear. 121
4.52 Mean number of equivalent uniform cycles at 65% of the peak stress versus earthquake magnitude. 124
4.53 Magnitude scaling factor values proposed by various researchers). 124
4.54 Laboratory data and compiled K_σ curves. 125
4.55 (a) K_σ curves for a range of $(N_1)_{60}$ and q_{c1N} (b) Comparison of derived K_σ relations to those recommended by Hynes and Olsen (1998). 126
4.56 Analysis of the effective stress paths obtained for different loading signals for Hostun sand without and with stress reversal (a) and (b) respectively. 127
4.57 Results of cyclic triaxial tests, showing the influence of the sample preparation method on the CRR of Monterey No. 0 sand at DR = 50%. 128
4.58 Comparison of cyclic resistance curves for loose air-pluviated and water-pluviated sands at the same relative density (D_r) and vertical effective stress ($\sigma_v^{'}$) combinations. 129
4.59 Comparative undrained cyclic triaxial response of undisturbed and reconstituted specimens of Gioia Tauro sand. 130
4.60 Summary of recommended values for K_α proposed by Harder and Boulanger. . . 131
4.61 Effect of the relative state parameter index, ξ_r, on the static shear stress ratio correction factor K_α. 132
4.62 K_α versus α for Fraser River sand at different density states at: (a) $\sigma_h^{'}$ = 100 kPa; (b) $\sigma_h^{'}$ = 400 kPa. 133
4.63 (a) Dependence of K_α on loading mode in semi-angular Fraser River sand; (b) Dependence of K_α on loading mode in sub-rounded silica sand. 135

4.64 (a) Stress ratio versus number of cycles to 15% double amplitude strain for wet tamped and air-pluviated no. 0 sand at D_r =60%; (b) Stress ratio versus relative density for failure defined as 15% double amplitude shear strain in the tenth loading cycle for wet tamped and air-pluviated Monterey No.0 sand. 136
4.65 (a) K_σ under simple shear and triaxial stress conditions for Fraser Delta sand; (b) The ratio c_r of cyclic resistance of Fraser Delta sand under simple shear and triaxial stress conditions). 137
4.66 Comparison of stress conditions causing liquefaction in cyclic loading under simple shear, triaxial and field conditions. 137
4.67 Liquefaction resistance of Ottawa sand in constant volume and undrained simple shear. 138
4.68 Schematic of yield surface softening induced by principal stress rotation. 139

5.1 Distribution of liquefaction during the Bourmedès earthquake, May 21, 2003 . . 142
5.2 Liquefaction-induced sand boils (a) and lateral spreading (b) of the banks of Isser River; (c) sand boils in an orange grove in Zemmouri; (d) time sequence of QuickBird images, showing apartments in western Boumerdes (1) prior to and (2) soon afer the 5/21/03 earthquake. Scene 3 was acquired on 6/18/03, and shows progress made with clean-up operations 143
5.3 Liquefaction consequences in structural damages: (a), (b) Differential settlement between quays wall and backland in Port of Algiers and the Harbor of Zemmouri-El-Bahri (JAEE); and, (c), (d) Bridges in the basin of the Isser River 143
5.4 Sand uplifted flow to the Mediterranean Sea in Isser River, 22 May 2003 144
5.5 Grading curve of Algeria Sand 145
5.6 Grain shape of Algeria sand 146
5.7 Definition of the normal consolidated isotropic (NCLISO) and odometer (NCLEDO) lines and the critical state line (CSL) of Algeria sand 147
5.8 Simplified procedure for Algeria sand 147
5.9 *"Basic Berkeley School liquefaction assessment chart"* for Algeria sand 148
5.10 (a) Isoseismal (MSK) map of the earthquake of 1 November 1755. Disputed positions of the epicentre are located. (b) Intensity data points and tentative isoseismal curves for the 1909 Benavente event 150
5.11 Location of probable liquefaction features recognized in aerial photos (1:18,000 scale) of the Benavente region (crop of photo showing example). Gray area, Upper Pleistocene fluvial terrace; white area, alluvial plain of the Tagus and Sorraia rivers; 1, linear features interpreted as remnants of the surface trace of cracks injected with liquefied sands generated during the 1909 earthquake; 2, lineament corresponding to small scarp; 3, area with circular features interpreted as remnants of sand blows generated by the 1909 earthquake 151
5.12 Return period of liquefaction for Portugal continental 152
5.13 Grading curve of Coimbra Sand 153
5.14 Grain shape of Coimbra sand – Microstructural analysis 153
5.15 CSL for Coimbra sand 154
5.16 CSL for Coimbra sand 155
5.17 Relation between CSR and number of cycles for confining pressures of 50 and 200 kPa and relative density of 20% 156
5.18 Simplified procedure for Coimbra sand 157
5.19 *"Basic Berkeley School liquefaction assessment chart"* for Coimbra sand 157

5.20 (a) Grading curve of the artificial silica; (b) Grading curves of Coimbra mixed with 20% and 40% of artificiall fines . . . 158
5.21 Distribution of the number of incidents according to cause in the World and in Europe . . . 160
5.22 Tailing dams heightening . . . 161
5.23 Deposition methods of tailings - (a) Hydro-cyclone, (b) Spray bar, (c) Spigot . . . 162
5.24 Examples of a method for tailings deposition) . . . 162
5.25 (a) Gold tailings; (b) Gold tailings plant of the Industrial Complex Mina-Usina Fazenda Brasileiro, from Teofilândia, Bahia, Brazil . . . 163
5.26 Grading curve of gold tailings and of the silt . . . 164
5.27 Grain shape of gold tailings – Microstructural analysis . . . 165
5.28 Results of triaxial compression tests and critical state analysis of gold tailings . . . 166
5.29 Grain shape of silt – Microstructural analysis . . . 167
5.30 Results of triaxial compression tests and critical state analysis of silt . . . 168
5.31 Grading curve of gold tailings and of the silt (LabGeo) all of them determined at LabGeo at FEUP in the scope of the present research) . . . 169
5.32 RETSCH Planetary Ball Mills . . . 170
5.33 Comparison of the grading curves of the silt, Osorio sand and the mixture (all of them determined at LabGeo at FEUP in the scope of the present research) . . . 171

6.1 Wykeham Farrance® Oedometer device (LabGeo). . . . 175
6.2 Scheme of a conventional triaxial cell . . . 177
6.3 "Bishop-Wesley" triaxial cell at LabGeo: a) smaller cell; b) larger cell. . . . 178
6.4 Distinct stress-paths by using "Bishop-Wesley" triaxial cell. . . . 179
6.5 Scheme of "Bishop-Wesley" cell . . . 180
6.6 GDS® (GDS Instruments®); Bishop-Wesley cell being controlled by a GDS® device (LabGeo). . . . 181
6.7 Hydraulic oil press, designed for reproducing cyclic loads at LabGeo, with a conventional triaxial cell (LabGeo). . . . 182
6.8 a) Oil hydraulic press with a high-pressure triaxial cell; b) detail of a soil specimen while being placed inside the high-pressure triaxial cell (LabGeo). . . . 183
6.9 LDT . . . 184
6.10 Hall-Effects . . . 185
6.11 LVDT . . . 186
6.12 Scheme and picture of an automatic volume change gauge by VJ Tech® . . . 187
6.13 a) Membrane adjustment to the bipartite mold; b) e c) Moist tamping technique . 188
6.14 (a) Internal/local transducers (inductive hall-effect calipers); (b) Freeze technique (procedure to determine the void ratio during all test stages after the saturation) (comment: on this test the water on the pores migrate to the top of the specimen during the freezing). . . . 190
6.15 Effect of cyclic loading frequency on cyclic shear strength of Toyoura sand . . . 191
6.16 DSS device at UWA . . . 192
6.17 a)Teflon coated stacked rings; b)and c) detail of the Teflon coated stacked rings during and after the cyclic shear of a soil sample (Geotechnical laboratory at UWA) 193
6.18 DSS apparatus: a)and b) horizontal load cell; c) display screen of the horizontal load; d) vertical load cell; e) display screen of the vertical load (Geotechnical laboratory at UWA) . . . 193
6.19 Bender-Extender Elements installed on a "Bishop-Wesley" cell (LabGeo) . . . 195
6.20 Schemes of the piezoeletric motion: a) bender elements; b) extender elements . . 195

6.21 Associated electronic equipments required for seism waves measurement 196
6.22 Identification of the compression index C_c and the swelling index C_s on a compression curve 198

7.1 Stress-strain and volumetric-strain behavior of drained triaxial tests of Algeria sand 219
7.2 Stress-strain and strain-volumetric behavior of the high-pressure triaxial test Tx_CID_12 220
7.3 Evolution of the grain size distribution of the Tx_ CID_ 12 high-pressure triaxial test ($p_i^{'} = 7.5$ MPa) 221
7.4 Stress-strain and strain-pore water pressure behavior of undrained triaxial tests of Algeria sand at low to medium confining pressures 222
7.5 Stress-strain and strain-pore water pressure behavior of undrained triaxial tests of Algeria sand at low confining pressures 223
7.6 Construction of the critical state and steady state lines for Algeria sand 224
7.7 Critical state and steady states lines of Algeria sand 225
7.8 Stress-strain and stress-path behavior of Tx_ CIU_ 2, Tx_ CIU_ 6, Tx_ CIU_ 7 and Tx_ CIU_ 12 tests 225
7.9 Stress-strain and stress-path behavior of Tx_ CIU_ 12 and Tx_ CIU_ 13 tests . . 226
7.10 Stress-strain and strain-volumetric behavior of some low-pressure triaxial tests Tx_ CID_ 6, Tx_ CID_ 8 and Tx_ CID_ 9 227
7.11 Variations of the Brittleness Index with the steady state parameter, ψ_{SSL}, and the ratio $p^{'}/p_{SSL}^{'}$ from left to right, respectively, for Algeria sand 229
7.12 Steady state parameter expressed as a function of normalized peak shear strength (q_1) and shear stiffness for Algeria sand 230
7.13 a) Detail of the stress-path of the triaxial tests; b) Instability Line (IL) for Algeria sand 231
7.14 a) Peak shear strength as function of the soil stiffness; b) Correlation between the normalized peak shear strength and the ratio between shear stiffness and the peak shear strength for Algeria sand 232
7.15 Stress-strain and volumetric-strain behavior of drained triaxial tests of Coimbra sand 236
7.16 Evolution of the grain size distribution for the Tx_ CID_ MT_ 8 high-pressure triaxial test (p'$_i$ = 9.5 MPa) 236
7.17 Stress-strain and strain-pore water pressure behavior of undrained triaxial tests of Coimbra sand 237
7.18 Stress-strain and strain-pore water pressure behavior of undrained triaxial tests of Coimbra sand at low to medium confining pressures 238
7.19 Construction of the critical state and steady state lines for Coimbra sand 239
7.20 Critical state and steady state lines of Coimbra sand 240
7.21 Stress-strain and strain-pore water pressure behavior of Tx_ CIU_ MT_ 4, Tx_ CIU_ MT_ 11, Tx_ CIU_ PL_ 1, Tx_ CIU_ PL_ 3 tests 241
7.22 Variations of the Brittleness Index with the steady state parameter, ϕ_{SSL}, and the ratio $p^{'}/p_{SSL}^{'}$ or ratio $p^{'}/p_{CSL_{Graincrushing}}^{'}$, from left to right, respectively for Coimbra sand 242
7.23 Steady state parameter expressed as a function of normalized peak shear strength (q_1) and shear stiffness for Coimbra sand 243
7.24 a) Peak shear strength as function of the soil stiffness; b) Correlation between the normalized peak shear strength and the ratio between shear stiffness and the peak shear strength for Coimbra sand 244
7.25 a) Detail of the stress-path of the triaxial tests; b) Instability Line (IL) for Coimbra sand 245

7.26 Construction of the critical state line for Coimbra 20 249
7.27 Critical state and steady state lines of Coimbra 20 250
7.28 Evolution of the grain size distribution of the Tx_CID_2 high-pressure triaxial test (p'_i = 9.4 MPa) 250
7.29 Construction of the critical state line for Coimbra 40 252
7.30 Critical state and steady state lines of Coimbra 40 253
7.31 Evolution of the grain size distribution of the Tx_CID_2 high-pressure triaxial test (p'_i = 9.2 MPa) 253
7.32 Stress-strain and volumetric-strain behavior of drained triaxial tests of Osorio sand at low to medium confining pressures 255
7.33 Stress-strain and strain-volumetric behavior of the high-pressure triaxial test Tx_CID_7256
7.34 Evolution of the grain size distribution of the Tx_CID_7 high-pressure triaxial test (p'_i = 9.3 MPa) 256
7.35 Stress-strain and strain-pore water pressure behavior of undrained triaxial tests of Osorio sand at low to high confining pressures 257
7.36 Construction of the critical state line for Osorio sand 258
7.37 Critical state and steady state lines of Osorio sand 258
7.38 Stress-strain and stress-path of the set of triaxial tests with decreasing p'; study under applied CSSM 260
7.39 Variations of the Brittleness Index with the steady state parameter, ψ_{SSL}, and the ratio p'/p'_{SSL}, from left to right, respectively, for Osorio sand 261
7.40 Steady state parameter expressed as a function of normalized peak shear strength (q_1) and shear stiffness for Osorio sand 262
7.41 a) Peak shear strength as function of the soil stiffness; b) Correlation between the normalized peak shear strength and the ratio between shear stiffness and the peak shear strength for Osorio sand 263
7.42 a) Detail of the stress-path of the triaxial tests; b) Instability Line (IL) for Osorio sand 264
7.43 Stress-strain and volumetric-strain behavior of drained triaxial tests of Mixture . 268
7.44 Stress-strain and strain-volumetric behavior of the high-pressure triaxial test Tx_CID_15269
7.45 Evolution of the grain size distribution of the Tx_CID_15 high-pressure triaxial test (p'_i = 9.4 MPa) 269
7.46 Stress-strain and strain-pore water pressure behavior of undrained triaxial tests of Mixture at low to high confining pressures 270
7.47 Construction of the critical state and steady state line for the Mixture 271
7.48 Critical state line and steady state line of the Mixture 271
7.49 Stress-strain and stress-path of the set of triaxial tests with decreasing p' and constant q; study under applied CSSM 273
7.50 Stress-strain and stress-path of the set of triaxial tests with constant and decreasing mean confining stress and increasing deviator stress; study under applied CSSM . 275
7.51 Variations of the Brittleness Index with the state parameter, ψ, and the ratio p'/p'_{CS}, from left to right, respectively, for the Mixture 276
7.52 Steady state parameter expressed as a function of normalized peak shear strength (q_1) and shear stiffness for Mixture 277
7.53 a) Peak shear strength as function of the soil stiffness; b) Correlation between the normalized peak shear strength and the ratio between shear stiffness and the peak shear strength for the Mixture 278
7.54 a) Detail of the stress-path of the triaxial tests; b) Instability Line (IL) for the Mixture279

7.55 Stress-strain and volumetric-strain behavior of drained triaxial tests of Silt 283
7.56 Stress-strain and strain-volumetric behavior of the high-pressure triaxial test Tx_CID_7285
7.57 Evolution of the grain size distribution of the Tx_CID_12 high-pressure triaxial test (p'_i = 7.4 MPa) 285
7.58 Stress-strain and strain-pore water pressure behavior of undrained triaxial tests of Silt at low to high confining pressures 286
7.59 Stress-strain and strain-pore water pressure curves comparison with distinct saturation degrees 287
7.60 Construction of the critical state and steady state line for Silt 288
7.61 Critical state line and steady state line of Silt 289
7.62 Extension triaxial tests under applied CSSM 291
7.63 Stress-strain and stress-path of the set of triaxial tests with decreasing p' and constant q; study under applied CSSM 292
7.64 $T_{x_{q=constant}}_CK_0D$ tests ultimate state positioning on e: ln p' space 293
7.65 a) Stress-paths of $T_{x_{q=constant}}_CK_0D$ tests; b) Detail of the stress-paths of $T_{x_{q=constant}}_CK_0D$ tests under lower pressures 294
7.66 Variations of the Brittleness Index with the steady state parameter, ψ_{SSL}, and the ratio p'/p'_{SSL}, from left to right, respectively, for the Silt 295
7.67 Steady state parameter expressed as a function of normalized peak shear strength (q_1) and shear stiffness for Silt 296
7.68 a) Peak shear strength as function of the soil stiffness; b) Correlation between the normalized peak shear strength and the ratio between shear stiffness and the peak shear strength for the Silt 297
7.69 a) Detail of the stress-path of the triaxial tests; b) Instability Line (IL) for Silt . . 298
7.70 Variations of the Brittleness Index with the state parameter, ψ, and the ratio p'/p'_{CS}, from left to right, respectively, for the for $T_{x_{q=constant}}_CK_0D$ tests of Silt 299
7.71 Steady state parameter expressed as a function of normalized peak shear strength (q_1) and shear stiffness for the $T_{x_{q=constant}}_CK_0D$ tests of Silt 300
7.72 Stress-strain and volumetric-strain behavior of drained triaxial tests of Gold tailings 304
7.73 Stress-strain and strain-volumetric behavior of the high-pressure triaxial test Tx_CID_5 and Tx_CID_7 304
7.74 Evolution of the grain size distribution of the high-pressure triaxial tests Tx_CID_5 and Tx_CID_7 (4.7 and 9.5 MPa) 305
7.75 Stress-strain and strain-pore water pressure behavior of undrained triaxial tests of Gold tailings at low to high confining pressures 306
7.76 Stress-strain and strain-pore water pressure behavior of undrained triaxial tests of Gold tailings at low confining pressures 306
7.77 Construction of the critical state and steady state line for Gold tailings 307
7.78 Critical state line and steady state line of Gold tailings 308
7.79 Stress-strain and stress-path of the set of triaxial tests with decreasing or constant p'; study under applied CSSM 309
7.80 Stress-strain and stress-path of $T_{x_{p'=constant}}_CID_2$, $T_{x_{p'=constant}}_CID_3$ and $T_{x_{p'=constant}}_CID_4$ triaxial tests 310
7.81 Variations of the Brittleness Index with the steady state parameter, ψ_{SSL}, and the stress ratio p'/p'_{SSL}, from left to right, respectively, for Gold tailings 311
7.82 Steady state parameter expressed as a function of normalized peak shear strength (q_1) and shear stiffness for Gold tailings 312

7.83 a) Peak shear strength as function of the soil stiffness; b) Correlation between the normalized peak shear strength and the ratio between shear stiffness and the peak shear strength for Gold tailings . . . 313
7.84 a) Detail of the stress-path of the triaxial tests; b) Instability Line (IL) for Gold tailings . . . 314
7.85 CSL varying positioning with varying fines content for Osorio sand . . . 317
7.86 a) CSL as function of the Fines content for Osorio sand; b) CSL of Osorio sand, Mixture and Silt . . . 318
7.87 SSL varying positioning with varying fines content for Osorio sand . . . 319
7.88 SSL varying positioning with varying fines content and varying ξ for Osorio sand 320
7.89 Effect of Cu on CSL and SSL positioning parameters . . . 320
7.90 CSL varying positioning with varying fines content for Coimbra sand . . . 321
7.91 CSL varying positioning for distinct sands . . . 322
7.92 Correlations between CSL parameter, Γ, and e_{max} and e_{min}; data set compiled and completed with present data . . . 323
7.93 Correlations between CSL parameters, Γ and λ, and Cu . . . 324
7.94 Correlations between CSL parameter, Γ and λ, and A . . . 324
7.95 Effect of particle shape on friction angle; data set compiled and completed with present data . . . 325
7.96 Peak shear strength as function of the soil stiffness . . . 326
7.97 Correlation between the normalized peak shear strength and the ratio between shear stiffness and the peak shear strength . . . 327
7.98 Simplified Procedure to evaluate static liquefaction . . . 328
7.99 Correlation between the coefficient of uniformity and the ratio V_{s0}/q_{peak} which define the limiting boundary between a strain softening and strain hardening behavior 328

8.1 Flow liquefaction due to (a) contractive deformation in compression with no rotation of principal stresses and (b) with shear stress reversal; Cyclic mobility for (c) cyclic loading with no shear stress reversal, and d) with shear stress reversal . . . 331
8.2 Cyclic resistance curves for Algeria sand under triaxial stress conditions for anisotropic specimens (with initial static shear stress, $\alpha = 0.33$) . . . 332
8.3 Cyclic resistance curves for Algeria sand under triaxial stress conditions for isotropic specimens (without initial static shear stress, $\alpha = 0$) . . . 333
8.4 Liquefaction resistance of Algeria sand under triaxial stress conditions: effect of initial relative density for 3 cycles . . . 334
8.5 Liquefaction resistance of Algeria sand under triaxial stress conditions, effect of initial confining stress for relative densities of: a) 30%; b) 44% . . . 335
8.6 Cyclic resistance curves for Algeria sand under triaxial stress conditions for isotropic and anisotropic specimens (without initial static shear stress, $\alpha = 0$, and with initial static shear stress, $\alpha = 0.33$, respectively) . . . 336
8.7 Cyclic stress ratio CSR, or Cyclic resistance ratio, CRR, versus relative density under triaxial stress conditions for Algeria Sand (Mw = 7.5) . . . 337
8.8 K_α versus α for Fraser River Sand at different density states at σ'_{nc} = 100 kPa complemented with results for Algerian Sand . . . 338
8.9 Anisotropic cyclic triaxial tests in the semi-logarithmic space e: log p' under applied CSSM . . . 339
8.10 Isotropic cyclic triaxial tests in the semi-logarithmic space e: log p' under applied CSSM . . . 340

8.11 Basic Berkeley Assessment chart with reference to the CSL (Mw = 7.5); Liquefaction resistance of Algeria sand under triaxial stress conditions 341
8.12 Basic Berkeley Assessment chart with reference to the SSL (Mw = 7.5); Liquefaction resistance of Algeria sand under triaxial stress conditions 342
8.13 "Simplified Procedure" of Algeria sand under triaxial stress conditions 343
8.14 Shear work (W) as function of shear wave velocity for Algeria sand 344
8.15 Comparison between the measured G_0, for Algeria sand, and the predicted G_0 . . 345
8.16 Dependence of cyclic resistance on relative density for 100 and 300 kPa of confining stress for Algeria sand under direct simple shear stress conditions 347
8.17 Cyclic stress ratio CSR, or Cyclic resistance ratio, CRR, versus relative density for Algeria Sand under direct simple shear stress conditions (Mw = 7.5) 347
8.18 Cyclic resistance curves for Algeria sand under direct simple shear stress conditions (without initial static shear stress, $\alpha = 0$) 348
8.19 Stress-strain, stress-path, and excess pore pressure with and without normalization, from left to right respectively, for 13° test_100k Pa and 10° test_300 kPa for Algeria sand 349
8.20 K_σ values for Fraser Delta sand and Algeria under direct simple shear and triaxial stress conditions 351
8.21 Basic Berkeley Assessment chart with reference to the CSL (Mw = 7.5); Liquefaction resistance of Algeria sand under direct simple shear stress conditions . . . 352
8.22 Cyclic stress ratio CSR, or Cyclic resistance ratio, CRR, versus relative density for Algeria Sand under both triaxial and direct simple shear stress conditions (Mw = 7.5) 353
8.23 Basic Berkeley Assessment chart with reference to the SSL (Mw=7.5); Liquefaction resistance of Algeria sand under both triaxial and direct simple shear stress conditions 354
8.24 Variations of the Brittleness Index with the steady state parameter, ψ_{SSL}, of Algeria sand tested on Triaxial and DSS devices 355
8.25 Flow liquefaction due to (a) contractive deformation in compression with no rotation of principal stresses; Cyclic mobility for (c) cyclic loading with no shear stress reversal 356
8.26 Cyclic resistance curves for Coimbra sand under triaxial stress conditions for anisotropic specimens (with initial static shear stress, $\alpha = 0.33$) 357
8.27 Cyclic stress ratio CSR, or Cyclic resistance ratio, CRR, versus relative density under triaxial stress conditions for Coimbra sand (Mw = 7.5) 357
8.28 Anisotropic cyclic triaxial tests in the semi-logarithmic space e: log p' under applied CSSM 359
8.29 Basic Berkeley Assessment chart with reference to the CSL (Mw = 7.5); Liquefaction resistance of Coimbra sand under triaxial stress conditions 360
8.30 Basic Berkeley Assessment chart with reference to the SSL (Mw = 7.5); Liquefaction resistance of Coimbra sand under triaxial stress conditions 361
8.31 "Simplified Procedure" of Coimbra sand under triaxial stress conditions 362
8.32 Shear work (W) as function of shear wave velocity for Algeria sand 362
8.33 Comparison between the measured G_0, for Coimbra sand, and the predicted G_0 by using the empirical equations 364
8.34 Dependence of cyclic resistance on relative density for 100, 300 and 500 kPa of confining stress for Coimbra sand 365

8.35 Cyclic stress ratio CSR, or Cyclic resistance ratio, CRR, versus relative density for Coimbra Sand under direct simple shear stress conditions (Mw = 7.5) 366
8.36 Cyclic resistance curves for Coimbra sand in DSS conditions (without initial static shear stress, $\alpha = 0$) 367
8.37 Stress-strain, stress-path, and excess pore pressure with and without normalization, from left to right respectively, for 12 test_100 kPa and 7° test_300 kPa for Coimbra sand 368
8.38 K_σ values for Fraser Delta sand and Coimbra sand under direct simple shear and triaxial stress conditions 369
8.39 Basic Berkeley Assessment chart with reference to the CSL (Mw = 7.5); Liquefaction resistance of Coimbra sand under direct simple shear stress conditions . . 370
8.40 Cyclic stress ratio CSR, or Cyclic resistance ratio, CRR, versus relative density for Algeria Sand under both Tx and direct simple shear stress conditions (Mw = 7.5) 371
8.41 Basic Berkeley Assessment chart with reference to the SSL (Mw = 7.5); Liquefaction resistance of Algeria sand under both triaxial and direct simple shear stress conditions 372
8.42 Variations of the Brittleness Index with the steady state parameter, ψ_{SSL}, of Coimbra sand tested on Triaxial and DSS devices 373

9.1 Schematic of yield surface and main ingredients plotted in effective stress space. The shaded area represents the elastic region whose inclination is dictated by α. Other important ingredients are the bounding stress ratio M_b, dilatancy stress ratio M_d and critical state ratio M 379
9.2 Comparison between the drained triaxial tests achieved with SANISAND and the real tests for Osorio sand 388
9.3 Comparison between the undrained triaxial tests achieved with SANISAND and the real tests for Osorio sand 388
9.4 Detail of the comparison between the drained triaxial tests achieved with SANISAND and the real tests for Osorio sand 389
9.5 Detail of the comparison between the undrained triaxial tests achieved with SANISAND and the real tests for Osorio sand 390
9.6 Sensitivity analysis of the void ratio for Osorio sand 391
9.7 Detail of the comparison between the $T_{x_{q=constant}}_CK_0D$ tests achieved with SANISAND and the real tests for Osorio sand 391
9.8 Comparison between the drained triaxial tests achieved with SANISAND and the real tests for Mixture 393
9.9 Comparison between the undrained triaxial tests achieved with SANISAND and the real tests for Mixture 394
9.10 Detail of the comparison between the drained triaxial tests achieved with SANISAND and the real tests for Mixture 394
9.11 Detail of the comparison between the undrained triaxial tests achieved with SANISAND and the real tests for Mixture 395
9.12 Comparison between the undrained triaxial tests achieved with SANISAND calibrated with the drained triaxial tests from those achieved with SANISAND calibrated and with the real tests for Mixture 395
9.13 Detail of the comparison between the $T_{x_{q=constant}}_CK_0D$ tests achieved with SANISAND and the real tests for Mixture 396

A.1 Volumetric strain as function of the initial modelling void ratio for Algeria sand; Linear regression model used on triaxial tests marked with * on table A.1, A.9 and A.10 443
A.2 Volumetric strain as function of the initial modelling void ratio for Coimbra sand; Linear regression model used on triaxial tests marked with * on table A.2 and A.11 443
A.3 Volumetric strain as function of the initial modelling void ratio for Osorio sand; Linear regression model used on triaxial tests marked with * on table A.3 444
A.4 Volumetric strain as function of the initial modelling void ratio for Mixture; Linear regression model used on triaxial tests marked with * on table A.4 444
A.5 Normal consolidation lines of Mixture determined with internal instrumentation (NCL old) and by using the freezing technique (NCL new); Corrections used on triaxial tests marked with ** on table A.4 445
A.6 Volumetric strain as function of the initial modelling void ratio for Silt; Linear regression model used on triaxial tests marked with * on table A.5 and A.6 445
A.7 Normal consolidation lines of Silt determined with internal instrumentation (NCL old) and by using the freezing technique (NCL new); Corrections used on triaxial tests marked with ** on table A.5 and A.6 446
A.8 Normal consolidation lines of Gold tailings determined with internal instrumentation (NCL old) and by using the freezing technique (NCL new); Corrections used on triaxial tests marked with ** on table A.7 446

B.1 Relation between P-wave velocity and B for Silt and Gold tailings. 449

List of Tables

1.1 Resume of the soils studied in the scope of the present work; Loading conditions and major factors assessed 4

2.1 Some cases of tailing dams failure due to liquefaction and some few other cases (source: Bulletin 121: *"Tailings dams risk of dangerous occurrences. Lessons learnt from practical experiences"*, 2001 12
2.2 Cont.: Some cases of tailing dams failure due to liquefaction and some few other cases (source: Bulletin 121: *"Tailings dams risk of dangerous occurrences. Lessons learnt from practical experiences"*, 2001 13

3.1 Changes in soil behaviour with strain and respective adapting interpretation model. 41
3.2 Reference void ratio functions. 49

4.1 Undrained strength behaviour and respective definition for sands and silty-sands. 83
4.2 Equivalent number of cycles. 123

5.1 Lisbon: return periods for different earthquakes 150

6.1 List of the oedometer tests performed 204
6.2 List of the monotonic triaxial tests performed with Algeria sand, complemented with previous researches 204
6.3 List of the monotonic triaxial tests performed with Coimbra sand, complemented with previous researches 205
6.4 List of the monotonic triaxial tests performed with Coimbra sand with 20% of FC 205
6.5 List of the monotonic triaxial tests performed with Coimbra sand with 40% of FC 206
6.6 List of the triaxial tests performed with Osorio sand, complemented with previous researches 206
6.7 – List of the triaxial tests performed with Mixture, complemented with previous researches 207
6.8 List of the monotonic triaxial tests performed with Silt, complemented with previous researches – part 1 208
6.9 List of the triaxial tests performed with Silt – part 2 209
6.10 List of the triaxial tests performed with Gold tailings, complemented with previous researches 210
6.11 List of the cyclic triaxial tests performed with Algeria sand, complemented with previous researches – part 1 211
6.12 List of the cyclic triaxial tests performed with Algeria sand, complemented with previous researches – part 2 212

6.13 List of the cyclic triaxial tests performed with Coimbra sand, complemented with previous researches . . . 213
6.14 List of the direct simples shear tests performed with Algeria sand . . . 214
6.15 List of the direct simples shear tests performed with Coimbra sand . . . 215

7.1 Basic physical characterization of Algeria sand . . . 218
7.2 Resume of the ultimate states for Algeria sand according to the type of test . . . 233
7.3 Limiting values between liquefaction and stable behavior for Algeria sand . . . 234
7.4 Basic physical characterization of Coimbra sand . . . 234
7.5 Resume of the ultimate states for Coimbra sand according to the type of test . . . 246
7.6 Limiting values between liquefaction and stable behavior for Coimbra sand . . . 247
7.7 Basic physical characterization of Coimbra sand with 20% FC . . . 248
7.8 Basic physical characterization of Coimbra sand with 40% FC . . . 251
7.9 Basic physical characterization of Osorio sand . . . 254
7.10 Resume of the ultimate states for Osorio sand according to the type of test . . . 265
7.11 Limiting values between liquefaction and stable behavior for Osorio sand . . . 266
7.12 Basic physical characterization of Mixture . . . 267
7.13 Resume of the ultimate states for the Mixture according to the type of test . . . 280
7.14 Limiting values between liquefaction and stable behavior for the Mixture . . . 281
7.15 Basic physical characterization of Silt . . . 282
7.16 Resume of the ultimate states for the Silt according to the type of test . . . 301
7.17 Limiting values between liquefaction and stable behavior for the Silt . . . 302
7.18 Basic physical characterization of Gold tailings . . . 303
7.19 Resume of the ultimate states for Gold tailings according to the type of test . . . 315
7.20 Limiting values between liquefaction and stable behavior for Gold tailings . . . 316

9.1 Constitutive model parameters and initial state values . . . 385
9.2 SANISAND parameters for Osorio sand . . . 387
9.3 SANISAND parameters for Mixture . . . 392

A.1 List of the triaxial tests performed with Algeria sand completed with initial state values, strength and stiffness parameters . . . 431
A.2 List of the triaxial tests performed with Coimbra sand completed with initial state values, strength and stiffness parameters . . . 432
A.3 List of the triaxial tests performed with Osorio sand completed with initial state values, strength and stiffness parameters . . . 433
A.4 List of the triaxial tests performed with Mixture completed with initial state values, strength and stiffness parameters . . . 434
A.5 List of the triaxial tests performed with Silt – part 1 completed with initial state values, strength and stiffness parameters . . . 435
A.6 List of the triaxial tests performed with Silt – part 2 completed with initial state values, strength and stiffness parameters . . . 436
A.7 List of the triaxial tests performed with Gold tailings completed with initial state values, strength and stiffness parameters . . . 437
A.8 List of the cyclic triaxial tests performed with Algeria sand – part 1 completed with initial state values, strength and stiffness parameters . . . 438
A.9 List of the cyclic triaxial tests performed with Algeria sand – part 2 completed with initial state values, strength and stiffness parameters . . . 439

A.10 List of the cyclic triaxial tests performed with Coimbra sand completed with initial state values, strength and stiffness parameters 440
A.11 List of the direct simple shear tests performed with Algeria sand 441
A.12 List of the direct simple shear tests performed with Coimbra sand 442

B.1 Saturation degree of undrained triaxial tests performed with Silt and Gold tailings 448

Abbreviations and Symbols

Abbreviations

ADVDPC	Advanced Pressure/Volume Controller
AP	Air Pluviation
ASTM	American Society for Testing and Materials
BP	Back-Pressure or pore water pressure
BPT	Becker Penetration test
BS	British Standards
CEN	Comité Europeu de Normalização
CIU	Compression Isotropic Undrained
CK_0U	Compression Anisotropic Undrained
CP	Confining Pressure
CPT	Cone penetration test
CPTU	Undrained Cone Penetration test
CSL	Critical State Line
CRR	Cyclic Resistance Ratio
CSR	Cyclic Stress Ratio
CSSM	Critical State Soil Mechanics
Cu	Uniformity coefficient
CVR	Critical Void Ratio
DEM	Discrete Element Analysis
DMT	Flat Dilatometer
DSS	Direct Simple Shear
FC or f_c	Fines Content
FCTUC	Faculdade de Ciências e Tecnologia da Universidade de Coimbra
FEA	Finite Element Analysis
FEUP	Faculdade de Engenharia da Universidade do Porto or Faculty of Engineering of Porto University
FFD	fast funnel deposition
GAG	gap graded soil size distribution
HCT	Hollow Cylinder Tests
ICL	Imperial College of London
IL	Instability line
INEGI	Instituto de Engenharia Mecânica e Gestão Industrial
ISO	International Organization for Standardization
IST	Instituto Superior Técnico de Lisboa
LabGeo	Laboratory of Geotechincs at FEUP
LL	Liquid limit

LVDT	Linear Variable Differential Transformers
MDD	mixed dry deposition
Msc	Master's degree
MSF	Magnitude Scaling Factor
MSK	Medvedev-Sponheuer-Karnik scale
MT	Moist tamping
NAG	Narrowly Graded soil size distribution
NCEER	National Center for Earthquake Engineering Research
NCL	Normal Consolidation Line
NGI	Norwegian Geotechnical Institute
NRC	National Research Council
NSF	National Science Foundation
OCR	OverConsolidation Ratio
PhD	Doctor of Philosophy
PI	pasticity index
PT	Phase-transformation
QSS	Quasi-Steady State
R	Roundness
RAM	
SANISAND	Simple Anisotropic Sand plasticicity model
SAWS	Spectral Analysis of Surface Waves
SD	Slurry deposition
SPT	Standard Penetration test
SS	Simple Shear
SSL	Steady State Line
TFC	Transitional Fines Content
TFD	Tapped Funnel Deposition
Tx	Triaxial
U.S.	United States
UBC	University of British Colombia
UFRGS	Universidade Federal do Rio Grande do Sul
USTHB	University of Science and Technology of Houari Boumediene
WG	Well-Graded soil
WP	Water Pluviation
WS	Water Sedimentation

Symbols

$(V_{S1})_{csa1}$	equivalent clean young sand normalized shear wave velocity
$(N1)_{60} = N_1(60)$	standard penetration ratio /effective stress normalized values for an energy ratio of 60%
t_{100}	time at the end of the consolidation
$(q_{c1N})_{cs}$	equivalent clean sand CPT normalized cone penetration resistance
$(N_1)_{60cs}$	equivalent clean sand SPT normalized penetration resistance
$\varnothing$ or D_i	Specimen diameter
A – generalized area of the specimen	
A and n	parameters function of the soil shear strain; used to determine G_{max}
A_0	initial area of the specimen

A_d	function of the state variables used to calculate the dilatancy rate on SANISAND
A_i or A_c	area of the specimen
a_{max}	maximum acceleration of an earthquake
B	Bulk modulus
b	Effect of magnitude of intermediate principal stress parameter; parameter used to analyse HTC results
B	Skempton parameter
c	CSL extension/compression
C_c	compression Index
C_C	shape coefficient
C_N	correction factor for the effective overburden pressure in the sand
C_Q	factor of normalization of static cone penetration resistance, q_{c1N}
c_r	correction factor between simple shear and triaxial results
C_s	swelling Index
c_z	control of the pace evolution of z
D_i	effective diameters where i is the percentaige of particles which passed the sieve with D diameter
D_r	relative density
e	void ratio
E	Young's modulus
e_0	initial void ratio; during the initial Chapters defined as void ratio after consolidation; during the results analysis used as void ratio after modeling the specimen
$e_{c,eq}$	active intergrain contacts
e_{c0}	limiting value of e at p = 0 of the SSL
e_{CS}	void ratio at the critical state
e_f	interfine void ratio
$e_{f,eq}$	interfine void ratio
E_h	Young's modulus on the horizontal direction
e_{max}	maximum void ratio
e_{min}	minimum void ratio
ER_r	energy ratio of the specific test equipment
e_{sk}	intergranular void ratio
e_{SS}	void ratio at the steady state
E_v	Young's modulus on the vertical direction
f	exponent function of the in situ conditions; used to determine K_σ
$f(\gamma_{av})$	function of the average cyclic strain γ_{av}
F	total load
$F(e)$	void ratio function
F_h	horizontal load applied on a specimen
f_s	sleeve resistance
F_v	vertical load applied on a specimen
g	acceleration of gravity
G_0	shear modulus

G_{crit}	shear modulus at the critical state
G_s	specific gravity of the soil
h	depth
h	function of the state variable used to calculate the hardening modulus
H	plastic hardening modulus
h_0 and c_h	hardening modulus parameters
H_c	height of the specimen at the end of the consolidation
I_B	brittleness index
I_c	material index for CPT test
I_c	soil behaviour type index used on the calculation of $(qc1N)_{cs}$
I_D	compact index
I_d	material index for DMT test
k	empirical exponent of the overconsolidation ratio OCR
K_0	at rest earth coefficient pressure
K_{a1}	correction factor which accounts with the age of the soil; used to calculate $(V_{S1})_{csa1}$
K_b	stiffness modulus
KC K_c	deviator stress ratio
K_{cs}	correction factor which accounts for the fines content; used to calculate $(V_{S1})_{csa1}$
K_D	horizontal stress index
K_M	magnitude correction factor
K_α	correction factor which takes into account the pre-existing shear stress on a horizontal plane
$K_{\alpha\sigma}$	factor which corrects both pre-existing shear stress on a horizontal plane and the overburden stress level
K_σ	correction factor which takes into account the initial overburden stress
L	distance between benders
m	half vertex angle of the yield surface
M or M_0	elastic constrained modulus
M_b	bounding surface
M_c or M_{tc}	CSL slope in p':q space
M_d	dilatancy surface
M_f	mass of fines of the specimen; used to determined e_{sk}
M_t	total mass of the specimen; used to determined e_{sk}
m_v	volumetric compressibility
M_w or M	Ricther magnitude scale
n	exponent which varies with the type of the soil used to normalize the static cone penetration resistance, q_{c1N}
N	SPT blowcount
N_1	normalized penetration strength
n^b	factor for the stress projection on the boundary surface
n^d	factor for the stress projection on the dilatancy surface
n_i and n_j	empirical stress exponents
$p^{'}$	mean effective stress
$p_0^{'}$	initial effective mean stress
$P_{CS}^{'}$	mean effective stress at the critical state

P'_{SS}	mean effective stress at the steady state
p_0	soil pressure against the membrane when it is flush with the blade; value used to calculate K_D
p_1	soil pressure against the membrane when its centre is expanded 1.10 mm; value used to calculate K_D
P_a	atmospheric pressure
P_A	pressure that must be applied to the back of the membrane to expand its centre 0,05 mm in soil; value used to calculate K_D
P_B	pressure that must be applied to the back of the membrane to expand its centre 1,10 mm in soil; value used to calculate K_D
q	deviator stress
Q	dimensionless CPT tip resistance
q_1	normalized shear strength
q_c	cone penetration resistance
q_{c1N}	normalized values of static cone penetration tests
r_d	stress reduction coefficient (m)
R_d	ratio between D50 and d50
S	degree of saturation
S	soil factor
S	sphericity
S_{ij}	non-dimensional material constant reflecting the fabric and structure of the soil
t	initial thickness of membrane; to not be confused with the wave travel time
t	time of stress waves travel
u_0	in situ pore water pressure prior to blade insertion; value used to calculate K_D
V_i or V_c	generalized volume of the specimen
v_{max}	maximum shear rate to be applied in a compression triaxial test
V_p	primary or compression wave's velocities
V_s	shear wave velocity
V_{s1}	normalized shear/distortional seismic waves
V^*_{S1}	maximum limit for V_{S1} for liquefaction occurrence
V_{Sfield}	Shear wave velocity measured in field
V_T	total volume of the specimen; used to determined e_{sk}
W	accumulated dissipated energy
w	water content
W_d	dry weight of the specimen
z	soils depth
z_{ij}	fabric dilatancy internal variable
Z_m	gauge pressure deviation from zero when venting the blade to atmospheric pressure; values used to calculate K_D
z_{max}	maximum attainable value of z
λ_s	SSL slope
$(\varepsilon_1)_m$	vertical strain of membrane (expressed as a ratio)
$(\varepsilon_{vol})_m$	volumetric strain of membrane
$(\Delta\sigma_1)_m$	correction to the total vertical stress
$(\Delta\sigma_3)_m$	correction to the total horizontal stress

α	back-stress ratio
α	ratio of the design ground acceleration on type A ground
α	ratio of the initial static shear by the normal effective stress action on the plane of maximum shear stress
α_σ	inclination of the major principal stress direction to the vertical
γ_s	shear strain
γ	unit weight of the soil
τ	intersection point of the CSL on the y axis
$\Delta\sigma_v^{'}$	variation of the vertical effective stress
Δe	void ratio variation
ΔQ	energy which has flowed into the structure from its surrounding
ΔU	total energy of a system
ΔW	incremental work
ΔH	axial displacement
Δu	excess of pore pressure
$\Delta\sigma_3$	increment of confining pressure
ΔP_A and ΔP_B	membrane calibration pressure; values used to calculate K_D
ε_a	axial strain
ε_e	elastic strain
ε_p	plastic strain
ε_q	shear strain
ε_s^e	elastic shear strain
ε_s^p	plastic shear strain
ε_v	volumetric strain
ε_v^e	elastic volumetric strain
ε_v^p	plastic volumetric strain
η_{IL}	stress ratio correspondent to the IL
η	stress ratio
κ	elastic compressibility
λ	correction factor for energy losses due to the rod length in the sand – used in equation (3.7); do not confuse with the CSL slope
λ	CSL slope
ν	Poisson's ratio
ξ_r	relative state parameter
ρ	mass density
ρ	regularity
ρ_w	water density
$\sigma_1^{'}$	maximum principal stress
$\sigma_3^{'}$	minimum principal stress
$\sigma_{3c}^{'}$	minimum principal stress direction on triaxial shear stress conditions
$\sigma_c^{'}$	initial confining stress
$\sigma_{cs}^{'}$	stress at the critical state
$\sigma_{d(min)}$	minimum shear strength after peak deviator stresses
$\sigma_{d(peak)}$	peak strength of a soil
σ_{dc}	cyclic shear stress on triaxial shear stress conditions
σ_{h0} or σ_r	total horizontal stress
$\sigma_i^{'}$ and $\sigma_j^{'}$	principal effective stress in the wave propagation direction where i and j are the wave polarization direction

σ_{v0}	total overburden stress or total vertical stress
$\sigma_{y0}^{'}$	initial vertical effective stress
$\sigma_{hi}^{'}$	initial horizontal effective confining stress
$\sigma_{m}^{'}$	medium confining stress
τ_{av}	average cyclic shear stress
τ_{cyc}	cyclic shear stress on simple shear plane
τ_{e}	equivalent shear stress of an earthquake
$\phi_{cv}^{'}$ or $\phi_{c}^{'}$	constant volume friction angle or critical friction angle
ϕ_{p}	peak strength angle
ψ or ξ_r or ξ_0	state parameter
Ψ or d	soil dilatancy; not to be confused with state parameter
ψ_{SSL}	steady state parameter

Chapter 1

Introduction

1.1 Prologue

Soil liquefaction is one of the major concerning hazards of geotechnical engineering. While constitutive modelling keeps prospering, the evaluation of soil liquefaction potential still relies on accumulated, well-founded, data.

Constitutive models are a simplification of the macromechanical soil behaviour, which describe the changes in strain and changes in stress, developed to be implemented in Finite Element Analysis (FEA) based software, for geotechnical engineering design. Despite the increasing efforts that have been being made, the complexity involved in the latest elasto-plastic models is very high and most of the times not enough to predict accurately the soil behaviour. In fact most of the actual models are still very limited for reproducing stress-paths other than compression or extension or to accurately predict phenomena such as soil liquefaction.

During liquefaction, more properly flow liquefaction, the soil crosses a transitory phase, passing from a solid phase to a liquid phase. Thus the presupposition that the soil is a continuous medium is no longer valid. As stated by Molano (2011) *"Geomaterials are complex multi-phase media usually characterized by a highly non-linear, irreversible and path-dependent response to the applied loads."*

Due to such complexity soil liquefaction susceptibility evaluation still relies on empirical or semi-empirical frameworks. These abacus have been being developed and calibrated in the past 30 years, and aim to predict soil stability by using stiffness or strength parameters. This is the core of the present research which aims to contribute to the performance of these tools, by analysing their limitations and by suggesting new procedures, or even by improving the predictability of the current correction factors. Plus this work aims to provide a structured and well founded reasoning basing on Critical State Soil Mechanics (CSSM). Therefore this document more than predicting soil instability also intends to contribute on clarifying the soil behaviour under both drained and

undrained conditions, and under both low and high confining pressures sheared under distinct stress-paths.

By knowing the limiting state conditions for which the soil starts exhibiting a stable behaviour it is required, for those which display instability, to be mitigated. Regardless mitigation techniques, like soil densification and dewatering or even jet grouting, were not contemplated and not investigated in the scope of the present work.

The soils are granular media, like any other materials, subjected to the 3rd law of Newton. Thus when the soil is externally sheared a stress transference chain is created between the grains. As the soil possess, unlike the other civil construction materials, beyond a solid phase, a liquid or a gas phase this external disturbance is reflected as displacement and possibly a volume change, due to the particles rearrangement. Therefore it could be imagined that a lots of factors might influence the soil response and more importantly that those factors play a major role on liquefaction onset.

1.2 Scope and Objectives

Aware of the influence of such distinct factors, a set of distinct soils were tested under distinct state conditions, by varying the initial confining stress, the initial relative density, the initial induced anisotropy (i.e. by making varying the coefficient of earth pressure, by increasing the vertical confining stress), and even, in the case of Coimbra sand, by varying the reconstitution method used for the specimens, therefore by varying the inherent anisotropy. The research focused on three distinct sands, Algeria sand and Coimbra sand, both tested under cyclic and monotonic triaxial loading conditions, and Osorio sand, studied exclusively under monotonic triaxial loading conditions. Plus a Silt and a Mixture, both obtained by grinding Osorio sand, were also studied under monotonic triaxial loading conditions. Whilst the variants of Osorio sand aimed to assess the influence of the fines content on both Critical State Line (CSL) positioning and on liquefaction susceptibility, Argelia and Coimbra sand were studied under monotonic loading conditions with the purpose to contribute for a construction of a CSSM based framework for a further assessment of it cyclic liquefaction potential. Furthermore the study of Algeria and Coimbra sand also included the performance of a set of cyclic Direct Simple Shear (DSS) tests in order to evaluate the influence of principal stress rotation on the undrained cyclic shear strength.

The study of Algeria sand, from Ain Beniam, arose from the necessity of evaluating the liquefaction events during the Bourmèdes earthquake that occurred in 2003 (Viana da Fonseca et al., 2011b). On the other hand the study of Coimbra sand also follows the conceptual idea of having a framework able to dictate the improvement of the initial state conditions required to prevent events such as the 1755 Lisbon Earthquake or the 1909 Benavente earthquake, where liquefaction events were registered. Finally the study of Silt, Osorio sand and Mixture, aimed to assess the influence

of the fines content on the liquefaction potential of a same mineralogical material. Regardless the proliferated studies, the initial idea actually arose from the comparison of the silt with the gold tailings geomechanical behaviour, as materials with similar grain size distributions, although chemically stable (Bedin, 2010; Bedin et al., 2012). However, later on, it was realized that in fact the grain size distributions of both materials are actually distinct. The gold tailings were collected in the Fazenda Brasileira disposal plant from Bahia State in Northeast Brazil (Bedin, 2010; Bedin et al., 2012; Schnaid et al., 2013).

The table 1.1 is a summary of the materials studied, the type of performed tests and the study addressed to each factor.

The study of soil liquefaction potential basing on CSSM is physically well founded and has being developed over the past 30 years. Conceptually this evaluation is performed by using the state parameter, ψ , a parameter which combines the influence of both void ratio and overburden stress, with a reference to an ultimate (steady or critical) state to describe the soil behaviour (Been and Jefferies, 1985). Plus the adoption of such a powerful parameter has undeniable advantages associated to a new generation of elasto-plastic models based on CSSM theory.

Jointly a set of frameworks were built relying on the stiffness parameter, i.e. basing on shear wave velocity, following the conceptual idea of the "Simplified Procedure" initially proposed by Seed and Idriss (2004), and later adapted by Andrus and Stokoe (1997).

At last the behaviour of Osorio sand and Mixture, i.e. stress-strain curves and stress-paths, were compared with those achieved by using an elasto-plastic constitutive model, SANISAND, initially developed by Manzari and Dafalias (1997) based on a previous model idea proposed by Lade et al. (1988), and improved by many other authors (Li and Dafalias, 2000; Dafalias et al., 2004; Dafalias and Manzari, 2004; Taiebat and Dafalias, 2008). The input parameters were properly calibrated basing on the laboratory data. After that the real and the predicted behaviour were compared aiming to rationally equate the limitations of the model for a future enhancement.

Table 1.1: Resume of the soils studied in the scope of the present work; Loading conditions and major factors assessed

Soil ID	**Monotonic compression loading conditions**				**Cyclic loading conditions**			
	Triaxial conditions				**Triaxial conditions**			**DSS**
	Classic drained and undrained shear tests			Other stress-paths	Shear stress-reversal – K_0=1	No shear stress-reversal – $K_0 \neq 1$		Principal stress rotation
	Same sample reconstitution technique		Effect of inherent anisotropy – Fabric effect			Same sample reconstitution technique	Effect of inherent anisotropy – Fabric effect	
	K_0=1	Effect of induced anisotropy - $K_0 \neq 1$						
Algeria sand	✓	✓			✓	✓		✓
Coimbra sand	✓		✓			✓	✓	✓
					Observations			
Coimbra sand 20% FC	✓				✓ Study of FC effect on CSL positioning of Coimbra sand			
Coimbra sand 40% FC	✓							
Osorio sand	✓			✓	✓ Study of FC effect on CSL positioning of Osorio sand and on soil liquefaction potential; ✓ CSL positioning corrected over data published by Bedin (2009)			
Mixture	✓	✓		✓				
Silt	✓			✓				
Gold Tailings	✓			✓	CSL positioning corrected over data published by Bedin (2009)			

1.3 Structure of Presentation

The present document is organized in ten distinct chapters and the thesis is splitted in two main parts.

The first part incorporates a brief introduction in Chapter 1, a historical overview in Chapter 2 and the studies developed over the past 30/40 years around the liquefaction theme in Chapter 3 and 4. On the other hand the second part is mainly related with the work and research developed over the

last 4 years. Starting with Chapter 5, this section presents the soils studied, the continuity given to past researches and the justification of their research. Chapter 6 follows with a presentation of the laboratory equipment and techniques adopted and performed according to the current National and European standards. Finally in Chapter 7 and 8 are presented the results achieved complemented with a careful and reasoning evaluation. This study was always accomplished within founded theories and when even devoid a supporting reasoning was presented. Therefore Chapters 3 and 4 support, through references, Chapter 7 and 8 founding's.

Whilst Chapter 7 exclusively accesses the onset of liquefaction of laboratory tests developed under a non-cyclic condition, Chapter 8 focuses on cyclic liquefaction and on the main contributing factors on cyclic undrained shear strength.

Chapter 9, which is, somehow disconnected from the others, is an extra-Chapter addressed to the constitutive modelling. SANISAND (Simple Anisotropic Sand plasticity model), is presented and calibrated for two distinct soils, Osorio sand and Mixture. It study aimed to analyse it ability to predict the soils behaviour, empathizing it ability to predict soil liquefaction.

Finally Chapter 10 presents a summary of the most important conclusions and contributions of the present work and research. It also provides a set of distinct issues which were not clarified and are a little dashed that whereby should be developed on further research projects.

Chapter 2

Soil Liquefaction – An Historical Overview

2.1 Introduction

The confluence between population locations and areas exposed to natural hazards like soil liquefaction, is not something new. Since Neanderthal the men always tried to fixate in fertile areas with water supply, therefore nearby riverbanks or seaside. However, whilst the more fertile areas are in the vicinity of volcanic zones and in the confluence of tectonic plates boundaries which occurs along the seaside, these locals also configures zones more susceptible to natural catastrophes. Therefore if population density is highly increased in such places, the role of engineering is to help preventing catastrophes, through the implementation of mitigation techniques.

Within the most devastating natural disasters, soil liquefaction is not the worst one, but certainly, jointly with landslides, is the less understandable geomechanical phenomena. In fact even some cases of landslides are mainly associated to soil liquefaction. Plus, curiously, the mechanics behind an avalanche is the same of soil liquefaction.

During the next sub-sections a description of the event is made, followed by an historical overview of the most striking liquefaction events, not only associated to earthquakes but also to tailing dams failures and even to civil construction works. This chapter attempts to warn the emergency of soil liquefaction study by describing the injuries reported in the past.

2.2 Liquefaction – Lexical Disambiguation

Soil liquefaction has been reported since antiquity, sometimes in manuscripts and others through the marks left in the Nature, such as soil dikes or soil boils, created by the fluid escape (see Figure

2.1).



(a) (b)

Figure 2.1: a) Dikes filled with sediments in the road to Falésia beach in Algarve, south of Portugal (ERSTA) (APNC, 2010); b) Sand boils beneath elevated West Grand Avenue distribution structure adjacent to Interstate Highway 80 east of San Francisco-Oakland Bay Bridge Toll Plaza during Loma Prieta, California, Earthquake of October 17, 1989 (Kayen et al., 1989).

Controversial definitions of soil liquefaction are often found in literature. In 1985, the US National Academy of Science's National Research Council (NRC, 1985) defined flow liquefaction as *"the condition where a soil mass can deform continuously under a shear stress less than or equal to the static stress applied to it. Equilibrium is restored, if at all, after enormous displacements or failures"*. In the same year, Sladen defined liquefaction as *"a phenomenon wherein a mass of soil loses a percentage of its shear resistance, when subjected to monotonic, cyclic or shock loading, and flows in a manner resembling a liquid until the shear stresses acting on the mass are as low as the reduced shear resistance"*. Both definitions are quite similar, regardless the NCR defined it as flow liquefaction while Sladen defined liquefaction by itself. Adding there is a phenomenon, usually designated by cyclic mobility, associated to the accumulation of plastic strains, without liquid-like flow, during a cyclic loading, which is often confused with the first term.

Later Rauch (1997) designated as liquefaction the tendency of soils to decrease in volume when subjected to shearing stresses, either monotonic or cyclic shear, and as cyclic mobility the propensity of dense, saturated sands to progressively soften in undrained cyclic shear and stiffen when monotonically loaded. If the cyclic load is lower than the steady state resistance the soil will also exhibit cyclic mobility. Such definition is used in the scope of the present research. Regardless no distinction is made between the differences in behaviour followed by stress-reversal during cyclic loading.

During this work, while Chapter 7 only concerns on flow liquefaction triggered under monotonic loading conditions, Chapter 8 reports to cyclic liquefaction, either flow liquefaction of cyclic mobility. The definition was used by simplification in order to assess and differentiate the phenomena carried out by the cyclic and non-cyclic loading types.

Unlike flow liquefaction, cyclic mobility detection in nature is not as obvious as the mark left by flow liquefaction type (see Figure 2.1).

A scientific and more detailed explanation between both phenomena is presented in Chapter 4.

2.3 Past Soil Liquefaction Events

2.3.1 Remarkable Case Histories

- Hydraulic dams

  The first time liquefaction terminology was used was by Hazen, in 1918, during the Calaveras Dam construction.

  Yet, it was in the year of 1938, during the hydraulic fill of Fort Peck Dam that liquefaction failure took larger attention (see Figure 2.2). Fort Peck Dam was designed by Casagrande by using the critical void ratio concept (see Chapter 3). The cause of failure was later studied by Casagrande, in 1965, and despite concluding the sand in-situ to be denser than it critical state it misleading was attributed to the interpretation guided by *"laboratory tests that can measure reliably the susceptibility of a sand to liquefaction"*. Nevertheless a majority defended a shear failure of the shale foundation which led to liquefaction triggering. The failure involved a 500 m section, with a total of 7.5 m^3, and was preceded by bulging ((Jefferies and Been, 2006)).

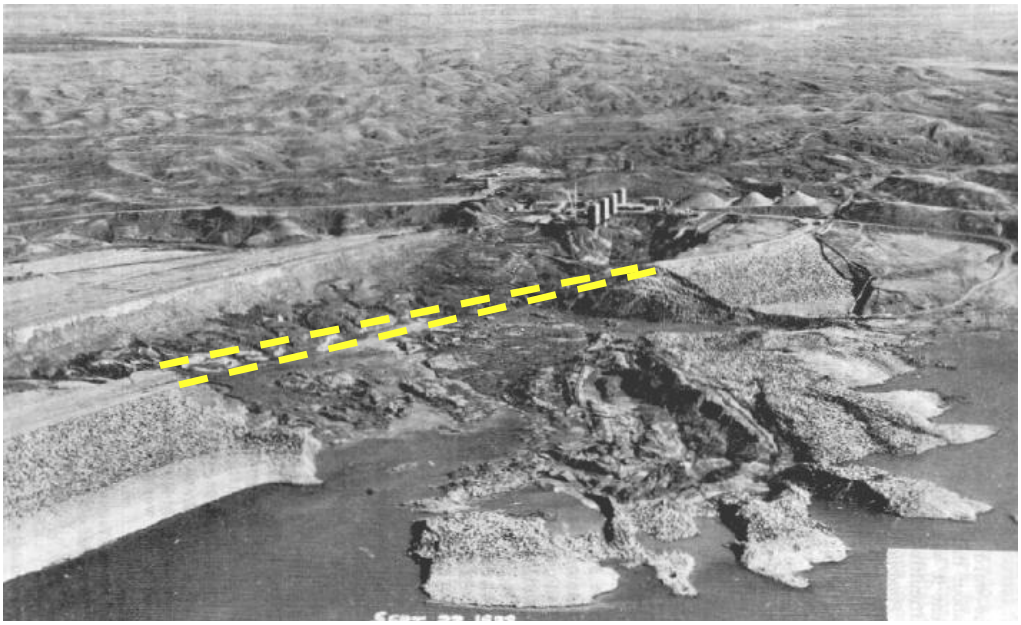
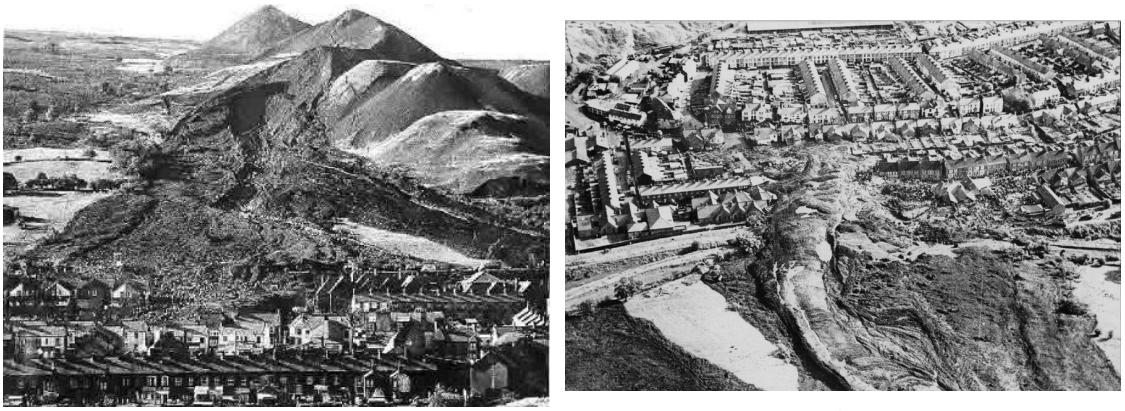


Figure 2.2: Oblique view of Fort Peck Dam Failure, in 1938 (Davies et al., 2002).

- Tailing dams

  While most of disasters involving hydraulic dams have been prevented some years ago, the same has not yet been observed with tailing dams. As described by Carrera (2008) tailings dams are *"big basins where these tailings, in the form of a slime, are poured into to decant"*, being the tailings *"the residual material of the rock milling process necessary to extract minerals"*. The majority of the problems are obviously related, not only to the tailings liquefaction but mainly to the structure which is not designed to support the liquefied material. In fact the tailings dams are usually constructed as embankments to resist the lateral forces imposed by the reservoir, however with increasing material to be deposited the dam is raised usually using the tailings material itself (Carrera, 2008). As quoted by Azam and Li (2010) the lack of regulations on design criteria and the sequential dam raise with an increase in effluents with residual materials from the mining operations are, jointly with external loads such as heavy rains, the reasons behind tailing dams failure. Plus according to both author' study, these are the reasons beyond the 1.2% of failure cases of 18 401 mines over the last century. Statistical studies reveal that liquefaction hazard is far from being solved.

  One of the first cases being reported was the failure of Aberfan mine waste in South Wales in 1966 (Figure 2.3). The colliery waste of the mine was tipped from rail trucks over the face of the tip on the side of the hill. The liquefaction onset succeeded after heavy rain and both the waste and the soil moved about 600 m, involving the failure of 107 000 m^3.



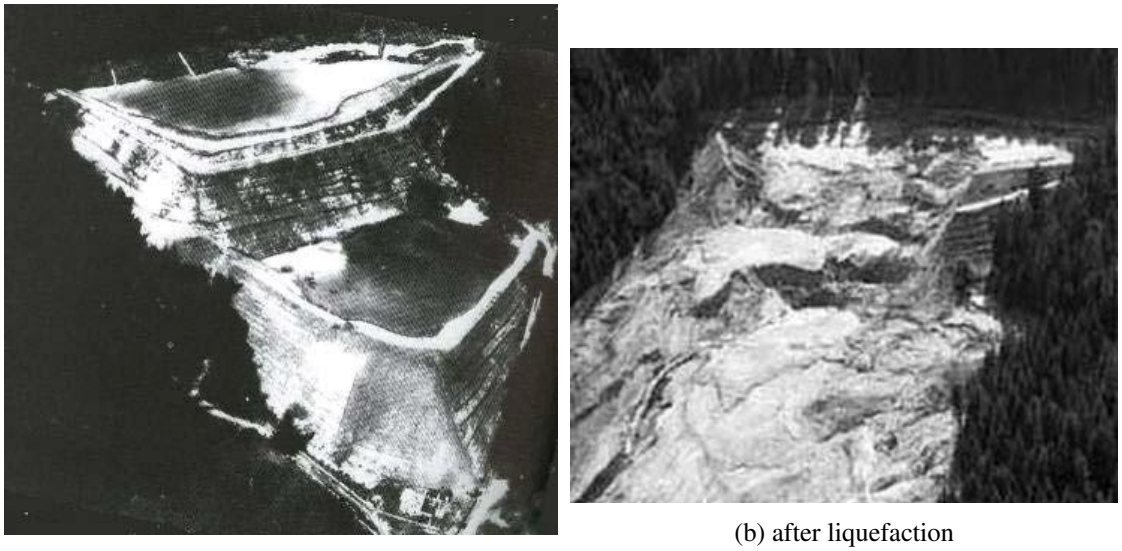
(a) (b)

Figure 2.3: Oblique view of Aberfan disaster (figure (a): Petcher (2010); figure (b): Dave (2011)).

One year before one of the biggest disasters ever occurred in El Cobre New Dam in Chile, during a 7.6 earthquake magnitude. This incident led to more than 200 fatalities and destroyed the city of El Cobre, involving a flood wave of about 2 250 00 m^3.

More recently, in 1985, Stava tailings dam, from fluorite mine, collapsed near Stava in northern Italy (Figure 2.4). The liquefied mass of 240 000 m^3 travelled more than 4 km obliterating everything in its path. The flow slide destroyed the entire village of Stava and

claimed 268 human lives. The dams, upstream constructed, collapsed due to the rising phreatic surface, under drained conditions followed by induced increasing pore-pressures which triggered liquefaction in the retained sublimes (Jefferies and Been, 2006; Morgenstern, 2001). Furthermore the steep slopes indicated a height surprisingly higher than failure in excess of the collapse surface irrespective of stress path (Jefferies and Been, 2006).



(a) before liquefaction

(b) after liquefaction

Figure 2.4: Stava tailing dams before and after the collapse (Tosatti, 2003).

Tailing dams collapse cases history have been showing that soil liquefaction is far from being triggered by the same external loading condition. In fact most of the reported tailings failures have been associated to heavy rains and to earthquakes. Thus research should be redirected according to the most concerning types of failure, instead of highlighting liquefaction triggered by a loading increase under undrained conditions, which in practice is not common.

Table 2.2 presents ones of the most important cases of liquefaction in tailing dams. For a more detailed list of tailings collapse, either by liquefaction or not Bulletin 121 *"Tailings dams risk of dangerous occurrences. Lessons learnt from practical experiences"* should be consulted.

Table 2.1: Some cases of tailing dams failure due to liquefaction and some few other cases (source: Bulletin 121: *"Tailings dams risk of dangerous occurrences. Lessons learnt from practical experiences"*, 2001 (Davies et al., 2002; Jefferies and Been, 2006)

Date	Location	Ore type	Type of Incident	Release	Impacts
2010	Kolontár, Hungary	Aluminium Bauxite	Triggered by a shear failure in the dike probably due to increased pore water pressures	700 000 m^3	10 victims; 8 km^2 flooded with toxic tailings; 472 million € for environmental damages
2000	Placer, Surigao del Norte, Philippines	Gold; Cooper	Tailings spill from damaged concrete pipe in tailings pond 7	700 000 m^3 of cyanide	268 victims; 40 hectares affected; 51 hectares of riceland swamped
1998	Los Frailes Mine, Spain	Lead Zinc	**Liquefaction** failure was induced, triggered by the construction of the waste rock lift	4 500 000 m^3	Contamination of the subsoil; 86 400 liters of acidic water per day; 240 million € for the clean-up; 90 million € for the environmental restoration and abandonment of the mine
1994	Merriespruit Harmony, South Africa	Gold	**Liquefaction** due to heavy storm; 50 mm of rain in 30 minutes	600 000 m^3	17 victims; tailings flowed within 1 km of distance;
1991	Sullivan Mine, British Columbia, Canada	Iron	Foundation failure and consequent **liquefaction**	Another tailings dyke contained the flow	
1985	Stava, North Italy	Fluorite	**Liquefaction** due to the rising phreatic surface	240 000 m^3	268 victims; Slurry wave flowed within 4 km of distance at 90 km/h velocity
1985	Marga, Chile		**Liquefaction** due to earthquake Mw=7.8	750 000 m^3	

Table 2.2: Some cases of tailing dams failure due to liquefaction and some few other cases (source: Bulletin 121: *"Tailings dams risk of dangerous occurrences. Lessons learnt from practical experiences"*, 2001 (Davies et al., 2002; Jefferies and Been, 2006)

1972	Bufallo Creek, West Virginia, USA	Coal	Sinkhole opened on the surface allowing surface water	500 000 m^3	125 victims; 4 000 were left homeless; 507 houses were destroyed; $292 million dollars in damages, in 2011 dollars,
1970	Mufulira, Zambia	Cooper		1 000 00 m^3	89 victims (miners)
1964	Bilbao, Spain	Rockfill	**Liquefaction** due to heavy rain	115 000 m^3	
1968	Hokkaido, Japan	Coal	**Liquefaction** due to earthquake Mw=8.0	90 000 m^3	
1966	Sgorigrad, Bulgaria				488 victims
1965	El Cobre New Dam, Chile	Cooper	**Liquefaction** due to earthquake Mw=7.6	2 250 00 m^3	>200 victims
1965, Mar. 28	Los Maquis; La Patagua New Dam; Bellavista; Cerro Negro No.3; all in Chile	Cooper	**Liquefaction** due to earthquake Mw=7.6	35 000 m^3, 21 000 m^3, 21 000 m^3 70 000 m^3 and 85 000 m^3, respectively	
1965	Aberfan	Coal	Liquefaction due to heavy rain	107 000 m^3	144 victims

- Earthquakes (not related with tailings)

  (i) Mino-Owari Earthquake, 1891

  On October 28, 1891, an earthquake reached the Nagoya area with a magnitude of 8.4 lasting for 15 minutes. During the event 7 500 persons lost their lives. The region, covered with soft alluvium, suffered disruption and a large number of liquefaction phenomena were reported. The tracks left by the occurrence of liquefaction were significant. In villages the soil was much easier to cultivate, as was loosened by the shaking, (which explains why liquefaction is a recurrent phenomena, i.e. often occurs more than once in the same place). A large number of cavities were opened from which streams of water spouts developed, plus sands deposits were observed in the houses roofs, meaning that those jets of water reached a height of about 2.0 m (adapted from Ishihara (2006)).

  (ii) Great Kanto Earthquake, 1923

  On September first of 1923, the most disastrous earthquake of Japanese history stroke Tokyo. The 7.9 magnitude earthquake which lasted longer than one minute victimized 14 000 persons, mostly due to fires after the quake. Constructions were more damaged in the downtown of Tokyo due to fissures and to formation of sand boils. Liquefaction phenomena were mainly reported on alluvial deposits, in the downstream delta area of big rivers (adapted from Ishihara (2006)).

  (iii) Fukui Earthquake, 1948

  On 28 June 1948 an earthquake with a magnitude of 7.2, with an epicenter 5 kilometres of Fukui city, reached and nearly destroyed this city. The area, of 15 km x 30 km, was mostly affected due to the geological conditions, mostly constituted by alluvial soils. Structures built on the alluvium plain were accompanied the large damages, leading to the destruction of 75% of the houses, whilst those built on bed rock hardly suffered minor damages. It was also observed sand boils formations along former stream channels and along the fault zone, which is geographically coincident with the fan deposit formed by the outflow of the Kuzuryu river. The detailed information about the sequential liquefaction phenomena observed is not clear, but is speculated to be due to the severity of shaking or with the abundance of pressurized underground water, which induced both sands and gravels soils to simultaneously liquefy (adapted from Ishihara (2006)).

  (iv) Alaska Earthquake, 1964

  On Good Friday, March 27, 1964, an 8.6 earthquake magnitude stroke Alaska. The city most affected was Anchorage, and the damage property was estimated in 300

million dollars (1967 dollars). Among the 130 deaths, 120 persons were drowned by tsunami.

Slides and lateral spreading of soft clays and sands caused the greatest damage and resulted from soil liquefaction induced by the cyclic stress waves (Figure 2.5). *"In the depressed areas, the ground dropped an average of 11 meters during the sliding. Houses in the area, some of which moved laterally as much as 150 or 180 meters, were completely destroyed"* (for Earth. Eng.).



Figure 2.5: Liquefaction during the 1964 Good Friday earthquake in Alaska results in lateral spreading collapse of the coastline (Elliott, 2011).

(v) Niigata Earthquake, 1964

Niigata earthquake is perhaps one of the present events most reported within earthquake history, despite it disproportional gauged 7.5 magnitude earthquake. This event which occurred on June 16, in the same year of Alaska earthquake, is perhaps one of the most remembered due to the wave of destruction almost exclusively related with soil liquefaction. The damages of the earthquake were estimated to be around $ 1 billion and near 30 persons were victimized. In Niigata, where sand deposits in lowland areas are widespread, buildings not embedded deep in firm strata sank or tilted (see Figure 2.6). On the other hand deep foundations as piles due to a large loss of their lateral resistance bent excessively causing girders fall. Also underground structures felt the effects of soil liquefaction, floating up a meter or two above ground level. Sand boils and mud volcanoes led to the coverage of the entire city with deposits of 20 to 30 cm thickness (adapted from Ishihara (2006)).



(a) (b)

Figure 2.6: (a) Building build on sands tilted (U.S.Department and U.S.Geological) and (b) Bridges collapsed due to liquefaction, during Niigata Earthquake, 1964 (Johansson, 2000a).

(vi) Loma Prieta Earthquake, 1989

During the Loma Prieta earthquake, on October 12, 1989, several counties in California, USA, experienced damages. Nevertheless it was in Sand Francisco and in some Alameda counties that major losses were registered. The earthquake of 7.0 of magnitude, beyond leading to 62 deaths, resulted in $5.9 billion in monetary losses.

The central San Francisco Bay area was the zone which suffered more damages, mainly due to it geological conditions. This area, mainly constituted by thick deposits of soft clayey soils, suffered large damages due to an amplification effect "at soft soils" of relatively moderate levels of "bedrock" shaking to much stronger levels of ground surface shaking. Such effect led to soil liquefaction of the coastal area, in the extent of 112 km, causing extensive damage to waterfront facilities, structures, and buried pipelines. The coastal area had typically loose sandy fill which was underlain by deep cohesive soils, responsible for the amplification effect of the ground shaking, sufficiently to trigger liquefaction (adapted from for Earth. Eng.).

(vii) Chi-Chi Earthquake, 1999

Chi-Chi earthquake occurred on September 21, 1999, and, with a magnitude of 7.6, stroked Taiwan and destroyed part of Wu-Feng. Due to geological conditions liquefaction induced ground failures including subsidence, lateral spreading and sand boils have occurred extensively over most plain area of Wu-Feng (Figure 2.7). This small town, located in central Taiwan, is formed by laterite deposit interlayered with high fine content silty sand deposits. This resulted on ground failures leading to structures damages including building collapses, foundation settlement, and ground surface cracks (adapted from Lee et al. (2011)).



Figure 2.7: Sand boils and ground surface cracking caused by liquefaction at Wu-Feng during Chi- Chi earthquake (Lee et al., 2011).

(viii) Christchurch Earthquake, 2011

On 22 February 2011, an earthquake with a magnitude, Mw, of 6.3 occurred with an epicenter located at Port Hills, near Lyttelton at about 10 km from Christchurch in Canterbury region on the South Island of New Zealand. This short distance between the epicenter and Christchurch led to significant damages to pipelines, traffic facilities, residential houses/properties and multi-story buildings. Furthermore a lot of liquefaction events were registered.

Canterbury Plains, New Zealand's largest flat land, have been formed by the overlapping fans of glacier-fed rivers issuing from the Southern Alps and are derived from the greywacke of the mountains or from loess. In addition, clay and volcanic rock are present near Christchurch from the Port Hills slopes of Banks Peninsula. The city of Christchurch, located at the coast of the Canterbury Plains, is mainly swamp, behind beach dune sand, and estuaries and lagoons. These set of geological conditions was crucial for liquefaction onset.

Soil liquefaction led to ground deformations, houses tilting (see Figure 2.8), bridges tilting in their abutments, as a result of lateral spreading and loss of bearing capacity. Plus a massive amount of sands were ejected and deposited around the houses (adapted from Yamada et al. (2011)).



(a)



(b) (c)

Figure 2.8: (a) Liquefaction-induced damages in CBD (Yamada et al., 2011); (b) and (c) Liquefaction on Kilmore St (Burton and Scobie; Woodfor, 2011).

2.3.2 Case Histories In Portugal

- Earthquakes

  Soil liquefaction within the national territory is not a common phenomenon. Beyond Portugal not possessing a large number of tailing dams, earthquake activity is not often. However case histories, local geological conditions and the high probability of a future strong earthquake in the south of the country justify the experts' concern. Among past researches it was collected and identified 53 points were soil liquefaction occurred in past events (Vaz, 2010).

  The first description of what could be a soil liquefaction event in Portugal is dated to 1531 and presented by **Garcia Resende (1973: 379 – 380)**:

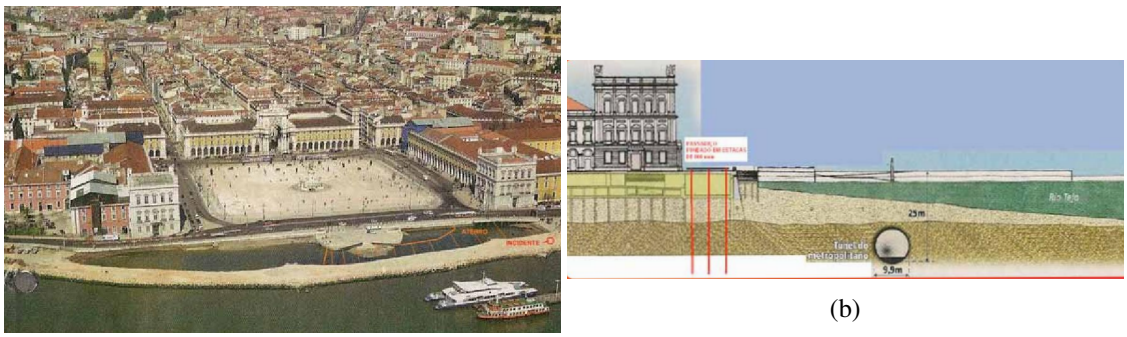
  In Portugal massive destructions and soil liquefaction events are mainly reported in 1755 Lisbon Earthquake and 1909 Benavente Earthquake. The reported occurrences are also corroborated by geological imprints, like the sand dikes displayed in Figure 2.1. A detailed description of both events is presented in Chapter 5, not justifying a further repetition.

"[...] Gretas, Buracos fazia	*"Cracks, Holes did*
ha terra, e se abriu,	*the soil, it opened,*
água, e areia sahía,	*water, and sand went out,*
que a enxufre fedia;	*which sulfur stank;*
isto em Almeirim se vio:	*this was seen in Almeirim:*
e porque logo vieram	*and because soon came*
grandes chuvas que choveram	*heavy rains that rained*
e alguos dias duraram,	*and some days lasted,*
as aberturas taparam,	*holes closed,*
que nunca mais aparecerao."	*and will never appear."*
(in Portuguese)	(translated in English)

- During construction

The study of soil liquefaction is beyond natural disasters. Examples like Nerlek Berm failure (1983), where sandfill liquefied after being hydraulically placed in loose conditions to promote displacement of clays before the construction of the offshore structure, or like Molikpaq (1986), an offshore structure where sandfill core, inside the caisson, liquefied during the subsequent cyclic thick ice induced vibrations, are not something new (see full description on Jefferies and Been (2006)).

In 1996, blue line of the Lisbon Metropolitan was decided to be extended (Figure 2.9). The tunnel was constructed without incidents till the end of 1999. Despite, in 2000, during the construction of the connection between of Terreiro do Paço metro station and the tunnel, flow liquefaction occurred. The connection was decided to be constructed through jet grouting columns, as the site is located behind alluvium soils beside Tejo river. It was during soil drilling that the event was observed. According to LNEC ("Laboratório Nacional de Engenharia Civil") experts static liquefaction would only stop when difference between the phreatic surface of the river and the one inside the tunnel would be less than 12.6 m (Salgado, 2012).



(a) (b)

Figure 2.9: (a) Terreiro do Paço; (b) Scheme of the tunnel and piles location on Terreiro do Paço (Salgado, 2012).

2.3.3 Liquefaction Hazard Mapping

Liquefaction hazard is a recurrent phenomenon, not only due to the recurrent earthquake activity, but also, as reported above, due to soil loosening during the cyclic loadings. Therefore liquefaction hazard mapping or zonation is very important for future constructions.

While liquefaction hazard mapping is useless for flow liquefaction triggered by static conditions it may be a powerful tool to mitigate liquefaction events induced by earthquakes. The open access to information which can provide the delimiting areas where liquefaction was often observed, basing on past events, geological and hydraulic conditions, on earthquakes opportunity maps, or even on in situ testing, etc., might be very valuable, even for small constructors, which in most cases do not characterize the soil properly.

For this purpose a relation, which can predict the maximum range of liquefaction for a particular magnitude of earthquake, given the presence of potentially liquefiable Holocene sediments, can be used (Kuribayashi and Tatsuoka, 1975; Ambraseys, 1988; Wakamatsu, 1993). Although some countries or cities already possess a liquefaction opportunity map further efforts should be made for a detailed information access. In 1994 Jorge developed a liquefaction opportunity map for Portugal continental, which is displayed in Figure 5.12, in Chapter 5. Despite providing valuable information it very large scale could be detailed, mainly on the most populated cities. For example the U.S. Geological Survey built a liquefaction-scenario seismic-hazard map of the greater Oakland, California, area for a magnitude 7.1 earthquake basing on the Cone Penetration Testing ("CPT") (see Figure 2.10). The U.S. Geological Survey CPT truck is a fast and inexpensive way to conduct shallow subsurface exploration, providing detailed data immediately.

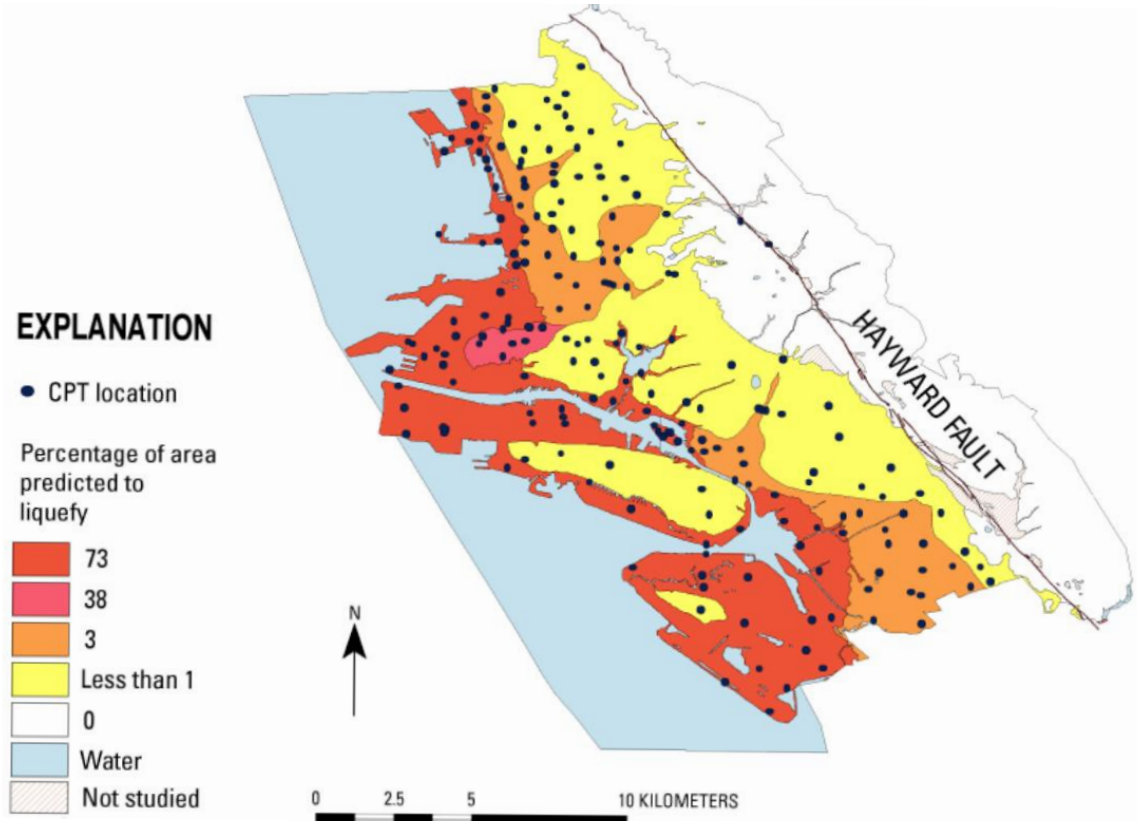


Figure 2.10: Liquefaction-scenario seismic-hazard map of the greater Oakland, California, area for a magnitude 7.1 earthquake on the Hayward Fault. Geologic units were geotechnically characterized with 210 cone-penetration-test (CPT) soundings (Noce and Holzer, 2003).

Chapter 3

Liquefaction Susceptibility Criteria

3.1 Specifications And Standards To Assess Liquefaction Susceptibility

It is now commonly accepted that the evaluation of soil liquefaction triggered by earthquakes, in spite of the type of phenomena (flow liquefaction or cyclic mobility), is conventionally done by using semi-empirical frameworks. Among them, "Simplified Procedure" stands out and remains as the one and only included in design codes, such as eur (2005). These frameworks are built upon and rely on accumulated experience of a widespread data values from well documented case-histories.

Professors Seed and Idriss, following the disastrous earthquakes which took place in Alaska and in Niigata, Japan in 1964, which reached a magnitude of 9.2 and 7.5, respectively, developed and published a methodology termed "Simplified Procedure" for evaluating liquefaction resistance analysis. This procedure basically requires the estimation of two variables: the Cyclic Stress Ratio (CSR), the seismic demand on a soil layer, and the Cyclic Resistance Ratio (CRR), the capacity of the soil to resist liquefaction (Youd et al., 2001).

The cyclic stress ratio concept, firstly proposed by Seed and Idriss (2004) results in the relationship between the average cyclic shear stress (τ_{av}) acting in a horizontal plane, induced by the vertically propagating seismic wave - estimated by site response analysis for the recorded strong ground motion, and the initial effective vertical (overburden) stress, σ'_{v0}. This normalization will give a measure of the imposed loading of the ground by an earthquake:

$$CSR = \frac{\tau_{av}}{\sigma'_{v0}} = 0.65 \left(\frac{a_{max}}{g} \right) \left(\frac{\sigma_{v0}}{\sigma'_{v0}} \right) r_d \tag{3.1}$$

where τ_{av} is the average cyclic shear stress generated by the earthquake of a maximum acceleration of a_{max}, σ_{v0} is the total overburden stress, g is the acceleration of gravity, and r_d stands for a stress reduction coefficient.

For noncritical projects it was accepted, during the workshops of 1996 NCEER and 1998 NCEER/NSF, to estimate average values of r_d according to the following equations proposed by Liao and Whitman (1986):

$$r_d = 1.0 - 0.00765z \qquad \text{for } z \leq 9.15m \tag{3.2}$$

$$r_d = 1.174 - 0.0267z \qquad \text{for } 9.15 < z \leq 23m \tag{3.3}$$

where z is the soils depth.

The stress reduction factor intents to correct the theoretical assumption that the maximum shear stress, normalized by the vertical effective stress, CSR, is determined assuming that the soils column behaves like a rigid body.

To evaluate the capacity of the soil to resist liquefaction, CRR, several field tests have gained common practice. Among them, Standard Penetration tests (SPT) and Cone Penetration test (CPT) are generally preferred due to the more extensive database and past experience. The SPT and CPT based frameworks to assess liquefaction potential are obtained by correlating the CSR with the normalized standard penetration (SPT) resistance $(N_1)_{60}$ (Seed and Idriss, 2004), and the normalized static cone penetration (CPT) resistance, q_{c1} (Robertson et al., 1992), respectively. The CRR becomes the curve which separates, conservatively, regions of liquefaction from nonliquefaction for earthquakes with a reference magnitude of 7.5 in Richter scale. This magnitude is associated to events of 10 to 20 seconds in frequencies roughly around 1 Hz and the reproduction of such a cyclic action will correspond roughly to 15 cycles.

The use of an earthquake magnitude correction factor, K_M, to adjust CRR curves to other magnitudes, is a current practice of soil liquefaction evaluation. Seed and Idriss (1982) firstly established K_M as an earthquake magnitude correction factor to a reference earthquake magnitude of 7.5. This resulted from the inability to constrain bounds between liquefaction and non-liquefaction regions on CRR plots for magnitudes other than 7.5 (Youd et al., 2001).

The CRR curves were developed for granular soils with less than 5% of fines content, and posterior extended for soils with fines content of 15 and 35%.

From the necessity to extrapolate the Simplified Procedure to larger overburden pressure and static shear stress conditions than the case history data from which "Simplified Procedure" is based on,

Seed (1983) started developing correction factors to enlarge it practice to other cases. In order to incorporate such factors, Seed generalized the Cyclic Resistance Ratio:

$$CRR = CRR_{15} \times K_M \times K_\sigma \times K_\alpha \tag{3.4}$$

where CRR_{15} is the limit condition for 15 cycles in action, and K_M, K_σ, K_α are correction factors to take into account the earthquake magnitude, the stress-level, and the pre-existing shear stress on a horizontal plane.

During this chapter it will be mentioned how to assess liquefaction triggered by cyclic or monotonic loadings. Nowadays standards for geotechnical design stands only for the first type of loading conditions, not making any kind of reservation for instabilities generated by other type of loading conditions. Flow liquefaction triggered by monotonic loadings despite not being covered by standards is most of the times assessed according to the CSSM theory as will be explained in Chapter 4.

3.1.1 Eurocode

3.1.1.1 Evaluation of soil liquefaction potential

Eurocode 8 – Part 5 is the European standard which regulates the performance-based design for earthquake resistance in foundations, retaining structures and geotechnical aspects.

Soil liquefaction potential can be evaluated according to the subsection 4.14 of Eurocode 8, where are expressed the requirements to fulfil in order to assure soil stability. It states that *"an evaluation of the liquefaction susceptibility shall be made when the foundation soils include extended layers or thick lenses of loose sand, with or without silt/clay fines, beneath the water table level, and when the water level is close to the ground surface..."*, and it requires *"...the execution of either in situ Standard Penetration Tests (SPT) or Cone Penetration Tests (CPT), as well as the determination of grain size distribution curves in the laboratory."*.

The determination of the grain size distribution curve of the soil is necessary to first assess soil liquefaction susceptibility, according to the ranges of grain size curves separating the liquefiable and nonliquefiable soils, proposed by (Tsuchida, 1970).

For the SPT the measured values of the blowcount N_{SPT}, expressed in blows/30 cm, shall be normalized to a reference effective overburden pressure of 100 kPa, and to a ratio of impact energy to theoretical free-fall energy of 0,6". The normalization shall be made by multiplying the N_{SPT} by the factor $(100/\sigma'_{v0})^{1/2}$, where σ'_{v0} is the effective overburden stress at the depth where the SPT was performed. The energy normalization is obtained by multiplying the value N_1 by the factor

ER/60, where ER is one hundred times the energy ratio specific of the testing equipment. The EC8 also recommends a reduction of 25% of the measured N_{SPT}, for depths of less than 3 m.

As it is well known, liquefaction hazard only takes place in soils under a set of conditions. Thus EC8 suggests:

- *"(7) For buildings on shallow foundations, evaluation of liquefaction susceptibility may be omitted when the saturated sandy soils are found at depths greater than 15 m from the ground surface."*;
- *"(8) The liquefaction hazard may be neglected when* α *.S < 0.15 and at least one of the following conditions is fulfilled:*
  - *The sands have a clay content greater than 20% with plasticity index PI > 10;*
  - *The sands have a silt content greater than 35% and, at the same time, the SPT blow-count value normalised for overburden effects and for the energy ratio* $N_1(60) > 20$*;*
  - *The sands are clean, with the SPT blowcount value normalised for overburden effects and for the energy ratio* $N_1(60) > 30$*."*

For the cases where liquefaction might take place, it evaluation shall be made *"based on field correlations between in situ measurements and the critical cyclic shear stresses know to have caused liquefaction during past earthquakes."* According to EC8, seismic shear stress might be estimated from the simplified expression:

$$\tau_e = 0.65 \alpha S \sigma_{v0} \tag{3.5}$$

where σ_{v0} is the total overburden stress, α is the ratio of the design ground acceleration on type A ground, a_g to the acceleration of gravity, and S is the soil factor. It is recommended to not apply this expression for depths larger than 20 m.

The empirical liquefaction chart proposed in EC8, the "Simplified Procedure" and the limiting curve, graphically represented in Figure 3.1, were both firstly proposed by Seed and Idriss (2004). A more extensive study about the SPT procedure will be presented on subsection 3.2.2.1.

Soils shall be considered susceptible to liquefaction whenever the earthquake-induce shear stress exceeds 0.8 of the critical state, which implies a safety factor of 1.25.

For earthquakes magnitudes others than 7.5, cyclic stress ratio needs to be multiplied by a correction factor CM, equivalent to the K_M correction factor which will be further presented, according to the surface wave-magnitude given in the table B.1 of EC8.

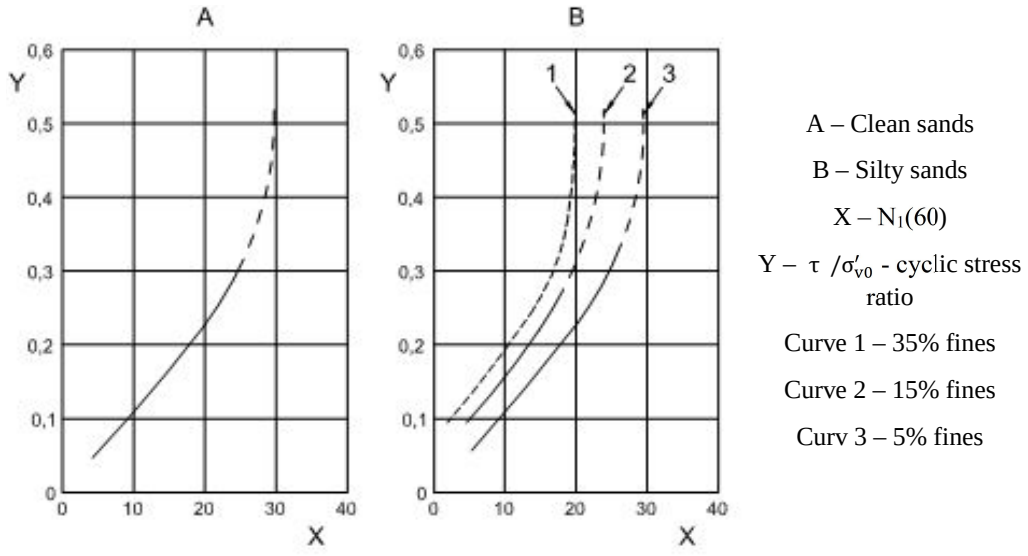


Figure 3.1: Relationship between stress ratios causing liquefaction and $N_1(60)$ values for clean and silty sands for Mw = 7.5 earthquakes (eur (2005)).

EC8 allows the resource to the charts based on the CPT resistance, also similar to the original one, i.e. "Simplified Procedure" being the limiting curves, which separate liquefaction from nonliquefaction events, were firstly proposed by Robertson et al. (1992). It is also highlighted that it employment shall not be done by correlating directly the q_{c1} with the $N_1(60)$.

Plus European standards indicates that, charts based on correlations with shear wave velocity, shall not be used by nonspecialists as they are still under development.

3.1.1.2 Mitigation

After proceeding to the liquefaction evaluation, if required, the engineer should: i) proceed with a more advanced analysis technique; ii) design the facility to resist the anticipated deformations; iii) remediate the site to reduce the anticipated deformations to acceptable levels; iv) or choose an alternative site (quoted from Kavazanjian et al. (1997))

If economically feasible, EC8 proposes as mitigation measure against liquefaction hazard either compact the soil, in order to increase its penetration resistance, or use drainage to reduce the excess pore-water pressure generated during the earthquake.

3.2 From Field-Based Procedures To Laboratory Studies

Because of the difficulties involved in extracting undisturbed soil cores, liquefaction potential analysis has always been preferred to be developed and studied basing on in situ testing. As stated

previously, conventionally, liquefaction potential frameworks are built with input variables, relating an action index, CSR, with a resistance index, CRR, usually expressed by the normalized values of in situ tests (SPT, CPT, DMT or Seismic Geophysical Surveys). These liquefaction potential charts, usually designated as "Simplified Procedures", were firstly proposed by Seed and Idriss (2004), correlating CRR with the normalized standard penetration (SPT) resistance $(N_1)_{60}$, giving rise lately to correlations between CRR and normalized static cone penetration (CPT) resistance, q_{c1N} (Robertson et al., 1992), and more recently between CRR and the normalized values of low energy shear waves' velocities, V_{s1} (Andrus and Stokoe, 2000; Andrus et al., 2004) or Flat Dilatometer (DMT) horizontal stress Index, K_D (Marchetti, 1982; Monaco et al., 2005).

Plus in situ tests can be done relatively quickly, when compared with laboratory tests, as a large number of data are provided and vertical and lateral variability can be assessed (Huang and Chang, 2011). Despite the numerous advantages, when testing in situ, variables dispersion is inherent to field conditions and uncontrollable and consequently misunderstood. Moreover the local boundary conditions created by most of the in situ intrusive testing methods are very difficult to perceive.

Notwithstanding, when comparing in situ and laboratory data, is necessary to understand that field boundary conditions differ from those developed in laboratory. As pointed out by Peacock and Seed (1968) in field, when an earthquake takes place, there is a cyclic reorientation of the principal stress directions of the soil element, which is initially consolidated under K_0 conditions, deformations are presumed to occur under plane-strain conditions and soil loading is multiaxial.

During the following subsections the most common ways to evaluate soil liquefaction potential, either in situ or under laboratory conditions, will be presented.

3.2.1 Empirical Criteria

"Not all soils are susceptible to liquefaction, consequently the first step in a liquefaction hazard is usually the evaluation of liquefaction susceptibility" (Kramer, 1996). The following empirical criteria, historical, geological and compositional criteria arise from the necessity to better assess liquefaction hazards, before proceeding with in situ and/or laboratory tests. From what follows it will be easily understood that purely empirical interpretations of the field case histories, without any physics-based framework, would leave unclear the conditions for which the empirical relations are suitable (Idriss and Boulanger, 2004). Whereby frameworks based on semi-empirical or empirical based-correlations emerge from the lack of response of the empirical relations.

3.2.1.1 Historical and Geological Criteria

Mapping liquefaction susceptibility can be a very helpful tool to assess where liquefaction often takes place. Thus case histories can help identifying specific sites, but more importantly it can help identifying the general conditions more prone to liquefaction hazard (Kramer, 1996).

On the other hand geological criteria helps out knowing which are the hydrogeologic and geologic conditions affecting liquefaction hazard. Depositional process and grain size distribution, drainage conditions and distances to groundwater affects expectedly the geomechanical behaviour of soils. For example fluvial, colluvial and aeolian deposits when saturated are susceptible to liquefaction (Kramer, 1996).

An example of the use of this empirical criteria was presented by **Ishihara (1974)**. According to the author, basing on Japanese case histories, there are three types of alluvium more prone to liquefaction hazard: i) Sands deposits existing in layers down to depths of at least 20 m; ii) Sandwished sand deposits: sands layers with thicknesses between 3 and 10 m, intercalated with silt or clay soils; iii) Thin sand layers lying on gravelly sand.

3.2.1.2 Compositional Criteria

As the name speaks for itself, compositional criteria is based on the parametrization of the characteristics of the soil, including shape, size and gradation. Those, highly related with volume change potential of the soil, help out to establish boundaries from which soils stop liquefying.

Initially liquefaction potential was commonly associated to sandy soils; however the bounds of the gradation criteria have broadened to include silty and coarser soils, ambiguities which, later, were proved to be prone to liquefaction (Kramer, 1996).

Tsuchida (1970), summarized the results of the grain size distribution of cohesionless, alluvial and diluvial, soils known to have liquefied or to not have liquefied during case history earthquakes. The analysis of the set of grading curves resulted into the achievement of a range between grain size curves separating the liquefiable and nonliquefiable soils as shown in Figure 3.2.

Despite being Tsuchida (1970) the first author proposing a compositional criteria, the most popular one was proposed by Wang (1980), widely known as Chinese criteria. As reported by Wang (1980), these criteria established a range board over a set of characteristics of soils and was developed basing on observations of liquefaction in fine-graded soils at various sites in China during strong earthquakes (Boulanger and Idriss, 2004). Later Seed and Idriss (1982) adapted Wang's findings and published what would become the most widely used criteria to assess soils liquefaction potential, the "Modified Chinese Criteria" (Figure 3.3a). According to these criteria, soils for being considered to be susceptible to liquefaction have to fulfill the following requisites:

- Fraction finer than 0.005 mm $\leq$ 15%;

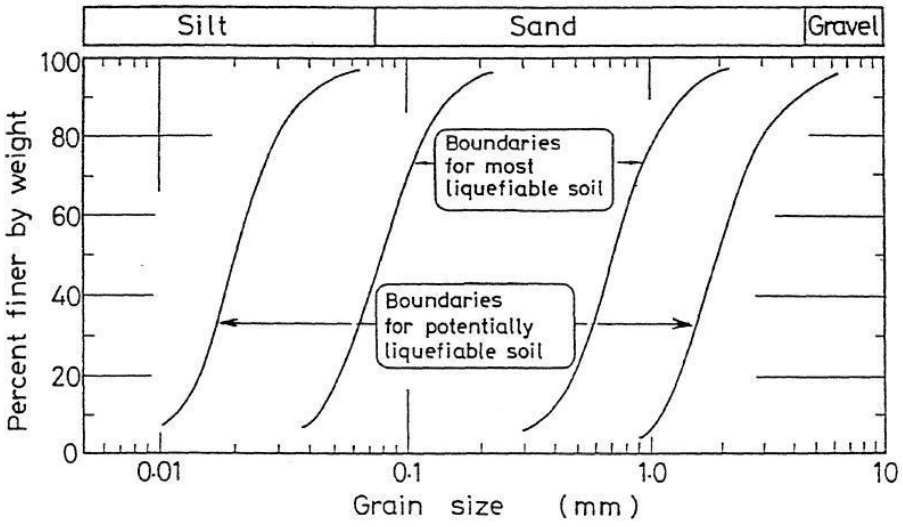
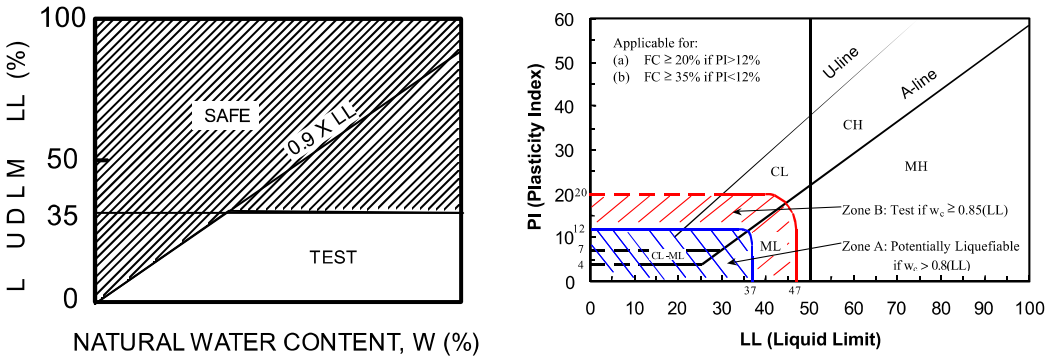


Figure 3.2: Limits in the gradation curves separating liquefiable and nonliquefiable soils (Tsuchida, 1970).

- Liquid limit, LL $\leq$ 35%;
- Water content $\geq$ 0.9(LL).



(a) (b)

Figure 3.3: "Modified Chinese Criteria" (after Wang (1980), from Seed and Idriss (1982)).

Countless re-examination has been being done in an effort to obtain a unified and consistent framework where engineers can rely when delaying with geotechnical issues related to strata stability. However, as pointed out by Seed et al. (2003), a misleading on liquefaction disambiguation is becoming an obstacle on the development of new procedures. In fact, soils with higher plasticity, despite not suffering "true" liquefaction, consequently accomplished by a complete loss of strength, might develop a positive excess pore pressure that might led to a loss of strength and a consequent strain softening, not compatible with the deformation limits of super and/or infrastructures in the vicinity.

Plus, as concluded by Bray and Sancio (2006), the indicators above-mentioned might not be absolute criterions as other factors, like mineralogy void ratio and overconsolidation, age, among other prominent factors which affects liquefaction susceptibility as well.

Seed et al. published recently, in 2003, a framework to assess liquefaction hazard, substitute of the "Modified Chinese Criteria", which intents to be "a good summary of what we know to the date" (Figure 3.3b). This new proposed framework tends to incorporate what the others mislead, such as the quantification of "clay-size" percentage, that should be accounted jointly with it activity.

Whereas grain shape and size constitute a not unanimous criterion, soil water content of at least 90%(LL) is widely accepted as a necessary condition for soil liquefaction.

3.2.2 Procedures Developed From Field/ In Situ Performance Studies

Among field and laboratory studies, field-based procedures are commonly preferred over the laboratory ones. Two main reasons support it popularity: i) the accumulated past case histories experiences, and ii) the better reliability over soil liquefaction resistance characteristics. Despite mostly in situ tests being intrusive methods, which clearly misrepresent the boundary conditions or even the stress conditions, generally they are preferred over the laboratory tests which are mostly performed over reconstituted specimens, leading to erroneous interpretations of the liquefaction resistance of the soil.

The "landmark" of the liquefaction hazard assessment is the original "Simplified Procedure", proposed by Seed and Idriss (2004), which correlates the CSR with the standard penetration resistance $(N_1)_{60}$, remaining as the one and only framework universally accepted for geotechnical design.

Adding to the numerous and constant refinements done over the original "Simplified Procedure", over the past thirty years many others in situ index tests branched out, such as the CPT, Undrained Cone Penetration test (CPTU), Becker Penetration test (BPT), Dilatometer test (DMT), geophysical techniques (e.g. Spectral Analysis of Surface Waves (SAWS)), helping out clarifying what SPT test misleads. While the SPT and CPT are the most used in practice, BPT test is usually used for evaluating the liquefaction potential in gravelly soils (Harder and Seed, 1986), finally the recourse to geophysical techniques for measuring shear wave velocities emerged as potential alternative to the BPT, having earned some relevance more recently.

Being the present study developed on laboratory conditions, a greater relevance is given over traditional seismic methods, focusing the shear wave velocity. Small-strain, shear wave velocity measurements is a promising alternative and/or supplement to the penetration base-approach. Despite the numerous critics on relating the small-strain parameter, (G_0-read V_s), with a large-strain parameter, the CRR, while working under undrained conditions the presumption is valid as the volumetric strain is zero, thus the elastic strain equalizes the plastic strain, $\varepsilon_v = 0 \Longleftrightarrow \varepsilon_e = -\varepsilon_p$.

3.2.2.1 Method based on SPT test

A high correlation between soil liquefaction resistance under earthquake shaking and soil SPT resistance in level ground conditions was observed from the field performance of sands and silty sands during actual earthquakes in the western United States, Alaska, South America Japan and China (Tokimatsu and Yoshimi, 1983; Seed, 1979; Seed et al., 1983, 1985). "Simplified Procedure" blossomed from this study, which, with the accumulated data and others authors' contributions, started to be a very powerful and most trustable framework to assess liquefaction potential.

The CSR, soil liquefaction resistance under earthquake shaking, is determined as expressed above, in equation 3.1, and was a simplified procedure for evaluating the induced shear stress in a soil deposit during an earthquake (Seed and Idriss, 2004). To determine the CSR Seed and Idriss (2004) admitted a soil column, above a soil element at depth h, behaving as a rigid body, being the maximum shear stress on the soil element expressed by:

$$\tau_{mass} = \gamma \times h \times \frac{a_{max}}{g} \tag{3.6}$$

where a_{max} is the maximum ground surface acceleration and γ is the unit weight of the soil.

As for the soil SPT resistance, $(N_1)_{60}$, is determined in the USA according to the d60, and in Europe according to eur (1997).

Eurocode 7, part 3 – Geotechnical design assisted by field tests – covers, in Chapter 5, the determination of the standard penetration resistance of the soil. As it is widely known, N, is the number of blows necessary to achieve a dynamic penetration of the sampler of 300 mm, by dropping a hammer of 63,5 kg mass from a height of 760 mm. This test is performed in two phases, the first one by penetrating the sampler, twice, 150 mm, recording the number the number of blows. The number of blows required to penetrate 300 mm, shall not pass 50, registering which of the both occurs first.

After performing the test, $(N_1)_{60}$ is determined by correcting the blow count N in relation with the energy delivered to the drive rods to a reference energy ratio of 60%, the effect of the overburden stress and the energy losses of the rods:

$$(N_1)_{60} = \frac{ER_r}{60} \times \lambda \times C_N \times N \tag{3.7}$$

where ER_r is the energy ratio of the specific test equipment, λ is the correction factor for energy losses due to the rod length in the sand (given in table 5.1 of Eurocode 7 – part 3), C_N is the correction factor for the effective overburden pressure in the sand (given in table 5.2 of Eurocode 7 – part 3).

In USA, (d60) is the practice which regulates the *"normalized resistance of sands to the penetration of a standard sampler driven by a standard energy for estimating soil liquefaction potential during earthquakes"*. This practice, limited for cohesionless soils, mostly saturated, does not include procedures for the determination of the liquefaction potential for gravelly soils and lithified soils or fine grained soils. This document only provides a set of instructions for performing one or more specific operations and energy adjustments for SPT test (d60).

Similarly to Eurocode 8, penetration resistance, N, is expressed as the number of hammer blows required to drive the sampler 30 cm distance and shall be normalized to an estimated energy deliver and to an effective overburden stress of 100 kPa. This practice adverts that if the drilling method created disturbance, an alternate method should be performed (d60).

To assess if a soil is liquefiable or not, after determining the $(N_1)_{60}$, it should be compared with the collected data history and analysed, for a certain CSR, following the boundary proposed on the workshop NCEER/NSF 1997, representative of a Magnitude 7.5 earthquake. It is necessary to point out that a data limitation does not offer appropriates boundaries for different earthquake magnitudes. Nevertheless a magnitude scaling factor, MSF, was suggested by Seed and Idriss (1982), and constant corrections have been proposed by various investigators, in order to adjust the induced CSR during earthquake magnitude M to an equivalent CSR for an earthquake magnitude M=7.5. A more detailed study over CSR correction factors is presented in section 4.4.

The CRR-$(N_1)_{60}$ relation put forth by Seed et al. (1984) for sands, developed over 125 cases of liquefaction/ non-liquefaction in 19 earthquakes, of which 65 cases concern to sands with fines, suffered minor adjustments till the workshop NCEER/NSF 1997 (Figure 3.4). Rauch (1998), on a personal communication to Youd et al. (2001), approximated the clean-sand (i.e. with a Fines Content (FC) $\leq 5\%$) base curve by the following equation which remains, according to Seed et al. (2001) as the one suggested to routine engineering calculations:

$$CRR_{7.5} = \frac{1}{34-(N_1)_{60}} + \frac{(N_1)_{60}}{135} + \frac{(N_1)_{60}}{[10\times(N_1)_{60}+45]^2} - \frac{1}{200} \tag{3.8}$$

However, more recently Seed et al. (2003) described this relationship as "dated" as it does not include *"field case history data from seismic events that occurred since 1984"*. Plus it determination did not use a probabilistic method, providing some uncertainty (Seed et al., 2003). Bayesian methods are pointed as a method to grant a reduced uncertainty and it is suggested that more studies should be developed in order to achieve a better resolution. Pursuing a new curve, Idriss and Boulanger (2004) revised the boundary curve, including also the study of the revised case history data set complied by Cetin et al. (2000), and suggested the following expression:

$$CRR = exp\left[\frac{(N_1)_{60cs}}{14.1} + \left(\frac{(N_1)_{60cs}}{126}\right)^2 - \left(\frac{(N_1)_{60cs}}{23.6}\right)^3 + \left(\frac{(N_1)_{60cs}}{25.4}\right)^4 - 2.8\right] \tag{3.9}$$

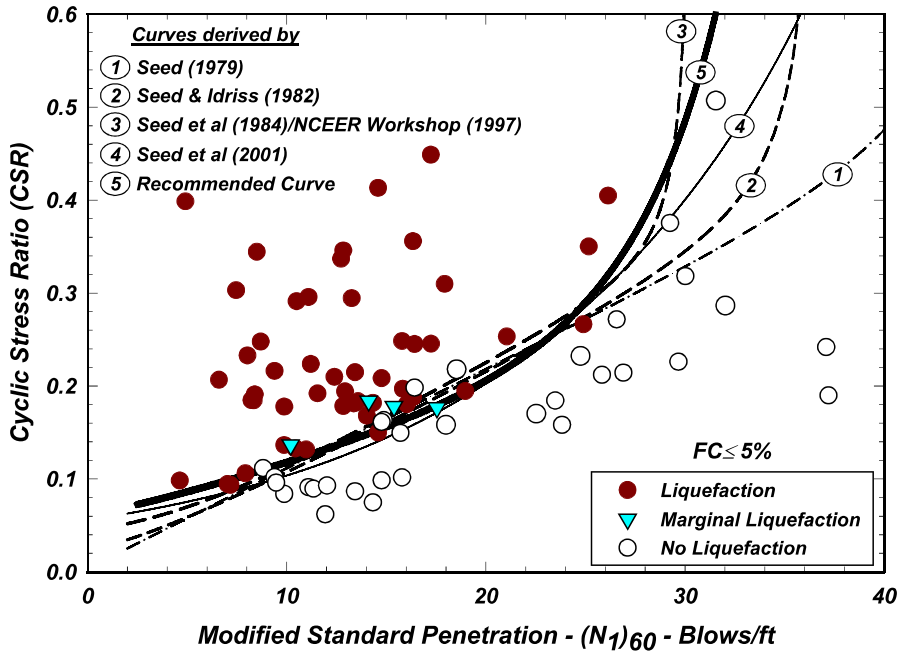


Figure 3.4: Curves relating CRR to $(N_1)_{60}$ published over the past 24 years for clean sands, including the one currently accepted for geotechnical design (curve 4 proposed by Seed et al. (2001)) and the recommended curve by Idriss and Boulenger in 2004 for M=7.5 and $\sigma'_{v0} = 1$ atm (Idriss and Boulanger, 2004).

$(N_1)_{60cs}$ is the SPT penetration resistance adjusted to an equivalent clean sand and can be determined, as suggested by (Idriss and Boulanger, 2004).

When in the presence of cohesionless fines in sands, the increasing resistance to liquefaction moves the boundary curve to the left. Thus a re-evaluation of the SPT-based procedures was also developed by Cetin et al. (2000) and summarized in Seed et al. (2001), in order to give a better consistency for liquefaction potential assessment of soils with a FC>5%. As the current practice still relies, and according to the workshop NCEER/NSF 1997, following the corrections suggested by Idriss and Seed, the SPT penetration resistance adjusted to an equivalent clean sand, to substitute in equation 3.7, can be determined as:

$$(N_1)_{60cs} = \alpha + \beta\,(N_1)_{60} \tag{3.10}$$

$$FC \leq 0.5\% \qquad \begin{matrix} \alpha = 0 \\ \beta = 1 \end{matrix} \tag{3.11}$$

$$0.5\% \leq FC \leq 35\% \qquad \begin{matrix} \alpha = exp\left(1.76 - 190/FC^2\right) \\ \beta = \left(0.99 + FC^{1.5}/100\right) \end{matrix} \tag{3.12}$$

$$FC \geq 35\% \quad \begin{matrix} \alpha = 5 \\ \beta = 1.2 \end{matrix} \tag{3.13}$$

Unless for the large data that provides a much more accurate and reliable SPT-based correlations, the SPT presents the disadvantage of having to be performed every 300 mm, being a discontinuous test which might miss liquefiable strata between deposits.

3.2.2.2 Method based on CPT test

CPT test is an alternative/ complementary in situ test to perform for evaluating the liquefaction resistance of the soil. CPT test has numerous advantages when compared to SPT test. Despite not providing a large number of data set case histories to assess liquefaction hazard, CPT is a more efficient, consistent and repeatable test than SPT, as borehole is not required and the variability between equipment and operators does is smaller (Youd et al., 2001). Nevertheless, the best advantage relies on the nearly continuous profile of penetration resistance which is developed for stratigraphic interpretation, not missing any possible liquefiable strata.

As advised in Eurocode 8, when an evaluation of the liquefaction potential is required throughout the CPT test results, no correlations with SPT test shall be made, but rather an evaluation following the existent CPT-based procedures.

The CPT test is performed by pushing vertically into the soil a penetrometer constituted by a series of rods and a penetrometer tip, at a constant rate of approximately 20 ($\pm$5) mm/s, thus allowing the measurement of both penetration resistances of the cone as well as the local friction along the cylindrical shaft through sensing devices. The procedures to calculate both cone resistance, q_c, as well as the local unit side friction, f_s, are disposed in Chapter 3 of the Eurocode 7 – part 3. However for liquefaction potential purpose only the cone resistance is needed.

The CPT test, such as SPT, requires the normalization of the cone resistance, q_{c1N}:

$$q_{c1N} = C_Q \left(q_c / P_a\right) \tag{3.14}$$

$$C_Q = \left(P_a / \sigma'_{v0}\right)^n \tag{3.15}$$

where C_Q is the factor of normalization of the cone resistance, P_a is the atmospheric pressure (1 atm), n is an exponent which varies with the type of the soil.

Several case history data, including those compiled by Stark and Olson (1995) and Suzuki et al. (1995), allowed Robertson and Wride (1997) to establish, empirically, the curve of CRR for

clean sands (FC $\leq$ 5%) as a function of dimensionless, corrected and normalized CPT resistance q_{c1} (Figure 3.5). Similarly to the SPT, CPT-based curve separates regions that liquefied from non-liquefied regions for an earthquake magnitude of 7.5, and is given by the following equation:

$$\begin{array}{ll} if\,(q_{c1N})_{cs} < 50 & CRR_{7.5} = 0.833 \times [(q_{c1N})_{cs}/1] + 0.05 \\ if 50 \leq (q_{c1N})_{cs} < 160 & CRR_{7.5} = 93 \times [(q_{c1N})_{cs}/1]^3 \end{array} \tag{3.16}$$

$(q_{c1N})_{cs}$, the clean-sand cone penetration resistance normalized to approximately 100 kPa, is corrected for grain characteristics by K_c as defined by the following relationships:

$$(q_{c1N})_{cs} = K_c q_{c1N} \tag{3.17}$$

$$\begin{array}{ll} if I_c \leq 1.64 & K_c = 1 \\ if I_c > 1.64 & K_c = -0.403 I_c^4 + 5.581 I_c^3 - 21.63 I_c^2 + 33.75 I_c - 17.88 \end{array} \tag{3.18}$$

where I_c, soil behaviour type index, is defined by

$$I_c = \left[(3.47 - \log Q)^2 + (1.22 + \log F)^2\right]^{0.5} \tag{3.19}$$

$$Q = [(q_c - \sigma_v)/P_a]\left[P_a/\sigma_v'\right]^n \tag{3.20}$$

$$F = [f_s/(q_c - \sigma_v)]\,100\% \tag{3.21}$$

where Q is dimensionless CPT tip resistance, σ_v is the vertical confining stress, σ_v' is the vertical effective confining stress, f_s is the sleeve resistance and P_a is the atmospheric pressure (=100 kPa).

As reflected by Seed et al. (2003), similarly to the SPT, CPT-based curves are in progression, now basing on a much more reliable and amount of case history data and using much stronger statistical tools, such as Bayesian methods. The re-evaluation proposed by Idriss and Boulanger (2004), which can be seen in Figure 3.5, for cohesionless soils (FC $\leq$ 5%) is expressed as:

$$CRR = exp\left[\frac{q_{c1N}}{540} + \left(\frac{q_{c1N}}{67}\right)^2 - \left(\frac{q_{c1N}}{80}\right)^3 + \left(\frac{q_{c1N}}{114}\right)^4 - 3\right] \tag{3.22}$$

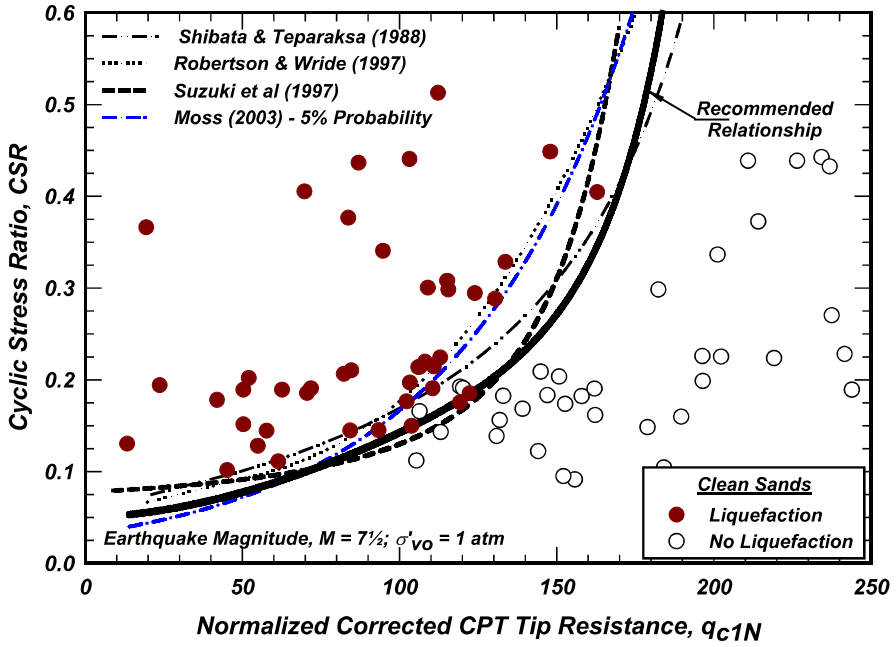


Figure 3.5: Curves relating CRR to q_{c1N} proposed by various investigators for clean, including the one currently accepted for geotechnical design design (curve proposed by Robertson and Wride (1997)) and recommended curve by Idriss and Boulanger (2004) for M=7.5 and $\sigma'_{v0} = 1$ atm.

It should be also pointed out that the determination of q_c, to assess soil liquefaction potential, needs to be corrected using a spherical expansion approach for contractive loose to medium dense sands and a cylindrical cavity expansion approach for dilatant dense sands (Seed and Olsen, 2006 adapted from Gupta, 2007). The implementation of this corrections are required in order to not overpredict the cone penetration resistance, q_c, due to the substantial increase of the horizontal stresses in the soil around the cone and the cone rodes during the penetration process.

Furthermore soil strength penetration, obtained from SPT or CPT, depends on soils properties, however, as pointed out by Youd et al. (2001), for a certain specific value of the normalized strength, the only difference between the soils prone to liquefaction and the stable ones relies exclusively on the fines content.

3.2.2.3 Method based on DMT test

The flat dilatometer test DMT allows the determination of the in situ strength and deformation properties of fine grained soils, clays, silts and sands, using a blade shaped probe. The blade provided with a thin expandable circular steel membrane mounted flush on one face allows the measurement of the pressure necessary to cause a displacement of 1.10 mm of the soil. A thrust machine is required to push the blade vertically with a penetration rate between 10 and 30 mm/s.

This device stands out not only for allowing the determination of a reliable shear modulus but also because it causes less distortion than the other penetration tests. Plus the arching effect is nearly nonexistent, meaning that the stiff soil ring created around the probe almost does not exist, resulting in a higher sensitivity to σ_h.

Unlike the other penetration devices, DMT test results gives a parameter, K_D, sensitive to stress/ state history, pure prestraining, aging, cementation and structure. This higher sensitivity is an advantage when comparing with the other in situ tests, appearing as an alternative to evaluate the liquefaction resistance, as suggested by Marchetti (1982).

Plus the DMT test can predict, with a certain precision, the relative density in situ, which is, like CPT, a deniable advantage over other in situ tests (Tanaka and Tanaka, 1998). Knowing the relative density and the in situ stress state, the state parameter can be obtained, supplied by some laboratory triaxial tests, and used to also assess the soil liquefaction resistance (Boulanger and Idriss, 2004). The state parameter consists in a good parameter to characterize the geomechanical behaviour of the soil, combining the effects of both relative density and stress level in a rational way (Monaco and Marchetti, 2007). Such a relation between K_D and the state parameter (Figure 3.6), which is a parameter very used in soils constitutive modelling, having a strong physical basis, supports the use K_D to assess soil liquefiability. As can be observed from Figure 3.6 the state parameter, ε_0 (ψ is also the nomenclature used for state parameter by other authors), depends on the type of soil. Despite an average expression is represented in the following Figure. The state parameter approach is discussed in the subsection that follows for laboratory studies.

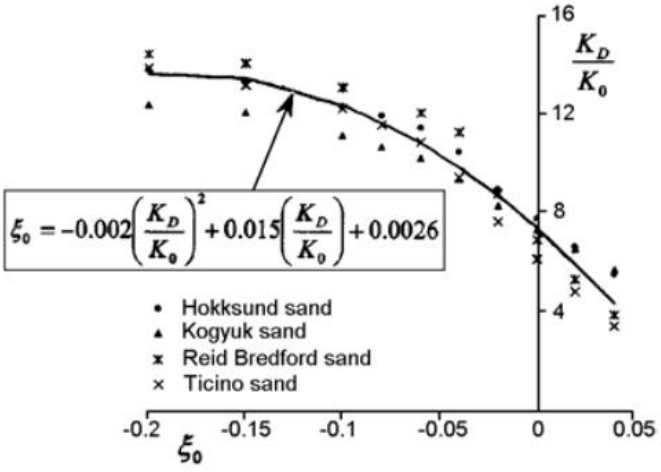


Figure 3.6: Average correlation for deriving the in situ state parameter using the normalized dilatometer horizontal index K_D/K_0 obtained by the DMT tests (Yu, 2006)

The K_D parameter, following the Eurocode 7 procedures, might be determined according to the following equations:

$$K_D = (p_0 - u_0)/\sigma'_{v0} \tag{3.23}$$

$$p_0 = 1 - 05\,(P_A + \triangle P_{A;avg} - Z_m) - 0.005 p_1 \tag{3.24}$$

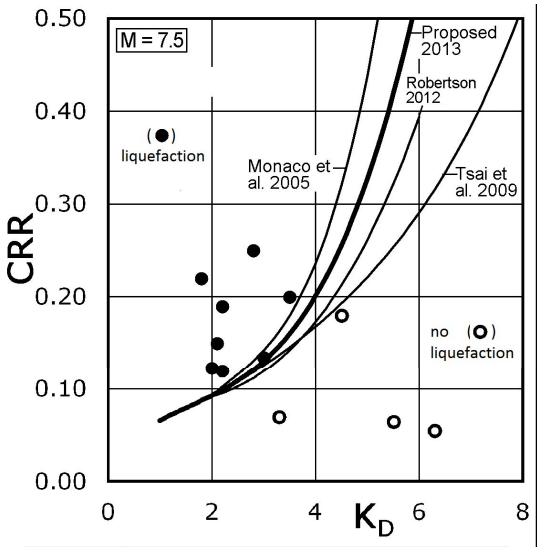
$$p_1 = P_B - \triangle P_{B;avg} - Z_m \tag{3.25}$$

where u_0 is the in situ pore water pressure prior to blade insertion, σ'_{v0} is the in situ vertical stress, p_0 is the soil pressure against the membrane when it is flush with the blade, p_1 is the soil pressure against the membrane when its centre is expanded 1.10 mm, P_A is the pressure that must be applied to the back of the membrane to expand its centre 0,05 mm in soil, P_B is the pressure that must be applied to the back of the membrane to expand its centre 1,10 mm in soil, $\triangle P_A$ and $\triangle P_B$ is a membrane calibration pressure and Z_m the gauge pressure deviation from zero when venting the blade to atmospheric pressure.

The latest CRR-K_D correlation (Figure 3.7), is expressed by the following equation, which separates regions that liquefied from non-liquefied regions:

$$CRR = 0.0038K_D^3 - 0.0176K_D^2 + 0.0532K_D + 0.0264 \tag{3.26}$$

was formulated by Marchetti (2014) as a result of the previous proposed correlations by Monaco et al. (2005) and Robertson (2012), combined with a refined study and comparison over the CPT liquefaction results.



Monaco et al 2005	$0.0107\ K_D^3 - 0.0741\ K_D^2 + 0.2169\ K_D - 0.1306$
Tsai et al. 2009	$\exp\left[\left(\frac{K_D}{8.8}\right)^3 - \left(\frac{K_D}{6.5}\right)^2 + \left(\frac{K_D}{2.5}\right) - 3.1\right]$
Robertson 2012	$93\,(0.025\ K_D)^3 + 0.08$
Proposed 2013	$0.0038\ K_D^3 - 0.0176\ K_D^2 + 0.0532\ K_D + 0.0264$

Figure 3.7: Average correlation for deriving the in situ state parameter using the normalized dilatometer horizontal index K_D/K_0 obtained by the DMT tests (Yu, 2006)

Aiming to predict the liquefaction resistance of soils with fines, Marchetti (2014) developed a fines correction to obtain an equivalent clean sand K_D. Basing on the correlation among the material

index Id, for the DMT test, and the material index I_c, for the CPT test:

$$I_c = 2.5 - 1 - 5\log(I_d) \tag{3.27}$$

Marchetti (2014) also demonstrated that there is an imperfect match between the K_d and q_{c1N} parameters, as the first one can predict accurately the stress/strain history, unlike the cone penetration resistance.

3.2.2.4 Method based on stress waves velocities measurement

- Shear wave velocity, V_S

  The major inherent disadvantages of SPT and CPT tests, and also, but less DMT test, are the creation of complex boundary conditions, difficult to interpret (Huang and Chang, 2011; Moss et al., 2006). These conventional in situ tests are preferred over nonintrusive seismic methods as, beyond having a strong background support based on the immense data accumulated, their use to assess liquefaction potential are based on the correlation of a plastic strength parameter, $(N_1)_{60}$, q_{c1N} or K_d, with CRR, which is also a plastic strength parameter. Such intrusive, in situ, techniques, which create plastic deformations on the soil, may change the real soil state condition. On the other hand seismic field methods, nonintrusive methods, which are also being, successfully, applied for the assessment of liquefaction potential, by correlating the normalized shear wave velocity V_{S1}, which is a small strain parameter, with the CRR, a large strain parameter, became somehow a little contested (see table 3.1) (Youd et al., 2001). The use of V_S for liquefaction-resistance evaluation is also contested for not providing a sample for soil characterization and because it might not detect thin, low V_{S1}, strata (Youd et al., 2001). Nevertheless, and as cited above, while working under undrained conditions the presumption is valid as the volumetric strain is zero, thus , which led, as stated by (Roy, 2005) to predictable profiteering.

  Nonintrusive seismic field methods beyond not disturbing the in situ soil state, are also a time and cost-saving technique, as drilling is not necessary. Their relative quick execution results in the possibility of covering a large area for further analysis, plus it can be particularly useful for sites underlain by difficult to penetrate strata (Andrus and Stokoe, 1997; Stokoe et al., 2004). Surface reflection method, surface refraction method and surface-wave method are examples of nonintrusive seismic methods (Stokoe et al., 2004).

  Nonetheless there are also intrusive seismic methods, such as downhole, crosshole, seismic cone penetration, seismic dilatometer penetration or suspension logger.

  Despite geophysical techniques not being of simple interpretation, they become a very prominent way to estimate the liquefaction potential as they allow direct measurement of

Table 3.1: Changes in soil behaviour with strain and respective adapting interpretation model (adapted from Ishihara (1996)).

Shear strain	10^{-6}	10^{-5}	10^{-4}	10^{-3}	10^{-2}	10^{-1}
Phenomenon	**Wave propagation, Vibrations**		Differentiate settlements, Cracks		Sliding, Compaction, Liquefaction	
Mechanical characteristics	**Elastic**		Elasto-Plastic		Collapse/ Failure	
Properties	**Shear modulus, Poisson coefficient, Damping**				Friction angle, cohesion	
Soil behaviour adapting model	**Linear elastic model**		Linear equivalent model		Non-linear cyclic model	

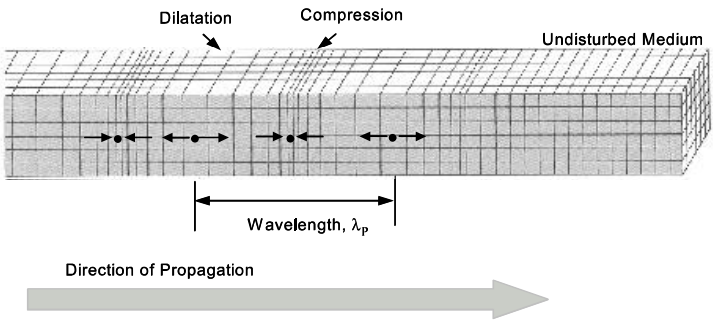
mechanical properties in situ. The small shear-strain modulus, (G_0), which might be calculated from the V_S waves measurement, is in practical terms independent of the type of loading, number of loading cycles, strain rate and stress/ strain history, being a fundamental parameter of dynamic properties of the ground (Viana da Fonseca et al., 2011a). The small-shear strain stiffness of a soil reflects the nature of interparticle contacts such as the Hertzian deformation of contacting smooth spherical particles (Cho et al., 2006).

Moreover, beyond being influenced by void ratio, effective confining stress, it has been recently proved that this property is very sensitive to structure and ageing (Moss and Schneider, 2011; Viana da Fonseca et al., 2011a). Plus in situ V_S waves might be compared with laboratory test results, with the use of bender-extender elements implemented on triaxial apparatus, which will facilitate calibrations in between (Andrus and Stokoe, 1997).

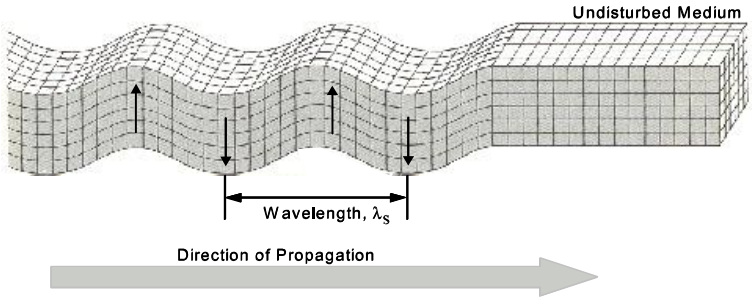
The main disadvantage of this technique relies on it less sensitivity to the relative density (or compact index I_D) of the soil, which is the major important factor reflecting on sands undrained cyclic response, when compared with the $(N_1)_{60}$, q_{c1N} or K_d parameters. Idriss and Boulanger (2004) compared the capacity of changing response by increasing the relative density of a soil from 20% to 80%. While the SPT blow count changed by a factor of 7.1, the CPT tip resistance by a factor of about 3.3, the Vs only changed by a factor of 1.4 basing on available correlations. Thus Idriss and Boulanger (2004) suggested an improvement on the V_s-based correlations, as well as an assessment of their accuracy basing on the CPT and SPT-based correlations.

Either in the field, as in the lab, S wave is generated artificially and the wave propagation is recorded. The distance divided by wave travel time is the S-wave velocity, V_S. S waves have particle motion perpendicular to the direction of the wave propagation (Figure 3.8).

Being stress waves, both P and S waves, non-dispersive in a uniform elastic medium, thus independent on the frequency, it interpretation and measurement can be performed assum-



a. Compression (P) wave



b. Shear (S) wave

Figure 3.8: Body waves propagation mode within a uniform, infinite medium (after Bolt (1976), adapted from Stokoe et al. (2004)).

ing the first-wave arrival method. Unlike in the laboratory, where tested samples are relatively homogeneous, stratigraphy and heterogeneity that exist in the field cause frequency-dependency of stress waves, being it interpretation not so straight forward.

According to Youd et al. (2001), (and after Kayen et al. (1992); Sykora (1987); Robertson et al. (1992)), the determination of the normalized shear wave must take into account the polarization of the propagation wave along the principal stress directions. Thereby shear wave velocity depends on the principal stress and on the direction of the propagated wave.

$$V_{S1} = V_{Sfield} \left(\frac{P_a}{\sigma'_{v0}} \right)^{0.25} \tag{3.28}$$

where P_a is the earth pressure (1 atm). This equation assumes a constant coefficient of earth pressure K_0 of 0.5, approximately (Youd et al., 2001). According to Belloti et al. (1996), V_S can be expressed by the following equation:

$$G_{max} = A' F(e) \left(\sigma'_m \right)^n \tag{3.29}$$

with

$$G_{max} = \rho V_s^2 \tag{3.30}$$

being

$$V_s = A^{'} F(e) \left(\sigma_m^{'}\right)^{0.25} = A^{'} F(e) \left[(1+2k_0)\,\sigma_v^{'}/3\right]^{0.25} \tag{3.31}$$

where $A^{'}$ is a constant material, n is a constant who varies with the type of soil and the level of shear deformation, K_0 is the effective earth pressure ratio, $\sigma_m^{'}$ is the medium confining stress, and $F(e)$ is a void ratio function, generally adopted as $F(e) = 1/\left(0.3+0.7e^{(}2)\right)$.

The assessment of soil liquefaction potential through the use of small-strain shear wave velocity was successfully achieved by Andrus and Stokoe (1997), throughout the validation, with history case data points, of a procedure developed mainly based on analytical and laboratory studies (Figure 3.9). Regardless it study was also followed by other authors such as Stokoe et al. (1988), Tokimatsu et al. (1991) and Robertson et al. (1992), among others.

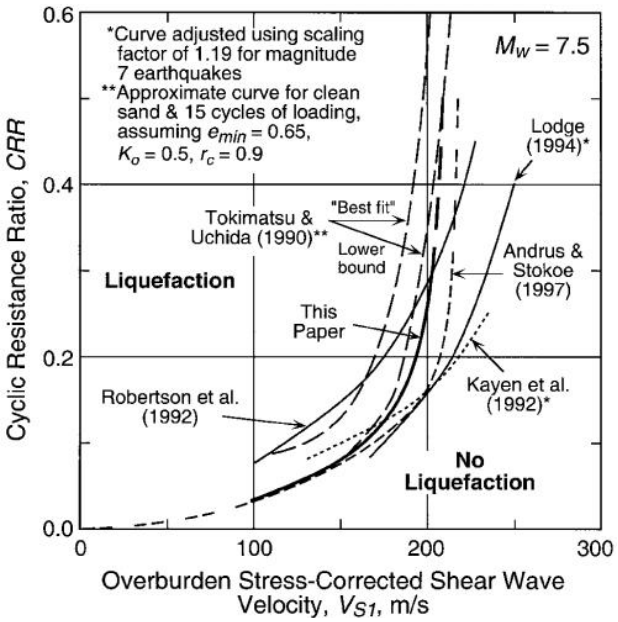


Figure 3.9: Curve recommended for calculation of *CRR* from V_{s1} measurements by Andrus and Stokoe (2000).

The boundary whom separates the liquefaction region from the not liquefaction region is given by the line defined as the limit ratio of the cyclic resistance (CRR). Andrus and Stokoe

(1997) proposed the following relationship basing on field performance data from 20 earthquakes and 50 measurements developed over uncemented, Holocene-age soils with 5% or less of fines content:

$$CRR = a\left(\frac{(V_{s1})_{csa1}}{100}\right)^2 + b\left(\frac{1}{V_{s1}^* - (V_{s1})_{csa1}} - \frac{1}{V_{s1}^*}\right) \tag{3.32}$$

where V_{s1}^* is the maximum limit for V_{s1} for liquefaction occurrence and a and b are both curve adjustment parameters (0.022 e 2.8, respectively). V_{s1}^* varies linearly between 200 m/s and 215 m/s for soils with a fines content (FC) between 5% and 35%, while for soils with FC < 5% the value is of 215 m/s. The first component of the previous equation, initially proposed by Dobry (1996), is based on a modified relationship, of the equation 3.33, between V_{s1} and *CRR* for an average cyclic deviatoric stress. While the second term is a hyperbola with lower values for lower values of V_{S1}, and higher values as the V_{S1} approaches V_{S1}^* (quoted from Youd et al. (2001)). The equation expressed above arises from semi-theoretical considerations as a result of the existent correlation between the *CSR* and the shear waves velocities:

$$CSR = \frac{\tau_{av}}{\sigma_v'} = f(\gamma_{av})\, V_{s1}^2 \tag{3.33}$$

where $f(\gamma_{av})$ is a function of the average cyclic strain, γ_{av}, equal to $f(\gamma_{av}) = (\rho/P_a)\,\gamma_{av}\,(G/G_{max})_{\gamma_{av}}$.

On its turn the equivalent young and clean soil value of V_{s1} is determined, according to Andrus et al. (2004), as it follows:

$$(V_{s1})_{csa1} = K_{a1}\,(V_{s1})_{cs}\,K_{cs}V_{s1} \tag{3.34}$$

where $(V_{s1})_{csa1}$ is the equivalent V_{s1} for clean young sands, $(V_{s1})_{cs}$ is the equivalent V_{s1} for clean sands not corrected from the age effect, K_{cs} is the correction factor which accounts for the fines content and K_{a1} is the correction factor which accounts with the age of the soil:

$$\begin{array}{ll} if FC \leq 5\% & K_{cs} = 1,0 \\ if 5\% < FC \leq 35\% & K_{cs} = 1,0 + (FC-5)\,T \\ if FC \geq 35\% & K_{cs} = 1,0 + 30T \end{array} \tag{3.35}$$

$$T = 0,009 - 0,0109\left(\frac{V_{s1}}{100}\right) + 0,0038\left(\frac{V_{s1}}{100}\right)^2 \tag{3.36}$$

where FC is the fines content.

(Roy, 2005) during his study also found dependency between the correlation $CRR - V_{s1}$ with the fines content and aging of the soil.

After some contestation in the 1996 NCEER workshop, Andrus and Stokoe (2000) studied seven other proposed curves, which can be seen in Figure 3.9, for calculation of CRR from V_{s1} measurements concluding that it dispersion was due to different levels of conservatism assumed with limited data and the use of different methods for selecting the site and the assumption of different correction factors. These conclusions strengthened V_s-based correlation curves to assess soil liquefaction potential.

Moreover, as demonstrated by Andrus et al. (2004), the V_s evaluation methods provide similar predictions of liquefaction resistance, as the CPT and SPT method, when the data lies on the implied curve. Plus the V_s method provides a more conservative method (see Figure 7. published by Andrus et al. (2004)).

- Compression wave velocity, V_p

  In the measurement of stress waves in situ, the measurement of the P wave velocity becomes prominent in the determination of the degree of saturation of cohesionless, not very structured soils. As it is widely known liquefaction is a process that is triggered in soils mostly saturated, thus, being the CRR function of the degree of saturation of the soil becomes necessary to assess it saturation conditions. Ishihara (2001), Yang and Sato (1998), Yang and Sato (2001), Vieira Faria et al. (2006) and Yang (2002c) observed that, for a specific CSR, the number of cycles required to trigger liquefaction is substantially less with a decreasing degree of saturation. Assuming the water as an incompressible element, when sheared under undrained conditions,if beyond water there is also some air, the air element, when sheared under undrained conditions will compress, decreasing the volume of the soil sample and whereby increasing CRR.

  In the field the soil is obviously saturated when below the water table. The position of the water table might be determined by measuring the P wave velocity that shall be around 1500 m/s, which corresponds to the speed of a compression sound wave in water.

  For degrees of saturation below 99%, the velocity of P waves is essentially controlled by the stiffness of the soil skeleton. However, as can be observed from Figure 3.10, when the degree of saturation is approximately 100%, the P wave velocity is controlled by the water (Stokoe et al., 2004).

  For a homogeneous, isotropic material, compression and shear wave velocities are related through the Poisson's ratio, υ:

$$V_P = V_S \sqrt{\frac{1-\upsilon}{0.5-\upsilon}} \tag{3.37}$$

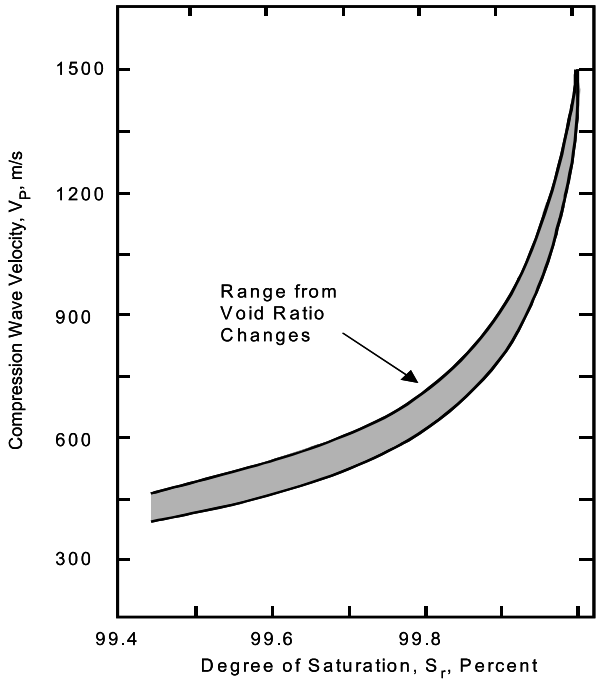


Figure 3.10: Typical variation in compression wave velocity with degree of saturation changing from 99.4 to 100% for sand (after Allen et al. (1980), and adapted from Stokoe et al. (2004)).

Besides allowing the determination of the saturation degree and of the stiffness of the soil skeleton, for soils underlying the water table, the velocity of P and S waves, respectively, also provides the achievement of important parameters for Geotechnical design, such as M, B, G and E, the constrained, bulk, shear and Young's moduli, respectively:

$$V_P = \sqrt{\frac{M}{\rho}} = \sqrt{\frac{B+4/3G}{\rho}} = \sqrt{\frac{E}{\rho}\frac{(1-\upsilon)}{(1+\upsilon)(1-2\upsilon)}} \tag{3.38}$$

$$V_s = \sqrt{\frac{G}{\rho}} \tag{3.39}$$

where ρ is the mass density.

3.2.3 Theoretical Background On Stiffness At Very Small Strains

As explained before stress wave velocities are responsible for very small motions of particles inside a soil element. These movements are so small that the soil behaviour is assumed elastic and the stress wave velocities might be used to determine the elastic stiffness of the soil such as the elastic shear modulus of the soil (G_0), expressed by equation (3.29), and the elastic constrained modulus, (M_0), by knowing the shear and compression waves velocities, respectively.

Factors such as confining pressure, void ratio, temperature, porosity, anisotropy, saturation, etc, affect both shear wave velocity and the elastic shear modulus (G_0). Hardin and Richard (1963) were pioneers on this research and, while studying the major factors affecting the shear wave velocity, they found shear wave velocities varying with the initial confining pressure raised to an exponent of 1/4. If this exponent was suitable for all range of stresses for the angular sand, for Ottawa rounded sand it applicability was limited to stresses higher than 96 kPa. For confining pressures lower than 96 kPa the exponent found to be most suitable was 3/10. During their research the authors also found shear wave velocity to decrease with increasing void ratio apart grains size, as can be seen in Figure 3.11.

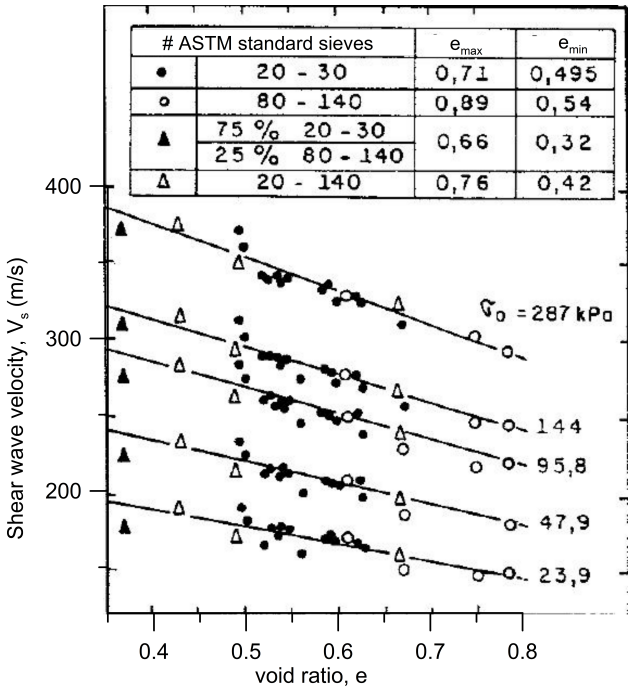


Figure 3.11: V_s as function of the void ratio and confining pressure – Ottawa sand (Hardin and Richard, 1963).

Later, Hardin and Black (1969) found G_0 to be independent of anisotropic consolidation, while Yu and Richard (1984) and Alarcon-Guzman et al. (1988) noticed G_0 to be lower for anisotropic consolidated sands. However it was Roesler (1979) who firstly showed G_0 not being dependent on the medium confining pressure, but on each of the individual components of confining pressure. Furthermore (Stokoe et al., 1985) found shear wave velocity to be independent on the third principal confining pressure. However, more recently, Li and Zeng (2014) discovered fabric anisotropy to affect G_{max} or G_{vh} parallel to the bedding plane, effect amplified under anisotropic consolidation. On its turn this effect is mainly associated to the shape which controls the fabric evolution. During this research the authors also found Ottawa sand, the one with highest sphericity, to exhibit the highest shear wave velocity.

Looking closely to Figure 3.12a it is difficult to perceive the influence of the relative density on the effect of the induced anisotropy for distinct relative densities. However in Figure 3.12b, comparing the Toyoura sand prepared with Dr=80% and 40% it can be assessed that the anisotropy effect is influenced by the relative density in a non-linear way difficult to perceive.

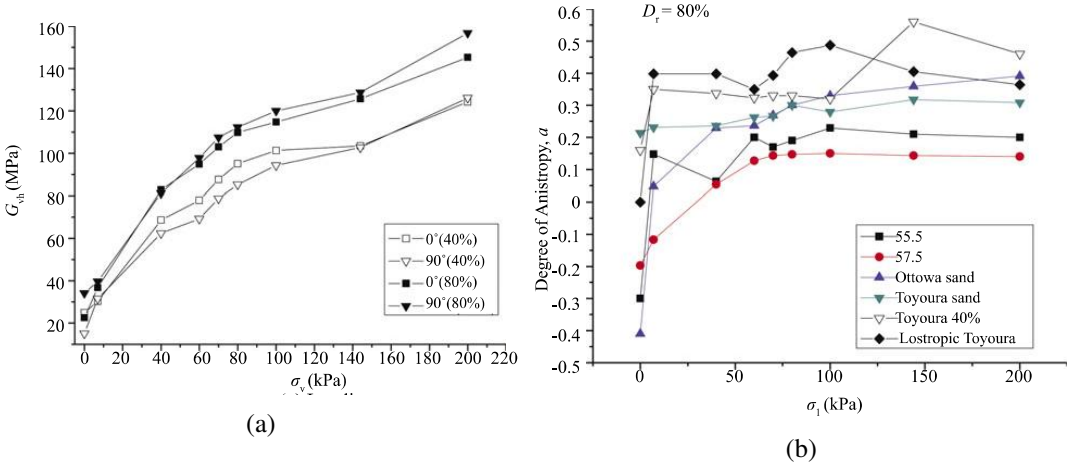


Figure 3.12: (a) G_{vh} of 0 deg and 90 deg deposition angles measured for Toyoura sand; (b) Relationship between degree of anisotropy and axial stress (Li and Zeng, 2014).

Aiming to achieve a unified correlation between G_0 and the factors affecting the soil response Hardin and Black (1969) proposed an empirical equation to estimate G_0 basing on a set of resonant column tests performed within the small-strain domain. This equation was then adapted by Hardin and Drnevich (1972) and Hardin (1978) and Kokusho (1980) and Lo Presti (1995), among other authors Table 3.2. Nonetheless the formula took the form proposed by Hardin and Blandford (1989) in function of the most important parameters:

$$G_{0ij} = S_{ij} \times F(e) \times OCR^k p_a^{\left(1-n_i-n_j\right)} \times \left(\sigma_i^{'}\right)^{n_i} \times \left(\sigma_j^{'}\right)^{n_j} \tag{3.40}$$

where $\sigma_i^{'}$ and $\sigma_j^{'}$ principal effective stress in the wave propagation direction, i and wave polarization direction, j; k is an empirical exponent of the overconsolidation ratio OCR depending of the plasticity index, IP; $F(e)$ is a void ratio function, S_{ij} is a non-dimensional material constant reflecting the fabric and structure of the soil; n_i and n_j are empirical stress exponents or indices and pa represents a reference stress (which is often considered equal to the atmospheric pressure, 100 kPa). The empirical exponents, n_i and n_j, are usually assumed the same for sandy soils (adapted from Ferreira, 2008).

The void ratio function, $F(e)$, have a lot of reference expressions. Despite, only few were addressed during this work and might be consulted in table 3.2.

As can be assessed the equation above does not have a parameter which takes into account the effect of the induced anisotropy beyond the consideration of the vertical confining pressure raised to

Table 3.2: Reference void ratio functions.

General expression	References
$\frac{(2.17-e)^2}{1+e}$	Hardin and Richart, 1963; Kokusho, 1980
$\frac{(2.973-e)^2}{1+e}$	Hardin and Drnevich, 1972
$\frac{1}{0.3+0.7\times e^2}$	Hardin, 1978
e^{-x}, with x=1.3	Lo Presti, 1995

an exponent which is often assumed the same as the exponent adopted for the horizontal confining pressure.

Finally if for sandy soils the shear wave velocity is independent on the grain size, the presence of fines and the coefficient of non-uniformity influences G_0, for soils with fines. Thus, for these soils, Iwasaki and Tatsuoka (1977) proposed the following expression to determine G_0:

$$G_{max} = A(\gamma) \times B \times F(e) \times \sigma_0^{n(e)} \tag{3.41}$$

where A and n are function of the soil shear strain, γ, and B is a parameter function of the percentage of the fines content (Figure 3.13).

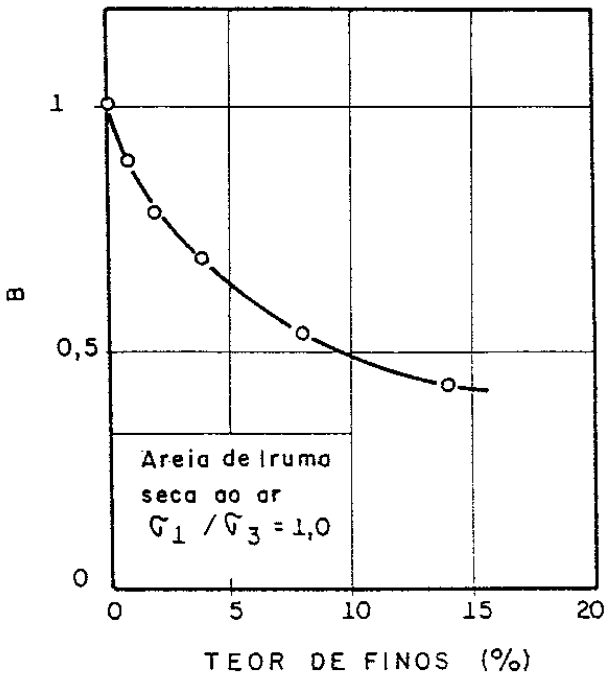


Figure 3.13: B parameter as function of the fines content (Iwasaki and Tatsuoka, 1977).

3.2.4 Procedures Developed From Laboratory Studies

Despite the term spontaneous liquefaction being attributed to Terzaghi and Peck (1948), its effects were first presented by Casagrande (1936) and it laboratory evaluation initiated later on, by Seed and Lee (1966), Lee and Seed (1967) and Lee and Fitton (1969). This first approach began by testing, under undrained conditions, saturated sand samples, consolidated in triaxial apparatus, under appropriate stress conditions and alternating shear loads of controlled magnitudes and frequencies.

Similarly to in field conditions, liquefaction potential frameworks are built with input variables, relating an action index, CSR, with a resistance index usually expressed by large or small-strain parameter, determined, obviously, through laboratory testing.

The CSR is defined differently for diverse types of tests. The CSR for simple shear tests is taken, according to Peacock and Seed (1968) as the ratio of the cyclic shear stress to the initial vertical stress, (i.e. $(CSR)_{SS} = \tau_{cyc}/\sigma_{v0}^{'}$), and liquefaction is deemed to occur when the single amplitude of shear strain exceeded 3.75%. For cyclic triaxial tests CSR, as proposed by Seed and Lee (1966) is defined as the ratio of the maximum cyclic shear stress to the initial lateral confining stresses, (i.e. $(CSR)_{tx} = \sigma_{dc}/2\sigma_{3c}^{'}$), when the double-amplitude axial strain DA reaches 5% or when the effective confining stress becomes or approaches zero (Seed, 1979). The CSR that is required to reach liquefaction in a specified number of loading cycles is the sand's cyclic resistance ratio (CRR), and according to Tokimatsu et al. (1991), the conversion of the CRR_{tx} to an equivalent field cyclic resistance ratio is done by the following expression:

$$CRR_{field} = \frac{\tau_{cyc}}{\sigma_{v0}^{'}} \cong 0.9\,(CRR)_{ss} = 0.9 c_r\,(CRR)_{tx} \tag{3.42}$$

being c_r the correction factor between simple shear and triaxial results, and 0.9 the correction factor accounting for the earthquakes multidirectional shaking effect.

The laboratory study of soil liquefaction is only fully understand under generalized stress-path loading, which is only granted if specific equipments, different from axisymmetric triaxial cells (Tx), such as cyclic Simple Shear (SS), cyclic Direct Simple Shear (DSS), Hollow Cylinder Tests (HCT), Torsional Shear Apparatus and Shake Table Tests, are included in these calibration studies.

Still, triaxial tests remain the most widely used laboratory technique for soil mechanical characterization mainly due to its simplicity. Their interpretation is easily comprehensive, being responsible for most of the developments on constitutive modelling and parametrical calibration. However, although enabling principal stresses reversal or inversion, Tx tests do not allow principal stress rotation, a key factor that conditions soil behaviour subjected to cyclic loading. In the extreme, HCT allows an independent control of the three principal stresses enabling the conduction of well

diversified stress-paths. However, the difficulty of the specimens preparation and the complexity of the involved instrumentation, turns this test highly time consuming and inaccessible for most research groups.

On the other hand, DSS apparatus is attractive at first sight, but leaves horizontal stress unmeasured and suffers from non-uniform stress distribution. As any simple shear testing technique, DSS has the same disadvantages but, as a constant volume test, becomes an easy performing and timesaving test, leaving however the amplitude and the direction of principal stresses difficult to trace. Thus as stress conditions are unknown, the interpretation of the results is limited to the consideration of the shear and of the normal stresses on the horizontal plane. Plus DSS hasn't the necessary compliance of other well controlled undrained tests performed in others systems. According to De Alba et al. (1976), the overestimation of the excess pore pressure, due to the compliance of test systems, with supposedly undrained saturated specimens, may reach 30%.

Notwithstanding an effort has been being made over the last decades by many authors in order to conceive a framework able to be applied to cohesionless soils in general, especially in sandy soils as they are especially sensitive to cyclic actions. Initially it seemed to be a good idea to have a framework able to predict the cyclic resistance of a soil independently of the anisotropy, initial confining stress or relative density, etc, based on few and simple laboratory Tx tests. However as the studies are progressing, in order to achieve this, it is becoming clear not being as straightforward as it was thought initially.

3.2.4.1 Liquefaction resistance curves

The first ways to evaluate soil liquefaction resistance, under laboratory conditions, are commonly done using liquefaction resistance curves (Figure 3.14). These curves are obtained by plotting the CRR and the number of cycles required for a condition of zero effective stress (ru=100%) or single amplitude shear strain of 2.5% or 3.75%, for triaxial and simple shear test, respectively. A greater CSR will trigger liquefaction in fewer loading cycles, whereas a smaller CSR will require more loading cycles.

3.2.4.2 Method based on the state parameter

- Critical state soil mechanics - CSSM

  Volume change is the feature that distinguishes soils from the other engineering materials. Thus when sheared while denser soils show a volume increase, loose soils exhibit a volume contraction. This tendency is designated by dilatancy (positive for dense soils and negative for loose soils) and has been known since Reynolds (1885).

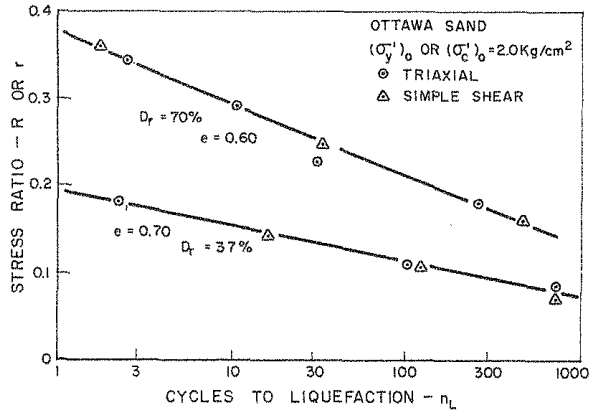


Figure 3.14: Comparison of liquefaction resistance of Ottawa sand in simple shear and triaxial compression (Finn et al., 1971).

Regardless their initial state, soils will always tend to their critical state. The critical state, defined by Roscoe et al. (1958) as the state at which a soil continues to deform at constant stress and constant void ratio, is the formalization of Casagrande's idea (Figure 3.15).

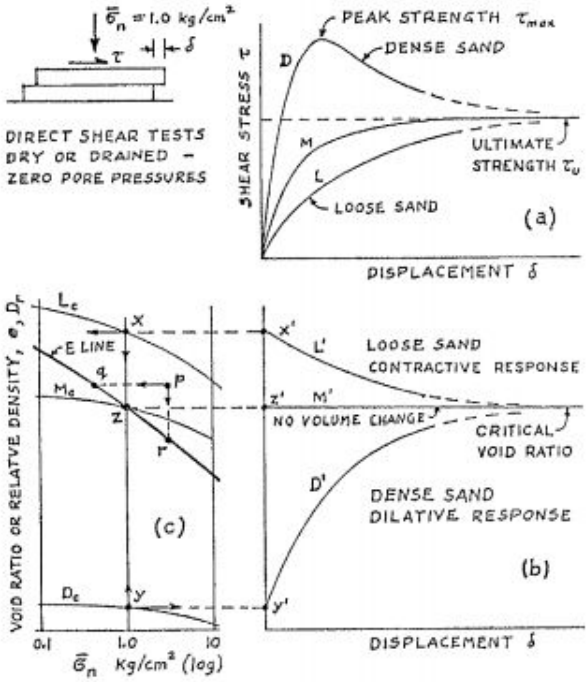


Figure 3.15: Early hypothesis of critical void ratio from direct simple shears (Casagrande (1975), adapted from Jefferies and Been (2006)).

Later on Castro (1969) termed his critical void ratio line a Steady State Line (SSL), which was found not being coincident with the term Critical State Line (CSL) defined by Casagrande. The differences were found on the load controlling device used by Castro, which by using weights on a hanger placed on a triaxial loading piston led to a rapidly increase on the strain

rate (adapted from Jefferies and Been (2006)).

According to Poulos (1981) the steady state is: *"the deformation of any mass of particles is that state in which the mass is continuously deforming at constant volume, constant normal effective stress, constant shear stress and constant velocity"*.

To sum up the differences between the definition of the critical state and steady state has a velocity term, which Been et al. (1991) and Jefferies and Been (2006) assume to be so small that the two points become identical.

The representation of the critical state is usually done in the void ratio-mean stress space, as represented in Figure 3.16:

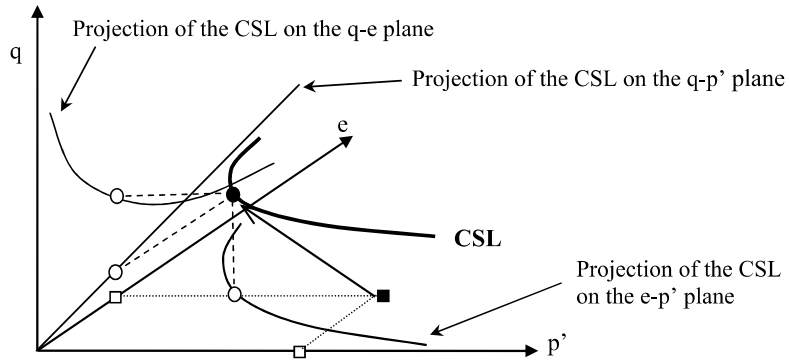


Figure 3.16: Dimensional Critical State Line. The balck dot is the CSL. The white dots represent the projections in the three planes. The black square dot is the starting point before undrained shearing. The white square dots are its projections (Carrera, 2008).

$$e_{CS} = \Gamma - \lambda \ln\left(p'_{CS}\right) \tag{3.43}$$

where e_{CS} is the critical void ratio, Γ is the intersection point of the CSL on the y axis, λ is the slope of the CSL and p'_{CS} is the pressure state correspondent to e_{CS}.

In the p': q space the critical state line is commonly represented as the Mohr-Coulomb failure line. The slope of the Mohr-Coulomb failure line in the shear-mean stress space is commonly designated by critical shear stress ratio, M_{tc}, which, for triaxial compression, is function of the constant volume friction angle, ϕ'_{cv}, also known as critical friction angle, ϕ'_c:

$$M_{tc} = \frac{q_c}{p'_q} = \frac{6\sin\phi'_c}{3-\sin\phi'_c} \tag{3.44}$$

Thus the critical state line is a line, as represented in Figure 3.16, in a three dimension space, $e : p' : q$, being the semi-logarithmic representation a modelling detail.

For critical state soil mechanics concepts, it is accepted that for a same void ratio, loose specimens monotonically loaded are more contractive with increasing confining stresses, while dense specimens are more dilatant with lower confining stresses. Undrained response of dense specimens is controlled by dilatancy, developing negative excess pore-water pressure, while undrained response of loose specimens is controlled by contractiveness, generating positive pore-water pressure (Figure 3.17). When submitted to cyclic shear stress any type of soil will contract, causing a progressive development of positive pore-water pressure under undrained conditions.

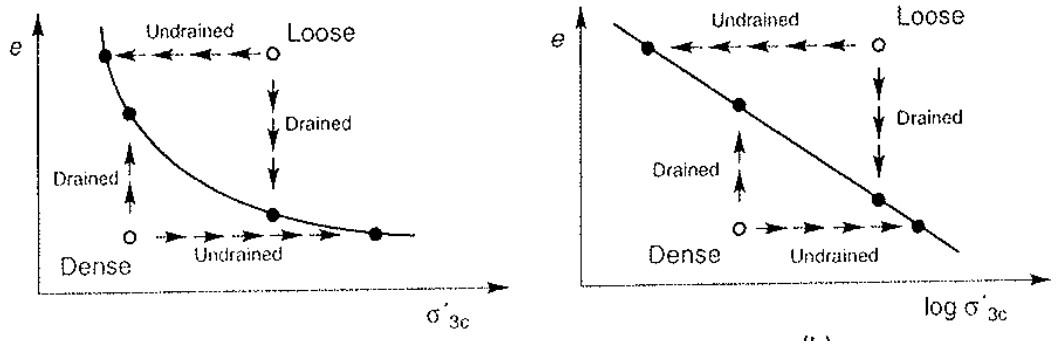


Figure 3.17: Behaviour of initially loose and dense specimens under drained and undrained and undrained conditions for (a) arithmetic and (b) logarithmic effective confining pressure (Kramer, 1996).

The determination of the CSL is commonly achieved by performing a set of triaxial tests. However a special care is necessary when choosing the tests to be performed, as there are some uncertainties on the determination of the CSL. Special attention is mainly required on tests performed over drained dense specimens as shear planes might develop (Mooney et al., 1998; Finno and Rechenmacher, 2003), through tests subjected to distinct stress paths, such as triaxial compression and triaxial extension (Vaid et al., 1990; Negussey and Islam, 1994), and for high confining pressures where grain crushing might occur (Konrad, 1998; Coop et al., 2004; Viana da Fonseca et al., 2011a; Muir Wood, 2008). Thus as advised by Jefferies and Been (2006), the determination of CSL is preferred over the performance of a series of triaxial compression tests on loose samples, and shall be performed under undrained conditions as the strains required to reach the critical state are well within the limits of triaxial equipment.

- Evaluation of soil liquefaction potential basing on CSSM – Static liquefaction

The evaluation of soil liquefaction potential through laboratory techniques was initiated by Casagrande (1936) when he proposed the Critical Void Ratio line (CVR), (nowadays known as CSL), as a boundary which separate soils prone to liquefaction from soils not susceptible to liquefaction (Figure 3.18). Nevertheless when Fort Peck Dam Montana suffered a static flow liquefaction of its upstream slope during construction in 1938, the initial soil state

was plotted below the CRV line. Casagrande attributed the fault to the inability of strain-controlled drained tests to replicate soil flow liquefaction (adapted from Kramer (1996)).

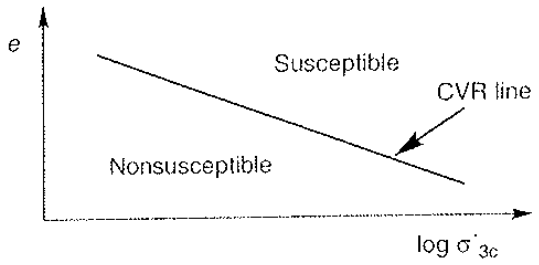


Figure 3.18: Use of CVR line as a boundary between initial states that are and are not susceptible to liquefaction (Kramer, 1996).

Later, in Been and Jefferies (1985) proposed *"an appropriate physical parameter that combines the influence of void ratio and stress level, with a reference to an ultimate (steady) state to describe soil behaviour"*:

$$\psi = e_0 - e_c \tag{3.45}$$

being e_0 the initial void ratio of the soil, after consolidation, and e_c the critical void ratio for the same initial confining pressure. When the state parameter was adopted to predict sandy soil behaviour, Been and Jefferies (1985) recognized their limitation of not assessing the anisotropic fabric of the sand. Regardless the use of the state parameter is used to normalize the large strain behaviour, where the influence of the initial fabric is small, and not to characterize a large strain behaviour.

State parameter suitability is based on the compressibility, key feature of the instability developed during the liquefaction, and it applicability relies on CSL singularity. As quoted by Jefferies and Been (2006) and Jefferies and Shuttle (2011) *"If the end state is known ... you always know where you are going"*. Plus the uniqueness of the CSL was demonstrated by numerous other authors (Been and Jefferies, 1986; Jefferies and Been, 2006; Atkinson, 2007; Carrera, 2008; Bedin, 2010).

The physical bases stand for the CSSM, where the relative density is connected to a current stress state now well established in the description of the mechanics of sands: Been and Jefferies (1985); Pestana and Whittle (1995); Lade and Yamamuro (1996); Verdugo and Ishihara (1996); Viana da Fonseca et al. (2011a).

Despite not existing, on geotechnical design codes, a framework to assess flow liquefaction triggered by monotonic shear (also designated by static liquefaction), it evaluation is commonly accepted to be done throughout the state parameter (Jefferies and Been, 2006). By

correlating ψ with the brittleness index I_B, a good prediction of the soil liquefaction potential might be obtained (Jefferies and Been, 2006; Uthayakumar and Vaid, 1998; Sadrekarimi and Olsen, 2011). Bishop (1976) defined the brittleness index, as a degree of strain softening of a contractive sand, expressed by the following equation:

$$I_B = \frac{\sigma_{d(peak)} - \sigma_{d(min)}}{\sigma_{d(peak)}} \tag{3.46}$$

where $\sigma_{d(peak)}$ is the the peak strength of a soil and $\sigma_{d(min)}$ is the minimum shear strength after peak deviator stresses, respectively as might be seen in Figure 3.19.

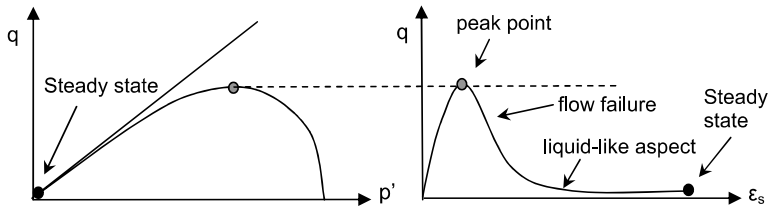


Figure 3.19: Concept of liquefaction reached through a strain controlled test (Carrera, 2008).

When correlating the ψ with I_B Jefferies and Been (2006) found it to be dependent on the type of soil and/or type of test. Similarly and following the initial idea of Sladen et al. (1985) also Wang et al. (2002) and Sadrekarimi and Olsen (2011) correlated and also found I_B to be a unique function $\sigma_c^{'}/\sigma_{cs}^{'}$ for all sandy soils, (being $\sigma_c^{'}$ the initial confining stress and $\sigma_{cs}^{'}$ the stress at the critical state). The use of such ratio, according to Sladen et al. (1985) and Ishihara (1993) , similarly to the ψ, can also represent the soil state. Yet the adoption of this ratio by Sadrekarimi and Olsen (2011) arose from the idea of normalizing the dispersion observed between the $I_B - \psi$ (see Figure 3.20 and 3.21). Such a consideration is however found, by the author, to be a bit redundant as both I_B and $\sigma_c^{'}/\sigma_{cs}^{'}$ may, in some cases, depend on the same variables, exhibiting a consequent strong statistical correlation. Nevertheless the idea beyond the ψ, firstly suggested by Wroth (1984), and earlier correlated with I_B, by Hird and Hassona (1990) and more recently by Jefferies and Been (2006), seems to provide, according to Figure 3.20, a good framework to predict liquefaction or strain softening. As can be observed from Figure 3.20 brittleness increases with increasing ψ/λ.

The brittleness index is a powerful parameter as is considered indicative of the flow potential of contractive sand, ranging from 0 for dilative sands to 1 for highly contractive sands (Uthayakumar and Vaid, 1998; Jefferies and Been, 2006; Sadrekarimi and Olsen, 2011). Thus the higher the difference between $\sigma_{d(peak)}$ and $\sigma_{d(min)}$ the higher the shear resistance drop, being on the limit equal to 1 when $\sigma_{d(min)}$ is 0. The state reached in $\sigma_{d(min)}$, for contractive soils, is named "quasi-steady" state, when there is no annulment of the deviatoric stress. If a complete loss of σ_d occurs, that is if $\sigma_{d(min)} = 0$, $I_B = 1$ and an extreme condition of instability is created, corresponding to true liquefaction, while the former cases is

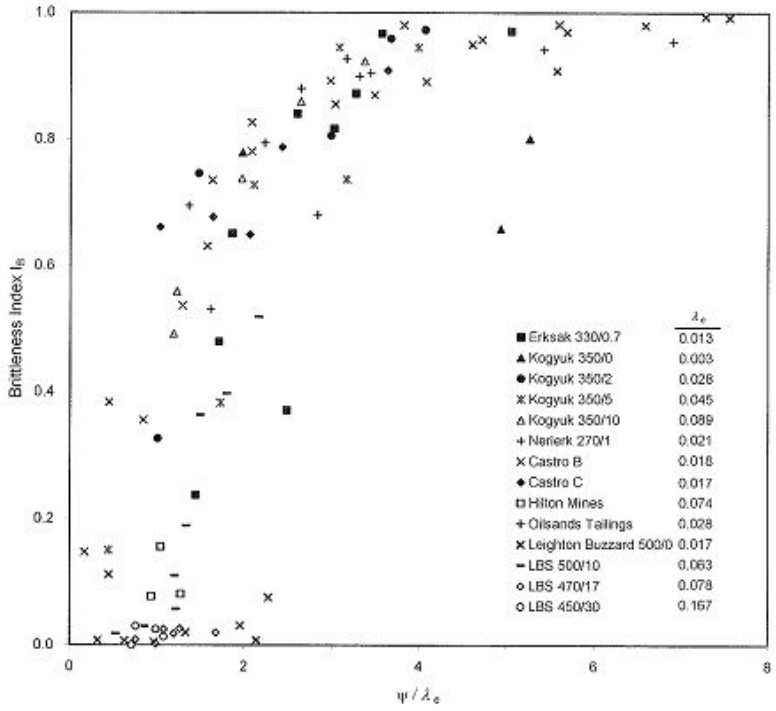
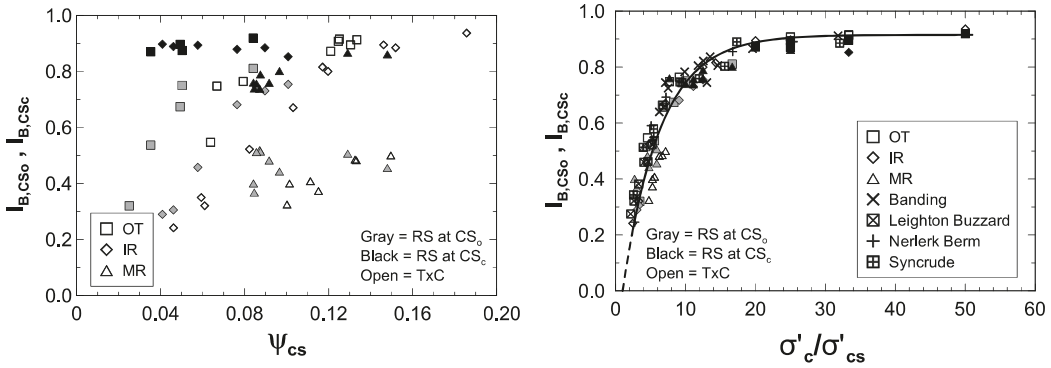


Figure 3.20: Britleness index of sands with a range of λ (Jefferies and Been, 2006).



(a) (b)

Figure 3.21: (a) Variations of the Brittleness Index with ψ_{cs} in 3 sands tested in Triaxial (TxC, C for compression) and Ring Shear (RS) in damaged and undamaged conditions by the end of the tests; (b) Variations of I_B with $\sigma_c^{'}/\sigma_{cs}^{'}$ in OT, IR and MR sands (Sadrekarimi and Olsen, 2011).

designated by limited or temporary liquefaction with strain softening (Yamamuro and Lade, 1998). The quasi steady state (QSS) concept was firstly proposed by Alarcon-Guzman et al. (1988) and is defined as the point where contractive behaviour changes to dilative behaviour, concept much explored by Yamamuro and Lade (1998) to assess liquefaction potential. The existence of a quasi steady state concept to assess soil liquefaction relies on the acceptance of soil behavioural divergence when sheared under drained and undrained conditions. Thus for those soils situated above the SSL, the QSS point is reached for a zero shear stress due to their inability to invert the positive pore pressure generation to a negative pore pressure gen-

eration, as a consequence of the disruption of the stress chain transference between grains. On the other hand if I_B is near 0, it means that soil is completely stable (Figure 3.20 and 3.21).

Nevertheless this type of approach as also requires the determination of the CSL is a not easy and expensive way to assess soil liquefaction. Plus the presence of fines, beyond changing sharply the CLS positioning, it also hinders it accurate determination, unless the freezing technique proposed by Sladen and Handford (1987) is adopted. This topic will be target of this study and thus further details about it influence are found in section 4.4.

- Evaluation of soil liquefaction potential basing on CSSM – Cyclic liquefaction (Flow liquefaction, triggered by cyclic shear and Cyclic mobility)

  In an attempt to also predict the cyclic undrained shear strength of soils, through laboratory techniques, Jefferies and Been (2006) proposed the *"Basic Berkeley School liquefaction assessment chart"* (Figure 3.22). This framework that correlates CRR with ψ has a clear validity under applied CSSM theory.

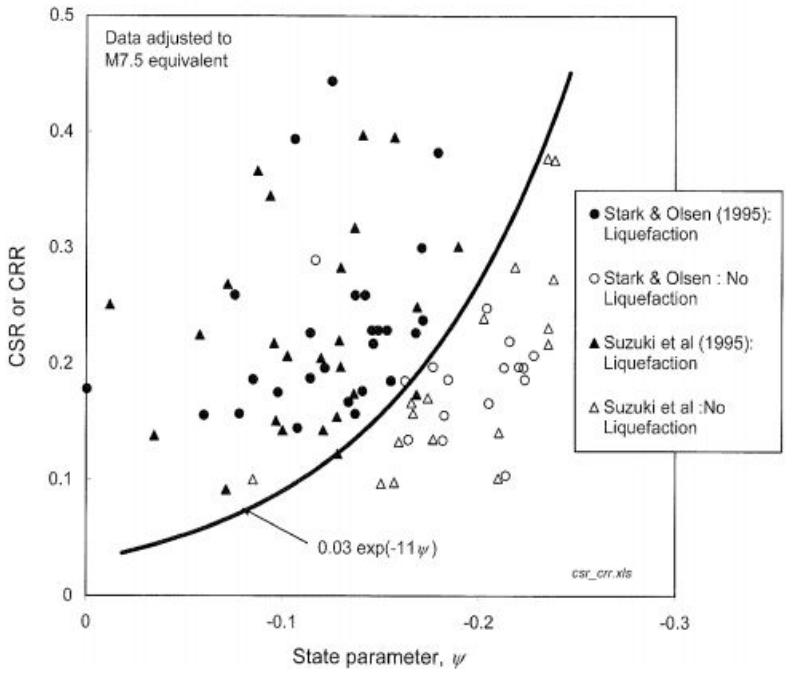


Figure 3.22: *"Basic Berkeley School liquefaction assessment chart"* - Field history data representation (Jefferies and Been, 2006).

As can be seen in Figure 3.22, the line which separates cases of liquefaction from no liquefaction is given by the following exponential function:

$$CRR = a \times exp\left(-b \times \psi\right) \tag{3.47}$$

where a and b, are parameters function of the soil properties, equal to 0.03 and 11, respectively, for the "clean sands" studied by Stark and Olson (1995) and Suzuki et al. (1995), respectively.

There is an additional advantage of associating the *CRR* with the ψ, as both are function of density and the stress state. As reported by Jefferies and Been (2006), when liquefaction potential is assess through the state parameter, then no correction of the initial overburden stress is required. As might be easily understood, ψ explains the influence of the changing stress level for a constant void ratio. Thus, unlike the "Simplified Procedure", often used on field, frameworks which rely on the ψ are disburdened of implementing a correction factor to take into account the initial stress state condition of the soil.

The main disadvantage of using the state parameter, on liquefaction assessment, is associated to the usual determination of the CSL through reconstituted samples of soil. Although fabric influence is a well-known factor that affects the mechanical response of soils, and consequently ψ, it is also known that undisturbed sampling of cohesionless soils is still currently very difficult and expensive (few successful attempts have been made recently: Cresswell and Powrie (2004) and Ventouras and Coop (2009)). For this reason, samples have to be reconstituted in laboratory using techniques like moist tamping, pluviation or slurry deposition. Further details about the fabric effect are presented in section 4.3.3.1.

Unlike laboratory tests, the determination of the in situ state parameter is compromised by the incapacity of the in situ tests to measure direct parameters. Thus for a rational interpretation, some laboratory is required when evaluating soil liquefaction potential basing on in situ tests Jefferies and Been (2006).

3.2.4.3 Method based on stress waves velocities measurement

Andrus and Stokoe (1997), proposed a "Simplified Procedure" based on the evaluation of liquefaction resistance through the use of small-strain 10^{-6} shear wave velocity (V_s). The procedure, already presented in the subsection 3.2.2.4, initialized with analytical studies developed by Stokoe et al. (1988) based on a parametric study of sandy soils in Imperial Valley. Despite the initial idea of correlating the *CRR* with the normalized small-strain shear wave velocity V_{s1}, was in fact firstly developed, under laboratory conditions, by Tokimatsu et al. (1991) (Figure 3.23).

The implementation of bender elements on triaxial apparatus, came to help out the measurement of the shear waves before cyclic shearing (Ishibashi and Capar, 2002; Viana da Fonseca et al., 2011b; Zhou and Chen, 2007; Zhou et al., 2009; Huang et al., 2004; Liu and Mitchell, 2006). Before bender elements, V_s waves measurement used to be determined by testing the soil specimens on a resonant column apparatus, with maximum shear strains of 10^{-4} in order to generate elastic waves and not to be a destructive test. Plus the measurement of small strain parameters might be also

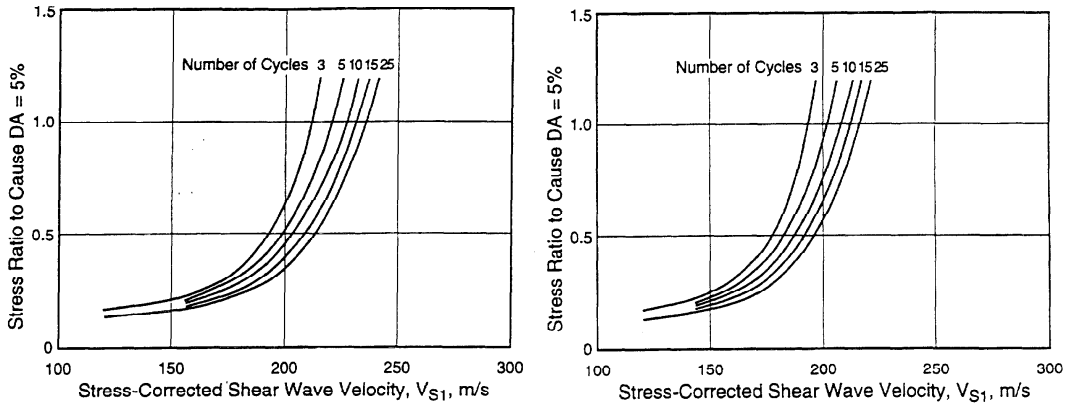


Figure 3.23: Liquefaction assessment charts based on V_{s1} proposed by Tokimatsu et al. (1991) (Andrus and Stokoe, 1997).

done, not only by using bender elements or by testing specimens in resonant column apparatus, but also by using accelerometers in a specimen.

- Method based on the first wave arrival – stress waves interpretation in time domain

  The method based on the first wave arrival relies on the assumption that stress waves are non-dispersive in a uniform elastic medium, thus independent on the frequency.

  As reported previously the velocity of the wave is determined by dividing the distance (L) between the transmitter and the receptor, by the time travel of the wave (t), (see Figure 3.24):

$$V_s = L/t \tag{3.48}$$

- Evaluation of soil liquefaction potential basing on shear wave velocity – Cyclic liquefaction

  The liquefaction resistance based on the correlation between CRR_{tx} and V_s using bender elements was also corroborated by Zhou and Chen (2007) through semi-theoretical considerations. Thus and according to them, the correspondent laboratorial "cyclic resistance ratio" (CRR_{tx}) can be related with V_s as it follows:

$$CRR_{tx} = \frac{1}{\sigma_m^{'}} \left[k \frac{\rho V_s^2}{F\,(e_{min})} \right]^{1/n} \tag{3.49}$$

  This equation comes from the replacement of the deviatoric stress of $CSR_{tx} = \sigma_d / 2\sigma_0^{'}$ by:

$$(\tau_d)^{n/f} = k \frac{G_{max}}{F\,(e_{min})} \tag{3.50}$$

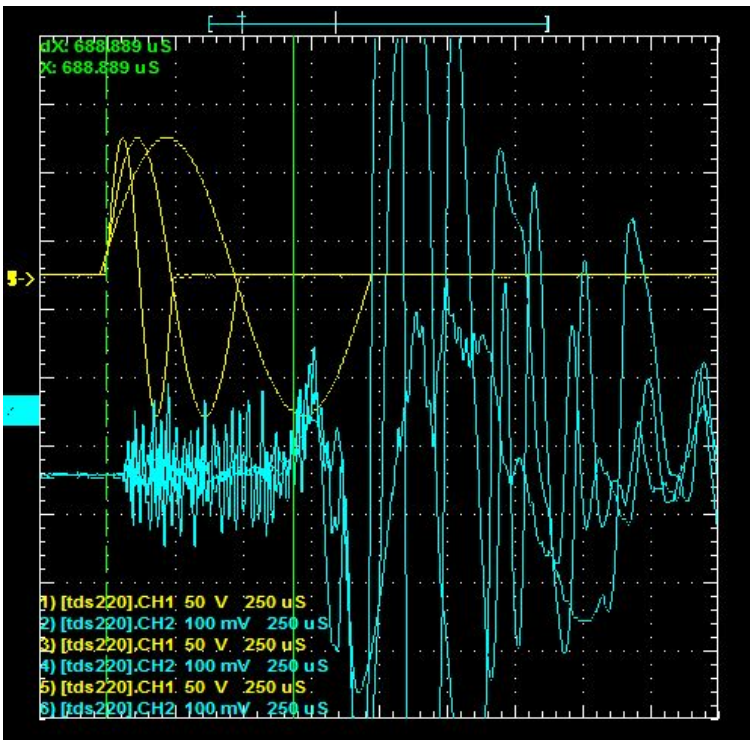


Figure 3.24: Method of first wave arrival; Stress waves measurement using bender-extender elements (Lab-Geo).

which on it turn is obtained through:

$$\left(\tau_d = \frac{\sigma_d}{2}\right)^{n/f} \propto G_{max} \tag{3.51}$$

This previous equation comes from the combination between the empirical expression of G_{max} (Hardin and Drnevich, 1972) with the equation derived from the relationship defined by Tokimatsu with the expression $K_\sigma = \left(\sigma'_m/P_a\right)^{f-1}$ that takes into account the non-linearity existent between *CRR* and the confining stress (adapted from Zhou and Chen (2007)).

Thus after determining the *CRR* in situ, following the equation (3.42), and determining the V_{s1}, the data points of liquefaction and no liquefaction can be plotted on the "Simplified Procedure", proposed by Andrus and Stokoe (1997), of Figure 3.9. As the liquefaction boundary, given by equation (3.32), depends on two adjustment factors, a and b, which also depend on the soil properties and on V^*_{s1}, their change might be required.

The determination of V_{s1}, under laboratory conditions, is done according to the following equation:

$$V_{s1} = V_{s1field}\left(\frac{P_a}{\sigma'_{v0}}\right)^{0.25} = V_{slab}\left(\frac{1+2k_0}{3}\right)^{0.25}\left(\frac{P_a}{\sigma'_m}\right)^{0.25} \tag{3.52}$$

where P_a is the atmospheric pressure (approximated by 100 kPa), K_0 is the at rest coefficient of earth pressure and σ'_m the medium effective confining pressure. As emphasized by Zhou and Chen (2007), this assumption in lab conditions is a direct consequence of the fact that V_S depends both on principal stresses in the direction of wave propagation and particle motion.

- Evaluation of soil liquefaction potential basing on shear wave velocity – Flow liquefaction

  "Approaches based on strength and stiffness measurement are predominant in engineering practice, and given their empirical nature, there are gaps in linking soil liquefaction to the stress-strain behaviour of soils, which renders modelling of the static and dynamic mechanical response difficult" (quoted form Schnaid et al. (2013)).

  Till recently the assessment of liquefaction potential through V_S waves measurement was usually performed basing on the "Simplified Procedure", being its use limited to liquefaction triggered by cyclic/ dynamic shear conditions. In order to overcame the inability of using stiffness parameters to predict static liquefaction, more recently Schnaid et al. (2013) and Bedin et al. (2012), proposed a framework to assess liquefaction of tailings, by connecting both large-strain parameters ψ, with small strain-parameters, G_0 (derived from V_S). As can be seen from Figure 3.25 the correlation between the state parameter, ψ, and initial or dynamic stiffness to strength ratio shows to provide good predictors of the soils susceptibility to static liquefaction.

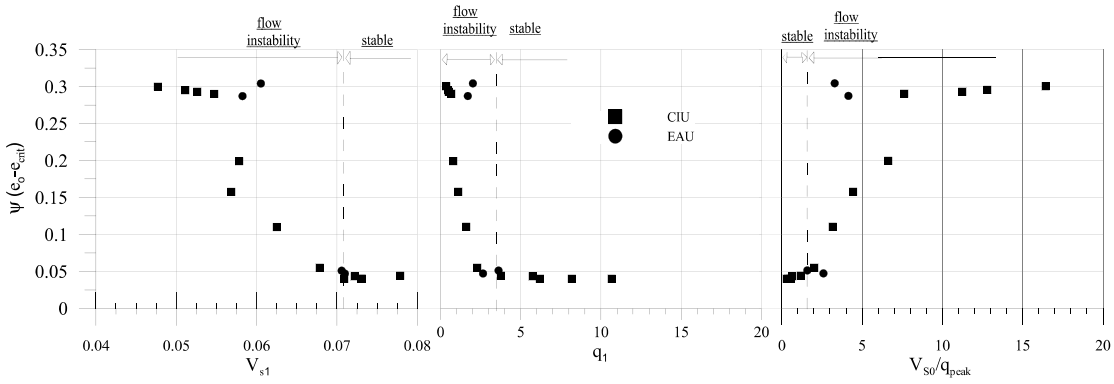


Figure 3.25: Critical state parameter expressed as a function of normalized peak shear strength (q_1) and shear stiffness (Schnaid et al., 2013).

From Figure 3.25 it is recognized that flow instability is function of the initial state of soils,

as previously demonstrated by Jefferies and Been (2006). Besides allowing the determination of soil stability under laboratory conditions, it also allows it achievement under field conditions, as ψ is correlated to the normalized shear strength q_1, normalized shear-wave velocity V_{S1}, and the stiffness-to-strength ratio V_{S0}: q_{peak} (Schnaid et al., 2013). Being V_{S1} determined according to the equation (3.52) and normalized shear strength according to the following equation:

$$q_1 = \left(\frac{q_{peak}}{P_a}\right)\left(\frac{P_a}{\sigma'_{v0}}\right)^{1/2} \tag{3.53}$$

From the stiffness-to-strength ratio V_{S0}: q_{peak}, which inherently include the effects of mean stress, Schnaid et al. (2004), Schnaid et al. (2013), Schnaid (2005) and Schnaid and Yu (2007) found these two measurements, which are function of the same parameters, useful in predicting soil parameters (Figure 3.26). Considering the combination of both shear-wave velocities and peak strength, a general framework was obtained and validated for distinct stress-paths to predict soil liquefaction, as can be observed in Figure 3.26.

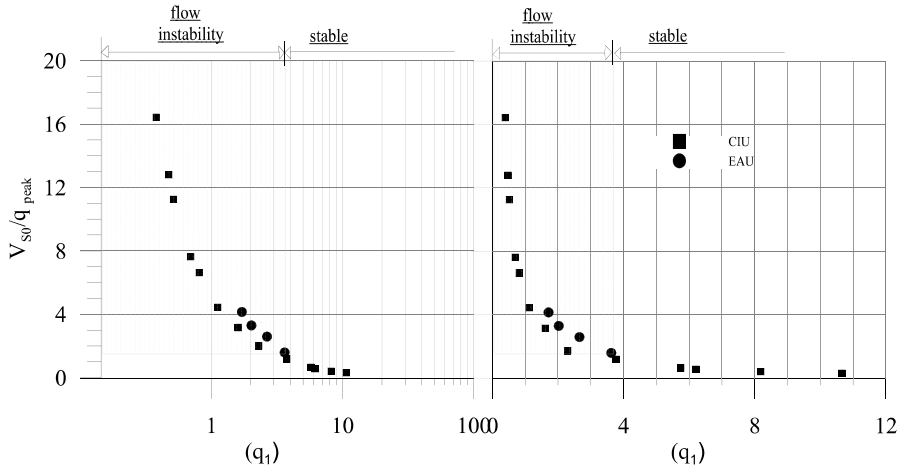


Figure 3.26: Effects of mean stress, normalized peak shear strength (q_1), and stiffness (Schnaid et al., 2013).

However it seems obvious the evident strong statistical correlation between both variables as both "y" and "x" are function of a same parameter. Thus for the case above in Figure 3.26, V_{S0}: q_{peak} and q_1 are found to be both function of q_{peak}.

- Compression wave velocity, V_P

If in field conditions the soil is obviously saturated when below the water table, in laboratory conditions, the degree of saturation might be determined through the Skempton parameter, B, or by measuring the compression P wave. As mentioned above, V_P, for saturated soils shall be around 1500 m/s, which correspond to the velocity of the sound in water.

On the other hand the determination of the Skempton parameter is conventionally done by measuring the response of the pore water pressure inside a specimen by increasing the confining pressure under undrained conditions. Thus it might be determined according to the soil response, as it follows:

$$B = \frac{\triangle u}{\triangle \sigma_3} \tag{3.54}$$

where $\triangle u$ is the excess of pore pressure and $\triangle \sigma_3$ the increment of confining pressure applied in the triaxial apparatus.

On the other hand the P wave velocity might be determined by using piezoelectric transducers inside the triaixal, or other laboratorial devices.

According to Yang (2002a), the velocity of the P waves and the Skempton parameter have the following correlation:

$$V_p = \left(\frac{\frac{4G}{3} + K_b/(1-B)}{\rho} \right)^{1/2} \tag{3.55}$$

where G is the shear modulus, B the Skempton parameter, ρ the mass density of the soil, V_p the velocity of P waves and K_b the stiffness modulus. It correlation is plotted in Figure 3.27.

3.2.4.4 Method based on energy approaches

Most researchers keep trying to assess liquefaction resistance of soils through the consideration of correction factors, which take into account the stress level adjustment factor (K_σ), the effect of the initial static shear stress on resistance against liquefaction (K_α), and some other factors which account for geological history, being each of these factors function of the relative density. Nevertheless, soil liquefaction evaluation can be also performed using the amount of energy dissipated in the soils during the propagation of seismic waves through soil deposits (Okur and Umu, 2012). This energy is dissipated throughout the soil during strain accumulation under cyclic loads while the other part of the energy is dissipated into the soil.

Figueroa et al. (1994) proposed a way to assess soil liquefaction potential, by comparing the energy per unit volume generated with the dynamic motion in the deposit.

The main reasons that support the development of an energy approach in liquefaction evaluations are: the possibility of earthquakes' energy quantification, the strong relationship that exists between the energy dissipated and the generated pore-pressure, and the fact that both cyclic stress and strain histories are taken into account when considering this parameter (Okur and Umu, 2012).

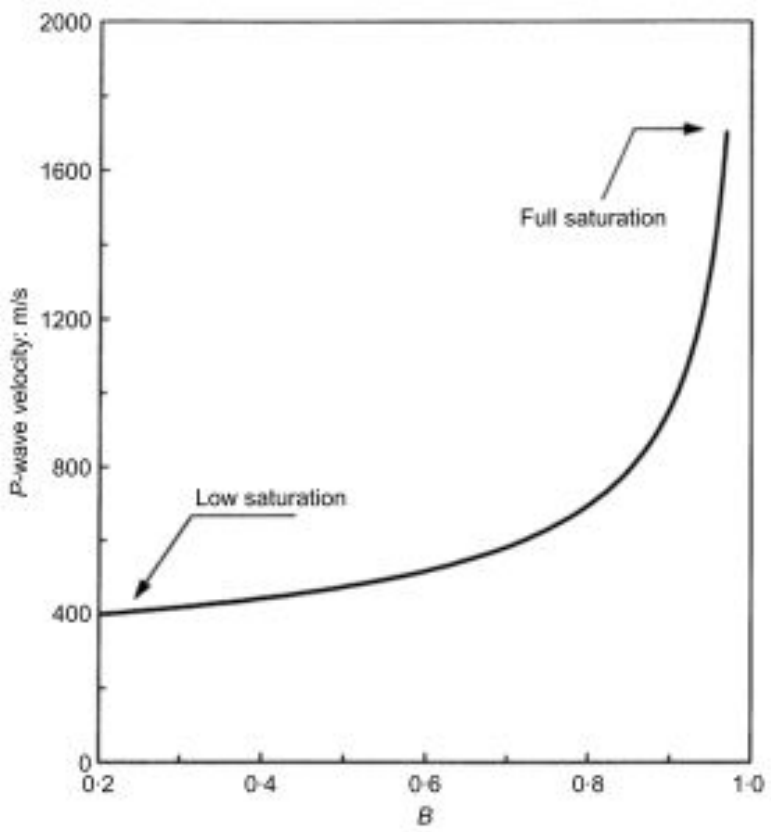


Figure 3.27: Relation between P-wave velocity and B for Toyoura sand (Yang, 2002a).

Considering that the dynamic instability of any soil is based on the ability to accumulate from cycle to cycle a part of the energy to be dissipated, soils' damage potential can be described as a function of the energy dissipated during loading, in an attempt to understand how the undrained cyclic resistance converge.

In fact, the structural collapse of the soil skeleton, while submitted to an external force, is associated to a sudden loss of energy, and this "the cumulative energy loss up to liquefaction" has been previously identified as a good index for the assessment of liquefaction potential (adapted from Okur and Umu (2012)). The employment of an energy approach is theoretically well supported as there is a unique relationship between the dissipated energy and the dynamic soil response in terms of dynamic strength, shear modulus and permanent strain. Plus the theory of using an energy approach is based on the preposition that, while under drained conditions, a certain amount of energy is involved in changing the void ratio, while under undrained conditions, then this tendency to decrease the void ratio will result in an increasing pore pressure. This, in turn, results in a decrease in the intergranular forces and so the incremental energy decreases with increasing pore-water pressure u, while the accumulated energy, W, increases during plastic strain accumulation (Figueroa et al., 1994).

The accumulated dissipated energy (W) might be calculated from the hysteresis loops, cyclic response of the soil, through the following equation (Figueroa et al., 1994):

$$W\left(\frac{kJ}{m^2}\right) = \sum_{1=N}^{N} \frac{1}{2}(\sigma_i + \sigma_{i+1})(\varepsilon_{i+1} - \varepsilon_i) \tag{3.56}$$

$$W\left(\frac{kJ}{m^2}\right) = \sum_{1=N}^{N} \frac{1}{2}(\tau_i + \tau_{i+1})(\gamma_{i+1} - \gamma_i) \tag{3.57}$$

,where σ is the applied deviator stress, ε is the axial strain at load increment in triaxial test, τ is the shear stress and γ the shear strain in simple shear test, and while N is the number of points recorded until zero effective stress or single amplitude shear strain of 2.5% or 3.75% is reached, for triaxial and simple shear test, respectively.

As cleared up by Figueroa et al. (1994) the liquefaction potential, thus the accumulated dissipated energy, of a soil deposit is influenced by grain-size relative distribution, relative density of the deposit, type of applied loading, drainage characteristics of the deposit, confining pressures acting on the deposit, soil structure and cementation of the sand forming on the deposit, intensity and duration of ground shaking, strain history of the deposit, amount of entrapped air in the deposit and thickness of the deposit.

Aware of such dependency between the energy per unit of volume and the initial state variables of the soils, Baziar et al. (2011) and Liang et al. (1995), tried to predict the energy per unit of volume as function of the main statistical soil parameters, following a relationship similar to:

$$\log W = a + b \times \sigma_c^{'} + c \times D_r + (d \times C_u + e \times FC + ...) \tag{3.58}$$

where a, b, c, d, e, etc are parameters function of the soil characteristics.

Equations like the one expressed above enables the prediction of the capacity energy for a certain soil deposit. By comparing the capacity energy with the demand energy, released by any kind of source, soil stability is assured if the first one is higher than the second one. Baziar et al. (2011), making use of the equation proposed estimated the capacity energy of a soil deposit, showing its ability to preview soils stability, by comparing a set of centrifuge tests (see Figure 3.28).

The energy-based approaches are consistent due to the strong theoretical correlation between the generations of excess pore water pressures with the dissipated energy during undrained cyclic loading. However in field requiring the seismic loading represented in terms of energy, this approach has not advanced further, because of the potentially large variations in Arias intensity (the integral of acceleration sqaured over time) versus depth in a soil profile, and also due to questions

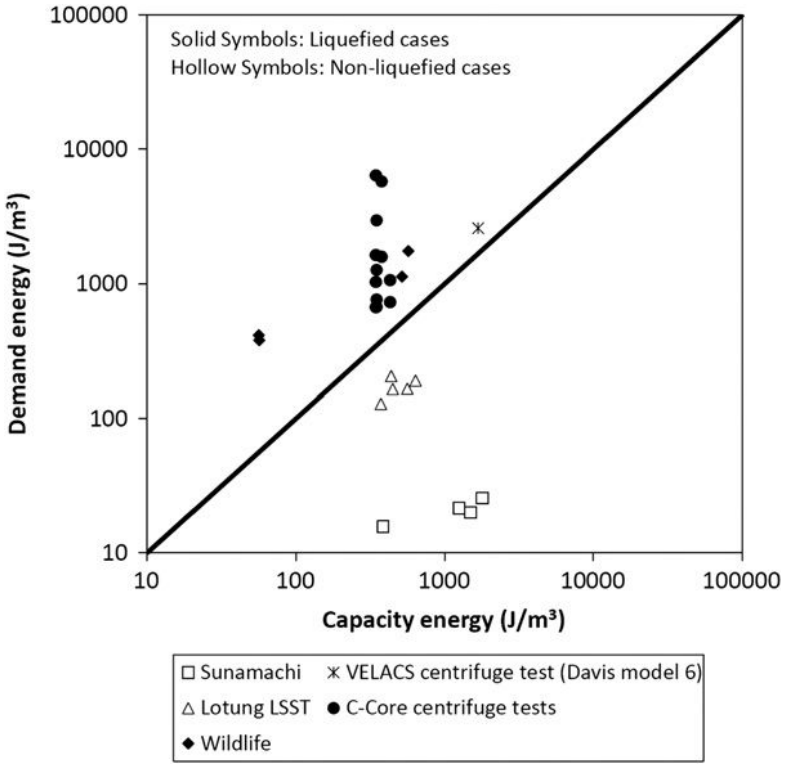


Figure 3.28: Comparison of demand energy imported by the soil and capacity energy predicted by GP-based model for various real sites and centrifuge tests (Baziar et al., 2011).

relating Arias intensity, at a specific depth, to that at the ground surface (adapted from Idriss and Boulanger (2008)).

Chapter 4

Mechanics Of Soil Liquefaction

4.1 Introduction

The main difference that distinguishes cohesionless sands or silty sands, while in a loose condition, is the aptitude to develop positive pore pressures in such a rate that constrains the ability of the soil to hold a shear static stress, which will lead to a null effective stress condition. Being the soil governed by the 3rd Newton's law, it is able, as any other continuous material to transmit, correctly, stresses between particles, through the action-reaction principle. However when soil, assembles a set of condition, and is sheared in a way that is no longer able to keep this stress-chain between particles, soil starts behaving like water (Figure 4.1). As can be seen in Figure 4.1, during the rupture of the stress-chain, particles get suspended in water and, as water density is less than the particles density, the soil gets deposited in the bottom and water comes up, which might be expressed in field as sand boils.

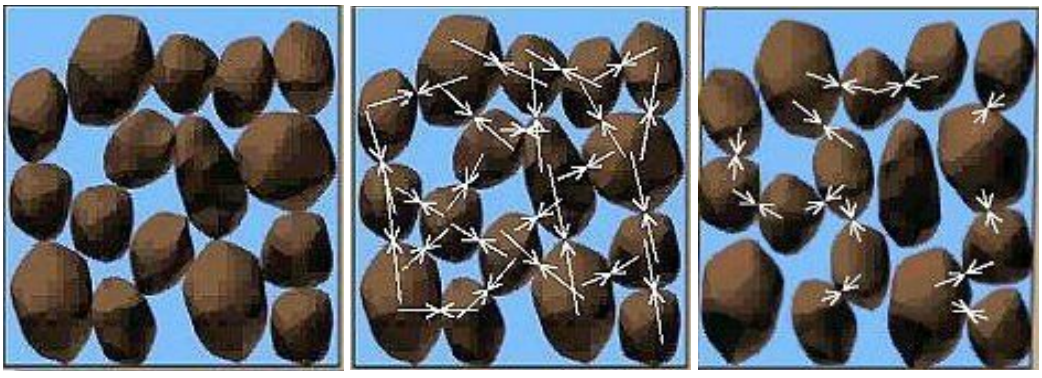


Figure 4.1: Inter-particle forces after and before liquefaction (Johansson, 2000b).

Soils are constituted by two different phases, the fluid phase, associated to void ratio, and the solid, associated to the skeleton, while under saturated conditions. Thus when sheared, particles are highly affected by the interstitial fluid, which naturally changes their stress state condition. As

liquids are of isotropic caraway, they do not have shear resistance. As liquefaction only takes place when soils are sheared, and the interstitial fluid do not have a tangential component, the shear will, occasionally, reflect as change on water pressure.

Before proceeding it was decided to present a brief note in order to clarify the main differences between flow liquefaction and cyclic mobility. In Chapter 2 a lexical disambiguation was made between flow liquefaction and cyclic mobility. According to Rauch (1997) three types of phenomena might be distinguished: flow liquefaction, when static shear stress exceeds residual strength of the soil, apart from being triggered under cyclic or monotonic loading (Figure 4.2); cyclic liquefaction, when a large deformations occurs and a zero effective stress might be reached due to shear stress reversal (Figure 4.3); cyclic mobility, when soil also develops deformations but no zero effective stress is reached as no shear stress reversal occurs (Figure 4.3). Notwithstanding, during this work, liquefaction is distinguished according to the type of loading conditions. Thus liquefaction triggered by monotonic and cyclic loading, are denominated as static and cyclic liquefaction, respectively. It means that despite flow liquefaction being also triggered under cyclic loading conditions, it is jointly studied with the cyclic mobility phenomena. Differences related with or without shear stress reversal are not taken into account, as it was found unnecessary.

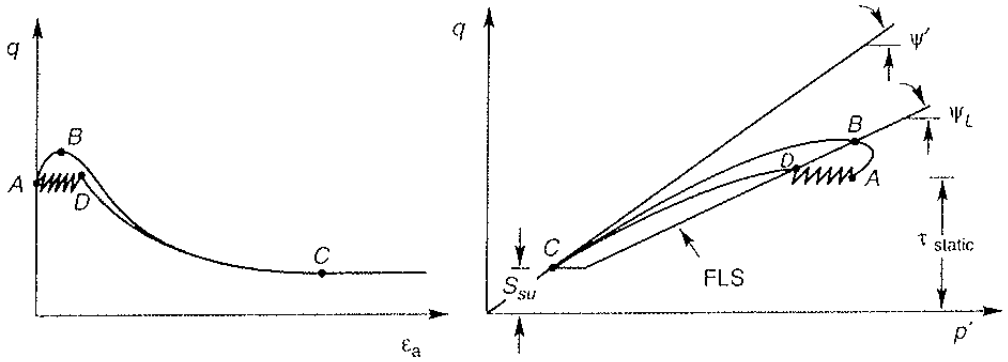


Figure 4.2: Initiation of flow liquefaction by cyclic and monotonic loading (Kramer, 1996).

While cyclic mobility is not a phenomena related to instability, but rather to plastic strain accumulation, strain softening during cyclic loading is very much like flow liquefaction triggered by monotonic shear. For strain softening to occur under cyclic loading is required, simultaneously: i) the sand is strain softening under static loading; ii) the maximum shear stress exceeds the SS or QSS strength on the compression or extension side; and iii) a sufficient number of loading cycles occur (Kramer, 1996; Vaid and Sivathayalan, 1996).

In order to understand both flow liquefaction and cyclic mobility under applied mechanics, first of all, is necessary to understand soil stress-strain and stress-path response. But more importantly is to understand how factors, such as the initial confining stress, relative density, initial static shear stress, fines content, among others influence the soil response. This chapter aims to cover all the aspects that influence the soil response under both cyclic and monotonic loading conditions, being each of the announced factors explored basing on previous researches.

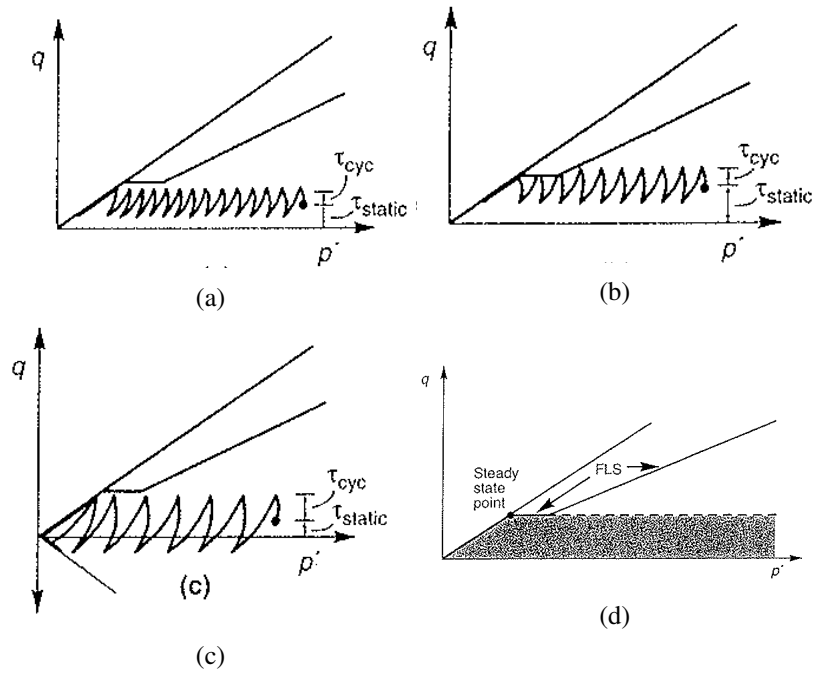


Figure 4.3: Three cases of cyclic mobility: (a) no stress reversal and no exceedance of the steady-state strength; (b) no stress reversal with momentary periods of steady-state strength exceedance; (c) stress reversal with no exceedance of the steady-state strength; (d) zones of susceptibility to cyclic mobility (Kramer, 1996).

4.2 Static Liquefaction Of Sands Within The Context Of Critical State Soil Mechanics

4.2.1 Drained Behavior

Sands and generally cohesionless soils, thus silts and silty sands, as particles are governed exclusively by gravitational forces, and exhibit, while under drained conditions, a regular and stable behaviour. Regular means that, while on the wet side of the CSL, thus in loose conditions ($e > e_c$), cohesionless soils exhibit a volume contraction towards the CSL, and while on the dry side ($e < e_c$), thus in dense conditions, cohesionless soils exhibit a positive dilation towards the CSL. Both of each cases exhibit drained stress-path which is typically characterized by a slope equal to 3, and the general expression is given by:

$$q = 3 \times p' - 3 \times \sigma'_{hi} \tag{4.1}$$

being q and p' the deviator and medium effective stress, respectively, and σ'_{hi} the initial effective confining stress.

Beyond the distinct volumetric behaviour, between loose and dense soils, when sheared, while loose sands exhibit a stress path which ends at the point of intersection of the failure line (or Mohr-Coulomb failure line or critical state), dense sands exhibit a peak strength, which surpasses Mohr-Coulomb failure line (Figure 4.4). This peak strength, represented by the peak angle ϕ_p, is commonly associated to the particles imbrications, which corresponds to the ability of the soil to dilate (Figure 4.4). Soil dilation takes place, after a minimum initial contraction, while peak strengths start to exhibit. Through a critical state soil mechanics point of view, as denser the soil, for a same initial confining stress, higher the magnitude dilation. Similarly, for a same relative density, as lower the initial confining stress higher the magnitude dilation. Bolton (1986) proposed a comprehensive empirical expression to determine peak angle ϕ_p through a relationship between the critical state friction and maximum dilation rate for several tests on the same material:

$$\phi_p^{'} = \phi_{cv}^{'} + 0.8 \times \psi_{max} \tag{4.2}$$

Usually represented by the critical state friction angle, $\phi_{cv}^{'}$, the failure line is expressed, in terms of stress invariants through the critical stress ratio.

$$q_c = M \times p_c^{'} \tag{4.3}$$

being M expressed, in terms of the critical friction angle, given by the equation (3.44). Both M and $\phi_p^{'}$ or $\phi_{cv}^{'}$ are soil properties used to describe the strength of the soil.

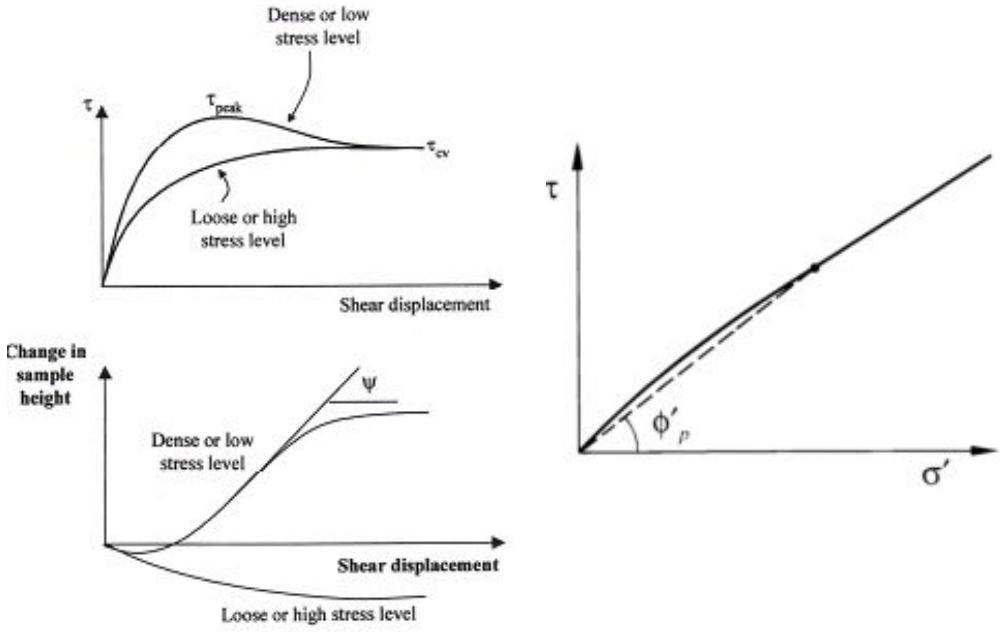


Figure 4.4: (a) Dilation and contraction of dense and loose sand in a simple shear test; (b) Curved peak strength envelope on Mohr's circle plot (Houlsby, 1991).

4.2.2 Undrained Behaviour

When monotonically sheared, while under drained conditions, sandy and silty soil exhibit a stable behaviour, under undrained instability might take place (i.e. flow liquefaction). As described earlier and according to many authors, (Castro, 1969; Castro and Poulos, 1977; Poulos et al., 1985; Kramer and Seed, 1988; Alarcon-Guzman et al., 1988), the conditions for flow liquefaction to take place are: soil must be in loose conditions (ψ>0); loading path must not allow for excessive volume changes prior to the collapse; soil must be saturated; soil permeability shall be low enough to sustain the generated pore pressures; plus the ultimate shear strength must be less than the initial driving shear stress.

From the above conditions some still remain unclear. Uncertainty remains on the following subjects: soil must be in loose conditions (ψ>0) and the loading path must not allow for excessive volume changes prior to the collapse jointly with the condition of saturation. While the first postulation is discussed below, the second one is discussed further ahead, addressed to the subsection "Instability under drained conditions".

As explained earlier in Chapter 3, the state parameter, ψ, is a parameter that measures the vertical distance of the initial from the critical state line for the same initial confining stress, $p_i^{'}$. This parameter commonly used to assess soil liquefaction potential, is build upon the CSSM theory. According to the CSSM a single and unique line of failure points, CSL, is defined from both drained and undrained tests. Plus when normalizing stress-strain and stress-path curves, with respect to the initial confining stress, all curves collapse into a unique curve (Figure 4.5).

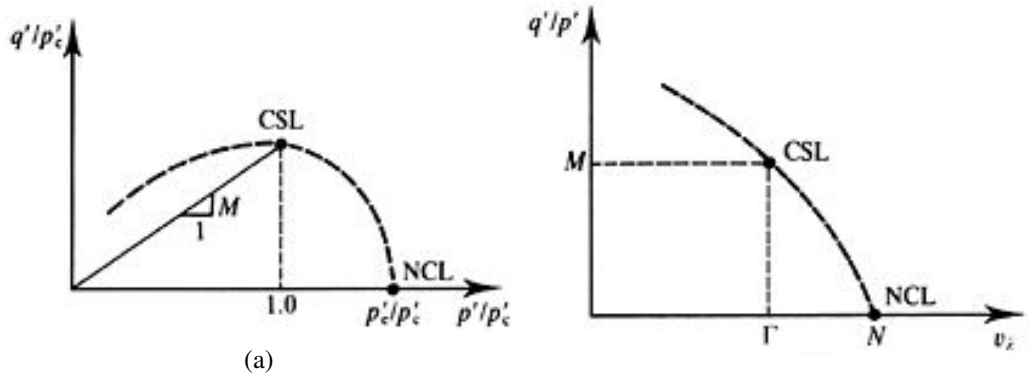


Figure 4.5: Normalized critical state and normal consolidation lines (Atkinson, 2007).

The CSL uniqueness, well accepted by a majority of authors (Atkinson, 2007; Been and Jefferies, 1986; Jefferies and Been, 2006; Carrera, 2008; Bedin, 2010), making ψ a functional parameter, not only to assess soil liquefaction potential, but also for normalization purposes. However, for some particular soils (mainly sands), CSL have a curved shape making it a less useful parameter (Rios Silva, 2011). However this curved shape might be an erroneous idea of what might be a bifurcation related to the velocity term during shear.

Been et al. (1991) and Jefferies and Been (2006) refer the CSL, derived from drained tests, and SSL, derived from undrained tests, to fundamentally a same condition. However distinction between both paths followed by drained and undrained conditions were previously found by Sladen et al. (1985), Alarcon-Guzman et al. (1988) and Yamamuro and Lade (1998), and respectively distinguished the CSL from the SSL. As stated by Alarcon-Guzman et al. (1988) *"if the sand structure is not inherently brittle, no collapse will take place; thus, the pore pressure response will be due solely to sand compressibility, and the S and F lines will tend to merge"*, being F the line for undrained tests and S the line for drained tests.

Figure 4.9 shows Nevada sand behaviour (with 7% fines), for drained and undrained conditions. While a divergence is found for lower confining stresses, a convergence of the SSL and the CSL takes place for higher confining stresses. First is necessary to throw off the scent that the 7% of fines in Nevada sand have an influence on the stress-strain and/ or stress-path behaviour, as the soil behaviour is entirely governed the sand fraction. Second is necessary to explain that what is commonly designated by Yamamuro and Lade (1998) by "reverse behaviour" is seen just as a consequence of the increasing stability with increasing confining stress and increasing relative density, a common behaviour of sands and silts. A misunderstood interpretation is made when all tests are compared regardless the initial void ratio after the consolidation, being only referred that they were prepared with the same relative density of 30%.

Moreover also Yang et al. (2006) found a divergence between the ultimate state reached for drained and undrained tests, for confining stresses lower than 200 kPa, while testing soils with different fines content (Figure 4.11).

A same similar curved shape for the ultimate stress state was found for CIU tests for Toyoura and Fujian sand by Verdugo and Ishihara (1996) and Yang and Sze (2011), respectively, (Figure 4.6), and for Stava tailings and gold tailings by Carrera et al. (2011) and Schnaid et al. (2013), respectively, (Figure 4.7 and 4.8). Also Wan and Guo (2001) have found a curved SSL (or CSL). Curiously none of the above authors performed drained tests at lower confining stresses; thereby no conclusions might be inferred about CSL uniqueness.

For such curved equation CSL classical definition, given by equation (3.43), stops being suitable, thus Li et al. (1999) proposed the following correlation:

$$e_{SS} = e_{c0} - \lambda_s \left(\frac{p_{ss}}{p_a} \right)^{\xi} \tag{4.4}$$

being e_{c0} the limiting value of e at $p = 0$, p_a is the atmospheric pressure, λ_s and ξ are constants which depend on soil characteristics. For simplification this curve was assumed to be the SSL, where SS refers to steady state, while the CS refer to critical state.

Thereby a question arises on using the ψ for analysing liquefaction potential of soils. Plus a doubt arises on how legitimate can be the assumption of a same normalized undrained behaviour for

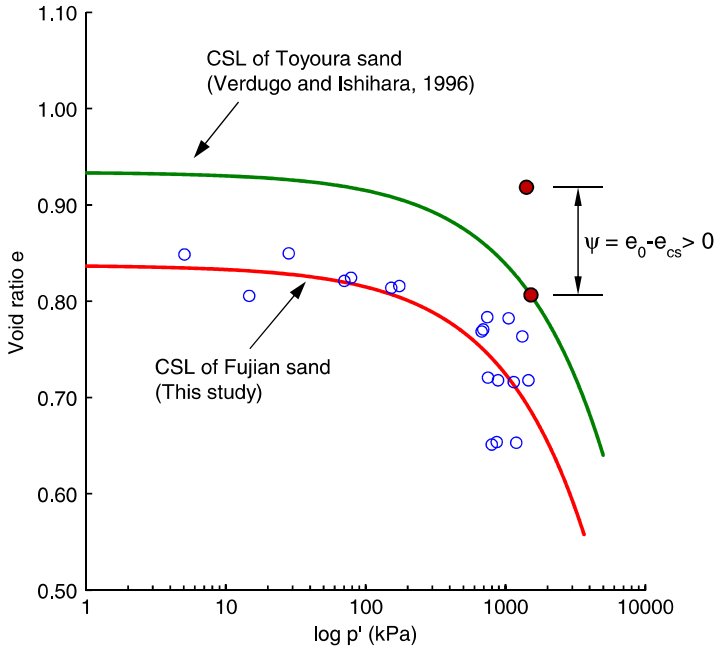


Figure 4.6: Critical state lines of Fujian sand and Toyoura sand (Yang and Sze, 2011).

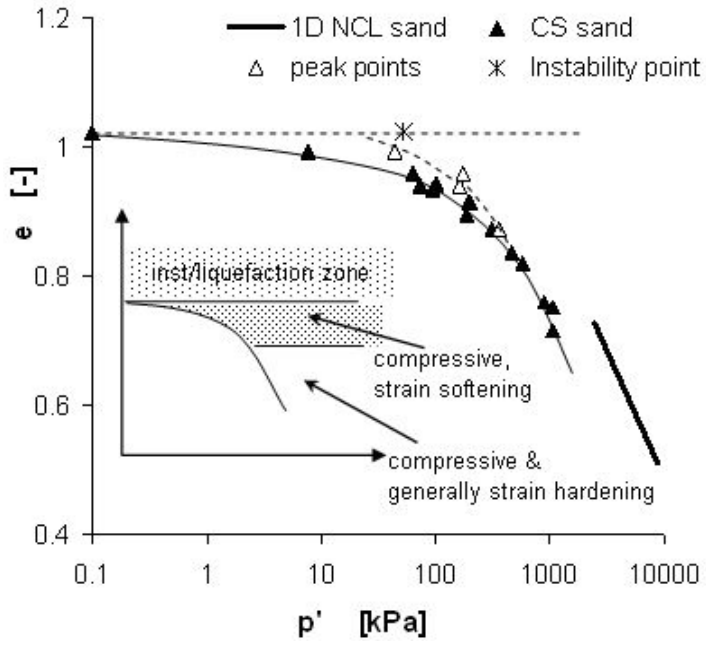


Figure 4.7: Critical state line of Stava tailings; Suggested scheme of subdivision of the area of the area above the CSL intro three different regions connected to different behaviour (Carrera et al., 2011; Viana da Fonseca et al., 2011a).

sands and / or silty sands. As pointed out by Jefferies and Been (2006) the definition of the state parameter is completely independent of the equation adopted for the CSL.

The following Figure 4.10 shows the undrained effective stress-paths and stress-strain response of

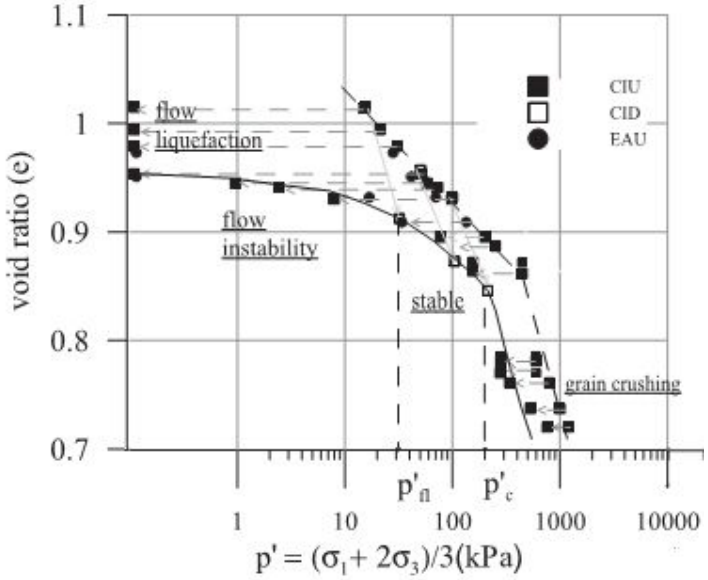


Figure 4.8: Critical state lines of gold tailings (Schnaid et al., 2013; Bedin, 2010).

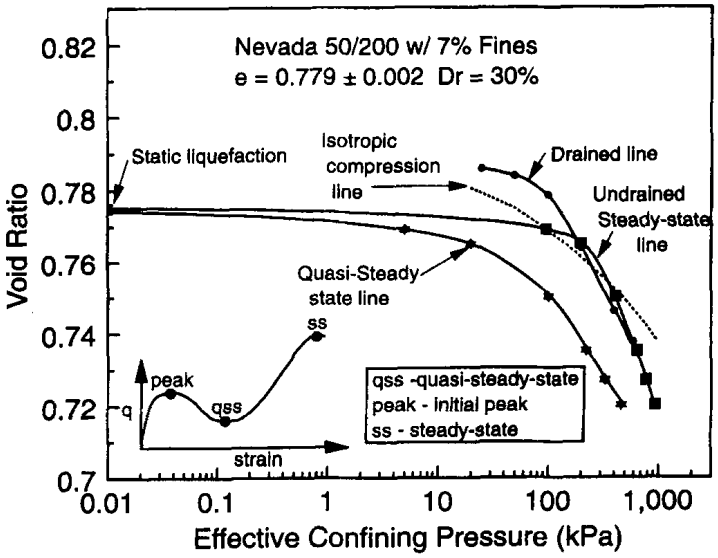
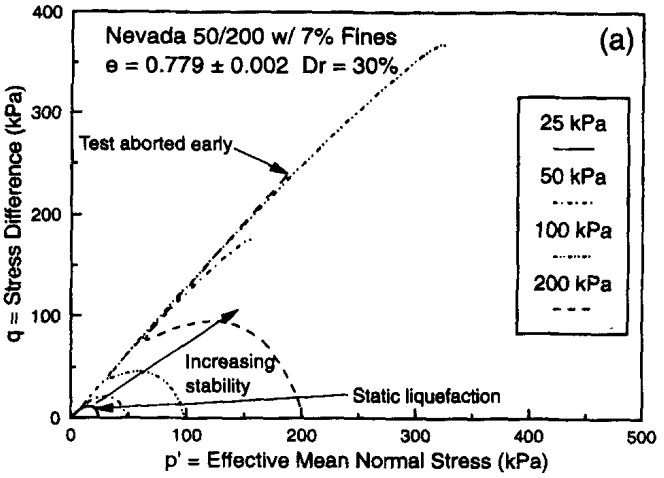
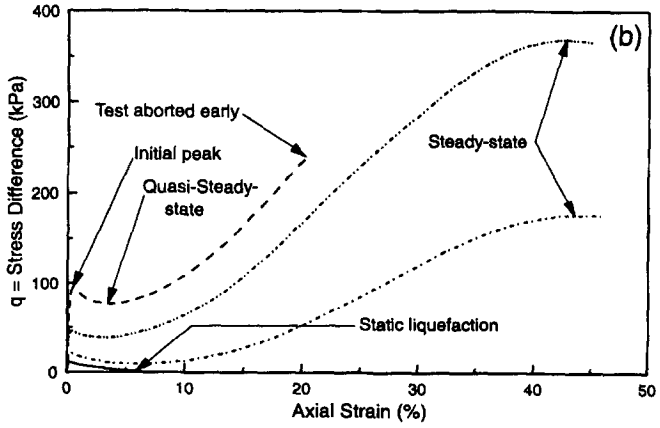


Figure 4.9: Steady State Diagram obtained from drained and undrained tests sheared from a single isotropic consolidation line on Nevada sand with 7% fines (Yamamuro and Lade, 1998).

Nevada sand (with FC = 7%), for confining stresses between 25 and 200 kPa. While the lower consolidated test completely liquefied, the other ones have not liquefied, reaching the CSL for a large axial strain. The steady state diagram, represented in Figure 4.9 exhibits an ICL, for initial relative densities of, approximately, 30%, below the CSL, and above the SSL. As can be observed soils in-between the CS and the horizontal branch of the SS lines dilate, while sheared under drained conditions, and liquefy, while sheared under undrained conditions. When the CSL and the SSL converge, the soil stops exhibiting instability and an undrained stable behaviour is reached.



(a)



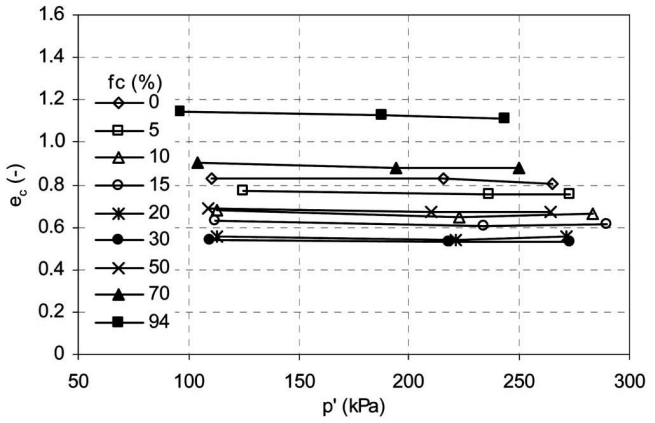
(b)

Figure 4.10: Undrained compression tests on Nevada sand with 7% of fines between 25 and 200 kPa initial confining pressure: (a) Effective stress-path; (b) Stress-strain relationship (Yamamuro and Lade, 1998).

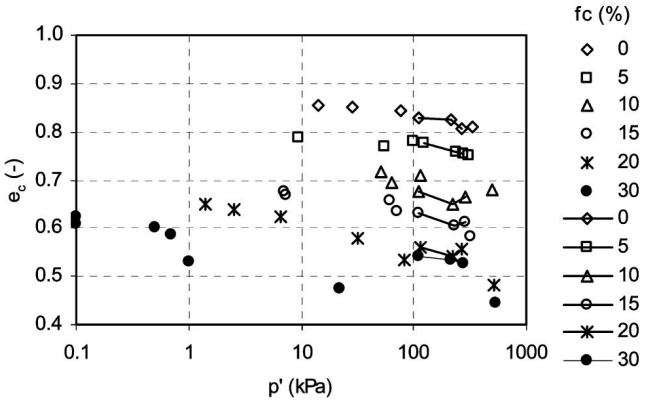
However, as can be observed from Figure 4.10, it does not mean that the soil is prevented from having a loss on shear strength before reaching it ultimate state (i.e. it critical state).

From what can be observed should the ψ measurement be used on soil liquefaction assessment? When CSL and SSL bifurcate is it a suitable parameter? From Figure 4.9, for Nevada sand, it employment does not make sense as the soil which liquefies have a $\psi < 0$ and the ones more stable, confined with higher confining pressures, have a $\psi > 0$, when is measured in relation to the CSL. On the other hand, if the state parameter is measured in relation to the SSL, than for decreasing confining stresses, higher the ψ and higher the liquefaction susceptibility. Due to uncertainty and to a lack of information, this issue remains open.

During the following work CSL and SSL are not considered the same, depending on the drainage process during shear. Elusive convergence might be referred during this chapter as it is supported by most of the authors that developed works on liquefaction hazard assessment.



(a)



(b)

Figure 4.11: (a) SSL for samples of various fines content (fc), tested under drained conditions and based on the void ratio; (b) Steady-state points from samples with fines content ranging from 0% to 30%, tested under drained and undrained conditions, being the connected points data obtained from the drained tests (Yang et al., 2006b).

4.2.2.1 Stress and strain paths - Peak, phase-transformation, critical and steady-state strength

When soils are sheared, perceiving the influence of the initial state conditions on their stress and strain paths, a world of distinct responses can be imagined. In the Figure 4.12 it can be observed three different soil responses, confined with a same initial confining stress, and three different void ratios. For the example given by Carrera (2008) soils located below the SSL exhibit, what would be dilation under drained conditions, negative pore pressures under undrained conditions, towards the SSL. When the soil is located below the SSL a peak strength below the failure surface (or Mohr-Coulomb surface) does not exist, contrary, after a phase transformation point a strain hardening, associated to dilation, takes place above the failure surface. The Phase-transformation (PT) line is the locus of points where a decrease in pore-water pressure takes place (Ishihara et al., 1975; Ishihara, 1993). According to some authors, (Negussey and Wijewckreme, 1988), if the soil is initially on a loose state condition then the mobilized friction angle at the phase transformation and constant-volume friction angle may be close.

The misgivings usually appear on soil liquefaction definition. As can be seen in Figure 4.12, some authors (Castro, 1969; Been and Jefferies, 1985; Sladen et al., 1985; Vaid and Chern, 1985), defined liquefaction what other authors designate by strain softening (Alarcon-Guzman et al., 1988; Lade and Yamamuro, 1997; Yamamuro and Lade, 1998; Viana da Fonseca et al., 2011a) or flow instability (Schnaid et al., 2013; Bedin, 2010). The misleading and confusions of the liquefaction term are not something new, and simply occur due to some labels imposed on particular behaviours of sands. Morris (1983) definition is an example: *"liquefaction is a phenomenon where a mass of soil loses a large percentage of its shear resistance, when subjected to monotonic, cyclic or shocking loading, and flows in a manner resembling a liquid until the shear stresses acting on the mass are as low as the reduced shear resistance"*. Also Castro et al. (1982) associated liquefaction to a process which evolves a huge loss of strength, and not to a complete loss of strength. However liquefaction is, defined during the present work, and in agreement with some other authors (Alarcon-Guzman et al., 1988; Ishihara, 1993; Lade and Yamamuro, 1997; Yamamuro and Lade, 1998; Yamamuro and Covert, 2001; Carrera, 2008; Schnaid et al., 2013; Bedin, 2010; Viana da Fonseca et al., 2011a) definition, associated to a complete loss of strength and to a zero effective stress condition (Figure 4.13). However both behaviours, flow liquefaction and strain softening, typically occur for soils in loose conditions, i.e. above the SSL (or CSL) (Figure 4.12 and 4.13). Yet for flow liquefaction to take place, under monotonic conditions, the loose soil must be lower confined. Very high confining stresses impose lower void ratios, thus a stronger soil skeleton, unable to suffer a complete loss of shear strength.

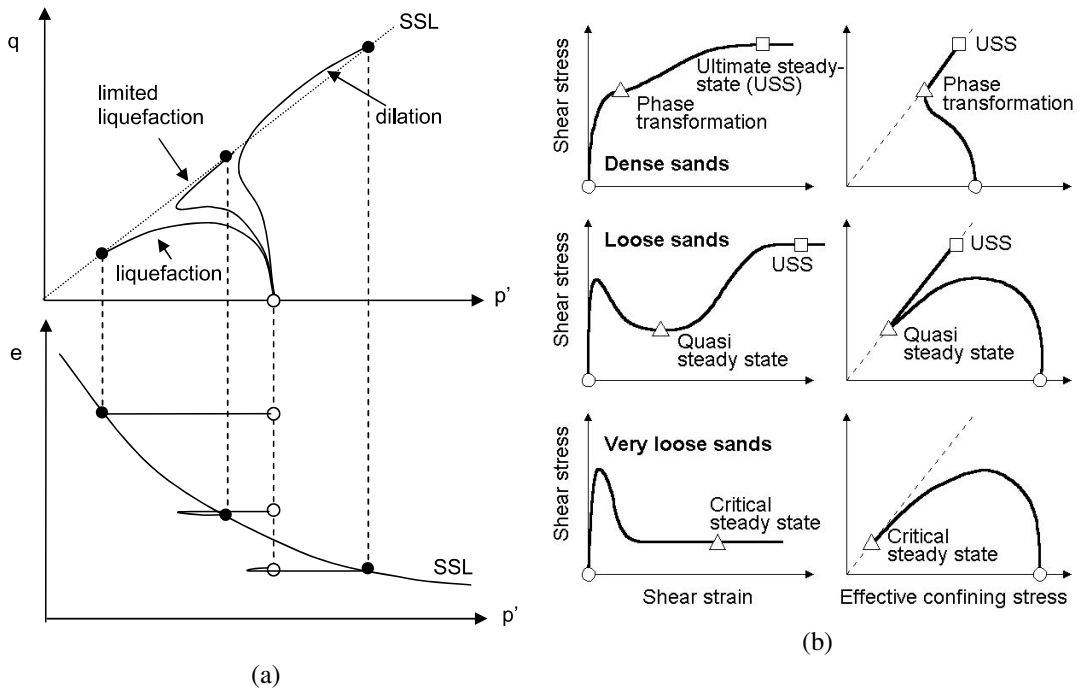


Figure 4.12: (a) Stress paths for three specimens of different initial densities consolidated at the same confining pressure (the white dots represent the initial states) and the position of the Steady States (black dots) on the Steady State Line (Carrera, 2008); (b) Undrained strength of sands (Yoshimine et al., 1999).

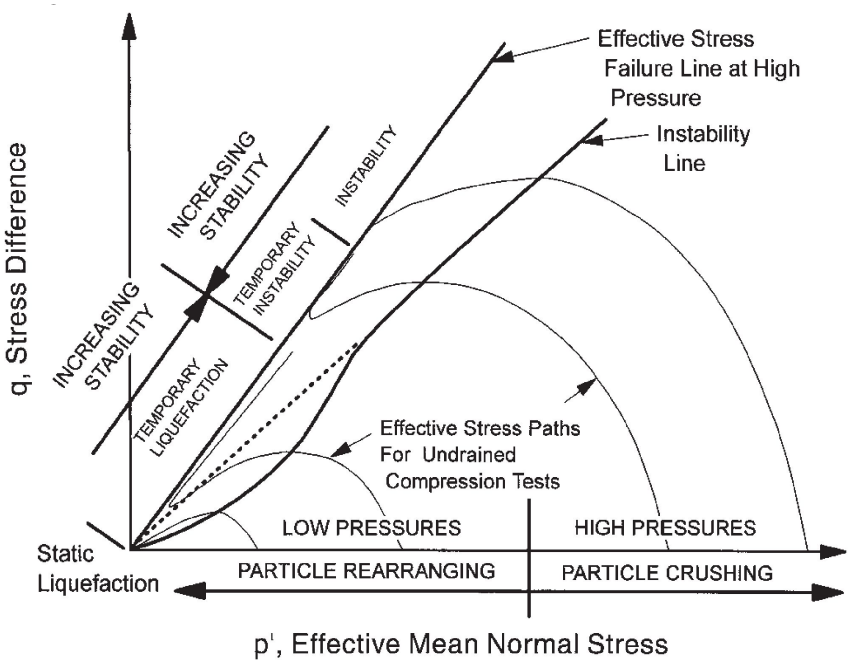


Figure 4.13: Four distinctly different general types of undrained effective stress paths for loose silty sands: Static liquefaction, temporary liquefaction; temporary instability, and instability shown in $p' - q$ diagram (Lade and Yamamuro, 1997).

Lade and Yamamuro (1997) go further and *"identified four different characteristics types of undrained behaviour under monotonic loading in either very loose clean sands or loose silty sands"*. In addition to static liquefaction (i.e. flow liquefaction triggered by monotonic shear), they also defined temporary liquefaction, in a stress region above static liquefaction and temporary instability and instability at higher pressures. Notwithstanding the last two instabilities are simply associated to an evolution of the grain size distribution, i.e. grain crushing. Thus as the percentage of fines increase a new soil is created and the instability is simply associated to the initial state condition of the new material.

In the present document temporary liquefaction is also distinguished between temporary liquefaction with strain softening, represented by liquefaction on Carrera (2008) $p' - q$ diagram (Figure 4.12), from temporary liquefaction with strain hardening represented by temporary liquefaction by Lade and Yamamuro (1997) $p' - q$ diagram (Figure 4.13). The main feature which distinguishes both behaviours is related to the ability of the soil to, after reaching a minimum strength, designated by quasi steady state (QSS), increase it strength with increasing axial strain, towards the SSL (or CSL).

According to Alarcon-Guzman et al. (1988) and Ishihara (1993) the quasi steady state is the point at which the soil changes from contractive to dilative behaviour. This point of lowest strength usually occurs at moderate strains (4-5%) and is typical of temporary liquefaction with strain hardening. Yet QSS is a temporary unstable deformation state at which the sand specimen is deforming at constant volume, constant mean effective stress, and constant shear stress (Ishihara,

1993; Wan and Guo, 2001). Plus, according to Vaid and Sivathayalan (2000), the friction angle at the quasi-steady state, ϕ_{QSS}, is a material property as the QSS line is unique, as long as strain softening occurs, regardless the initial state or stress-path. Despite QSS/SS being unique in stress space, it is not unique in the void ratio-stress space. These findings corroborate the existence of a SSL, non-unique, which is not the coincident with the CSL. Regardless not being unique, QSS line is strongly dependent on the initial stress state conditions. Yet Wan and Guo (2001) prefer to link the QSS to internal state parameters such as fabric and dilatancy, as the undrained response of Nevada sand prepared through different reconstitution techniques led to a strain hardening in one case and to strain softening in the other case.

The quasi steady state point is preceded by a peak strength, at low strains (1-2%) and is followed by a strength hardening, towards the SSL (or CSL) at large strains (Yamamuro and Lade, 1998).

Quasi-steady state line and phase-transformation line are assumed to be the same on loose contractive soils which deem to exhibit strain softening when monotonically sheared, under undrained conditions. Plus for soils under these circumstances, as suggested by Vaid and Chern (1985), the mobilized friction angles, for the phase transformation line and the steady state, are slightly smaller, independent of initial stress state conditions and density states. Notwithstanding phase-transformation line depends on the initial state condition of the soil and may be found even in dense sands (Alarcon-Guzman et al., 1988; Hyde et al., 2006; Wan and Guo, 2001).

Earlier Alarcon-Guzman et al. (1988), following previous studies (Castro, 1969; Been and Jefferies, 1985; Sladen et al., 1985; Vaid and Chern, 1985), established three regions in the p'-q diagram according to the stress-strain behaviour of sands. From the diagram, represented in Figure 4.14, the author, for a same initial void ratio, established two different regions, for loose sands, separating the soils which strain softens, for higher confining stresses, from those closer to the SSL (F line) which exhibit strain hardening after reaching a minimum strength. Nevertheless, and excluding stress-path A, looking closer at the ultimate state of each other stress-paths, it is observed that those located in this transient region, closer to SSL, do not fall in the same ultimate state as those which suffer limited liquefaction with strain softening. The ultimate state points of those exhibiting strain softening are leftmost than those exhibiting strain softening. This might be a hint of CSL and SSL divergence. In fact, according to Yamamuro and Lade (1998) data, SSL and CSL convergence are found for Nevada sand (with 7% FC), when it starts exhibiting, under undrained conditions, strain hardening after the quasi-steady state.

An additional typical behaviour, designated by grain crushing, might be found for some soils, in a wide range of very high confining stresses, which are only usually achieved by testing material in a high-pressure triaxial apparatus (e.g. Figure 4.8 and 4.13). Such behaviour has been well stated in granular materials (Coop et al., 2004) and is clearly associated to an evolution of the inclination of both normal consolidation and critical state lines in e-log p' space. Grain crushing is not something new in the scope of soil mechanical behaviour and is an irreversible phenomenon,

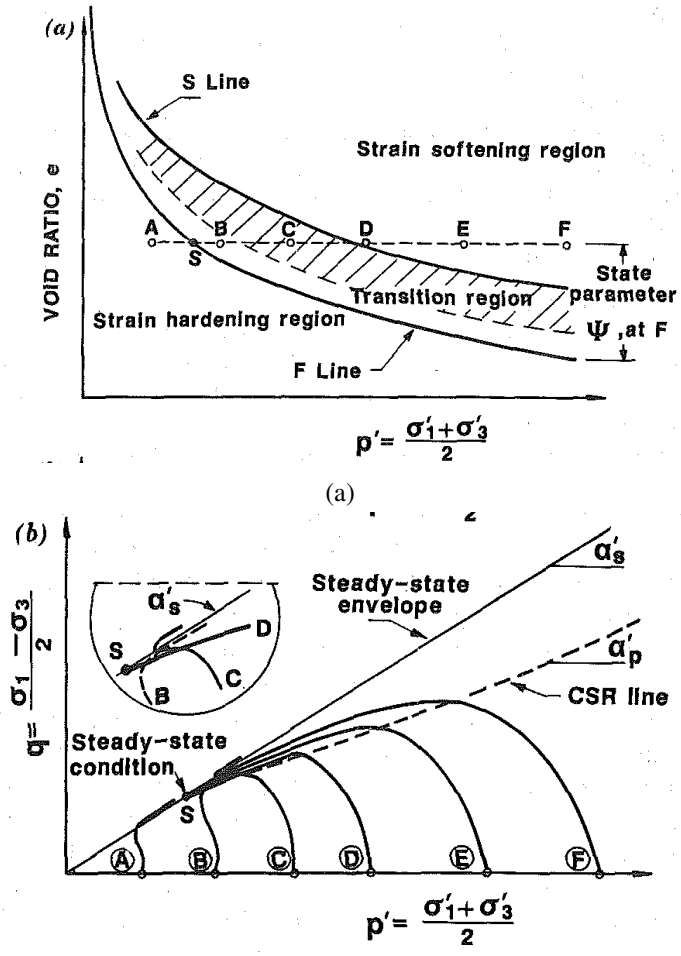


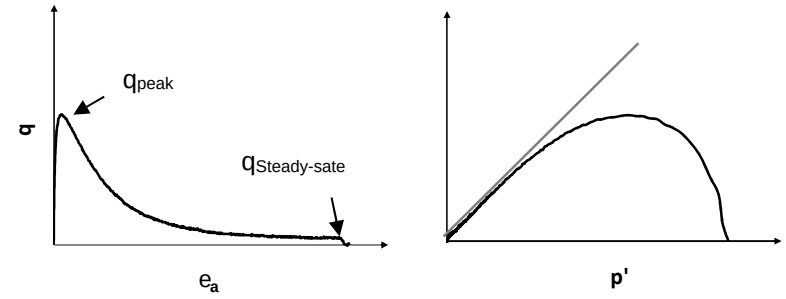
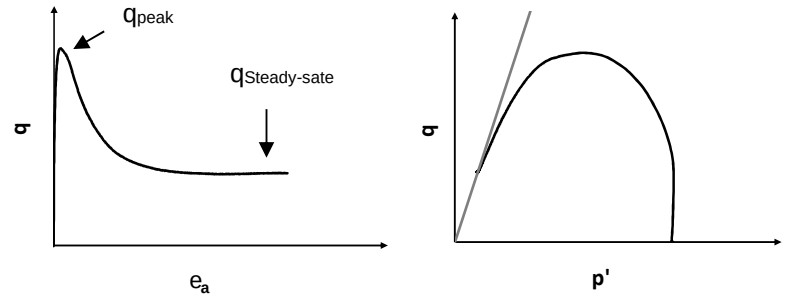
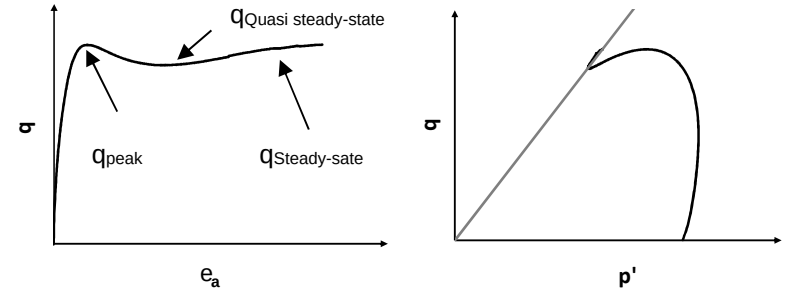
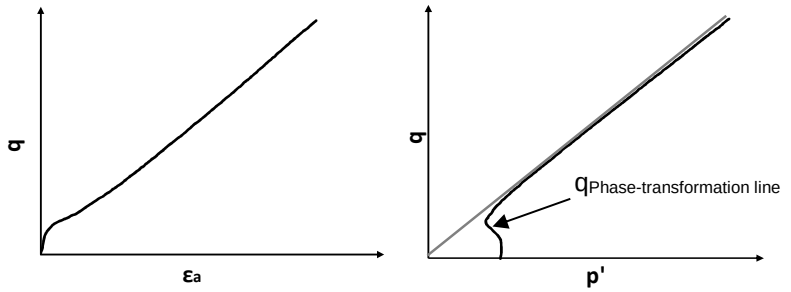
Figure 4.14: Monotonic undrained behaviour at constant relative density: a) State diagram; b) Stress path plot (Alarcon-Guzman et al., 1988).

(Muir Wood, 2008), leading to an evolution of the critical state line position, going downwards in the y-axis.

Table 4.1 shows the definitions adopted for sands and silty-sands undrained strength behaviour during this work.

Despite the occurrence or not of divergence between the CSL and the SSL, moderate strains (4-5%) occur at minimum strengths (QSS points), and might not be compatible with the displacements of nearby structures. Thus shall the infrastructures design be based on the ultimate state of soils? Nevada sand (7% FC) steady state strength is, for the specimen confined with 100 kPa, four times higher than the minimum strength reached under undrained conditions. It becomes imperial to understand how can be evaluated the strength of soils, while under undrained conditions, not only for liquefaction assessment purpose, but also for a correct infrastructures design. If modeling purposes are inferred then an overall knowledge over soil behaviour is required, however and as pointed out by Jefferies and Been (2006), for engineering purposes, a greater attention is

Table 4.1: Undrained strength behaviour and respective definition for sands and silty-sands.

Sress-path and stress-strain graphs	Soil behaviour
	Liquefaction (100% excess pore pressure) - ψ>0; - Low confining stresses
	Limited liquefaction with strain softening - ψ>0; - Medium confining stresses
	Limited liquefaction with strain hardening - ψ>0; - High confining stresses
	Dilation - ψ<0

mandatory for soils confined between 20 and 500 kPa.

4.2.2.2 Instability concept

"Classical equilibrium methods of geotechnical engineering consistently overestimate the factor of safety of these structures, because they are based on ultimate friction values and prefailure pore pressures" (Skopek et al., 1994).

As we might infer from loose undrained strength of sands (Figure 4.15), the peak deviator stress of sand, exhibited during undrained monotonic shear, reflects it maximum reachable strength, before instability is found. Although, as highlighted by Lade (1992) instability is not a synonymous of failure, however both may originate disastrous events.

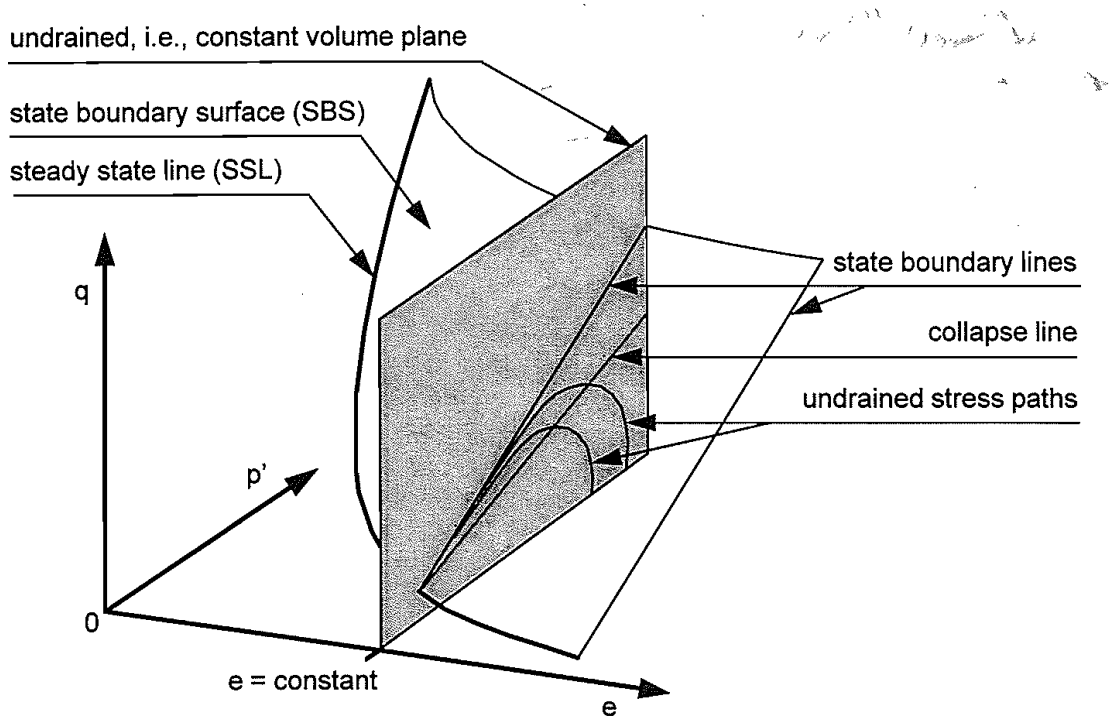


Figure 4.15: Definition of the elements of state boundary surface. The collapse line is below the state boundary in the undrained plane (Skopek et al., 1994).

These peak strengths are, for some loose state conditions, the highest strength of soils and the onset of instability, being important to define their locus in the p'-e-q space. In addition it becomes essential to assess the influence of some external factors on the position of this yield surface.

The term of collapse surface, was introduced by Sladen et al. (1985), as the line joining the peaks of the stress-paths to the ultimate state in p'-e-q space. Sladen et al. (1985) also observed, while studying the Nerlerk subsea berm flow slide, that the peaks of the undrained effective stress-path at the same void ratio but at various initial stress states fell on a unique straight line, which eventually would reach the same steady state. Nevertheless while testing distinct void ratios, despite the collapse line having the same slope, they ended at different steady states.

Later Lade (1992) defined the locus of peak shear strength points as Instability Line (IL), constituting the limit of the region of the instability line. The differences between the collapse line and the IL are on it intersection, while the first one intersects the SSL, Lade assumed IL intersection on the origin of the stress space (Figure 4.13). When the instability line is reached, granular soils start to deform plastically under decreasing shear stress. Notwithstanding, as pointed out by Carrera (2008), not all peak points imply the failure of the soil.

As it could be expected with increasing closeness of the initial soil state to the SSL, increasing becomes the stability and less pronounced is the peak strength. Thus the soils become more stable when it initial state condition is closest to it ultimate state, being completely stable when on the dry side. Supporting Lade and Yamamuro (1993), Lade and Yamamuro (1997) and Yamamuro and Lade (1998) founding's, Chu and Leong (2002) found IL to be also dependent on the initial void ratio. In the same year Yang supported IL to be dependent on the initial void ratio but also dependent on the initial confining stress (Figure 4.16). Thus, as found my numerous authors (Yamamuro and Lade, 1997, 1998; Carrera, 2008; Carrera et al., 2011; Schnaid et al., 2013; Bedin, 2010), liquefaction resistance increases with increasing initial confining stress. This feature is also easy to picture, as with increasing confining stress, for very loose conditions, lower is the void ratio, and higher the contact surface between particles. Nontheless this might be a result of the relative positioning of the initial state of the soil on the p'-q-e space.

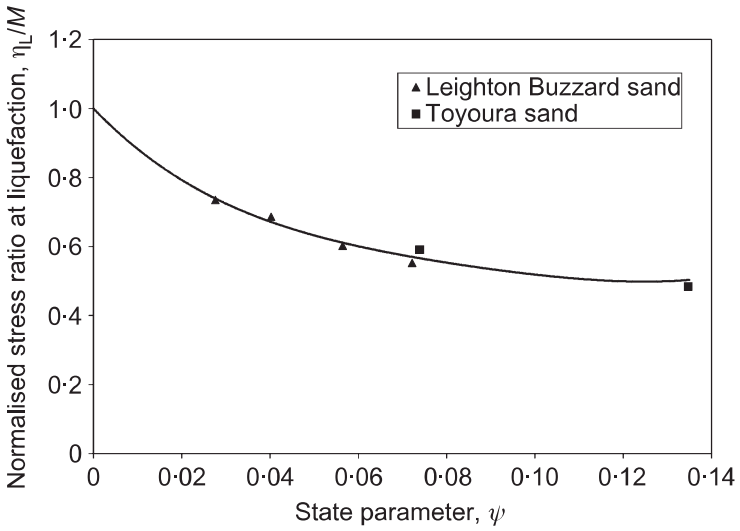


Figure 4.16: Stress ratio at peak undrained strength of loose sand expressed in terms of current state parameter ψ at onset of liquefaction (Yang, 2004).

Aware of the the simultaneous effect of both initial void ratio and initial confining stress on liquefaction onset, Yang (2002b) proposed a correlation making feasible the prediction of the stress ratio, η_{IL}, correspondent to the onset of liquefaction, by knowing the state parameter ψ of a certain soil (Figure 4.16).

In a modelling point of view the concept evolved in the instability line is difficult to percept and

have different interpretations when it stands to it definition. However, as highlighted by Jefferies and Been (2006), while sheared monotonically under drained conditions, loose soils would not exhibit collapse, instead a stable classical failure would be displayed. Thus if meta-stable is not created while under drained conditions, which mechanism is associated to the IL? Is it just a boundary conditions problem? (adapted from Viana da Fonseca and Soares (2012)).

Usually most of the current constitutive models do not adopt IL as soil characteristic, instead soil collapse prediction is performed through the nullity of the second-order work, $d^2W = 0$, originally proposed by Hill (1958) (Sanisand, from Dafalias and Manzari (2004)). The vanishing of the second-order work leads to loss of stability and coincides with the loss of uniqueness in the incremental response (Ramos, 2010).

4.2.2.3 Instability under drained conditions

Instability mechanisms of sand created under drained conditions is not something and is a very concerning issue due to the occurrence of flow slides in slopes deposited with inclinations lower than angle of repose of the sand. It occurrence are addressed, not only to saturated sands, but also to dry sands, meaning that the condition of saturation is required but not necessary as it also depend on the loading path.

In fact Skopek et al. (1994) demonstrated that while testing dry loose Ottawa sand, when subjected to constant deviator stress path, an increasing compressibility followed by instability took place at a certain discreet stress state. This collapse occurred in tests with slow decreasing cell pressure. Yet according with Skopek this change occurs at a mobilized friction angle smaller than the critical state friction angle. Thus geotechnical design cannot always relay on the ultimate mobilized friction angle as a guarantee of safety. Furthermore, according to Skopek, this structural collapse is responsible for the pore-pressure generation during the collapse of very loose saturated sand, resulting in flow liquefaction.

Notwithstanding, unsaturated sands are not studied and therefore not addressed in the present thesis.

Nevertheless a same stress path was studied, for saturated soils, by many authors (Sasitharan et al., 1993; Chu et al., 2012; Mattioti et al., 1995; Leroueil and Wanatowski, 2009). This stress-path, illustrated in Figure 4.17, was firstly suggested by Sasitharan et al. (1993), and the importance of it study reports to real field cases, when instability occurs not only by increasing shear stress, but also by a reduction in the effective stress due to, for example, water infiltration into slopes (Chu et al., 2012). According to Mattioti et al. (1995) the entire process may be considered drained as a virtually full-drainage is guaranteed while the water table is slowly risen.

According to the previous authors despite the phenomena, instability, due to pore water pressure increase under drained conditions, and due to an increasing monotonic shear, under undrained

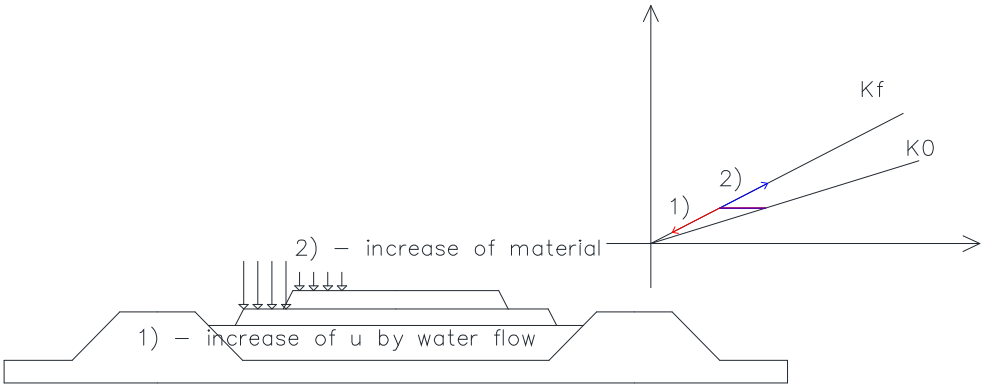


Figure 4.17: Flow liquefaction due to: 1) increase of u due to water infiltration; 2) increase of q due to increasing material deposition.

conditions, have differences and similarities. While the first one is caused by an unstable microstructural fabric rearrangement, the second one is due to a compactive condition mechanical behaviour of loose granular material and consequent pore pressure increase (Matiotti et al., 1995). Neverthless similarities among both stress-paths are found on the Instability line (IL), as it influences both drained and undrained stress-paths (Chu et al., 2012).

From what follows it is comprehensive that while instability under undrained classical stress-paths may be determined using the state parameter proposed by Been and Jefferies (1985), the prediction of instability due to pore water pressure increase, under drained conditions, is beyond agreement.

Leroueil (2001) found that this instability is not controlled by initial stress state conditions, but rather by the relative position of the point at yielding, with respect to the CSL. Later Chu et al. (2003) proposed a modified state parameter ψ - with reference to the yield surface, i.e. with respect to the initial state at the IL (Figure 4.18 and Figure 4.19).

"For large plastic strain to develop the soil must be in a yielding state" (quoted from Chu et al. (2003)). Being the IL defined based on the yielding conditions, it is recognized that this surface may be characterized similarly to a friction angle. Notwithstanding it shall not be used as a friction angle, as it position changes with soil fabric and induced anisotropy, among other factors (Lade and Yamamuro, 2011). As pointed out by Di Prisco et al. (1995) the evaluation of this type of instability, basing on isotropically consolidated, undrained triaxial compression tests, K_0 consolidated specimens will have a yield surface rotated around the stress origin, located higher up (Figure 4.20). Thus the immediate response of anisotropically consolidated soils is to deform elastically, as the current state is inside the yield surface, liquefying only after passing the yield surface, as can be seen in figure 4.21 (Vaid and Eliadorani, 1998; Lade and Yamamuro, 2011). According to Vaid and Eliadorani (1998), soil triggering occurs after the stress path enters a region bounded by the IL, the PT line and a horizontal cutoff, correspondent to the steady state strength of the soil. Similarly to Kramer (1996) they found out stability in the region below the cutoff,

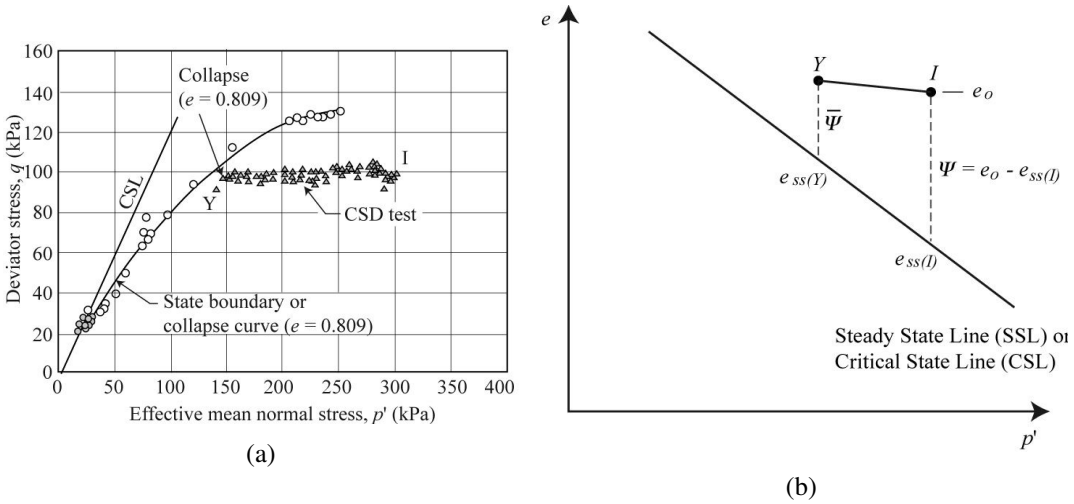


Figure 4.18: (a) Instability or collapse curve at e = 0.809 and CSD test, i.e. triaxial tests with deviator stress and mean stress controlled, (q = 100 kPa) on Ottawa sand (after Sasitharan et al. (1993) by Leroueil and Wanatowski (2009)); (b) Definition of the state parameter ψ and the modified state parameter (after Chu et al. (2003) by Leroueil and Wanatowski (2009))

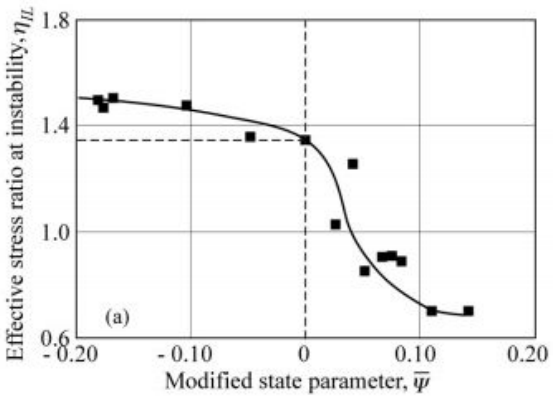


Figure 4.19: Relationships between the effective stress ratio at instability and the modified state parameter for Changi sand in triaxial conditions (Chu et al., 2003).

meaning basically that if the deviator stress is lower than the steady strength of the soil, then it exhibits a stable behaviour.

Notwithstanding the IL obtained from isotropically consolidated, undrained triaxial compression tests defines the lower bound of all the possible unstable conditions (Chu et al., 2003). Thus it is physically substantiated to predict drained instability upon IL definition, obtained by shearing undrained isotropically consolidated specimens (Lade and Yamamuro, 2011).

Furthermore is necessary to point out that instability takes place not only for loose soils but also for soils denser than the CSL. According to some authors, (Chu et al., 2003, 2012; Leroueil and Wanatowski, 2009), instability occurs for denser soils at an angle of strength mobilization slightly larger than the critical state friction angle, and if dilation is allowed, failure may be followed by

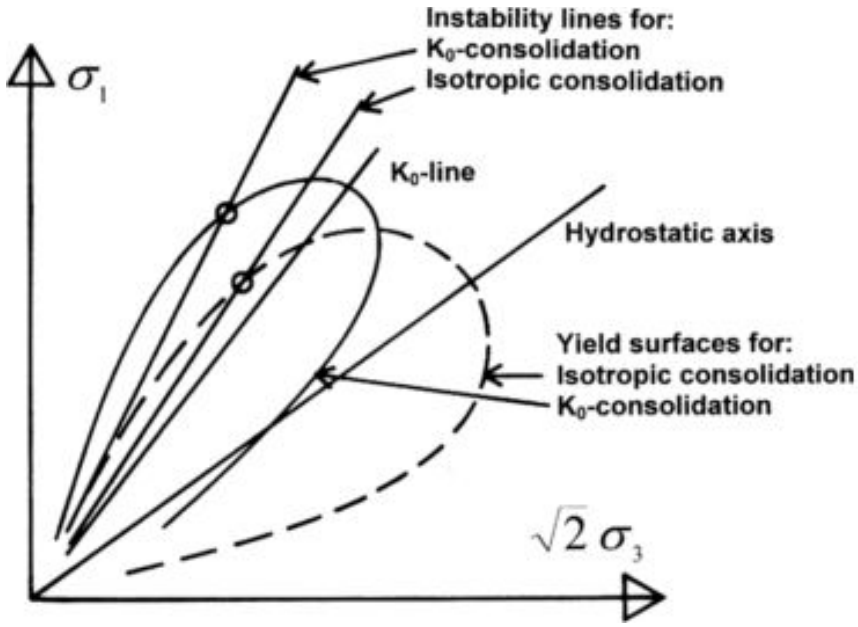


Figure 4.20: Schematic diagram of locations of yield surfaces and instability lines for isotropically and K_0-consolidated soil elements (Lade and Yamamuro, 2011).

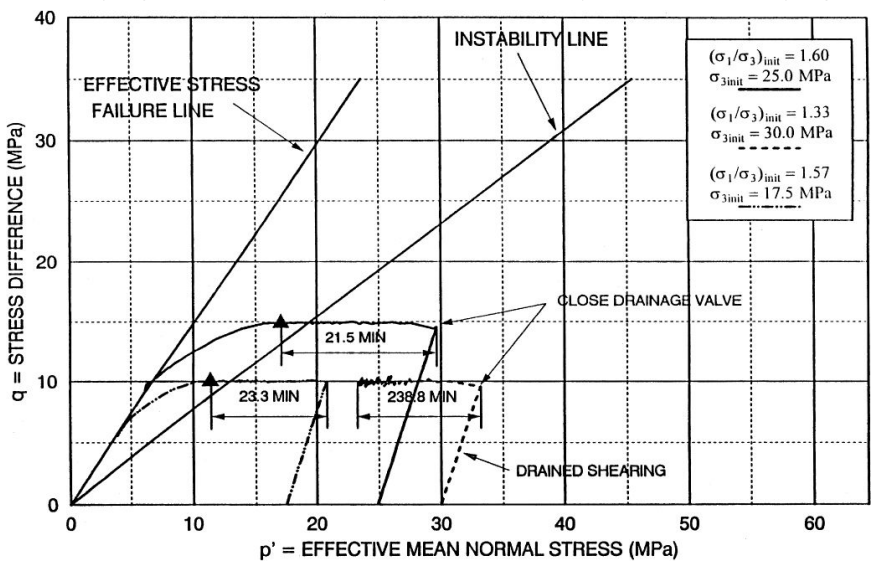


Figure 4.21: Effective stress-paths in p'-q diagram for three triaxial compression tests on medium-dense Cambrian sand exposed to undrained creep initiated outside the instability region. Two tests eventually exhibited instability inside the instability region (Lade and Yamamuro, 2011).

run-away post failure. An example of this situation is when seism originates a migration of pore water pressure from loose to denser zones (Vaid and Eliadorani, 1998).

4.3 Factors Affecting Static Liquefaction

There are lots of factors affecting the undrained shear response of cohesionless soils. During this section only factors related to liquefaction triggering and to the SSL (or CSL) positioning will be discussed. Realizing that liquefaction onset is characterized by IL position, it is important to evaluate how it changes with changing factors, such as relative density, confining stress, fines content, inherent and induced anisotropy, and the rotation of principal stress directions during shear.

4.3.1 Influence Of Initial Confining Stress Level And Relative Density

Through CSSM is well recognized that, for a same void ratio, loose specimens subjected to monotonic or cyclic loads, are more contractive with higher confining stresses. On the other side undrained response of dense specimens is controlled by dilatancy, which is associated with the development of negative excess pore-water pressure. Whereas undrained response of loose specimens, controlled by contractiveness, is associated with positive pore-water pressure. On the other side, while submitted to cyclic shear stress or shear strain the tendency of the sand is to compact causing a progressive development of positive pore-water pressure, while under undrained conditions, or to a progressive reduction in vertical pressure on the loading head, under constant volume conditions. Nevertheless the basics of CSSM are or should be also applied in cyclic conditions. *"The influence of the level of the confining stress on the response is fairly well understood both under cyclic and monotonic loading conditions. Increasing confining stresses have been shown to increase the contractive tendency at a given initial density (Vaid and Eliadorani, 1998; Vaid and Thomas, 1995)"* (Sivathayalan and Ha, 2011).

As explained earlier the initial state conditions of soils, i.e. initial relative density and initial confining stress, with relation to its final state, i.e., the critical state, allows the evaluation of liquefaction potential. While specimens located on the dry side exhibit a dilative behaviour, thus a stable behaviour, specimens located on the wet side may be prone to liquefaction. Soil liquefaction susceptibility, for these cases, can be evaluated by determining experimentally the locus of the instability line and it dependency on the state parameter. Such a correlation was proposed by Yang (2002b) for Toyoura sand and Leighton Buzzard sand (Figure 4.16).

Yamamuro and Lade (1998) also recorded distinct SSL for specimens prepared with distinct initial void ratios (Figure 4.22). Thus, beyond IL, also SSL changes positioning moving upward in the e – p' space, for lower initial relative densities. SSL non-uniqueness was observed in Nevada sand 50/200, with 6% of fines content, and it was attributed, by the authors, to the "reversal" behaviour typical of silty sands, i.e. to liquefaction susceptibility even for higher densities with different combinations of lower confining pressures. As can be observed in Figure 4.22 if a unique SSL existed then all the specimens prepared with 12% would have liquefy. Notwithstanding SSLs did

not converge for higher confining pressures which the authors attribute to a loss of their capacity to dilate before reaching the steady state. Plus is the 6% of FC, near 5% of FC for being considered as clean sands, enough to cause such a distinct behaviour?

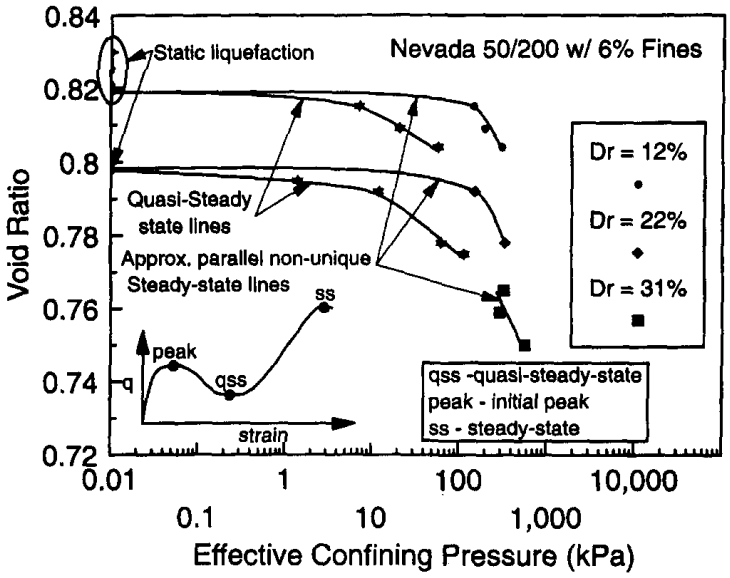


Figure 4.22: Steady state diagram from undrained tests on three densities of Nevada sand with 6% of fines showing non-uniquess of SSLs and QSSLs (Yamamuro and Lade, 1998).

4.3.2 Influence Of Non Plastic Fines Content

The presence of cohesionless fines on soils is not only very common in nature but also as a product of industrialized processes from industrial mining. From the increasing problems related to tailing damns and slopes instability arose the concern of studying the effect of the fines content on the undrained shear strength of the soil, becoming one of the most important issues on the evaluation of liquefaction hazard. Plus due to the occurrence of grain crushing when soils, subjected to high confining pressures, are sheared, the study of fines content gained greater relevance.

The study of silty-sandy and silty soils have revealed in past studies many stability problems, mainly related with flow liquefaction and strain softening. As has been mentioned along this chapter, instability triggered by an increasing loading might be easily assessed experimentally by determining the locus of the IL, for isotropically consolidated specimens. Notwithstanding, as reported by Carrera (2008), not all peak strengths reflect liquefaction onset, thereby it is also important to determine SSL (or CSL) location, as well as the limit boundary for which soils stop liquefying.

However as it is widely known the performance of an extensive laboratorial work is expensive and time consuming. Thus in an attempt to reduce implied time and cost, many researchers have been

studying the effect of fines on the SSL (or CSL) positioning in order to normalize the SSL (or CSL) to the one of the clean base sand.

Jointly to the IL, flow liquefaction is also associated to the relatively low conductivity and high compressibility of fine graded sands and silts (Yamamuro and Lade, 1997, 1998; Lade et al., 2009). While a low permeability induces difficulties on the dissipation of excess pore pressure, which may cause soil liquefaction due to its inability to bear shear static stress, on the other hand the high compressibility of well graded silty-sandy soils is responsible for a high contractibility for low confining stresses. It compressibility is very high when compared with clean sands, which reflects on SSL (or CSL) and NCL slope, λ. Plus, comparatively, sands are only prone to flow liquefaction under laboratory conditions, through reconstitution techniques, while silty-sands and silts only exhibit a stable behaviour for higher confining stresses (Yamamuro and Lade, 1997, 1998; Lade et al., 2009).

The Silty high susceptibility of silty-sand soils to liquefaction hazard comes from the loose meta-stable configuration created between bigger and smaller grains. Then when a shear stress is applied in such a meta-stable structure it will force smaller particles to fill in the spaces in-between the bigger grains, creating a large volumetric contraction, and a possible collapse (Figure 4.23).

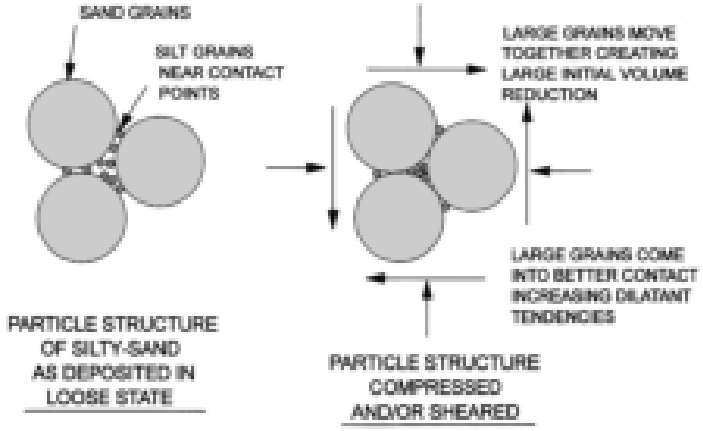


Figure 4.23: Schematic diagram showing silty sand deposited in a loose state with silt grains between large grains. Application of stresses causes silt grains to move into void spaces, resulting in large volumetric contraction in static liquefaction (Lade and Yamamuro, 1997).

Figure 4.23 shows a schematic diagram of silty soils configurations. As can be expected with increasing confining stress, lower the maximum reachable void ratio, turning soil configuration less unstable. Thus with IL nearness to CSL (or SSL), more stable is the soil behaviour.

Aiming to predict liquefaction susceptibility of soils with varying fines content, Lade and Yamamuro (1997) and Yamamuro and Lade (1998) proposed a three-dimensional framework which combines the fines content, with volume compressibility and the void ratio (Figure 4.24). Such a framework arose from the inability, reported by Yamamuro and Lade (1998), of the steady-state diagram to predict soil liquefaction.

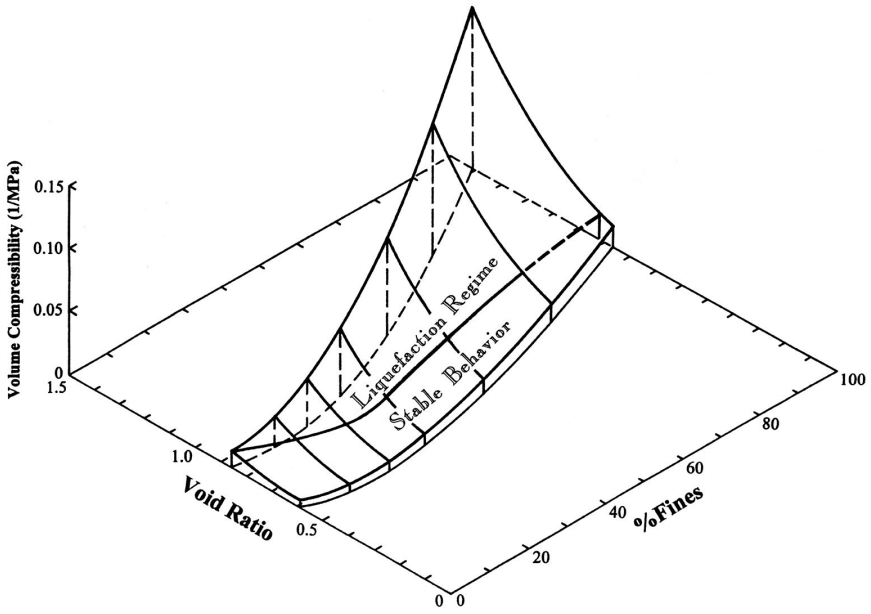


Figure 4.24: Three-dimensional diagram showing static liquefaction related to volumetric compressibility, which in turn is influenced by fines content and void ratio for specimens of fine Ottawa sand and Loch Raven fines (Lade et al., 2009).

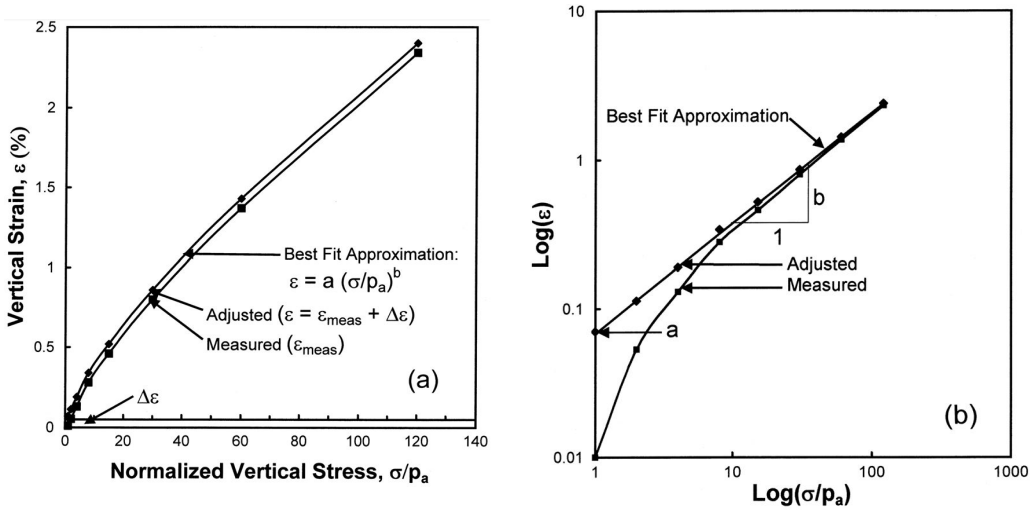
Soil volumetric compressibility might be obtained by performing a set of one-dimensional compression tests. Such variable is mainly controlled by the major principal stress, which in one-dimensional compression tests is the vertical stress, and might be determined by the following equation (Lade et al., 2009):

$$m_v = \frac{d\varepsilon}{d\sigma} = a.b.\left(\frac{\sigma}{p_a}\right)^{b-1} \tag{4.5}$$

being a and b the best-fitting parameters determined from the one-dimensional compression curve on log-log scales as shown in Figure 4.25.

Volumetric compressibility is a key parameter on undrained shear strength, as the contractibility tendency is compensated by a generation of an excess pore pressures, being the magnitude of such variation a contra-balance between elastic and plastic volumetric deformation, as $\varepsilon_v = 0$. Through applied CSSM, compressibility is usually incorporated through CSL inclination, λ, and elastic bulk modulus K. Elastic compressibility is represented by k, which is related with K, and λ captures the plastic behaviour of soil (Jefferies and Been, 2006). Notwithstanding and for sands, parallelism between the NCL and the CSL is not required, being compressibility, (e.g. NorSand model), related to a plastic hardening modulus which is also related with λ (Jefferies and Shuttle, 2011).

The inability, reported by Yamamuro and Lade (1998),of the steady-state diagram to predict soil



(a) (b)

Figure 4.25: Measured and adjusted one-dimensional compression curves shown on (a) arithmetic, and (b) log-log scales with best fitting lines for description by power functions (Lade et al., 2009).

instability is a result of the occurrence of whta they designated as reversal behaviour for sands with fines. According to them sands normally exhibit increasing instability with increasing confining pressure, unlike sands with fines. From these observations they designated "reversal behaviour" for Nevada sand with 7% of fines content (Figure 4.9). A misleading led to such conclusions as the authors were comparing specimens with increasing confining pressure, and decreasing void ratio. Thus it is expected that, within a range of confining pressures that no grain size evolution occurs, both sands, silty-sands and sands exhibit an increasing stability for initial states sheared along the NCL. With increasing confining pressures there are some soil configurations unable to be created for lower confining pressures. The increasing contact forces in-between particles obligate a higher contact surface, thus a decreasing void ratio. Then soil instability, i.e. liquefaction potential, might be properly assessed through a state parameter by measuring the initial distance of the soil to the SSL, obtained by undrained tests (for the cases where CSL and SSL do not coincide) (Figure 4.26).

However when the state parameter is measured relatively to the CSL, when the CSL and SSL do not coincide, it becomes a useless parameter to predict soil liquefaction potential. While cases prone to liquefaction would have a negative state parameter, soils exhibiting a stable behaviour would have a positive state parameter.

Figure 4.26 shows schematically a resume of the distinct soil behaviours according to each initial state condition (i.e. the combination between the initial void ratio and the initial confining stress).

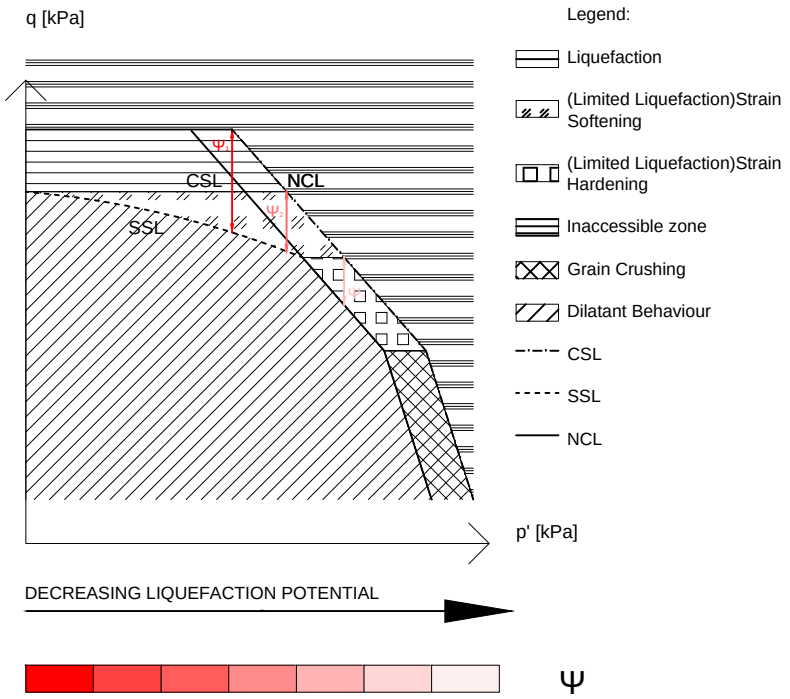


Figure 4.26: CSL and SSL for sands and silts; Undrained shear strength of soils delimited in a diagram e-log p'; Measurement of liquefaction potential through the state parameter ψ.

4.3.2.1 Effect of fines content on critical state parameters

Coming back to the effect of fines content it is important to assess which are the main parameters influenced by its presence, mainly those which influence on first hand soil liquefaction potential. As referred before compressibility, void ratio and hydraulic conductivity stands out among other factors. The void ratio might be assessed through the relative density, which depends on the maximum and minimum void ratio, but more importantly to its position in relation to the CSL (or SSL). Thus it becomes important to figure out how the fines influence CSL (or SSL) positioning. Jointly volume compressibility are related to the soil initial state condition relatively to it ultimate state (CSL or SSL). Hydraulic conductivity becomes a very important feature to analyse liquefaction potential of soils, however it effect is only perceptible while in the presence of drainage boundaries. While performing undrained laboratory tests, hydraulic conductivity becomes useless, only affecting the time rate of plastic strains accumulation.

From Figure 4.27 and 4.28 is observed that CSL (or SSL), with increasing fines content, goes downward in the semi-logarithmic e: log p' space, till a, commonly called, transitional fines content of 30%-40% is reached, beginning to move upwards for higher fines content (Zlatovic and Ishihara, 1997; Thevanayagam et al., 2002; Naeini and Baziar, 2004; Yang et al., 2006b,a; Rahman and Gnanendran, 2008; Bobei et al., 2009; Carrera et al., 2011).

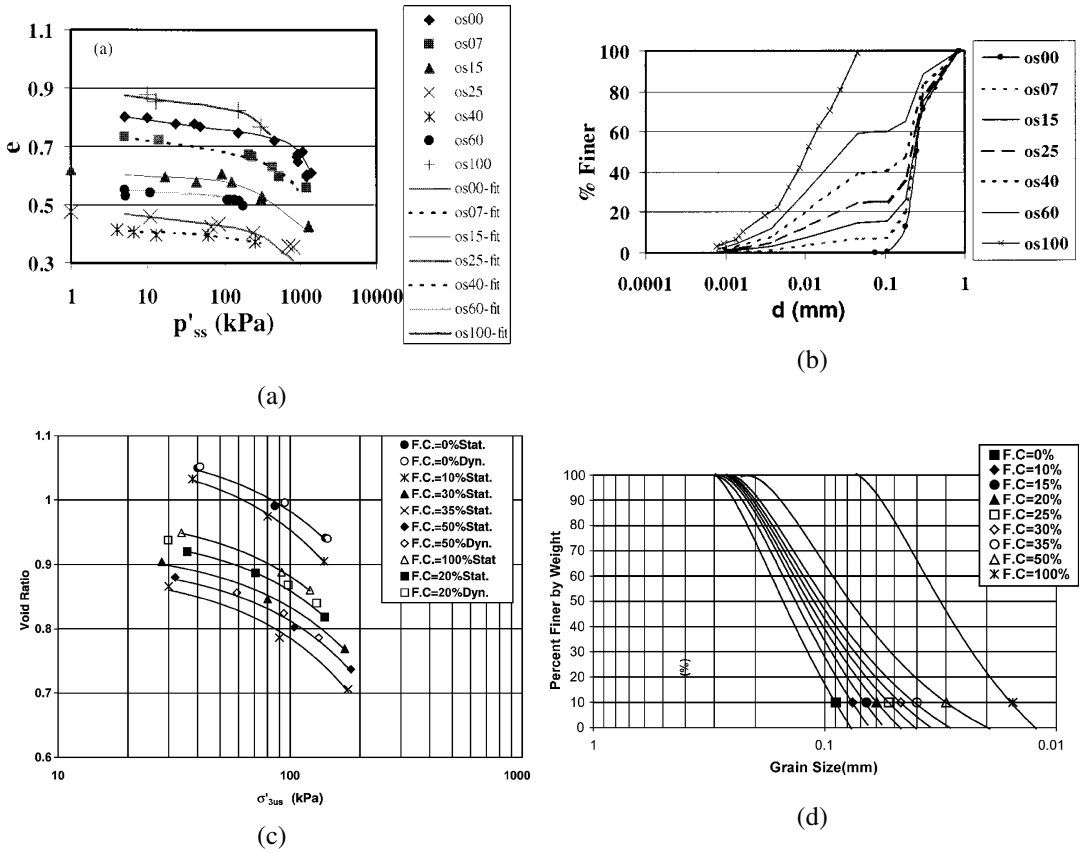


Figure 4.27: (a) SSL for samples of various fines content; (b) Grain size distribution curves for the nonplastic host silt (Sil co sil No. 40) and the host sand (F55, Foundry Sand, U.S. Silica Company, Ottawa, Ill.) (Thevanayagam et al., 2002); (c) SSL for static and dynamic triaxial tests (mixed under compaction) for Ardebil sand with fines; (d) Grain size distribution curves of Ardebil sand being the fines natural particles collected from the natural Ardebil sand (Naeini and Baziar, 2004).

However, as can be seen in Figure 4.29, other authors, (Been and Jefferies, 1985; Bouckovalas et al., 2003), demonstrated that increasing fines content also causes a steepening of the CSL (or SSL).

An explanation of such distinct conclusion results from the set of different factors affecting CSL (or SSL) positioning.

Poulos et al. (1985) demonstrated that CSL (or SSL) slope increases for well graded soils and grains angularity. On the other hand Yan and Dong (2011) demonstrated, in a DEM, that wider particle size distributions downward CSL positioning. It position might be explained by the loose configuration of both silty-sand or sandy-silt soils. A non-uniform sand has lower void ratios, e, as the smaller particles tend to fill the void spaces between the bigger ones, while irregular and angular shapes rises the e (Carrera, 2008). As can be observed from Figure 4.30, with increasing fines content the maximum and minimum void ratios decrease until the transactional fines content is reached, limit from which starts increasing again (Lade and Yamamuro, 1997; Yang et al., 2006b,a; Carrera et al., 2011; Lade et al., 2009).

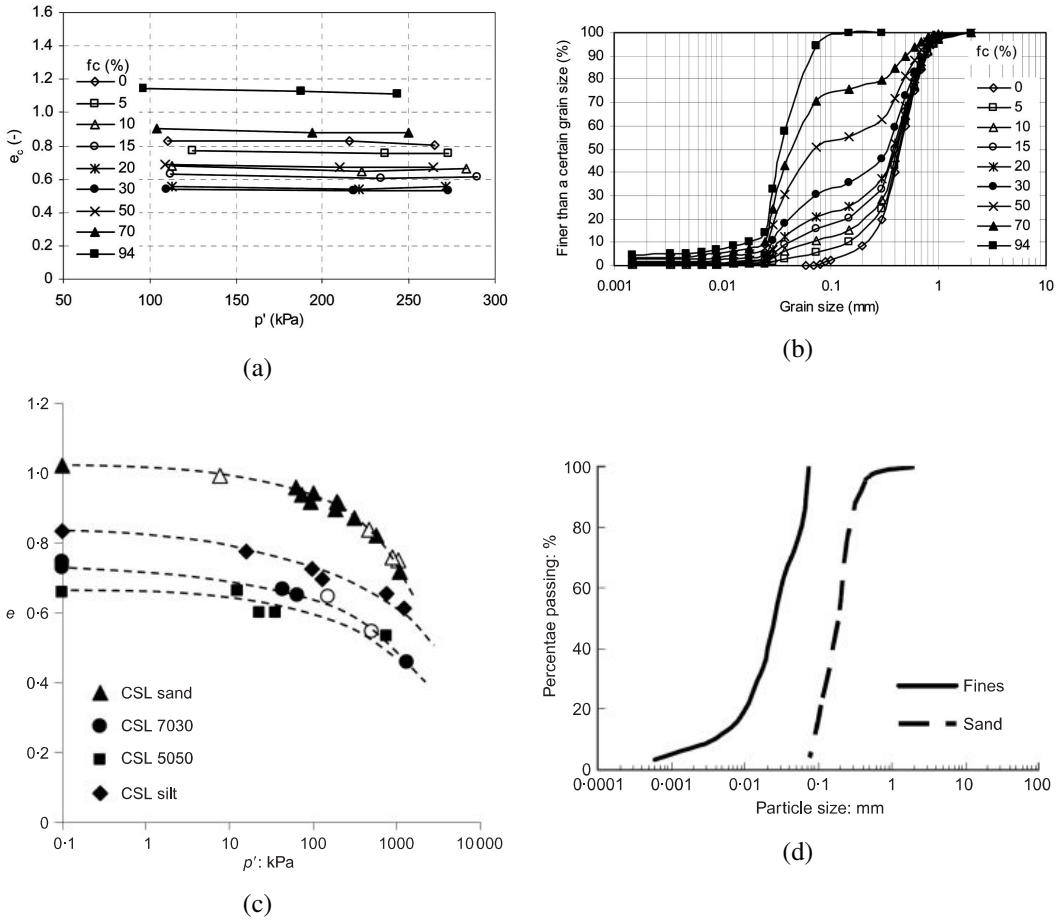


Figure 4.28: a) SSL for samples of various fines content, tested under drained conditions on the void ratio after consolidation; (b) Grain size distribution curves for mixtures obtained with an host silt (Chengbei nonplastic silt) and an host sand (clean Hokksund sand) (Yang et al., 2006b); (c) CSL for samples of various fines content; (d) Grain size distribution curves of sand and silt of Stava tailings (Carrera et al., 2011).

As reported by Cho et al. (2006) maximum and minimum void ratios have a major influence on CSL positioning (Figure 4.31). Comparing Figures 4.28a and 4.28c it can be observed that both materials Hokksund with fines and Stava tailings CSL interception Γ reach it minimum for the mixture which haves also the minimum maximum and minimum void ratios (see Figure 4.30a and 4.30b). This takes place for fines content between 30% and of 50% either for Hokksund with fines and Stava tailings.

On the other hand, as concluded by Cho et al. (2006) the maximum and minimum void ratios depend and decrease with increasing roundness (R), regularity (ρ) and sphericity (S) of grains (Figure 4.32). Despite, both correlations obtained by Cho et al. (2006) were exclusively achieved for sands with a uniformity coefficients lower than 2.5. Being roundness the average radius of curvature of surface features relative to the radius of maximum sphere that can be inscribed in the particle, and sphericity the diameter of the largest inscribed sphere relative to the diameter of the smallest circumscribed sphere. Regularity is obtained as an average between the roundness and the sphericity (Cho et al., 2006).

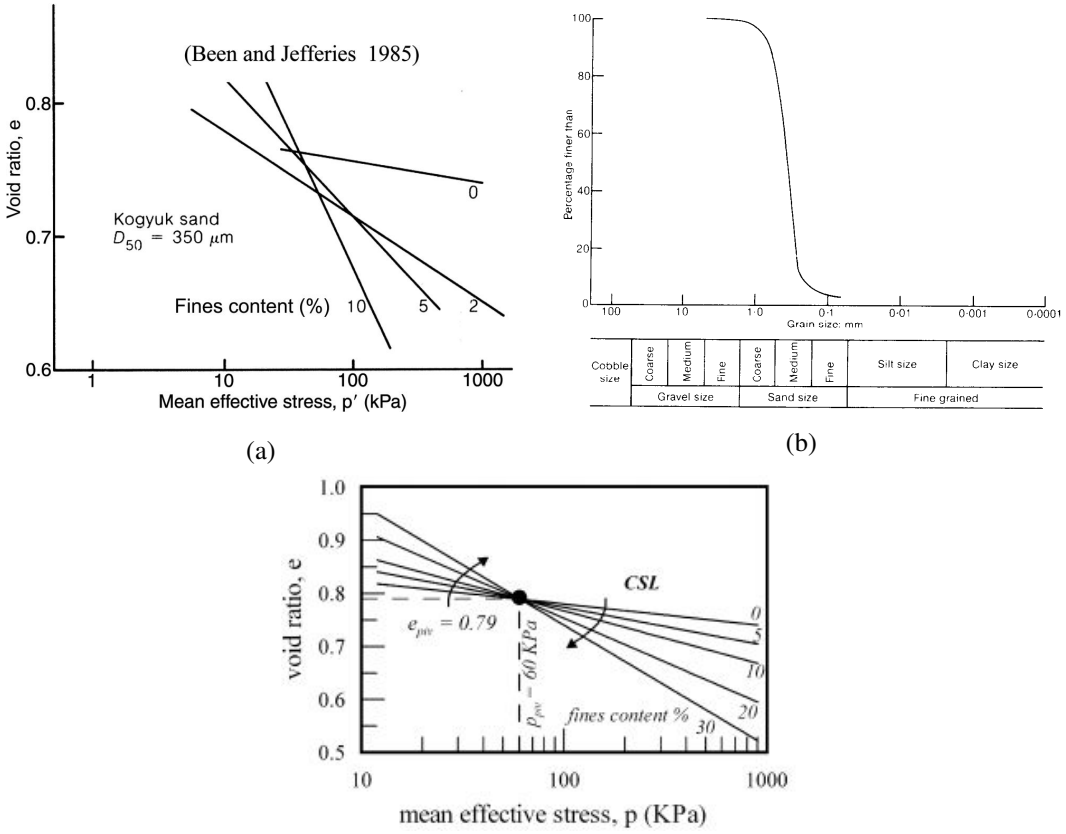


Figure 4.29: (a) SSL for Kogyuk 350 sand with different silt content; (b) Grain size distribution curve of Kogyuk 350 sand with 2% silt; the fines content was varied by adding fines to previously washed Kogyuk 350 sand (Been and Jefferies, 1985); (c) Iddealized effect of fines content on CSL determined statically for 42 different parent sands (Bouckovalas et al., 2003).

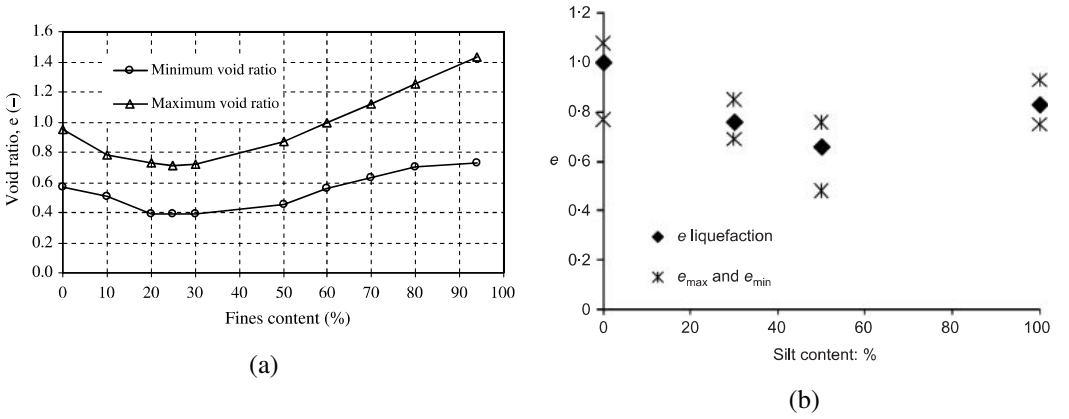


Figure 4.30: (a) Extreme void ratios for soils obtained for mixtures obtained between Hokksund and Chengbei non-plastic silt (Yang et al., 2006a); (b) Variation of potential for static liquefaction with silt content for Stava tailings (Carrera et al., 2011).

Furthermore Cho et al. (2006) and Poulos et al. (1985), among other authors, found the CSL slope to increase with increasing grains angularity (Figure 4.33). Conclusively particle shape conceives

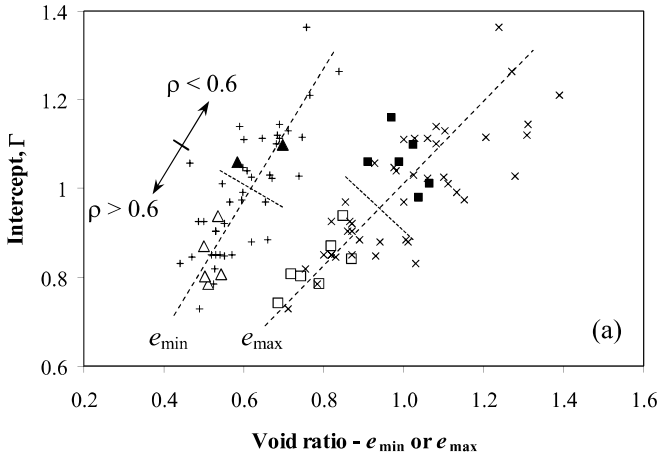


Figure 4.31: Correlation between CSL interception, Γ, and the maximum and minimum void ratio (Cho et al., 2006).

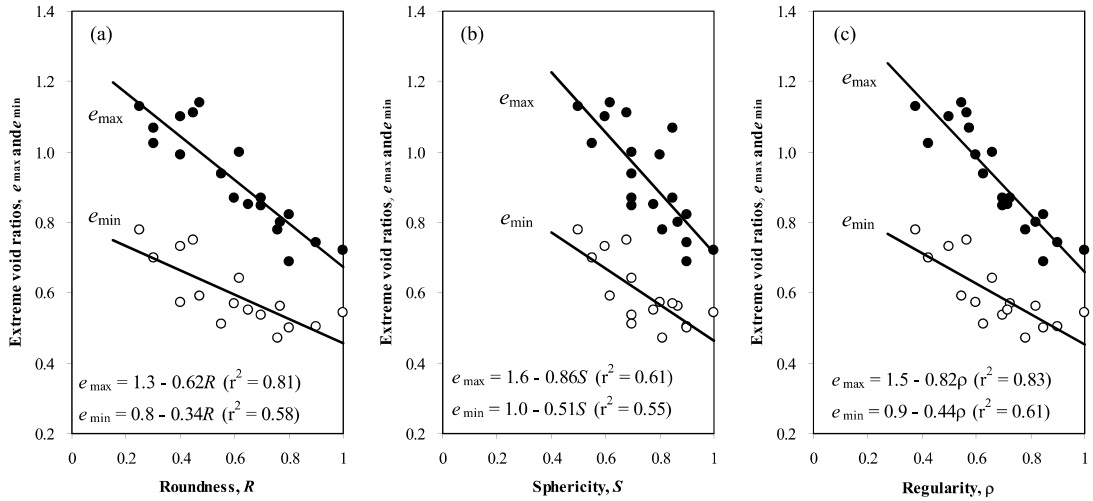


Figure 4.32: Effect of particle shape on extreme void ratios (natural sands with CU $\leq$ 2.5) (Cho et al., 2006).

an important feature to study. In fact platiness is predominant on finer soils which might explains the increasing slope of the CSL (thus of λ).

Thus the differences observed for the CSL between Been and Jefferies (1985) and Bouckovalas et al. (2003), perhaps resulted from studying sands with their natural fines, and thus roundest than the ones tested by other authors (Zlatovic and Ishihara, 1997; Thevanayagam et al., 2002; Naeini and Baziar, 2004; Yang et al., 2006b,a; Bobei et al., 2009; Carrera et al., 2011; Rahman et al., 2008). From it analysis it is concluded that with increasing graduation soils increases their packing capacity, increasing also λ, and decreasing the interception, Γ, but not the sufficient to surpass grains angularity effect. Then if both angularity and soil gradation increases the CSL slope and it interception Γ it becomes necessary to assess which one influences on first place for CSL to rotate and or decrease on the semi-logarithmic space e: log p'. Plus the slopes observed in

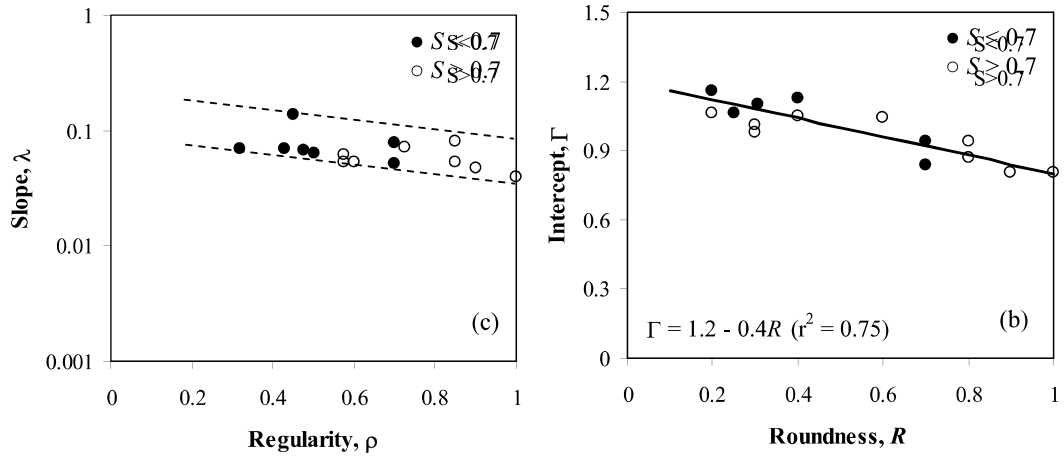


Figure 4.33: Effect of particle shape on critical state parameters (Cho et al., 2006).

most of the figures above were determined for low/ medium confining pressures and CSL with a curved shape just starts incurving for higher confining pressures. Thus for comparing purposes it just makes sense when comparing the slopes in a rage between the medium and higher confining pressures, even though liquefaction takes place for low confining pressures.

4.3.2.2 Effect of fines content on residual friction angle

When assessing the influence of fines on soil behaviour becomes prominent to analyse the influence of particles shape on the residual strength. Residual strength depends on the fraction of platy particles and on the soil mineralogy, i.e., particle thickness and slenderness (Skempton, 1985). While plattiness decreases stiffness and residual friction angle (Santamarina and Cho, 2004), Figure 4.34 shows that increasing roundness decreases the residual friction (Cho et al., 2006; Santamarina and Cho, 2004). Thus being the silts platter than sands lower is the residual friction angle, notwithstanding being sands rounder, lower is the residual friction angle. Therefore not major conclusions can be inferred.

Aiming to assess grain size distribution effect Lambe and Whitman (1979), O. et al. (2012), Igwe et al. (2007), demonstrated a higher peak and residual shear strengths on well-graded ("WG") soil than on monogranular soil ("NAG", i.e. narrowly graded), due to their highest packing capacity (Figure 4.35). Increasing packing capacity results from smaller particles filling in the void ratios in-between larger particles, producing a stronger interlocking, responsible for a greater resistance.

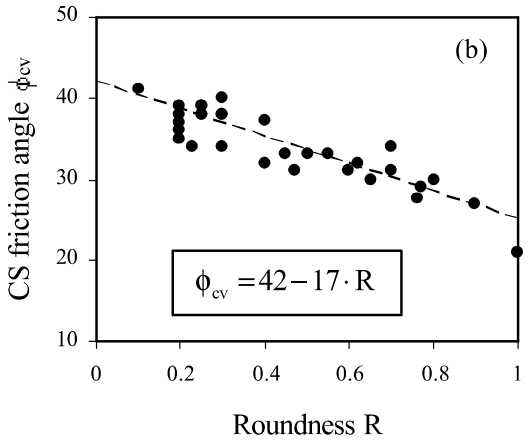


Figure 4.34: Effect of particle roundness on constant volume friction angle (Cho et al., 2006; Santamarina and Cho, 2004).

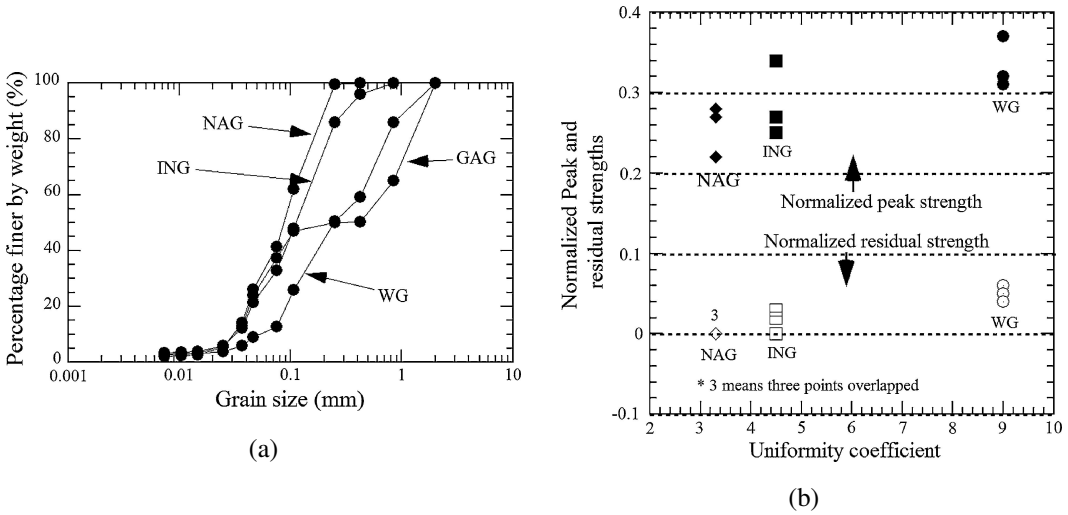


Figure 4.35: (a) Particle size distribution curves of the reconstituted sands ;(b) Relationship between uniformity coefficient and normalized strength of loose specimens (O. et al., 2012).

4.3.2.3 Effect of fines content on undrained shear strength

In an attempt to predict soils liquefaction potential, more importantly than prediction the residual friction angle, becomes to assess fines content influence on the peak shear strength. Undrained shear strength might be evaluated through the IL positioning, and through the range of confining stresses, for which loose specimens suffer liquefaction or limited liquefaction (i.e. strain softening).

O. et al. (2012) while testing loose industrial silica sand, composed of sub-angular to angular quartz and a small amount of feldspar, found well-graded specimens ("WG") to exhibit a higher peak and residual shear strengths than poorly graded ones (Figure 4.35). *"Stronger interlocking may offer greater resistance to forces inducing relative sliding between grains, and in effect, de-*

form less than the weaker interlocking between the particles in poorly graded specimens". Plus it was only observed complete liquefaction on narrowly graded specimens ("NAG") attributed to the weaker interlocking. Thus if the curve was left shifted than the silt would dominate the overall soil behaviour, and the platter particles would certainly reduce both peak and residual strengths (Skempton, 1985). However this is only true if the grains have a low angularity. Notwithstanding is important to highlight that the well-graded soil have a minor amount of fines content (FC 20%), being the soil behaviour predominantly governed by the sand behaviour.

O. et al. (2012) also discovered that gap graded ("GAG") specimens exhibited the lowest peak and residual strength, attributing this behaviour to the silt overall dominant behaviour over sand particles.

Knowing that the overall soil behaviour might be dominated by sands or soils, according to their grain size distribution curves, it becomes necessary to infer their transactional fines content in order to perceive the dominating soil behaviour (Figure 4.36).

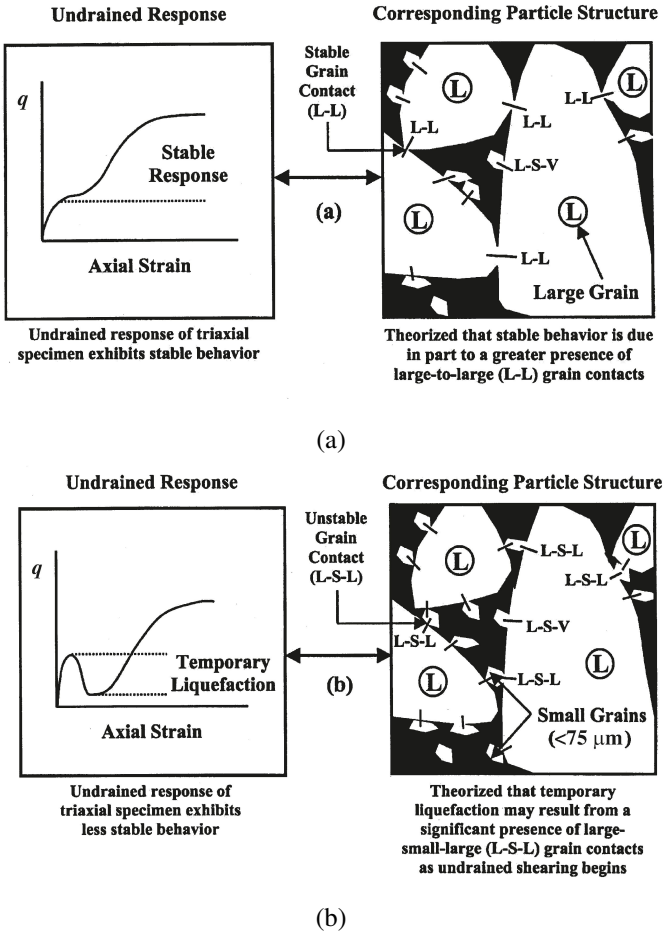


Figure 4.36: (a) Stable undrained triaxial behaviour due to Large-to-Large grain contacts (L-L) – Behaviour predominantly governed by sand behaviour; (b) Unstable undrained triaxial behaviour due to Large-Small-Large grain contacts (L-L) – Behaviour predominantly governed by silt behaviour (adapted from Yamamuro et al. (2008)).

Silt particles usually are platter and irregular than sand grains, which are usually more rounded (which might also be characterized as angular to sub-angular, but not as pronounced as silts). Angularity and plasticity of fines are also very influent in liquefaction potential and in the residual strength (Rahman and Gnanendran, 2008). From undrained triaxial tests, Santamarina and Cho (2004) observed that the rounder the sand is, the lower the strain at peak strength and at phase transformation.

As suggested by Goddard (1990) grains irregularity promotes looser packing, lower coordination number, and hence a softer matrix, thus exhibiting a more deformability. Irregular grains contact might be compared to a cone-to-plane contact versus a sphere-to-plane contact, producing a lower stiffness and a higher sensitivity of stiffness to the state of stress (Cho et al., 2006).

Despite CSL positioning, the fines content which provides the soil more susceptible to liquefaction is usually the transitional fines content.

While studying mixtures between Hokkusand and Chengbei non-plastic silt, Yang et al. (2006b) and Yang et al. (2006a) observed the instability line moving from right to left, in the q – p' space, when the fines content changed from 0 to 30%, moving back for fines content higher than 30%. The percentage of 30% is the transitional fines content (TFC) for the mixtures studied by the authors. This means that, for a same confining stress, the peak shear strength is lower for mixtures near it TFC.

Also Carrera et al. (2011) found Stava tailings having a higher liquefaction potential for the silt content of about 30%, correspondent to the mixture near the TFC. As explained by the authors this have major consequences on dam embankments made of sand mixed with a relative small of fines, which are significantly more prone to liquefaction. These mixtures are often obtained by using a hydro-cyclone.

While IL moves from right to left till the FC equalizes the TFC, moving back for mixtures with a fines content higher than TFC, it slope (i.e. inclination) remains nearly unchanged (Figure 4.37). The IL maximum often occurs when the FC is near the TFC.

4.3.2.4 Intergranular void ratio

Due to LEC divergence for soil mixtures with distinct fines content, Mitchell (1976) introduced a new parameter, the intergranular void ratio:

$$e_{sk} = \frac{V_v + V_f}{V_s} = \frac{V_T \times G_s \times \rho_w}{M_t - M_f} - 1 \tag{4.6}$$

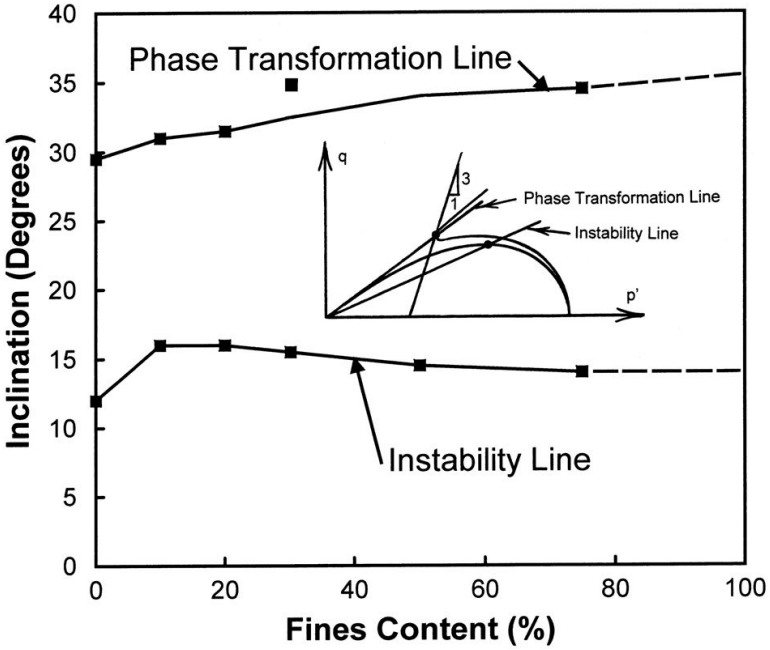


Figure 4.37: Variation of inclination of the phase transformation line and the instability line with fines content for fine Ottawa sand and Loch Raven fines (Lade et al., 2009).

where V_T is the total volume G_s the specific gravity of the sand, ρ_w the density of water and M_t and M_f respectively the total mass of the specimen and the mass of the fines respectively. If it is assumed that the G_s of the sand is equal to that of the fines, the equation becomes:

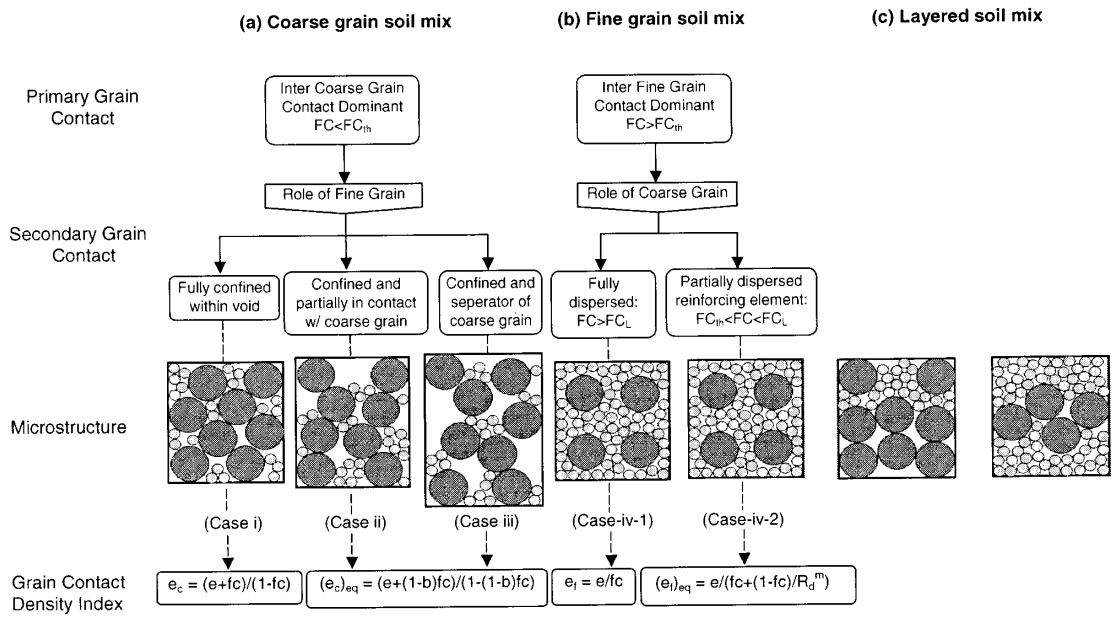
$$e_{sk} = \frac{e + (f_c/100)}{e - (f_c/100)} \tag{4.7}$$

where f_c is the fines content of the soil mixture. The intergranular void ratio can only be used for soil mixtures with a FC which ensures the soil is governed by the sand behaviour. For higher FC, (f_c), the behaviour of the soil begins to be governed by the silts content being the intergranular void ratio unsuitable (Carrera, 2008).

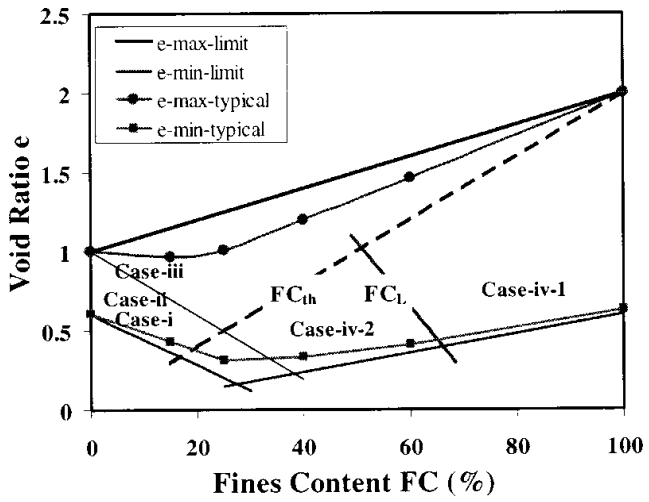
Later, Thevanayagam et al. (2002) found equation (4.7) to be insufficient and go further. Also basing on previous studies Thevanayagam and Mohan (2000) proposed an equivalent intergranular void ratio according the role played by both sands and silt grains (Figure 4.38).

For mixtures with FC < TFC, which represent cases ii) and iii) of Figure 4.38, Thevanayagam and Mohan (2000) adapted equation (4.7) introducing a new parameter, b, which takes into account the portion of the fine grains that contributes to the active intergrain contacts:

$$e_{c,eq} = \frac{e + (1-b)\left(\frac{f_c}{100}\right)}{1 - (1-b)\left(\frac{f_c}{100}\right)} \tag{4.8}$$



(a)



(b)

Figure 4.38: (a) Intergranular soil mix classification; (b) Intergranular matrix diagram classification (Thevanayagam and Mohan, 2000).

being b=0, which represent case i), when the fines do not participate actively in supporting the coarse-grain skeleton, and b=1 when all of the grains participate actively in supporting the coarse-grain skeleton. The parameter b depends on grain size disparity ratio and grain characteristics. The c designs for coarse grains.

For a two size particle system with large size disparity considering a reinforcement effect by the coarse grains (case iv)-2), Thevanayagam and Mohan (2000) proposed the equivalent interfine

void ratio:

$$e_{f,eq} = \frac{e}{f_C + \frac{1-f_c}{R_d^m}} < e_f \tag{4.9}$$

where m is a coefficient, varying between 0 and 1, that depends on grain characteristics and fine grain packing, and R_d is the grain size disparity ratio. Being R_d the ratio between D_50 and d_50, which are the mean grain sizes of the coarser and finer grains (Yang et al., 2006b). The interfine void ratio, e_f, is the ratio between the void ratio and the fines content. The f designation stands for fine grains.

Finally, the case iv)-1, which is applied to soils with high percentage of FC might be normalized by applying the interfine void ratio:

$$e_f = \frac{e}{f_c} \tag{4.10}$$

As can be observed from Figure 4.39, both data for FC < TFC and FC > TFC fall into the vicinity of the clean sand SSL and into the vicinity of the pure silt SSL, respectively. Thus, following their studies, Thevanayagam et al. (2002) by applying the intergranular and interfine void ratios normalization concept achieved a unique CSL.

Thevanayagam et al.' findings reveal to be prominent for future studies and it suitability shall be verified, such as the calibration of the b and m parameters.

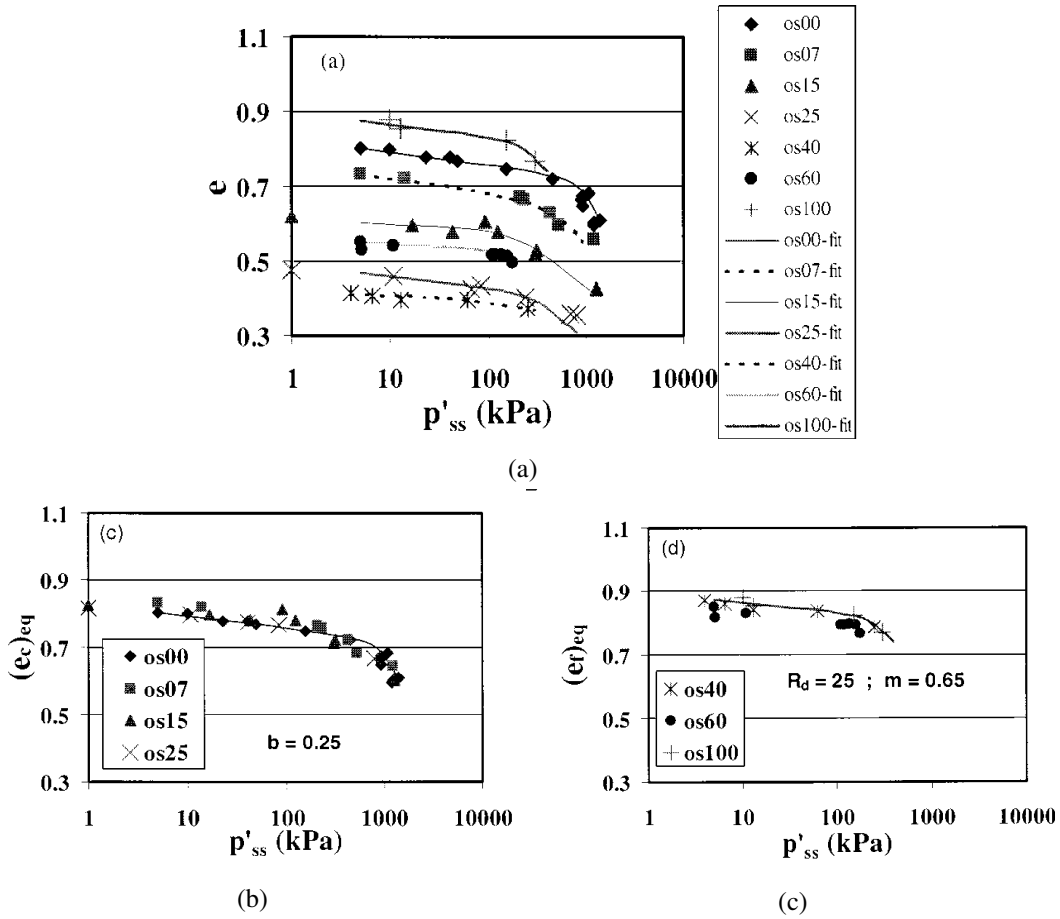


Figure 4.39: SSL data : (a) e vs p'_{SS}; (b) $(e_c)_{eq}$ vs p'_{SS}; (c) $(e_f)_{eq}$ vs p'_{SS} for granular mixes between F55, Foundry Sand, U.S. Silica Company, Ottawa, Ill. and nonplastic crushed silica fines (Sil co sil No. 40) (Thevanayagam et al., 2002).

4.3.3 Influence Of Anisotropy

Mostly soils have anisotropic strength and deformation characteristics (Saada, 1988). This anisotropy might be of two types: the inherent anisotropy and the induced anisotropy. The first one is attributed to the preferred particle arrangement during gravitational sedimentation, and might differ according to grains shape, angularity and roughness. The second one is the stress-induced type. As might be expected the second one influences the first one.

The emergence of understanding both anisotropies arises from the differences of the peak shear strength of soils. As observed by many authors both anisotropies provide diversified liquefaction susceptibility.

Perceiving the effect of both, inherent and induced anisotropy, on soil strength and stiffness is one of the most delicate subjects. As stated by Hareb and Doanh (2012) *"experimental scientists still struggle to figure out exactly what are the parameters controlling the induced anisotropy"*.

4.3.3.1 Influence of inherent anisotropy

Inherent anisotropy is perhaps the trickiest factor affecting liquefaction susceptibility and the overall undrained shear strength of cohesionless soils, being early recognized as a factor also affecting cyclic liquefaction (Lee and Fitton, 1968). As samples reconstituted through different reconstitution techniques have proven to produce distinct undrained shear responses, it means that, as long as testing reconstituted specimens, the in situ soil strength might be over or underpredicted. Although fabric influence is a well-known factor that affects the mechanical response of soils, it is also recognized that undisturbed sampling of cohesionless soils is still currently very difficult and expensive (few successful attempts have been made recently: Cresswell and Powrie (2004); Ventouras and Coop (2009)). For this reason, samples have to be reconstituted in laboratory using techniques like moist tamping, pluviation (air or water pluviation) or slurry deposition.

Among the sample reconstitution techniques, moist tamping is the most practiced, (Carrera, 2008; Bedin, 2010), and preferred one. Usually moist tamping technique produces a fabric potentially collapsible (Vaid and Sivathayalan, 2000), which has been often criticized. Casagrande (1975) pointed out this technique responsible to create a metastable honeycomb structure produced by capillarity, which are more prone to liquefaction. Notwithstanding most of the other techniques does not allow the reproduction of much loose void ratios. Plus, as pointed out by Ishihara (1996) moist tamping is able to produce the widest range in void ratio with satisfactory uniformity allowing for a clear definition of the CSL.

Yet *"Specimens pluviated in water have been shown to mimic the behaviour of natural fluvial and hydraulic fill sands, under both static and cyclic loading"* (Vaid et al., 2001). Despite some authors found water pluviation technique to capture the same fabric as the intact samples, (Vaid and Sivathayalan, 2000; Vaid et al., 2001; Ghiona and Porcino, 2006), thus to capture their stress-induced response, in a modeling point of view it becomes fundamental to interpret distinct soil fabrics stress-induced responses. Plus there are some influent factors such as aging, either caused by particle interlocking or chemical reactions through cementation, which might also be very difficult to reproduce under laboratory conditions.

On the other hand for silts and tailing silts the reconstitution technique which may reproduce a same shear strength behaviour as the intact specimens are usually obtained by the slurry deposition technique (Heymann et al., 2011).

Inherent anisotropy for each soil is exclusively attributed to the preferred particle arrangement. The distinct peak shear strengths, thus non-unique SSL, might be attributed to grains shape, angularity and roughness. If soils were constituted by homogenous spheres, same peak shear strength would be exhibited, despite soil fabric. As in nature soils only have grains with different shapes, angularity and roughness, then it is expected, that, while differently deposited, they will reorient their grains producing fabric anisotropies. Thus when sheared, even for a same principal stress direction, they will exhibit different peak shear strengths. As explained by Nougier-Lehon et al.

(2005) and Muir Wood (2008) inherent anisotropy prevents any extensive reorganization, meaning that the strain required to reach constant fabric may, sometimes, be very large, even reaching values of 100%. As initial anisotropy increases with increasing aspect ratio of particles (i.e. length to width ratio of particle), then soil reorganization increases as well.

Non-cohesive soils are difficult to sample in undisturbed conditions, as the most adequate techniques, such as freezing, remain very expensive. Plus in order to perform a representative number of tests it would become unsustainable. Thus, samples must be prepared through multiple reconstitution techniques as Moist Tamping, Air Pluviation, Slurry Deposition, etc, looking at which one can capture the representative fabric of the soil condition under study, as this has clear influence on stress-strain response. The study of different generated fabrics is therefore very important as it must enable the reproduction of representative in situ conditions, due to the natural or anthropic deposition processes, with relevant consequences in the results that condition the calibration of any constitutive model. The position of plastic yielding surfaces and how they evolve during the stress induced paths are highly affected by the anisotropy (Chang et al., 2011).

From Figure 4.40 it can be realized that the majority of the grains lays in a position close to the horizontal and the majority of the contacts in-between particles is preferentially vertical. Then if for a monotonic compression shear (α = 0), where the force is perpendicular to the bedding deposition, the evolution of the structure stops when the axial strain reaches 20%. On the other hand if the loading is different from that of the inherent anisotropy ($\alpha = \pi/2$), soil samples might require 100% of axial strain to reach the CSL (Nougier-Lehon et al., 2005).

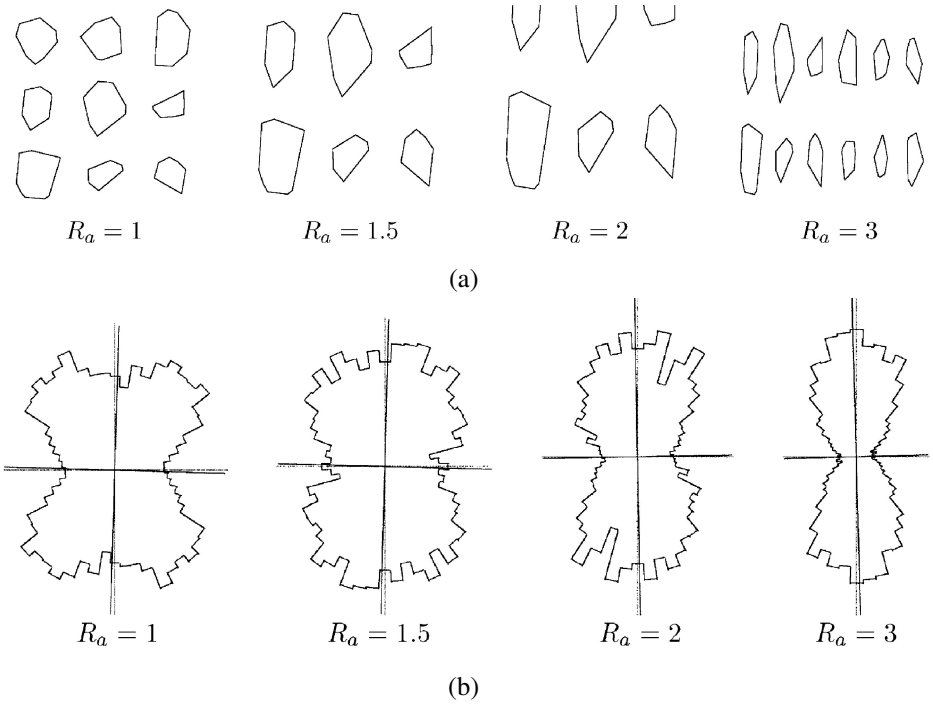


Figure 4.40: (a) Examples of grain shapes for each aspect ratio; (b) Distribution of contact orientations at the end of the dry pluviation process (Nougier-Lehon et al., 2005).

Despite sometimes requiring extensive reorganization, according to some authors, (Nougier-Lehon et al., 2005; Muir Wood, 2008), the critical state can always be reached in granular material. Also other authors, (Castro, 1969; Castro et al., 1985; Poulos, 1981; Alarcon-Guzman et al., 1988; Jefferies and Been, 2006; Sadrekarimi and Olson, 2013; Casagrande, 1975; Poulos, 1981; Been and Jefferies, 1985), despite being aware of the influence of fabric on the behaviour at small shear strains, defend that the initial fabric has no effect on the large shear strain characteristics of sands.

The undrained response of sands prepared with different sample reconstitution methods was studied by many authors, (Zlatovic and Ishihara, 1997; Tsukamoto et al., 1998; Vaid and Sivathayalan, 2000; Wood et al., 2008), in order to assess inherent anisotropy influence, and for some cases it was perceived their influence on the large strains, thus on the achievement of distinct SSL.

Vaid and Sivathayalan (2000) studied the effect of sample reconstitution method, testing both Syncrude sand and Fraser River sand. The reconstitution techniques chosen to study the undrained shear strength of Syncrude sand was water pluviation (WP), air pluviation (AP) and moist tamping (MT), while for Fraser River sand only the two first ones were adopted (Figure 4.41). As can be observed the reconstitution technique results in a very distinct response, resulting in a very strain softening response for the MT, an also strain softening, but to a lesser extent for the AP, and a strain hardening for the WP specimen reconstitution. Despite the sand and the equipment, it seems that, unlike what some authors stated, and at least for undrained conditions, the influence of fabric on the behaviour at small shear strains is insignificant, being much higher for large strain deformations.

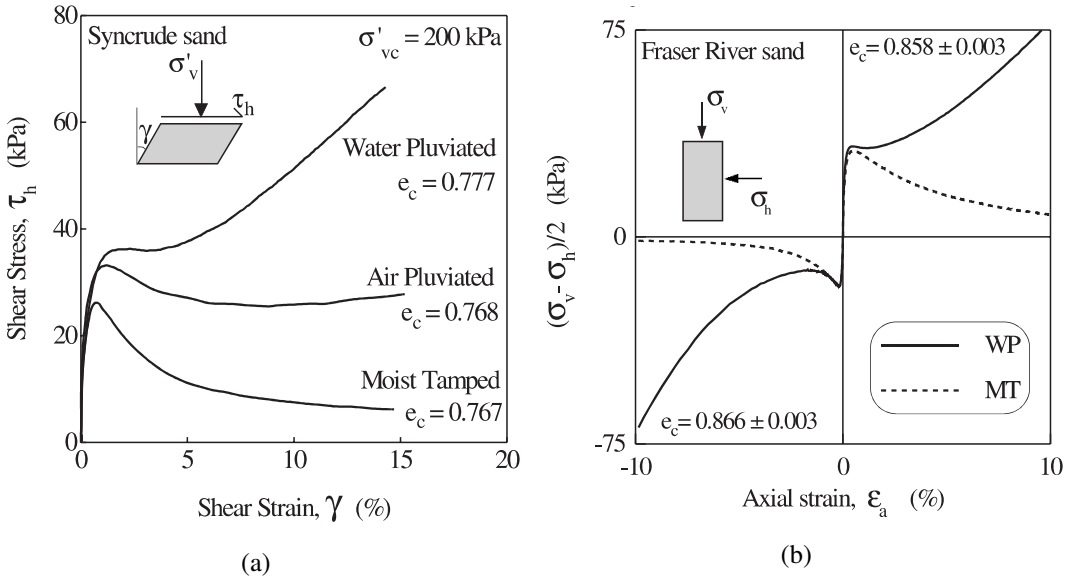
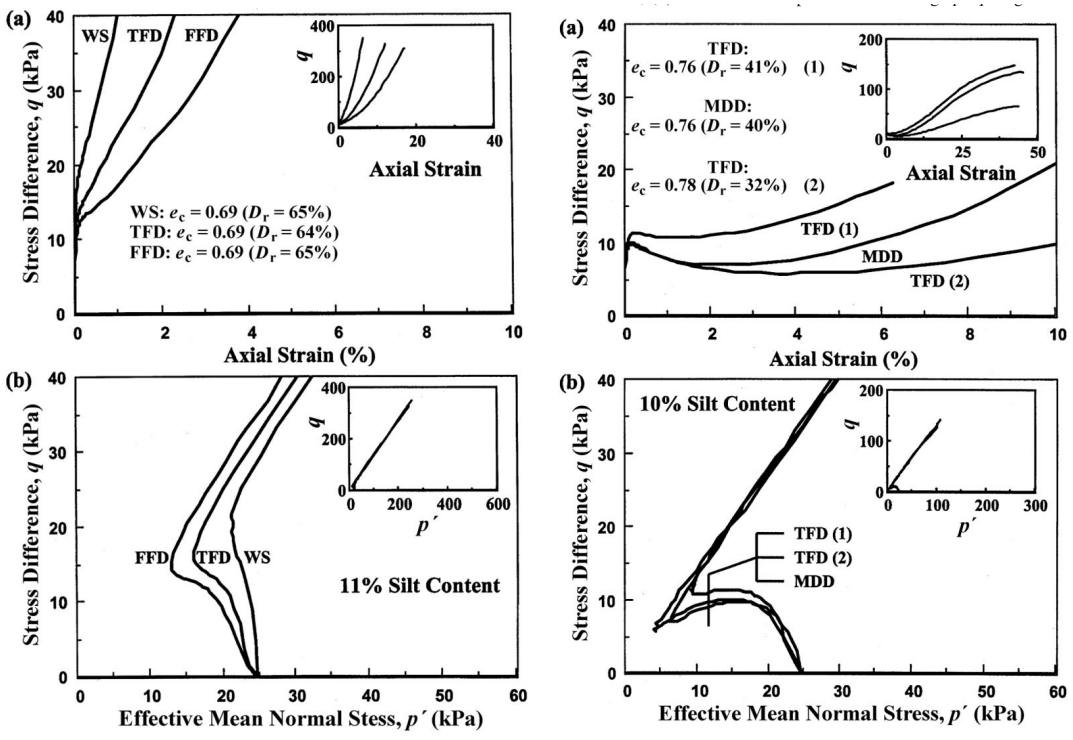


Figure 4.41: Stress-strain response comparing water pluviation (WP), air pluviation (AP): (a) and moist tamping (MT) for medium density Syncrude sand specimens tested under simple shear conditions; (b) for low density Fraser River sand specimens tested under triaxial conditions, both on compression and extension (Vaid and Sivathayalan, 2000).

Also Wood et al. (2008) studied the influence of the depositional method, thus of inherent anisotropy, on undrained shear strength of Nevada sand with fines. The reconstitution methods adopted were: tapped funnel deposition (TFD), water sedimentation (WS), slurry deposition (SD), mixed dry deposition (MDD), air pluviation (AP) and fast funnel deposition (FFD). While the authors observed a similar undrained response for specimens with high densities, regardless the depositional method, loose and medium densities indicated significant differences among the distinct reconstitution techniques.

From Figures 4.42 and 4.43 it can be observed that specimens formed by water sedimentation (WS) exhibit the behaviour more stable, while those formed by TFD and MDD in some cases underwent temporary liquefaction or even true liquefaction for the loosest specimens. Plus, as expected, with increasing silt content, increasing is the liquefaction tendency, regardless of depositional method. It is also necessary to point out that the differences in undrained behaviour among specimens, created by wet and dry deposition methods, also increased with silt content. The authors also alerted the necessity to ascertain when choosing the method to prepare specimens with silt content as an eventual segregation of the material might take place.



(a) (b)

Figure 4.42: (a) Stress-strain and stress-path response of undrained triaxial test comparing water sedimentation (WS), tapped funnel deposition (TFD), and fast funnel deposition (FFD) for medium density Nevada sand specimens, with 11% of FC; (b) Stress-strain and stress-path response of undrained triaxial test comparing mixed dry de- position (MDD) with tapped funnel deposition (TFD) for low density Nevada sand specimens, with 10% of FC (Wood et al., 2008).

By analysing the figures above it might be assessed that IL and SSL are not unique and depend

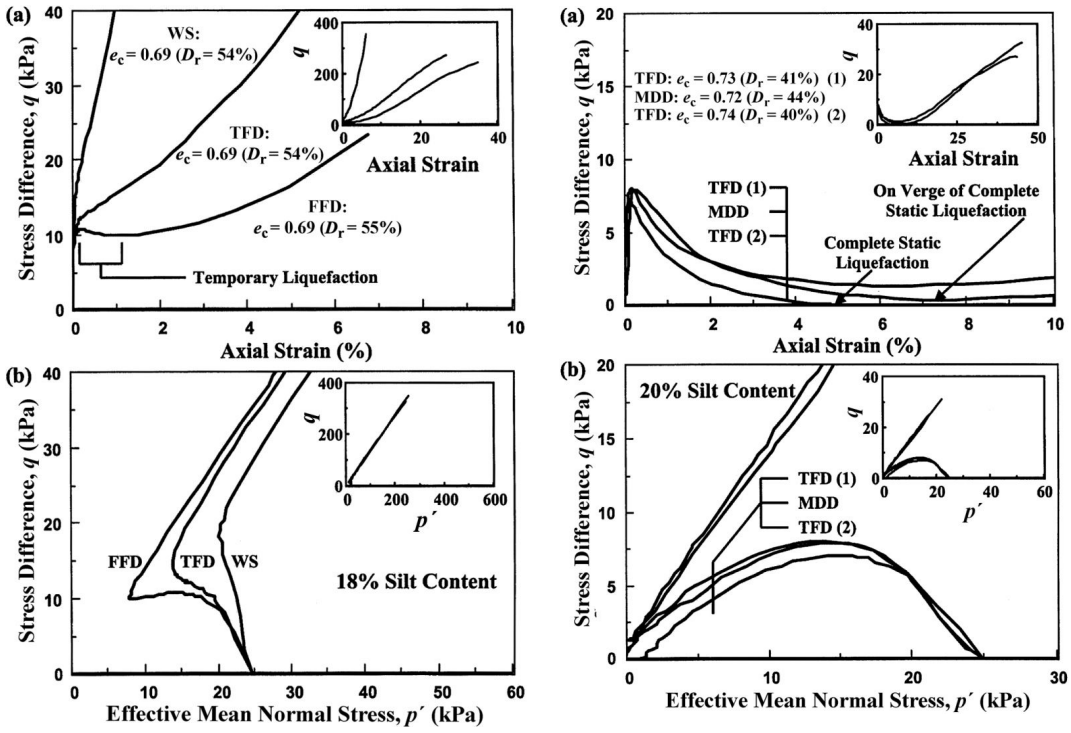


Figure 4.43: (a) Stress-strain and stress-path response of undrained triaxial test comparing water sedimentation (WS), tapped funnel deposition (TFD), and fast funnel deposition (FFD) for medium density Nevada sand specimens, with 18% of FC; (b) Stress-strain and stress-path response of undrained triaxial test comparing mixed dry deposition (MDD) with tapped funnel deposition (TFD) for low density Nevada sand specimens, with 20% of FC (Wood et al., 2008).

on the initial fabric of the soil. Thus it becomes prominent to know how to assess soil inherent anisotropy, not only for the development of frameworks able to predict soil liquefaction potential, but also for further implementation on constitutive modelling.

Inherent anisotropy might be assessed, as described previously, throughout laboratory large strain tests by comparison of peak shear strength, or more accurately through the determination of elastic deformation properties. Small strain parameters are inherently anisotropic and might be obtained by using bender elements or mini-accelerometers, or by local displacement-transducers, during very small amplitude cyclic loading or cyclic torsional test, aligned with principal strain directions (Hoque and Tatsuoka, 1998).

Hoque and Tatsuoka (1998) measuring both vertical and horizontal strains, on a triaxial device, achieved distinct Young modulus (E) larger on the vertical direction than in the horizontal direction. This is something already expected as, for all sample preparation techniques, a horizontal bedding is developed perpendicularly to the falling or tamped directions. The authors also concluded Young modulus to be function of the normal stress in the direction of the major principal strain increment.

Also Ishibashi and Capar (2002), while studying cyclic liquefaction resistance on sand specimens reconstituted with distinct techniques, found that when the level of anisotropy increases, the ratio E_v/E_h increases, and the shear modulus (G) decreases in all directions.

Instead comparing different sample reconstitution techniques, the influence of fabric on the behaviour of sands can be also investigated experimentally, by varying the angle between the applied external major principal stress and the bedding plane (Wan and Guo, 2001). The direction-dependent undrained behaviour of sand is a reflection of its inherent anisotropy (Vaid and Chern, 1985; Vaid and Sivathayalan, 2000; Uthayakumar and Vaid, 1998; Vaid and Sivathayalan, 2000). Despite inherent and stress-path linkage, the last one is discussed in the next subsection 4.3.3.2.

4.3.3.2 Influence of stress-path

As pointed out by some authors (Vaid et al., 1990; Vaid and Sivathayalan, 2000; DeGennaro et al., 2004; Yang and Sze, 2011) sands are weaker in extension than in compression due to transverse isotropy, exhibiting consequently stiffer elastic characteristics in the vertical direction than in the horizontal direction. Therefore, independently on the reconstitution method, sands are usually stiffer in the vertical direction as their grain orientation in deposition is controlled by gravitational forces. Besides, as "in many geotechnical problems", soil loading conditions are multiaxial and may also be accompanied by principal stress rotations (Wijewickreme and Vaid, 1993), a continuous change in soil fabric, i.e., with soil anisotropy evolving on loading.

Many researchers (Castro and Poulos, 1977; Been et al., 1991) argue that final stress state (i.e., the steady state line) are unique apart the shear mode. Others disagree (Vaid et al., 1990; Riemer and Seed, 1997; Yoshimine and Ishihara, 1998), and demonstrated the stress-path, among other factors, to strongly influence the final stress state. Notwithstanding Jefferies and Been (2006) and Been et al. (1991) showed that, although liquefied shear strengths differ according to the shear mode, the steady state line is unique. However, as reported by some authors, (Vaid and Chern, 1985; Vaid et al., 1990; Vaid and Sivathayalan, 2000; Uthayakumar and Vaid, 1998), sands undrained stress response is stress-path dependent, being this non-uniqueness attributed to the binomial: stress-path and inherent anisotropy.

Plus second-order effects may affect the achievement of the SSL. While extension test results are contested by some authors due to the influence of necking (Lade et al., 1996; Usmani et al., 2011; J., 2005), other authors support the idea of soils reaching the SSL (or CSL) before necking takes place, (Uthayakumar and Vaid, 1998), or even when necking is completely inhibited when specimens are consolidated at high confining pressures (DeGennaro et al., 2004).

In triaxial compression loading, the major principal stress direction, $\sigma_1^{'}$, coincides with the sand depositional direction, $\alpha_\sigma = 0^o$, which results in a less contractive or even strain-hardening responses. On the other hand in triaxial extension, $\alpha_\sigma = 90^o$, or in simple shear $\sigma_1^{'}$ rotates from

0° till close to 45°, the loading direction coincides with the weakest plane, resulting in contractive responses. As demonstrated by Vaid and Sivathayalan (1996), despite the initial shear stress being smallest for the sample tested on the simple shear device, due, most probably, to the plane of maximum shear stress being initially 45° to the horizontal, it can be observed that it behaviour is in-between triaxial compression and extension (Figure 4.44). Furthermore only the triaxial compression test exhibits strain-hardening, while the other two exhibits a much more contractive behaviour, which may lead to in distinct ultimate states, thus in distinct SSL (Figure 4.44). Also Yoshimine et al. (1999) found simple shear to be a behaviour in-between triaxial compression and extension for Toyoura sand. Thus soil liquefaction resistance may be overpredicted by exclusively relying on triaixal compression tests.

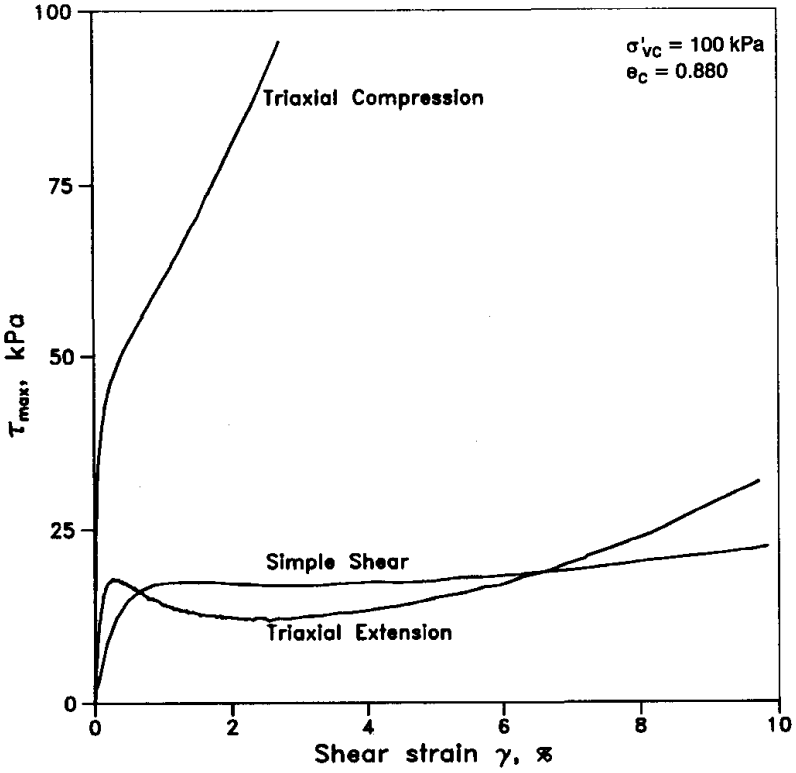


Figure 4.44: Comparison of simple shear, triaxial compression and extension behaviour for Fraser Delta sand (Sivathayalan, 1994; Vaid and Sivathayalan, 1996).

However, as this behaviour is also associated with the inherent anisotropy of soil, it does not mean that it overrules all granular material. In fact Jefferies and Been (2006) achieved, for Bonnie silt, an higher contractiveness under simple shear than under triaxial extension.

If the main goal to achieve is the evaluation soil anisotropy effect, particularly under generalized stress-path loading, only specific equipments, different from axisymmetric triaxial cells (Tx), such as cyclic simple shear (SS), cyclic direct simple shear (DSS), Hollow Cylinder Tests (HCT), Torsional Shear Apparatus and Shake Table Tests, can guarantee a comprehensive study.

Regardless strain localization or other second order effect influences, not only triaxial extension

or simple shear tests may be used to assess stress-path influencing on SSL (or CSL) localization. However, only the HTC device allows an independent control of the three principal stresses enabling the conduction of well diversified stress-paths. HTC device allows the study of such influence by being the unique which enables an independent control of the four derived stress parameters σ_m, α_σ, b, and σ_d, which are considered to influence granular soils behaviour, where $\sigma_m = 1/3\left(\sigma_1^{'} + \sigma_2^{'} + \sigma_3^{'}\right)$, is the mean normal stress; α_σ is the inclination of the major principal stress direction to the vertical; $b = \left(\sigma_2^{'} - \sigma_3^{'}\right) / \left(\sigma_1^{'} - \sigma_3^{'}\right)$ is the effect of magnitude of intermediate principal stress parameter; and $\sigma_d = \left(\sigma_1^{'} - \sigma_3^{'}\right)$, the deviator stress or the stress ratio, $K_c = \left(\sigma_1^{'}/\sigma_3^{'}\right)$ (Figure 4.45).

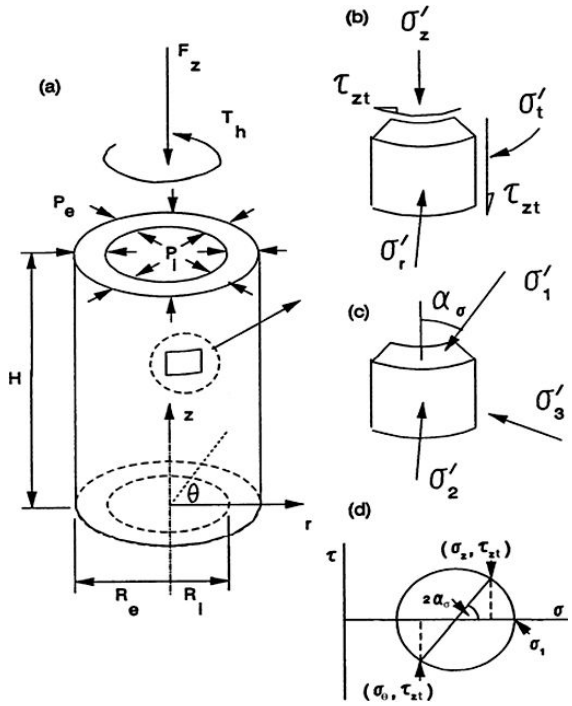
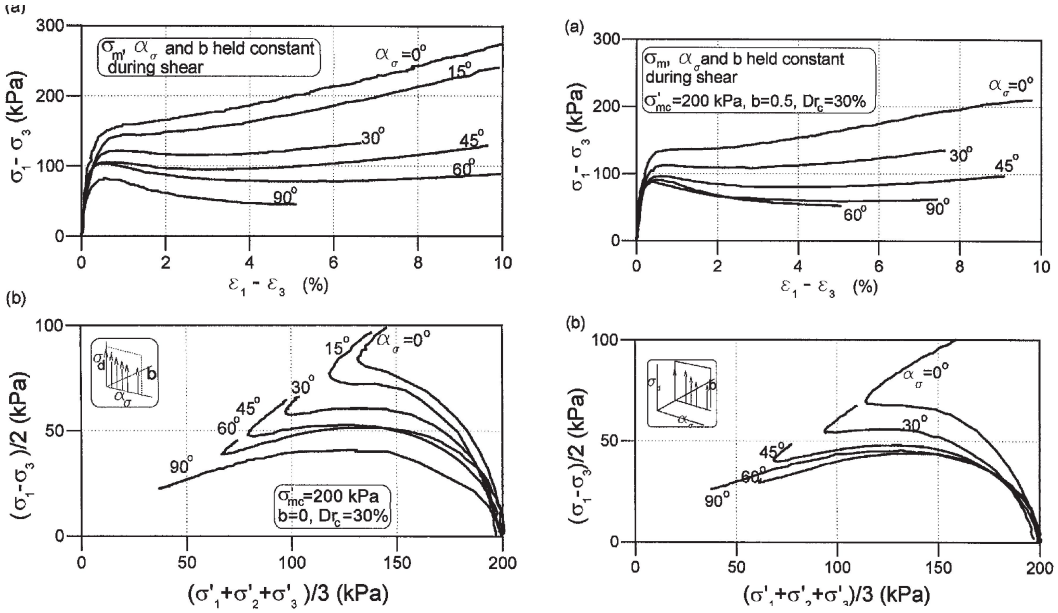


Figure 4.45: Loading and stress conditions in HTC specimens (Wijewickreme and Vaid, 2008).

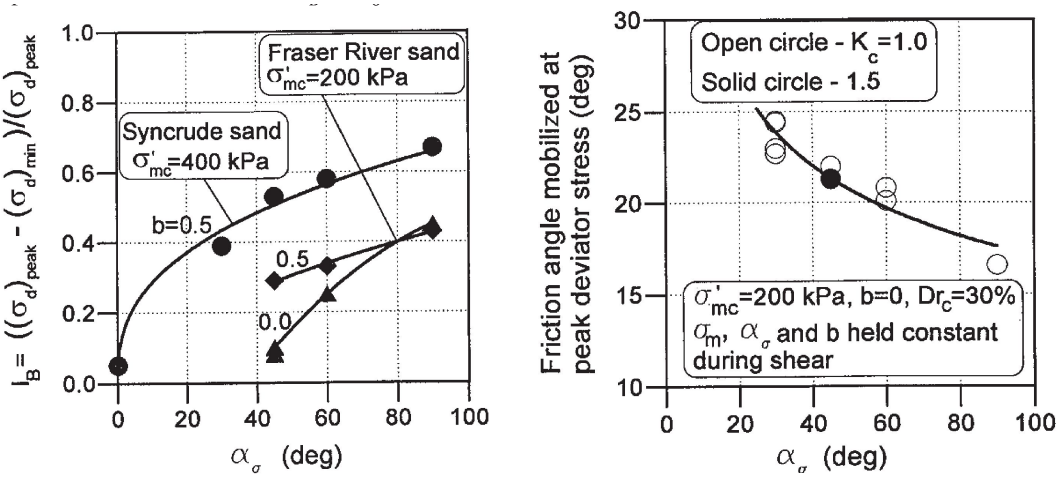
Fraser River sand undrained response was studied, by Uthayakumar and Vaid (1998), in a HTC device, by varying the principal stress direction $\sigma_1^{'}$ from the deposition direction towards the bedding plane (Figure 4.46 and Figure 4.47).

The remarkable differences in the undrained response with α_σ were attributed to the inherent fabric anisotropy created by the parallel alignment of the particles during the deposition process. Consequently, deformability is higher when the $\sigma_1^{'}$ is acting on the bedding direction, the weakest plane. From Figure 4.46 Fraser River sand, with an initial relative density of 30% and initial confining stress of 200 kPa, exhibits a limited liquefaction for α_σ values, except for 15^o and 0^o which is characterized by a strain hardening. During this study the authors reinforced the idea of a non-unique SSL as is suggested by similar extensive laboratory data in the literature, and a further straining will led to a unique SSL. Also Kumruzzaman and Yin (2010) found soil contractiveness



(a) (b)

Figure 4.46: Strain and stress-paths for Fraser River sand: (a) at b = 0; (b) at b = 0.5 (Uthayakumar and Vaid, 1998).



(a) (b)

Figure 4.47: (a) Dependence of friction angle mobilized at peak deviator stress on α_σ for Fraser River sand; (b) Dependence of brittleness index IB on α_σ for Fraser River and Syncrude sand (Uthayakumar and Vaid, 1998).

to increase with increasing inclination of the major principal stress direction towards the bedding planes, while testing completely decomposed granite in a hollow cylinder triaxial test. Thus shear strength decreases with an increase in principal stress direction angle α_σ (Figure 4.47a). The degree of peak shear strength associated to anisotropy in loose Fraser River sand under non-axisymmetric stress states suggests that with increasing b, increasing is the soil contractiveness (Figure 4.47b). This may explain the very distinct undrained shear responses of soils while tested

under triaxial compression (α_σ = 0° and b = 0) and extension (α_σ = 90° and b = 1) responses. However it will not explain the overall behaviour, as triaxial compression or extension are not equivalent. As stated by DeGennaro et al. (2004): *"even an isotropic material behaves differently in compression and in extension; thus, the explanation using sand anisotropy only is not easy"*. Even in the absence of initial inherent anisotropy of the sand, IL and the overall stress response of soils may not be independent of the initial state of stress due to its influence on the magnitude of the rotation of the planes of principal stress and their orientation with respect to the principal axes of anisotropy (Alarcon-Guzman et al., 1988).

Despite the interesting studies that the HTC device may supply, the difficulty of the specimens preparation and the complexity of the involved instrumentation, turns this test highly time consuming and inaccessible for most research groups. Thus, triaxial tests still remain the most widely laboratory technique used for soil mechanical characterization, due to its simplicity when compared with the others devices. Their interpretation is easily comprehensive, being responsible for most of the developments on constitutive modelling and parametrical calibration. Plus *"no single test can duplicate all aspects of a particular loading situation, but combinations of triaxial compression, triaxial extension and direct simple shear test may be used to analyse many practical situations"* (quoted by Dyvik et al. (1987)) (Figure 4.48).

Therefore each particular situation of soil instability, including liquefaction, might be evaluated through the performance of a representative set of tests. Figure 4.48 gives examples of the stress-path, and correspondent laboratory tests, at which the soil is subjected to in: (a) limiting equilibrium stress states beneath an embankment; (b) limiting equilibrium stress states beneath a gravity platform (Uthayakumar and Vaid, 1998) and (c) lateral spreading failure of level to mildly sloping ground (Olson and Mattson, 2008).

4.3.3.3 Influence of induced anisotropy

Granular soils, while in situ, are usually anisotropically consolidated with a K_0 between 0.4 and 0.5, which is in agreement with the semi-empirical formula $K_0 = 1 - \sin\phi'_{cv}$, proposed by Jaky (1944), thus the study of it influence on flow liquefaction triggering have some relevance.

Induced anisotropy occurs as elongated sand grains become aligned in a direction perpendicular to the major principal stress as a sand mass is sheared and is caused by a strain developed during shearing (adapted from Olson and Mattson (2008)). Following what was previously explained about inherent inosotropy it becomes obvious, as demonstrated by Hoque and Tatsuoka (1998), that with increasing anisotropy, more anisotropic is the granular material.

While studying Merriespruit gold tailings Fourie and Tshabalala (2005) found an increasing brittleness of the material with increasing induced anisotropy, thus with increasing K_0 (Figure 4.49). As can be observed from Figure 4.49, K_0-consolidated specimens exhibited an higher peak shear

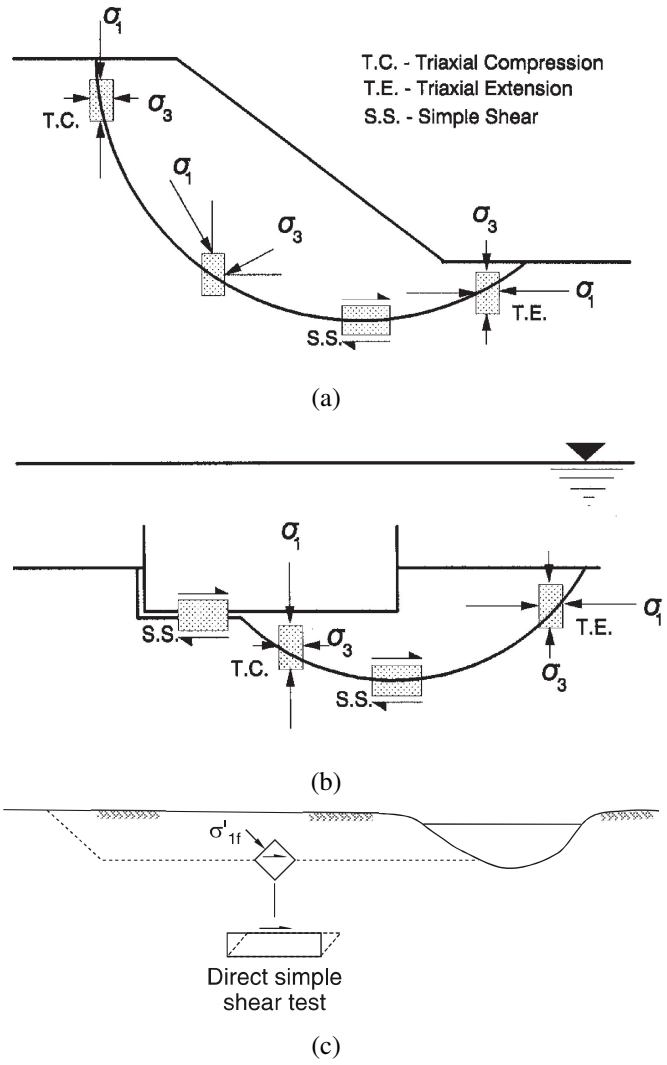


Figure 4.48: Examples of principal stress direction variation along potential failure surfaces: (a) Limiting equilibrium stress states beneath an embankment; (b) Limiting equilibrium stress states beneath a gravity platform (Uthayakumar and Vaid, 1998); (c) Lateral spreading failure of level to mildly sloping ground (Olson and Mattson, 2008).

stress for very small-strains (0.1 0.2%) when compared with the isotropically consolidated specimens. Despite the IL being significantly steeper for K_0-consolidated specimens, the contractiveness was observed to be higher, as a greater drop of the shear strength was observed. This was pointed out as the reason beyond Merriespruit gold tailings dam failure, as the factor of safety of 1.05 using the Bishop method, i.e., very close to unity. Therefore both authors recommended the determination of peak shear stresses developed during undrained compression of K_0 consolidated specimens.

Also Vaid and Sivathayalan (2000) and Vaid et al. (2001) denoted a slight increase in the degree of strain softening with increasing anisotropy at constant $\sigma_3^{'}$, despite the associated increase in density, for Fraser River sand under monotonic triaxial compression loading. A similar trend was

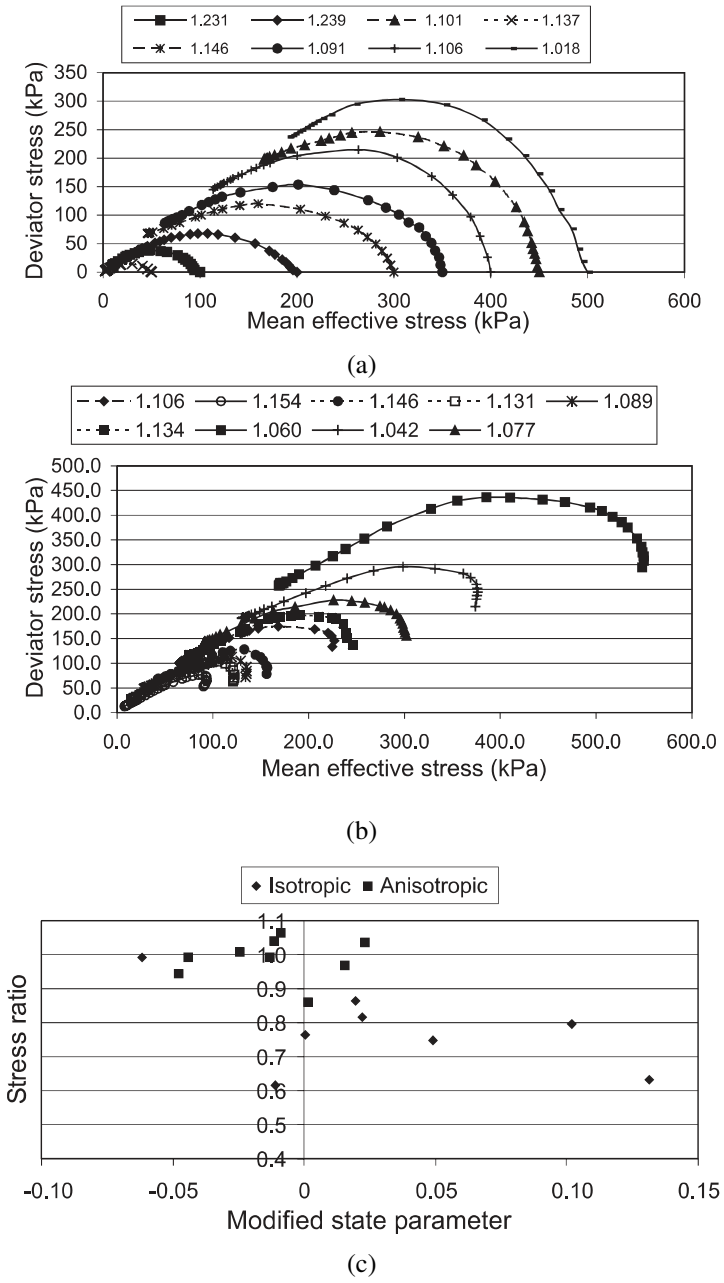


Figure 4.49: Stress paths from undrained triaxial compression tests of loose tailings with 0% fines: (a) on isotropically consolidated specimens; (b) on K_0-consolidated specimens; (c) Variation of modified state parameter with stress ratio at initiation of liquefaction for isotropically and anisotropically consolidated specimens of loose Merriespruit gold tailings, with 0% fines (Fourie and Tshabalala, 2005).

observed by Tsukamoto et al. (2000) for Omigawa sand and Jamuna River sand.

This goes against other authors suggestions, (Chu et al., 2003; Lade and Yamamuro, 2011), which defend the use of IL, obtained from isotropically consolidated undrained triaxial compression tests, to be used to predict soil liquefaction potential, as it defines the lower bound of all the possible unstable conditions.

Joining the facts: i) if IL steepness increases with increasing K_0; ii) and the brittleness increases with increasing K_0; iii) but the SSL is the same for isotropically and anisotropically consolidated specimens; thus something needs to be figured out, as the correlation proposed by Jefferies and Been (2006), between the brittleness index and the normalized state parameter, ψ/λ, would no longer be able to predict soil liquefaction susceptibility, at least for K_0-consolidated specimens. As stated by Sivathayalan and Vaid (2002) the original brittleness index was intended to characterize the flow potential of initially hydrostatically consolidated soils, thus not being able to fully characterize flow potential for initially anisotropically consolidated sands. Notwithstanding the SSL (or CSL) was quite undefined and difficultly to perceive K_0 influence on SSL positioning (see Figure 4.50), which could result on distinct state parameters.

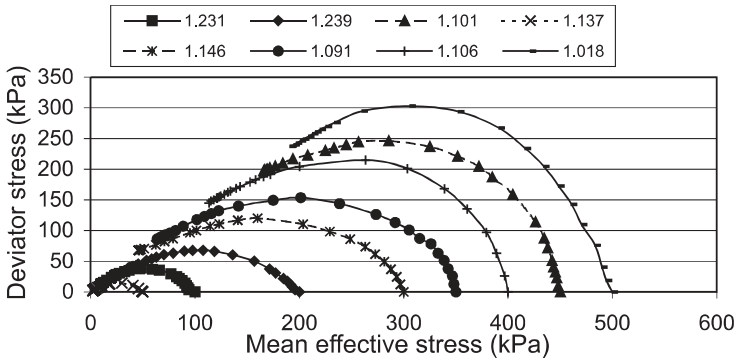


Figure 4.50: Comparison of steady state lines derived from isotropically and K_0-consolidated specimens of loose Merriespruit gold tailings, with 0% fines (Fourie and Tshabalala, 2005).

Yet Sivathayalan and Vaid (2002) while studying Fraser River sand on a HTC device observed that IL (designated by the authors as CSR) depends on α_σ alone, and not on K_c (or K_0). The authors found, as can be observed in Figure 4.51, a unique IL for a given α_σ regardless the initial K_c.

Beyond distinct stress-paths, initial relative densities, initial confining and static shear stresses, soils undrained response also depends on principal stress directions rotation. In situ principal stress rotation especially occurs in the embankments of dams, under sloping ground and below foundations of structures, or due to wave action (Sivathayalan and Vaid, 2002).

Sivathayalan and Vaid (2002) complemented the study of Fraser River on a HTC device, developed by Uthayakumar and Vaid (1998), by evaluating it undrained response with principal stress rotation on initially non-axisymmetrically consolidated Fraser River sand. The undrained behaviour of the sand consolidated to an identical initial state (void ratio at the end of consolidation $e_c = 0.898$, $\sigma_m^{'}$ = 200 kPa, $b = 0.5$, $K_c = 2.00$, and $\alpha_\sigma = 30^o$) and subjected to shear under an identical degree of stress rotation, softens when α_σ increases and hardens as α_σ decreases. The authors also concluded that the minimum undrained strength mobilized (SS) under principal stress rotation depends on the direction of major principal stress at the instant of quasi steady state (QSS).

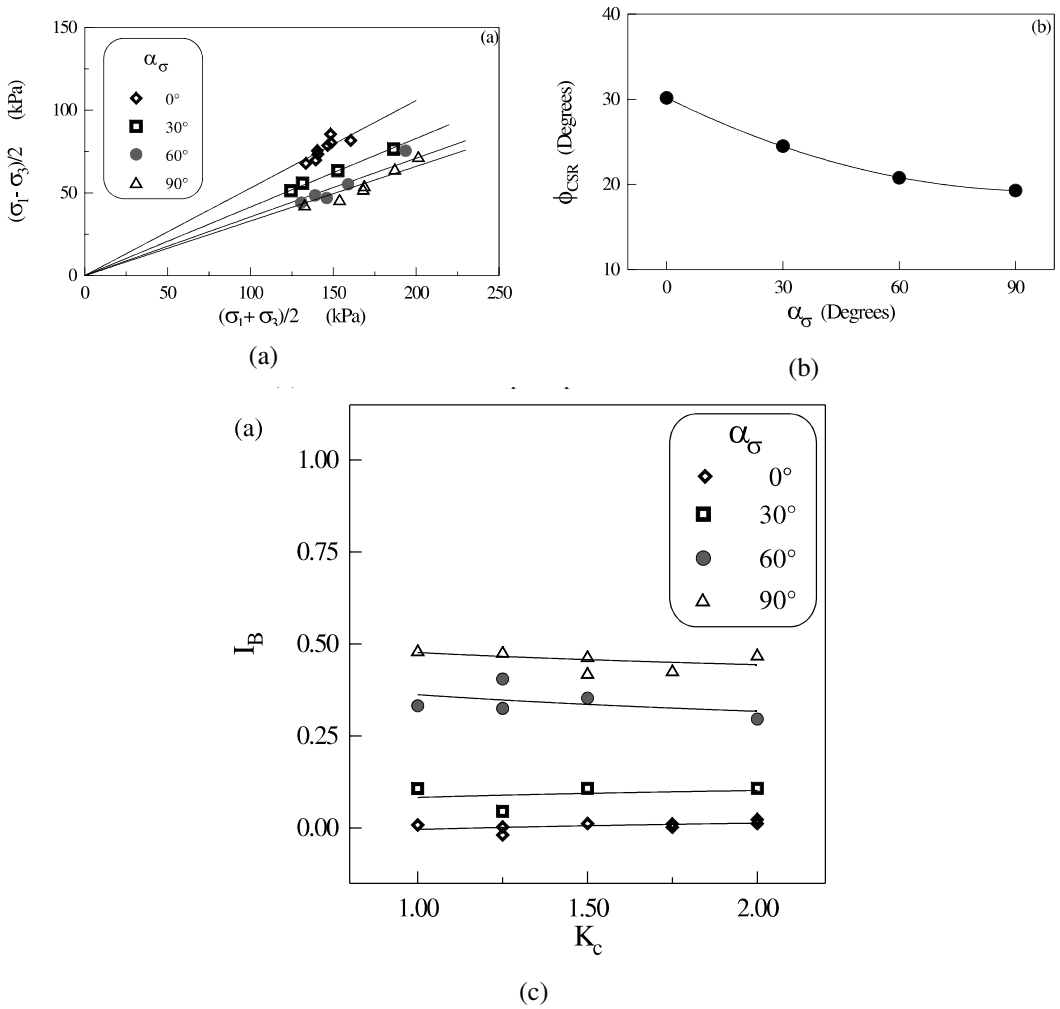


Figure 4.51: Conditions at the instant of the trigger of strain softening: (a) effective stress states, and (b) dependence of mobilized friction angle ϕ_{CSR} on α_σ; (c) Modified brittleness index with static shear (Sivathayalan and Vaid, 2002).

From the facts exposed above it might be concluded that undrained shear strength of cohesionless involves parameters very difficult to assess, mainly when in loose conditions. The extraordinary dependency of the undrained response on the initial stress state or the stress path justifies the increased difficulty on soil liquefaction evaluation. Plus it study is not contemplated on most of the current analytical methods used for geotechnical design against liquefaction hazard.

4.4 Factors Affecting Cyclic Liquefaction

As stated above, for liquefaction to take place is necessary that the soil is completely saturated and cohesionless, or with a very light cohesive component, so that the Van-der-Walls forces won't be able to compete with the gravitational forces for the control of the particles re-arrangements. Differently from flow liquefaction, cyclic mobility also takes places in soil denser than the critical

state, as far as it is subjected to cyclic shear stresses. Due to the enormous losses associated it study became very important for seismic design, or even, but less recurrent, for the study of the seabed during storms.

In Chapter 3 were introduced the many experimental ways used to assess cyclic liquefaction potential. While some of them, like the SPT and the CPT are already a standard for geotechnical design, others remain in experimental development, such as the DMT, or V_{S1}.

In earthquake-induced liquefaction, ground motion is idealized as a vertically propagating shear wave in the soil from the underlying rock. Resistance of sand against liquefaction may be evaluated in laboratory by running undrained cyclic triaxial tests on undisturbed soil specimens. Cyclic stress with a constant amplitude is loaded repeatedly, and the number of cycles are counted until excess pore water pressure equal the initial effective stress or peak-to-peak (i.e., double amplitude) axial strain equal to 2.5%, 5%, 10%, etc.

As explained before, the analysis of liquefaction susceptibility, triggered by cyclic loadings, is commonly made by comparing the CSR , the seismic demand on a soil layer, and the CRR, the capacity of the soil to resist liquefaction (Youd et al., 2001).

Being the generalized Cyclic Resistance Ratio determined, according to Seed (1983), by:

$$CRR = CRR_{15} \times K_M \times K_\sigma \times K_\alpha \tag{4.11}$$

where CRR_{15} is the limit condition for 15 cycles in action, and K_M or MSF, K_σ, K_α are correction factors to take into account the earthquake magnitude, the stress-level, and the pre-existing shear stress on a horizontal plane.

During this section are presented some of the literature which investigate the influence of many factors, such as initial confining stress, density, initial static shear stress, specimen preparation, on the cyclic strength of sands. These influencing factors are usually implemented in the form of correction factors, following the expression above. Laboratory element tests have also shown that the CRR of saturated sands depends on prior stress-strain history, age, cementation, and other environmental factors (Idriss and Boulanger, 2008).

Similarly to the literature presented for the monotonic liquefaction, there are a lot of factors influencing cyclic strength of cohesionless soils. Unlike for liquefaction triggered by monotonic loading conditions, literature addressed to cyclic strength of soils with fines is beyond the scope of this work.

4.4.1 Influence Of Earthquake Magnitude Scaling

A magnitude scaling factor (MSF) is used to adjust the CSR and/or CRR to a common value of earthquake magnitude, M or Mw, (conventionally taken to be M = 7.5), because of the CRR dependency on the number of loading cycles, which correlates with M. The basic definition of the magnitude scaling factor (MSF) is:

$$MSF = K_M = \frac{CRR_M}{CRR_{M=7.5}} \tag{4.12}$$

The MSF or K_M, is a magnitude adjustment factor which shows the idea of Seed and Idriss (1982) who replaced an irregular time history of earthquake loading by an equivalent stress history with a constant amplitude (Table 4.2). Despite being largely arbitrary, the equivalent stress amplitude is a reference stress and was defined, by 65% of the maximum shear stress in the irregular history, by Seed and Idriss (1982). Then, the number of cycles changing with the earthquake magnitude is taken into account by reducing the soil resistance for quakes of greater magnitude, or to increase soil resistance for quakes of fewer magnitudes. The trends of N, i.e. number of cycles required for liquefaction to take place, for simplicity may be expressed solely as a function of earthquake magnitude (Figure 4.52). Figure 4.53 shows the correlation, obtained by Idriss, for MSF scaling factor basing on the earthquake magnitude, M.

Table 4.2: Equivalent number of cycles Idriss.

Richter scale of earthquake magnitude (M)	Equivalent number of stress cycles (estimate)	K_M
8.5	30-32	0.8
7.5	15	1
6.75	8	1.2
6	5-6	1.5
≤5.25	2-3	1.8

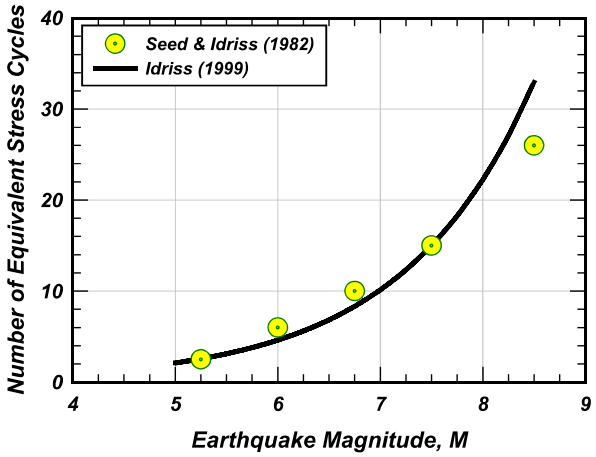


Figure 4.52: Mean number of equivalent uniform cycles at 65% of the peak stress versus earthquake magnitude (Idriss and Boulanger, 2004, 2008).

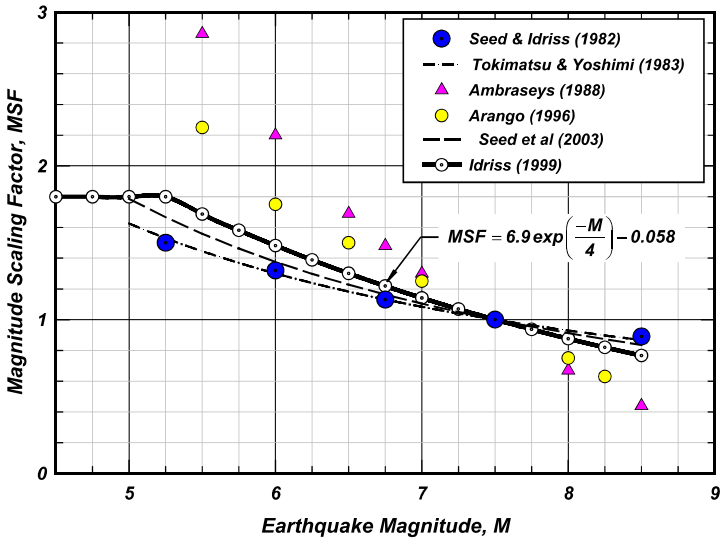


Figure 4.53: Magnitude scaling factor values proposed by various researchers (Idriss and Boulanger, 2004, 2008).

4.4.2 Influence Of Initial Confining Stress Level And Relative Density

Cyclic strength of sands dependency on confining stress is well stated and corrected through the empirical correction factor K_σ, which is also dependent on the relative density of the soil.

Monotonic shear of sand under different consolidation pressures reveal that the higher is the confining pressures, for a similar void ratio, more contractive is the soil. The same applies on cyclic liquefaction, as the development of excess pore water pressure is a consequence of (negative) dilatancy. Thus theoretically cyclic liquefaction is the more likely to occur, for a same void ratio and a same external solicitation (i.e. a same CSR), under higher initial confining stresses, despite it does not mean that exist a higher liquefaction risk in deep layers in nature. It means that liquefaction

susceptibility is not only based on the initial state conditions, based on the initial confining stress and on the initial void ratio, because sand at a greater depth is more aged and the liquefaction resistance of sand increases with the number of years after deposition (Towhata, 2008). Generally, for recent deposits, liquefaction resistance increases with the confining stress in a non-linear way (Figure 4.54), being K_σ expressed by the equation:

$$K_\sigma = \left(\sigma'_{v0}/P_a\right)^{f-1} \tag{4.13}$$

,where f is an exponent function of the in situ conditions, including the relative density, the effect of past stresses, ageing and overconsolidation ratio. For relative densities between 40 and 60% f =0.7–0.8 and for relative densities between 60 and 80% f =0.6–0.7 (Youd et al., 2001).

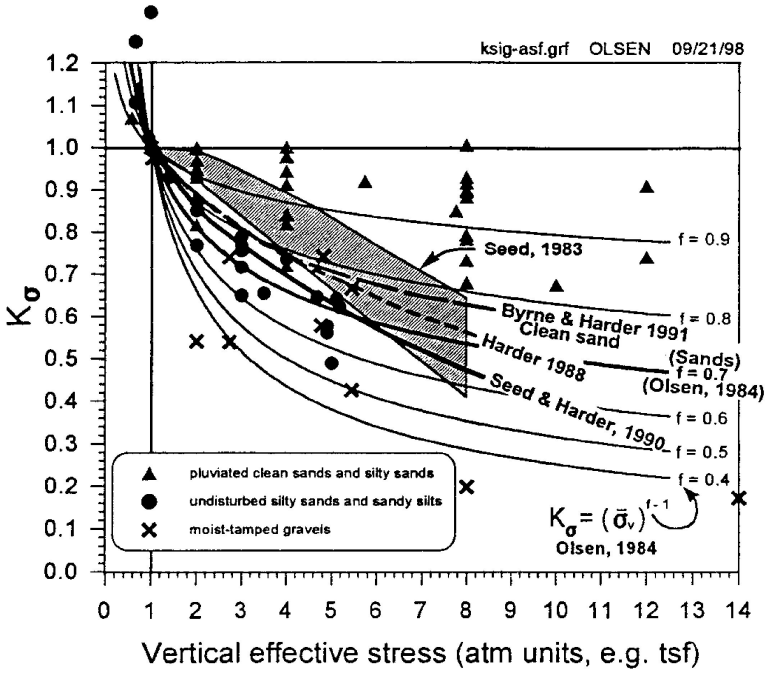


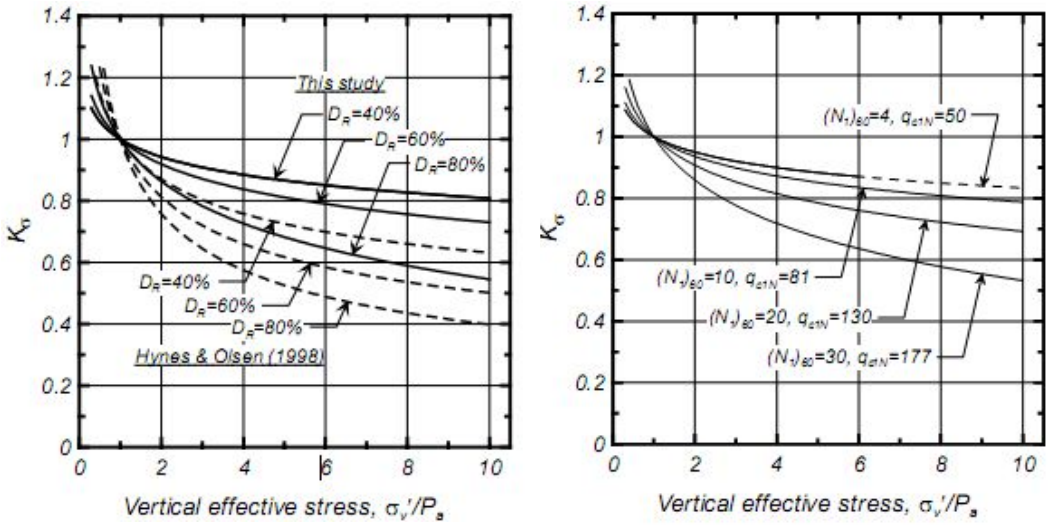
Figure 4.54: Laboratory data and compiled K_σ curves (reproduced from Hynes and Olsen (1999)) – (Youd et al., 2001).

The overburden correction factor, K_σ, was recently reviewed by Boulanger and Idriss (2004) (Figure 4.55a), which proposed the following relationship:

$$K_\sigma = 1 - C_\sigma \ln\left(\frac{\sigma'_{v0}}{P_a}\right) \leq 1.0 \tag{4.14}$$

$$C_\sigma = \frac{1}{18.9 - 17.3 D_r} \leq 0.3 \tag{4.15}$$

, where D_r is the relative density of the soil and P_a is the atmospheric pressure. This re-evaluation corresponds to a progressive change of a relative state parameter, and was suggested due to the combined effects of Dr and σ'_{v0} on CRR.



(a) (b)

Figure 4.55: (a) K_σ curves for a range of $(N_1)_{60}$ and q_{c1N} (b) Comparison of derived K_σ relations to those recommended by Hynes and Olsen (1999) (Boulanger and Idriss, 2004).

Idriss and Boulanger (2003) also re-evaluated the correlations between $(N_1)_{60}$, q_{c1N} and D_r (Figure 4.55b), and recommend the following expressions for clean sands:

$$D_r = \sqrt{\frac{(N_1)_{60}}{46}} \tag{4.16}$$

$$D_r = 0.478\,(q_{c1N})^{0.264} - 1.063 \tag{4.17}$$

To correct the overburden stress effects on CRR for CPT and SPT tests, the authors expressed the c_σ in terms of $(N_1)_{60}$, q_{c1N} by:

$$C_\sigma = \frac{1}{18.9 - 2.55\sqrt{(N_1)_{60}}} \leq 0.3 \tag{4.18}$$

$$C_\sigma = \frac{1}{37.3 - 8.27\sqrt{(q_{c1N})^{0.263}}} \leq 0.3 \tag{4.19}$$

Although values higher than 1 are typically found in K_σ curves for initial confining stresses lower than 100 kPa, according to the ASCE workshop in 2001, it is recommended that the correction

factor be restricted to 1. To achieve K_σ curves tests are necessary the performance of a set of laboratorial tests on hydrostatically consolidated sands.

Overburden correction factor, K_σ, was firstly identified from cyclic triaxial tests and later on from other different apparatus. The differences related to both equipments are partially explained by inherent and induced anisotropy. The comparison arisen from different laboratory equipments is presented in the subsection 4.4.4.

4.4.3 Influence Of Anisotropy

Similarly to monotonic undrained shear response, cyclic undrained shear response also depends on inherent and induced anisotropy. Yet it influence may be more difficult to assess due to the principal stress rotation or shear-stress reversal, or even when principal stress direction remains constant, and to changing orientation with respect to the principal axes of anisotropy.

When a soil, hydrostatically consolidated, is subjected to a cyclic shear with principal stress-reversal, it is expected a large plastic strain accumulation during extension than during compression. This distinct shear response is partially attributed to inherent anisotropy of sand caused by non-uniform particle shapes.

Another way to assess soil inherent or induced anisotropy effect is by determining the Young's modulus E_v and E_h or through the loading and unloading stress-paths during cyclic shear. DeGennaro et al. (2004), basing on the Graham and Houlsby (1983) simplified procedure, found the inclination of the effective stress paths during unloading able to be described with an elastic anisotropic model. During unloading the stress paths with a positive slope are typical of soils stiffer in the vertical direction, (see Figure 4.56a), and if the stress path has a negative slope, the soil samples are stiffer in the horizontal direction. The authors observed Hostun sand samples to be stiffer in the vertical direction than in the horizontal direction, describing a nearly vertical stress-path during one-way stress reversal, (see Figure 4.56b).

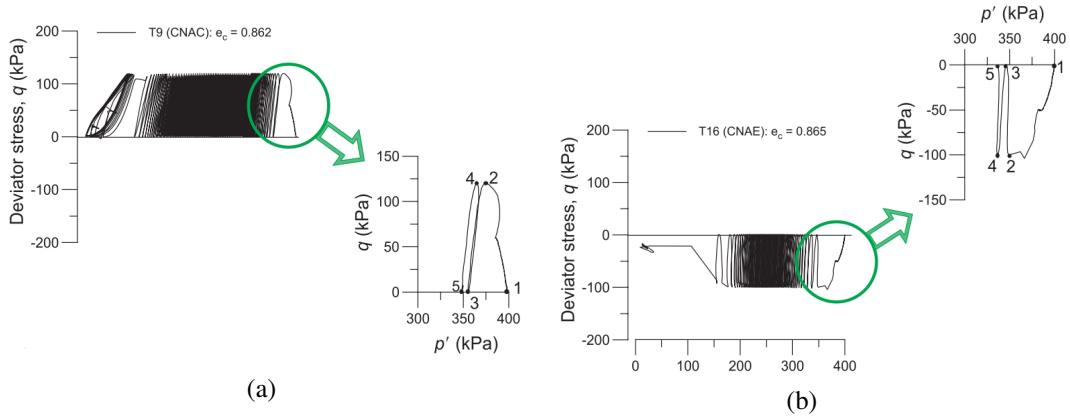


Figure 4.56: Analysis of the effective stress paths obtained for different loading signals for Hostun sand without and with stress reversal (a) and (b) respectively (DeGennaro et al., 2004).

Unlike induced anisotropy, which effect is introduced through the K_α correction factor, used on the determination of the CRR, i.e. the capacity of the soil to resist liquefaction, inherent anisotropy is usually neglected. Yamada et al. (2010) during their study of Toyoura sands' reliquefaction resistance concluded that anisotropy is a major factor influencing liquefaction resistance. They stated that *"anisotropy is a crucial factor that surpasses even the importance of density"*. It is expected that dense soils under high values of confining stresses can strain soften.Yamada et al. (2010) concluded that, even with the increase of relative density due to the drainage of water after liquefaction, cyclic resistance increase is not always observed. Instead, sometimes, denser soils become more prone to liquefaction. Anisotropy was identified, by Yamada et al. (2010), as the key factor influencing soil liquefaction resistance. In fact, *"during liquefaction, continuous and orderly changes in anisotropy are repeated with dizzying speed"*. According to these authors, in cases where the level of anisotropy after liquefaction becomes appreciable low, when compared with the situation before liquefaction, the soil behaviour will never be similar to an extremely loose sand in any shear direction.

4.4.3.1 Influence of specimen preparation technique

The influence of the depositional method, thus of inherent anisotropy and fabric on the CRR of saturated sands might be as large as a factor of 2 from highest to lowest, as might be observed from Figure 4.57 (Mulilis et al., 1977).

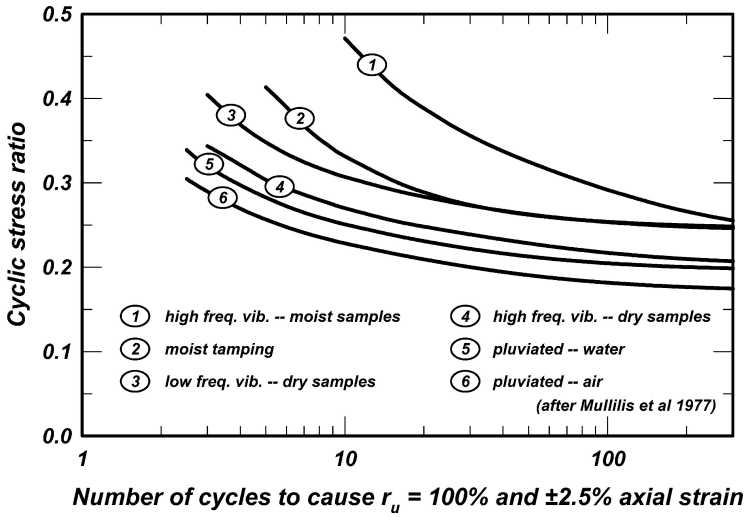


Figure 4.57: Results of cyclic triaxial tests, showing the influence of the sample preparation method on the CRR of Monterey No. 0 sand at DR = 50% (after Mulilis et al. (1977), with permission from ASCE, from Idriss and Boulanger (2008)).

Also according to Figure 4.57 moist tamping seems to be the technique which produces the most resistant specimens, when compared with the others reconstitution techniques. However, as the reconstitution technique also depends on the shape of the grains, suitability of Figure 4.57 is limited to that particular soil (Monterey No. 0).

Somasundaram (2004) while studying Fraser River sand, on a UBC simple shear apparatus is of the NGI type, observed, similarly to Mulilis et al. (1977), a higher CRR for specimens prepared by water pluviation than on those prepared by air-pluviation. Additionally, Somasundaram (2004) and Wijewickreme et al. (2005) reported an increasing CRR for loose Fraser River sand with increasing initial vertical confining stress, for specimens prepared by air-pluviation formed with the same energy, i.e. with the same initial void ratio (Figure 4.58). Such occurrence was associated by the authors to a densification effect created by the sample reconstitution method. As stated by Wijewickreme et al. (2005) *"for the air-pluviated sand the gain in CRR due to stress densification exceeds the potential reduction in CRR arising from increase* $\sigma_v^{'}$*"*. Additionally, Al-Tarhouni et al. (2011) found, while studying the behaviour of gold tailings, that regardless the initial confining stress, a same number of cycles was required to induce liquefaction, for a given void ratio. Following the same ideology it is concluded that the reconstitution technique might have a densification effect which surpasses the potential reduction in CRR, arising from increase $\sigma_v^{'}$.

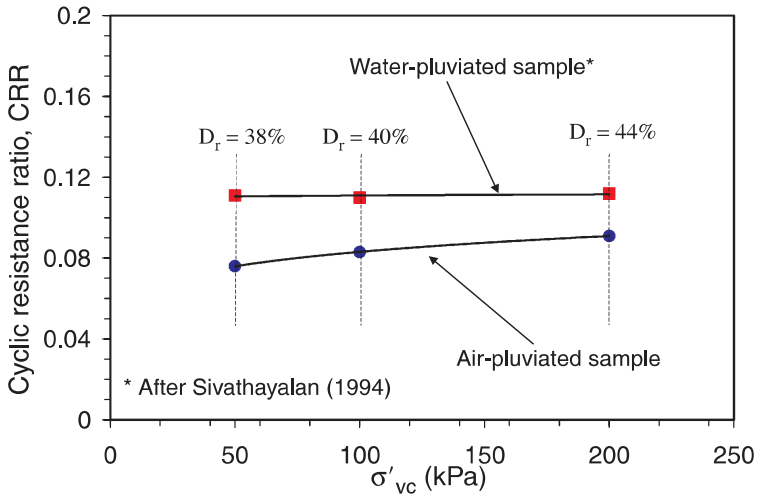


Figure 4.58: Comparison of cyclic resistance curves for loose air-pluviated and water-pluviated sands at the same relative density (D_r) and vertical effective stress ($\sigma_v^{'}$) combinations (Wijewickreme et al., 2005).

The relevance of understanding the effect of fabric anisotropy reflects on an accurate ability to predict CRR of soils in situ. Aiming to understand it effect Ghiona and Porcino (2006) studied the fabric effect by comparing the cyclic undrained shear strength of of Gioia Tauro Sand reconstituted by water sedimentation and air pluviation with undisturbed samples. The authors concluded undrained monotonic and cyclic triaxial strength to be greatly influenced by reconstitution method. Similarly to the effect on undrained monotonic shear strength, reports state water sedimentation (WS) to be the technique which betters represent cyclic undrained shear strength of undisturbed frozen specimens (Figure 4.59). On the other hand, sand specimens prepared by air pluviation led to a weaker undrained response (see Figure 4.59).

Being the sample reconstitution such an important factor affecting undrained soil response how is it possible to know which one is the most accurate to predict liquefaction susceptibility, with

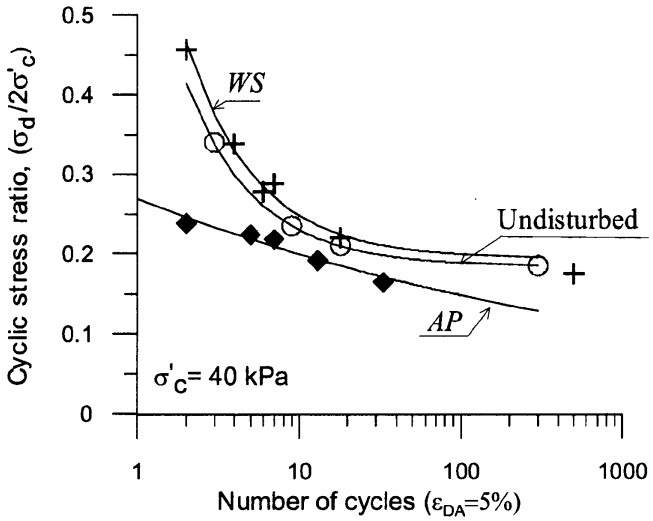


Figure 4.59: Comparative undrained cyclic triaxial response of undisturbed and reconstituted specimens of Gioia Tauro sand (Ghiona and Porcino, 2006; Porcino et al., 2008).

reference to those in situ? Is it the water pluviation the best reconstitution technique which better reproduces all soils undrained strength?

In a recent work, Wang et al. (2006), found the same shear wave velocity for reconstituted and intact offshore samples to predict liquefaction and a same strength resistance for a 6% peak-to-peak axial strain. The reconstitution method adopted by the authors was the moist tamping technique. In order to achieve a same shear wave velocity, the reconstituted specimen was submitted to a combination of overconsolidation and pre-shearing stress. These findings support the idea of evaluating soil liquefaction susceptibility based on the Simplified Procedure which correlates CSR with V_{S1}.

4.4.3.2 Influence of static shear stress (or induced anisotropy)

Loading direction during shear can be properly specified by α, which measures the ratio of the initial static shear by the normal effective stress action on the plane of maximum shear stress. It is defined differently, according to the apparatus used for testing, by normalizing the maximum shear stress with the normal effective stress acting on the plane of maximum stress (Vaid et al., 2001):

(simple shear)

$$\alpha = \frac{\tau_{st}}{\sigma'_{vc}} \tag{4.20}$$

(triaxial shear)

$$\alpha = \frac{\sigma'_{1c} - \sigma'_{3c}}{\sigma'_{1c} + \sigma'_{3c}} \tag{4.21}$$

In order to account with this effect Seed (1983) developed the K_α factor, which corrects the CRR by considering the initial static shear stress ratio (α) (Figure 4.60). The K_α is defined as the ratio between the cyclic resistance for some value of α, by the cyclic resistance for $\alpha = 0$:

$$K_\alpha = \frac{CRR_\alpha}{CRR_{\alpha=0}} \tag{4.22}$$

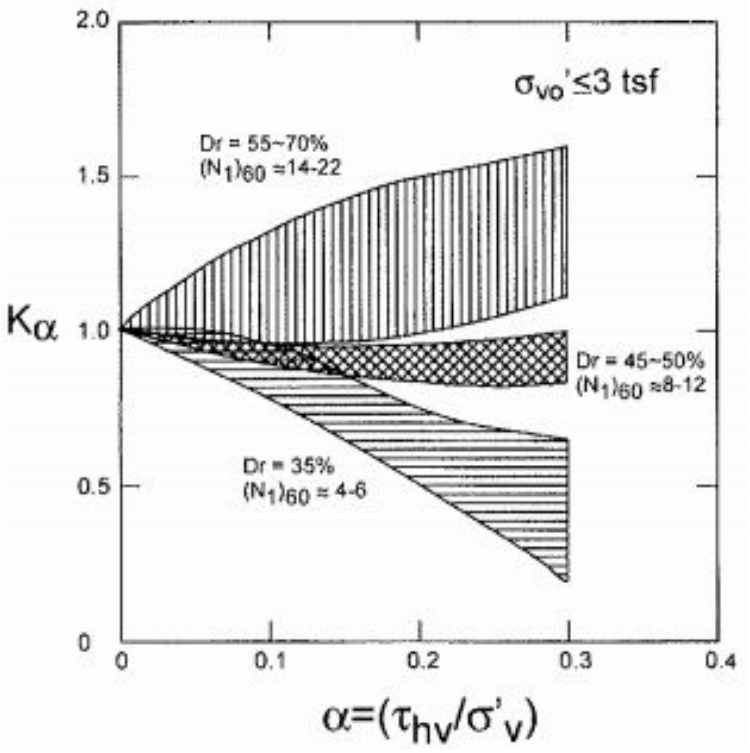


Figure 4.60: Summary of recommended values for K_α proposed by Harder and Boulanger (Jefferies and Been, 2006).

K_α, differently of K_σ, can increase or decrease depending jointly on the density and confining stress. In addition, K_α also depends on the failure criteria used to define the CRR and on the laboratory test device. Usually, simple shear device is preferred as it allows for principal stress rotation to occur, making it nearest to in situ stress conditions during earthquake shaking (Idriss and Boulanger, 2008).

Though, as observed by many other authors (Vaid and Chern, 1985; Vaid et al., 2001; Sivathayalan and Ha, 2011; Viana da Fonseca and Soares, 2012; Chiaro et al., 2012), cyclic resistance increases

with increasing static shear if liquefaction results in cyclic mobility, and decreases with initial static shear if strain softening takes place.

As revised by several researchers, strain softening during cyclic loading will trigger only if the sand strain soften under static loading and the maximum shear stress exceeds the steady or quasi steady state strength (Kramer, 1996; Vaid and Sivathayalan, 2000).

Because of the lack of convergence and consistency in the existing data, static shear stress effects on liquefaction susceptibility are still under research. Thus, according to the workshop of the National Centre for Earthquake Engineering Research, the current proposals *"shouldn't be used by non-specialists"* (Youd et al., 2001).

More recently Boulanger (2003) published a new framework for K_α based on a relative state parameter, ξ_r, in order to take into account both initial relative density and initial confining stress (Figure 4.61).

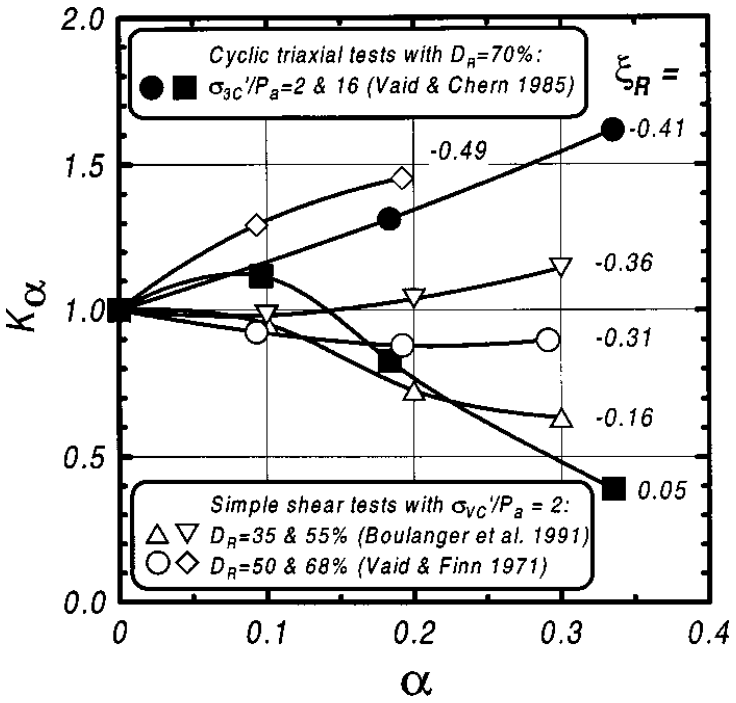


Figure 4.61: Effect of the relative state parameter index, ξ_r, on the static shear stress ratio correction factor K_α (Boulanger, 2003).

Boulanger proposal appeared as an answer to the misgivings founnd by previous authors on the ability of K_α and K_σ to accurately correct undrained cyclic shear strength.

In fact, earlier, Vaid et al. (2001), from studies developed with Fraser River sand on triaxial apparatus, found K_α to be highly dependent on relative density, at a given confining stress. The authors also found K_σ values very close to 1, regardless of the confining stress level, thus grossly underestimated by Seed and Harder curve (1990). The authors compared the predictions obtained by

multiplying K_σ and K_α with a new single site-specific correction factor, termed $K_{\alpha\sigma}$ herein, that would empirically relate the reference $(CRR)_{\sigma'=100,\alpha=0}$, to $(CRR)_{\sigma',\alpha}$ for the effects of the levels of static shear and confining pressure. The huge differences recorded for Fraser River sand at an initial confining stress of 400 kPa can be observed in Figure 4.62.

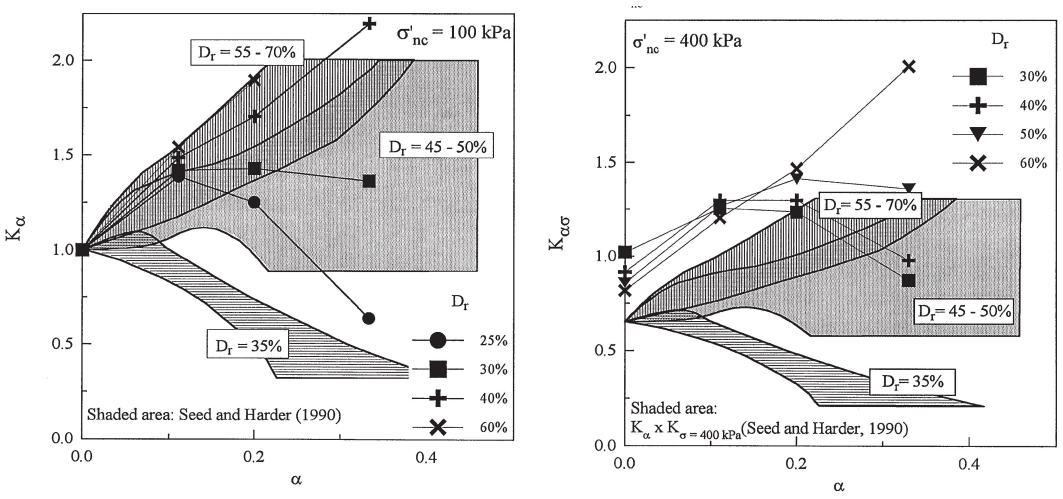


Figure 4.62: K_α versus α for Fraser River sand at different density states at: (a) $\sigma_h^{'}$ = 100 kPa; (b) $\sigma_h^{'}$ = 400 kPa (Vaid et al., 2001).

While Vaid et al. (2001) found Seed and Harder correlations to underpredict undrained cyclic shear strength of Fraser River sand, Sivathayalan and Ha (2011) found it to overpredict undrained cyclic shear strength of a Silica sand tested in a NGI type simple shear apparatus. Sivathayalan and Ha (2011) associated such differences to the distinct nature of response between the two sands, (i.e., strain-softening versus strain-hardening), to be dictated jointly by dilatancy, soil fabric, and particle shape and on loading conditions. The authors also suggest that K_α should not be determined basing on the initial relative density but on the anticipated deformation characteristics, (i.e. strain softening versus strain hardening), of soils.

Nevertheless the differences reported above might be associated not only to anisotropic stress conditions but also to the shear mode. In fact huge differences have been recorded in the past few years between both devices, mainly associated to principal stress rotation. Aiming to perceive such differences on both correction factors an extensive laboratory study, using the HCT, would be required.

4.4.4 Undrained Cyclic Shear Strength Obtained From Distinct Laboratory Testing Devices

4.4.4.1 Comparison

Usually cyclic liquefaction potential (both flow liquefaction and cyclic mobility) might be evaluated through four distinct laboratory devices: torsional shear apparatus, shaking table; cyclic triaxial device; cyclic simple shear or cyclic direct simple shear device. Among all equipments the HTC is usually more used to evaluate non-cyclic shear as valuable information is obtained. The expensive device, difficulty associated to the preparation of the specimens and the complexity of the instrumentation, turned HTC tests less performed.

Still, Tx tests remain the most practiced laboratory technique for soil mechanical characterization, mainly due to its simplicity. Plus their interpretation is easily comprehensive, being responsible for most of the developments on constitutive modelling and parametrical calibration. However, although enabling principal stresses reversal or inversion, Tx tests do not allow principal stress rotation, a key factor which conditions soil behaviour.

On the other hand, DSS apparatus is attractive at first sight, but similarly to SS device, leaves horizontal stress unmeasured and suffers from non-uniform stress distribution. As any simple shear testing technique, DSS has the same disadvantages but, as a constant volume test, becomes an easy performing and timesaving test, leaving however the amplitude and the direction of principal stresses difficult to trace. Thus as stress conditions are unknown, the interpretation of the results is limited to a consideration of the shear and the normal stresses on the horizontal plane. Tests interpretation shall be based on the presumption that the horizontal plane is the plane of maximum shear stress (Sivathayalan and Ha, 2011). Despite it disadvantages, DSS tests beyond allowing principal stress rotation, is also devoid of compliance. According to De Alba et al. (1976), the overestimation of the excess pore pressure due to the compliance of test systems with supposedly undrained saturated specimens may reach 30%.

Stress and strain conditions during cyclic loading differ significantly between simple shear and triaxial tests. Several researchers, aiming to obtain a better correction factor to apply to the triaxial cyclic resistances, pointed out that cyclic triaxial might not be suitable to asses liquefaction susceptibility induced by earthquake actions. Sivathayalan and Ha (2011) state that inherent anisotropy due to in situ natural fabric and the one induced by specimens reconstitution in lab by pluviation is responsible for the increased resistance when tested under tiaxial conditions, due to it higher stiffness on the vertical direction than on horizontal plane. The authors found cyclic SS undrained shear strength to be, in extreme cases, three times lower than the resistance obtained for triaxial tests (Figure 4.63b). The authors also attributed such differences to soil fabric and particle shape, as Fraser River, a semi-angular sand exhibited a more dilative behaviour and the sub-rounded silica sand exhibited a more contractive behaviour (Figure 4.63).

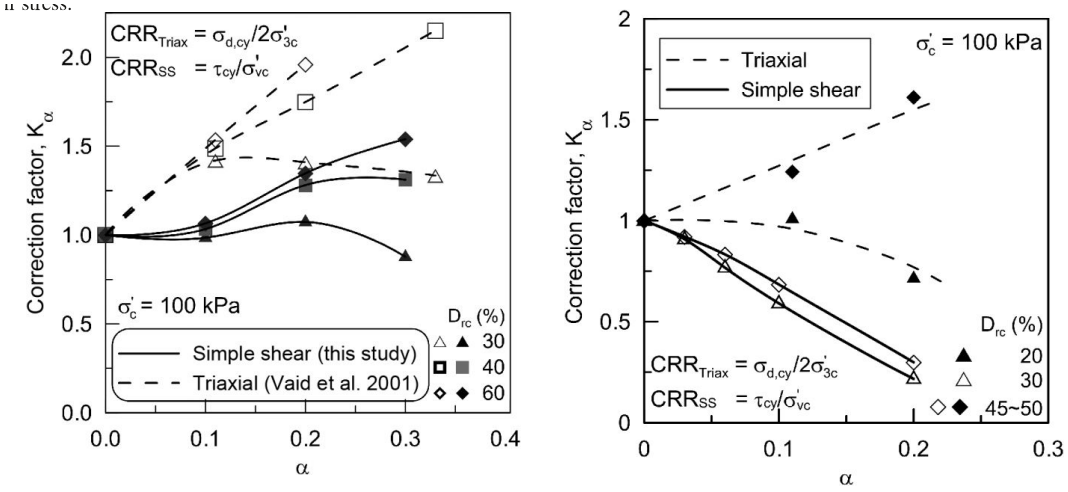


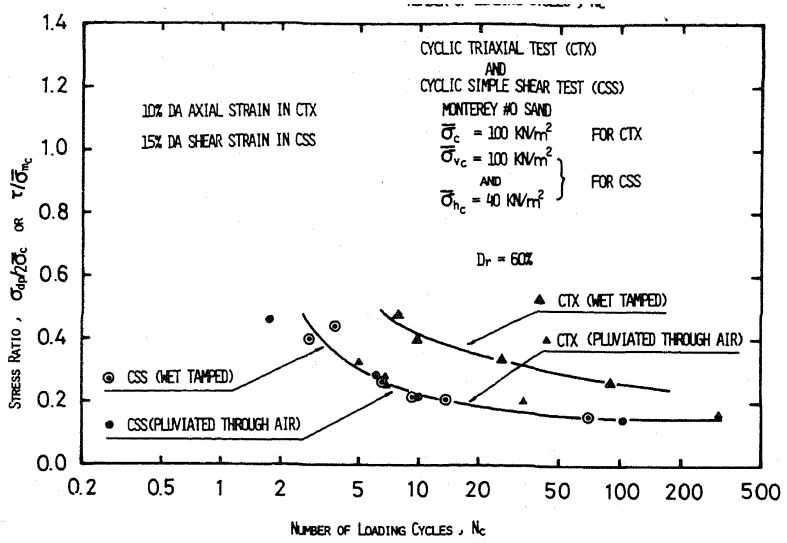
Figure 4.63: (a) Dependence of Ka on loading mode in semi-angular Fraser River sand; (b) Dependence of K_α on loading mode in sub-rounded silica sand (Sivathayalan and Ha, 2011).

Earlier, Silver et al. (1980) during their studies realized that the comparison between triaxial and simple shear devices is not as simple as it has been suggested. They concluded that specimens prepared by moist tamping are significantly more resistant than those prepared by air pluviation under triaxial conditions (Figure 4.64). However for both techniques, the cyclic resistance was the same under simple shear conditions (Figure 4.64). Therefore comparison between different apparatus is not so simple and is apparently conditioned by the sample preparation method, i.e., by the inherent anisotropy, jointly with induced anisotropic fabric.

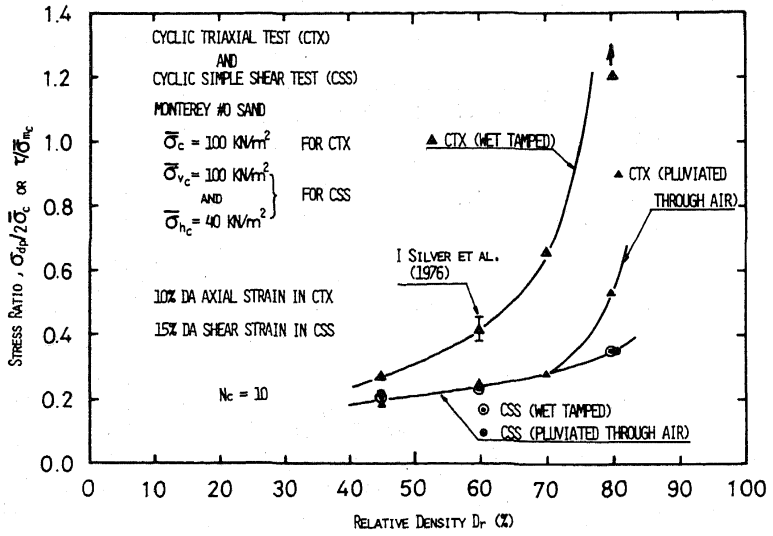
As outlined by Tatsuoka et al. (1986b) comparisons in-between simple shear and triaxial devices for a given sand element depend on several factors, including the kind of sand, the sample preparation, the relative density, the strain value for which liquefaction is deemed to occur and the number of loading cycles.

Also Vaid and Chern (1985) identified that K_σ, for cyclic SS devices, to be close to 1 for loose sand specimens and significantly smaller than 1 for denser states. As emphasized by Vaid, it appears that cyclic triaxial test conditions overestimate K_σ, when compared to the cyclic simple shear conditions.

During their studies of static and cyclic liquefaction potential over Fraser Delta sand, Vaid and Sivathayalan (1996) have also concluded that the reduction factors currently applied to cyclic triaxial resistance to make the correspondence to simple shear response may involve a large degree of conservatism for design purposes and depend jointly on relative density and on confining stress (Figure 4.65a). The authors found the reduction factor c_r used to correct triaxial cyclic resistance to an equivalent simple shear, to be conservative and that it should not be considered just a function of K_0, as it also depends on both initial relative density and initial confining stress (see Figure 4.65b).



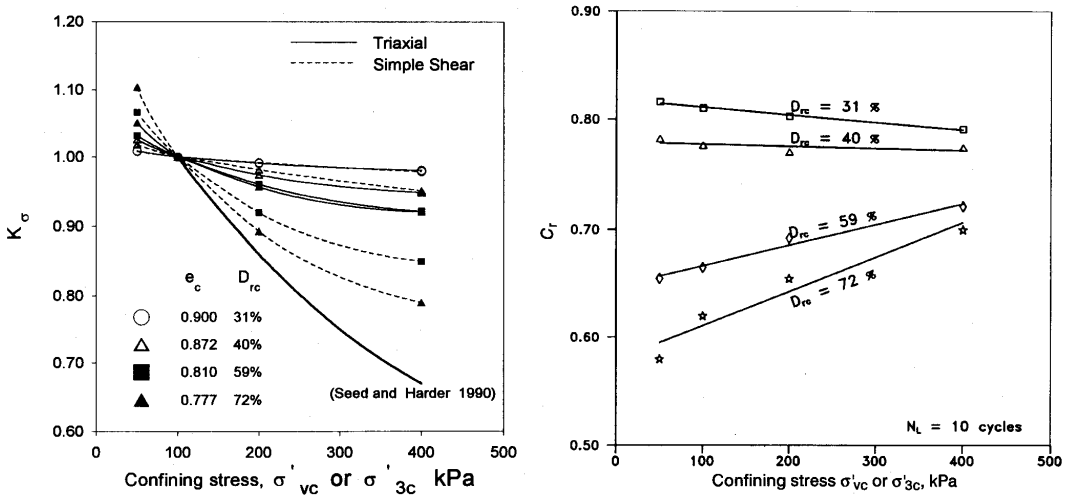
(a)



(b)

Figure 4.64: (a) Stress ratio versus number of cycles to 15% double amplitude strain for wet tamped and air-pluviated no. 0 sand at D_r =60%; (b) Stress ratio versus relative density for failure defined as 15% double amplitude shear strain in the tenth loading cycle for wet tamped and air-pluviated Monterey No.0 sand (Silver et al. (1980)).

It is possible that these differences are associated, not only to different equipments (where anisotropy is induced), but also to the simultaneous effect of the level of confining stress, relative density and inherent anisotropy. Vaid et al. (2001) state that K_σ and K_α should not be considered independent, therefore, changes in anisotropy with principal stress reorientation during cycling and their dependence with the relative density and confining stress should be taken into account. As highlighted by Jefferies and Shuttle (2011), *"CSR may hide the periodic change in principal stress direction that actually occurs, which appears to be the fundamental driver of soil response at micromechanical level"*. Additionally, these factors are also dependent on grain shape, roughness and sphericity



(a) (b)

Figure 4.65: (a) K_σ under simple shear and triaxial stress conditions for Fraser Delta sand; (b) The ratio c_r of cyclic resistance of Fraser Delta sand under simple shear and triaxial stress conditions (Sivathayalan, 1994; Vaid and Sivathayalan, 1996).

and on grain size of soils. Figure 4.66 reveals cyclic shear strength dependency on mean grain size and on the type of device, by results reported by Seed and Peacock (1971) jointly with data obtained and compiled by Porcino et al. (2008), for Gioia Tauro sand.

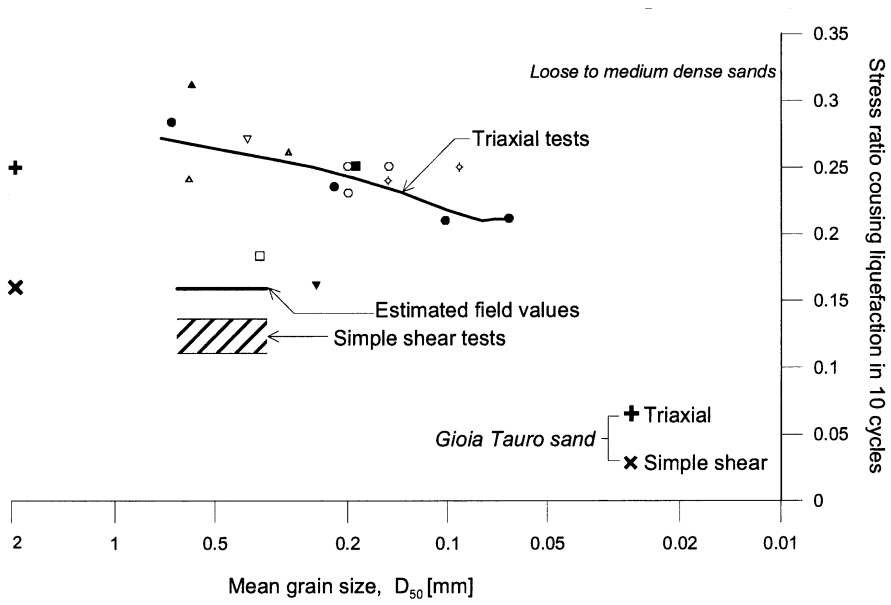


Figure 4.66: Comparison of stress conditions causing liquefaction in cyclic loading under simple shear, triaxial and field conditions (modified by Porcino et al., 2008, from Seed and Peacock, 1970).

As far as it can be considered, new alternative methods to evaluate cyclic resistance have to be considered. Currently correction factors proposed to evaluate liquefaction susceptibility are variables that depend on each other and that should not be considered separately.

Notwithstanding, it is necessary to take into account that specimens can be isotropically or anisotropically consolidated (in undrained conditions designated, CIU and CK_0U, respectively) in triaxial apparatus (Tx), while in direct simple shear, there is no lateral strain developing during consolidation (that is anisotropically consolidated). Finn et al. (1971) recognized that, explaining the differences on cyclic resistances by the fact that in simple shear tests, initial vertical effective stress can be misleading due to sample confinement. In fact, the soil specimen, being laterally constrained by the Teflon rings, is under a K_0 consolidation condition (typically 0.4-0.5 for sands). Liquefaction susceptibility analysis considered an initial effective stress ratio of $2 \triangle \tau_{xy} / \left(\sigma_y^{'} p K_0 \sigma_y^{'}\right)_0$, giving an approximate gain of 30%, being $\sigma_{y0}^{'}$ the initial vertical effective stress.

Nevertheless, despite cyclic triaxial tests not allowing for principal stress rotation, these tests cannot be devalued, since they offer two great advantages over simple shear: principal stresses control and a large amount of data for different undrained cyclic resistances, working with a wide variety of sands and initial states. As each sand has different grain shapes, and consequently different inherent anisotropy, the study of this variable could start with tests already performed willing to understand, on first hand, of how inherent anisotropy and particle shape influences stress-strain response.

In spite of liquefaction potential analysis of cohesionless soils being usually performed through different kinds of equipments in undrained conditions, as pointed out by Finn and Vaid (1977), constant volume drained tests are considered to be timesaving tests, with extraordinarily high reproducibility with more accurate cyclic soil response. According to both authors compliance in the constant volume test is less than 1/20 when compared with undrained tests, giving consequently more realistic estimation of liquefaction potential (Figure 4.67).

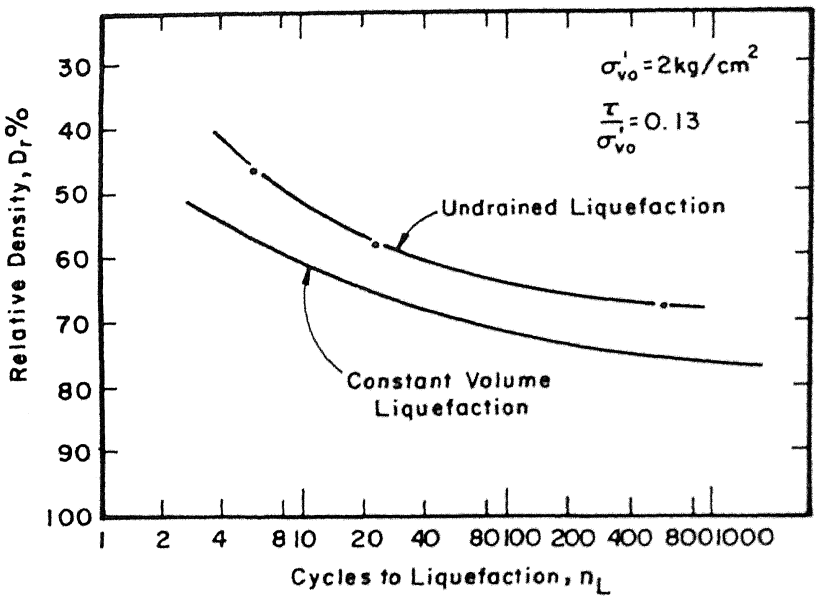


Figure 4.67: Liquefaction resistance of Ottawa sand in constant volume and undrained simple shear ((Finn and Vaid, 1977)).

4.4.4.2 Influence of principal stress rotation

Most of the cyclic liquefaction phenomena involve principal stress rotation, however its study started in the 70's, from the study of large cyclic loadings from storm waves acting on offshore platforms (Jefferies and Been, 2006). Nowadays this topic has been widely studied, being one of the keys to assess soil cyclic liquefaction potential.

The effect of principal stress rotation on fabric is related to the fact that it *"can move the stress point further into the yield surface until further yielding would only be triggered on the opposite side of the yield surface"* (quoted from Jefferies and Been (2006)). As *"the yield surface reflects the mobilization of particle contacts at a micromechanical level"* and a *"fabric evolution during cycles"* might occur ((DeGennaro et al., 2004; Papadimitriou and Bouckovalas, 2002)), a constant shrinkage and dilation of the yield surface dominates the cyclic undrained behaviour, over any other factor (Figure 4.68). As both fabric evolution and particle contacts differ from soil to soil, due to differing on grain shape and roughness, it is likely that different soils may have distinct undrained cyclic shear responses. (Oda and Iwashita, 2000) stated: *"Rotational resistance arises not only from contractive behaviour, but also from particle shape. It can be one of the dominant components to control the strength of granular media"*.

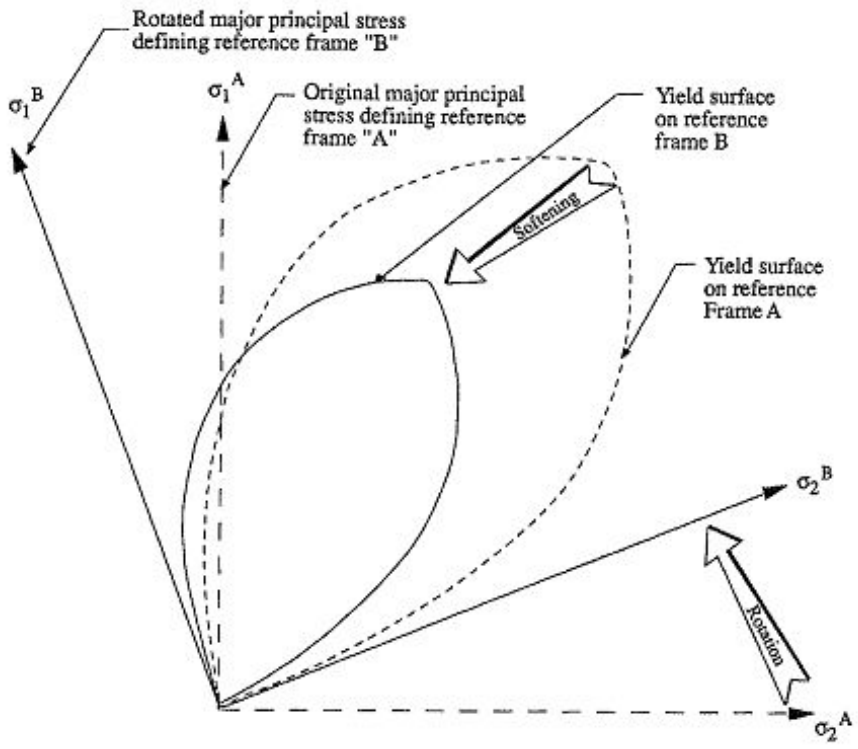


Figure 4.68: Schematic of yield surface softening induced by principal stress rotation (from Jefferies and Been (2006)).

Nevertheless precaution is required when inferring principal stress rotation influence. As explained by (Park et al., 2005) rotation of principal stresses does not occurs if K_0=1, as by the moment any horizontal shear stress is applied, the horizontal plane become the plane where principal stress direction is applied remaining as such during all test. However if K_0 = 0.5, principal stress direction acts on the 45^o plane and the plane of maximum shear gradually rotates and becomes approximately horizontal at failure (Roscoe, 1970). Cyclic DSS is an example where principal stress rotation gradually rotates as the soils samples are inherently consolidated by the Teflon coated stacked rings.

Plus principal stress rotation causes soil yielding, being responsible for lowest undrained cyclic shear strength of soils. This explains why CRR obtained by specimens tested on cyclic SS or DSS devices are much lower than the ones tested on triaxial devices.

From what was previously described about DSS or SS and Triaxial comparisons, much of the differences are associated do the possibility of the first one to allow principle stress rotation. And being the constant changes on the yield surface associated to the micromechanical grains contact then it becomes implicit that during these tests a continuous change on fabric succeeds. Intriguing (DeGennaro et al., 2004) demonstrated, while testing Hostun sand on a cyclic triaxial device under undrained conditions, that the *"elastic parameters remained nearly constant during most of the test (i.e., constant slope of the unloading paths), until cyclic mobility or liquefaction was reached, demonstrating that cycles did not significantly alter the initial fabric"*, even when testing with shear stress-reversal. Curiously most of the correction factors (K_σ and K_α), which correct CRR, were born from triaxial tests, thus and considering the non-dependency between each other it becomes clear that perhaps corrections factors are not suitable for other types of devices where elastic parameters do not remain constant (thus the contact between the grain particles).

Chapter 5

Scope Of The Research And Characterization Of The Materials

5.1 Introduction

The research program, mainly laboratorial, covers six distinct materials (exclusively natural soils) and an extra work which encompasses the study of two more materials (mixes between natural soils and manmade materials), but in a less intensive way. The main scope of this work is centered into the evaluation of the liquefaction potential of these six materials, thus it becomes prominent to understand the reasons behind the choice of each soil. This chapter aims to enclose the beginning of the research by making an historical overview of the interest of each one of the studied materials.

Additionally all the results already published by other authors (both Msc and PhD) are presented, highlightening the main contributions for the evaluation of soil liquefaction potential. All results which are intended to be continued, thus fundamental for the present research, are also presented and later on complemented in Chapter 7 and 8.

5.2 Algeria Sand

In the scope of liquefaction risk assessment, extensive laboratory studies have been completed on a sand from Ain Beniam, involved in well documented liquefaction events during the Bourmèdes earthquake that occurred in 2003 (Viana da Fonseca et al., 2011b).

5.2.1 Historical Overview - The Boumerdès Earthquake

On May 21, 2003, an earthquake occurred in Boumerdès, a province 50 km east of the Algerian capital Algiers. Reaching a 6.8 on Richter scale and a IX (Destructive) on Merchalli scale, it became one of the most destructive earthquake since January 1716. The epicenter of the earthquake was offshore, 7 km of Zemmouri in the province of Boumèrdes, about 50 km east of the capital city of Algiers The devastating event claimed the lives of 2287 people, injured 11.500 and left around 160.000 people homeless (Bouhadad et al., 2004). In this case, buildings with foundations on sands would be seriously affected by soil liquefaction, resulting in rapid loss of support, giving rise to significant settlements and consequently serious structural damages. Many liquefaction occurrences were documented especially on the coastline and margins of the local rivers (Figure 5.1). Figure 5.2 illustrates how the liquefaction features vary in size and morphology, while Figure 5.3 shows some damages in buildings and transportation systems observed in the area. The port of Algiers, responsible at that time by approximately 40% of the national cargo traffic, suffered several damages due to soil liquefaction including large settlements (see Figure 5.3a and 5.3b).

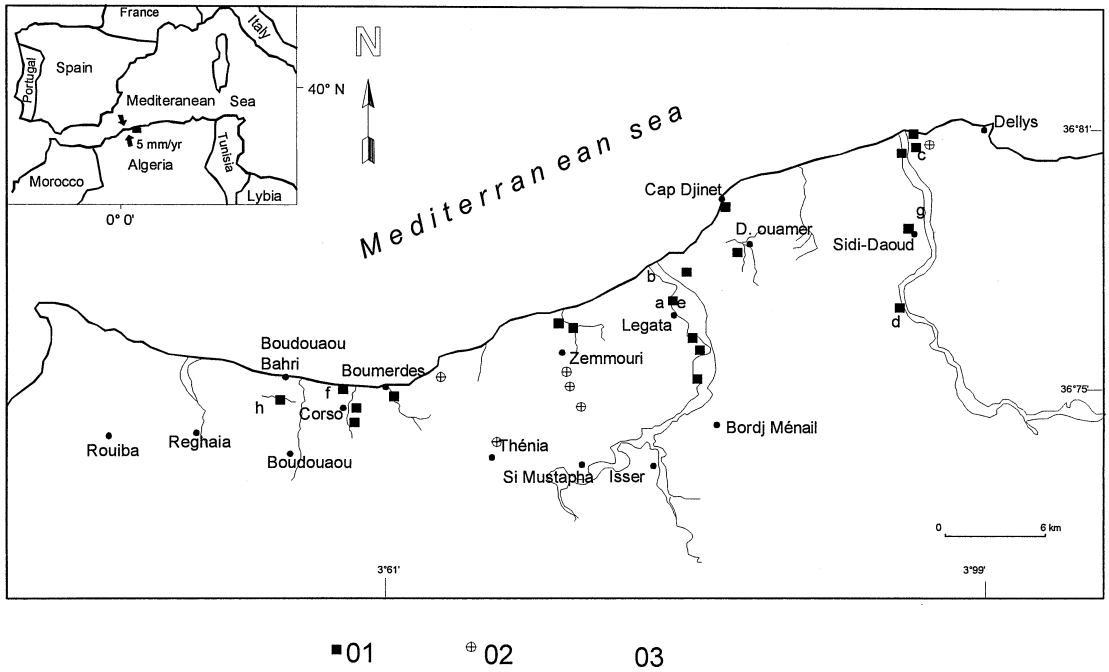
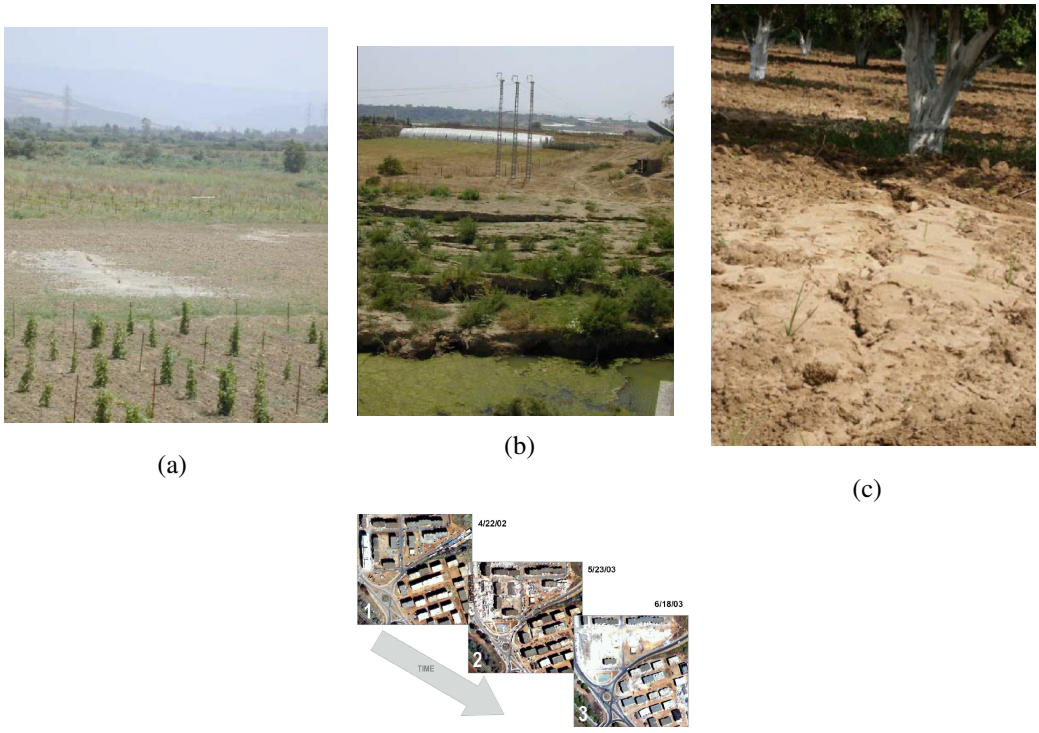


Figure 5.1: Distribution of liquefaction during the Bourmedès earthquake, May 21, 2003 (Bouhadad et al., 2004)

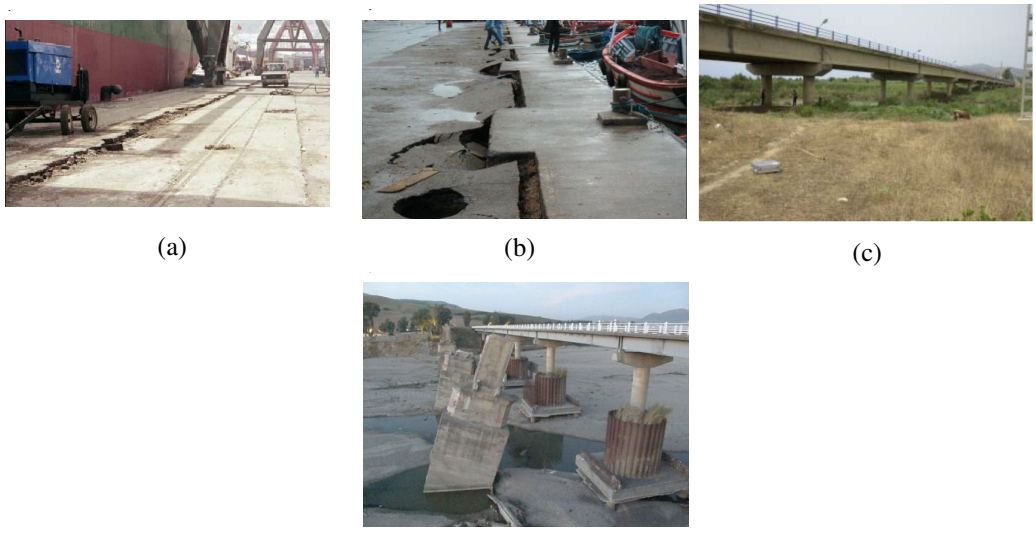
Serious damage induced by soil liquefaction occurred in the basin of the Isser and Sebaou Rivers (see Figure 5.1). The earthquake triggered the liquefaction of sandy deposits, forcing the excess water to come to the ground surface along the Isser River, where a large solid flow (mostly sand) was transported to the Mediterranean Sea (see Figure 5.4).

This relevant liquefaction phenomena had expression on classical sand boils and surface cracks (craters), appearing on both banks of Isser River, as in other places. Examples of these features are



(a) (b) (c) (d)

Figure 5.2: Liquefaction-induced sand boils (a) and lateral spreading (b) of the banks of Isser River; (c) sand boils in an orange grove in Zemmouri; (d) time sequence of QuickBird images, showing apartments in western Boumerdes (1) prior to and (2) soon afer the 5/21/03 earthquake. Scene 3 was acquired on 6/18/03, and shows progress made with clean-up operations (Bendimerad et al., 2003)



(a) (b) (c) (d)

Figure 5.3: Liquefaction consequences in structural damages: (a), (b) Differential settlement between quays wall and backland in Port of Algiers and the Harbor of Zemmouri-El-Bahri (JAEE); and, (c), (d) Bridges in the basin of the Isser River ((Bendimerad et al., 2003), and author personal photo)



Figure 5.4: Sand uplifted flow to the Mediterranean Sea in Isser River, 22 May 2003 (**Google-Earth**)

shown in Figure 5.3, where damage on roads and the collapse of retaining structures are included (Figure 5.3c and 5.3d). Figure 5.3 also shows the damage caused by loss of ground support due to soil liquefaction.

The emergence of assessing soil liquefaction potential on countries as Algeria is becoming prominent. In fact Algeria has experienced not only Bourmèdes earthquake, but also many destructive earthquakes over the last century. On October 10, 1980, an earthquake, reaching 7.1 of magnitude, devastated the city of El Asnam killing at least 5000 people. Earlier on September 9, 1954, the same city and Orleansville, had been heavily damaged by a magnitude 6.7 earthquake that killed over 1000 people (Bendimerad et al., 2003).

Liquefaction mitigation becomes very important, mainly in megacities where the risks and the vulnerability are higher due to unregulated construction, leading to heavy material and human losses.

The University of Science and Technology of Houari Boumediene (USTHB), in Alger, and the University of Porto have established a protocol to develop common research programmes, including the studies of development of significant extents of liquefied areas during the 2003 Boumerdès earthquake. For that purpose, and under a doctorate program, a sand from Ain Beniam in Alger, Algeria, which liquefied during the earhquake, was selected for complete evaluation of the factors implied in the phenomena.

5.2.2 Past Research

The laboratorial study of Ain Beniam sand was started by Ghili (2003), and continued by Pinheiro (2009), Fonseca (2009) and Rocha (2010), till the present research. As the study, mainly developed

under monotonic shear conditions, culminated with Rocha (2010) work, it will only be referred and presented part of his publishing.

During their investigation the authors characterized Ain Beniam sand, (designated by Algeria sand during the present work), including the grain size distribution curve, the specific gravity G_s and the determination of the maximum and minimum void ratio, (e_{max} and e_{min}). They also defined the CSL by performing a set of triaxial tests with loose reconstituted specimens, under both drained and undrained conditions. Plus a set of cyclic triaxial tests were initially performed by the authors in order to obtain a framework for assessing Algeria sand liquefaction potential.

The soil is a siliceous medium monogranular sand with effective diameters of D_{10} = 0.2 mm, D_{30} = 0.26 mm, D_{60} = 0.35 mm and D_{100} = 0.85 mm (corrected over those published in Viana da Fonseca and Soares (2012)). The coefficients of uniformity and shape are respectively C_U = 1.76 and C_C = 0.97, revealing a poorly graded sand (Figure 5.5). The mean grain size, D_{50}, is about 0.31 mm and the specific gravity, G_s, is 2.70. The values of the maximum and minimum void ratio are respectively: e_{max} = 0.89 and e_{min} = 0.531. Algeria Sand is predominantly quartz sand with a minimal amount of feldspars. As can be seen in Figure 5.6, the grain shapes are, in general, relatively spherical.

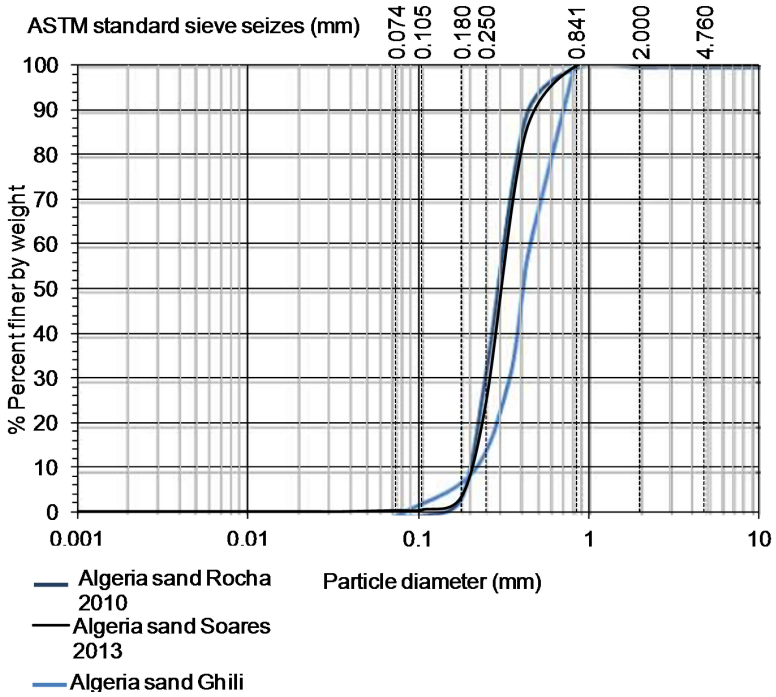
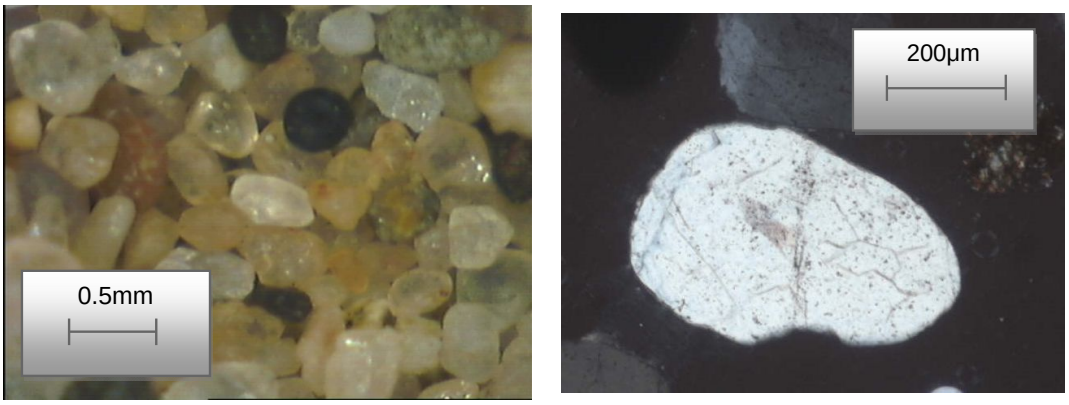


Figure 5.5: Grading curve of Algeria Sand

It should also be pointed out that the grading curve of Algeria sand determined by Ghili (2003) is very different, revealing a coarser sand when compared with that determined by Rocha (2010) and more recently (2013) in the scope of the present work. The recent grading curve was determined with the purpose to evaluate if any grading evolution occurred due to the large amount of tests performed over Algeria sand (Figure 5.5). Nonetheless as during three years of performing triaxial



(a) (b)

Figure 5.6: Grain shape of Algeria sand

tests the soil haven't evoluted, it is believed that the differences between the grain size distributions is mainly due to the different laboratory procedures to determine the grain size distribution of the soil.

Rocha (2010) performed a set of triaxial tests with specimens reconstituted by moist tamping, with an optimum water content of 5%. Among other techniques, moist tamping was chosen as it is able to produce the widest range in void ratio with satisfactory uniformity (Ishihara, 1996), allowing for a clear definition of the CSL. The optimum water content was determined through the compaction curve of Algeria sand using a standard weighted hammer ("the Kangoo hammer") according to the British Standards BS 1924: Part 2:1990 (Rocha, 2010).

The triaxial tests allowed a confirmation of the critical friction angle determined by a set of direct shear tests, of 32.4°, corresponding to a critical shear stress ratio M_{tc} of 1.30.

As reported by Rocha (2010), expectedly according to CSSM theory, Algeria CSL indicates a parallelism with the NCL. Notwithstanding CSL is only linearly defined by drained triaxial tests and undrained triaxial tests with initial confining pressures higher than 100 kPa (Figure 5.7). For lower confining pressures the specimens deemed to liquefy. Plus as might be seen in Figure 5.7 NCL determined through the odometer, revealed for higher confining pressures (> 1000 kPa), an inflection of the soil behavior, possibly due to the occurrence of grain crushing (Rocha, 2010).

The CSL equation obtained for Algeria sand by Rocha (2010) was:

$$e_c = 0.97 - 0.023 \ln\left(p_c'\right) \tag{5.1}$$

Moreover a loose low confined specimens exhibited, while tested under drained conditions, a distinct behavior from those tested under undrained conditions (see Figure 5.7). Thus the bifurcation once reported by Yamamuro and Lade (1998) for Nevada sand (with 7% FC), seems to also occur on Algeria sand.

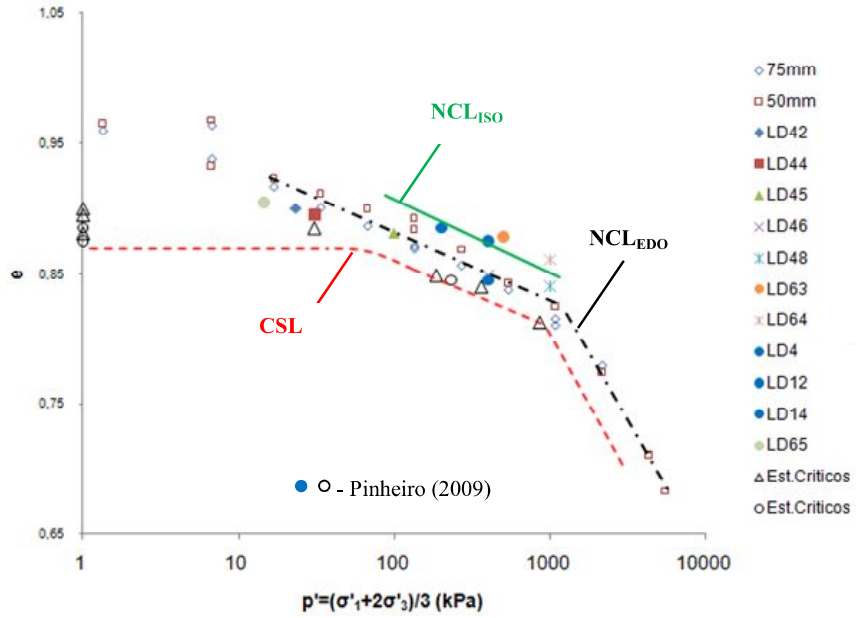


Figure 5.7: Definition of the normal consolidated isotropic (NCLISO) and oedometer (NCLEDO) lines and the critical state line (CSL) of Algeria sand (Rocha, 2010; Viana da Fonseca et al., 2011b)

Aiming to perceive cyclic liquefaction potential Rocha plotted two distinct frameworks, the simplified procedure, and the *"basic Berkeley school liquefaction assessment chart"*. The first one, proposed by Andrus and Stokoe (1997) is displayed in Figure 5.8, and the other one, proposed by Jefferies and Been (2006), which relies on CSSM theory, is displayed in Figure 5.9.

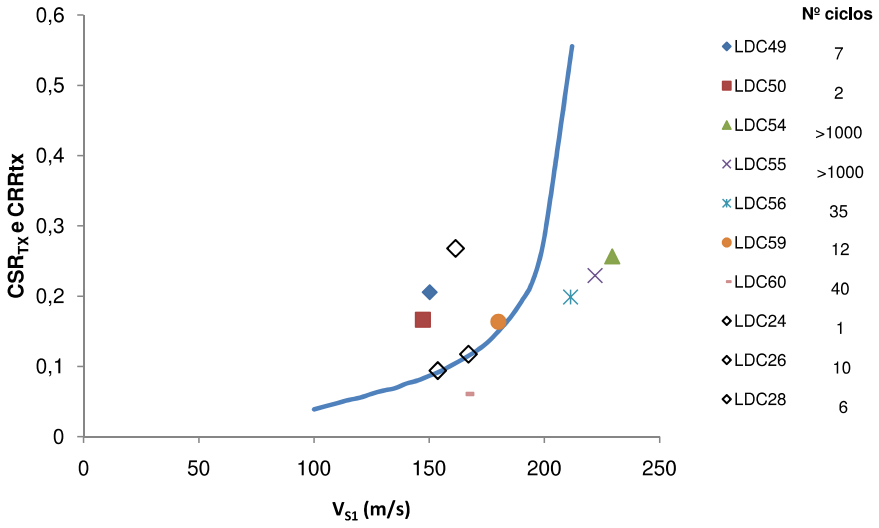


Figure 5.8: Simplified procedure for Algeria sand (Rocha, 2010)

Both frameworks feet well and deem to accurately predict soil liquefaction potential, at least under laboratorial conditions as the boundaries separate quite well tests which liquefied from non-liquefied tests. Both these Figures (5.8 and 5.9) were prepared with reference to earthquakes of

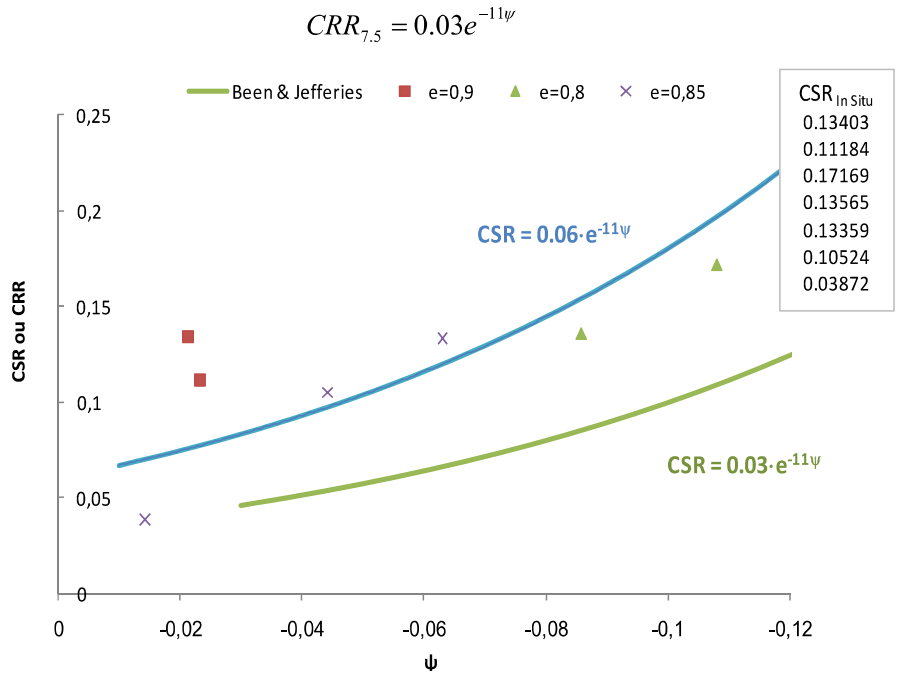


Figure 5.9: *"Basic Berkeley School liquefaction assessment chart"* for Algeria sand (Rocha, 2010; Viana da Fonseca et al., 2011b)

a magnitude of 7.5 on the Richter scale, meaning that liquefaction is distinguished from non-liquefaction for a number of cycles of 15, according to the magnitude scaling factors proposed by Idriss.

5.3 Coimbra Sand

In Portugal, due to past earthquakes, such as the 1755 Lisbon Earthquake, Coimbra's region has been identified as a region with several alluvial sandy deposits susceptible to liquefaction. Aiming to assess the geomechanical behavior of one of Coimbra's soils a predominantly quartz sand was prepared artificially from a quarry. This sand is one of the soils studied in a common research program between the Universities of Porto, Coimbra and Technical University of Lisbon.

5.3.1 Historical Overview – Lisbon And Benavente Earthquakes

In Portugal, due to its geographical localization, some seismic risk requires mitigation. Historical data shows that, depending on the construction importance and purchase, seismic action should be taken into account for projects design. A brief résumé is made upon Lisbon and Benavente earthquakes as being two of the most destructive taking place in national territory, which justify on the laboratorial study of Coimbra sand.

On November 1, 1755, Lisbon was stroke by an earthquake reaching a 9 in Richter magnitude scale. Killing up to 100 000 people and injuring more than 40 000 people, the Lisbon earthquake of 1755 is probably the greatest seismic disaster to have struck Western Europe. With an epicenter situated in the Atlantic Ocean, SW of Cape San Vicente, at several hundred kilometers from this city, the earthquake lasted 6 to 10 minutes affecting an area of 800 000 km^2 (Mezcua et al., 1991).

Lisbon is characterized by a complex and heterogeneous geology. While basalt, limestone and marble of Cretaceous cover the western part of the city, Miocene formations dominate the south and the east, while the centre is composed by low-lying valleys filled with water-saturated alluvial sediments. Expectedly damages were much stronger in the centre zone, not only due to building concentration but also due to the dominant geology highly susceptible to liquefaction hazard, including slope failures. As in soft unconsolidated sediments, restraints on acceleration and seismic wave velocities are much lower, the layers when shaken, are subjected to an increase of the pore water pressure until liquefaction is triggered (adapted from Chester (2001)).

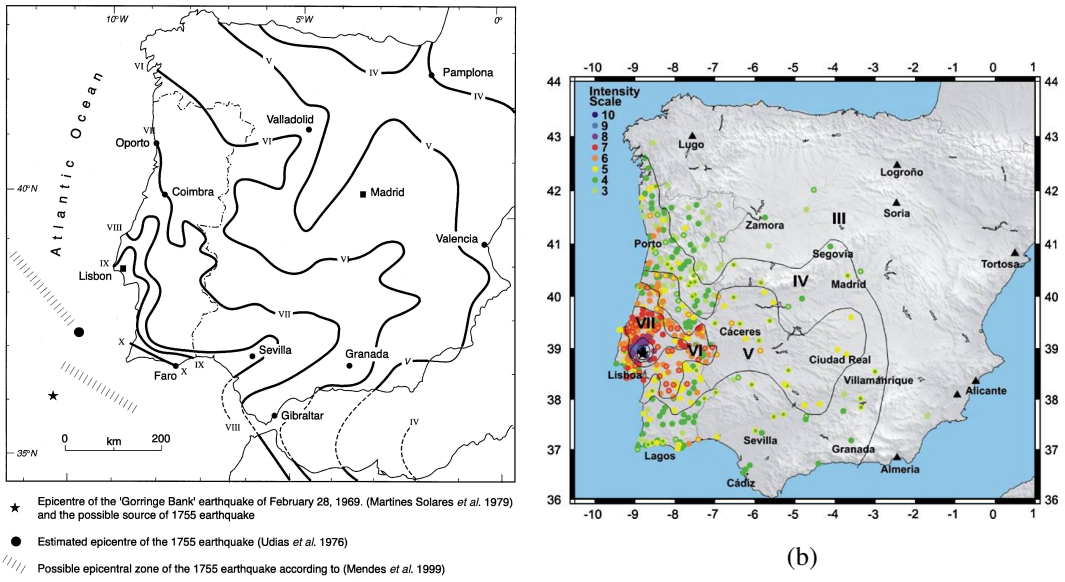
Regardless, sub-soil conditions and the seismic intensity cannot explain such catastrophe, yet a combination of both factors. The massive destruction which took place in Lisbon was in effect a result of what is commonly designated by "three-way harmonic interaction" between the attenuation of high frequency seismic motions from distant earthquakes, building styles and subsoil conditions (Degg, 1992).

The 1755 also reached Algarve, as might be seen in isoseismal (MSK) map of the earthquake (Figure 5.10a), devastating almost totally the towns of Lagos, Alvor, Portimão, Albufeira, Quarteria and Faro. Curiously the city of Tavira was hardly affected by ground shaking as was built on 'hard' limestone rather than superficial sands.

Table 5.1 shows the return periods for earthquakes of differing type magnitudes according to the distance to a distant 'Gorringe' source and a near source, Lower Tagus Valley (Chester, 2001). This table is a good source to be considered for some design projects by also considering the life service required for the structure or infrastructure.

Later, on 23 April 1909, an earthquake, with epicenter near the village of Benavente (Portugal), and a magnitude of 6.0 (Cabral et al., 2013), destroyed several small towns located in the Tagus Rive valley. Benavente earthquake, designation attributed to the complete destruction of village of Benavente, was the largest crustal earthquake in the Iberian Peninsula during the twentieth century (see Isoseismal (MSK) map of the earthquake of 23 April 1909, in Figure 5.10b).

The excessive destructions caused by the earthquake were also associated to local site effects or regional geology-dependent effects, indicating complex seismic propagation and low attenuation processes.



(a) (b)

Figure 5.10: (a) Isoseismal (MSK) map of the earthquake of 1 November 1755. Disputed positions of the epicentre are located. Figure modified from Degg and Doornkamp (1994) by Chester (2001) (b) Intensity data points and tentative isoseismal curves for the 1909 Benavente event (Teves-Costa and Batlló, 2011)

Table 5.1: Lisbon: return periods for different earthquakes. (Reproduced by permission of Kluwer Academic Publishers, Dordrecht, Issues in urban earthquake risk, 1994, Mendes-Victor et al. (1994), table 1, p. 269) - Chester (2001)

Magnitude	Return period (years)	
	Gorringe Bank area	Lower Tagus Valley area
5.0	3	5
5.5	7	10±1
6.0	15±1	21±2
6.5	30±2	41±6
7.0	63±7	84±13
7.5	135±17	170±33
8.0	288±42	344±80
8.5	614±105	695±188

Among other devastating events caused by the earthquake, liquefaction phenomena stands out as one of the frequently observed in the Tagus and Sorraia rivers alluvial plain (e.g. sand blows, soil cracks and ejected sand) (Teves-Costa and Batlló, 2011). A scheme of the probable liquefaction features might be observed in Figure 5.11.

Aware of liquefaction occurrence consequences, lately some authors have been attempting to reproduce a liquefaction mapping hazard for Portugal continental. Jorge (1994) has published, after compiling information relying on the description of the phenomena, and since XX century basing on the seismic instrumentation recordings, and also basing on geological and geomorphologic

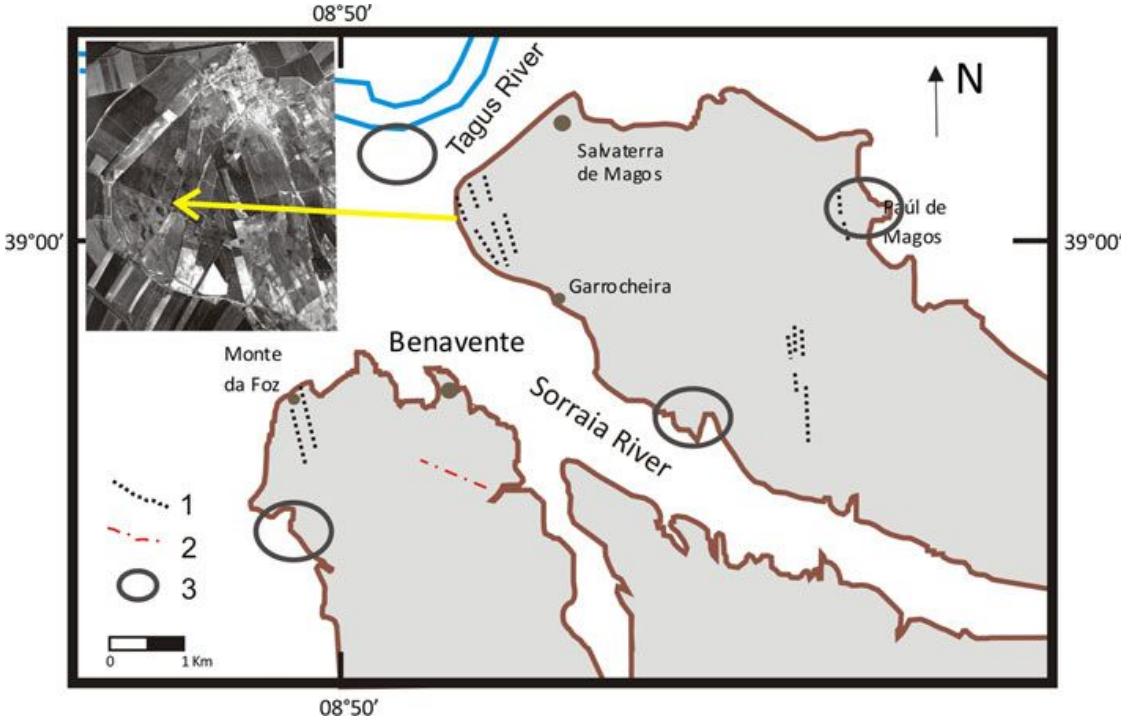


Figure 5.11: Location of probable liquefaction features recognized in aerial photos (1:18,000 scale) of the Benavente region (crop of photo showing example). Gray area, Upper Pleistocene fluvial terrace; white area, alluvial plain of the Tagus and Sorraia rivers; 1, linear features interpreted as remnants of the surface trace of cracks injected with liquefied sands generated during the 1909 earthquake; 2, lineament corresponding to small scarp; 3, area with circular features interpreted as remnants of sand blows generated by the 1909 earthquake (Cabral et al., 2013)

data, the liquefaction opportunity map for Portugal continental (Figure 5.12). The map shows return periods for earthquake shaking strong enough to generate liquefaction in susceptible materials. The map was built upon the presupposition that the main seismic sources were the Euro-Asian plate and the African plate. Thus by using the empirical relations between the magnitude earthquake and the logarithm of the liquefaction limit, proposed by some authors (Kuribayashi and Tatsuoka, 1975; Midorikawa and Wakamatsu, 1988), and the return periods for earthquakes, Jorge (1994) obtained the liquefaction opportunity map.

Coimbra, University City of Portugal, located between a seismic risk zone of VII and VIII, lodge the sand that is being studied in the scope of liquefaction assessment. It is widely recognized that while a proper constitutive model is being developed, semi-empirical data remains as the one and only way to assess liquefaction "risk" on sandy soils.

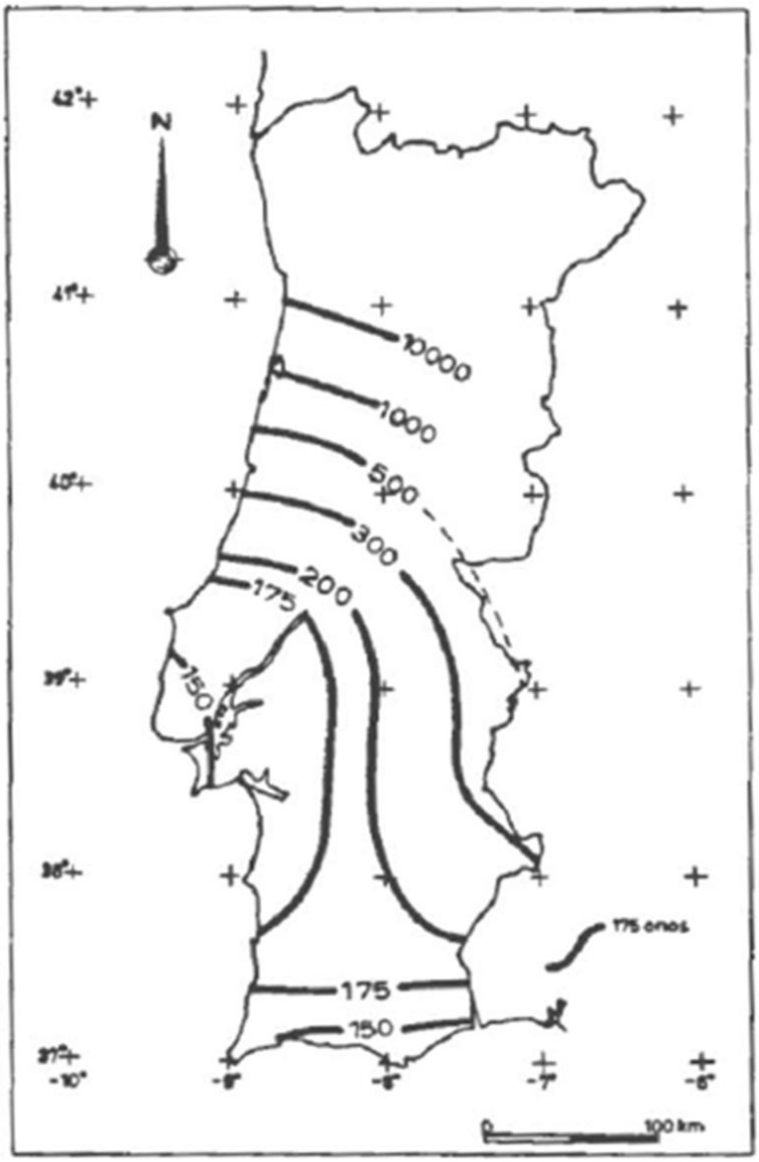


Figure 5.12: Return period of liquefaction for Portugal continental (Jorge, 1994)

5.3.2 Past Research

The study of Coimbra sand geomechanical behavior was initiated during this research and complemented in meantime by Abreu (2012). The author characterized Coimbra sand, which includes the grain size distribution curve, the specific gravity G_s, whilst the maximum and minimum void ratio, (e_{max} and e_{min}), were determined by Santos (2009). Abreu (2012) also defined the CSL by performing a set of triaxial tests with loose reconstituted specimens, under drained and undrained conditions. Furthermore the author sketched the framework to assess liquefaction susceptibility to cyclic shearing, in the scope of evaluating Coimbra sand performance if subjected to an earthquake.

Coimbra sand, a predominantly quartz sand was prepared artificially from a quarry in order to obtain a gradation between the sieves no. 10 (2 mm) and no. 200 (0.075 mm) of ASTM series, having effective diameters of D_{10} = 0.19 mm, D_{30} = 0.32 mm, D_{60} = 0. 4 mm and D_{100} = 1 mm. The coefficients of uniformity and shape are respectively C_U = 2.13 and C_C = 1.37, being also a poorly graded sand (Figure 5.13). The mean grain size, D_{50}, is about 0.36 mm and the specific gravity, G_s, is 2.66. The minimum and maximum void ratios are e_{min} = 0.48 and e_{max} = 0.81, respectively, and the grains are generally angular to sub-angular (see Figure 5.14).

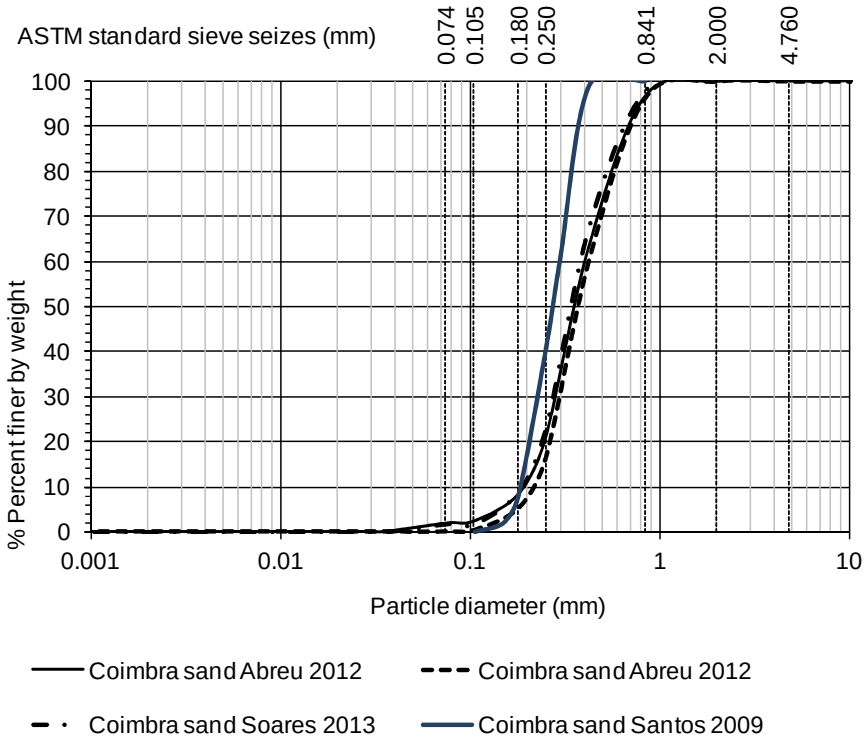
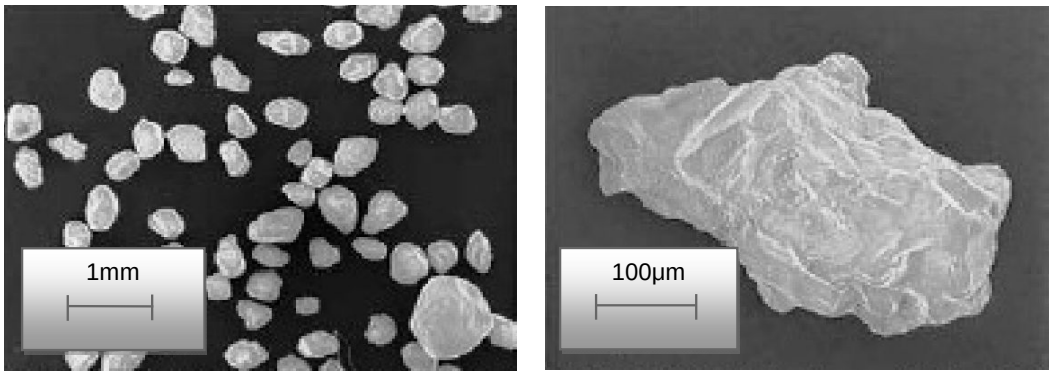


Figure 5.13: Grading curve of Coimbra Sand



(a) (b)

Figure 5.14: Grain shape of Coimbra sand – Microstructural analysis (adapted from Santos (2009))

Curiously Coimbra sand grading curve was very distinct from the one previously determined by

Santos (2009). The recent grading curve was determined with the purpose to evaluate if any grading evolution occurred due to the large amount of tests performed over Coimbra sand. Apparently, by observing Figure 5.13, Coimbra sand was not subjected to a grain size distribution evolution.

The set of triaxial tests allowed the determination of the critical shear stress ratio M of 1.3, which corresponds to a critical friction angle of 32.3º.

Expectedly, and in agreement with CSSM, Abreu (2012) observed a contractive behavior for specimens prepared with higher void ratios, while dense specimens exhibited a dilatant behavior, corresponding to the generation of positive pore pressure and negative pore pressure, respectively, while tested under both drained and undrained conditions (see Figure 5.15).

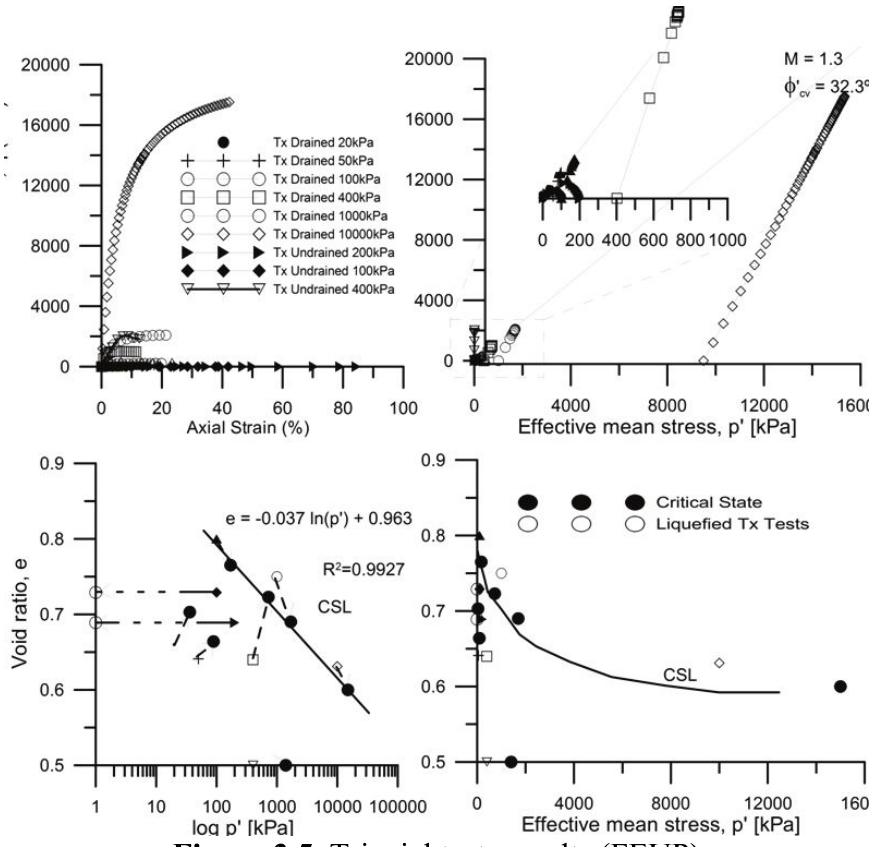


Figure 5.15: CSL for Coimbra sand (Santos et al. (2012) adapted from Abreu (2012))

Liquefaction deems to occur, for Coimbra sand specimens, tested from an initial condition starting on the NCL, till a confining pressure of 200 kPa. Curiously, while sheared under undrained conditions, only tests confined with very high confining pressures (p' > 5000 kPa) seem to reach the CSL. Specimens tested within these interval, and for medium densities (e > 0.65; Dr > 50%), exhibited a limited liquefaction behavior, whilst the others did not reached the CSL due to a not stabilization of the generated negative excess pore pressures.

As for the drained tests only those which started from the NCL were able to end up into the CSL, while those initially on the dry side have not reached the CSL as did not stabilized for large axial strains compatible within the equipment limits.

Therefore critical state line was only reached by some drained tests and by some undrained tests (Figure 5.15 and 5.16). Figure 5.16, referent to the CSL, was published later on by Abreu (2012) with a more complete data set.

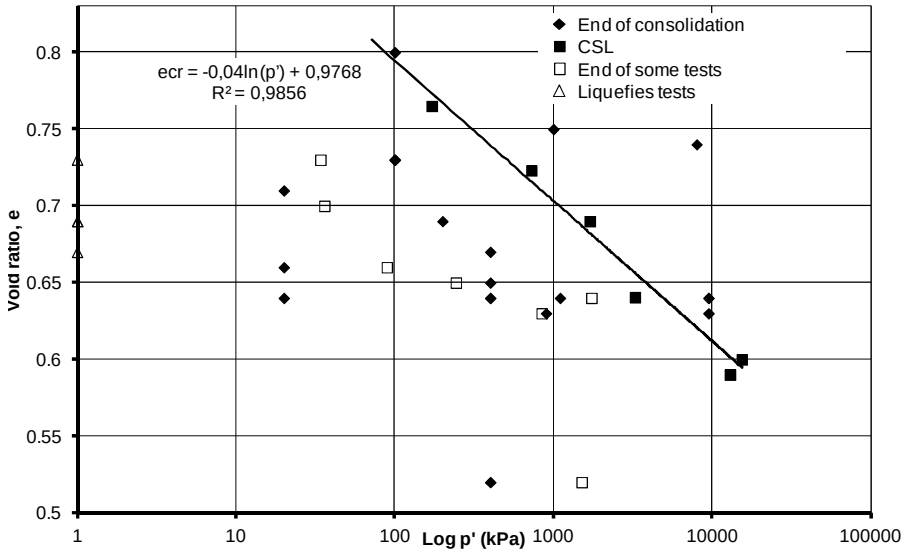


Figure 5.16: CSL for Coimbra sand (Abreu, 2012)

The CSL equation obtained for Coimbra sand was:

$$e_c = 0.97 - 0.037 \ln\left(p_c^{'}\right) \tag{5.2}$$

As pointed out by Santos et al. (2012), the CSL inclination (λ) of 0.037 is lower than the usual values for river sands, which are the order of 0.16 (Atkinson, 1993). The authors conjectured the existence of a critical state defined by a curve instead of a line, and an increasing λ for higher confining pressure tests. However is necessary to point out that the high inclination suggested by Atkinson (1993) is a reflect of grain crushing. As stated by Carrera (2008) both clays and sands reach a unique envelope of states due to different physical mechanisms. *"While in clays, the compression mechanism is governed most of all by superficial, electro-static forces, in clean sands, the load is supported by grains contacts, and the plastic volumetric strains are mainly due to particle breakage, so that the NCL is only reached when the particle breakage is prevalent (Coop and Lee, 1993; McDowell and Bolton, 1998)"* (quoted from Carrera (2008)).

Furthermore loose low confined specimens exhibited, while tested under drained conditions, a distinct behavior from those tested under undrained conditions. Similarly to Algeria sand and to

Nevada sand (with 7% FC – Yamamuro and Lade (1998)), also Coimbra sand exhibit a bifurcation between drained and undrained triaxial tests, for a wide range of confining pressures when prepared from the NCL.

The set of cyclic triaxial tests were presented by Santos et al. (2012) jointly with cyclic torsional shear tests performed on Instituto Superior Técnico de Lisboa (IST) and with the ones performed on the Bishop-Wesley apparatus on Faculdade de Ciências e Tecnologia da Universidade de Coimbra (FCTUC).

As might be observed in Figure 5.17, in line with the behavior observed in monotonic tests, for a same applied loading (i.e. same "CSR"), loose sample tends to generate larger excess of pore water pressure, $\triangle u$. Figure 5.17 also shows the relation between CSR and number of cycles for confining pressures of 50 and 200 kPa and relative density of 20%. It can be seen that the lines for p=50 and p=200 kPa are almost parallel, exhibiting a decreasing cyclic resistance with increasing confining pressure.

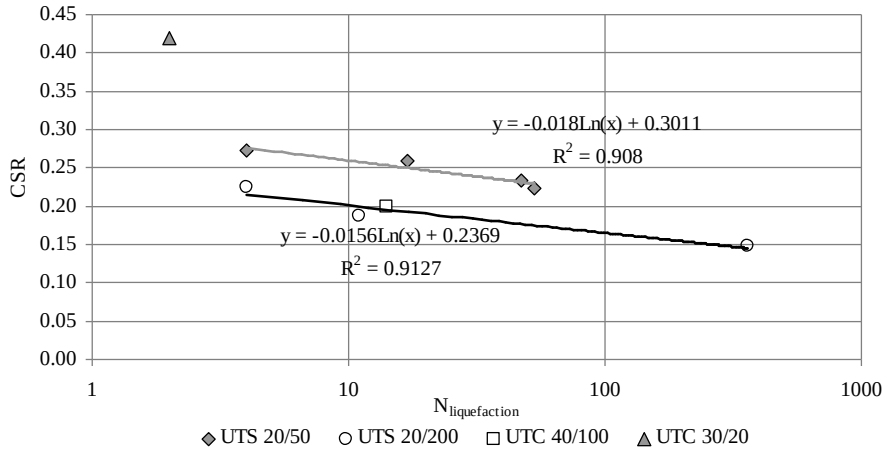


Figure 5.17: Relation between CSR and number of cycles for confining pressures of 50 and 200 kPa and relative density of 20% (Santos et al., 2012)

It is also necessary to point out that, after a careful examination of Figure 5.17, a comparison between the results of the two equipments cannot be made.

Coimbra sand cyclic triaxial results were also compiled on the Simplified Procedure, initially proposed by Andrus and Stokoe (1997) (Figure 5.18), and on the *"basic Berkeley School liquefaction assessment chart"* (Figure 5.19), initially proposed by Jefferies and Been (2006). The tests presented in Figure 5.18 and 5.19 were exclusively developed on FEUP, by Abreu (2012), on a cyclic triaxial device and on a Bishop-Wesley apparatus. Both equipments supplied with bender-extender elements allowed the determination of the soil stiffness prior to cyclic shearing.

The study of Coimbra sand also intended to assess the effect of fines content on both CSL positioning and liquefaction potential. In an agreement between the three institutions involved in this

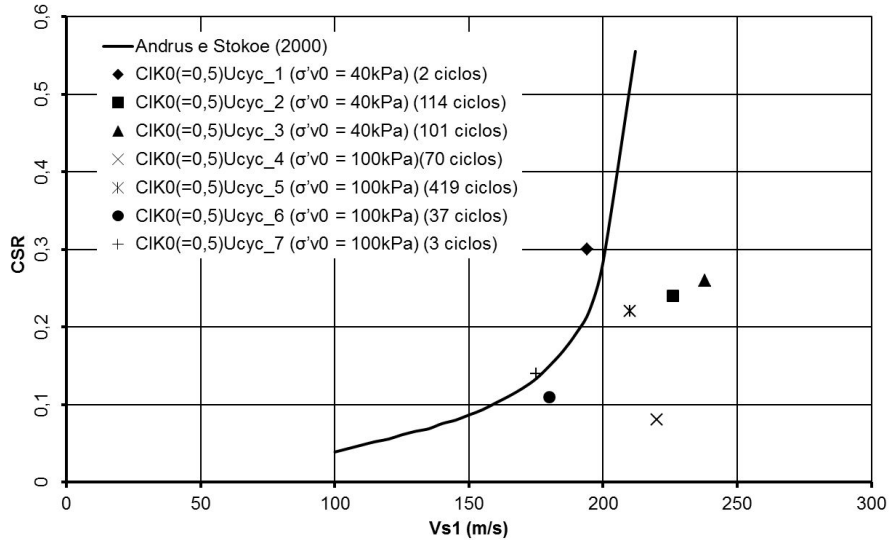


Figure 5.18: Simplified procedure for Coimbra sand (Abreu, 2012)

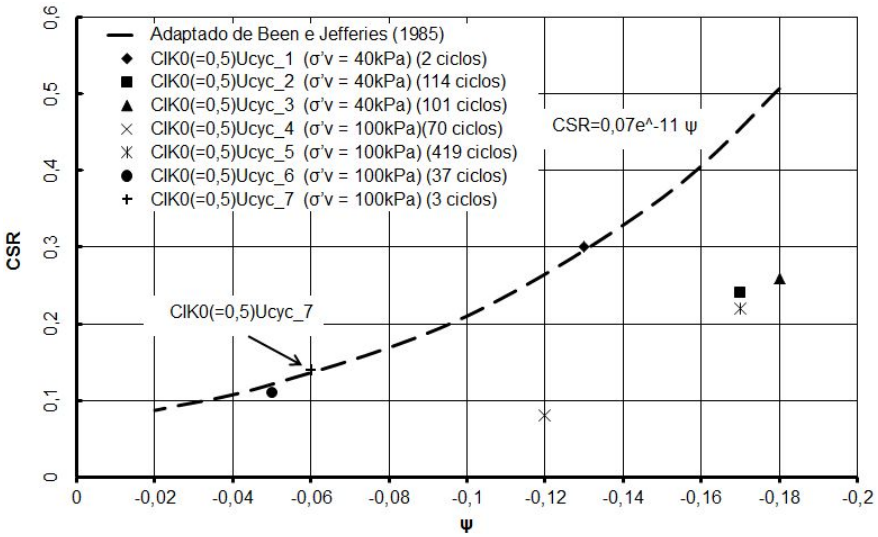
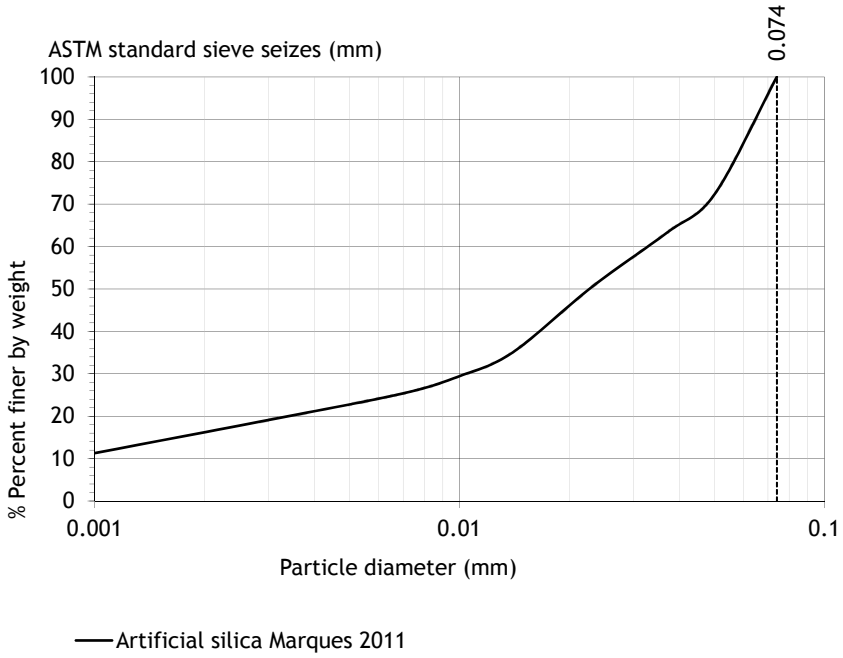


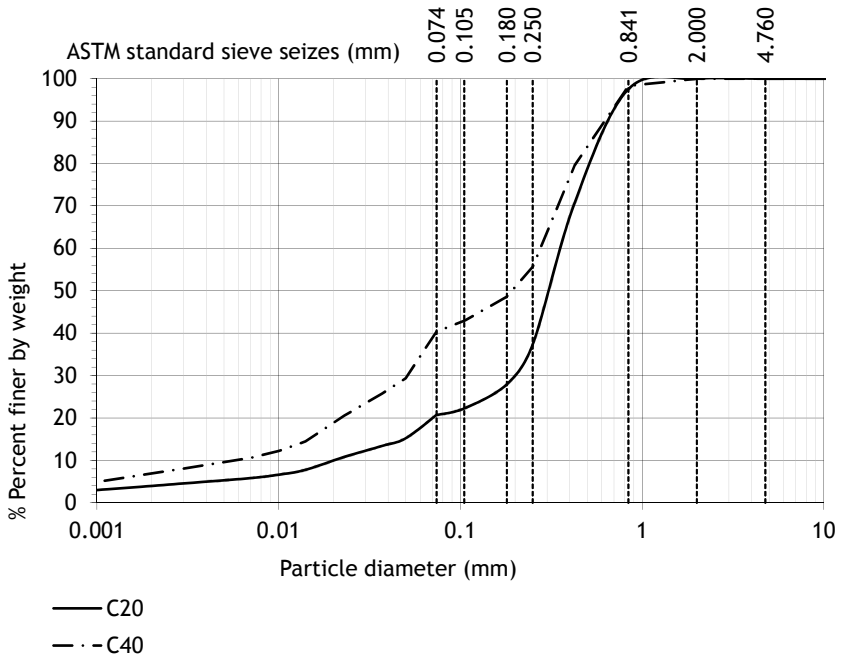
Figure 5.19: *"Basic Berkeley School liquefaction assessment chart"* for Coimbra sand (Abreu, 2012)

project research an artificial silica was adopted to produce the soil mixtures with 20% and 40% of FC (see Figure 5.20b). This material, a silt, presents the grain size distribution plotted in Figure 5.20a.

Unfortunately the study of this subject was very limited and due to a lack of time only a small number of triaxial tests were able to be carried out.



(a)



(b)

Figure 5.20: Grading curve of the artificial silica (Marques, 2011); (b) Grading curves of Coimbra mixed with 20% and 40% of artificiall fines

5.4 Silt, Osorio Sand And Mixture

The evaluation of the geomechanical behavior of a silt arose from the idea of it comparison with the gold tailings geomechanical behavior, while subjected to instability due to static liquefaction, with partial or overall failure, of the perimeter dike or dike foundation (Bedin, 2010). Therefore the Silt, an artificial material, was prepared by grinding Osorio sand aiming to achieve a similar grain size distribution with 85% of fines content, although chemically stable, of gold tailings.

Unfortunately, sometimes, tailing dams are associated to some catastrophic events mainly related with static liquefaction, due to the very loose configuration in which the tailings are deposited on the tailing dam. In order to prevent such event, liquefaction susceptibility is usually studied under laboratorial conditions and or/ in situ. The emergence of studying tailing stability aims not only to provide a better knowledge of soils mechanical behavior, particularly focused on liquefaction, but also to provide a consistent framework which could be used on tailings mitigation.

As described by Carrera *"tailings are the residual material of the rock milling process necessary to extract minerals. Tailings dams are big basins where these tailings, in the form of a slime, are poured into to decant"* (quoted from Carrera (2008)). The gold tailings, used in this research, were collected in the Fazenda Brasileira disposal plant from Bahia State in Northeast Brazil (Schnaid et al., 2013; Bedin, 2010; Bedin et al., 2012).

The original material, Osorio sand represent a monogranular, uniform, clean, with sub-rounded grains, sand. When grinded, a continuously grains breakage took place resulting in a new material with angular, uneven edges, similar to the gold mining waste seen in Brazil (Bedin, 2010; Bedin et al., 2012).

To complement this study also Osorio sand and a mixture (45% FC) were assessed aiming to achieve the influence of fines content on liquefaction onset. Moreover, while assessing soil behavior through CSSM theory, it becomes also important to evaluate CSL positioning with increasing fines content. In fact the achievement of a unified framework becomes a very important tool for saving time and money; furthermore understanding such influence would be very helpful for developing consistent constitutive models.

The study of fines content influence it's very useful, not only due to the widespread grain size distribution of the tailings materials, but also on the study of in situ deep foundations stability. Deep foundations, such as piles, due to the extremely high bearing solicitation might be responsible for grain crushing occurrence. Also erosion processes might lead to a grain size evolution.

5.4.1 Historical Overview – Liquefaction Of Tailings

The first liquefaction event ever recorded was in Calarevas dam failure, in Alameda County, east of Milpitas, USA, by Hazen in 1918. Yet the first mitigation being implemented, through a densi-

fication process, was made by Colon Lyman on Franklin Fill dam, basing on the critical void ratio concept earlier introduced by Casagrande (1936).

The mining industry currently faces a lot of challenges, mainly related with tailings dam stability issues. According to Azam and Li (2010), these containment facilities are *"vulnerable to failure because of the following reasons: dyke construction with residual materials from the mining operations; sequential dam raise along with an increase in effluents; lack of regulations on design criteria, especially in developing countries; and high maintenance cost after mine closure"*. According to these authors, for a world inventory of 18401 mines, the failure is estimated to be 1.2 percent, over the last century. Among the causes of failures, methereologic conditions are responsible for the biggest share of total incidents. Also Rico et al. (2008) within a study of 147 tailings dam disasters, from which 26 located in Europe, related the majority to unusual rainfall events/periods and snow, accounting for 25% of worldwide cases and 35% in Europe (Figure 5.21).

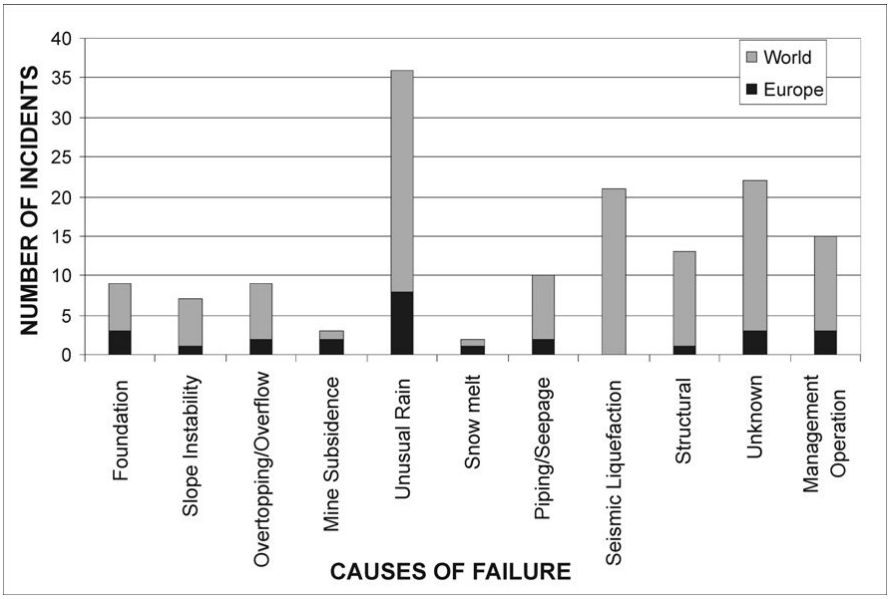


Figure 5.21: Distribution of the number of incidents according to cause in the World and in Europe (Rico et al., 2008)

The construction of tailing dams comes from the necessity of depositing the residual material of the rock milling process necessary to extract minerals. While initially tailings are deposited inside reservoirs contained by well designed embankments, during their life-times, and to the necessity of increasing capacity, these are subjected to heightening processes made with the coarser fractions of tailing materials. An embankment can be heightened in three different ways (Figure 5.22):

(i) Upstream method: the embankment rises towards upstream by placing partly on the embankment below, partly on the consolidated silt; it occupies a minor volume than the others methods;

(ii) Downstream method: the embankment rises towards downstream by depositing the sand outside the embankment; it is the most spacious;

(iii) Centerline method: the embankment rises vertically.

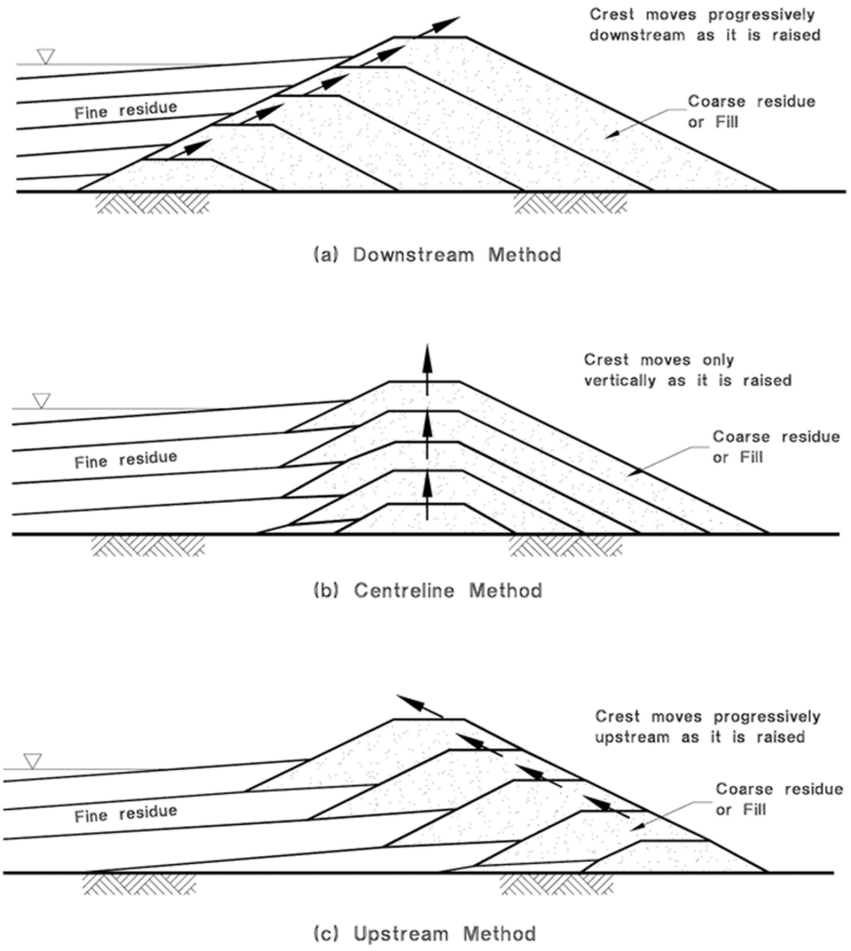


Figure 5.22: Tailing dams heightening (fig, 2014)

The upstream method is the most common, due to spatial and economical advantages, but the less stable and safer, being much more susceptible to piping, erosion and liquefaction (Carrera, 2008). The less safety upstream method is well recognized being, for example, prohibited in Chile, according to the Decree No. 86 (Barrera et al., 2011).

The heightening process is a money saving technique which increases the capacity of the reservoir. However if no compaction is made, liquefaction may take place on the beach leading to the failure of the embankments, not designed to support such pressures. Most of liquefaction on tailings takes place due to the inexistence of an efficient drainage system which, due to the high-rate deposition process of the residual material, may generate increasing pore-pressures leading to a complete loss of the bearing capacity. Afterwards if the beach liquefies and the embankment have no bearing

capacity, due to it loose configuration, then a complete liquefaction process might take place, accompanied by a flow of a large mass of material.

Tailing materials might be deposited on the reservoirs, through dry or wet method. Usually the material is pumped from the ore or the mill to the basin through pipelines in the form of slurry. Once there, the material is deposited through spray bars, spigots or hydro-cyclones (Figure 5.23). Among them the hydro-cyclones are usually more suitable as they allow a separation of the materials by fraction, obtaining a finer fraction designated by overflow, and a coarser fraction named underflow.

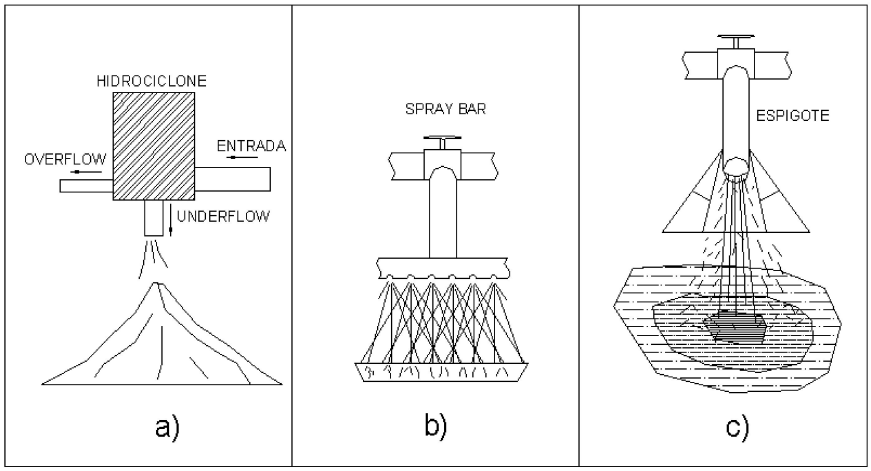


Figure 5.23: Deposition methods of tailings - (a) Hydro-cyclone, (b) Spray bar, (c) Spigot (Mendes, 2007)

As might be seen in Figure 5.24 the finer fraction is usually deposited as slurry with a minimum velocity of approximately 150-300cm/s (Bedin, 2010). Then the water must flow away through drainage pipes to allow for the residual materials to consolidate. Consolidation, which is reached through water drainage, guarantees the stabilization of the dam, otherwise their consistence is that of a fluid mud.



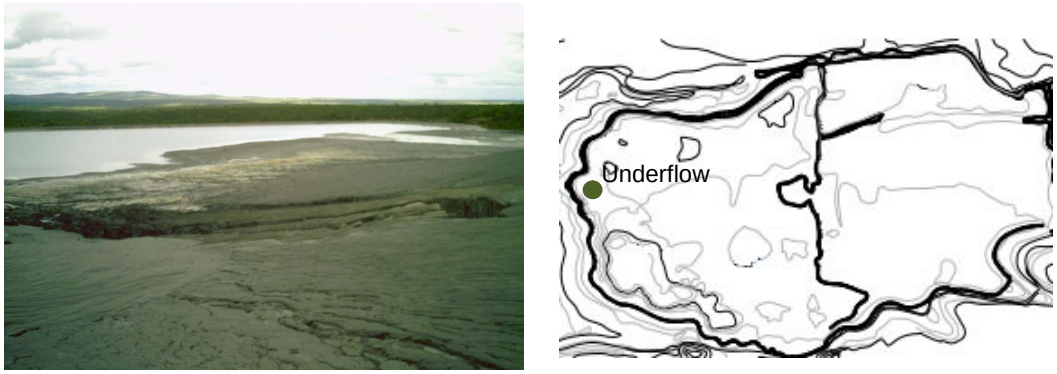
Figure 5.24: Examples of a method for tailings deposition (Bedin, 2010)

Among the causes of tailing dams failures flow failure is the worst one, as a large volume of tailings inside the dam or from the embankment liquefies and flew out.

Aiming to avoid such catastrophic events a large number of studies have been carried out by many researchers (Fourie and Tshabalala, 2005; Wijewickreme et al., 2005; Carrera, 2008; Al-Tarhouni

et al., 2011; Heymann et al., 2011). The study of gold tailings geomechanical behavior started with Bedin (2010) with an intensive study carried out by performing a large set of triaxial tests, allowing the achievement of a framework able to separate the stable behavior from flow instability.

These gold tailings are residual materials obtained from the process necessary to extract the gold from the rocks greenstone belt, of the Industrial Complex Mina-Usina Fazenda Brasileiro, from Teofilândia, Bahia, Brazil (Figure 5.26). This rock is mainly constituted from volcanic and sedimentary rocks submitted to a low metamorphism, from the archean or paleoproterozoic era (Bedin, 2010).



(a) (b)

Figure 5.25: (a) Gold tailings; (b) Gold tailings plant of the Industrial Complex Mina-Usina Fazenda Brasileiro, from Teofilândia, Bahia, Brazil (Bedin, 2010)

The gold tailings initially studied by Bedin (2010) are the finer fraction (overflow) of the processed material.

5.4.2 Past Research

In the scope of evaluating tailings liquefaction susceptibility, Bedin (2010), studied the geomechanical behavior of gold tailings and of an inert material obtained from Osorio sand grinding. Among other materials, the study of the gold tailings and of the inert material, designated by silt during this work, was developed under CSSM theory and performed by carrying out a set of triaxial tests.

The study of gold tailings geomechanical behavior was completed and published by Schnaid et al. (2013),Bedin (2010) andBedin et al. (2012). The author characterized gold tailings, namely the grain size distribution curve, the specific gravity G_s, and the maximum and minimum void ratio, (e_{max} and e_{min}). Besides defining the CSL from undrained triaxial tests results, the author also defined some frameworks in order to evaluate the material liquefaction potential.

On the other hand, the study of the silt also performed by (Bedin, 2010), but not completely completed during her PhD program, was continued in the scope of this work.

5.4.2.1 Gold tailings – Underflow

The gold tailings are chemically constituted by quartz (32.5%), albite (24.3%), chlorite (23.0%), and sulfides (3–6.5%) (Schnaid et al. (2013); Bedin (2010); Bedin et al. (2012)). The material disposed in ponds is predominantly sandy silt (Sand 57%; Silt 39%), with a solid content of approximately 30%, an in situ water content of 35%, low plasticity values, and a high density of solid particles ($2.89 < G_s < 3.2 \Leftrightarrow \overline{G_s} = 3$ g/cm^3). The hydraulic conductivity determined by constant-head permeability tests yielded an average value of $2\text{x}10^{-6}$ (Bedin, 2010; Bedin et al., 2012).

According to the author, the gold tailings have a gradation below the sieve no. 40 (0.425 mm) of ASTM series with a fines content near 40%, having effective diameters of D_{10} = 0.001 mm, D_{30} = 0.046 mm, D_{60} = 0.077 mm and D_{100} 0.4 mm. The coefficients of uniformity and shape are respectively C_U = 7.7 and C_C = 2.8, revealing a graded sandy silt (Figure 5.26). The mean grain size, D_{50}, is about 0.06 mm and the grains are generally sub-angular with uneven edges (see Figure 5.27).

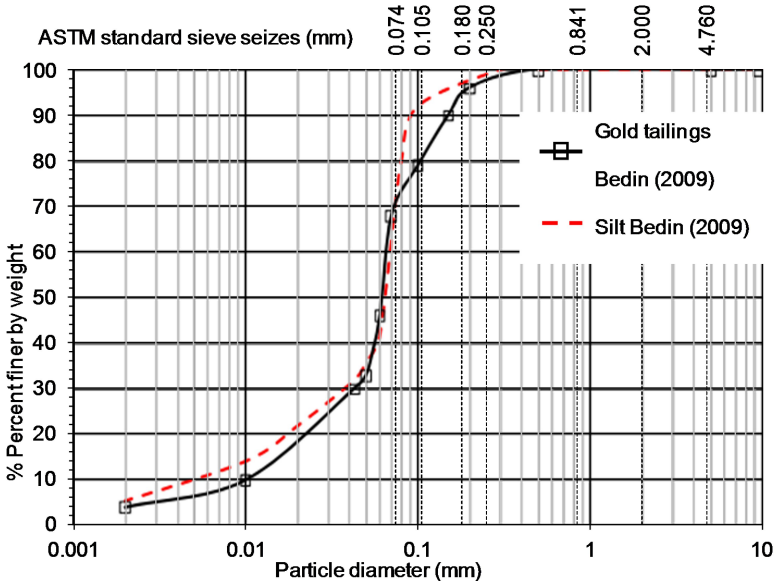


Figure 5.26: Grading curve of gold tailings and of the silt (Bedin, 2010; Bedin et al., 2012)

The moist tamping method was used to reconstitute specimens at their average in situ density, prepared with a small amount of water content.

One-dimensional compression test allowed determining the compressibility of the soil, which seems to have a slope equal to 0.048 at high stresses and for an interception void ratio of 2.0 (Bedin, 2010; Bedin et al., 2012).

A set of isotropic triaxial tests were conducted under drained and undrained conditions allowing a further evaluation of the gold tailings stress-path and stress-strain behavior.

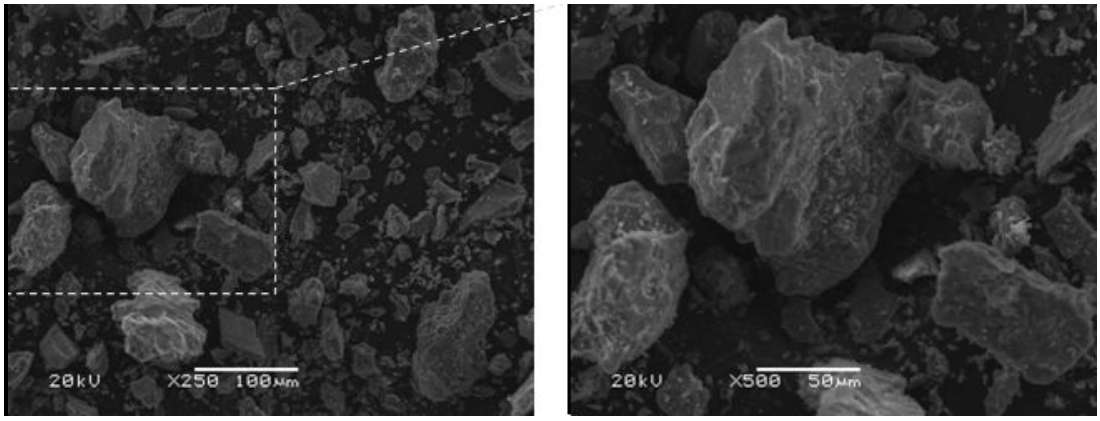


Figure 5.27: Grain shape of gold tailings – Microstructural analysis (Bedin, 2010)

From the evaluation of the final results, displayed in Figure 5.28, it can be observed that at lowest confining stress range, $\left(p_i' < 100kPa\right)$, the tests revealed a strong strain-softening response, followed by a complete loss of the bearing capacity. For higher confining stresses the behavior changes to gentle limited liquefaction accompanied by strain-softening. On the other hand, for confining pressures higher than 400 kPa, the tailings, according to the author, exhibit grain crushing. The reason behind the occurrence of grain crushing within medium confining pressures is attributed to the tailings constitution: alumina, magnesium and iron (Bedin, 2010; Bedin et al., 2012).

The large contractive volumetric strain combined with the high initial void ratio and low pressure justify it liquefiable potential. This high contractivness is associated to a high development of excess pore pressures when the soil is sheared under undrained condition; this tendency is gradually suppressed with increasing confining pressures and decreasing void ratios (Bedin, 2010; Bedin et al., 2012).

As both drained and undrained extension triaxial tests confirmed trends observed under compression triaxial tests, the material seems to achieve a unique ultimate state (Bedin, 2010; Bedin et al., 2012). Therefore the results show the idealized behavior of a unique critical state line (CSL), despite not being captured by a semi-logarithm line, rather by a curve (Figure 5.28).

Aiming to predict tailings liquefaction susceptibility, Schnaid et al. (2013) proposed a framework, already presented in subsection 3.2.4.3 (*"Method based on shear wave velocity measurement"*), which correlates stiffness-to-strength ratio V_{S0}: q_{peak}, with the normalized peak shear strength, q_1. The authors also correlated the state parameter, ψ, with q_1, with V_{S0}: q_{peak} and with V_{S1}. Both correlations were found to be good predictors of the transactional behavior of gold tailings (Schnaid et al., 2013).

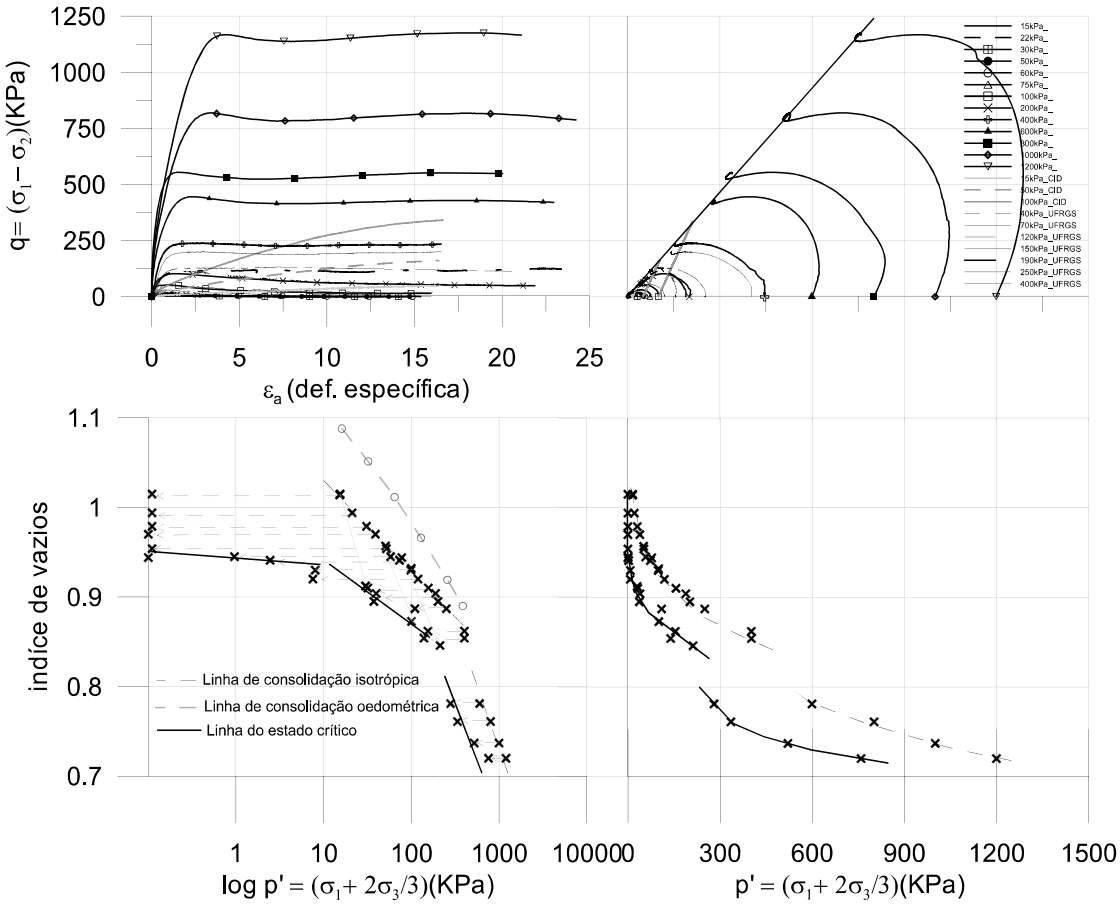


Figure 5.28: Results of triaxial compression tests and critical state analysis of gold tailings (Bedin, 2010; Bedin et al., 2012)

5.4.2.2 Silt (Inert material)

The silt, an inert material obtained from a milling process performed over Osorio sand, is a soil chemically stable (Schnaid et al., 2013; Bedin, 2010; Bedin et al., 2012). The material was produced at Universidade Federal do Rio Grande do Sul (UFRGS) on a ball mill, with a ratio of balls/soil equal to 3:1, for 1.8 kg of soil during a period of 8 hours. The proportions established above allowed the achievement of the grading curve represented in Figure 5.26.

The sandy silt (Sand 10%; Silt 90%) is mainly constituted by quartz particles, like Osorio sand. The density of solid particles, determined at UFRGS, was of $G_s = 2.7$ g/cm^3 (Bedin, 2010).

The grading curve determined for silt at UFRGS shows a gradation below the sieve no. 40 (0.425 mm) of ASTM series with a fines content near 40%, having effective diameters of $D_{10} < 0.001$ mm, $D_{30} = 0.04$ mm, $D_{60} = 0.07$ mm and D_{100} 0.4 mm (Figure 5.26). The mean grain size, D_{50}, is about 0.063 mm and the grains are generally angular with uneven edges (see Figure 5.29).

Bedin (2010) through the performance of a set of undrained triaxial tests found loose specimens,

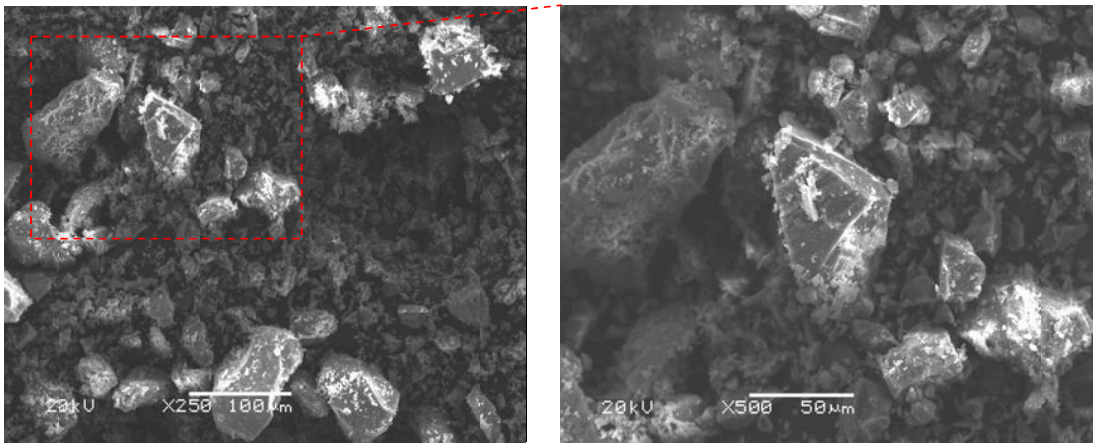


Figure 5.29: Grain shape of silt – Microstructural analysis (Bedin, 2010)

with confining pressures lower than 50 kPa, to liquefy, while in a range between 50 and 100, deem to exhibit a strain-softening behavior. The specimens displayed a stable behavior for the undrained compression triaxial tests, confined with 700 and 1200 kPa.

Similarly to the gold tailings three distinct behaviors occur with increasing confining pressures, static liquefaction, proceeded by a strain-softening and followed by a stable behavior, accomplished with strain-hardening. Grain crushing was not observed for the silt. These three pattern behavior result on the two distinct slopes of the CSL (Figure 5.30).

From the silt triaxial tests results (Bedin, 2010) found with increasing ψ an increasing susceptibility of the silt to liquefaction. Plus by correlating the state parameter with G_{crit} e G_{crit}/G_0 or between these and the final confining pressures Bedin (2010) identified the clearly changing behaviors, indentifying the liquefaction, the meta-stable (associated to the strain-softening behavior), and the stable zone.

5.4.3 Present Research

Aiming to evaluate tailings and silt liquefaction susceptibility basic characterization tests were once more performed, this time at LabGeo (Geotechnical Laboratory) at FEUP. While the characterization of Osorio sand and of the mixture were developed aiming to appraise the influence of fines content on Osorio sand, the Silt and the Gold tailings characterization was carried out attempting to analyse a possible evolution of the material due to the large amount of tests performed.

The selection of Osorio sand by Bedin (2010), for the achievement of a material with an identical grain size curve as gold tailings, was based on the well documented grain size distribution and permeability, representing a well characterized and studied material at UFRGS.

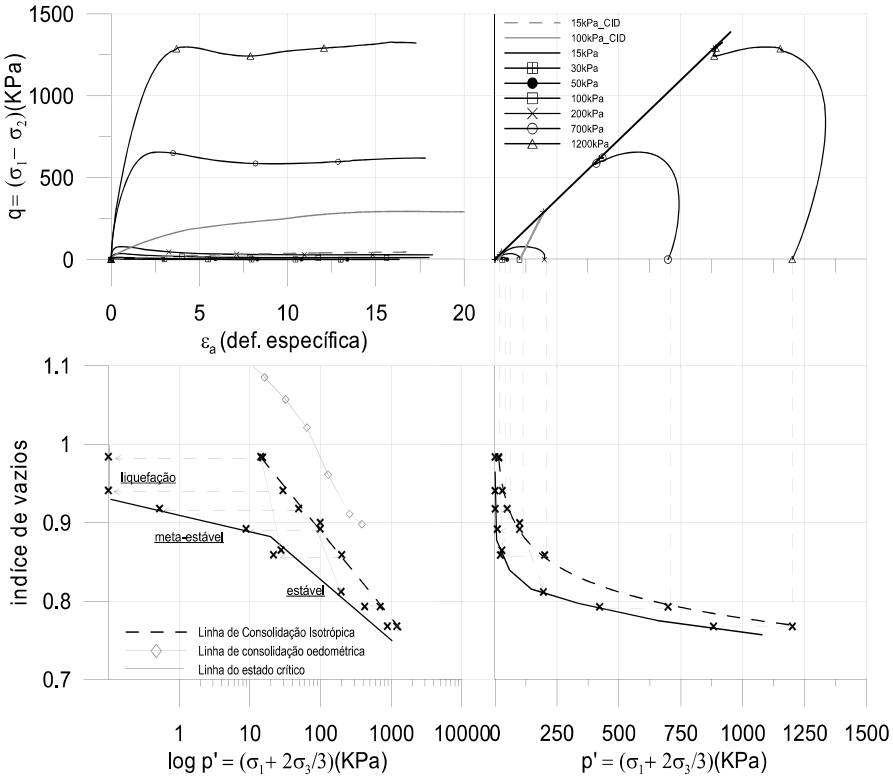


Figure 5.30: Results of triaxial compression tests and critical state analysis of silt (Bedin, 2010)

Unfortunately, after analyzing the grain size distribution of both materials large dissimilarities were observed. Plus, as can be seen from Figure 5.31, the distinct grain size distribution was not attributed to a possible grain crushing as the curves of both material, which were subjected to a large set of triaxial tests, were coincident to those determined in the beginning of the PhD program. Therefore a further comparison between the two materials was not justified in the scope of this work.

5.4.3.1 Gold tailings

The curve of the grain size distribution of the gold tailings revealed a distinct curve of the one determined previously by Bedin (2010) at UFRGS (Figure 5.31). According to the new grading curve the effective diameters of D_{10} = 0.006 mm, D_{30} = 0.022 mm, D_{60} = 0.059 mm and D_{100} 0.841 mm and a mean grain size, D_{50}, of 0.044 mm were determined, revealling a well-graded soil. Plus the coefficients of uniformity and shape are respectively C_U = 10 and C_C = 1.35 also supporting the good gradation of the soil.

Evaluated at LagGeo, gold tailings revealed a density of solid particles of G_s = 2.94 g/cm^3, which is very close to that obtained by Bedin (2010).

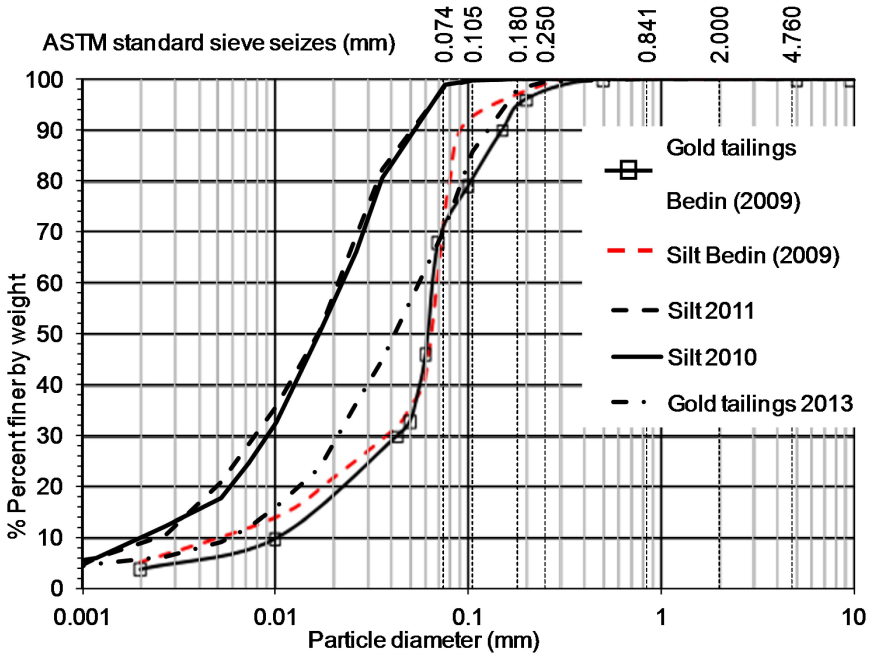


Figure 5.31: Grading curve of gold tailings and of the silt (LabGeo) all of them determined at LabGeo at FEUP in the scope of the present research)

5.4.3.2 Silt (Inert material)

The curve of the grain size distribution of the silt revealed a distinct curve of the one determined previously by Bedin (2010) at UFRGS (Figure 5.31).

The material, a pure silt with a minor amount of sand (Silt 99%; Sand 1%), also revealed a distinct density of solid particles of G_s = 2.65 g/cm^3. The distinct G_s was expected as the density of solid particles of Osorio sand was also confirmed to be 2.65 g/cm^3. Curiously Bedin obtained a G_s = 2.7 g/cm3 for the silt while Consoli et al. (2007) obtained a value of 2.3 g/cm^3 for Osorio sand.

The grading curve determined for silt at LabGeo shows a gradation below the sieve no. 140 (0.106 mm) of ASTM series with a fines content of 99.85%, having effective diameters of $_{D10}$ = 0.0002 mm, D_{30} = 0.009 mm, D_{60} = 0.022 mm and D_{100} 0.106 mm and a mean grain size, D_{50}, of 0.017 mm. The coefficients of uniformity and shape are respectively C_U = 9.6 and C_C = 1.47, revealing a well-graded silt (Figure 5.31).

5.4.3.3 Osorio sand

Osorio sand gradation curve and was determined at LabGeo, jointly with the particle specific weight (Gs).

The Osorio sand is a sand from the region of Osorio, in the southern Brazil, with a specific gravity of the particles of 2.65 g/cm^3, in contrast to 2.63 g/cm^3, found by Consoli et al. (2007, 2003).

According to the authors the soil is classified as a non-plastic uniform fine sand according to the Unified Soil Classification System (ASTM, D2487, 1993).

The material have a gradation between the sieves no. 40 (0.425 mm) and no. 20 (0.075 mm) of ASTM series with a minimum amount of fines (<4%), having effective diameters of D_{10} = 0.11 mm, D_{30} = 0.15 mm, D_{60} = 0.21 mm and D_{100} 0.42 mm. The coefficients of uniformity and shape respectively of C_U = 1.9 and C_C = 1.0, perceives a monogranular sand (Figure 5.33). The mean grain size, D50, is about 0.19 mm and the grains are generally rounded to sub-rounded, with a few sub-angular grains (Consoli et al., 2003, 2007) (see Figure 5.33).

5.4.3.4 Mixture

The mixture, also chemically stable, mainly constituted by quartz, is a silty sand (Sand 60%; Silt 40%), and has a density of solid particles of 2.65 g/cm^3, equal to the original sand and the silt.

This material was produced at FEUP aiming to achieve a material with an intermediate grain size distribution between the silt and Osorio sand. To obtain the mixture as there was not enough silt to mix with Osorio sand, a certain amount of Osorio sand was grind on a RETSCH Planetary Ball Mills at the Construction Materials Laboratory (Figure 5.32). Different trial milling times, 10, 7 and 5 minutes, were performed over 150 gr of material, with a rotational speed of 450 r.p.m.. An analysis of each grading curve led to the decision of adopting a mixture of the silt (obtained with 5 minutes of grinding), with a certain amount of Osorio sand so it could be obtained a material with 45% of fines content. Theoretically half of the fines content of the silt, determined at UFRGS, would be 45%, however beyond the fines content being almost 100%, when mixed with the 50% of Osorio sand, somehow the finer amount dropped to approximately 43%.



Figure 5.32: RETSCH Planetary Ball Mills (Mill)

The mixture exhibits a gradation below the sieve no. 40 (0.425 mm) of ASTM series with a fines of approximately 43%, having effective diameters of D_{10} = 0.004 mm, D_{30} = 0.037 mm, D_{60} = 0.13 mm and D_{100} 0.425 mm. The coefficients of uniformity and shape, C_U = 32.4 and C_C = 2.6, reveal a well graded sandy silt. The mean grain size, D50, is about 0.11 mm and the grains are generally sub-angular to angular with uneven edges, created by the grinding process (see Figure 5.33).

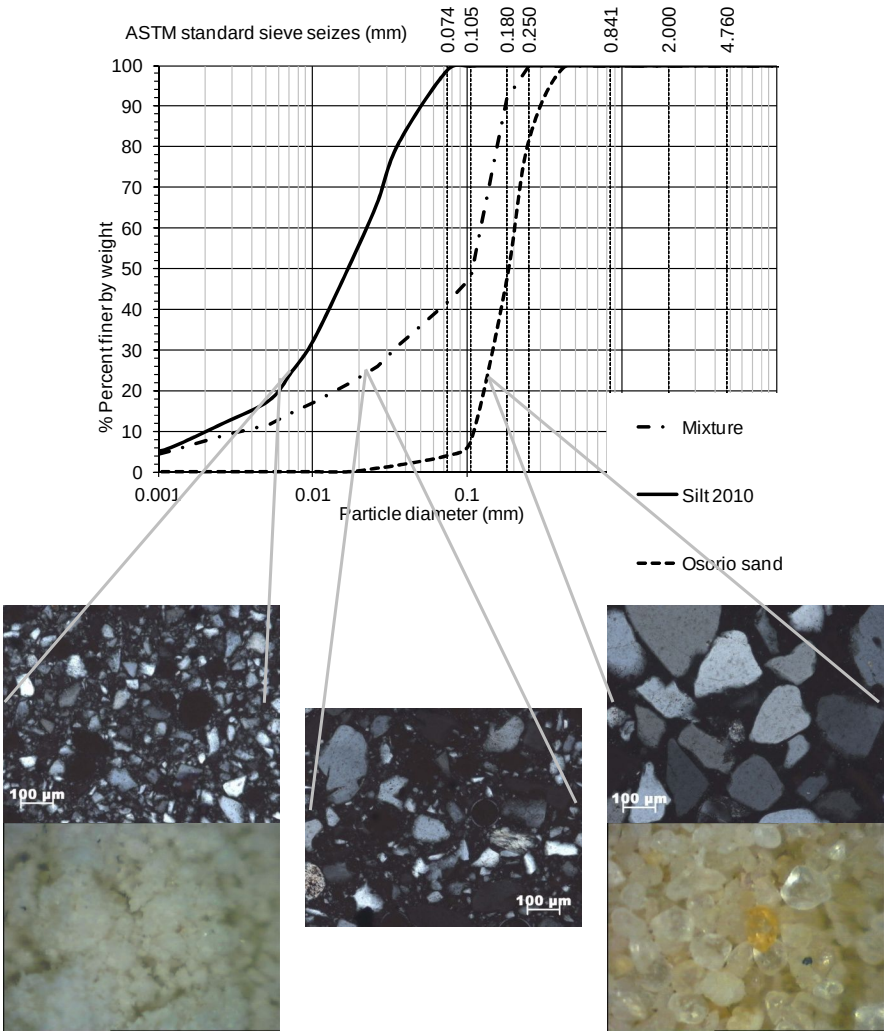


Figure 5.33: Comparison of the grading curves of the silt, Osorio sand and the mixture (all of them determined at LabGeo at FEUP in the scope of the present research)

The three grading curves of the silt, Osorio sand and the mixture are displayed in Figure 5.33.

Chapter 6

Equipments, Testing Procedures and Experimental Program

6.1 Introduction

During this chapter are presented the equipments used and the testing procedures performed in the scope of the experimental research.

As soil liquefaction, mainly cyclic liquefaction, is not straightforward, the experimental work presented has not followed a programmed list. Therefore the initial conditions of each test were decided in the meantime during the research by comparing with the previous results.

Within this research, the majority of the work was developed under laboratorial conditions at LabGeo at FEUP and a specific type of tests was performed at the Geotechnical Testing Laboratory at UWA. Aiming to understand the liquefaction under applied soil mechanics, this study was focused on triaxial tests, performed with some conventional triaxial apparatus, two "Bishop Wesley" devices, and a high pressure triaxial cell at LabGeo. Some few oedometers and direct shear tests were also carried in order to complement the triaxial tests. Furthermore a set of cyclic DSS tests were performed, within a program abroad, at UWA.

While static liquefaction focused on monotonic stress-paths, under both stress and strain control conditions, cyclic liquefaction was studied on Bishop-Wesley device and conventional triaxial devices, supplied with hydraulics, able to reproduce cyclic actions, controlled by a well programmed software developed at Institute of Mechanical and Industrial Management Engineer (in Portuguese *Instituto de Engenharia Mecânica e Gestão Industrial* - INEGI).

6.2 Equipments and Test Procedures

6.2.1 Oedometer

6.2.1.1 Oedometer

The oedometer test is a one-dimensional compression test as only the vertical displacement is allowed to change, while the radial displacements are constrained. This test allows the determination of the compressibility of the soil. Plus if carried out on saturated soil specimens, this test can be used to determine consolidation and swelling parameters.

The oedometer apparatus comprises a metal ring, where the sample is placed in. The sample is also placed vertically within one porous stones and one steel top cap supplied with a porous stone, which allows the sample to drain when a load is applied. After placing the sample, the cell is filled with distilled water.

A lever connected to the ram transmits the load to the sample, amplifying it by 10 times, while the axial displacement is measured using a Linear Variable Differential Transformers (LVDT), with a maximum range of 25 mm.

The confining rings used on this work were of 70 mm and 50 mm of diameter and the maximum vertical stress (σ_v) is of 3200 kPa and 6400 kPa, respectively. Increments of vertical static load are usually applied using dead loads.

The Wykeham Farrance® Oedometer device at LabGeo is manually controlled, while the acquirement is made through a data logger linked to a computer with ADU ® software (see Figure 6.1).

6.2.1.2 Experimental Procedure

Knowing the metal ring dimension and the required void ratio, the amount of soil necessary to place inside the oedometer ring can be determined.

Similarly to the triaxial tests, the reconstitution method adopted to remold the soil specimen was moist tamping. Basing on this technique the calculated weight of soil is posed inside the ring of the oedometer and pressed in a way that it height meets the ring height. Furthermore the surface of the sample must be as flat as possible to avoid errors in the height and further displacements measurement and for a good alignment with the top cap, thus with the applied vertical load.

The top cap is then placed over the sample and the whole cell is positioned and fixed at the base of the oedometer.



Figure 6.1: Wykeham Farrance® Oedometer device (LabGeo).

All the performed tests required a complete saturation of the specimens by filling the cell with distillated water. The specimen saturation is assured by ensuring the level of water always behind the top cap of the specimen. In order to avoid swelling, a very small load shall be positioned on the lever.

For the performance of this test, first of all is necessary to establish the set of loading steps increments to be applied to the sample.

At time $t = 0$ a first load is applied over the sample. For cohesionless specimens part of the load is applied to the soil skeleton, which corresponds to an immediate settlement while the other part is beard by the pore water pressure. As the time goes by, the pore pressures are dissipated. When the drainage process is completed, the load is exclusively transmitted to the solid phase at $t \longrightarrow \infty$.

The duration of the application of each load depends on each soil consolidation characteristics. Once the equilibrium is reached, the next increment might be applied.

The stress-void ratio representation in a semi-logarithmic scale allows for the determination of the Swelling Index (C_s), Compression Index (C_c) and Coefficient of Volume Compressibility (m_v).

6.2.2 Triaxial Cell

6.2.2.1 Conventional Triaxial Cell

The triaxial test is perhaps the most popular and used device to study soils geomechanical behavior. The binomial between a well controlled device, tests feasibility and easiness of performance makes triaxial cell a winner among the other devices. Furthermore the triaxial cell is, perhaps, among other sophisticated devices, such as HTC and SS, the cheapest one, despite not allowing principal stress rotation and principal stresses control other than the vertical and the horizontal ones.

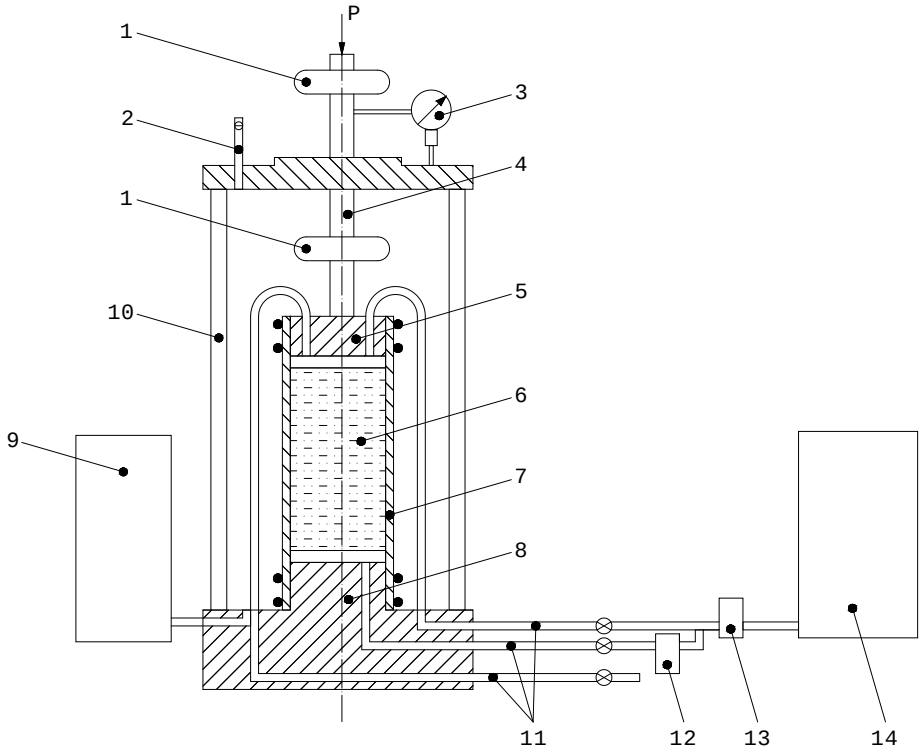
Figure 6.2 shows a scheme of a common triaxial device equivalent to the VJ Tech ® and Wykeham Farrance ® triaxial cells of LabGeo, both used during this research.

The triaxial tests is shortly described as a test where the soil specimen is saturated and confined via the difference between the confining pressure (CP), i.e. the surrounding fluid, and the back-pressure (BP), i.e. the fluid inside the specimen. Following that, the specimens are monotonically or cyclically sheared, under stress or strain control, depending on the hydraulic press and on the software installed.

All the triaxial cells of LabGeo have a limiting capacity of pressure of 1700 kPa, being the limiting pressure of the test also dependent of the limiting capacity of the pressure transducers. LabGeo triaxial devices are constituted by two or three pressure transducers, CP, BP and PN, an internal submersible load cell and a linear displacement transducer.

Most of these devices are prepared for samples of 70 mm of diameter and an approximately 140 mm of height.

While some tests were manually controlled and data acquisition was performed through a data logger linked to a computer with LabVIEW ® software or ADU ® software, others were also automatically controlled by the LabVIEW ® software.



Key:

1 alternative positions for load measuring device

2 air bleed

3 vertical compression measuring device

4 piston

5 top cap

6 soil specimen

7 membrane

8 pedestal

9 device for measurement and control of cell pressure

10 triaxial cell

11 drainage tubes

12 pore pressure sensor

13 volume change sensor

14 device for measurement and control of back pressure

P vertical load

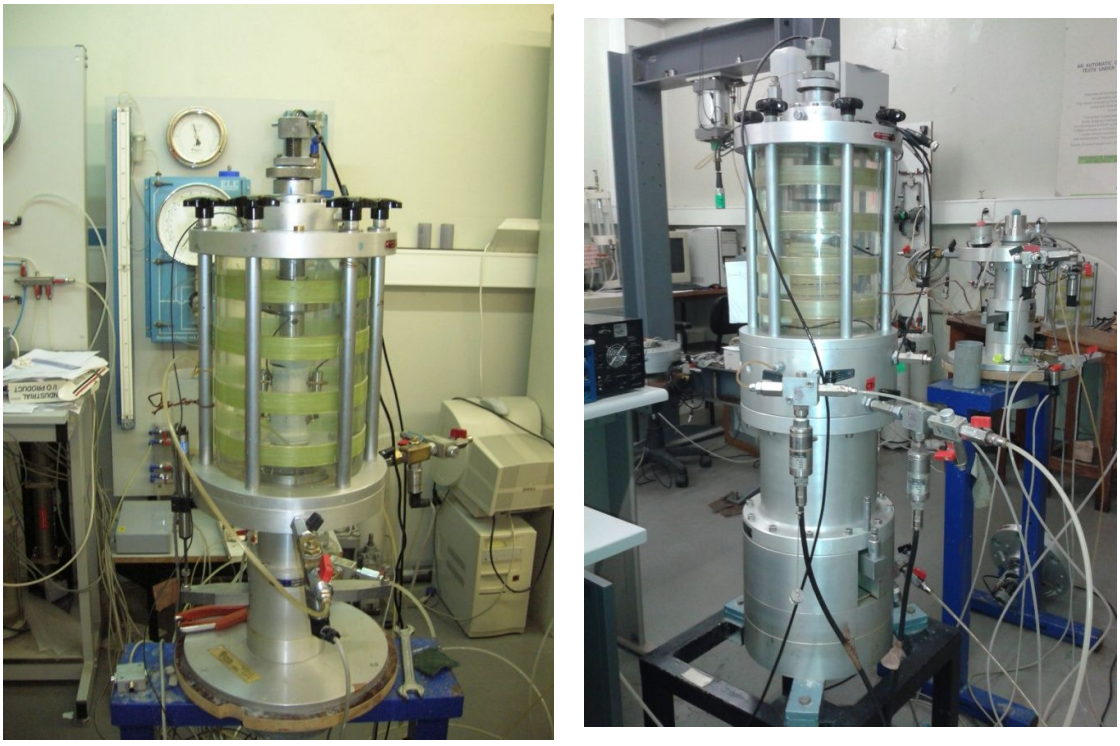
Figure 6.2: Scheme of a conventional triaxial cell (adapted from Standard (2004a))

The main disadvantages of the conventional triaxial cell are, as referred previously, the impossibility of controlling the direction of the principal stresses, and the inability of performing tests other then compression ones, regardless being cyclic or monotonic. Plus the shear stage has to be performed on a hydraulic press. During this research most of the monotonic shear stages were performed with a hydraulic press WF10056 RTITECH 50 of Wykeham Farrance ®.

Aiming to perform distinct stress-paths some of the triaxial tests were carried out by using a Bishop-Wesley triaxial device.

6.2.2.2 Bishop-Wesley Triaxial Cell

Bishop-Wesley or "stress-path" triaxial cell, as the name implies, allows the user to define the stress-path to be performed during shear. LabGeo is equipped with two of these devices (Figure 6.3), a smaller one, for specimens with 50 mm of diameter and an approximately 110 mm of height, and a bigger one, for specimens with 70 mm of diameter (⌀), and an approximately 140 mm of height.



(a) (b)

Figure 6.3: "Bishop-Wesley" triaxial cell at LabGeo: a) smaller cell; b) larger cell.

Both devices are constituted by four pressure transducers, CP, BP, PN and RAM, an internal submersible load cell and a linear displacement transducer. The distinct stress-paths might be reached with an automatic and independent control of the three controlling exes, of the radial and axial

components. A scheme of these equipments, shown in figure 6.5, perceives a better knowledge of the function mechanism.

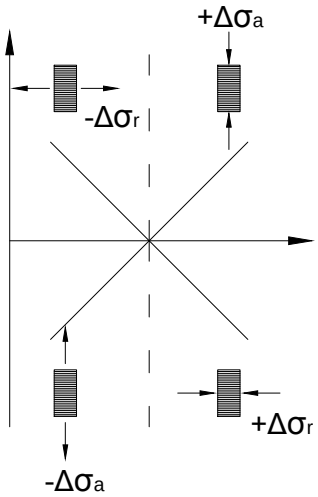


Figure 6.4: Distinct stress-paths by using "Bishop-Wesley" triaxial cell.

This system, unlike the conventional triaxial cells, which require a hydraulic press for shear to be performed, has the advantage of being able to shear the specimens by controlling both the axial and radial components (Figure 6.4).

Figure 6.5 shows that the Bishop-Wesley hydraulic system drives a piston fixed to the pedestal of the chamber, allowing the independence of the axial pressure. The axial hydraulic load is kept constant by sealing the hydraulic "Bellofram" that holds the pressure at the base of the chamber.

Despite these triaxial tests might being executed through the independent control of the axial and radial pressures, they actually depend on each other, as can be seen in Figure 6.5, through the following expression (Viana da Fonseca, 1996):

$$\sigma_v = \frac{1}{A_l}\left(p_a a - \sigma_r\left(a - A_0\right) - W\right) \tag{6.1}$$

where:

σ_v - vertical pressure applied on the specimen;

σ_v - horizontal pressure applied on the specimen;

p_a - axial pressure applied ;

W - piston and accesoirize weight;

a - loading piston area;

A_0 - Initial area of the specimen;

A_i - area of the specimen during the test.

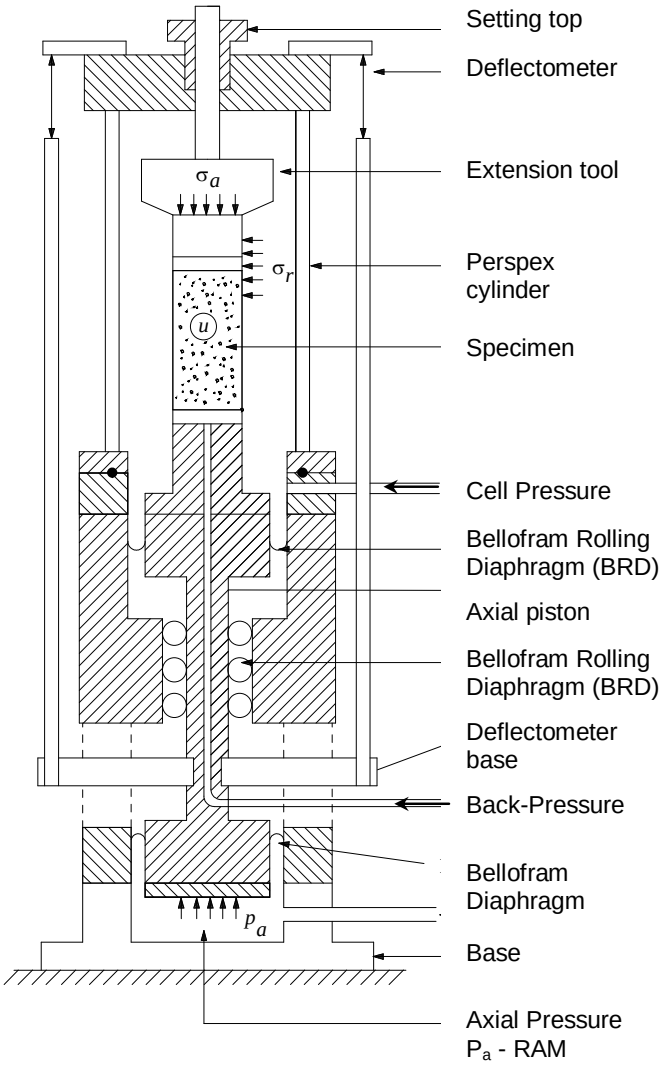


Figure 6.5: Scheme of "Bishop-Wesley" cell (adapted from Viana da Fonseca (1996))

Both devices can be automatically controlled by a TRIAX® software, developed by Dr. G. Toll from the Geotechnical Systems Group – School of Engineering and Computer Science Durham University, or by GDS® from GDS Instruments United® (Figure 6.6). The data acquisition, for both equipments, is also performed by the TRIAX® software.

The GDS® Advanced Pressure/Volume Controller (ADVDPC) is a general-purpose water pressure source and volume change gauge for the precise regulation and measurement of fluid pressure and volume change (GDS Instruments® manual). The ADVDPC used in LabGeo are exclusively water pressure controllers.

Also GDS® ADVDPC, which is commonly designated by GDS®, has a limiting pressure, a limiting volume and a limiting velocity for the regulation of the fluid pressure. During the performance of tests on the large Bishop-Wesley triaxial cell, a careful control was required, and an oil/ air interface pressure was used to assure a constant confining pressure under conventional monotonic loading stress-paths.



Figure 6.6: GDS® (GDS Instruments®); Bishop-Wesley cell being controlled by a GDS® device (LabGeo).

As these devices allow an automatic and independent control of the two controlling exes, a set of cyclic triaxial tests were performed on the small Bishop-Wesley cell. Although the TRIAX® software does not allow for the performance of sinusoidal waves, a set of ramps were programmed aiming to produce the same effect. However this equipment have the limitation of only allowing for the performance of approximately 20 cycles/ hour, due to a step-by-step motor constraint.

6.2.2.3 Cyclic Triaxial Apparatus

The cyclic triaxial tests were performed on a conventional triaxial cell sheared on a hydraulic oil press developed by INEGI, under specifications of the Geotechnical Laboratory of FEUP (Figure 6.7).

Mainly cyclic, but also some monotonic tests were performed on this apparatus being controlled with internal load cells with maximum capacity of 3 kN, 5 kN or 10kN.

The hardware which constitutes this hydraulic oil press are (quoted from Rios Silva (2011)):

- A motor and an hydraulic pump with a maximum pressure of 250 bar allowing the execution of static tests with a maximum load of 50 kN and cyclic tests up to 10 kN;
- An hydraulic unit and a servo actuator that contains an hydraulic cylinder with a displacement transducer and a load transducer (that permits introducing cyclic load with a frequency between 0.001 and 2 Hz);

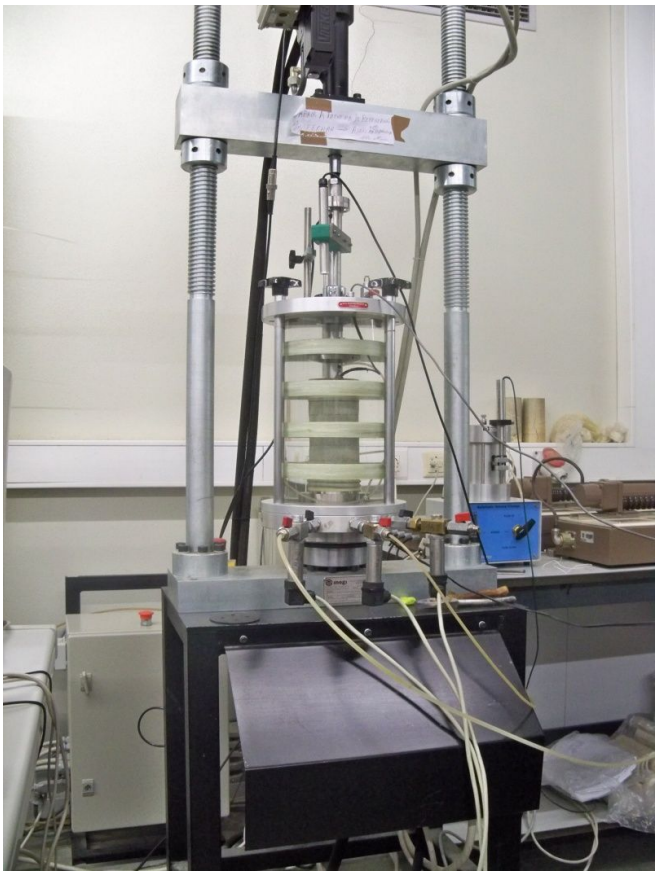


Figure 6.7: Hydraulic oil press, designed for reproducing cyclic loads at LabGeo, with a conventional triaxial cell (LabGeo).

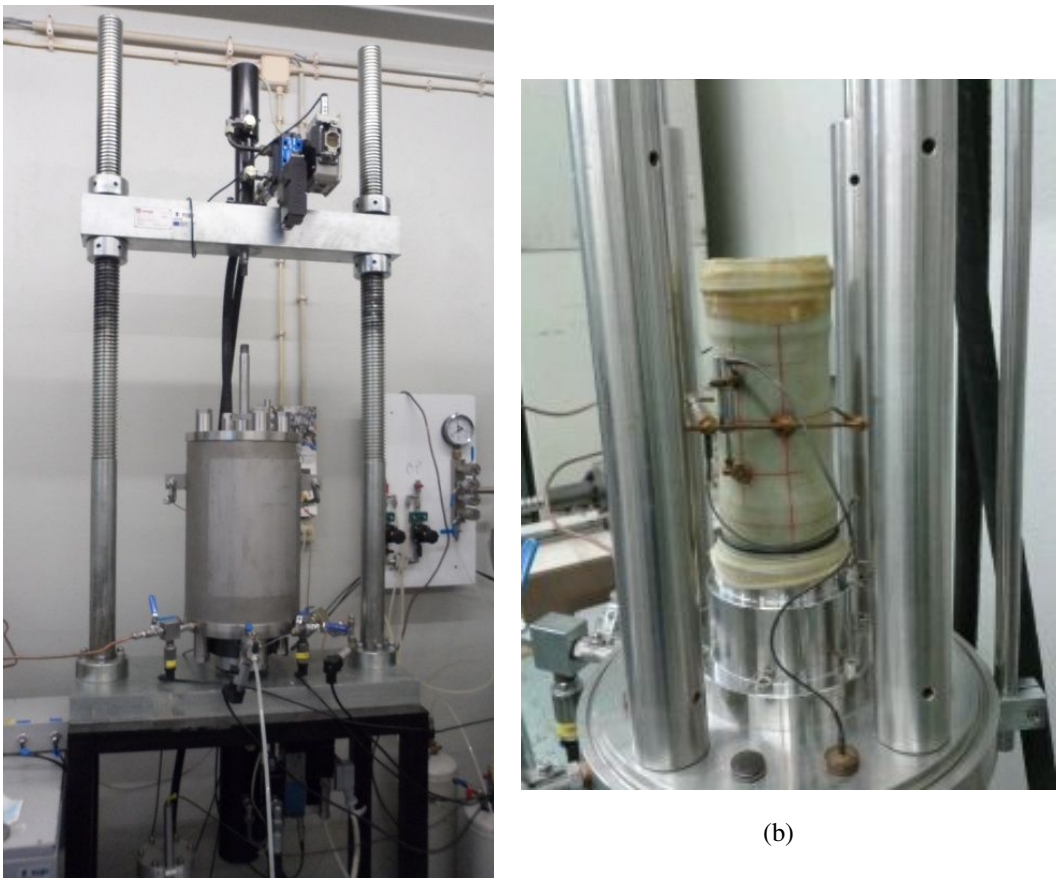
- An electrical panel with the protection of the motor and an emergency button.

The system also includes a data acquisition system supplied by space for several channels to be installed. Plus the controlling and acquiring software DynaTester V2.0® allows for the user to define a template with a set of stages, such as ramp, sinusoidal and constant, to be performed during the shear stage. Such functionality was very helpful for the evaluation of cyclic liquefaction on anisotropically consolidated specimens, which template includes a ramp before the cyclic loading. As for the performance of the isotropically consolidated cyclic triaxial tests it was necessary to adapt the triaxial device with a top cap supplied by a rubber, which allowed the creation of vacuum when coupled to the plate applied to the load cell. This plate was then connected to the top of the chamber through a tube, ending with a water tap to expel the water between the two pieces, for the creation of vacuum.

6.2.2.4 High-Pressure Triaxial Cell

Recently acquired by LabGeo the high-pressure triaxial cell, built at the Imperial College of London (ICL), (Figure 6.8), is a valuable equipment for a proper study of soils subjected to high con-

fining pressures. This equipment works exactly as a conventional triaxial cell, with the exception of allowing the specimens to be tested in a much wider range of confining pressures.



(a) (b)

Figure 6.8: a) Oil hydraulic press with a high-pressure triaxial cell; b) detail of a soil specimen while being placed inside the high-pressure triaxial cell (LabGeo).

The chamber, as well as the pressure transducers, have a limiting pressure of 10 MPa, while the internal load cell, and the external load cell existent on the base of the equipment, display a maximum range of 100 kN. Furthermore the chamber is made of stainless steel instead of Perspex, and the pipes, for the CP and BP connections, are made of cooper and stainless steel replacing the PVC, commonly used on the conventional triaxial cells.

The hydraulic oil press was developed, by INEGI, under specifications of the Geotechnical Laboratory of FEUP for the performance of high-pressures triaxial tests (Figure 6.8).

The acquisition and control of the triaixal tests is held by the software DynaTester V2.0®, which being the same as the one installed for the cyclic press, allows for the performance of templates which might include several test stages.

6.2.2.5 Internal and External Instrumentation

In the beginning of the research most of the tests were carried out in triaxial devices supplied with internal and external instrumentation. These are extremely important, mainly for materials which do not exhibit a structure collapse, thus with a medium/low volumetric strain variation during the percolation and saturation phases.

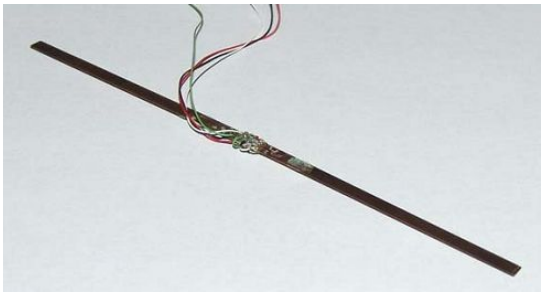
While internal instrumentation allows the achievement of the volumetric strains during the percolation and saturation phases, the external instrumentation is fundamental and irreplaceable for the accurate determination of the specimens void ratio, under saturated conditions.

Although and being aware of the non-accuracy of the internal instrumentation for silty soils, more recently a freezing technique has been applied. This freezing technique, firstly suggested by Sladen and Handford (1987) is described later in the next section.

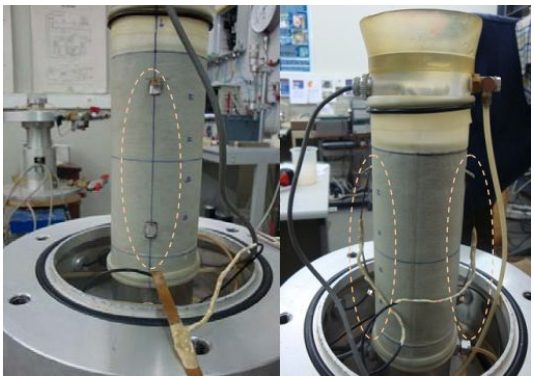
- Internal Instrumentation:

  (i) Linear Displacement Transducer (LDT)

  Some triaxial tests were performed using Linear Displacement Transducers (LDT), usually coupled to the specimen (Figure 6.9). The axial strain is detected by strain gauges fixed to a metal strip (Costa, 2008).



(a)



(b)

Figure 6.9: LDT: a) Costa (2008); b) Bedin (2010)

  (ii) Hall-Effects

  The axial displacements of the specimens were also measured using electromagnetic devices known by hall-effects (Figure 6.10).



Figure 6.10: Hall-Effects (adapted from Rocha (2010))

(iii) Mini-LVDTs

The mini-LVDTs are internal axial or radial displacement transducers, resistant to water and to high-pressure which allows for axial or radial strains of the soil specimens to be measured.

These devices work following the same principle as the external LVDT's described below.

A set of two axial and one radial mini-LVDTs were used, coupled to the soil specimen, for the high-pressure triaxial tests.

- External Instrumentation:

(i) Linear Variable Differential Transformers (LVDT)

The instruments for measuring external displacements are of LVDT type (Figure 6.11). These are constituted by three bobbins and a steel-magnetic cylindrical nucleon, which moves jointly with the object, whose displacement is desired to be measured (Costa, 2008).

The relative movement is given as the LVDT, while coupled to the piston, joins it movement. Special care is required for a perfect vertical positioning of this device.

Most of the LVDTs at LabGeo have a maximum range of 50 mm, providing enough range for loose specimens to reach the CSL.



Figure 6.11: LVDT

(ii) Automatic volume change gauge

The automatic volume change gauges, used during the triaxial tests, are devices constituted by a small hydraulic cylinder whose piston is coupled to a LVDT (Figure 6.12). The water volume change is easily determined as the cylinder diameter and the axial displacement of the piston are known (Costa, 2008).

This equipment can only be used when the soil specimen is well saturated.

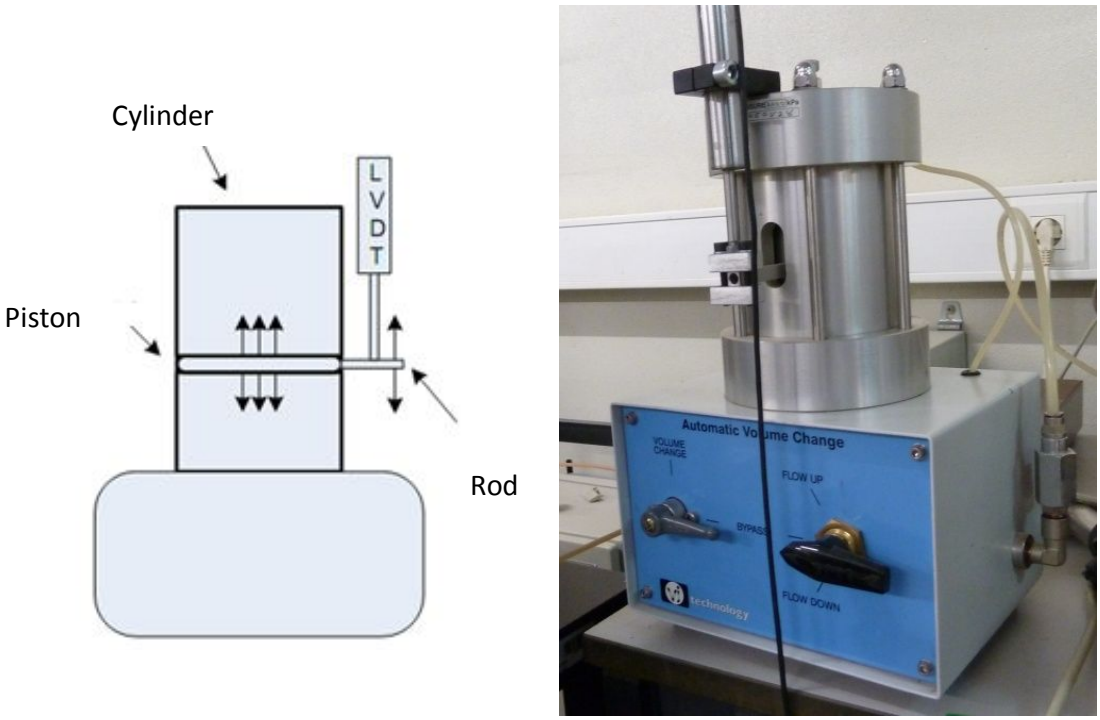


Figure 6.12: Scheme and picture of an automatic volume change gauge by VJ Tech® (adapted from Costa (2008))

6.2.2.6 Triaxial Test Procedures

In the scope of this research a large set of triaxial tests were performed over specimens of 70 mm of diameter and 140 mm height and over smaller specimens of 50 mm of diameter and 140 mm height.

The majority of the soil specimens were prepared by moist tamping with a certain water content, depending on the soil type, while a few set of tests were prepared with a dry air pluviation technique. Among other techniques, moist tamping was chosen as it is able to produce the widest range in void ratio with satisfactory uniformity (Ishihara, 1996), allowing for a clear definition of the CSL. Although being a popular laboratory technique, is commonly associated to the creation of a honeycomb fabric which leads to a higher susceptibility to liquefaction. Notwithstanding it is an easier, low time-consuming technique to perform, which does not segregate soil particles (such as dry air pluviation technique), beyond allowing the operator to control the final density much more readily (adapted from Chang et al. (2011)).

For the moist tamped reconstitution technique the soil specimens were prepared and assembled as follows (also see Figure 6.13):

(i) Guiding marks are first drawn on the membrane for guiding the soil deposition on each layer;

(ii) A filter is placed at the base of the cell, to prevent the passage of fines through the porous stones;

(iii) The membrane is attached to the base of the chamber by applying two "o-rings";

(iv) A cylindrical metallic bipartite mold is placed on the base and the membrane is subsequently adjusted. A 50 kPa of vacuum pressure is applied between the mold and the membrane for a perfect stretch;

(v) Knowing the mold dimensions, the required weight of sand to be used for the requested void ratio can be determined, for a certain water content;

(vi) In order to obtain homogeneous samples, the sand has to be placed in five or six layers in the mold;

(vii) Once the specimen is finished top cap can be then placed being the membrane wrapped on with the use of two "o-rings".

(viii) A small vacuum (negative pressure between 10 kPa to 15 kPa) is applied to the top of the sample for a safe remove of the mold, preventing a soil collapse; the final dimensions of the specimen are then measured helped by a caliper;

(ix) Finally, the Perspex cylinder is mounted on the base and then properly closed and filled with water; the internal pressure is replaced by the surrounding water confining pressure, (positive 10 to 15 kPa).



(a) (b) (c)

Figure 6.13: a) Membrane adjustment to the bipartite mold; b) e c) Moist tamping technique (Viana da Fonseca et al., 2011b)

On the other hand on the specimens prepared by dry air pluviation the soil was placed through a funnel by keeping as low as possible the height of fall. Aiming to not lose soil even the denser specimens were mounted following the same procedure with the particularity of being densified with the help of a rod.

Common phases were developed before shearing. After percolation, a complete saturation, with a B Skempton parameter of at least 0.97, was assured by increasing the back pressure up to 600 kPa, keeping the effective confinement of 10 kPa. A Skempton parameter of at least 0.97 is required for saturated specimens to be tested, according to the Standard (2004b) procedures. During the first stages, specimen dimensions were re-measured with the help of internal/local transducers (inductive hall-effect calipers) measuring axial and radial deformation (Figure 6.14a). Isotropic and anisotropic consolidation, for $K_0 = 0.5$, were also accompanied by redundant volume measurement with a volume change gauge. A good agreement with the void ratio after the consolidation was found through a freezing technique. This technique consists on freezing the sample in the end of the triaxial test (Figure 6.14b). With the freezing technique the volume was accurately determined by keeping the volume of water inside the specimen, which is completely saturated ($G \times w = S \times e$). With this final void ratio and the precise measurements of volume changes, the void ratio was easily determined at the end of both consolidation and shear stages. This freezing technique was initially proposed by Sladen and Handford (1987) in order to correct the potential systematic error in laboratory testing of very loose sands.

While in the beginning on this work, percolation and saturation phases were time-consuming, requiring between 5/6 days to be completed, more recently a previous CO_2 percolation has been done before water percolation. This technique is not new and was also used at LabGeo some years ago. Now, recently re-established, this technique allows reaching B Skempton parameters higher than 0.97 for low pressures ($\sigma_h = 300$ kPa).

Finally, monotonic or cyclic shearing was applied under stress or strain control. As already referred, monotonic tests were performed by constant strain rate, till reaching an axial strain around 20% or until the critical state was reached. On the other hand the cyclic liquefaction deemed to have liquefied when a single amplitude shear strain exceeded 2.5% or when a zero effective pressure was reached (Ishihara, 1996).

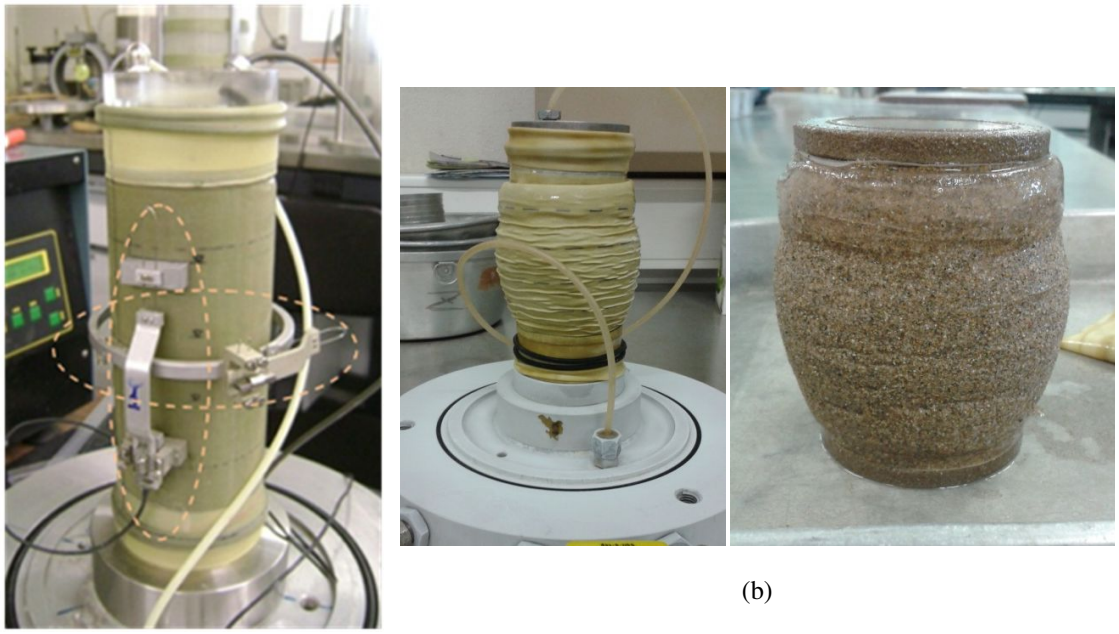
All triaxial tests were performed by fulfilling the requirements established on the actual standard procedures (Standard, 2004b).

The next items are a short resume of the steps followed for the performance of a triaxial test:

(i) Remolded specimens were directly prepared in the triaxial cell using a bi-parted mold and maintaining its integrity by 10 kPa vacuum pressure after de-molding;

(ii) The percolation of an equivalent to 1 liter of CO_2 , which has allowed the saturation to be reached more efficiently; de-aired water percolation followed; (the CO_2 percolation was something implemented only on the last set of tests);

(iii) The saturation was assured by checking the values of Skempton's parameter higher than 0.97, as required by current standards for undrained triaxial tests); The saturation process is



(a) (b)

Figure 6.14: (a) Internal/local transducers (inductive hall-effect calipers); (b) Freeze technique (procedure to determine the void ratio during all test stages after the saturation) (comment: on this test the water on the pores migrate to the top of the specimen during the freezing).

developed by applying a confining pressure of 10 kPa, while increasing the backpressure up to values higher that 300 kPa;

(iv) Isotropic consolidation was attained by increasing the confining pressure to the required effective pressures;

(v) Shearing in axial compression was imposed, under drained and/or undrained conditions, assuring an axial strain velocity compatible with the rate of excess pore pressure dissipation that would guarantee stress state, following recommended practices for v_{max} in reference to consolidation, t_{100} (Standard, 2004b); Shearing in cyclic compression/extension under undrained conditions was performed with a frequency of 0.1 Hz, (and of approximately 0.03 Hz on the Bishop-Wesley device).

Under strain control, the rate of shear depends if the tests are executed under drained or undrained conditions. While under undrained conditions the shear-rate depends exclusively on the frequency of acquisition of the software, under drained conditions the shear-rate depends on the soil permeability, which shall be determined according to the Standard (2004b) procedures. Although the triaxial tests might be performed with higher strain-rates usually, at LabGeo, drained tests are performed with a strain rate of 0.01 mm/min, while the undrained tests are carried out with a velocity of 0.05 mm/min.

Notwithstanding a higher strain-rate might be adopted, being the maximum speed permitted for soils to be sheared under drained conditions determined through the following equation:

$$v_{max} = \frac{H_c \times \varepsilon_a}{15 \times t_{100}} \tag{6.2}$$

Where H_c is the height of the specimen at the end of the consolidation, ε_a is the axial strain to be achieved at the end of the test (e.g. 20%) and t_{100} the time at the end of the consolidation.

6.2.2.7 Brief note about cyclic load frequency

Most of the cyclic triaxial tests were performed with a frequency of 0.1 Hz to ensure a better acquisition and for a better characterization of the geomechanical behavior of the soils. Furthermore this frequency was earlier recommended and used by Tatsuoka et al. (1986a) to study cyclic response of sands.

Independency of the undrained cyclic response of soils on the loading frequency was previously demonstrated by some authors (Peacock and Seed, 1968; Tatsuoka et al., 1986a). Peacock and Seed (1968) showed a small difference for simple shear tests cyclic sheared with frequencies between 1/6 and 4 Hz. Later on Tatsuoka et al. (1986a), after making the same experience for specimens cyclic sheared with frequencies between 0.05 and 1 Hz, concluded that the frequency did not affected significantly the undrained soils response (Figure 6.15).

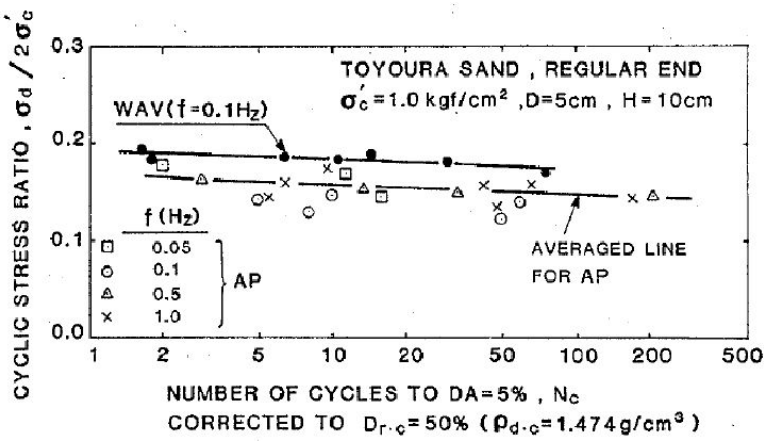


Figure 6.15: Effect of cyclic loading frequency on cyclic shear strength of Toyoura sand (Tatsuoka et al., 1986a)

6.2.3 Direct Simple Shear Device

Both monotonic and cyclic direct simple shear tests were performed, aiming to perceive the effect of principal stress rotation on the behavior of Algeria and Coimbra sand. These tests were carried

out using a Norwegian Geotechnical Institute (NGI) – simple shear device, by using the ShearTrac II-DSS system, in the Geotechnical Laboratory at the University of Western Australia (UWA) (Figure 6.16).

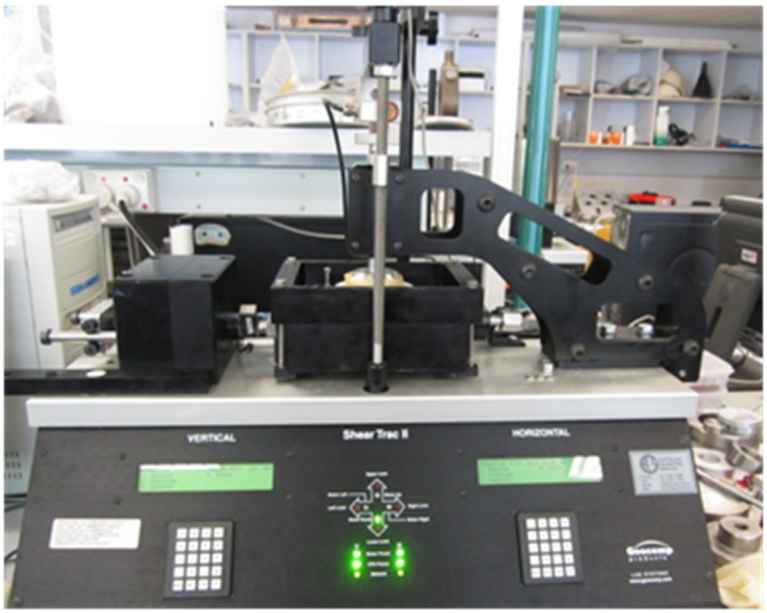


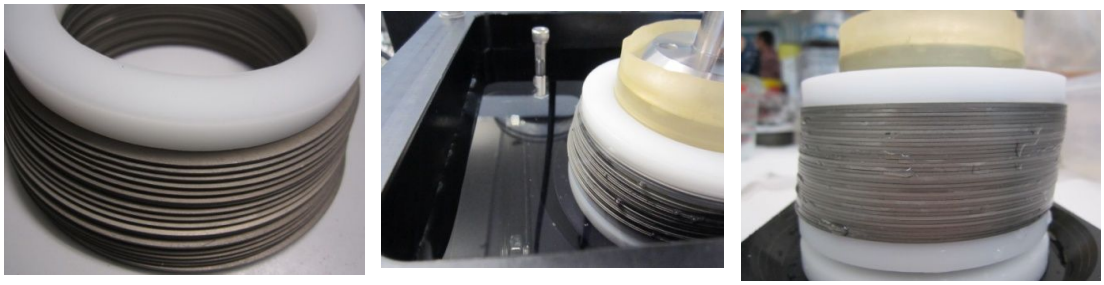
Figure 6.16: DSS device at UWA

6.2.3.1 DSS device

The "Shear Trac II – DSS" is a universal shear system which allows the performance of consolidations, cyclic and monotonic shear under automatic control. This equipment allows for the shear stage to be executed with 32 automatic increments. On the other hand, horizontal shearing has the possibility to be executed under shear or strain-control. Yet cyclic shear, performed under shear-control, may be applied within a limiting maximum frequency of 1 Hz (Manual, 1982-2010).

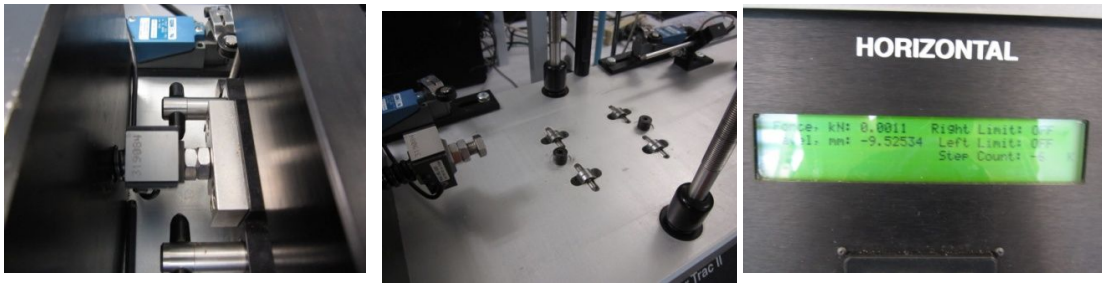
In this equipment the specimen is inherently confined inside a rubber membrane and Teflon coated stacked rings (Figure 6.17). The anisotropic consolidation is then achieved under permission of vertical displacement and preventing radial displacement (Figure 6.18) (Manual, 1982-2010).

During the shear stage only constant volume tests are allowed, which are considered equivalent to undrained tests (Bjerrum and Landva, 1966). Constant volume condition is assured by the vertical cell (Figure 6.18) adjustment through a closed computational loop controlled by a vertical LVDT.



(a) (b)

Figure 6.17: a)Teflon coated stacked rings; b)and c) detail of the Teflon coated stacked rings during and after the cyclic shear of a soil sample (Geotechnical laboratory at UWA)



(a) (b) (c)



(d) (e)

Figure 6.18: DSS apparatus: a)and b) horizontal load cell; c) display screen of the horizontal load; d) vertical load cell; e) display screen of the vertical load (Geotechnical laboratory at UWA)

DSS tests are controlled and acquired through a data logger linked to a computer with LabVIEW® software.

This equipment has also the advantages of not having a system compliance. As referred by Finn et al. (1978), "compliance in systems for conducting undrained cyclic shear tests on saturated sands is equivalent to partial drainage, being responsible for an overprediction of soil liquefaction

potential." The magnitude compliance is primarily function of the type of test and of the grain size of the soil. Thus while in the triaxial the compliance is fundamentally function of the membrane penetration effect, on the simples shear tests this is due to the expansion of the membrane on the sample boarders, generating cavitations with the pore pressure increase (Finn et al., 1978).

The main disadvantage of this system, as referred previously, is the unknown direction and magnitudes of principal directions. Thus it interpretation is limited, not being able to be directly compared with other equipments (Bjerrum and Landva, 1966).

6.2.3.2 Test Procedure

To study the influence of principal stress rotation a set of DSS tests were performed on specimens prepared by moist tamping with a water content of 5%. Beyond being required for further comparison with the triaxial tests, this technique may be the only one which can be used for testing cohesionless soils on a DSS device, as it is imperative to assure that the soil is compacted against the Teflon rings, without letting them to slide in between.

After placing the top cap and being inherently confined, inside a rubber membrane and Teflon coated stacked rings, the height of the specimen was measured using a caliper. Subsequently the set was placed inside the DSS machine and the vertical displacements during consolidation were measured using an external LVDT.

During the shear stage the constant volume condition is maintained by adjusting the vertical load, being the pore pressure equivalent to the change of the total vertical stress (Bjerrum and Landva, 1966). As the specimen is confined inside a rubber membrane and Teflon coated stacked rings, the constant volume condition is ensured only by controlling the vertical deformation.

The tests are not conventionally undrained, since there is no monitoring of pore pressures, but they are constant volume tests. As discussed by Reyno et al. (2005), this is an equivalent condition in the simple shear apparatus. Therefore, it was decided to perform tests with and without water, saturated or dry, inside the shear box where the specimen is contained. Afterwards all tests were plotted and, as expected, a convergence was found, as was previously found by Finn et al. (1978).

Simple shear specimens were deemed to have liquefied when a single amplitude shear strain exceeded 3.75% and/or reached a zero vertical effective stress within 15 cycles, for a 7.5 magnitude earthquake. This single shear strain is equivalent to 2.5% of single amplitude axial strain in a cyclic triaxial test (Ishihara, 1996).

6.2.4 Piezoeletric Transducers

Most of the triaxial devices are supplied with piezoeletric transducers, which allow the measurement of the soil stiffness. These transducers have a main role on this work, as the stiffness (G_0 - read V_s) is a parameter often used to evaluate soil liquefaction susceptibility and for the subsequent development of frameworks.

The majority of the triaxial devices at LabGeo have installed piezoeletric transducers of bender-extender elements type (Figure 6.19). While bender elements are examples of piezoelectric transducers, which can transmit and receive S-waves; extender and compression transducers can transmit and receive P-waves velocities.

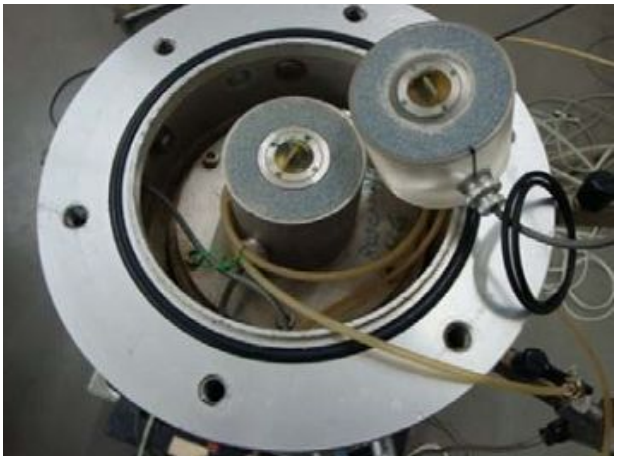


Figure 6.19: Bender-Extender Elements installed on a "Bishop-Wesley" cell (LabGeo)

These transducers implemented on the base and on the top cap of the triaxial chambers, allow for S and P waves measurement during each stage of the triaxial test.

Bender elements are composed by two piezoceramic thin plates rigidly connected to a central metalic foil and to the outer faces electrodes. The bending motion is generated when one plate expands while the other contracts (Figure 6.20). For it feasible interpretation is very important to take into account the directions of polarization.



(a) (b)

Figure 6.20: Schemes of the piezoeletric motion: a) bender elements; b) extender elements (adapted from Ferreira (2008))

On the other hand, extender elements are trasducers similar to the bender elements, which reproduce a distinct motion of compression-extention type (Figure 6.20).

The main feature which distinguishes bender-extender elements motion behavior relies uniquely and exclusively on the excitation frequency. While low frequencies (<10 kHz) induce a bending movement, larger frequencies (>10 kHz) induce a compression-extending motion.

For the measurement of seismic waves, besides the piezoelectric transducer, are also required an external signal source, i.e. a function generator, and an acquisition device for visualizing and recording the travel time and acquiring the signals, i.e. a digital Oscilloscope (Figure 6.21). Furthermore amplification is often fundamental for a clear and accurate interpretation of the emitted and received signals (adapted from Ferreira (2008)).

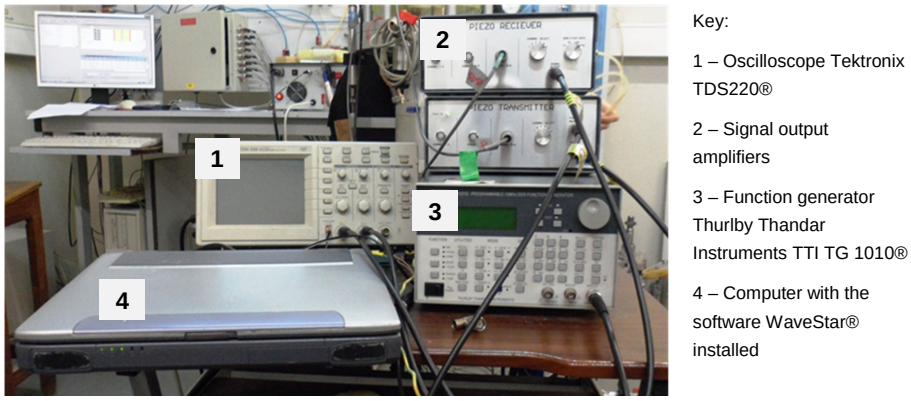


Figure 6.21: Associated electronic equipments required for seism waves measurement

The associated electronic equipments existent at LabGeo, for seismic waves to be measured, are a function generator Thurlby Thandar Instruments TTI TG 1010®, an Oscilloscope Tektronix TDS220® and a set of two signal output amplifiers designed and manufactured at UWA (Figure 6.21).

The function generator allows the generation of an electrical signal with various user-defined configurations (sinusoidal, square, ramp, arbitrary, in continuous or triggered mode); regardless only waves of the sinusoidal type were used. Sinusoidal signals allow an intuitive and straightforward interpretation in time domain. In fact these have been shown to give more reliable time measurements by reducing the frequency components and thus minimizing the velocity dispersion (Blewett et al. (2000), adapted from Ferreira (2008)).

For seismic wave measurements, in time domain, Tektronix oscilloscope is provided with the data acquisition program WaveStar®.

Time domain analysis of seismic waves is attached with a couple of problems, such as cross-talking (Ferreira, 2008). Notwithstanding and due to the author inexperience this method was the one adopted during the course of the present research.

As previously stated in Chapter 3, seismic wave's measurement is performed basing on the first arrival method. The method based on the first wave arrival relies on the assumption that stress waves are non-dispersive in a uniform elastic medium, thus independent on the frequency.

6.3 Test Analysis

6.3.1 Oedometer Tests

The oedometer tests allow for the compression curves to be drawn by plotting the void ratio against the vertical confining stress, after the settlement is complete, for each load stage.

The vertical confining stress, $\sigma_v^{'}$, is calculated as:

$$\sigma_v^{'} = \frac{F}{A} \times 10 \tag{6.3}$$

, where F is the total load, the value 10 is due to the amplification effect of the load by the lever, and A is the area of the sample, which is constant during all the test due to the horizontal displacement constrain.

As the area is kept constant during all test loading stages, then the axial strain is equal to the volumetric strain:

$$\varepsilon_a = \varepsilon_v = \frac{\Delta H}{H_0} \tag{6.4}$$

, where H_0 is the initial height of the sample and ΔH is the axial displacement correspondent to the final of each loading stage.

Then, by knowing the volume at the end of each loading increment, the void ratio, e, is calculated as:

$$e = G_s \frac{V_c}{W_d} - 1 \tag{6.5}$$

where G is the density of solid particles, V_c is the corrected volume and W_d is the dry weight of the specimen.

The corrected volume of the specimen can be determined as follows:

$$V_c = A \times (H - H_0) \tag{6.6}$$

For the compression curve to be plotted it is also required to determine the stress invariants p', by assuming a typical earth pressure coefficient for loose cohesionless soils of 0.5:

$$p' = \frac{\sigma_1' + 2 \times \sigma_3'}{3} = \frac{\sigma_v' + 2 \times \sigma_h'}{3} = \frac{\sigma_v' + 2 \times \sigma_v' \times K_0}{3} \tag{6.7}$$

Once the compression curve is plotted the compression index, C_c, displayed in Figure 6.22, can be obtained by determining it inclination:

$$C_c = -\frac{\Delta e}{\log(\Delta \sigma_v')} \tag{6.8}$$

On the other hand the swelling index, Cs is the inclination of the unloading stage, as can be seen in Figure 6.22, which might be performed in the middle of the compression stages, or at the end of the compression test.

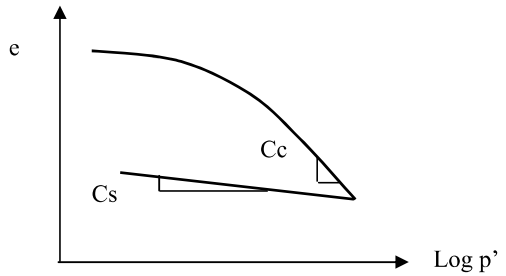


Figure 6.22: Identification of the compression index C_c and the swelling index C_s on a compression curve (Carrera, 2008)

6.3.2 Triaxial Tests

The scope of the present work is centered on the evaluation of soil liquefaction potential based on Critical State theory. For CSSM to be applied is necessary to determine both NCL and CSL on the semi-logarithmic space e – log p'. Therefore an accurate void ratio and corrected area are required for a proper evaluation of the triaxial results. Furthermore both deviator and mean effective stresses need also to be corrected for two more distinct effects: the membrane penetration effect and the restraining effect caused by the membrane rigidity.

6.3.2.1 Calculation procedure for the evaluation of a triaxial test

1st Hypothesis – The void ratio is determined by means of internal instrumentation

First of all is necessary to determine the void ratio changes during the percolation and saturation phases. While in some tests the sample volume change was obtained by using two axial hall-effects

and one radial hall-effect, on other tests the volume change was simply assessed by means of two axial LDTs. During the consolidation only the volumetric changing gauge was used, by assuming a complete saturation of the specimen. Finally during the shear stage, while under undrained conditions the volume is kept constant, under drained conditions the changes in volume are determined using the volumetric changing gauge and the axial strains by using an external LVDT. The calculations performed are displayed by the following equations, where the nomenclature 0, 1, 2 and 3, refers to the specimens measurements at the end of the remodeling, saturation, consolidation and shear stages, respectively, and f and i stands for the initial and end of the stage, respectively.

Percolation+	$\varepsilon_a = (\Delta h_1 - \Delta h_2) \times 100 / H_{target}$	$H_1 = H_0 - H_0 \times \varepsilon_a / 100$	(6.9)
Saturation using Hall-	$\varepsilon_r = \Delta r \times 100 / \varnothing_i$	$A_1 = A_0 - A_0 \times \varepsilon_r / 100$	(6.10)
effect or mini-LVDTs	$\varepsilon_v = 2 \times \varepsilon_r + \varepsilon_a$	$V_1 = V_0 - V_0 \times \varepsilon_v / 100$	(6.11)
Percolation +	$\varepsilon_a = (\Delta h_1 - \Delta h_2) \times 100 / H_{target}$	$H_1 = H_0 - H_0 \times \varepsilon_a / 100$	(6.12)
Saturation using LDTs	$\varepsilon_r = \varepsilon_a$	$A_1 = A_0 - A_0 \times \varepsilon_r / 100$	(6.13)
	$\varepsilon_v = \varepsilon_a / 3$	$V_1 = V_0 - V_0 \times \varepsilon_v / 100$	(6.14)
	$\varepsilon_v = \dfrac{\Delta V}{V_{1f}}$	$V_2 = V_1 - \Delta V$	(6.15)
Consolidation	$\varepsilon_a = \dfrac{\varepsilon_v}{3}$	$H_2 = H_{1f} - H_{1f} \dfrac{\varepsilon_a}{100}$	(6.16)
	$\varepsilon_r = 2\dfrac{\varepsilon_v}{3}$	$A_2 = A_{1f} - A_{1f} \dfrac{\varepsilon_r}{100}$	(6.17)
	$\varepsilon_v = \dfrac{\Delta V}{V_2}$	$V_3 = V_{2f} - \Delta V$	(6.18)
Shear - Drained	$\varepsilon_a = \dfrac{\Delta H}{H_2}$	$H_3 = H_{2f} - \Delta H$	(6.19)
	$\varepsilon_r = \dfrac{\varepsilon_v - \varepsilon_a}{2}$	$A_3 = \dfrac{V_{2f} - \Delta H}{H_{2f} - \Delta H}$	(6.20)
	$\varepsilon_v = 0$	$V_3 = V_{2f}$	(6.21)
Shear – Undrained	$\varepsilon_a = \dfrac{\Delta H}{H_2}$	$H_3 = H_{2f} - \Delta H$	(6.22)
$(e_3 = e_2)$	$\varepsilon_r = -\dfrac{\varepsilon_a}{2}$	$A_3 = \dfrac{V_{2f}}{H_{2f} - \Delta H}$	(6.23)
			(6.24)

2nd Hypothesis – Freezing technique

The hypothesis based on the freezing technique also assumes a complete saturation of the specimen, being the samples dimension determined with an inverse calculation procedure of the first hypothesis. The calculations performed are displayed by the following equations, where the nomenclature 0, 1, 2 and 3, refers to the specimens measurements at the end of the remodeling, saturation, consolidation and shear stages, respectively, and f and i stands for the initial and end of the stage, respectively.

$$\varepsilon_v = \frac{\Delta V}{V_{2i}} \qquad V_2 = V_3 + \Delta V \tag{6.25}$$

Consolidation

$$\varepsilon_a = \frac{\Delta H_2}{H_{2i}} \qquad H_2 = H_0 - \Delta H_2 \tag{6.26}$$

$$\Delta H_2 = \left\{ \left[\left(\frac{V_{2i} - V_0}{100} \right) / V_0 \right] / 3 \right\} \times \frac{H_0}{100} \tag{6.27}$$

$$\varepsilon_r = \frac{\varepsilon_v - \varepsilon_a}{2} \qquad A_2 = \frac{V_2}{H_2} \tag{6.28}$$

$$\varepsilon_v = \frac{\Delta V}{V_{3i}} \qquad V_3 = V_4 + \Delta V \tag{6.29}$$

Shear - Drained

$$\varepsilon_a = \frac{\Delta H_3}{H_{3i}} \qquad H_3 = H_0 - \Delta H_3 \tag{6.30}$$

$$\Delta H_3 = \Delta H + \left\{ \left[\left(\frac{V_{2i} - V_0}{100} \right) / V_0 \right] / 3 \right\} \times \frac{H_0}{100} \tag{6.31}$$

$$\varepsilon_r = \frac{\varepsilon_v - \varepsilon_a}{2} \qquad A_3 = \frac{V_3}{H_3} \tag{6.32}$$

$$\varepsilon_v = 0 \qquad V_3 = V_4 \tag{6.33}$$

Shear – Undrained

$$\varepsilon_a = \frac{\Delta H_3}{H_{3i}} \qquad H_3 = H_0 - \Delta H_3 \tag{6.34}$$

$(e_3 = e_2)$

$$\Delta H_3 = \Delta H + \left\{ \left[\left(\frac{V_{3i} - V_0}{100} \right) / V_0 \right] / 3 \right\} \times \frac{H_0}{100} \tag{6.35}$$

$$\varepsilon_r = \frac{\varepsilon_v - \varepsilon_a}{2} \qquad A_3 = \frac{V_3}{H_3} \tag{6.36}$$

After freezing

$$Gw = Se \longrightarrow e_4 \tag{6.37}$$

$$V_4 = \frac{W_d \times (e_4 + 1)}{G} \tag{6.38}$$

(6.39)

Finally with the dimensions of the specimens at the end of the consolidation is possible to determine the stress invariants, q and p' during the shear stage:

$$p' = \frac{\sigma_1' + 2 \times \sigma_3'}{3} = \frac{\sigma_v' + 2 \times \sigma_h'}{3} \tag{6.40}$$

$$q = \sigma_1' - \sigma_3' = \sigma_v' - \sigma_h' = \frac{F}{A_3} \tag{6.41}$$

,while the void ratio is determined according to the equation:

$$e = G\frac{V_3}{W_d} - 1 \tag{6.42}$$

6.3.2.2 Membrane Correction

The membrane penetration effect is the effect of the membrane to penetrate in void ratios between the grains at the interface. This effect tends to underestimate the pore pressure for loose specimens ($e > e_c$), and to overestimate the pore pressure of dense specimens ($e < e_c$).

According to Nicholson et al. (1993) this effect shall be corrected only if the D_{20} of the soil is higher than twice the membrane thickness. As none of the soils have a D_{20} higher than 0.8 this effect was not taken into account.

The membrane rigidity may, mainly when barreling occurs and for low confining pressures, have a restrain effect, overpredicting the final strength of the soil. The deviator and mean effective stress correction due to the membrane effect during the specimen barreling were calculated, during the present research, according to the Standard (2004b) standards:

$$\text{Correction to the total vertical stress} \qquad (\Delta\sigma_1)_m = \frac{4 \times t \times E}{D_i}\left[(\varepsilon_1)_m + \frac{(\varepsilon_{vol})_m}{3}\right] \tag{6.43}$$

$$\text{Correction to the total horizontal stress} \qquad (\Delta\sigma_3)_m = \frac{4 \times t \times E}{D_i} \times \frac{(\varepsilon_{vol})_m}{3} \tag{6.44}$$

where t is the initial thickness of membrane, E is the elastic modulus for membrane, measured in tension, D_1 is the initial diameter of membrane, $(\varepsilon_1)_m$ is the vertical strain of membrane (expressed as a ratio) and $(\varepsilon_{vol})_m$ is the volumetric strain of membrane (expressed as a ratio). While the thickness of the membrane was considered to be 0.4 mm, the Yong modulus, E, of the membrane was considered to be typically 1.3 MPa.

6.3.3 Direct Simple Shear Tests

Direct simples shear tests have the peculiarity of the user not knowing the magnitude and direction of principal stresses, being the only stresses known the vertical and the horizontal ones.

The initial measurements of the specimens are determined by measuring the height of the specimens with a caliper and by assuming a constant area determined by the interior diameter of the Teflon coated stacked rings.

As the area is kept constant, then during the consolidation, the axial strain is equal to the volumetric strain:

$$\varepsilon_a = \varepsilon_v = \frac{\Delta H}{H_0} \tag{6.45}$$

,where H_0 is the initial height of the sample and ΔH is the axial displacement correspondent to the end of the consolidation stage.

As the direct simple shear test is a constant volume test, then both the height and the area are kept constant, during both monotonic and cyclic shear.

The analysis of the shear stage is actually performed through the vertical and the shear stress calculation. The vertical confining stress, σ_v and the shear stress tau_{xy} are determined, respectively, as:

$$\sigma_v = \frac{F_v}{A} \tag{6.46}$$

$$\tau_{xy} = \frac{F_h}{A} \tag{6.47}$$

where F_v is the vertical load, F_h is the horizontal load and A is the area of the specimen.

For the stress-strain behavior to be plotted is also required the shear strain evaluation:

$$\gamma = \frac{\Delta h}{H_1} \times 100 \tag{6.48}$$

being Δh the horizontal displacement of the specimen during shear and H_1 the specimen height at the end of the consolidation.

As DSS tests are constant volume tests by adjusting the vertical load, the pore pressure generation is assumed to be the drop on the vertical confining stress:

$$\Delta u = \sigma_{v0} - \sigma_{vi} \tag{6.49}$$

where σ_{v0} is the initial vertical confining stress and σ_{vi} is the vertical confining stress at the instant i.

6.4 Introduction to the Experimental Work Done

The experimental work incorporated three distinct parts:

(i) Initially each of the studied materials were characterized through the determination of it grain size distribution and specific gravity, according to Standard (2004a). Some soils had already been studied by other authors, which already identified the maximum and minimum void ratios, the sandy particle morphology mineralogy and permeability. Unfortunately, as will be seen in Chapter 7, some basic characterization tests are still missing for some soils and shall be complemented on future researches. For a better organization of this thesis the author decided to present, previously, on Chapter 5 the basic characteristics of each soil, in order to confront with the previous researchers' publications;

(ii) The oedometer tests were performed, not only to complement the triaxial tests, but also to investigate the NCL positioning. In order to achieve the curve, all specimens were prepared with an initial high void ratio, on specimens prepared through moist tamping technique;

(iii) Finally, in order to achieve the distinct geomechanical behavior of each soil, a large set of both drained and undrained triaxial tests were performed. The basis of this research, relying on the critical state theory, required a previous determination of the CSL. Distinct initial conditions were pursued in order to understand the influence of distinct factors, both on the onset of liquefaction and on CSL positioning;

(iv) Algeria and Coimbra sand were also evaluated both under cyclic triaxial and direct simple shear conditions.

In table 6.1 are listed the oedometer tests performed and their main features, while Table 6.2 till table 6.13 display each of the performed triaxial tests with it respective initial state conditions. Finally table 6.14 and table 6.15 shows the list of DSS tests.

A total set of 9 oedemeter tests, 321 triaxial tests and 91 direct simple shear tests were studied and are presented in the scope of this research. Among the total set of tests, 8 oedemeters, 237 triaxial tests and 91 direct simple shear tests were performed during this PhD.

Table 6.1: List of the oedometer tests performed

Test ID	Φ mm	e_0	e_i 3 kPa	σ'_v max kPa	Soil	Method of samples preparation	Author
OE_A	70	-	0.959	3200	Argelia sand	Moist tamping w=5%	Rocha, 2010
OE_C	70	0.913	0.913	3200	Coimbra sand	Moist tamping w=5%	Present research
OE_C20	70	0.756	0.726	3200	Coimbra sand + 20% FC	Moist tamping w=8.25%	
OE_C40	70	1.008	0.862	3200	Coimbra sand + 40% FC	Moist tamping w=8.25%	
OE_O	70	0.875	0.863	3200	Osorio sand	Moist tamping w=5%	
OE_M_1	70	0.968	0.859	3200	Mixture	Moist tamping w=8..25%	
OE_M_2	50	1.207	0.934	6400	Mixture	Moist tamping w=8.25%	
OE_S_1	70	0.988	0.883	3200	Silt	Moist tamping w=11.5%	
OE_S_2	50	1.303	1.120	6400	Silt	Moist tamping w=11.5%	

Table 6.2: List of the monotonic triaxial tests performed with Algeria sand, complemented with previous researches (Pinheiro, 2009; Fonseca, 2009; Rocha, 2010)

	Test ID	e_0	e_i	p'_i kPa	K_0	Equipment	Method of samples preparation	Author
ALGERIA SAND	Tx_CID_1	0,882	0,767	500	1,0	Conventional Tx	Moist tamping w=5%	Rocha, 2010
	Tx_CID_2	0,862	0,859	14	1,0	Conventional Tx	Moist tamping w=5%	
	Tx_CID_3	0,862	0,808	1006	1,0	Conventional Tx	Moist tamping w=5%	
	Tx_CID_4	0,541	0,535	100	1,0	Conventional Tx	Moist tamping w=5%	Present research
	Tx_CID_5	0,612	0,608	31	1,0	Conventional Tx	Moist tamping w=5%	
	Tx_CID_6	0,783	0,784	10	1,0	Conventional Tx	Moist tamping w=5%	
	Tx_CID_7	0,790	0,741	1000	1,0	Conventional Tx	Moist tamping w=5%	
	Tx_CID_8	0,832	0,816	10	1,0	Conventional Tx	Moist tamping w=5%	
	Tx_CID_9	0,862	0,853	10	1,0	Conventional Tx	Moist tamping w=5%	
	Tx_CID_10	0,950	0,912	29	1,0	Conventional Tx	Moist tamping w=5%	
	Tx_CID_11	0,952	0,868	50	1,0	Conventional Tx	Moist tamping w=5%	
	Tx_CID_12	0,540	0,485	7433	1,0	High Pressure Tx cell	Dry pluviation	
	Tx_CIU_1	0,804	0,799	50	1,0	Conventional Tx	Moist tamping w=5%	Pinheiro, 2009
	Tx_CIU_2	0,873	0,833	402	1,0	Conventional Tx	Moist tamping w=5%	
	Tx_CIU_3	0,908	0,858	99	1,0	Conventional Tx	Moist tamping w=5%	
	Tx_CIU_4	0,866	0,845	50	0,9	Conventional Tx	Moist tamping w=5%	
	Tx_CIU_5	0,866	0,842	48	1,0	Conventional Tx	Moist tamping w=5%	
	Tx_CIU_6	0,866	0,809	200	1,0	Conventional Tx	Moist tamping w=5%	
	Tx_CK_0U_1	0,882	0,840	68	0,5	Conventional Tx	Moist tamping w=5%	Fonseca, 2009
	Tx_CK_0U_2	0,865	0,828	134	0,5	Conventional Tx	Moist tamping w=5%	
	Tx_CK_0U_3	0,840	0,799	267	0,5	Conventional Tx	Moist tamping w=5%	
	Tx_CK_0U_4	0,840	0,827	50	0,6	Conventional Tx	Moist tamping w=5%	
	Tx_CK_0U_5	0,833	0,807	76	0,5	Conventional Tx	Moist tamping w=5%	Ghili, 2009
	Tx_CIU_7	0,814	0,790	100	1,0	Conventional Tx	Moist tamping w=5%	
	Tx_CIU_8	0,868	0,854	23	1,0	Conventional Tx	Moist tamping w=5%	Rocha, 2010
	Tx_CIU_9	0,852	0,824	220	0,9	Conventional Tx	Moist tamping w=5%	
	Tx_CIU_10	0,871	0,859	31	1,0	Conventional Tx	Moist tamping w=5%	
	Tx_CIU_11	0,866	0,830	99	1,0	Conventional Tx	Moist tamping w=5%	
	Tx_CIU_12	0,841	0,805	400	1,0	Conventional Tx	Moist tamping w=5%	
	Tx_CIU_13	0,867	0,797	1001	1,0	Conventional Tx	Moist tamping w=5%	
	Tx_CIU_14	0,809	0,811	15	1,0	Conventional Tx	Moist tamping w=5%	
	Tx_CK_0U_6	0,871	0,779	1451	0,4	Conventional Tx	Moist tamping w=5%	
	Tx_CIU_15	0,783	0,746	529	1,0	Conventional Tx	Moist tamping w=5%	Present research
	Tx_CIU_16	0,799	0,734	1503	1,0	Conventional Tx	Moist tamping w=5%	
	Tx_CK_0U_7	0,833	0,823	13	0,4	Conventional Tx	Moist tamping w=5%	

Table 6.3: List of the monotonic triaxial tests performed with Coimbra sand, complemented with previous researches (Abreu, 2012)

	Test ID	e_0	e_i	p'_i kPa	K_0	Equipment	Method of samples preparation	Author
COIMBRA SAND	Tx_CID_MT_1	0.617	0.607	20	1.0	Stress-path	Moist tamping w=5%	Abreu, 2012
	Tx_CID_MT_2	0.672	0.672	20	1.0	Stress-path	Moist tamping w=5%	
	Tx_CID_MT_3	0.607	0.610	50	1.0	Stress-path	Moist tamping w=5%	
	Tx_CID_MT_4	0.789	0.750	101	1.0	Stress-path	Moist tamping w=5%	
	Tx_CID_MT_5	0.621	0.611	400	1.0	Stress-path	Moist tamping w=5%	
	Tx_CID_MT_6	0.766	0.717	1002	1.0	Stress-path	Moist tamping w=5%	
	Tx_CID_MT_7	0.670	0.564	8010	1.0	High-pressure Tx	Moist tamping w=5%	
	Tx_CID_MT_8	0.645	0.559	9500	1.0	High-pressure Tx	Moist tamping w=5%	
	Tx_CIU_MT_1	0.718	0.693	100	1.0	Stress-path	Moist tamping w=5%	Present research
	Tx_CIU_MT_2	0.710	0.691	100	1.0	Stress-path	Moist tamping w=5%	Abreu, 2012
	Tx_CIU_MT_3	0.685	0.653	201	1.0	Stress-path	Moist tamping w=5%	Present research
	Tx_CIU_MT_4	0.661	0.635	400	1.0	Stress-path	Moist tamping w=5%	Abreu, 2012
	Tx_CIU_MT_5	0.499	0.534	400	1.0	Stress-path	Moist tamping w=5%	
	Tx_CIU_MT_6	0.659	0.629	400	1.0	Stress-path	Moist tamping w=5%	
	Tx_CIU_MT_7	0.641	0.601	900	1.0	Stress-path	Moist tamping w=5%	
	Tx_CIU_MT_8	0.641	0.615	1100	1.0	Stress-path	Moist tamping w=5%	
	Tx_CIU_MT_9	0.691	0.559	9500	1.0	Stress-path	Moist tamping w=5%	
	Tx_CIU_MT_10	0.716	0.658	698	1.0	Stress-path	Moist tamping w=5%	Present research
	Tx_CIU_MT_11	0.690	0.641	1242	1.0	Stress-path	Moist tamping w=5%	
	Tx_CIU_MT_12	0.670	0.624	2505	1.0	High-pressure Tx	Moist tamping w=5%	
	Tx_CID_PL_1	0.656	0.526	5091	1.0	High-pressure Tx	Dry pluviation	
	Tx_CID_PL_2	0.620	0.602	202	1.0	Stress-path	Dry pluviation	
	Tx_CIU_PL_1	0.638	0.631	50	1.0	Conventional Tx	Dry pluviation	
	Tx_CIU_PL_2	0.655	0.610	509	1.0	Stress-path	Dry pluviation	
	Tx_CIU_PL_3	0.651	0.627	251	1.0	Stress-path	Dry pluviation	
	Tx_CIU_PL_4	0.626	0.620	896	1.0	Stress-path	Dry pluviation	
	Tx_CIU_PL_5	0.739	0.715	92	1.0	Stress-path	Partially-wet pluviation w=0.8%	
	Tx_CIU_PL_6	0.718	0.703	79	1.0	Stress-path	Partially-wet pluviation w=0.8%	
	Tx_CIU_PL_7	0.724	0.664	498	1.0	Stress-path	Partially-wet pluviation w=0.8%	
	Tx_CIU_PL_8	0.753	0.647	596	1.0	Stress-path	Partially-wet pluviation w=0.8%	

Table 6.4: List of the monotonic triaxial tests performed with Coimbra sand with 20% of FC

	Test ID	e_0	e_i	p'_i kPa	K_0	Equipment	Method of samples preparation	Author
COIMBRA 20% FC	Tx_CID_1	0.524	0.474	399	1	Conventional Tx cell	Dry pluviation	Present research
	Tx_CID_2	0.515	0.385	9448	1	High-pressure Tx cell	Dry pluviation	
	Tx_CIU_1	0.630	0.509	94	1	High-pressure Tx cell	Dry pluviation	
	Tx_CIU_2	0.505	0.399	9096	1	High-pressure Tx cell	Dry pluviation	

Table 6.5: List of the monotonic triaxial tests performed with Coimbra sand with 40% of FC

	Test ID	e_0	e_i	p'_i kPa	K_0	Equipment	Method of samples preparation	Author
COIMBRA 40% FC	Tx_CID_1	0.462	0.405	702	1	Conventional Tx cell	Dry pluviation	Present research
	Tx_CID_2	0.365	0.283	9200	1	High-pressure Tx cell	Dry pluviation	

Table 6.6: List of the triaxial tests performed with Osorio sand, complemented with previous researches (Festugato, 2008; Consoli et al., 2012; Oliveira, 2014)

	Test ID	e_0	e_i	p'_i kPa	K_0	Equipment	Method of samples preparation	Author
OSORIO SAND	Tx_CID_1	0.869	0.803	41	1	Conventional Tx	Moist tamping	Present research
	Tx_CID_2	0.861	0.796	25	1	Conventional Tx	Moist tamping	
	Tx_CID_3	0.815	0.795	15	1	Conventional Tx	Moist tamping	
	Tx_CID_4	0.783	0.697	704	1	Conventional Tx	Moist tamping	
	Tx_CID_5	0.852	0.758	450	1	Conventional Tx	Moist tamping	
	Tx_CID_6	0.749	0.749	20	1	Conventional Tx	Moist tamping	
	Tx_CID_7	0.717	0.582	9330	1	High-pressure Tx	Moist tamping	Oliveira, 2014
	Tx_CID_8	0.737	0.652	730	1	Conventional Tx	Moist tamping	Present research
	Tx_CID_9	0.785	0.706	1284	1	Conventional Tx	Moist tamping	
	Tx_CID_10	0.748	0.680	200	1	Conventional Tx	Moist tamping	Festugato, 2008
	Tx_CID_11	0.752	0.686	100	1	Conventional Tx	Moist tamping	
	Tx_CID_12	0.756	0.693	50	1	Conventional Tx	Moist tamping	
	Tx_CID_13	0.634	0.568	200	1	Conventional Tx	Moist tamping	Consoli et al., 2012
	Tx_CID_14	0.633	0.570	100	1	Conventional Tx	Moist tamping	
	Tx_CID_15	0.637	0.576	20	1	Conventional Tx	Moist tamping	
	Tx_CIU_1	0.830	0.769	100	1	Conventional Tx	Moist tamping	Present research
	Tx_CIU_2	0.864	0.802	50	1	Conventional Tx	Moist tamping	
	Tx_CIU_3	0.857	0.776	25	1	Conventional Tx	Moist tamping	
	Tx_CIU_4	0.834	0.787	100	1	Conventional Tx	Moist tamping	
	Tx_CIU_5	0.873	0.785	199	1	Conventional Tx	Moist tamping	
	Tx_CIU_6	0.863	0.749	299	1	Conventional Tx	Moist tamping	
	Tx_CIU_7	0.867	0.766	600	1	Conventional Tx	Moist tamping	
	Tx_CIU_8	0.830	0.746	1200	1	Conventional Tx	Moist tamping	
	Tx_CIU_9	0.850	0.758	600	1	Conventional Tx	Moist tamping	
	Tx_CIU_10	0.834	0.770	600	1	Conventional Tx	Moist tamping	
	Tx_CIU_11	0.848	0.794	132	0	Conventional Tx	Moist tamping	
	Tx_CIU_12	0.744	0.719	301	1	Conventional Tx	Moist tamping	
	$Tx_{q=constant}_CK_0D_1$	0.914	0.804	63	1	Conventional Tx	Moist tamping	
	$Tx_{q=constant}_CK_0D_2$	0.902	0.831	33	1	Conventional Tx	Moist tamping	
	$Tx_{q=constant}_CK_0D_3$	0.848	0.810	36	1	Conventional Tx	Moist tamping	

Table 6.7: List of the triaxial tests performed with Mixture, complemented with previous researches (Oliveira, 2014)

	Test ID	e_0	e_i	p'_i kPa	K_0	Equipment	Method of samples preparation	Author
MIXTURE	Tx_CID_1	0.897	0.777	40	1	Conventional Tx	Moist tamping w=8.25%	Present research
	Tx_CID_2	0.932	0.646	51	1	Conventional Tx	Moist tamping w=8.25%	
	Tx_CID_3	0.946	0.703	26	1	Conventional Tx	Moist tamping w=8.25%	
	Tx_CID_4	0.911	0.604	400	1	Conventional Tx	Moist tamping w=8.25%	
	Tx_CID_5	0.832	0.617	221	1	Conventional Tx	Moist tamping w=8.25%	
	Tx_CID_6	1.014	0.561	800	1	Conventional Tx	Moist tamping w=8.25%	
	Tx_CID_7	0.892	0.658	100	1	Conventional Tx	Moist tamping w=8.25%	
	Tx_CID_8	0.945	0.651	100	1	Conventional Tx	Moist tamping w=8.25%	
	Tx_CID_9	0.889	0.752	10	1	Conventional Tx	Moist tamping w=8.25%	
	Tx_CID_10	0.937	0.675	50	1	Conventional Tx	Moist tamping w=8.25%	
	Tx_CID_11	0.905	0.636	299	1	Conventional Tx	Moist tamping w=8.25%	
	Tx_CID_12	0.834	0.618	151	1	Conventional Tx	Moist tamping w=8.25%	
	Tx_CID_13	0.903	0.572	597	1	Conventional Tx	Moist tamping w=8.25%	Oliveira, 2014
	Tx_CID_14	0.932	0.587	602	1	Conventional Tx	Moist tamping w=8.25%	
	Tx_CID_15	0.481	0.406	9397	1	High-pressure Tx	Moist tamping w=8.25%	
	Tx_CID_16	0.571	0.450	3024	1	High-pressure Tx	Moist tamping w=8.25%	Present research
	Tx_CIU_1	0.800	0.663	50	1	Conventional Tx	Moist tamping w=8.25%	
	Tx_CIU_2	0.942	0.611	200	1	Conventional Tx	Moist tamping w=8.25%	
	Tx_CIU_3	1.042	0.671	25	1	Conventional Tx	Moist tamping w=8.25%	
	Tx_CIU_4	0.991	0.575	298	1	Conventional Tx	Moist tamping w=8.25%	
	Tx_CIU_5	0.954	0.578	399	1	Conventional Tx	Moist tamping w=8.25%	
	Tx_CIU_6	0.937	0.534	600	1	Conventional Tx	Moist tamping w=8.25%	
	Tx_CIU_7	0.953	0.541	571	0	Conventional Tx	Moist tamping w=8.25%	
	Tx_CIU_8	0.978	0.603	790	1	Conventional Tx	Moist tamping w=8.25%	
	Tx_CIU_9	0.880	0.536	999	1	Conventional Tx	Moist tamping w=8.25%	Oliveira, 2014
	Tx_CIU_10	1.001	0.608	220	1	Conventional Tx	Moist tamping w=8.25%	
	$Tx_{q=constant}_CK_0D_1$	0.821	0.697	38	1	Conventional Tx	Moist tamping w=8.25%	Present research
	$Tx_{q=constant}_CK_0D_2$	0.801	0.670	75	1	Conventional Tx	Moist tamping w=8.25%	
	$Tx_{q=constant}_CK_0D_3$	0.788	0.685	18	1	Conventional Tx	Moist tamping w=8.25%	
	$Tx_{q=constant}_CK_0D_4$	0.653	0.631	34	1	Conventional Tx	Moist tamping w=8.25%	
	$Tx_{p'=constant}_CID_1$	0.840	0.606	200	1	Stress-path	Moist tamping w=8.25%	Courtesy of LabGeo
	$Tx_{p'=diminishing}_CID_1$	0.872	0.650	101	1	Stress-path	Moist tamping w=8.25%	
	$Tx_{p'=diminishing}_CID_2$	0.868	0.646	50	1	Stress-path	Moist tamping w=8.25%	

Table 6.8: List of the monotonic triaxial tests performed with Silt, complemented with previous researches (Bedin, 2010; Silva, 2010) – part 1

	Test ID	e_0	e_i	p'_i kPa	K_0	Equipment	Method of samples preparation	Author
SILT	Tx_CID_1	1.255	0.809	16	1.0	Conventional Tx	Moist tamping w=11.5%	Bedin, 2010
	Tx_CID_2	1.255	0.726	99	1.0	Conventional Tx	Moist tamping w=11.5%	
	Tx_CID_3	1.285	0.834	19	1.0	Conventional Tx	Moist tamping w=11.5%	Silva, 2010
	Tx_CID_4	1.282	0.697	403	1.0	Conventional Tx	Moist tamping w=11.5%	
	Tx_CID_5	1.203	0.647	404	1.0	Conventional Tx	Moist tamping w=11.5%	Present research
	Tx_CID_6	1.195	0.634	804	1.0	Conventional Tx	Moist tamping w=11.5%	
	Tx_CID_7	0.602	0.501	7408	1.0	High-pressure Tx	Moist tamping w=11.5%	
	Tx_CID_8	1.033	0.763	41	1.0	Conventional Tx	Moist tamping w=11.5%	
	Tx_CID_9	1.112	0.777	30	1.0	Conventional Tx	Moist tamping w=11.5%	
	Tx_CIU_1	1.255	0.810	15	1.0	Conventional Tx	Moist tamping w=11.5%	Bedin, 2010
	Tx_CIU_2	1.244	0.767	30	1.0	Conventional Tx	Moist tamping w=11.5%	
	Tx_CIU_3	1.244	0.744	50	1.0	Conventional Tx	Moist tamping w=11.5%	
	Tx_CIU_4	1.244	0.718	99	1.0	Conventional Tx	Moist tamping w=11.5%	
	Tx_CIU_5	1.244	0.686	201	1.0	Conventional Tx	Moist tamping w=11.5%	
	Tx_CIU_6	1.212	0.649	699	1.0	Conventional Tx	Moist tamping w=11.5%	
	Tx_CIU_7	1.212	0.626	1199	1.0	Conventional Tx	Moist tamping w=11.5%	
	Tx_CIU_8	1.213	0.778	30	1.0	Conventional Tx	Moist tamping w=11.5%	
	Tx_CIU_9	1.208	0.718	70	1.0	Conventional Tx	Moist tamping w=11.5%	
	Tx_CIU_10	1.218	0.734	110	1.0	Conventional Tx	Moist tamping w=11.5%	
	Tx_CIU_11	1.218	0.707	220	1.0	Conventional Tx	Moist tamping w=11.5%	
	Tx_CIU_12	1.214	0.695	265	1.0	Conventional Tx	Moist tamping w=11.5%	
	Tx_CIU_13	1.218	0.679	342	1.0	Conventional Tx	Moist tamping w=11.5%	
	Tx_CIU_14	1.211	0.661	394	1.0	Conventional Tx	Moist tamping w=11.5%	
	Tx_CK$_0$U_1	1.127	0.755	38	0.5	Stress-path	Moist tamping w=11.5%	Present research
	Tx_CIU_15	1.274	0.726	101	1.0	Conventional Tx	Moist tamping w=11.5%	Silva, 2010
	Tx_CIU_16	1.303	0.793	20	1.0	Conventional Tx	Moist tamping w=11.5%	
	Tx_CIU_17	1.224	0.608	1499	1.0	Conventional Tx	Moist tamping w=11.5%	Present research
	Tx_CIU_18	1.224	0.844	20	1.0	Conventional Tx	Moist tamping w=11.5%	
	Tx_CIU_19	1.004	0.600	401	1.0	Conventional Tx	Moist tamping w=11.5%	
	Tx_CIU_20	1.006	0.630	499	1.0	Conventional Tx	Moist tamping w=11.5%	
	Tx_CIU_21	1.278	0.756	50	1.0	Conventional Tx	Moist tamping w=11.5%	Silva, 2010
	Tx_CIU_22	1.144	0.678	298	1.0	Stress-path	Moist tamping w=11.5%	Present research
	Tx_CIU_23	1.043	0.702	197	1.0	Stress-path	Moist tamping w=11.5%	
	Tx_CIU_24	1.098	0.658	400	1.0	Conventional Tx	Moist tamping w=11.5%	
	Tx_CIU_25	1.125	0.650	701	1.0	Conventional Tx	Moist tamping w=11.5%	Courtesy of LabGeo
	Tx_CIU_26	1.127	0.617	1185	1.0	Conventional Tx	Moist tamping w=11.5%	
	Tx_CIU_27	0.000	0.000	0	0.0	Conventional Tx	Moist tamping w=11.5%	

Table 6.9: List of the triaxial tests performed with Silt – part 2

	Test ID	e_0	e_i	p'_i kPa	K_0	Equipment	Method of samples preparation	Author
SILT	Tx_EK0U_1	1.127	0.800	77	0.6	Stress-path	Moist tamping w=11.5%	Present research
	Tx_EK0U_2	1.073	0.772	46	0.4	Stress-path	Moist tamping w=11.5%	
	Tx_EK0U_3	1.076	0.786	76	0.6	Stress-path	Moist tamping w=11.5%	
	Tx_EK0U_4	1.192	0.782	128	0.5	Stress-path	Moist tamping w=11.5%	
	$Tx_{q=constant}_CK_0D_1$	1.251	0.751	39	0.5	Conventional Tx	Moist tamping w=11.5%	
	$Tx_{q=constant}_CK_0D_2$	1.189	0.691	133	0.5	Conventional Tx	Moist tamping w=11.5%	
	$Tx_{q=constant}_CK_0D_3$	1.256	0.711	131	0.5	Conventional Tx	Moist tamping w=11.5%	
	$Tx_{q=constant}_CK_0D_4$	1.205	0.648	269	0.5	Conventional Tx	Moist tamping w=11.5%	
	$Tx_{q=constant}_CK_0D_5$	1.191	0.691	79	0.5	Conventional Tx	Moist tamping w=11.5%	
	$Tx_{q=constant}_CK_0D_6$	1.191	0.733	35	0.6	Conventional Tx	Moist tamping w=11.5%	
	$Tx_{q=constant}_CK_0D_7$	1.194	0.737	72	0.7	Conventional Tx	Moist tamping w=11.5%	
	$Tx_{q=constant}_CK_0D_8$	1.178	0.722	35	0.8	Conventional Tx	Moist tamping w=11.5%	
	$Tx_{q=constant}_CK_0D_9$	1.246	0.728	44	0.8	Conventional Tx	Moist tamping w=11.5%	
	$Tx_{q=constant}_CK_0D_10$	1.249	0.778	76	0.8	Conventional Tx	Moist tamping w=11.5%	
	$Tx_{q=constant}_CK_0D_11$	1.176	0.715	39	0.5	Conventional Tx	Moist tamping w=11.5%	
	$Tx_{q=constant}_CK_0D_12$	1.232	0.717	79	0.5	Conventional Tx	Moist tamping w=11.5%	
	$Tx_{q=constant}_CK_0D_13$	1.176	0.690	79	0.5	Conventional Tx	Moist tamping w=11.5%	
	$Tx_{q=constant}_CK_0D_14$	1.212	0.677	64	0.8	Conventional Tx	Moist tamping w=11.5%	
	$Tx_{q=constant}_CK_0D_15$	1.249	0.706	117	0.7	Conventional Tx	Moist tamping w=11.5%	
	$Tx_{q=constant}_CK_0D_16$	1.266	0.751	130	0.8	Conventional Tx	Moist tamping w=11.5%	
	$Tx_{q=constant}_CK_0D_17$	1.261	0.798	89	0.7	Conventional Tx	Moist tamping w=11.5%	
	$Tx_{q=constant}_CK_0D_18$	1.241	0.685	136	0.6	Conventional Tx	Moist tamping w=11.5%	
	$Tx_{q=constant}_CK_0D_19$	1.211	0.761	36	0.7	Conventional Tx	Moist tamping w=11.5%	
	$Tx_{q=constant}_CK_0D_20$	1.195	0.751	30	0.9	Conventional Tx	Moist tamping w=11.5%	
	$Tx_{q=constant}_CK_0D_21$	1.158	0.771	32	0.7	Conventional Tx	Moist tamping w=11.5%	

Table 6.10: List of the triaxial tests performed with Gold tailings, complemented with previous researches (Bedin, 2010)

	Test ID	e_0	e_i	p'_i kPa	K_0	Equipment	Method of samples preparation	Author
GOLD TAILINGS	Tx_CID_1	1.333	1.014	15	1.0	Classic Tx	Moist tamping w=11.5%	Bedin, 2010
	Tx_CID_2	1.336	0.940	50	1.0	Classic Tx	Moist tamping w=11.5%	
	Tx_CID_3	1.336	0.907	100	1.0	Classic Tx	Moist tamping w=11.5%	
	Tx_CID_4	1.184	1.059	8	1.0	Classic Tx	Moist tamping w=11.5%	Courtesy of LabGeo
	Tx_CID_5	0.880	0.512	4675	1.0	Classic Tx	Moist tamping w=11.5%	
	Tx_CID_6	1.239	0.859	299	1.0	Classic Tx	Moist tamping w=11.5%	
	Tx_CID_7	0.851	0.461	9500	1.0	Classic Tx	Moist tamping w=11.5%	
	Tx_CIU_1	1.350	1.031	15	1.0	Classic Tx	Moist tamping w=11.5%	Bedin, 2010
	Tx_CIU_2	1.350	1.004	22	1.0	Classic Tx	Moist tamping w=11.5%	
	Tx_CIU_3	1.350	0.990	30	1.0	Classic Tx	Moist tamping w=11.5%	
	Tx_CIU_4	1.350	0.959	50	1.0	Classic Tx	Moist tamping w=11.5%	
	Tx_CIU_5	1.350	0.943	60	1.0	Classic Tx	Moist tamping w=11.5%	
	Tx_CIU_6	1.350	0.936	75	1.0	Classic Tx	Moist tamping w=11.5%	
	Tx_CIU_7	1.350	0.927	100	1.0	Classic Tx	Moist tamping w=11.5%	
	Tx_CIU_8	1.350	0.883	200	1.0	Classic Tx	Moist tamping w=11.5%	
	Tx_CIU_9	1.197	0.790	400	1.0	Classic Tx	Moist tamping w=11.5%	
	Tx_CIU_10	1.350	0.794	600	1.0	Classic Tx	Moist tamping w=11.5%	
	Tx_CIU_11	1.350	0.774	800	1.0	Classic Tx	Moist tamping w=11.5%	
	Tx_CIU_12	1.350	0.758	1000	1.0	Classic Tx	Moist tamping w=11.5%	
	Tx_CIU_13	1.350	0.735	1200	1.0	Classic Tx	Moist tamping w=11.5%	
	Tx_CIU_14	1.247	0.869	100	1.0	Classic Tx	Moist tamping w=11.5%	Courtesy of LabGeo
	Tx_CIU_15	1.334	0.903	100	1.0	Classic Tx	Moist tamping w=11.5%	
	Tx_CIU_16	1.267	0.843	299	1.0	Classic Tx	Moist tamping w=11.5%	
	$Tx_{p'=diminishing}$_CID_1	1.314	0.938	38	0.5	Bishop-Wesley	Moist tamping w=11.5%	
	$Tx_{p'=diminishing}$_CID_2	1.282	0.978	50	1.0	Bishop-Wesley	Moist tamping w=11.5%	
	$Tx_{p'=diminishing}$_CID_3	1.333	0.991	30	1.0	Bishop-Wesley	Moist tamping w=11.5%	
	$Tx_{p'=diminishing}$_CID_4	1.283	1.015	15	1.0	Bishop-Wesley	Moist tamping w=11.5%	
	$Tx_{p'=constant}$_CID_1	1.305	0.857	300	1.0	Bishop-Wesley	Moist tamping w=11.5%	
	$Tx_{p'=diminishing}$_CID_5	1.256	0.869	300	1.0	Bishop-Wesley	Moist tamping w=11.5%	

Table 6.11: List of the cyclic triaxial tests performed with Algeria sand, complemented with previous researches (Fonseca, 2009; Rocha, 2010) – part 1

	Test ID	e_0	e_i	p'_i kPa	K_0	$\tau/(2x\sigma'_{h0})$	Equipment	Method of samples preparation	Author
ALGERIA SAND	CTx_CK$_0$U_1	0.851	0.856	94	0.6	0.09	Conventional Tx	Moist tamping w=5%	Fonseca, 2009
	CTx_CK$_0$U_2	0.837	0.825	133	0.5	0.12	Conventional Tx	Moist tamping w=5%	
	CTx_CK$_0$U_3	0.858	0.836	267	0.5	0.12	Conventional Tx	Moist tamping w=5%	
	CTx_CK$_0$U_4	0.863	0.855	67	0.5	0.11	Conventional Tx	Moist tamping w=5%	
	CTx_CK$_0$U_5	0.884	0.846	132	0.5	0.14	Conventional Tx	Moist tamping w=5%	
	CTx_CK$_0$U_6	0.853	0.834	31	0.5	0.11	Conventional Tx	Moist tamping w=5%	
	CTx_CK$_0$U_7	0.865	0.855	34	0.5	0.05	Conventional Tx	Moist tamping w=5%	
	CTx_CK$_0$U_8	0.847	0.821	133	0.5	0.06	Conventional Tx	Moist tamping w=5%	Rocha, 2010
	CTx_CK$_0$U_9	0.846	0.817	130	0.5	0.06	Conventional Tx	Moist tamping w=5%	
	CTx_CIU_1	0.845	0.814	202	1.0	0.12	Conventional Tx	Moist tamping w=5%	
	CTx_CIU_2	0.852	0.830	48	0.9	0.14	Conventional Tx	Moist tamping w=5%	
	CTx_CK$_0$U_2	0.760	0.753	132	0.5	0.07	Conventional Tx	Moist tamping w=5%	
	CTx_CK$_0$U_13	0.764	0.763	40	0.3	0.05	Conventional Tx	Moist tamping w=5%	
	CTx_CK$_0$U_14	0.805	0.785	132	0.5	0.07	Conventional Tx	Moist tamping w=5%	
	CTx_CK$_0$U_15	0.803	0.799	31	0.5	0.05	Conventional Tx	Moist tamping w=5%	
	CTx_CK$_0$U_16	0.813	0.807	20	0.5	0.03	Conventional Tx	Moist tamping w=5%	
	CTx_CK$_0$U_17	0.784	0.779	28	0.5	0.06	Conventional Tx	Moist tamping w=5%	Present research
	CTx_CK$_0$U_18	0.793	0.785	27	0.5	0.23	Conventional Tx	Moist tamping w=5%	
	CTx_CK$_0$U_19	0.819	0.803	25	0.5	0.10	Conventional Tx	Moist tamping w=5%	
	CTx_CK$_0$U_20	0.804	0.796	26	0.5	0.12	Conventional Tx	Moist tamping w=5%	
	CTx_CK$_0$U_21	0.833	0.816	29	0.5	0.07	Conventional Tx	Moist tamping w=5%	
	CTx_CK$_0$U_22	0.817	0.802	26	0.5	0.13	Conventional Tx	Moist tamping w=5%	
	CTx_CK$_0$U_23	0.791	0.783	28	0.5	0.12	Conventional Tx	Moist tamping w=5%	
	CTx_CK$_0$U_24	0.791	0.782	25	0.5	0.46	Conventional Tx	Moist tamping w=5%	
	CTx_CK$_0$U_25	0.762	0.758	27	0.5	0.34	Conventional Tx	Moist tamping w=5%	
	CTx_CK$_0$U_26	0.771	0.764	26	0.5	0.23	Conventional Tx	Moist tamping w=5%	
	CTx_CK$_0$U_27	0.761	0.753	27	0.5	0.28	Conventional Tx	Moist tamping w=5%	
	CTx_CK$_0$U_28	0.751	0.738	82	0.5	0.18	Conventional Tx	Moist tamping w=5%	
	CTx_CK$_0$U_29	0.745	0.732	86	0.5	0.17	Conventional Tx	Moist tamping w=5%	
	CTx_CK$_0$U_30	0.724	0.715	81	0.5	0.32	Conventional Tx	Moist tamping w=5%	
	CTx_CK$_0$U_31	0.724	0.767	79	0.5	0.30	Conventional Tx	Moist tamping w=5%	
	CTx_CK$_0$U_32	0.775	0.758	80	0.5	0.16	Conventional Tx	Moist tamping w=5%	
	CTx_CK$_0$U_33	0.748	0.736	67	0.5	0.22	Conventional Tx	Moist tamping w=5%	
	CTx_CK$_0$U_34	0.772	0.756	68	0.5	0.18	Conventional Tx	Moist tamping w=5%	
	CTx_CK$_0$U_35	0.749	0.736	66	0.5	0.08	Conventional Tx	Moist tamping w=5%	
	CTx_CK$_0$U_36	0.795	0.778	80	0.5	0.19	Conventional Tx	Moist tamping w=5%	
	CTx_CK$_0$U_37	0.771	0.763	26	0.5	0.22	Conventional Tx	Moist tamping w=5%	
	CTx_CK$_0$U_38	0.757	0.752	28	0.5	0.16	Conventional Tx	Moist tamping w=5%	
	CTx_CK$_0$U_39	0.729	0.728	26	0.5	0.22	Conventional Tx	Moist tamping w=5%	
	CTx_CK$_0$U_40	0.782	0.776	28	0.5	0.21	Conventional Tx	Moist tamping w=5%	
	CTx_CK$_0$U_41	0.734	0.732	27	0.5	0.23	Conventional Tx	Moist tamping w=5%	

Table 6.12: List of the cyclic triaxial tests performed with Algeria sand, complemented with previous researches – part 2

	Test ID	e_0	e_i	p'_i kPa	K_0	$\tau/(2x\sigma'_{h0})$	Equipment	Method of samples preparation	Author
ALGERIA SAND	CTx_CK$_0$U_42	0.735	0.733	27	0.5	0.27	Conventional Tx	Moist tamping w=5%	Present research
	CTx_CK$_0$U_43	0.733	0.732	26	0.5	0.32	Conventional Tx	Moist tamping w=5%	
	CTx_CK$_0$U_44	0.739	0.738	26	0.5	0.40	Conventional Tx	Moist tamping w=5%	
	CTx_CK$_0$U_45	0.781	0.776	27	0.5	0.49	Conventional Tx	Moist tamping w=5%	
	CTx_CK$_0$U_46	0.742	0.732	69	0.5	0.33	Conventional Tx	Moist tamping w=5%	
	CTx_CK$_0$U_47	0.758	0.750	54	0.5	0.43	Conventional Tx	Moist tamping w=5%	
	CTx_CK$_0$U_48	0.760	0.756	54	0.5	0.27	Conventional Tx	Moist tamping w=5%	
	CTx_CK$_0$U_49	0.709	0.704	439	0.6	0.50	Conventional Tx	Moist tamping w=5%	
	CTx_CK$_0$U_50	0.693	0.695	868	0.5	0.54	Conventional Tx	Moist tamping w=5%	
	CTx_CK$_0$U_51	0.703	0.675	866	0.5	0.64	Conventional Tx	Moist tamping w=5%	
	CTx_CK$_0$U_52	0.682	0.644	1225	0.4	0.42	Conventional Tx	Moist tamping w=5%	
	CTx_CK$_0$U_53	0.857	0.762	1064	0.5	0.23	Conventional Tx	Moist tamping w=5%	
	CTx_CK$_0$U_54	0.816	0.745	1066	0.5	0.20	Conventional Tx	Moist tamping w=5%	
	CTx_CK$_0$U_55	0.844	0.791	398	0.5	0.20	Conventional Tx	Moist tamping w=5%	
	CTx_CK$_0$U_56	0.802	0.774	396	0.5	0.15	Conventional Tx	Moist tamping w=5%	
	CTx_CK$_0$U_57	0.913	0.828	398	0.5	0.12	Conventional Tx	Moist tamping w=5%	
	CTx_CK$_0$U_58	0.869	0.812	399	0.5	0.16	Conventional Tx	Moist tamping w=5%	
	CTx_CK$_0$U_59	0.744	0.710	401	0.5	0.34	Conventional Tx	Moist tamping w=5%	
	CTx_CIU_3	0.761	0.756	40	0.9	0.13	Conventional Tx	Moist tamping w=5%	Present research
	CTx_CIU_4	0.778	0.769	38	0.9	0.14	Conventional Tx	Moist tamping w=5%	
	CTx_CIU_5	0.790	0.781	39	0.9	0.17	Conventional Tx	Moist tamping w=5%	
	CTx_CIU_6	0.787	0.774	40	1.0	0.23	Conventional Tx	Moist tamping w=5%	
	CTx_CIU_7	0.770	0.765	40	0.9	0.25	Conventional Tx	Moist tamping w=5%	
	CTx_CIU_8	0.819	0.804	40	0.9	0.19	Conventional Tx	Moist tamping w=5%	
	CTx_CIU_9	0.772	0.764	38	1.0	0.22	Conventional Tx	Moist tamping w=5%	
	CTx_CIU_10	0.733	0.730	38	0.9	0.29	Conventional Tx	Moist tamping w=5%	
	CTx_CIU_11	0.744	0.741	39	0.9	0.31	Conventional Tx	Moist tamping w=5%	
	CTx_CIU_12	0.793	0.786	40	1.0	0.32	Conventional Tx	Moist tamping w=5%	
	CTx_CIU_13	0.728	0.725	40	1.0	0.42	Conventional Tx	Moist tamping w=5%	
	CTx_CIU_14	0.759	0.755	39	1.0	0.43	Conventional Tx	Moist tamping w=5%	
	CTx_CIU_15	0.721	0.723	41	1.0	0.36	Conventional Tx	Moist tamping w=5%	
	CTx_CIU_16	0.806	0.791	38	0.9	0.22	Conventional Tx	Moist tamping w=5%	
	CTx_CIU_17	0.820	0.803	35	0.9	0.22	Conventional Tx	Moist tamping w=5%	
	CTx_CIU_18	0.848	0.784	690	0.7	0.27	Conventional Tx	Moist tamping w=5%	

Table 6.13: List of the cyclic triaxial tests performed with Coimbra sand, complemented with previous researches (Abreu, 2012)

	Test ID	e_0	e_i	p'_i kPa	K_0	$\tau/(2x\sigma'h0)$	Equipment	Method of samples preparation	Author
COIMBRA SAND	CTx_CK$_0$U_MT_1	0.680	0.680	26	0.5	0.2	Conventional Tx	Moist tamping w=5%	Abreu, 2012
	CTx_CK$_0$U_MT_2	0.628	0.628	26	0.5	0.4	Conventional Tx	Moist tamping w=5%	
	CTx_CK$_0$U_MT_3	0.624	0.624	26	0.5	0.3	Conventional Tx	Moist tamping w=5%	
	CTx_CK$_0$U_MT_4	0.658	0.658	68	0.4	0.2	Conventional Tx	Moist tamping w=5%	
	CTx_CK$_0$U_MT_5	0.601	0.601	67	0.5	0.6	Conventional Tx	Moist tamping w=5%	
	CTx_CK$_0$U_MT_6	0.742	0.742	65	0.5	0.2	Conventional Tx	Moist tamping w=5%	
	CTx_CK$_0$U_MT_7	0.737	0.737	67	0.5	0.2	Conventional Tx	Moist tamping w=5%	
	CTx_CK$_0$U_MT_8	0.709	0.690	72	0.5	0.1	Conventional Tx	Moist tamping w=5%	Present research
	CTx_CK$_0$U_MT_9	0.756	0.726	73	0.5	0.1	Conventional Tx	Moist tamping w=5%	
	CTx_CK$_0$U_MT_10	0.601	0.598	72	0.5	0.5	Conventional Tx	Moist tamping w=5%	
	CTx_CK$_0$U_MT_11	0.642	0.637	72	0.5	0.6	Conventional Tx	Moist tamping w=5%	
	CTx_CK$_0$U_MT_12	0.643	0.638	72	0.5	0.8	Conventional Tx	Moist tamping w=5%	
	CTx_CK$_0$U_MT_13	0.639	0.632	67	0.5	1.0	Conventional Tx	Moist tamping w=5%	
	CTx_CK$_0$U_MT_14	0.698	0.680	72	0.5	0.1	Conventional Tx	Moist tamping w=5%	
	CTx_CK$_0$U_MT_15	0.701	0.679	72	0.5	0.1	Conventional Tx	Moist tamping w=5%	
	CTx_CK$_0$U_MT_16	0.700	0.681	72	0.5	0.0	Conventional Tx	Moist tamping w=5%	
	CTx_CK$_0$U_PL_1	0.682	0.672	72	0.5	0.2	Conventional Tx	Moist tamping w=5%	
	CTx_CK$_0$U_PL_2	0.722	0.704	72	0.5	0.2	Conventional Tx	Moist tamping w=5%	
	CTx_CK$_0$U_PL_3	0.708	0.694	78	0.5	0.5	Conventional Tx	Moist tamping w=5%	
	CTx_CK$_0$U_PL_4	0.623	0.623	66	0.5	0.4	Conventional Tx	Moist tamping w=5%	
	CTx_CK$_0$U_PL_5	0.672	0.663	68	0.5	0.1	Conventional Tx	Moist tamping w=5%	
	CTx_CK$_0$U_PL_6	0.659	0.651	69	0.5	0.3	Conventional Tx	Moist tamping w=5%	
	CTx_CK$_0$U_PL_7	0.727	0.708	78	0.5	0.6	Conventional Tx	Moist tamping w=5%	
	CTx_CK$_0$U_PL_8	0.630	0.630	78	0.5	0.7	Conventional Tx	Moist tamping w=5%	
	CTx_CK$_0$U_PL_9	0.656	0.651	77	0.5	0.5	Conventional Tx	Moist tamping w=5%	
	CTx_CK$_0$U_PL_10	0.629	0.628	78	0.5	0.7	Conventional Tx	Moist tamping w=5%	
	CTx_CK$_0$U_PL_11	0.633	0.634	73	0.5	0.8	Conventional Tx	Moist tamping w=5%	
	CTx_CK$_0$U_PL_12	0.671	0.662	67	0.5	0.6	Conventional Tx	Moist tamping w=5%	
	CTx_CK$_0$U_PL_13	0.623	0.624	68	0.5	0.5	Conventional Tx	Moist tamping w=5%	

Table 6.14: List of the direct simples shear tests performed with Algeria sand

	Test ID	e_0	e_i	σ'_{vi} kPa	τ/σ'_{v0}	Method of samples preparation	Specimen Saturation Condition	Author
ALGERIA SAND	CDSS_2_100	0.638	0.605	100	0.20	Moist tamping w=5%	Saturated	Present research
	CDSS_3_100	0.924	0.847	100	0.12	Moist tamping w=5%	Saturated	
	CDSS_4_100	0.900	0.848	100	0.10	Moist tamping w=5%	Saturated	
	CDSS_5_100	0.900	0.816	100	0.08	Moist tamping w=5%	Saturated	
	CDSS_6_100	0.690	0.690	100	0.30	Moist tamping w=5%	Saturated	
	CDSS_7_100	0.735	0.689	100	0.22	Moist tamping w=5%	Saturated	
	CDSS_8_100	0.735	0.698	100	0.17	Moist tamping w=5%	Saturated	
	CDSS_10_100	0.734	0.690	100	0.15	Moist tamping w=5%	Dry	
	CDSS_11_100	0.835	0.775	100	0.08	Moist tamping w=5%	Dry	
	CDSS_12_100	0.648	0.606	100	0.17	Moist tamping w=5%	Saturated	
	CDSS_13_100	0.650	0.615	100	0.17	Moist tamping w=5%	Dry	
	CDSS_14_100	0.652	0.604	100	0.14	Moist tamping w=5%	Saturated	
	CDSS_15_100	0.647	0.616	100	0.14	Moist tamping w=5%	Dry	
	CDSS_16_100	0.741	0.693	100	0.07	Moist tamping w=5%	Saturated	
	CDSS_17_100	0.718	0.680	100	0.07	Moist tamping w=5%	Dry	
	CDSS_18_100	0.649	0.613	100	0.19	Moist tamping w=5%	Saturated	
	CDSS_19_100	0.651	0.615	100	0.19	Moist tamping w=5%	Dry	
	CDSS_20_100	0.646	0.613	100	0.20	Moist tamping w=5%	Saturated	
	CDSS_21_100	0.646	0.618	100	0.22	Moist tamping w=5%	Dry	
	CDSS_22_100	0.646	0.615	100	0.21	Moist tamping w=5%	Saturated	
	CDSS_23_100	0.646	0.619	100	0.07	Moist tamping w=5%	Dry	
	CDSS_24_100	0.654	0.620	100	0.07	Moist tamping w=5%	Saturated	
	CDSS_26_100	0.933	0.863	100	0.04	Moist tamping w=5%	Saturated	
	CDSS_27_100	0.938	0.864	100	0.06	Moist tamping w=5%	Dry	
	CDSS_28_100	0.936	0.869	100	0.10	Moist tamping w=5%	Dry	
	CDSS_29_100	0.940	0.871	100	0.10	Moist tamping w=5%	Saturated	
	CDSS_30_100	0.745	0.706	100	0.16	Moist tamping w=5%	Saturated	
	CDSS_31_100	0.739	0.705	100	0.16	Moist tamping w=5%	Dry	
	CDSS_32_100	0.739	0.703	100	0.11	Moist tamping w=5%	Saturated	
	CDSS_33_100	0.744	0.714	100	0.10	Moist tamping w=5%	Saturated	
	CDSS_34_100	0.733	0.692	100	0.12	Moist tamping w=5%	Dry	
	CDSS_1_300	0.924	0.810	300	0.12	Moist tamping w=5%	Saturated	
	CDSS_2_300	0.924	0.833	300	0.10	Moist tamping w=5%	Saturated	
	CDSS_3_300	0.924	0.826	300	0.08	Moist tamping w=5%	Saturated	
	CDSS_4_300	0.733	0.669	300	0.18	Moist tamping w=5%	Saturated	
	CDSS_5_300	0.733	0.683	300	0.14	Moist tamping w=5%	Saturated	
	CDSS_6_300	0.733	0.683	300	0.09	Moist tamping w=5%	Saturated	
	CDSS_7_300	0.646	0.598	300	0.23	Moist tamping w=5%	Saturated	
	CDSS_8_300	0.646	0.605	300	0.20	Moist tamping w=5%	Saturated	
	CDSS_9_300	0.646	0.598	300	0.15	Moist tamping w=5%	Saturated	
	CDSS_10_300	0.646	0.605	300	0.18	Moist tamping w=5%	Saturated	
	DSS_1	0.939	0.829	100		Moist tamping w=5%	Saturated	
	DSS_2	0.646	0.619	100		Moist tamping w=5%	Saturated	
	DSS_3	0.758	0.699	200		Moist tamping w=5%	Saturated	
	DSS_4	0.922	0.832	300		Moist tamping w=5%	Saturated	

Table 6.15: List of the direct simples shear tests performed with Coimbra sand

	Test ID	e_0	e_i	σ'_{vi} kPa	τ/σ'_{v0}	Method of samples preparation	Specimen Saturation Condition	Author
ALGERIA SAND	CDSS_2_100	0.638	0.605	100	0.20	Moist tamping w=5%	Saturated	Present research
	CDSS_3_100	0.924	0.847	100	0.12	Moist tamping w=5%	Saturated	
	CDSS_4_100	0.900	0.848	100	0.10	Moist tamping w=5%	Saturated	
	CDSS_5_100	0.900	0.816	100	0.08	Moist tamping w=5%	Saturated	
	CDSS_6_100	0.690	0.690	100	0.30	Moist tamping w=5%	Saturated	
	CDSS_7_100	0.735	0.689	100	0.22	Moist tamping w=5%	Saturated	
	CDSS_8_100	0.735	0.698	100	0.17	Moist tamping w=5%	Saturated	
	CDSS_10_100	0.734	0.690	100	0.15	Moist tamping w=5%	Dry	
	CDSS_11_100	0.835	0.775	100	0.08	Moist tamping w=5%	Dry	
	CDSS_12_100	0.648	0.606	100	0.17	Moist tamping w=5%	Saturated	
	CDSS_13_100	0.650	0.615	100	0.17	Moist tamping w=5%	Dry	
	CDSS_14_100	0.652	0.604	100	0.14	Moist tamping w=5%	Saturated	
	CDSS_15_100	0.647	0.616	100	0.14	Moist tamping w=5%	Dry	
	CDSS_16_100	0.741	0.693	100	0.07	Moist tamping w=5%	Saturated	
	CDSS_17_100	0.718	0.680	100	0.07	Moist tamping w=5%	Dry	
	CDSS_18_100	0.649	0.613	100	0.19	Moist tamping w=5%	Saturated	
	CDSS_19_100	0.651	0.615	100	0.19	Moist tamping w=5%	Dry	
	CDSS_20_100	0.646	0.613	100	0.20	Moist tamping w=5%	Saturated	
	CDSS_21_100	0.646	0.618	100	0.22	Moist tamping w=5%	Dry	
	CDSS_22_100	0.646	0.615	100	0.21	Moist tamping w=5%	Saturated	
	CDSS_23_100	0.646	0.619	100	0.07	Moist tamping w=5%	Dry	
	CDSS_24_100	0.654	0.620	100	0.07	Moist tamping w=5%	Saturated	
	CDSS_26_100	0.933	0.863	100	0.04	Moist tamping w=5%	Saturated	
	CDSS_27_100	0.938	0.864	100	0.06	Moist tamping w=5%	Dry	
	CDSS_28_100	0.936	0.869	100	0.10	Moist tamping w=5%	Dry	
	CDSS_29_100	0.940	0.871	100	0.10	Moist tamping w=5%	Saturated	
	CDSS_30_100	0.745	0.706	100	0.16	Moist tamping w=5%	Saturated	
	CDSS_31_100	0.739	0.705	100	0.16	Moist tamping w=5%	Dry	
	CDSS_32_100	0.739	0.703	100	0.11	Moist tamping w=5%	Saturated	
	CDSS_33_100	0.744	0.714	100	0.10	Moist tamping w=5%	Saturated	
	CDSS_34_100	0.733	0.692	100	0.12	Moist tamping w=5%	Dry	
	CDSS_1_300	0.924	0.810	300	0.12	Moist tamping w=5%	Saturated	
	CDSS_2_300	0.924	0.833	300	0.10	Moist tamping w=5%	Saturated	
	CDSS_3_300	0.924	0.826	300	0.08	Moist tamping w=5%	Saturated	
	CDSS_4_300	0.733	0.669	300	0.18	Moist tamping w=5%	Saturated	
	CDSS_5_300	0.733	0.683	300	0.14	Moist tamping w=5%	Saturated	
	CDSS_6_300	0.733	0.683	300	0.09	Moist tamping w=5%	Saturated	
	CDSS_7_300	0.646	0.598	300	0.23	Moist tamping w=5%	Saturated	
	CDSS_8_300	0.646	0.605	300	0.20	Moist tamping w=5%	Saturated	
	CDSS_9_300	0.646	0.598	300	0.15	Moist tamping w=5%	Saturated	
	CDSS_10_300	0.646	0.605	300	0.18	Moist tamping w=5%	Saturated	
	DSS_1	0.939	0.829	100		Moist tamping w=5%	Saturated	
	DSS_2	0.646	0.619	100		Moist tamping w=5%	Saturated	
	DSS_3	0.758	0.699	200		Moist tamping w=5%	Saturated	
	DSS_4	0.922	0.832	300		Moist tamping w=5%	Saturated	

Chapter 7

Static Liquefaction

7.1 Introduction

Soil liquefaction phenomenon demands for constitutive laws to be used in numerical modeling while led to failure through any type of stress-path. Despite the geomechanics being already well understood and progressing rapidly, the limited available laboratorial results, performed with distinct initial state conditions and stress-paths, leaves some uncertainty on the relevancy of each effect. Chapters 7 and 8 aim to contribute for a comprehensive study of the geomechanical behavior of cohesionless soils, providing a linkage between some of the key factors contributing on the onset of instability.

After a brief introduction, in Chapter 5, of the materials studied in the scope of the present research, these chapters are exclusively addressed to a comprehensive study and analysis of the experimental results. For a better analysis the two chapters are separated according to the type of loading condition. Chapter 7 is exclusively dedicated to the tests performed under a monotonic (non-cyclic) loading, including not only the classical compression stress-paths, but also a set of stress-paths, under constant deviator stress (q = const.), under constant mean effective stress (p' = const.), and under decreasing mean effective stress (p' = decreasing), and a few set, for the silt, of undrained extension triaxial tests. The analysis and further evaluation of the tests subjected to cyclic shear is reserved for Chapter 8. Even considering the fact that the phenomena can be considered similar, flow liquefaction trigered under both monotonic and cyclic loading shall be separated according to the type of loading.

During this chapter each section is dedicated to each tested soil. The results of each material are presented and a careful evaluation of the soil behavior is made and displayed, basing on critical state theory. Aiming to perceive the better way to assess soil liquefaction potential, a set of empirical frameworks is presented, based on both stiffness and strength parameters. Then is made a

comparison between frameworks in order to understand its precision on predicting flow liquefaction triggered under non-cyclic shear conditions.

All triaxial test results were treated following the procedure presented in Chapter 6. Due to their large size, the tables with the final results can be found in Annex A, being the present chapter exclusively addressed to the final plots.

Finally, the last section is addressed to a comparison between the behaviors observed for each soil, pursuing the identification of the major factors controlling both CSL and SSL positioning, and liquefaction onset.

7.2 Algeria Sand

7.2.1 Basic Characterization

Algeria sand basic characterization was previously presented in Chapter 5. Despite the mineralogy not being investigated during this PhD, some performed electronic microscopies allowed to observe and distinguish a predominant quartz constitution (brighter particles) complemented with a minimum amount of feldspar (darker particles) (Figure 5.6). A resume of the basic physical characteristics of the soil, previously presented in Chapter 5, is summarized on table 7.1.

Table 7.1: Basic physical characterization of Algeria sand

ID	Unit Weight volume of solid particles	Unit Weight volume	Grain size distribution ASTM sieves			FC	Cu	Cc	Maximum and Minimum void ratio	
	γ_s	$\bar{\gamma}$	Nº20	Nº60	Nº200	%			e_{max}	e_{min}
	(kN/m^3)	(kN/m^3)	0.841 mm	0.250 mm	0.075 mm					
Algeria sand	27.0	14.7	99.9	24.5	0.2	0.2	1.76	0.97	0.89	0.531

7.2.2 Triaxial Tests

The set of triaxial tests performed with the Algeria sand covered a range of low to medium/high confining pressures, performed under both drained and undrained conditions. Algeria sand behavior under triaxial conditions was complemented with a drained high-pressure triaxial test. The

tests, performed under isotropic and anisotropic consolidation, allowed the definition of the ultimate states and the soil liquefaction potential.

7.2.2.1 Drained Triaxial Tests

The set of 11 drained triaxial tests exhibit a conventional stress-strain-volumetric behavior typical of cohesionless soils. Figure 7.1 shows that while the loose specimens exhibit a contractive behavior $\varepsilon_v > 0\%$, the specimens prepared with lower void ratios ($0.5 < e < 0.6$), Tx_CID_4 and Tx_CID_5, show a dilative behavior, ($\varepsilon_v < 0\%$). Obviously the dilative behavior is accompanied by a peak strength higher than its ultimate ultimate state, associated to the particles imbrications during the shear, before achieving its ultimate friction strength. These expected stress-strain-volumetric behaviors follow the CSSM theory, thus while loose specimens, i.e. on the wet side of the CSL, contract towards the CSL, dense specimens, i.e. on the dry side of the CSL, dilate towards it ultimate state, meaning it critical state.

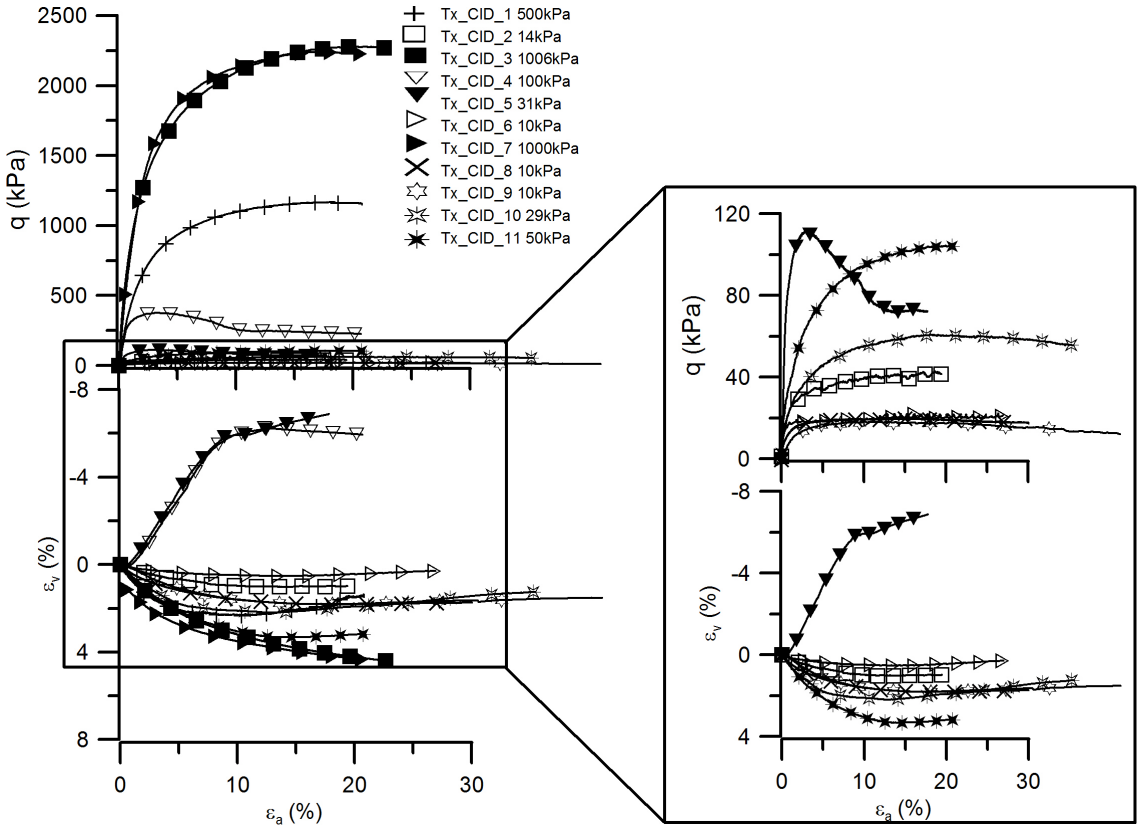


Figure 7.1: Stress-strain and volumetric-strain behavior of drained triaxial tests of Algeria sand

By analyzing carefully Figure 7.1, it can be observed that, among the loose prepared samples, the tests which exhibit a lower contraction are those tested under lower confining pressures. This succeeds as the tests are very near its critical state. In subsection 7.2.2.3 this will become clearer as the initial state can be compared with its ultimate state, defined by the CSL.

The test performed on the high-pressure triaxial cell, (Tx_CID_12), is shown in figure 7.2. Due to the high confining stress its representation is isolated for a better visibility. The Tx_CID_12 test was specially prepared by air pluviation, with the help of a funnel, which ensures an easier achievement of a lower void ratio than the moist tamping technique. While placing the soil inside the split mold it was also necessary to stir the sample with a metal rod, in order to better compact the soil. The necessity to achieve such a low void ratio for this particular test, because the blind cap of the chamber, as explained before, required a de-aired water percolation before closing the cell and proceed with the subsequent stages. This blind cap is required to ensure a proper seal of the specimen, preventing water to escape.

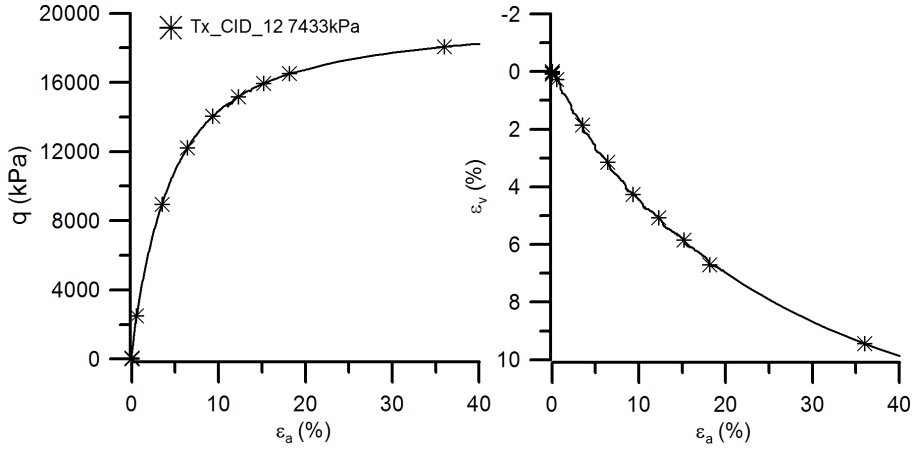


Figure 7.2: Stress-strain and strain-volumetric behavior of the high-pressure triaxial test Tx_CID_12

The high-pressure triaxial test, despite having an initial low void ratio, has achieved, after being consolidated, an initial state above the CSL, as can be concluded from the stress path and the contractive behavior exhibited during shear ($\varepsilon_v > 0\%$) (see Figure 7.2). Despite the test have finished with an axial strain of 20%, the Hyperbolic model was used to predict it behavior till 40% of axial strain. As can be observed in Figure 7.2, the volumetric strain does not stabilize even at 40% of axial strain, requirement necessary to define the critical state. This occurs as at high-pressures the soil evolves from its initial grain size distribution to a new grain size distribution. This process is commonly designated by grain crushing and had been widely referred in the literature (Konrad, 1998; Viana da Fonseca et al., 2011a; Muir Wood, 2008; Coop et al., 2004; Vilhar et al., 2013).

Figure 7.3 shows the initial grain size distribution (continuous line), common to all tests, and the grain size distribution at the end of the high-pressure triaxial test (dashed line). The grain size distribution shows that substantial changes occurred during the high-pressure triaxial test. The soil evolved from a monogranular curve to better graded soil, initially with a FC of 0.39%, to a FC of 14.51%.

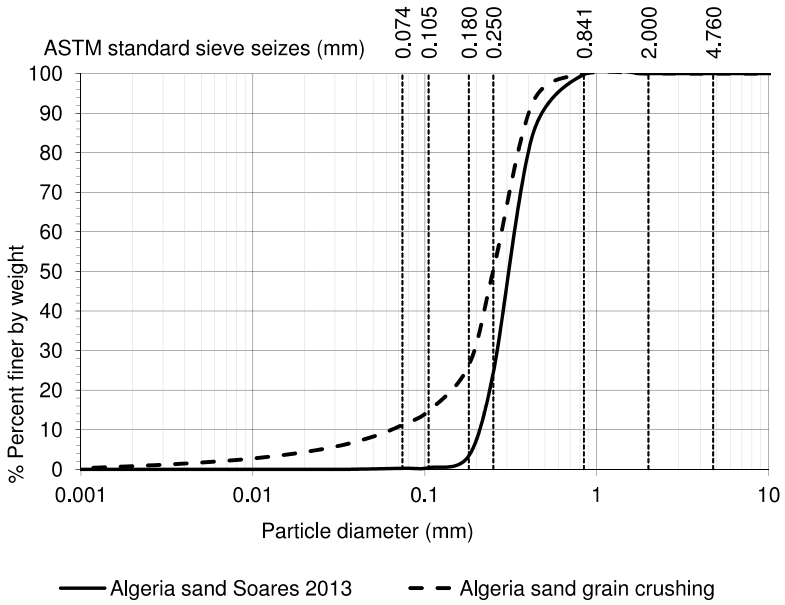


Figure 7.3: Evolution of the grain size distribution of the Tx_ CID_ 12 high-pressure triaxial test ($p_i^{'} = 7.5$ MPa)

7.2.2.2 Undrained Triaxial Tests

While the loose specimens, tested under drained compression triaxial, exhibited a typical contractive behavior, and the denser ones a dilative behavior, while tested under undrained conditions, the volumetric contraction leads to a generation of a positive pore pressure and the volumetric dilation is replaced by a generation of a negative pore pressure. Apart from tests Tx_ CIU_ 1, Tx_ CK_0U_ 4 and Tx_ CK_0U_6 which exhibited negative pore-pressure, all the other tests exhibited a positive pore water pressure. The unusual strain-water pressure graph exhibited by the Tx_ CK_0U_ 6 suggests an eventual problem during the shear stage, as a negative pore water pressure would be accompanied typically by a strain-hardening and not by a drop on the shear stress. Similarly to the drained tests, the tests which exhibit a positive pore-pressure are located, in this case, above the SSL and the ones located below the SSL develop a negative pore water pressure. As will be explained in the next section, during this work, the final state reached by the drained and undrained triaxial tests is distinguished by CSL and SSL, respectively, as suggested by Yamamuro and Lade (1998).

Looking carefully to Figure 7.4 it can be observed distinct stress-strain behaviors for each of the performed tests. While a minority suggests a peak strength followed by a strain-softening, the majority after the peak strength show a loss of strength quickly followed by a strain-hardening.

As the undrained geomechanical behavior, unlike drained triaxial tests, are so distinct from test to test it was opted to represent the stress-strain-pore water pressure, for lower confined triaxial tests, separated in Figure 7.5. As can be observed, apart Tx_ CIU_ 4 and Tx_ CK_0U_ 2, all the other tests

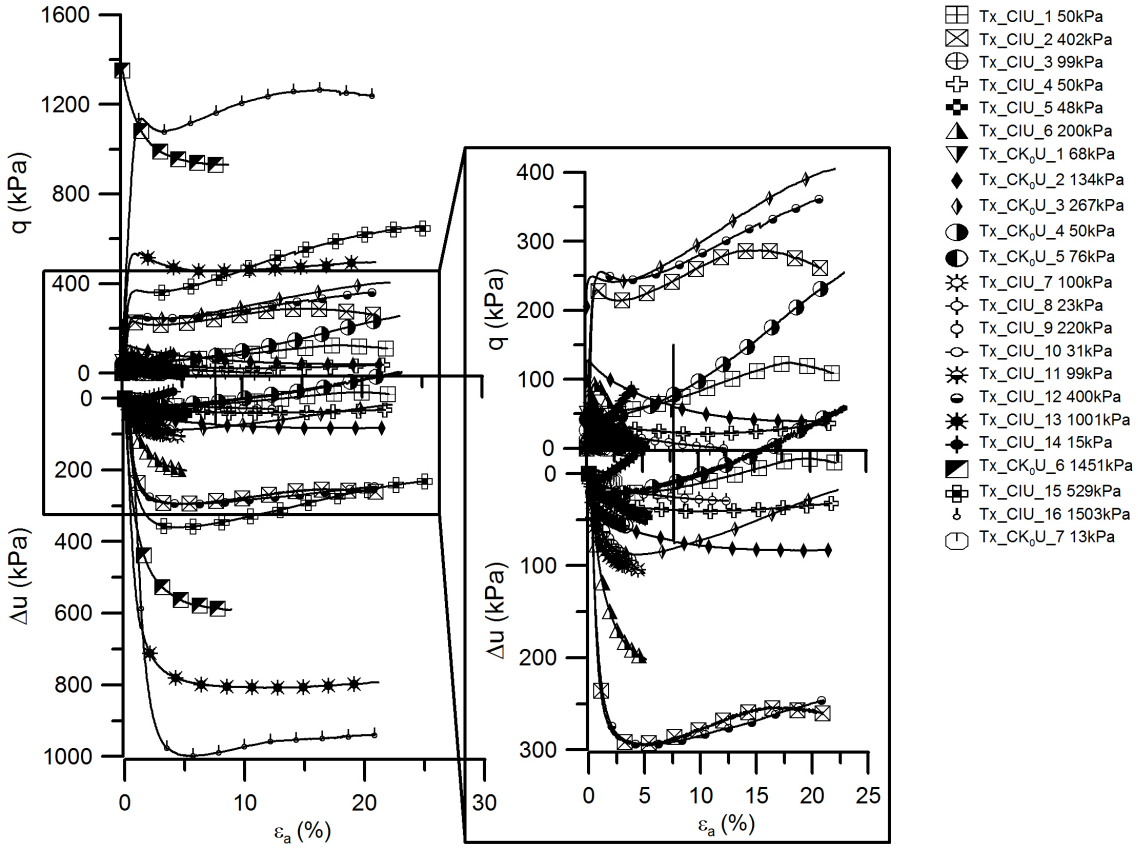


Figure 7.4: Stress-strain and strain-pore water pressure behavior of undrained triaxial tests of Algeria sand at low to medium confining pressures

after exhibiting a peak strength underwent on a complete loss of strength, which was accompanied by a large positive pore-pressure till a condition of zero effective stress (CP = BP). Thus, all tests displayed in Figure 7.5, apart from Tx_ CIU_ 4 and Tx_ CK_0U_ 2, experienced flow liquefaction triggered by monotonic loading condition. This phenomenon, as previously explained, occurs due to a disruption of the chain between the particles of the soil, which is responsible for the stress transference.

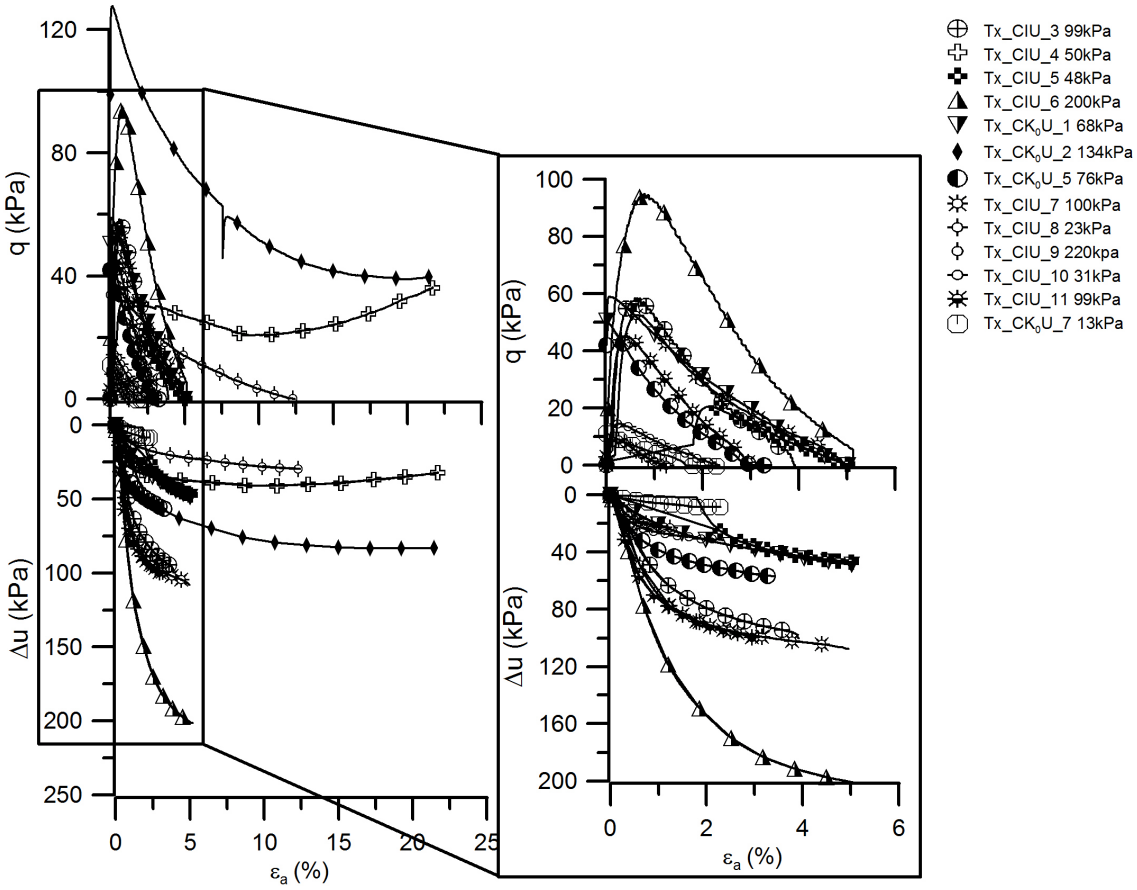


Figure 7.5: Stress-strain and strain-pore water pressure behavior of undrained triaxial tests of Algeria sand at low confining pressures

7.2.2.3 Soil Behavior Under Applied CSSM

Frameworks based on critical state theory have been used to describe monotonic behavior of sands (Jefferies and Been, 2006; Coop and Atkinson, 1993; Coop, 2003) and more recently to describe cyclic loading behavior (Jefferies and Been, 2006; Qadimi and Coop, 2007). The recourse to a parameter based on critical state theory, such as the state parameter (ψ), behind basing on a well-founded theory, also provides a good relationship with in situ tests results, such as the normalized cone resistance (q_{c1N}) of CPTu, (Jefferies and Been, 2006; Robertson, 2009).

Aiming at providing a consistent and reasonable soil behavior under applied CSSM, through both drained and undrained tests results, both CSL and SSL of Algeria sand were outlined (Figure 7.6).

According to the definition of the Critical State Line (CSL), $e_{cs} = \Gamma + \lambda \times \log\left(p'_{cs}\right)$, the values of the reference void ratio, Γ, and the slope, λ, determined based on the results of drained compression triaxial tests and some undrained triaxial tests, are 0.906 and -0.048, respectively (Figure 7.6 and 7.7). A value of 31.9° for the critical friction angle ϕ_{cv}, was found, which corresponds to a critical friction ratio, M, of 1.28. During the performance of undrained strain controlled monotonic

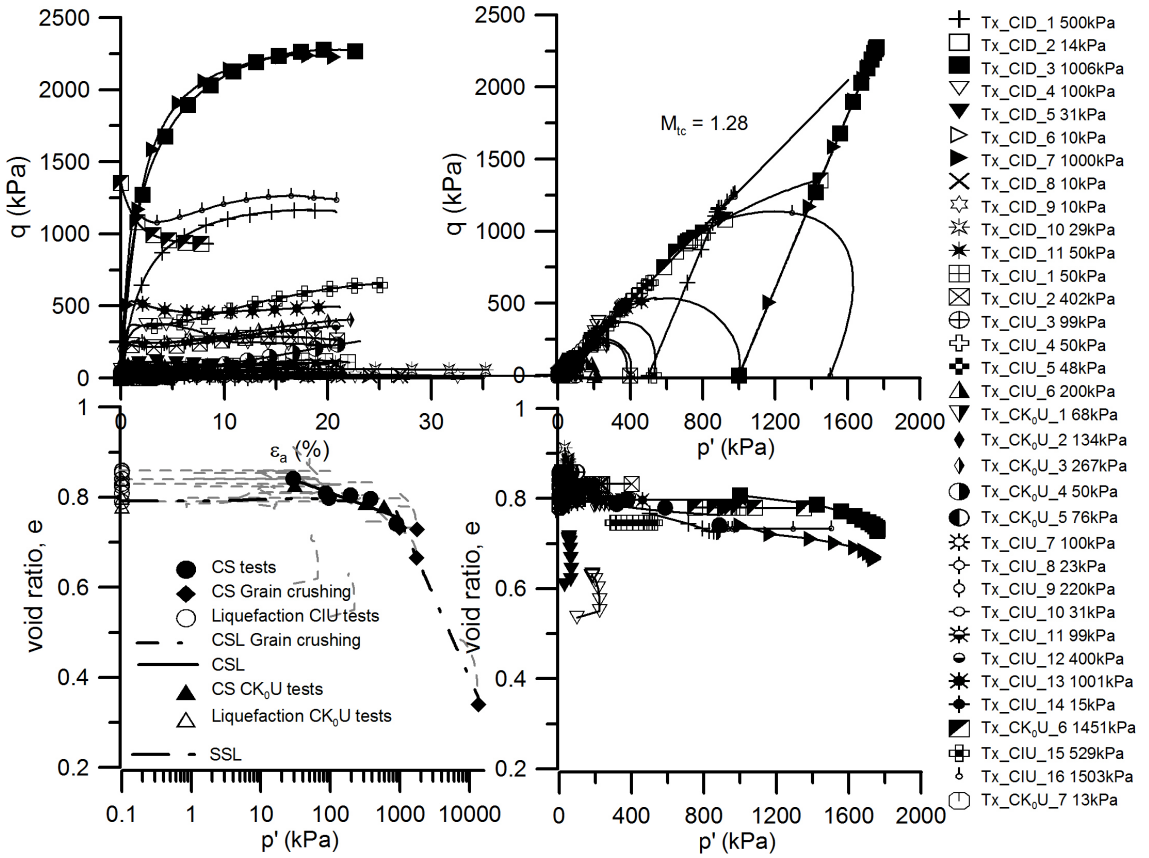


Figure 7.6: Construction of the critical state and steady state lines for Algeria sand (completed after Viana da Fonseca and Soares (2012))

tests, liquefaction occurred systematically for loose to medium/loose conditions for isotropic mean confining stresses lower than 300 kPa. For a smaller void ratio (e = 0.805) and a confining stress of 400 kPa, the soil starts exhibiting limited liquefaction with strain hardening (Figure 7.8). Only an imperceptible changing in behavior from true liquefaction to limited liquefaction with strain hardening is detected, for that it is believed that limited liquefaction with strain softening only occurs within a very limited range of void ratios and confining stresses (Figure 7.8). These patterns clearly identify a bifurcation when specimens are tested under drained or undrained conditions (Figure 7.7).

As defined by Sladen et al. (1985) the locus of peak strengths, defining a line in q - p' space is designated by "instability line". From Figure 7.6, it can be concluded that with increasing stress level, a reduction of strain softening is observed and the peak states are reached at higher stress ratios, closer to the CSL, followed by a new type of instability, this time due to particle crushing. Figure 7.7 also indicates, for Algeria sand, the occurrence of grain crushing for specimens tested with confining stresses higher than 1000 kPa. The grading curve evolution can be also confirmed with Figure 7.3. Grain crushing is not something new in the scope of soil geomechanical behavior and it is an irreversible phenomenon (Coop et al., 2004; Muir Wood, 2008) leading to an evolution of the critical state line position. The changing position of the CSL with the fines content was

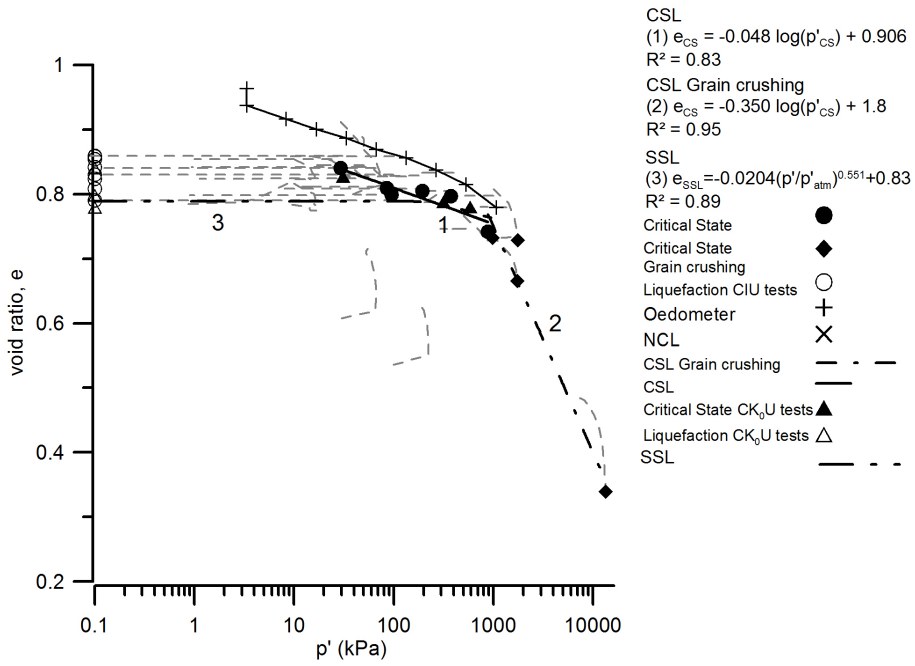


Figure 7.7: Critical state and steady states lines of Algeria sand (completed after Viana da Fonseca and Soares (2012))

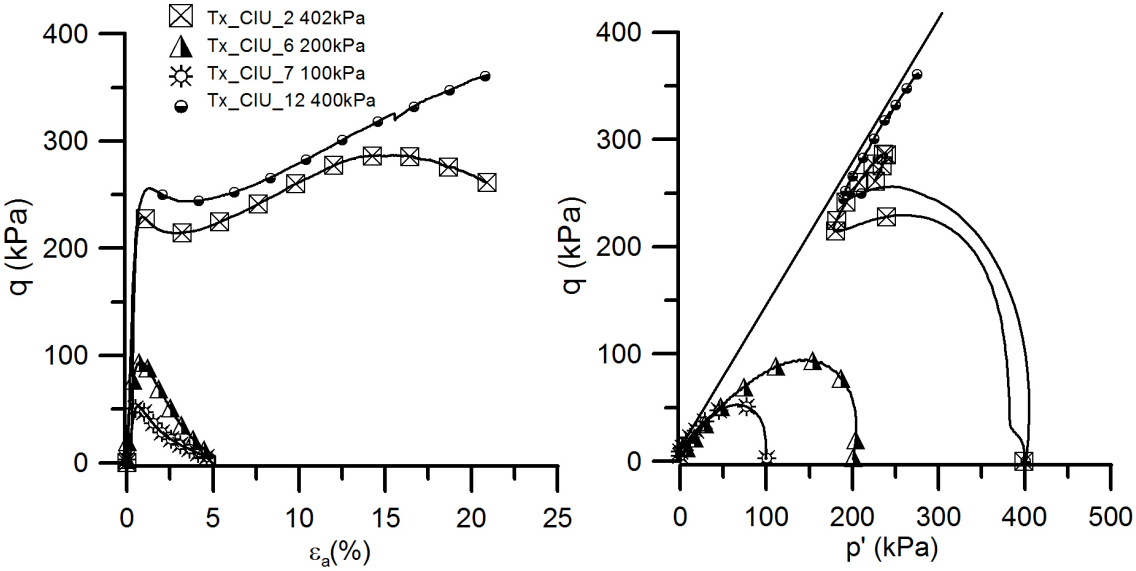


Figure 7.8: Stress-strain and stress-path behavior of Tx_ CIU_ 2, Tx_ CIU_ 6, Tx_ CIU_ 7 and Tx_ CIU_ 12 tests

previously reported by numerous authors, mainly in the scope of tailings liquefaction researches (Thevanayagam et al., 2002; Bouckovalas et al., 2003; Chang and Yin, 2011). Notwithstanding this high gradient is not only associated to grain crushing but also to the ability of the cohesionless grains to slide between them, which can only takes place when, during shear, the angularities are smoothed. As quoted by Carrera (2008) while "in clays, the compression mechanism is governed most of all by superficial, electro-static forces, in clean sands, the load is supported by grains

contacts, and the plastic volumetric strains are mainly due to the particle breakage". This means that both NCL and CSL, for clean sands, are only achieved when grain crushing occurs (Coop and Lee, 1993).

For Algeria sand, a clear and quick transformation was observed between the phases of true liquefaction and temporary liquefaction, with no evidence of a strain softening regime, clearly defined in figure 7.6 and 7.7 by a flatten line instead of a curve, as it is common in silty soils (Carrera et al., 2011; Bedin et al., 2012; Schnaid et al., 2013). So after true liquefaction, temporary liquefaction with strain hardening encompasses a large confining pressure range, similarly to the behavior observed for Nevada sand with 7% fines by Yamamuro and Lade (1998). The mechanism of contractiveness is associated to particle rearrangement during consolidation, and exhibits a typical quasi-steady state. Figure 4.26 helps to understand the differences in behavior observed in Figure 7.8, explaining that the test consolidated with 400 kPa cannot reach the void ratio of the test with 100 kPa as it would be located in an unreachable zone. Plus it seems obvious that the densification is enough for the soil to be more stable. Whereby for Algeria sand it is observed that the tests located within the NCL when sheared under undrained conditions will be developing liquefaction, strain softening, limited liquefaction with strain hardening and grain crushing, with increasing confining stress (and obviously with a consequent decreasing void ratio). These diverse stress-strain behavior only can be attainable, mainly for liquefaction and strain softening, when the soil samples are in a very loose condition, only reproduced by a moist tamping technique. However this does not mean that Algeria sand does not follow the critical state theory, in fact, as can be observed in Figure 7.9, the test confined with 1000 kPa exhibits more contractiveness than the test confined with 400 kPa, for a similar void ratio (after consolidation) of 0.80.

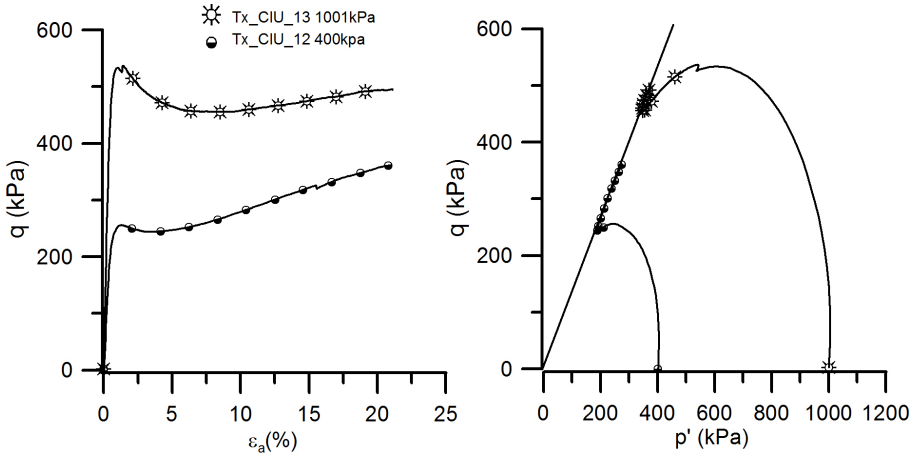


Figure 7.9: Stress-strain and stress-path behavior of Tx_ CIU_ 12 and Tx_ CIU_ 13 tests

The bifurcation of the CSL under different drainage conditions is already recognized. A similar behavior was found in Toyoura and Fujian sands by Verdugo and Ishihara (1996) and Yang and Sze (2011), respectively, while tested under undrained compression triaxial conditions. Figure 4.6, of Toyoura and Fujian sands, also exhibits a curved shape line, delineated by the ultimate stress states of both soils. Although it is necessary to point out that the flat part of the curve, which in the

case of Algeria sand is mostly horizontal, encompasses the tests which typically exhibited a strain softening behavior, while the steeper part of the curve is usually associated to the strain-hardening behavior, and usually converges with the CSL.

As a clear bifurcation between the CSL and SSL occurs for Algeria sand, it was decided to determine a suitable equation for the soils tested under undrained conditions. For a proper definition the SSL, the undrained tests which exhibited strain-hardening were also included, otherwise the SSL would be a horizontal line. Therefore the SSL adopted was determined according to the curved equation proposed by Li et al. (1999), $e_{SS} = e_{c0} - \lambda_s \left(\frac{p_{SS}}{p_a} \right)^{\xi}$, adopting the values of -0.0204, 0.551 and 0.83 for the λ_s, ξ and e_{c0} parameters.

It is also necessary to point out that even tests located below the CSL, such as Tx_ CK$_0$U_ 7 ($\sigma'_{hi} =$ 10 kPa, $K_0 = 0.4$ and $e_i = 0.79$) and Tx_ CIU_ 7 ($\sigma'_{hi} = 100$ kPa and $e_i = 0.79$) underwent on flow liquefaction. This proof supports the CSL and SSL divergence, as even the specimens initially located in the narrow zone between both lines will liquefy under undrained conditions.

Furthermore tests with an initial state condition located below the SSL, and tested under drained conditions, might not be able to reach its ultimate state. For these tests, located before the shear stage between the CSL and the SSL, an initial contraction takes place and dilation deems to occur only for very large axial strains, most of the times not being able to reach its ultimate state. Figure 7.10 shows three triaxial tests wich could not reach the CSL due to a strong contraction before dilation takes place. Such tests were excluded for the determination of the CSL positioning.

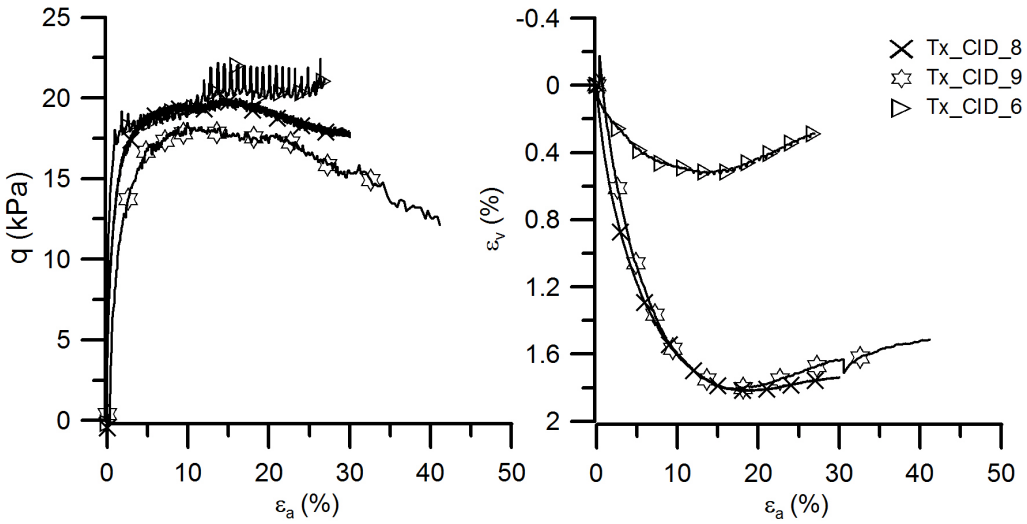


Figure 7.10: Stress-strain and strain-volumetric behavior of some low-pressure triaxial tests Tx_ CID_ 6, Tx_ CID_ 8 and Tx_ CID_ 9

7.2.3 Prediction of Liquefaction Resistance

The evaluation of soil liquefaction potential based on critical state theory may have some advantages, when compared with other commonly used liquefaction assessment charts. According to Jefferies and Been (2006), if ψ is chosen for a liquefaction assessment chart, then both void ratio and initial confining stress are taken into account to quantify soil liquefaction potential. However careful must be taken when CSL and SSL do not merge. For those cases, it may be inferred that, when the state parameter is measured relatively to the CSL, it becomes a less useful or even useless parameter to predict soil liquefaction potential. Tests Tx_ CK_0U_ 7 and Tx_ CIU_ 7 are examples of situations where the use of the state parameter might not have a correct effect. These tests have negative state parameter and experienced flow liquefaction while some other tests, exhibiting a stable behavior, display a positive state parameter.

Aiming at avoiding those errors the state parameter used to evaluate the soil liquefaction potential was measured with reference to the SSL, given by the equation proposed by Li et al. (1999). Expectedly, using the SSL as a reference ultimate state, makes more sense as this line is defined by the final states of the triaxial tests sheared under undrained conditions. However, when looking at Figure 7.11, it can be seen that some of the tests, which have liquefied, still have a negative ψ_{SSL}. This means that or the SSL equation does not suit all data points or few errors occurred while measuring the void ratio of the tests. This difficulty seems to be higher when the soil quickly changes from flow liquefaction to strain hardening within a narrow range of initial void ratios.

Ideally when measuring the liquefaction potential making use of a framework which correlates the brittleness index, I_B, with the ψ_{SSL}, all tests should follow the sketched line, having an $I_B = 1$ and higher values of ψ_{SSL}, in case of liquefaction. Plus soils exhibiting a limited liquefaction should follow the vertical section until stability is reached.

While the brittleness index, I_B when correlated with the ψ_{SSL} fails for some situations, being more sensitive for the zone nearby the CSL and the SSL, when correlated with ratio $p^{'}/p^{'}_{SSL}$ the same inaccuracy is found (Figure 7.11). This correlation was firstly proposed by Sladen et al. (1985) and Sadrekarimi and Olsen (2011), who found I_B to be a unique function of $p^{'}/p^{'}_{SSL}$ for all sandy soils. Such correlation seeks to avoid determining the CSL. The use of such ratio, according to Sladen et al. (1985) and later adapted by Ishihara (1993), appears as it can also represent the soil state. However, when looking carefully to both parameters it seems obvious that, for the soils which liquefy and the soils with exhibit a strain softening behavior, both depend on the minimum shear strength, $q_{min} = q_{cs/ss}$, of the soil. Furthermore this framework is not as straightforward as it seems. For example, if it is required to know if a dense sample confined with 10 kPa is susceptible to liquefaction, then the limiting ratios shall not be used. In fact such specimen will have an I_B equal or lower than 0 and a ratio $p^{'}/p^{'}_{SSL}$ very low (< 1). Thus it does not mean that by knowing the initial confining stress it will be known the soil behavior only by relying on such framework.

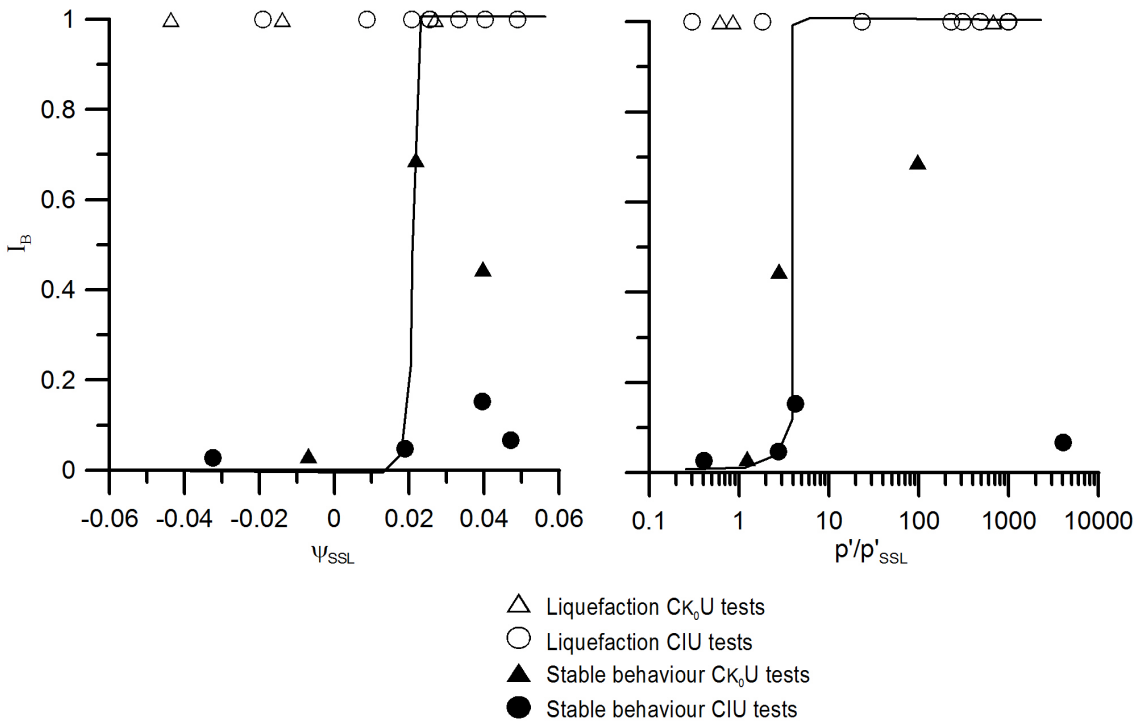


Figure 7.11: Variations of the Brittleness Index with the steady state parameter, ψ_{SSL}, and the ratio $p^{'}/p^{'}_{SSL}$ from left to right, respectively, for Algeria sand

For assessing such information it would be also required, at least, to know the peak strength of the soil if not it critical state.

For that reason the resource to the ψ_{SSL} is much more consistently practical.

As sometimes the use of ψ_{SSL} seems to be unreliable, Schnaid et al. (2013) proposed a more powerful framework which makes use of both strength and stiffness parameters.

Figure 7.12 expresses the steady state parameter ψ_{SSL} as function of the normalized peak shear strength (q_1) and normalized shear stiffness (V_{s1}). Despite the correlation, between ψ_{SSL} and the other parameters, not displaying a trend line, both q_1 and V_{s1} seem to provide and establish a limit border between liquefaction and stable behavior. Only one test, anisotropically consolidated, seems to escape and consequently dismiss this tendency. Furthermore, by evaluating the normalized shear wave velocity, it seems that the limit for which liquefaction does not occur is about 190/200 m/s for isotropically consolidated specimens. As for anisotropically consolidated specimens nothing can be concluded. Nonetheless these dissimilarities seem to vanish, for both isotropically and anisotropically consolidated soil samples, when adopting the ratio V_{s0}/q_{peak} equal to 2, which seems to establish the limit between liquefaction and stability. The lack of points between the three graphs are justified either by the inexistence of a peak strength and/or by the non measurement of shear waves.

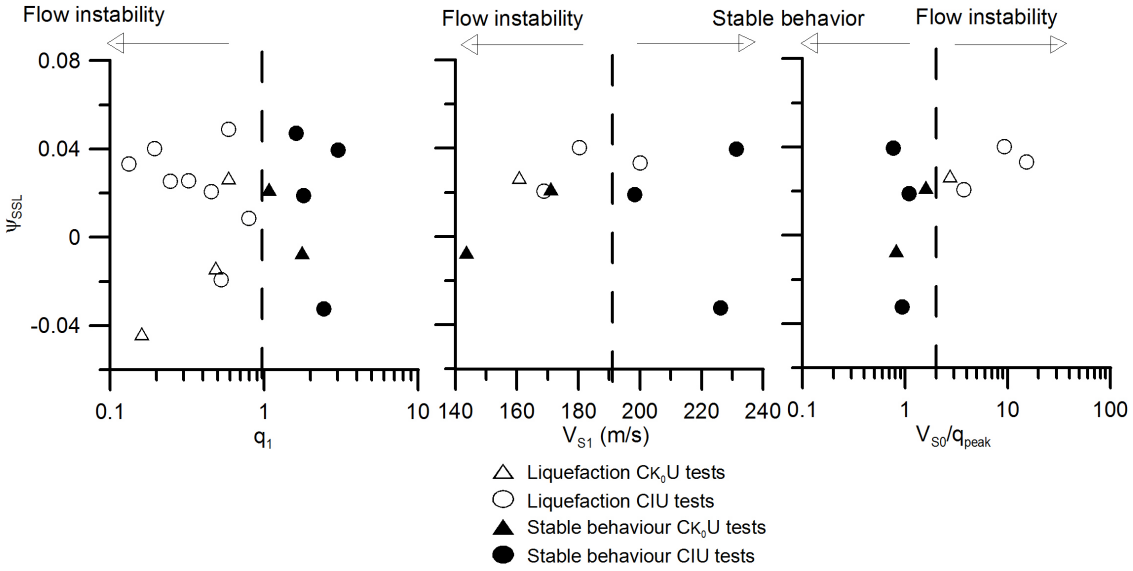
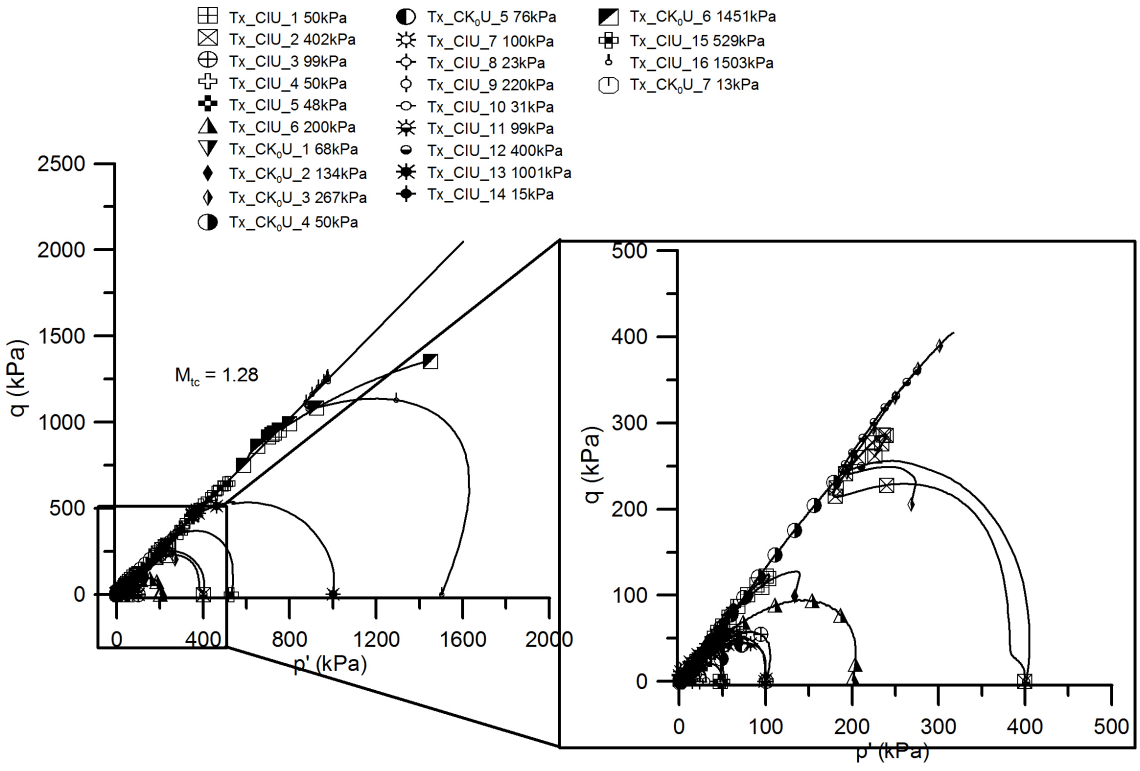


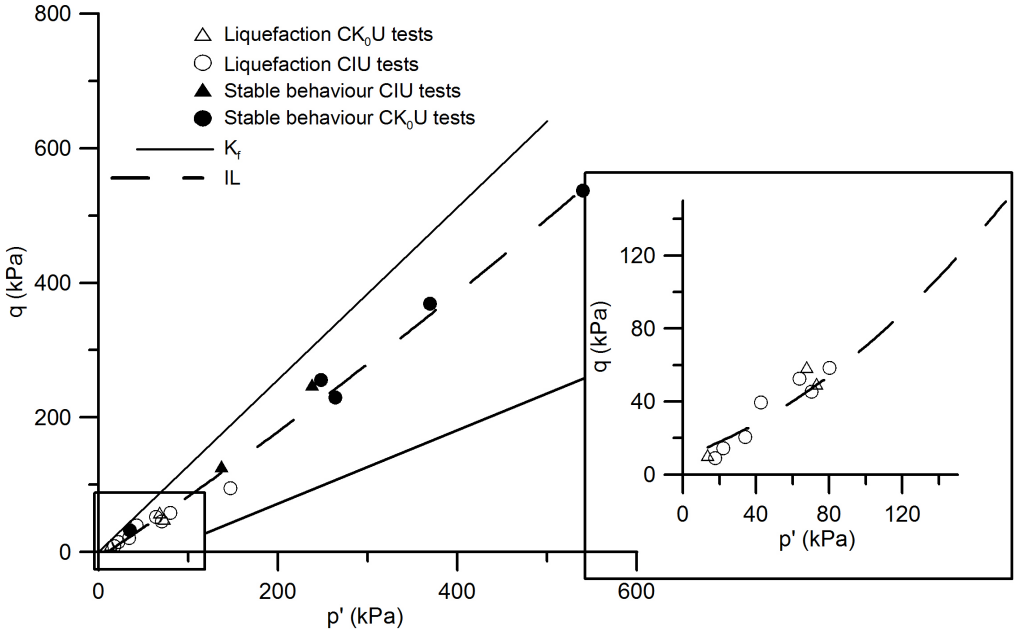
Figure 7.12: Steady state parameter expressed as a function of normalized peak shear strength (q_1) and shear stiffness for Algeria sand

While stability increases with increasing stiffness, thus with increasing V_{s1}, also the normalized shear strength seems to follow the same trend. Thus stability increases with both increasing q_1 and V_{s1} as reflect of an increasing contact between grains, due to both increasing confining pressure and decreasing voir ratio. The increase of the peak shear strength can be observed in Figure 7.13. Whilst IL appears to diverge more from the failure surface K_f with increasing p', in reality for lower confing pressure q_{peak} is approximatly half of p'_{peak}, while for higher confining pressures q_{peak} is approximately equal to p'_{peak}.

Figure 7.14a explains the correlation existent between both strength and stiffness parameters, q_{peak} and V_{s0}. Hence it employment, as ratio, becomes implicit for soil liquefaction susceptibility analysis. As reported by Schnaid et al. (2013) "because stiffness (G_0 – read V_s) and shear resistance (q_{peak}) are controlled (although) differently by the void ratio, mean stresses, compressibility, and soil structure and are, therefore, different functions of the same variables, it is possible to anticipate that as a ratio, these two measurements can be useful in predicting soil parameters". Conclusively Schnaid et al. (2013) proposed the following relationship for tailings, expressed in Figure 7.14b, which associates V_{s0}/q_{peak} and q_1. This relationship also suits, expectedly, Algeria sand. However careful must be taken as a strong statistical correlation exists between both variables. Thus the correlation shall be used as a limiting stress ratio differentiating liquefiable and non-liquefiable conditions, which for Algeria sand is when V_{s0}/q_{peak} approaches the value of 2 (see Figure 7.12 and 7.14). Furthermore by knowing the function between V_{s0} and q_{peak} it becomes possible, for this particular sand, to predict the peak shear through the correlation displayed in Figure 7.14.

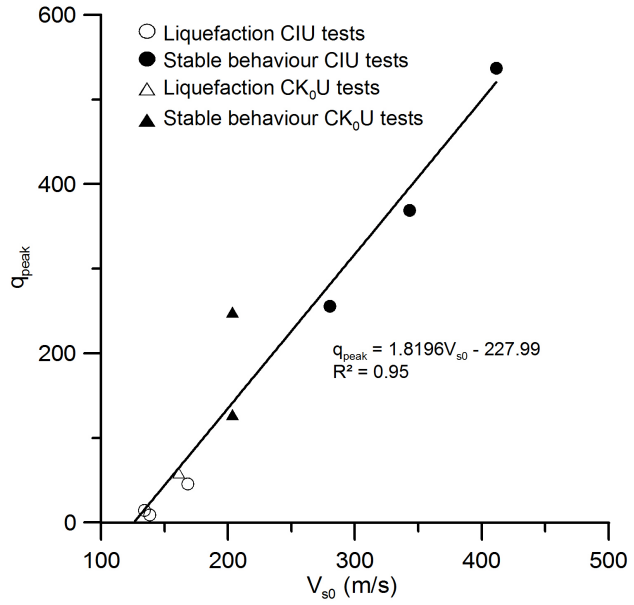


(a)

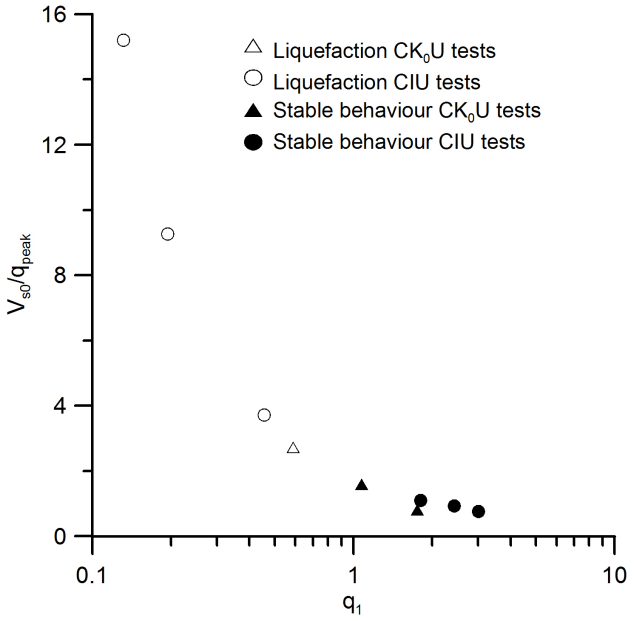


(b)

Figure 7.13: a) Detail of the stress-path of the triaxial tests; b) Instability Line (IL) for Algeria sand



(a)



(b)

Figure 7.14: a) Peak shear strength as function of the soil stiffness; b) Correlation between the normalized peak shear strength and the ratio between shear stiffness and the peak shear strength for Algeria sand

7.2.4 Partial Conclusions

Algeria sand strength and stiffness was evaluated through the performance of a set of compression triaxial tests, sheared both under drained and undrained conditions, on specimens isotropically and anisotropically consolidated.

The compression triaxial tests allowed determining both CSL and SSL for Algeria sand. The tests results are obvious and it seems that, for low confining stresses, the ultimate states achieved under drained and undrained conditions do not merge, originating two distinct ultimate state lines, the CSL and the SSL. Plus it was also concluded that for normal consolidated specimens the typical geomechanical behavior for Algeria sand is:

- For low confining stresses – Liquefaction;
- Medium confining stresses to high confining pressures – Limited liquefaction with strain hardening;
- Very high confining pressures ($p'_i > 1$ MPa) – Grain crushing.

It was also observed that the range of confining pressures for which strain softening takes place is too small as SSL exhibits a flat shape merging with the CSL for higher confining stresses, when the specimens start exhibiting a limited liquefaction with strain hardening. On the other hand for very high confining stresses the soil evolves due to grain crushing, changing the CSL positioning.

A resume of the distinct ultimate state lines can be consulted in the Table 7.2:

Table 7.2: Resume of the ultimate states for Algeria sand according to the type of test

	Soil behavior	Type of tests	Equation
CSL	Stable behavior	Drained and some undrained, which reveal a strain hardening, triaxial tests	(1) $e_{cs} = -0.048 \log(p'_{cs}) + 0.906$
CSL	Grain crushing	High-pressure triaxial tests	(2) $e_{cs} = -0.350 \log(p'_{cs}) + 1.8$
SSL	Liquefaction and strain softening	Undrained triaxial tests	(3) $e_{ss}=-0.0204(p'_{ss}/p'_{atm})^{0.551}+0.83$

Algeria liquefaction potential was evaluated and distinct correlations between distinct parameters were proposed. On one hand the state parameter revealed to have some limitations, even when using as reference the SSL, due to the lack of accuracy of the void ratios, and or changing behavior when compared to the narrow range of void ratio nearby the SSL. A same pattern was exhibited by the ratio between the initial state and the final critical state, p'/p'_{SSL}. Nonetheless both the soil stiffness (G_0 – determined by V_s registers) and the ratio stiffness-strength (V_{s0}/q_{peak}) revealed

to be good parameters to assess soil liquefaction potential, providing the limiting values between liquefaction and stability.

Table 7.3 provides a resume of the limiting ratios between liquefiable and nonliquefiable behavior for Algeria sand.

Table 7.3: Limiting values between liquefaction and stable behavior for Algeria sand

Parameter	Limiting value
ψ_{SSL}	Inconclusive
p'/p'_{SSL}	Inconclusive
V_{s1}	>170m/s anisotropically consolidated specimens >200m/s isotropically consolidated specimens
V_{s0}/q_{peak}	<2

7.3 Coimbra Sand

7.3.1 Basic Characterization

Coimbra sand, an artificial soil from a quarry, previously presented in Chapter 5, was investigated in the scope of the present research. Similarly to Algeria sand its mineralogy was not investigated during this PhD, yet some performed electronic microscopies allowed to observe and distinguish a predominant quartz constitution (Figure 5.14. In Table 7.4 some of its basic physical characteristics, previously presented in Chapter 5, can be consulted.

Table 7.4: Basic physical characterization of Coimbra sand

ID	Unit Weight volume of solid particles	Unit Weight volume	Grain size distribution ASTM sieves			FC	Cu	Cc	Maximum and Minimum void ratio	
	γ_s	$\bar{\gamma}$	Nº20	Nº60	Nº200	%			e_{max}	e_{min}
	(kN/m^3)	(kN/m^3)	0.841 mm	0.250 mm	0.075 mm					
Coimbra sand	26.6	14.8	97.8	22.9	1.8	<1.8	2.13	1.37	0.81	0.48

7.3.2 Triaxial Tests

Coimbra sand, unlike other quartz sands, has the particularity of having a low maximum void ratio, which results from its uneven and angular grains shape.

It study was, similarly to all the others materials, specified through the performance of a set of triaxial tests. Aiming at reproducing samples with the a similar fabric as in situ, which is known to be obtained by water pluvitation (Vaid and Sivathayalan, 1998, 2000; Vaid et al., 2001; Ghionna and Porcino, 2006), it was decided between the three Universities involved in the project, (FEUP, FCTUC and IST), to prepare Coimbra sand specimens by air pluviation. This technique was choosen over water pluviation as being of easier performance. Furthermore a large set of specimens were also prepared by moist tamping as some difficulties arose on achieving the CSL with the air pluviated specimens.

The set of triaxial tests performed with the Coimbra sand covered a range of low to very high confining pressures, performed under both drained and undrained condition, under both stress and strain control. A total of 30 triaxial tests were performed, among which 8 drained and 12 undrained were prepared by moist tamping technique, and 2 drained and 8 undrained were prepared by air pluviation.

The distinct reconstitution techniques not only allowed the evaluation of fabric influence on the ultimate stress state of the soil, but also allowed the comparison of soil liquefaction potential between the two techniques.

7.3.2.1 Drained Triaxial Tests

Coimbra sand triaxial tests results are presented in Figure 7.15, and with a more detail, for lower confining pressures. While a contractive behavior is observed for the specimens tested on the high-pressure triaxial device (Figure 7.15), the low confined specimens ($p'_i < 200$ kPa), tested on conventional triaxial devices, with exception of the Tx_ CID_ MT_ 4, experienced dilation accompanied by a peak shear strength, associated to particle imbrications during shear (Figure 7.15). This resulted from the difficulty to achieve very high void ratios with the specimens prepared by air pluviation.

High-pressure compression triaxial tests exhibited a similar behavior to Algeria sand as they did not stabilize the volumetric strain even for a very large axial strain. Attempting to predict the soil behavior of the Tx_ CID_ MT_ 8 test at higher axial strain, ($\varepsilon_a = 40\%$), an extrapolation, similarly to what was applied in Algeria sand, was made using the Hyperbolic model. Yet it recourse was not sufficient to stabilize the volumetric strain. This suggests an evolution of the grain size distribution of Coimbra sand within the range of high confining pressures, which can be confirmed in Figure 7.16. The differences between the original soil grain size distributions are evident, being Coimbra sand, by the end of the shear stage, a better graded material with a FC of 13.43%.

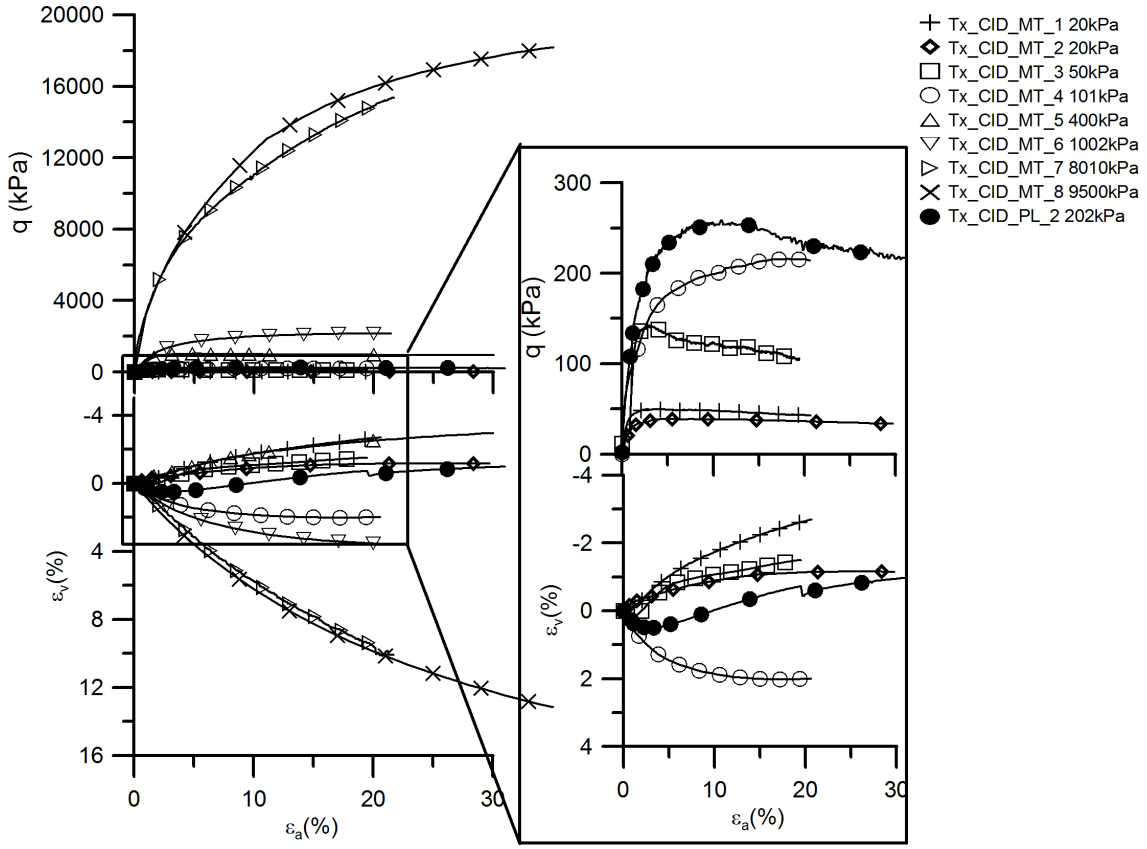


Figure 7.15: Stress-strain and volumetric-strain behavior of drained triaxial tests of Coimbra sand

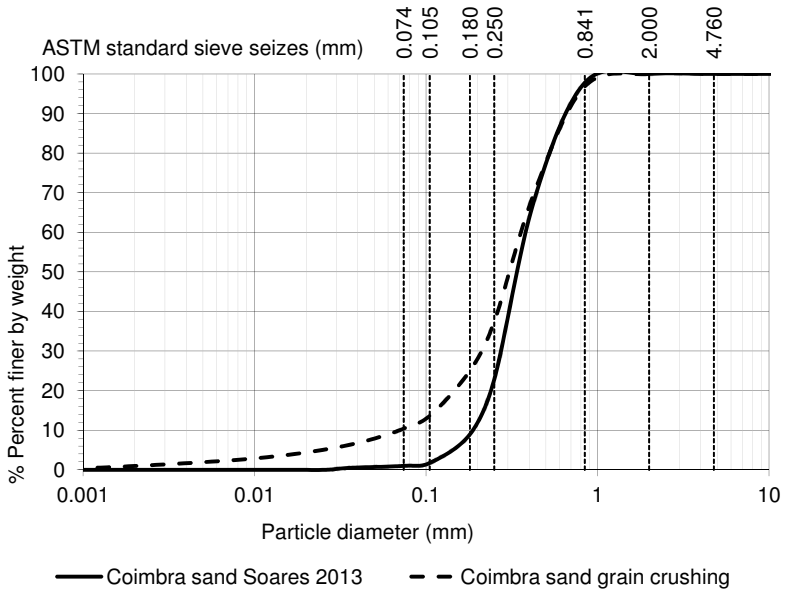


Figure 7.16: Evolution of the grain size distribution for the Tx_ CID_ MT_ 8 high-pressure triaxial test (p'_i = 9.5 MPa)

7.3.2.2 Undrained Triaxial Tests

The undrained triaxial tests results of Coimbra sand are exhibited very different behaviors according to it initial state conditions (both initial confining stress and void ratio).

Among all tests, Tx_ CIU_ MT_ 9 describes a different stress-strain behavior, characterized by a strain softening, which is clearly associated to the high-pressure confinement and to consequent grain crushing (Figure 7.17). As explained in Chapter 4 the presence of fines, either under large or low confining pressures, creates contacts of large-small-large type, forcing the small particles moving to the empty spaces between large particles, which creates a meta-stable structure. This is then translated, while sheared under undrained conditions, in a large positive pore pressure generation.

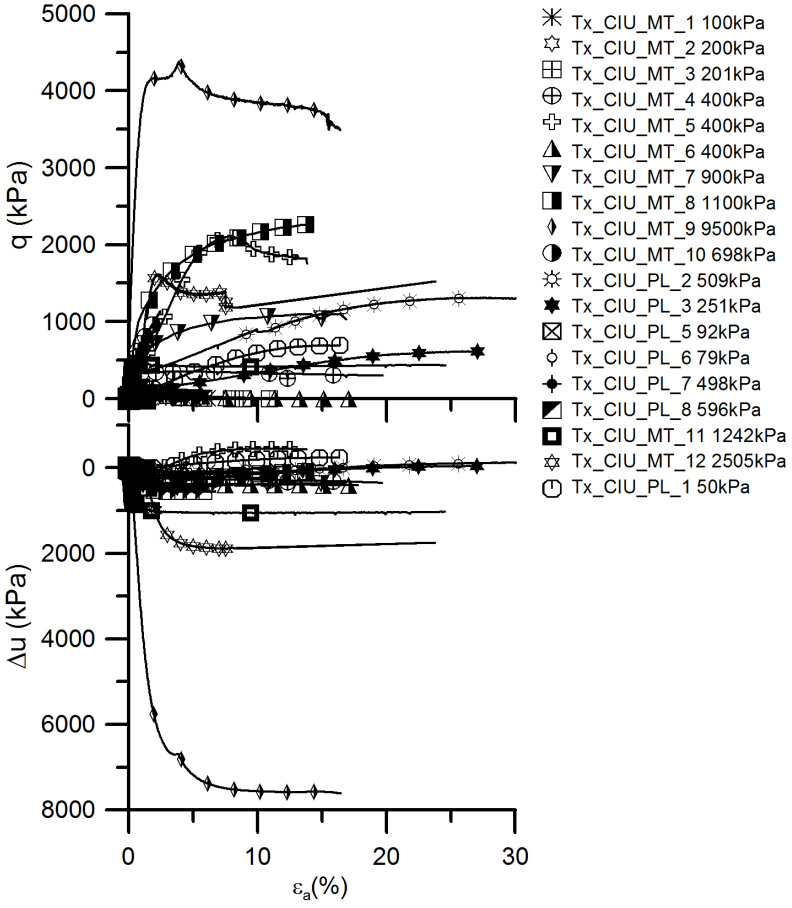


Figure 7.17: Stress-strain and strain-pore water pressure behavior of undrained triaxial tests of Coimbra sand

As for the other triaxial tests a same trend behavior as Algeria sand was observed by Coimbra sand. However Coimbra sand seems to experiment, within a large range of both void ratios and confining stresses, flow liquefaction, even when the tests did not initiate from the NCL. By consulting Table 6.4 and Figure 7.18 it can be concluded that liquefaction occurred for dry pluviated specimens consolidated with at least 600 kPa and for void ratios higher than 0.65, while the moist tamped

samples liquefied for confining pressures of at least 400 kPa and for void ratios higher than 0.63. Generally specimens with initial void ratios, (after consolidation), lower than 0.63, regardless the initial confining stress seem to exhibit a stable behavior.

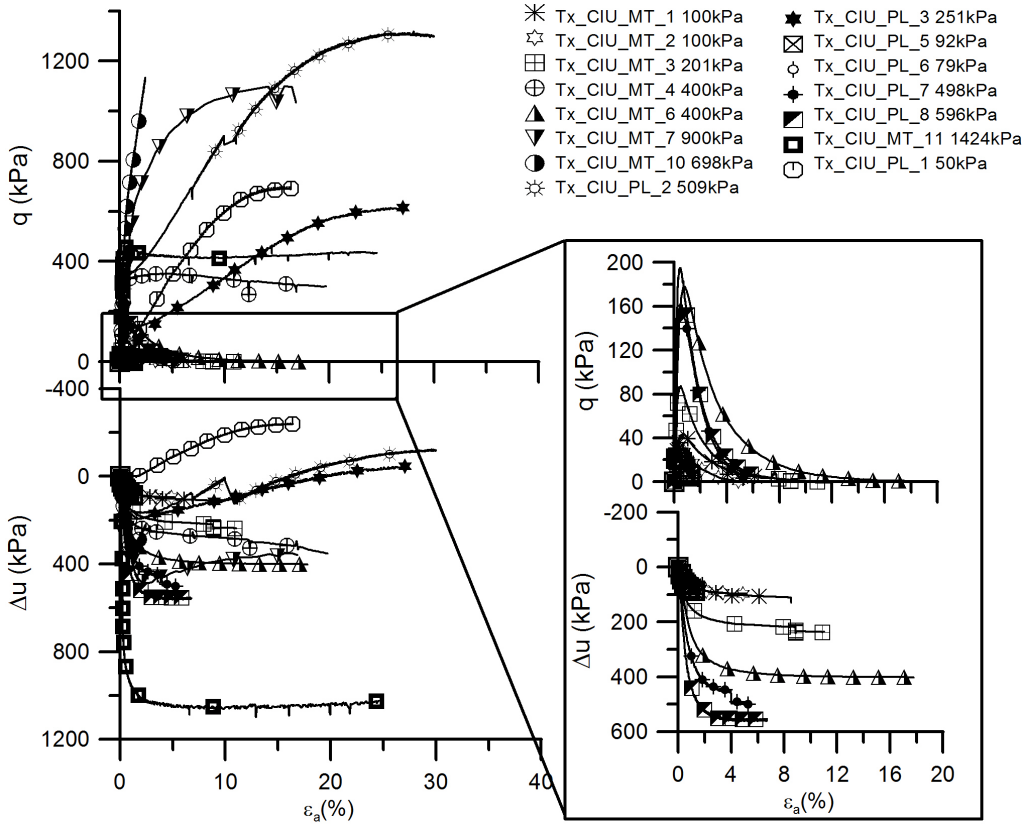


Figure 7.18: Stress-strain and strain-pore water pressure behavior of undrained triaxial tests of Coimbra sand at low to medium confining pressures

A more comprehensive evaluation of soil behavior sheared under undrained conditions is explained in the following section.

7.3.2.3 Soil Behavior Under Applied CSSM

The set of triaxial tests allowed defining the CSL of Coimbra sand (Figure 7.19), which splitted in two different patterns, one for low to medium confining stresses (< 1000 kPa) and a second one for higher confining stresses (> 1000 kPa). As refered previously this divergence is commonly associated to the occurrence of grain crushing.

Furthermore it was also observed a distinct geomechanical behavior among drained and undrained triaxial tests (see Figure 7.19 and Figure 7.20), being their ultimate states distinguished between CSL and SSL, respectively, according to Poulos (1981) definition for SSL. As stated by Alarcon-Guzman et al. (1988) *"if the sand structure is not inherently brittle, no collapse will take place; thus, the pore pressure response will be due solely to sand compressibility, and the S and F lines*

will tend to merge", being F the line achieved by tests sheared under undrained conditions and S the line achieved by tests sheared under drained tests. Curiously, for Coimbra sand merging only takes place for very high confining pressures, where grain crushing dominates the soil behavior. Even most of the grey points seem to be already part of the CSL defined by grain crushing (Figure 7.21), which explains the late convergence between the SSL and the CSL, when strain hardening starts dominating the soil behavior.

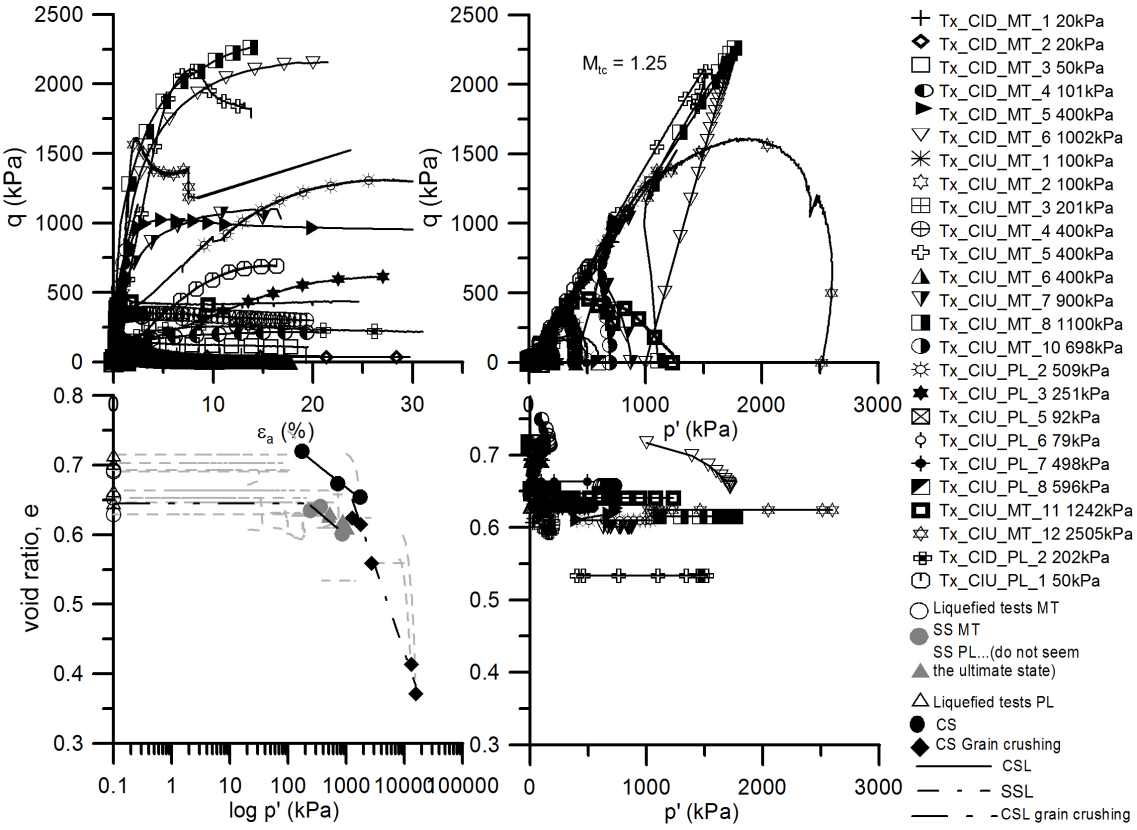


Figure 7.19: Construction of the critical state and steady state lines for Coimbra sand

On the other hand, unexpectedly, both samples reconstituted by air pluviation and moist tamping techniques deem to reach a unique SSL, which does not mean that both exhibit a similar liquefaction potential. Despite sometimes requiring extensive reorganization, according to some authors, (Muir Wood, 2008; Nouguier-Lehon et al., 2005), the critical state can always be reached in granular material. Plus, according to some authors, (Castro, 1969; Castro et al., 1985; Poulos, 1981; Poulos et al., 1985; Alarcon-Guzman et al., 1988; Jefferies and Been, 2006; Sadrekarimi and Olson, 2013; Been and Jefferies, 1985; Casagrande, 1976), despite the existent influence of fabric on the behavior at small shear strains, it seems that the initial fabric has no effect at large strains. However some authors, (Zlatovic and Ishihara, 1997; Tsukamoto et al., 1998; Vaid and Sivathayalan, 2000; Wood et al., 2008), detected, in some cases, distinct undrained responses of sands inclusively at large strains, thus on the definition of distinct SSL, by using different sample preparation methods.

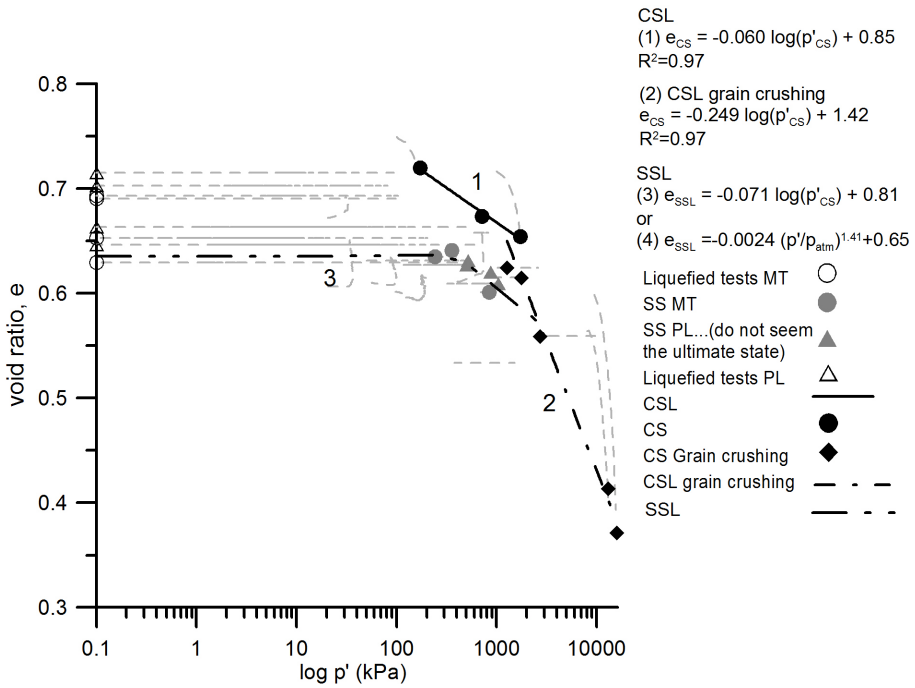


Figure 7.20: Critical state and steady state lines of Coimbra sand

Despite an apparent convergence of the ultimate states for samples prepared by moist tamping and air pluviation, a careful study was made in order to perceive the differences between both preparation techniques. Looking to the stress-strain curves of the two leftmost tests of the SSL (represented as grey circles), which are the tests CIU_ MT_ 4 and CIU_ MT_ 11, it is feasible to perceive a strain-softening behavior (Figure 7.21), whilst the other points are almost part of the CSL defined by grain crushing. On the other hand when analyzing the stress-strain curves of the two tests in the extreme left position of the SSL, which were prepared by air pluviation (represented with grey triangles), Tx_ CIU_ PL_ 1 and Tx_ CIU_ PL_ 13, a strain-hardening dominant behavior is observed (Figure 7.21). Then, it is necessary to understand if the Tx_ CIU_ PL_ 1 and Tx_ CIU_ PL_ 3 tests have achieved their ultimate state, as if they define a new CSL, distinct from the tests prepared by moist tamping. Nevertheless it seems obvious to accept that the tests have not achieved its real ultimate state despite seeming to define a same SSL, coinciding with the MT tests. From these tests results, it becomes obvious that the SSL is only defined by specimens which experienced strain softening during undrained shear and that the CSL is unique independently of the initial soil fabric.

Figure 7.20 also makes clear the particularity of Coimbra sand achieving liquefaction for a wide range of confining pressures and void ratios. This might be explained by the fictitious bridges created between the uneven grains. Thus, while sheared under undrained conditions it generates enough pore pressure to break the weak stress chains. When decreasing the void ratio, Coimbra sand starts approaching the flat part of the SSL, which starts bending only for very high-confining stresses. Whereby the SSL, instead of meeting the CSL, meets the CSL defined by tests which

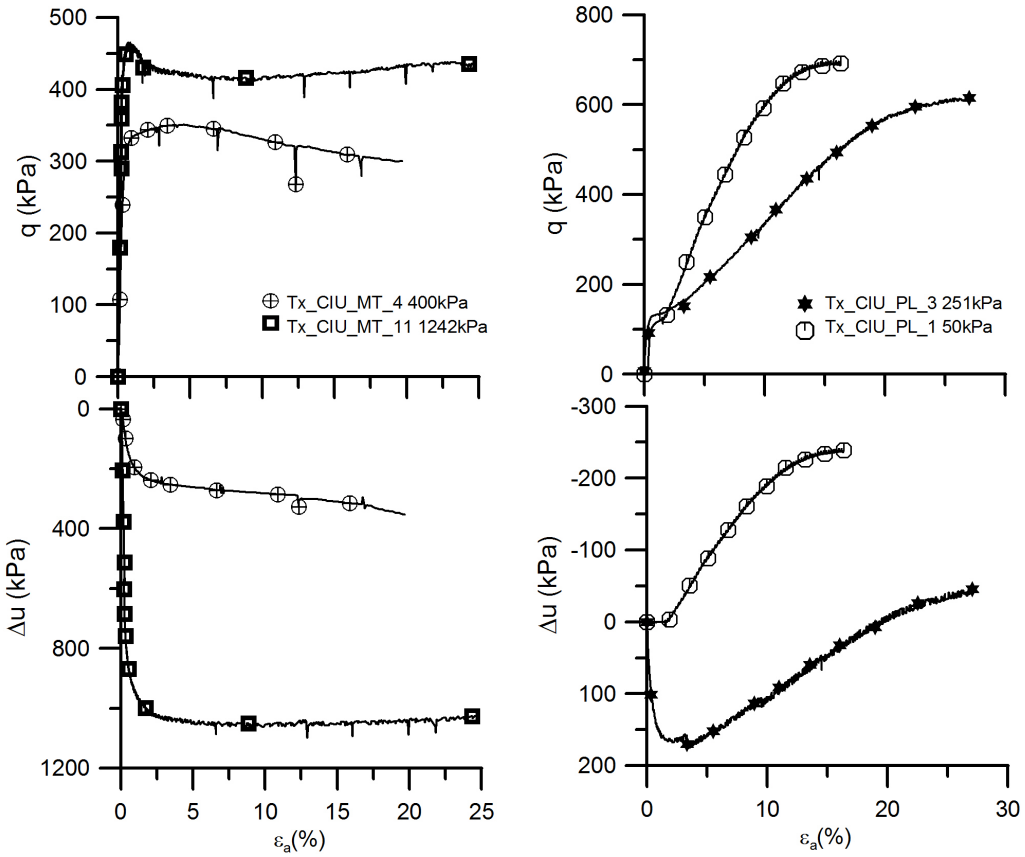


Figure 7.21: Stress-strain and strain-pore water pressure behavior of Tx_ CIU_ MT_ 4, Tx_ CIU_ MT_ 11, Tx_ CIU_ PL_ 1, Tx_ CIU_ PL_ 3 tests

suffered grain crushing. This is seemingly to occur as both drained and undrained tests ultimate states only converge for very high confining stresses.

The equations for both SSL and CSL (with or without grain crushing) are defined in Figure 7.20. For SSL, two equations are presented, one following the classical form of CSL, and a second one on the form proposed by Li et al. (1999) for curved shape critical states. According to the definition of the Critical State Line (CSL), $e_{cs} = \Gamma + \lambda \times \log\left(p'_{cs}\right)$, the values of the reference void ratio, Γ, and the slope, λ, were determined for Coimbra sand based on the results of classical drained triaxial tests, having the values of 0.85 and -0.060, respectively (Figure 7.20). Similarly to Algeria sand, as a clear bifurcation exists between the drained and the undrained soil behavior, it was decided to implement the curved equation proposed by Li et al. (1999), $e_{SS} = e_{c0} - \lambda_s \left(\frac{p_{SS}}{p_a}\right)^{\xi}$,which optimization resulted in the values of -0.0024, 1.41 and 0.65 for the λ_s, ξ and e_{c0} parameters, respectively.

A value of 31.1° for the critical friction angle, ϕ_{cv}, was found, obtaining a critical friction ratio, M, of 1.25.

7.3.3 Prediction of Liquefaction Resistance

A same set of frameworks presented for Algeria sand were plotted for the evaluation of the liquefaction potential of Coimbra sand.

Figure 7.22 display the correlation between the brittleness index, I_B, with the state parameter, ψ_{SSL} or ψ_{CSL}, and with the stress ratio $p^{'}/p^{'}_{SSL}$ or $p^{'}/p^{'}_{CSL_{Graincrushing}}$. Both correlations are reasoned on the same principles, i.e. the ultimate state of the soil, and require the previous definition of the SSL and/or CSL. Whilst the ψ_{SSL} was obviously determined as the difference between the initial state and the ultimate state defined either by the SSL or CSL, the stress ratio, $p^{'}/p^{'}_{SSL}$ or $p^{'}/p^{'}_{CSL_{Graincrushing}}$, was achieved by dividing the initial confining stress by the ultimate mean effective confining stress.

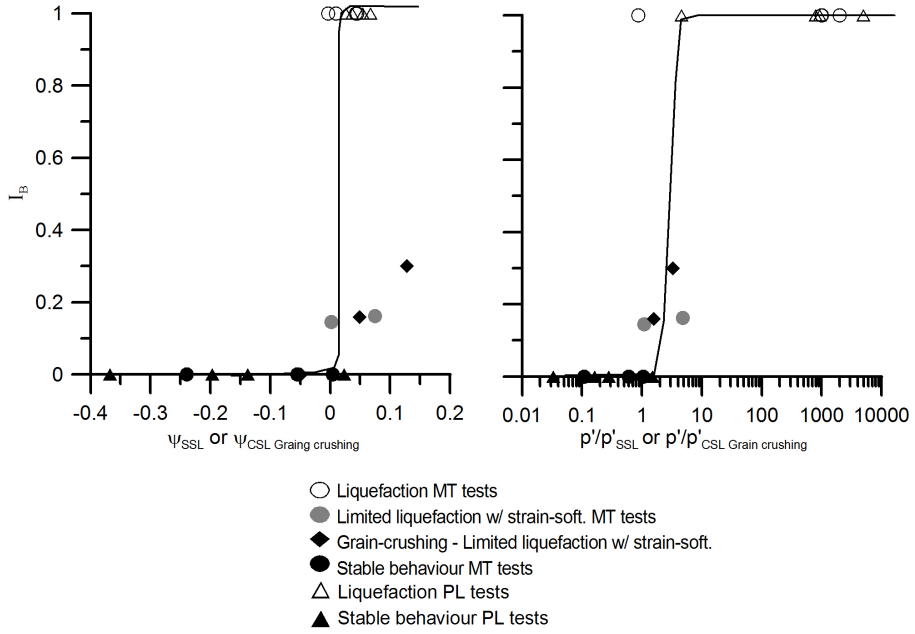


Figure 7.22: Variations of the Brittleness Index with the steady state parameter, ϕ_{SSL}, and the ratio $p^{'}/p^{'}_{SSL}$ or ratio $p^{'}/p^{'}_{CSL_{Graincrushing}}$, from left to right, respectively for Coimbra sand

Both correlations seem to be suitable to assess Coimbra sand liquefaction potential, although the second framework provides a strong statistical correlation between the two variables as explained previously. The small dispersion observed is somehow expected distinct from the one observed with Algeria sand probably due to a better determination of the SSL. The ψ was calculated with reference with the SSL for specimens above and below the SSL and with reference to the $CSL_{Graincrushing}$ crushing for specimens nearby.

Aiming to assess soil liquefaction potential, without depending on the use of soil state parameter, which requires CSL determination, stiffness parameters, G_0, thus V_s, were also determined.

To overcome the inability of using stiffness parameters to predict static liquefaction, Bedin (2010) and Schnaid et al. (2013) proposed a framework to assess liquefaction of tailings, by connecting

large-strain parameters indexes, ψ, with small strain-parameters, G_0 (derived from V_S). These correlations between the state parameter, the normalized shear wave velocity and the normalized peak shear strength are show in Figure 7.23 for Coimbra sand.

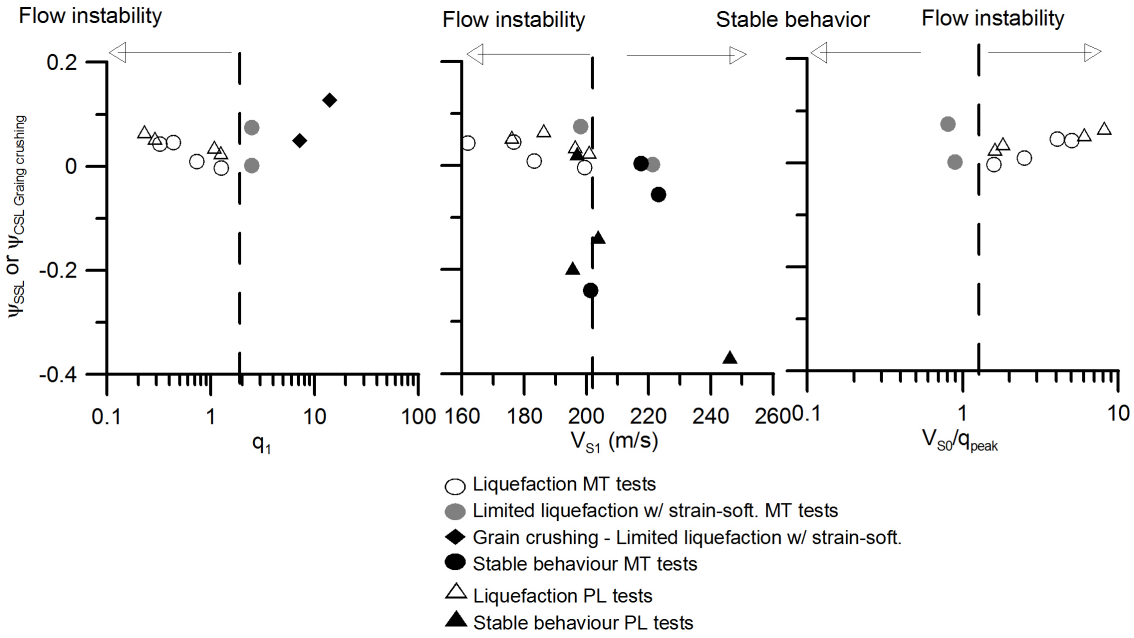


Figure 7.23: Steady state parameter expressed as a function of normalized peak shear strength (q_1) and shear stiffness for Coimbra sand

As might be inferred, the use of a state parameter, at least for sandy soils, is not as good as expected, mainly when grain crushing occurs. In this case, the soil starts exhibiting an instability associated to the increasing fines content for higher stress levels, exhibiting a consequent peak shear strength followed by a drop on shear strength (see Figure 7.19), associated to a positive state parameter, despite the soil not suffering flow liquefaction (see Figure 7.22 and 7.23). On the other hand, soils above the flat border line of the SSL, even with a very small state parameter will always experience flow liquefaction.

Notwithstanding both q_1 and V_{s1} parameters provide a limit value for which Coimbra sand stops being unstable, which takes the values of approximately 1 and 200 m/s, respectively.

Some points missing in Figure 7.23 were either due to the non measurement of shear waves or to the inexistance of peak shear strengths (including dilative tests). On the other hand soils tested on the high-pressure triaxial chamber were not accompanied with shear waves measurement, as the bender-extender elements in the geotechnical laboratory in FEUP are not yet prepared to be submitted to such high pressures, so they could not be considered in this approach.

Notwithstanding, for low/medium confining stresses, the use shear wave velocities seems to constitute a good way to assess soil liquefaction potential, being aware that all soils located above the horizontal branch of the SSL, even when situated very close to this critical zone - with an almost null value for the state parameter -, will always exhibit flow liquefaction.

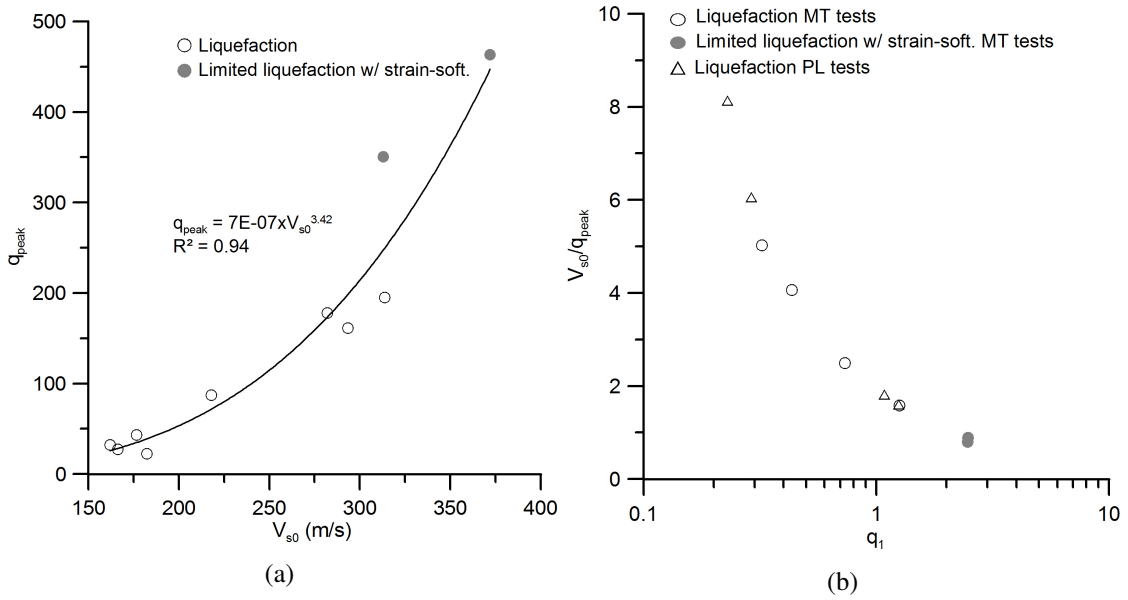


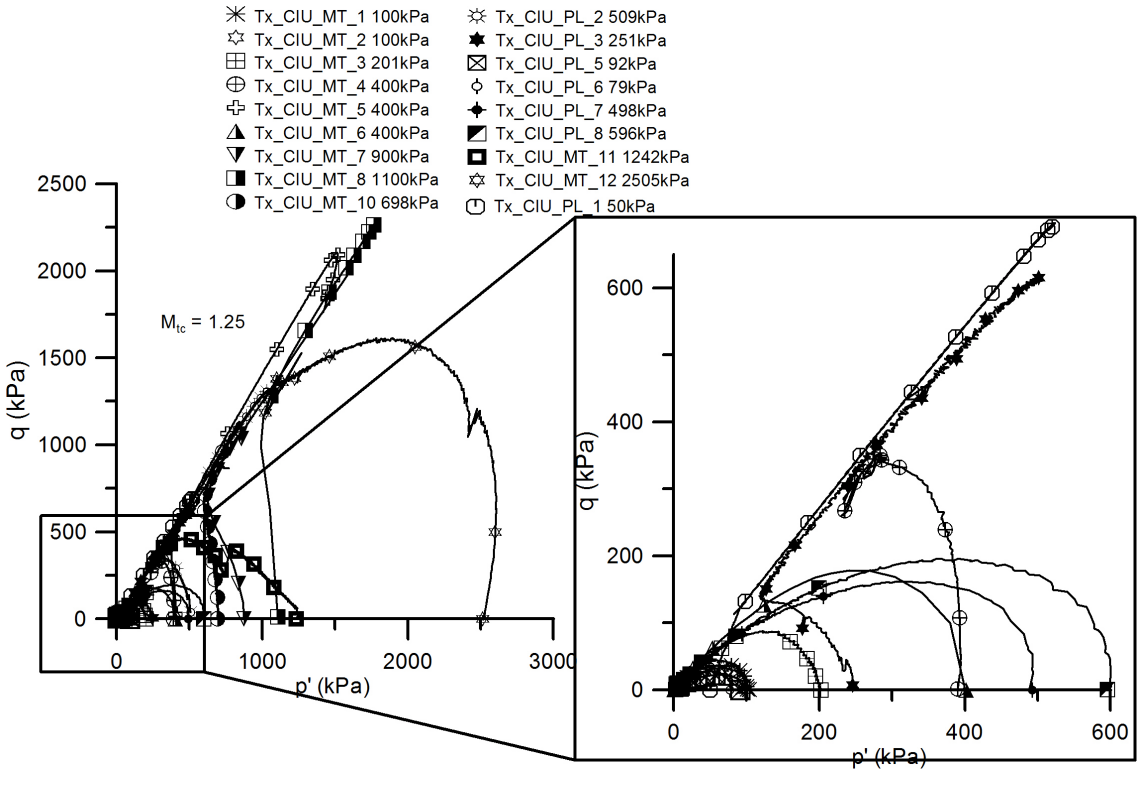
Figure 7.24: a) Peak shear strength as function of the soil stiffness; b) Correlation between the normalized peak shear strength and the ratio between shear stiffness and the peak shear strength for Coimbra sand

Thus, regardless the state parameter not being the most appropriate parameter to assess soil liquefaction susceptibility, the ratio between the initial shear wave velocity, V_{S0}, and the peak shear strength, q_{peak}, seem to be a good index to establish the boundary between soils liquefiable and stable. As reported by Schnaid et al. (2013) low values of q_1 and V_{s1} are associated with liquefiability, although at different levels of sensitivity. Figure 7.24a shows the correlation between both strength and stiffness parameters, q_{peak} and V_{s0}, which tend to justify how differently they are sensible to liquefiability analysis.

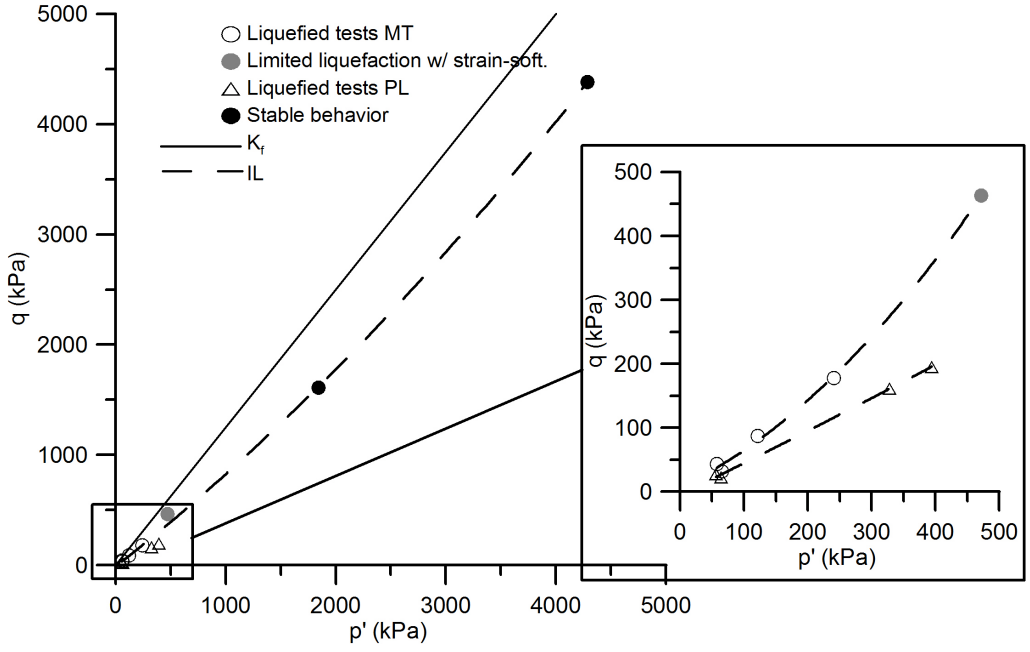
Figure 7.24b shows the relationship between the V_{s0}/q_{peak} ratio and q_1, which inherently include the effects of mean stress, strength, and stiffness. Despite Coimbra sand does not exhibit a smooth transition, associated to the occurrence of limited liquefaction accompanied by strain softening within a wide range of void ratios and mean effective stresses, typical of finer soils. From Figure 7.24b, it is clear that this relationship has a strong potential to differ liquefiability as both V_{s0}/q_{peak} and q_1 depend on the same parameter, the peak shear strength. Thus, this plot of V_{s0}/q_{peak} versus q_1 has its own limitations for predicting the undrained geomechanical behavior of soils. Nonetheless, it becomes very useful to define the boundary differentiating liquefiable and nonliquefiable conditions, which for Coimbra sand seems to be for ratios lower than 1, ($V_{s0}/q_{peak} < 1$).

Whilst not seeming necessary to distinguish both reconstitution techniques, in reality, distinct IL were achieved. By analyzing Figure 7.25, it is observed that the specimens reconstituted by air pluviation exhibit lower peak strengths. However as all specimens, prepared with this technique, which exhibited a peak strength, liquefied, the limit for which the soil is stable is not known, not being feasible it comparison with those prepared by moist tamping.

Yet, when assessing Figure 7.25 it seems that, regardless the initial void ratio, it is observed an increasing peak strength with increasing confining stress. Furthermore it seems, that, for the higher-confined specimens this tendency seems to prevail even when grain crushing takes place.



(a)



(b)

Figure 7.25: a) Detail of the stress-path of the triaxial tests; b) Instability Line (IL) for Coimbra sand

7.3.4 Partial Conclusions

Coimbra sand strength and stiffness was evaluated through the execution of a set of compression triaxial tests. During it research the influence of inherent anisotropy achieved through different, air pluviation and moist tamping, was also studied.

Similarly to Algeria sand, three distinct ultimate states lines were attained. Drained and undrained conditions led to distinct ultimate states, SSL and CSL, respectively. Plus the convergence between SSL and CSL did not occurred until grain crushing took place, i.e. for high-confining pressures.

As most specimens were not prepared from the NCL, no major conclusions can be outlined. Nevertheless it is true that for Coimbra sand:

- For void ratios higher than approximately 0.64 – Liquefaction seems to take place regardless the initial confining stress;
- Medium confining stresses to high confining pressures – Limited liquefaction with strain softening occurs, within a small range of void ratios of approximately 0.64;
- Medium confining stresses to high confining pressures – Limited liquefaction with strain hardening occurs, within a small range of void ratios of approximately 0.64; It is important to notice that in the vicinity of the SSL both strain hardening and strain softening might occurs;
- Very high confining pressures ($p'_i > 1$ MPa) – Grain crushing occurs;
- CSL was only achieved through the performance of very loose drained triaxial tests, prepared by moist tamping.

A resume of the distinct ultimate state lines are expressed in the table below:

Table 7.5: Resume of the ultimate states for Coimbra sand according to the type of test

	Soil behavior	Type of tests	Equation
CSL	Stable behavior	Drained triaxial tests	(1) $e_{cs} = -0.060 \log(p'_{cs}) + 0.85$
CSL	Grain crushing	High-pressure triaxial tests, sheared under drained and undrained conditions	(2) $e_{cs} = -0.249 \log(p'_{cs}) + 1.42$
SSL	Liquefaction and strain softening	Undrained triaxial tests with initial void ration lowe than, approximately, 0.64	(3) $e_{ss}=-0.024(p'_{ss}/p'_{atm})^{1.41}+0.65$

To assess liquefaction potential, distinct correlations, between different parameters, were proposed for Coimbra sand. On one hand the state parameter and the stress ratio despite being accurate

reveal some limitations, mainly due to the lack of accuracy of the void ratios when compared to the narrow range of void ratio nearby the flatten SSL. On the other hand soil stiffness (G_0 – from V_s readings) and the ratio stiffness-strength (V_{s0}/q_{peak}) show to be very accurate parameters, beyond not requiring CSL determination.

Table 7.6 provides a resume of the limiting ratios between liquefiable and nonliquefiable behavior for Coimbra sand.

Table 7.6: Limiting values between liquefaction and stable behavior for Coimbra sand

Parameter	Limiting value
Ψ_{SSL}; $\Psi_{CSL Grain\ crushing}$	$\Psi_{SSL} < 0$; $\Psi_{CSL Grain\ crushing} < 0$
p'/p'_{SSL}; $p'/p'_{CSL\ Grain\ crushing}$	<10
V_{s1}	>200m/s
V_{s0}/q_{peak}	<1

7.4 Coimbra Sand With 20% FC

7.4.1 Basic Characterization

The presence of fines in soils is not only very common in nature but it can also result from industrialized processes from the mining industry. As explained before, its study is mostly commonly associated to the study of tailing dams, slopes instability and due to the occurrence of grain crushing when soils are subjected to very high confining pressures.

The presence of fines in soils is one of the prominent factors affecting soil liquefaction potential due to increasing liquefaction susceptibility, associated to the increasing compressibility of the material.

As the investigation of liquefaction hazard remains associated to the state parameter, requiring CSL determination, it becomes important to assess it positioning with different fines content.Unfortunately due to the lack of time the evaluation of soil liquefaction potential must the asseted for future researches.

Aiming to assess the effect of the fines content on Coimbra sand CSL positioning a set of triaxial tests was performed with two different fines content. While the first group was asset with 20% of fines content, the second, presented on the following sub-section, were conducted with 40% of FC.

For simplicity the terminology used for Coimbra sand with 20% of fines content and with 40% of fines content are, in the present document, as Coimbra 20 and Coimbra 40 or C20 and C40,

respectively. Both materials presented in Chapter 5, within which Coimbra sand was presented in the last subsection, when mixed with fines present the following basic physical characteristics, according to tests performed at LabGeo (see Table 7.7).

Table 7.7: Basic physical characterization of Coimbra sand with 20% FC

ID	Unit Weight volume of solid particles	Unit Weight volume	Grain size distribution ASTM sieves			FC	Cu	Cc	Maximum and Minimum void ratio	
	γ_s	$\bar{\gamma}$	Nº20	Nº60	Nº200	%			e_{max}	e_{min}
	(kN/m^3)	(kN/m^3)	0.841 mm	0.250 mm	0.075 mm					
Coimbra sand 20%FC	26.6	18.1	97.2	34.8	20.7	<20.7	18.12	5.89	n.v	n.v

7.4.2 Triaxial Tests – Soil Behavior Under Applied CSSM

The study of Coimbra 20 only included a set of 4 triaxial tests, perfomed both under drained and undrained conditions. The CSL was achieved as all tests attained a stable ultimate state (see Figure 7.26). Despite the final void ratio not being confirmed through the freezing technique (see Sladen and Handford (1987)), an oedometer test allowed to ascertain CSL slope.

Although allowing defining CSL for high pressures, the set of tests was no sufficient for defining it positioning for low confining stresses, the region more prone to liquefaction (see Figure 7.26).

As explained before soil liquefaction potential is usually assessed by measuring the state parameter with reference to the ultimate states, and it is usually associated to very loose undrained compression triaxial tests. As no tests were performed with very loose specimens the liquefaction potential of C20 was not evaluated. In fact only one test exhibited a positive pore pressure generation, thus no major conclusions can be inferred.

Nonetheless CSL, $e_c = \Gamma + \lambda \times \ln\left(p'\right)$, positioning was determined for Coimbra 20, obtaining the values of 0.828 and -0.127 for the reference void ratio, Γ, and the slope, λ, respectively and according to Figure 7.27.

A value of 32.5º for the critical friction angle, ϕ_{cv}, was found for the lower confined triaxial tests, correspondent to a critical friction ratio, M, of 1.31. However this value was of 34.9º when including the high-pressure drained triaxial test, Tx_CID_2. This variation of the friction angle is

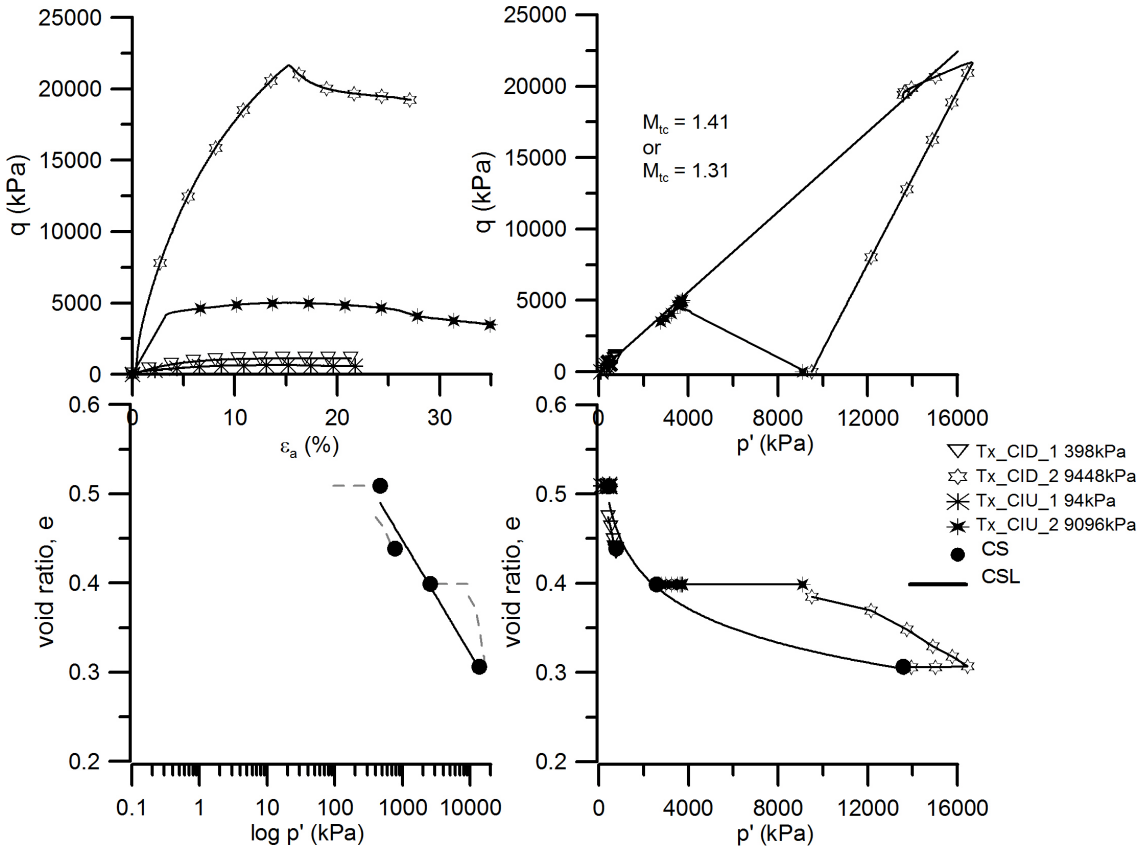


Figure 7.26: Construction of the critical state line for Coimbra 20

inconclusive but might be either a result of the grain size distribution evolution, which might not necessarily means that it occurs at a macroscale.

In what concerns to the high-pressure triaxial tests, there were no major signs of a grain size distribution evolution as might be seen in Figure 7.28. Beyond the volumetric strain have stabilized, the final grain size distribution was also determined and compared with the initial one. However it is important to highlight that the high-pressure triaxial test was performed under undrained conditions before the material achieved the failure envelope (Figure 7.28). This was required due to a limitation of the load cell. Nonetheless a stabilization of the pore pressure generation was also observed.

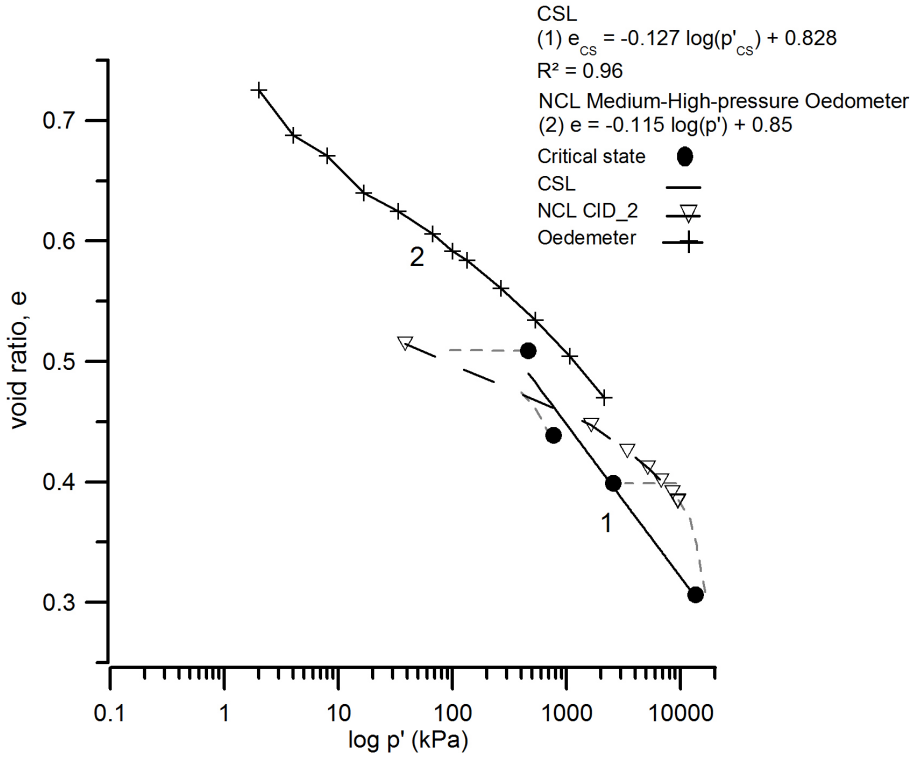


Figure 7.27: Critical state and steady state lines of Coimbra 20

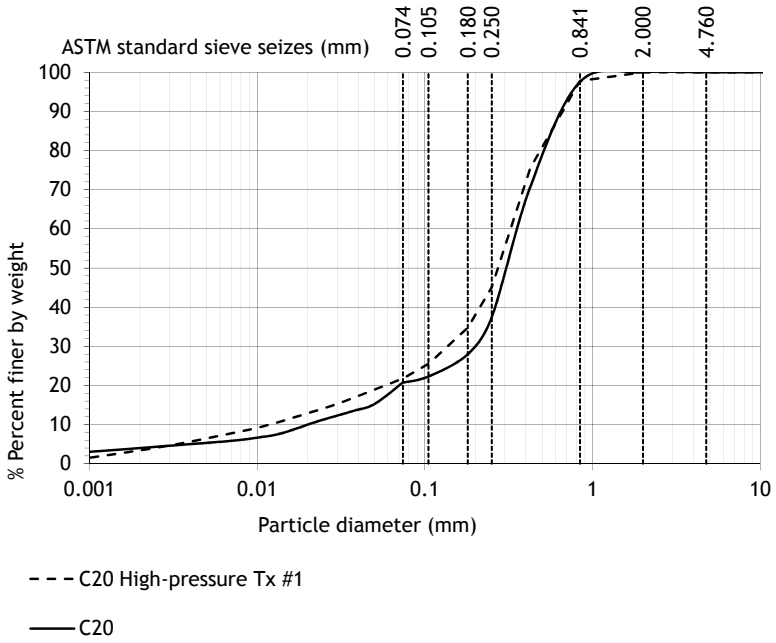


Figure 7.28: Evolution of the grain size distribution of the Tx_CID_2 high-pressure triaxial test (p'_i = 9.4 MPa)

7.5 Coimbra Sand With 40% FC

7.5.1 Basic Characterization

The mixture of Coimbra sand with 40% of rock powder was studied with the same purpose as Coimbra 20. Table 7.8 provides a resume of Coimbra 40 basic physical characteristics, previously presented in Chapter 5, according to tests performed at LabGeo.

Table 7.8: Basic physical characterization of Coimbra sand with 40% FC

ID	Unit Weight volume of solid particles	Unit Weight volume	Grain size distribution ASTM sieves			FC	Cu	Cc	Maximum and Minimum void ratio	
	γ_s	$\bar{\gamma}$	Nº20	Nº60	Nº200	%			e_{max}	e_{min}
	(kN/m^3)	(kN/m^3)	0.841 mm	0.250 mm	0.075 mm					
Coimbra sand 40%FC	26.6	15.0	97.9	51.1	40.5	<40.5	51.58	2.85	n.v	n.v

7.5.2 Triaxial Tests – Soil Behavior Under Applied CSSM

The study of Coimbra 40 was very limited and resulted in the performance of 2 single triaxial tests and one oedometer. Similarly to Coimbra 20 no evaluation of soil liquefaction potential was performed and the CSL positioning was, similarly, only achieved for very high-triaxial tests (Figure 7.29).

The limiting capacity of the load cell also prevented the Tx_CID_2 tests to be performed till the end under drained loading conditions, whereby part of the test was continued under undrained conditions (see Figure 7.29).

The CSL, $e_c = \Gamma + \lambda \times \ln\left(p'\right)$, positioning, determined for Coimbra 40 basing on two single triaxial tests, resulted on a reference void ratio, Γ, and slope, λ, of 0.807 and -0.131, respectively (Figure 7.30).

A critical friction angle, ϕ_{cv}, of 35.1^o, corresponding to a critical friction ratio, M, of 1.43 was found for Coimbra 40.

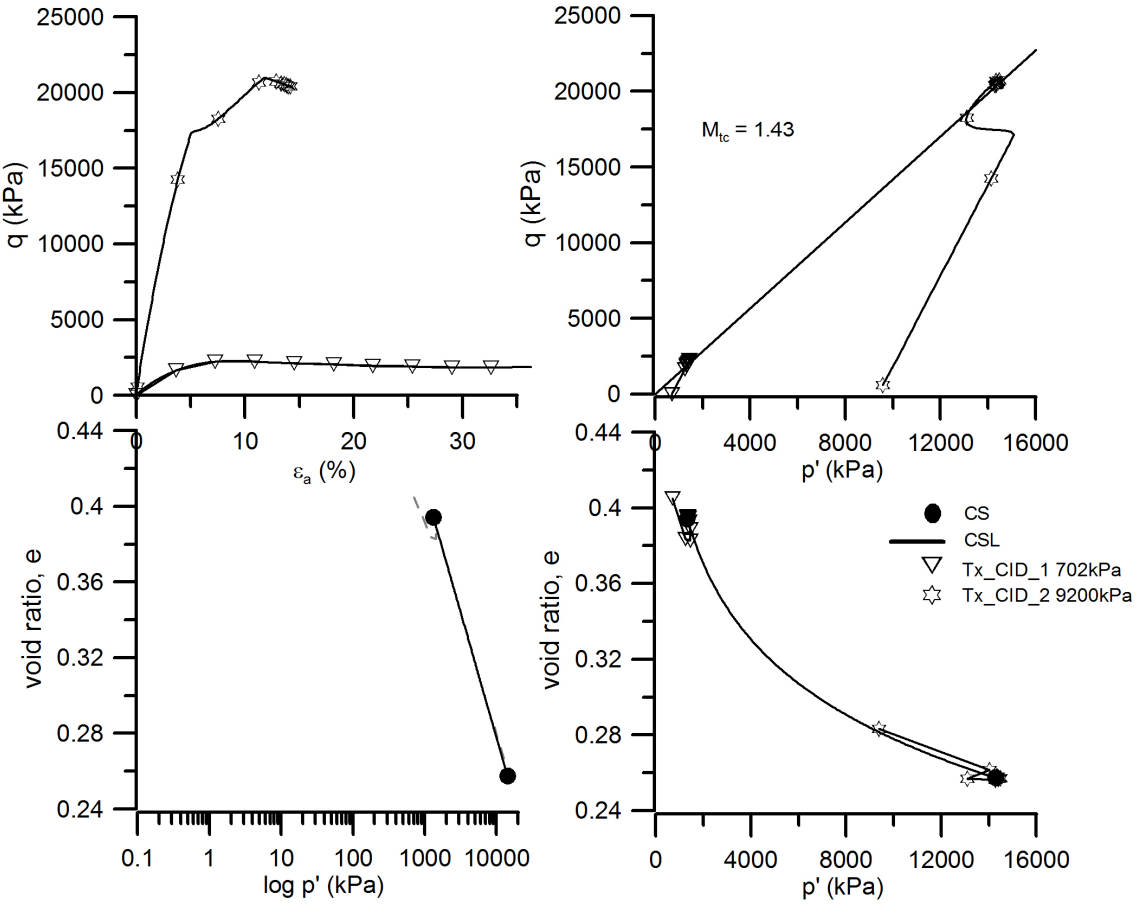


Figure 7.29: Construction of the critical state line for Coimbra 40

Despite no evidences were observed of grain crushing occurrence, since there was a linear CSL with no clear inflection (breakage), Coimbra 40 grain size distribution was still verified and compared to the initial and original one (see Figure 7.31). According to the plot it seems clear that a slight grain crushing occurred, even when is not clear from triaxial tests interpretation.

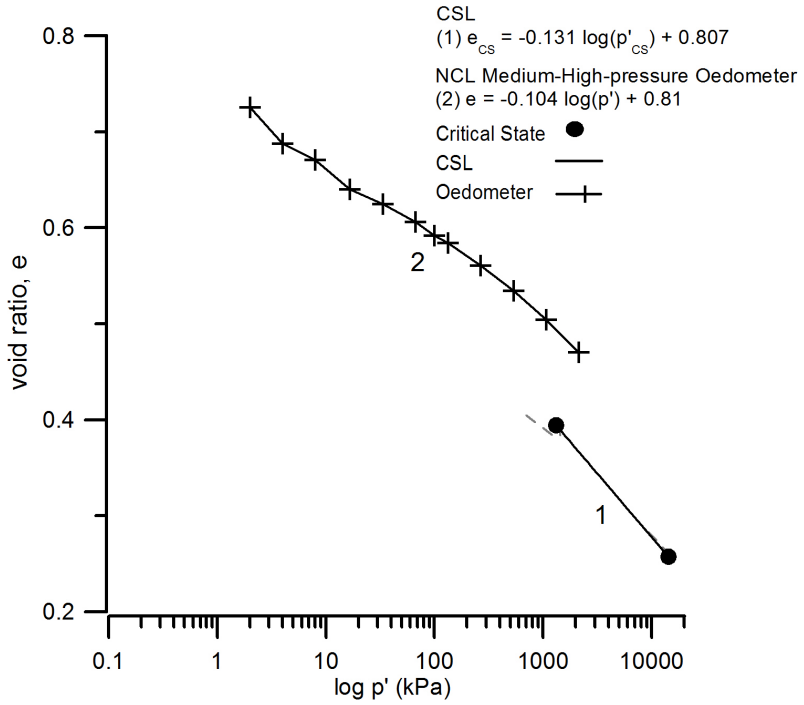


Figure 7.30: Critical state and steady state lines of Coimbra 40

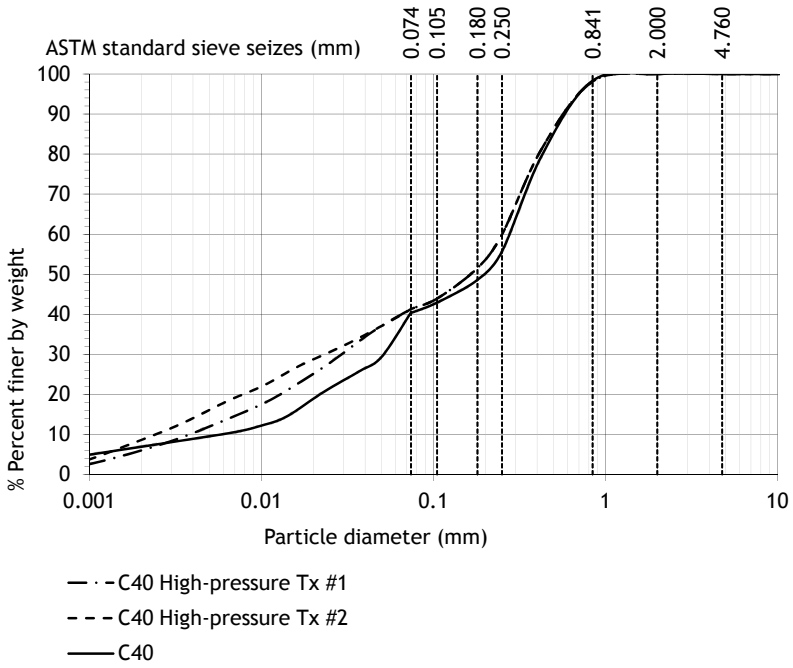


Figure 7.31: Evolution of the grain size distribution of the Tx_CID_2 high-pressure triaxial test (p'_i = 9.2 MPa)

7.6 Osorio Sand

7.6.1 Basic Characterization

Osorio sand, a natural soil from a coastal area in the state of Rio Grande do Sul, in Brazil, around the city of Osorio, was studied in the scope of the present research. Despite its mineralogy not being investigated during this PhD, well documented research provided the information of Osorio sands to be predominantly quartz (Consoli et al., 2007) (Figure 5.33). Table 7.9 provides a resume of Osorio sand basic physical characteristics, previously presented in Chapter 5, according to tests performed at LabGeo.

Table 7.9: Basic physical characterization of Osorio sand

ID	Unit Weight volume of solid particles	Unit Weight volume	Grain size distribution ASTM sieves			FC	Cu	Cc	Maximum and Minimum void ratio	
	γ_s	$\bar{\gamma}$	Nº20	Nº60	Nº200	%			e_{max}	e_{min}
	(kN/m^3)	(kN/m^3)	0.841 mm	0.250 mm	0.075 mm					
Osorio sand	26.5	15.0	100.0	81.0	4.0	<4	1.9	1.0	0.85	0.57

7.6.2 Triaxial Tests

In the scope of the present research, the study of Osorio sand was suggested in order to investigate the effect of the fines content on both stiffness and strength, particularly on soil liquefaction potential. The study was initiated with an inert material, obtained by Osorio sand grinding, by Bedin (2010) . Later the study was prolonged to include the original soil, Osorio sand, and to an intermediate soil, a mixture of silt and Osorio sand.

A set of compression triaxial tests, more precisely 15 under drained conditions and 12 under undrained conditions, were performed. The soil was studied under critical state theory and its liquefaction potential was investigated making use of the tools previously presented for the the other two soils, Algeria and Coimbra sands. Furthermore Osorio sand instability was also investigated through the performance of 3 triaxial tests with a distinct stress-path, by decreasing the mean effective stress, p', and keeping constant the deviatoric stress, q.

7.6.2.1 Drained Triaxial Tests

Osorio sand drained triaxial tests results are presented in Figure 7.32, being the unique high-pressure triaxial test represented separately in Figure 7.33.

With exception of the 6 last triaxial tests, all the other tests experienced a volume contraction. This occurred as all tests were prepared with high void ratios in order to be sheared from the NCL, thus on the wet side of the CSL. Despite not being very perceptible in Figure 7.32, all the dense tests exhibited a peak shear strength, followed by a strength loss towards the Mohr-Coulomb failure envelope, accompanied by an initial lower volume contraction, which precedes the volume dilation.

The high-pressure triaxial test, shown in Figure 7.33, seems, similarly to the other sands, to not stabilize it volume contraction. This phenomenon is associated, as previously referred, to an evolution of the soil grading curve, as might be seen in Figure 7.34.

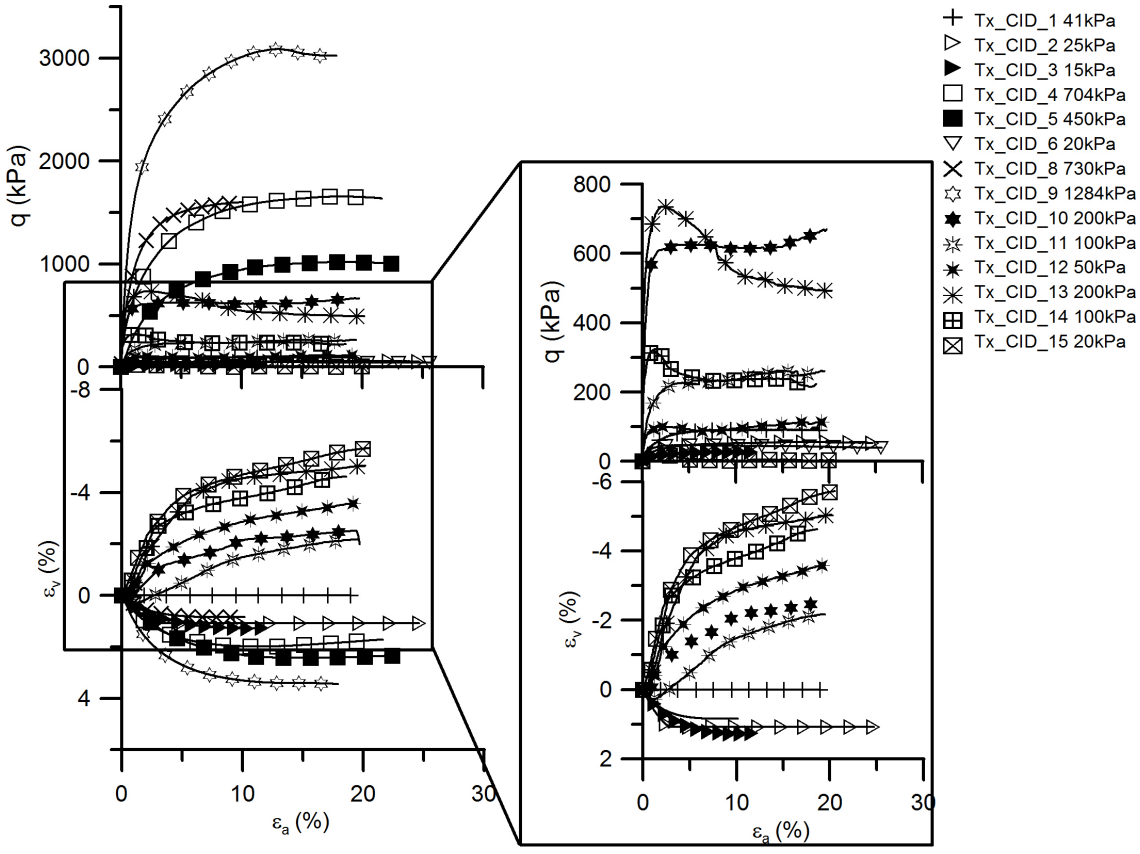


Figure 7.32: Stress-strain and volumetric-strain behavior of drained triaxial tests of Osorio sand at low to medium confining pressures

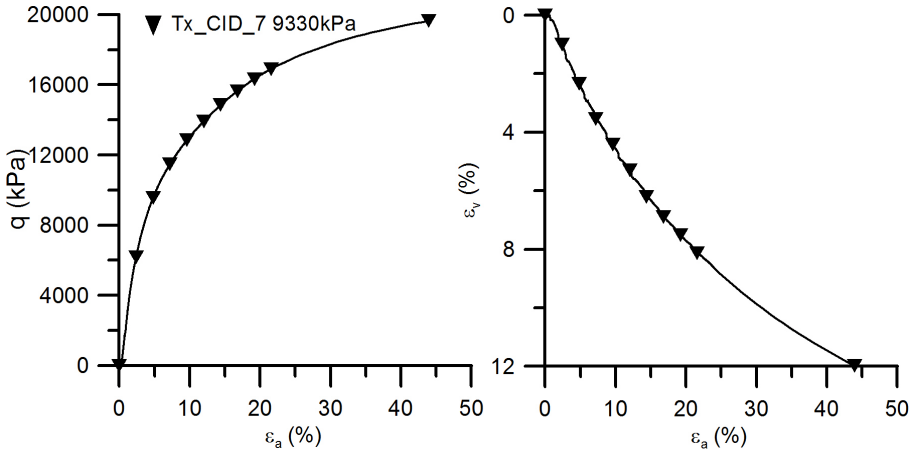


Figure 7.33: Stress-strain and strain-volumetric behavior of the high-pressure triaxial test Tx_CID_7

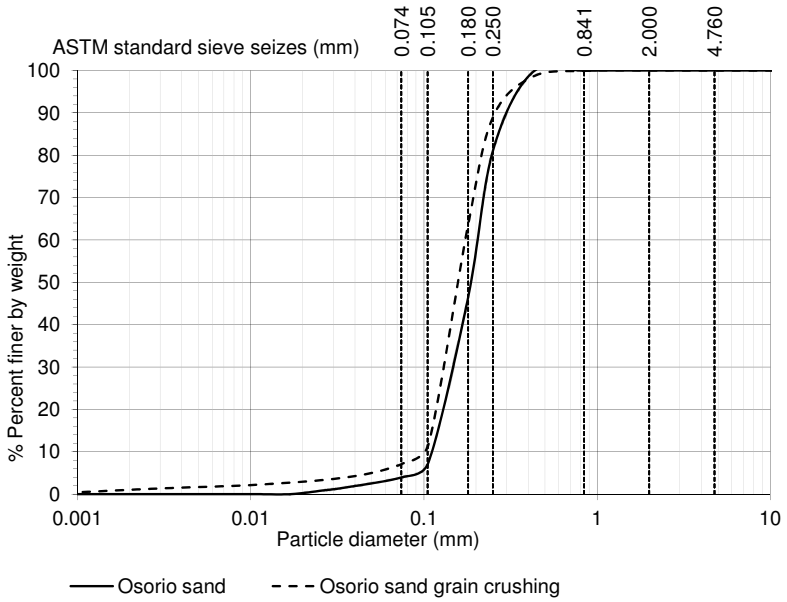


Figure 7.34: Evolution of the grain size distribution of the Tx_CID_7 high-pressure triaxial test (p'_i = 9.3 MPa)

7.6.2.2 Undrained Triaxial Tests

Osorio sand undrained triaxial tests results are shown in Figure 7.35.

Except for Tx_CIU_11 test, all tests exhibit a positive pore pressure generation associated to the high void ratios.

Once more two typical undrained behaviors are observed in Osorio sand compression triaxial tests: flow liquefaction and limited liquefaction with strain hardening. This means that when a certain contact between grains is ensured, either by volume contraction during consolidation, either because the existence of a limiting void ratio, then the pore pressure is not enough to in-

duce flow liquefaction. For Osorio sand this limit seems to be, for specimens prepared from the NCL, a confining pressure of 200 kPa, (for the Tx_CIU_2, Tx_CIU_3, Tx_CIU_4 and Tx_CIU_5 tests).

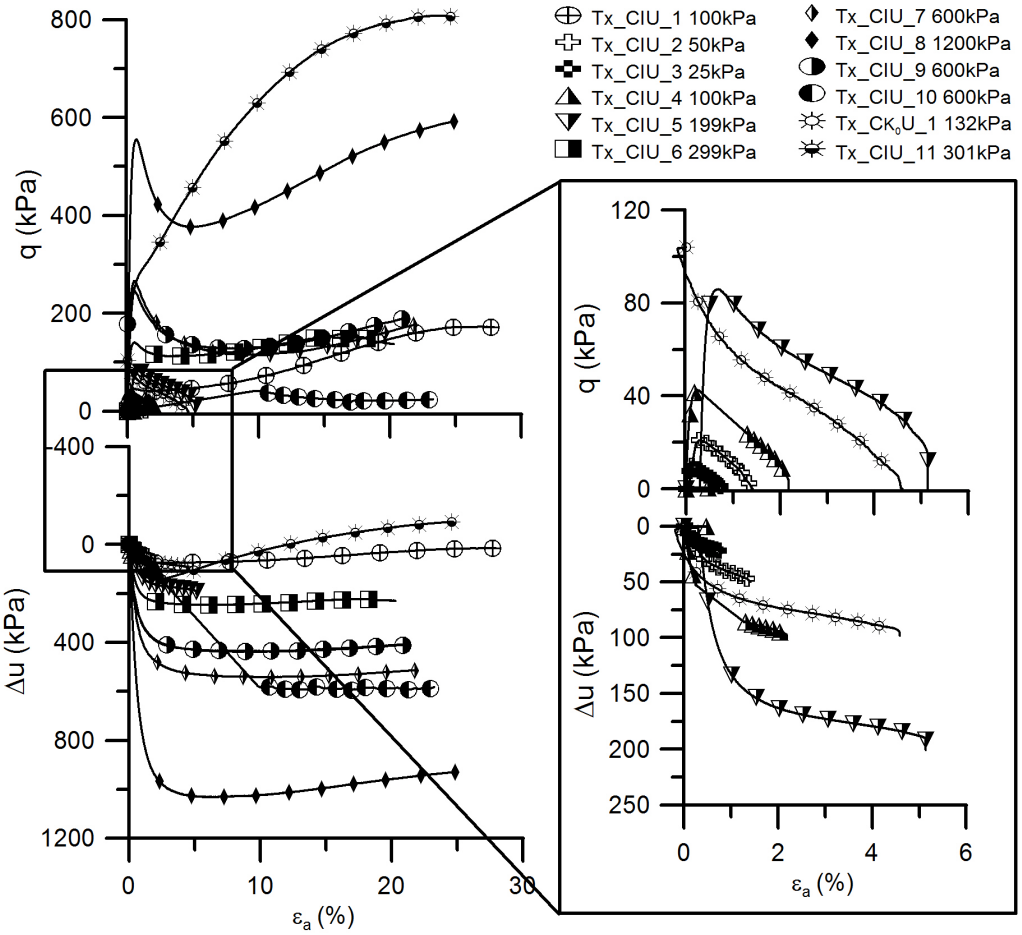


Figure 7.35: Stress-strain and strain-pore water pressure behavior of undrained triaxial tests of Osorio sand at low to high confining pressures

7.6.2.3 Soil Behavior Under Applied CSSM

The set of tests performed, under both drained and undrained conditions, allowed to achieve Osorio sand ultimate states, both CSL and SSL (see both Figures 7.36 and 7.37).

As explained earlier, Osorio sand deem to liquefy for confining stresses of at least 200 kPa, while initially normally consolidated. For higher confining stresses the soil exhibits a stable behavior, accompanied by strain hardening, which ultimate state deems to merge with the ultimate states achieved by drained low confined triaxial tests. Thus if divergence exists between CSL and SSL it occurs for confining pressures lower than 24 kPa, which is the ultimate state attained by test Tx_CID_3.

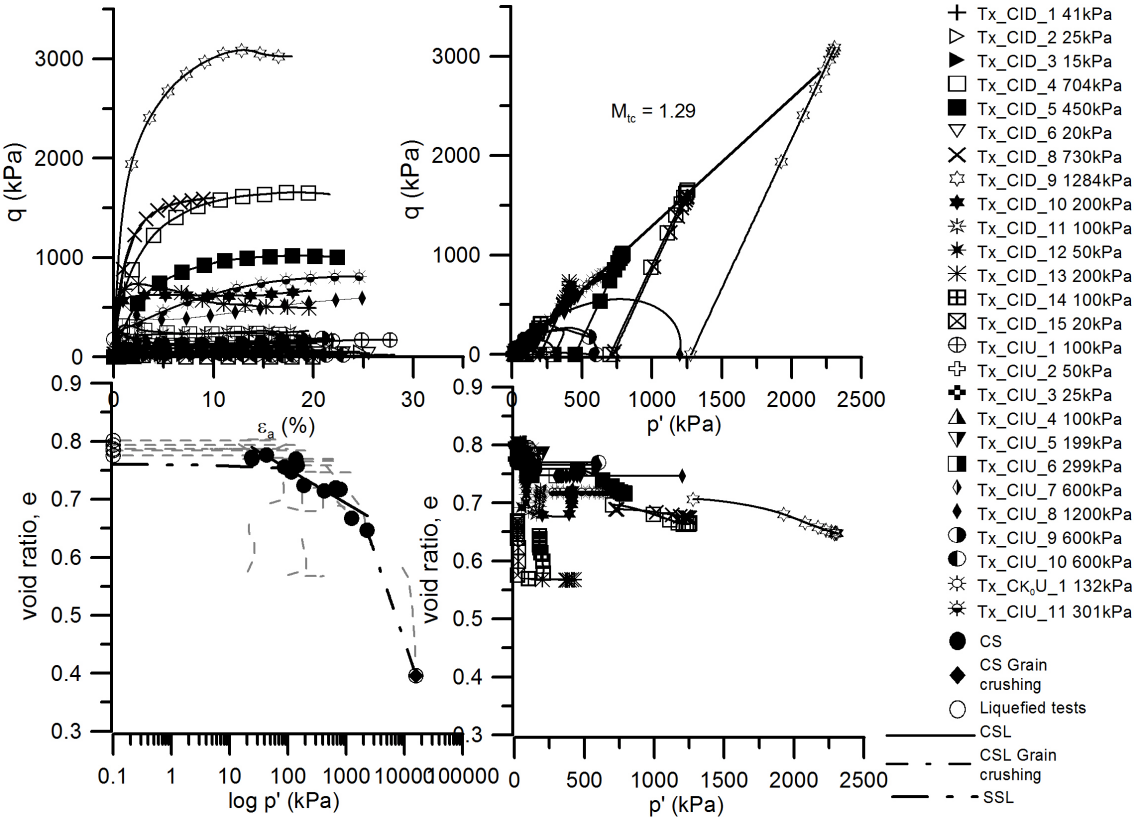


Figure 7.36: Construction of the critical state line for Osorio sand

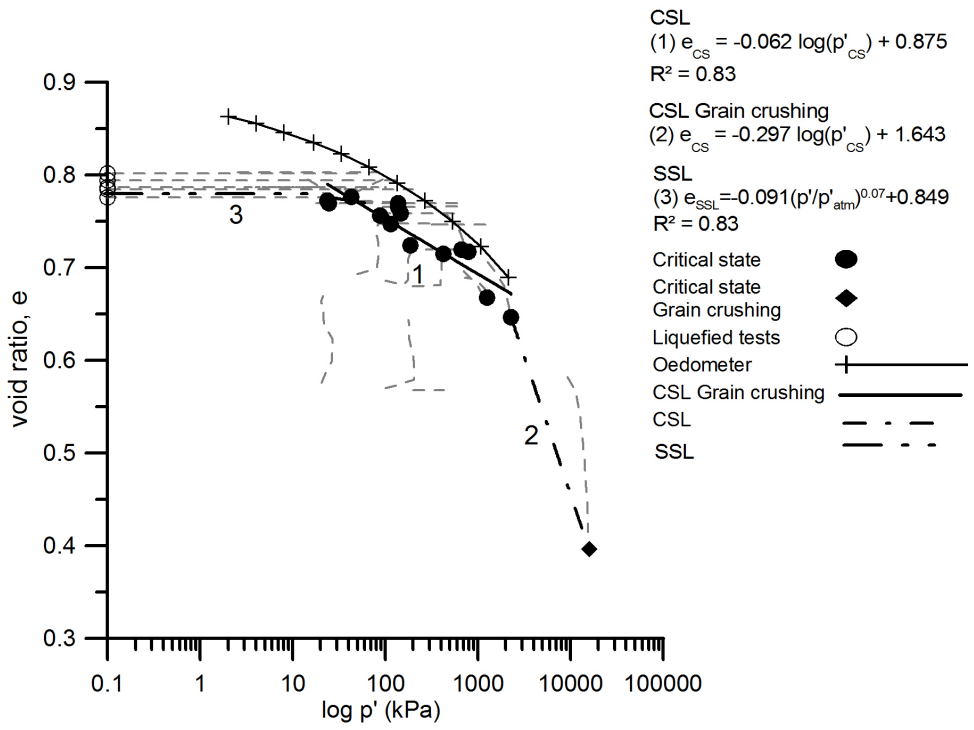


Figure 7.37: Critical state and steady state lines of Osorio sand

As for the high confining pressures, similarly to all the other sands, grain crushing seems to prevail the geomechanical behavior of Osorio sand. In Figure 7.37 grain crushing is also obvious by analyzing the compression line determined by the oedometer test. This suggests that the CSL of Osorio sand, similaly to the other sands, might not be linear in the semi-log e:p' space, but a curve.

Regardless Osorio sand not exhibiting a clear distinction between CSL and SSL, the last one was also determined for the purpose of being additionally used on the soil liquefaction assessment. As explained before it seems more reasonable to establish a state parameter with reference to the curved shaped line proposed by Li et al. (1999). This allows having a higher state parameters for lower confined specimens, which are more susceptible to liquefaction.

Both equations for SSL and CSL (with or without grain crushing), found for Osorio sand, are defined in Figure 7.37. According to the definition of the Critical State Line (CSL), $e_{cs} = \Gamma + \lambda \times \log\left(p'_{cs}\right)$, the values of the reference void ratio, Γ, and the slope, λ, were determined for Osorio sand, getting the values of 0.875 and -0.062, respectively. On the other hand the values adopted for λ_s, ξ and e_{c0} parameters, which define the curved SSL, are of -0.0091, 0.07 and 0.845, respectively.

For Osorio sand a value of 32.1º for the critical friction angle, ϕ_{cv}, was found, correspondent to a critical friction ratio, M, of 1.29, typical of cohesionless soils (see Figure 7.36).

7.6.2.4 Drained Triaxial Tests With Decreasing Mean Confining Stress And Constant Deviator Stress

Aiming to understand the phenomenon beyond the instability line and the onset of flow liquefaction, a set of three triaxial tests with a distinct stress-path was performed.

The tests were carried out on conventional triaxial tests and an initial anisotropic consolidation was applied. Then the specimens were led to failure by decreasing the mean effective stress by means of a pore-water pressure (BP) increase.

From Figure 7.38 stress-strain and stress-paths can be analyzed. While it is clear that $T_{x_{q=constant}}_CK_0D_1$ test have not liquefied, the other two tests are not so clear. Despite $T_{x_{q=constant}}_CK_0D_3$ seem to have liquefied, in reality the complete loss of strength only occurred when the back-pressure equalized the confining-pressure (CP=BP). Thus the only test which was actually considered to have liquefied was the $T_{x_{q=constant}}_CK_0D_2$, which was accompanied by a sudden loss of the bearing capacity.

Curiously it would be expected for the specimen to liquefy when reaching the IL. However the IL represented on Figure 7.38 was determined by plotting the peak strengths of the undrained isotropically consolidated specimens and not by the peak strengths achieved by the anisotropically consolidated specimens.

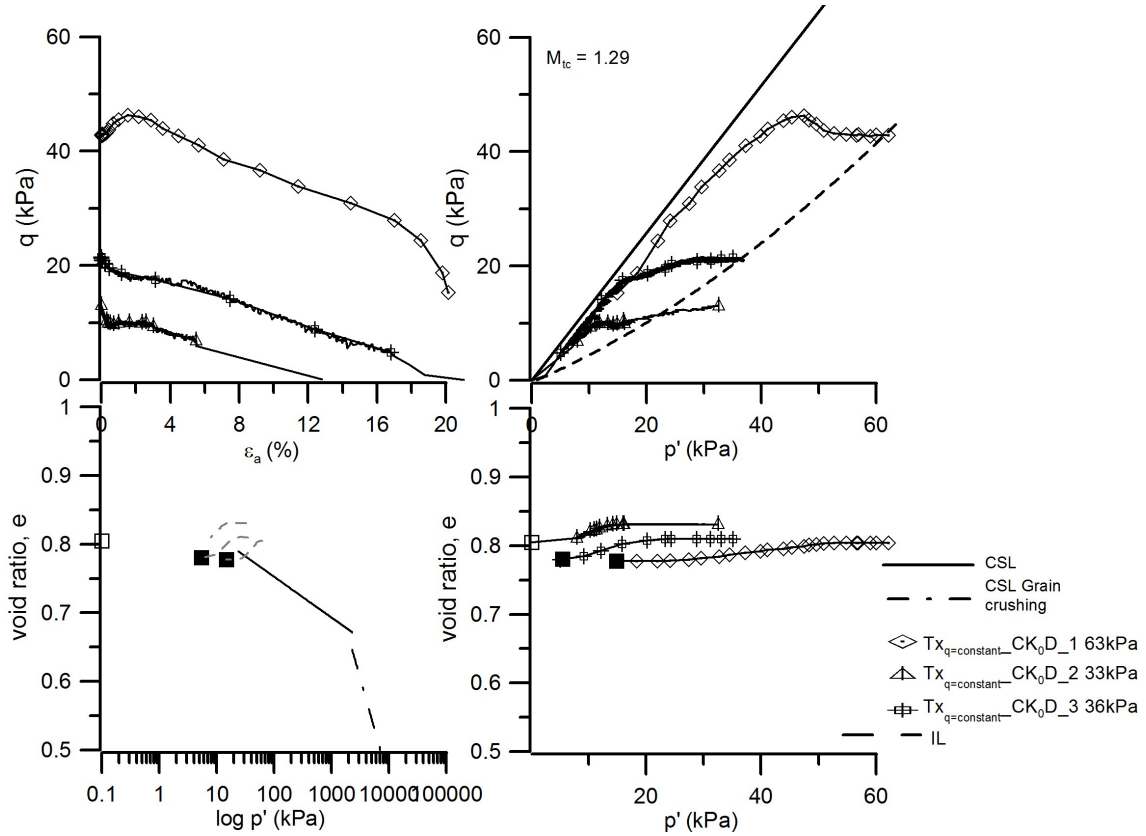


Figure 7.38: Stress-strain and stress-path of the set of triaxial tests with decreasing p'; study under applied CSSM

From Figure 7.38 it was found that the specimen which liquefied had the highest void ratio, which associated to a low confining pressure led to an instability. This means that flow liquefaction and therefore instability might not be only a function of drainage condition, but more importantly a function of the ability of the soil to carry on a stress transference, being therefore a function of the initial void ratio and of the initial confining stress. Therefore this stability is ensured by a greater contact between the particles of the soil.

Due to the reduced number of this type of triaxial tests performed with Osorio sand, a detailed study of instability associaed to this type of stress-path is presented on next subsections.

7.6.3 Prediction Of Liquefaction Resistance

Osorio sand liquefaction potential was evaluated following the same procedures adopted for the other soils. Beyond the conventional triaxial tests, also the $T_{x_{q=constant}}_CK_0D$ were included in these frameworks. Before going further it is important to highlight that the stress-paths presented on the previous subsections where deemed to fail either by reaching a zero mean effective stress when liquefaction takes place or by the point when the stress-path crossed the failure surface in case stability was reached.

When correlating both the ψ_{SSL} and the stress ratio p'/p'$_{SSL}$ with the brittleness index, I_B, a good trend line was outlined (Figure 7.39). Unlike the other two sands, this steady state parameter seems to be well determined, displaying an increasing stability with with decreasing I_B. This means that the liquefaction potential is highly related with the steady state parameter, as well as with the stress ratio p'/p'$_{SSL}$. Figure 7.39 shows that Osorio sand liquefied, (I_B = 1), for higher values of the steady state parameter, ($\psi_{SSL} > 0.02$), and for higher values of the stres ratio p'/p'$_{SSL}$, (p'/p'$_{SSL}$ > 10). For lower ψ_{SSL} a set of tests exhibit intermediate I_B which is associated to limited liquefaction with strain hardening. Finally for ψ_{SSL} < -0.01 or p'/p'$_{SSL}$ < 0.02 the soil exhibits a completely stable behavior. This Figure also reveals that it is possible that the anisotropically consolidated $T_{x_{q=constant}}_CK_0D$ tests tend to a distinct SSL, which would explain its dispersion from the trend observed with the isotropically consolidated specimens.

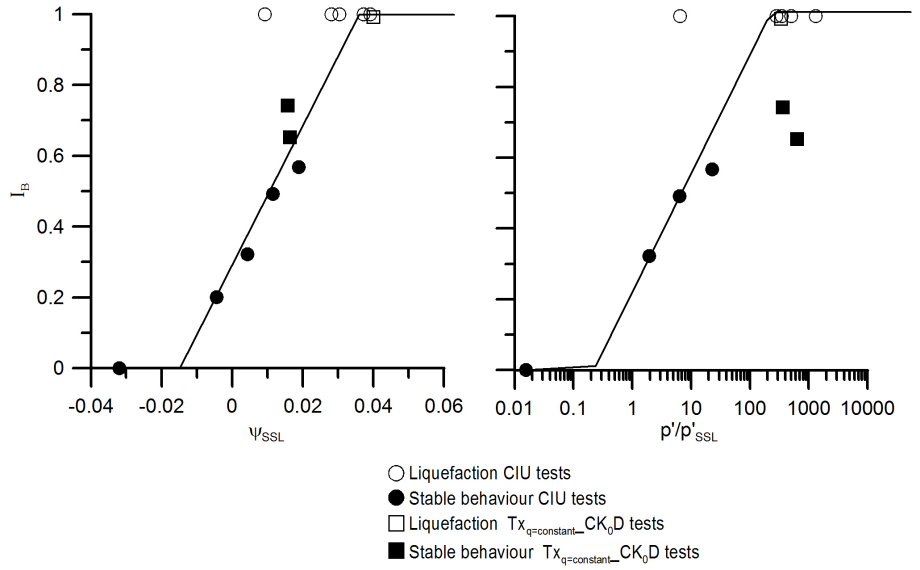


Figure 7.39: Variations of the Brittleness Index with the steady state parameter, ψ_{SSL}, and the ratio p'/p'$_{SSL}$, from left to right, respectively, for Osorio sand

The second framework to assess Osorio sand liquefaction potential can be seen in Figure 7.40, where the steady state parameter is represented as a function of the normalized peak shear strength, q_1, and of the shear stiffness, V_{s1}. According to this Figure a decreasing initial state parameter is associated with an increasing peak shear strength and with an increasing shear stiffness, as a reflection of an increasing stability. Furthermore the figure also exhibits a clear boundary, separating liquefaction from stability, which takes the values of 1 and of 225 m/s for q_1 and V_{s0}, respectively. Curiously this boundary seems to move from 1 to 0.5 for the q_1 and from 225 m/s to 215 m/s for the $T_{x_{q=constant}}_CK_0D$ tests, reflecting a more stable behavior for this type of stress-path. This increasing stability is expressed in terms of the limiting ratio V_{s0}/q_{peak} by an increase of it value from 2 to 10.

The relationship existent between shear strength and shear stiffness for Osorio sand can be seen in Figure 4.41a. This relationship reflects the ability of the grains to transfer the shear stresses

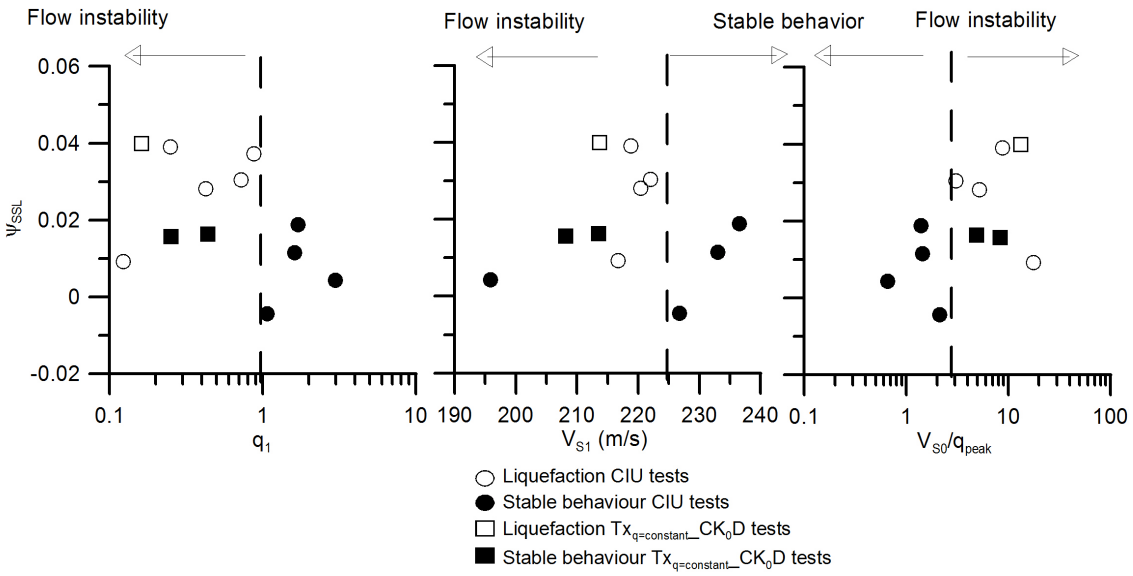
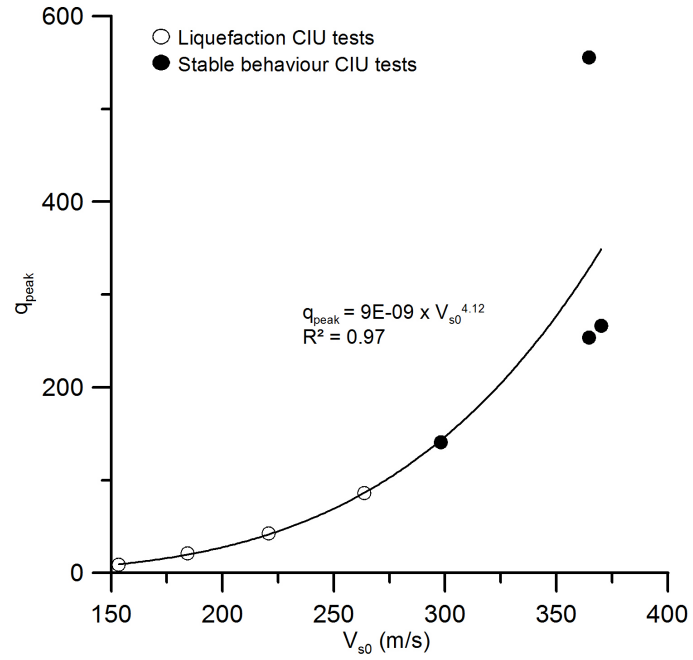


Figure 7.40: Steady state parameter expressed as a function of normalized peak shear strength (q_1) and shear stiffness for Osorio sand

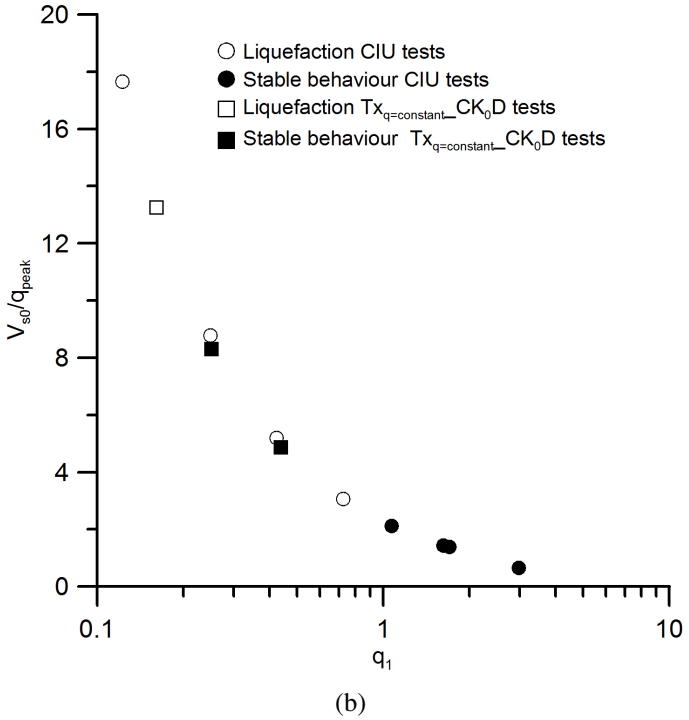
between particles contacts. From the plotted graph it is perceptible that Osorio sand, for higher shear wave velocities than approximately 275 m/s, assures the minimum required grains contact to hold up the shear stress without undergoing on a liquefaction process.

Aware of the relationship existent between shear strength and shear stiffness, the ratio V_{s0}/q_{peak} is proposed to assess soil liquefaction potential. Its use can be made as a function of the steady state parameter, ψ_{SSL}, as proposed above, or as function of the normalized peak shear strength, q_1, as can be seen in Figure 4.41b. Nonetheless the strong correlation between both V_{s0}/q_{peak} and q_1 disrupts the real sense of correlating two distinct variables. However it is perceptible that for lower ratios than 2, Osorio sand starts exhibiting a stable behavior. This ratio assumes the value of approximately 10 for the anisotropically consolidated specimens, led to failure by an increasing pore-water pressure. Thus soils subjected to this type of stress-paths are less susceptible to suffer from flow liquefaction. This can only mean that either the soil possesses a higher strength to this type of stress-path towards failure or the induced anisotropy is responsible for increasing it strength and stiffness. Despite not being included the study of the influence of the induced anisotropy on the liquefaction potential of Osorio sand, from the results observed for Algeria sand, induced anisotropy appears to have little influence on IL, thus not explaining the differences observed in Figure 4.41b. Therefore these differences are apparently exclusively associated to the influence which the stress-path has on the onset of instability.

Osorio sand IL can be consulted in Figure 7.42. According to this plot is observed an increasing in peak shear strength with increasing confining stress. However such difference is not as obvious as the ones observed for Coimbra and Algeria sand. In fact a p'_{peak} of 800 kPa is associated with a q_{peak} of approximately 550 kPa, which for any of the other two sands would be a value between 700 and 800 kPa. Thus Osorio sand is clearly more brittle than the other two sands, perhaps



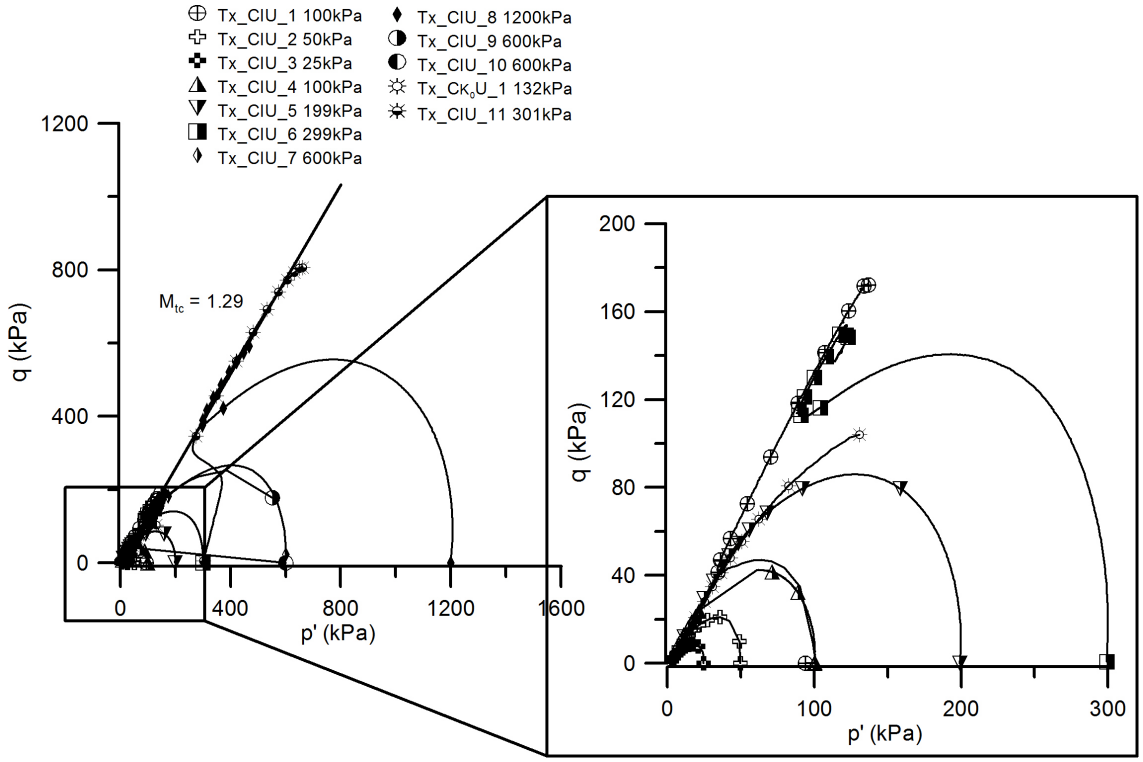
(a)



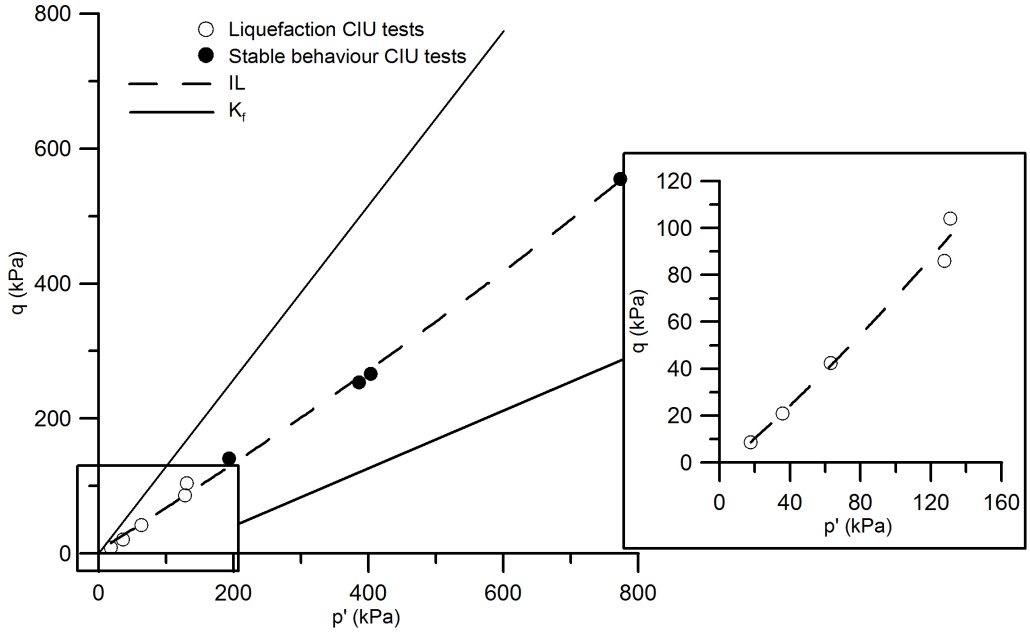
(b)

Figure 7.41: a) Peak shear strength as function of the soil stiffness; b) Correlation between the normalized peak shear strength and the ratio between shear stiffness and the peak shear strength for Osorio sand

because of its higher fines' content.



(a)



(b)

Figure 7.42: a) Detail of the stress-path of the triaxial tests; b) Instability Line (IL) for Osorio sand

7.6.4 Partial Conclusions

Osorio sand strength and stiffness was evaluated through the performance of a set of compression triaxial tests, completed with three triaxial tests led to failure by increasing the pore water pressure (BP).

Similarly to the other two sands, three distinct ultimate states lines were attained. Despite both drained and undrained conditions have not led to distinct ultimate states, a SSL was also defined for a proper evaluation of the soil liquefaction potential.

Being most of the specimens prepared from the NCL, it is conclusive that:

- For void ratios higher than approximately 0.78, and initial confining pressure lower than 200 kPa – Liquefaction takes place; (Note: it is important to highlight that liquefaction only takes place for confining stresses lower than 200 kPa as the void ratio of 0.78 is not attainable for higher initial confining stresses);
- Medium confining stresses to high confining pressures – Limited liquefaction with strain hardening occurs; When strain hardening rules the soil behavior, the ultimate states of both drained and undrained triaxial tests converge into a unique line;
- Very high confining pressures ($p'_i > 1$ MPa) – Grain crushing.
- CSL was achieved through the performance of both drained and undrained triaxial tests.

A resume of the distinct ultimate state lines are expressed in the table below:

Table 7.10: Resume of the ultimate states for Osorio sand according to the type of test

	Soil behavior	Type of tests	Equation
CSL	Stable behavior	Drained and undrained triaxial tests	(1) $e_{cs} = -0.062 \log(p'_{cs}) + 0.875$
CSL	Grain crushing	High-pressure triaxial tests, sheared under drained and undrained conditions	(2) $e_{cs} = -0.297 \log(p'_{cs}) + 1.643$
SSL	Liquefaction and strain softening	Undrained triaxial tests	(3) $e_{ss}=-0.091(p'_{ss}/p'_{atm})^{0.07}+0.849$

Soil liquefaction potential was properly assessed by using the steady state parameter, unlike what happened to the other two sands. However for this particular soil SSL and CSL converge for a much wider range of mean effective pressures and void ratios, meaning that the SSL is not flatten for such a wide range of mean effective pressures. Thus the ψ_{SSL} becomes more accurate and precise to evaluate soil liquefaction potential, similarly to the stress ratio p'/p'_{SSL}.

It should be emphasized, that soil stiffness (G_0 – read V_s) and the ratio stiffness-strength (V_{s0}/q_{peak}) are very accurate parameters, with the additional advantage of not requiring CSL determination.

Finally it was also concluded that the phenomenon of instability is not something exclusive of the drainage prevention. Regardless it seems to also occur under drained conditions. However this instability, at least for Osorio sand, is distinct under distinct stress-paths. As it was observed the $T_{x_{q=constant}}_CK_0D$ tests exhibited a much more stable behavior than the undrained compression isotropic triaxial tests. This occurs due to the dissimilarities existent between both stress-paths. While the instability due to the increasing pore water pressure is caused by an unstable microstructural fabric rearrangement, the instability due to undrained conditions is associated to a contractiveness condition mechanical behavior of loose granular material and consequent pore pressure increase (Matiotti et al., 1995). Regardless similarities are usually found on the Instability line (IL), as it seems to influence both drained and undrained stress-paths (Chu et al., 2012).

Table 7.11 provides a resume of the limiting ratios between liquefiable and nonliquefiable behavior for Osorio sand.

Table 7.11: Limiting values between liquefaction and stable behavior for Osorio sand

Parameter	Limiting value
ψ_{SSL}	ψ_{SSL}<0.02
p'/p'$_{SSL}$	<10
V_{s1}	>225m/s
V_{s0}/q_{peak}	<2

7.7 Silty Sand - Mixture

7.7.1 Basic Characterization

Mixture, a silty sand soil obtained by mixing a natural soil, Osorio sand, with an artificial soil, a silt, obtained by grinding Osorio sand, was studied aiming to understand the effect of the fines content on soil liquefaction potential. Despite it mineralogy not being investigated in the scope of this research project, well documented research provided the information of Osorio sand to be predominantly quartz (Consoli et al., 2003, 2007). Therefore the mixture is also predominantly constituted by quartz (Figure 5.33). Table 7.12 provides a resume of the Mixture basic physical characteristics, previously presented in Chapter 5, according to tests performed at LabGeo.

Table 7.12: Basic physical characterization of Mixture

ID	Unit Weight volume of solid particles	Unit Weight volume	Grain size distribution ASTM sieves			FC	Cu	Cc	Maximum and Minimum void ratio	
	γ_s	$\bar{\gamma}$	Nº20	Nº60	Nº200	%			e_{max}	e_{min}
	(kN/m^3)	(kN/m^3)	0.841 mm	0.250 mm	0.075 mm					
Mixture	26.5	15.0	100.0	99.9	41.9	<41.9	32.4	2.6	n.v.	n.v.

7.7.2 Triaxial Tests

Similarly to Osorio sand, the Mixture was also studied mainly to achieve not only CSL positioning, but also to determine the soil liquefaction potential for further comparison with the congener soils. Both stiffness and strength were quantified particularly to assess it sensitivity and precision, as function of the fines content, to measure soil liquefaction potential.

A set of compression triaxial tests, more precisely 15 under drained conditions and 10 under undrained conditions were performed. Following the same procedures used for the others soils, the Mixture was evaluated under applied CSSM, making also use of the measured stiffness parameters (G_0 – read V_s).

The onset of instability was also investigated through the performance of $T_{x_{q=constant}}_CK_0D$ tests, i.e. anisotropically consolidated triaxial tests lead to failure by increasing the pore-water pressure, therefore with drained conditions, and by the performance of $T_{x_{p'=constant}}_CID$ and $T_{x_{p'=decreasing}}_CID$ triaxial tests. These last type of triaxial tests were performed on a Bishop-Wesley cell, led to failure by decreasing or by keeping constant the mean effective stress. As reported before both instabilities, triggered due to drainage conditions or due to the unstable microstructural fabric rearrangement, are distinct but apparently both are affected by the IL positing. Furthermore, it becomes important to assess if the bifurcation between the CSL and the SSL is only a matter of drainage or if is also related to the microstructural fabric rearrangement.

7.7.2.1 Drained triaxial tests

The stress-strain-volumetric behavior of Mixture under drained conditions might be seen in Figure 7.43. This graph shows that all performed tests exhibit a contractive behavior, as no peak strength, associated to dilation, is found. This was already expected as the soils were prepared in very loose conditions, meaning on the wet side of the CSL.

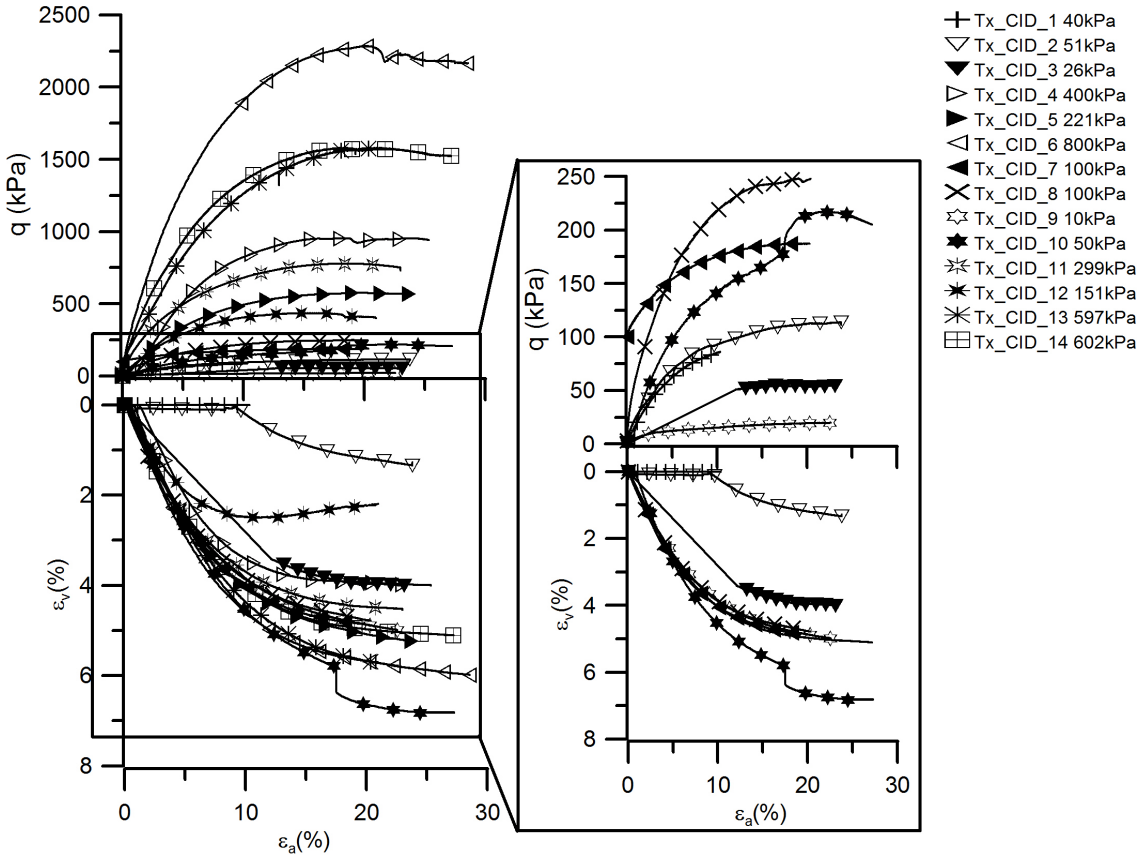


Figure 7.43: Stress-strain and volumetric-strain behavior of drained triaxial tests of Mixture

Furthermore, it can be verified that most of the specimens were sheared from the NCL as they display similar volumetric strains. This is more evident than on the sandy soils not only due to the higher slope of the NCL, which differentiates more the initial state of each test, but also due to the very high void ratio used to prepare all specimens, which ensured that all specimens begun with similar state conditions. It should be also pointed out that the Tx_CID_1 was not saturated at the time of shearing, whereby its volumetric strain was not measured, and the test was only carried out in order to contribute for the determination of the critical friction angle.

When comparing the Mixture with the other sandy soils a particularity arises on what concerns to the axial strain. Looking carefully for both graphs, of Figure 7.43 and 7.44, it is observed that the maximum strength is only achieved for considerably high axial strains, ($10\% < \varepsilon_a < 15\%$), unlike cohesionless monogranular sands, ($\varepsilon_a < 5\%$).

The high-pressure drained triaxial test, (Tx_CID_15), showed in Figure 7.44, was performed over a specimen prepared by air pluviation, for the same reasons pointed above for the other soils. Unlike the other high-pressure trixial tests performed on monogranular sandy soils, the Mixture clearly indicates a full stabilization of the shear strength and volumetric strain, for very low axial strains. This occurs as the soil can rearrange for very low void ratios without being subjected to grain crushing. Figure 7.45 confirms the minor evolution of the grain size distribution curve

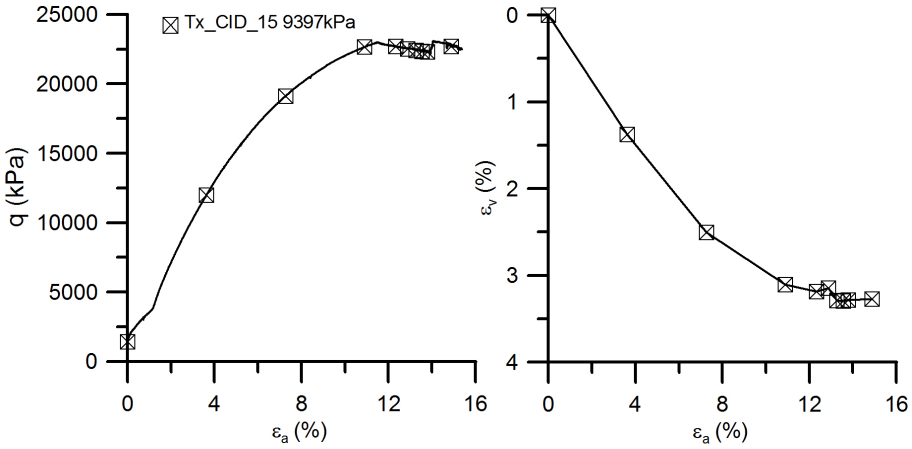


Figure 7.44: Stress-strain and strain-volumetric behavior of the high-pressure triaxial test Tx_CID_15

due to grain size distribution of the soil before and after the high-pressure triaxial test is very similar.

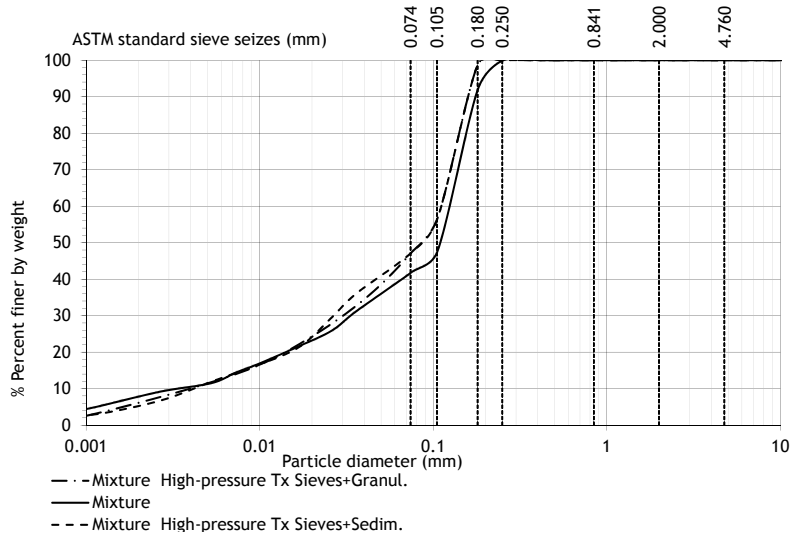


Figure 7.45: Evolution of the grain size distribution of the Tx_CID_15 high-pressure triaxial test (p'_i = 9.4 MPa)

7.7.2.2 Undrained Triaxial Tests

All the undrained compressive trixial tests, plotted in Figure 7.46, confirm that the Mixture exhibits a particular behavior when compared to monogranular sands. Fundamentally, it was observed complete liquefaction, for normally consolidated specimens, up to mean confining stress values of 200 kPa (see Figure 7.46). This would not be strange if the soil started exhibiting a stable behavior when tested under higher confining pressures. However this does not occur and despite not suffering a complete loss of shear strength, in reality all the other tests ends up with a minimum

shear strength. Even the test confined with 1000 kPa, (Tx_CIU_9), ended up with an ultimate shear strength of 96 kPa and an ultimate mean effective stress of 69 kPa.

Therefore, basically, the only undrained behaviors observed in the Mixture are flow liquefaction and limited liquefaction with strain softening, with the particularity of the last one dominating the soil behavior for a wide range of initial confining stresses.

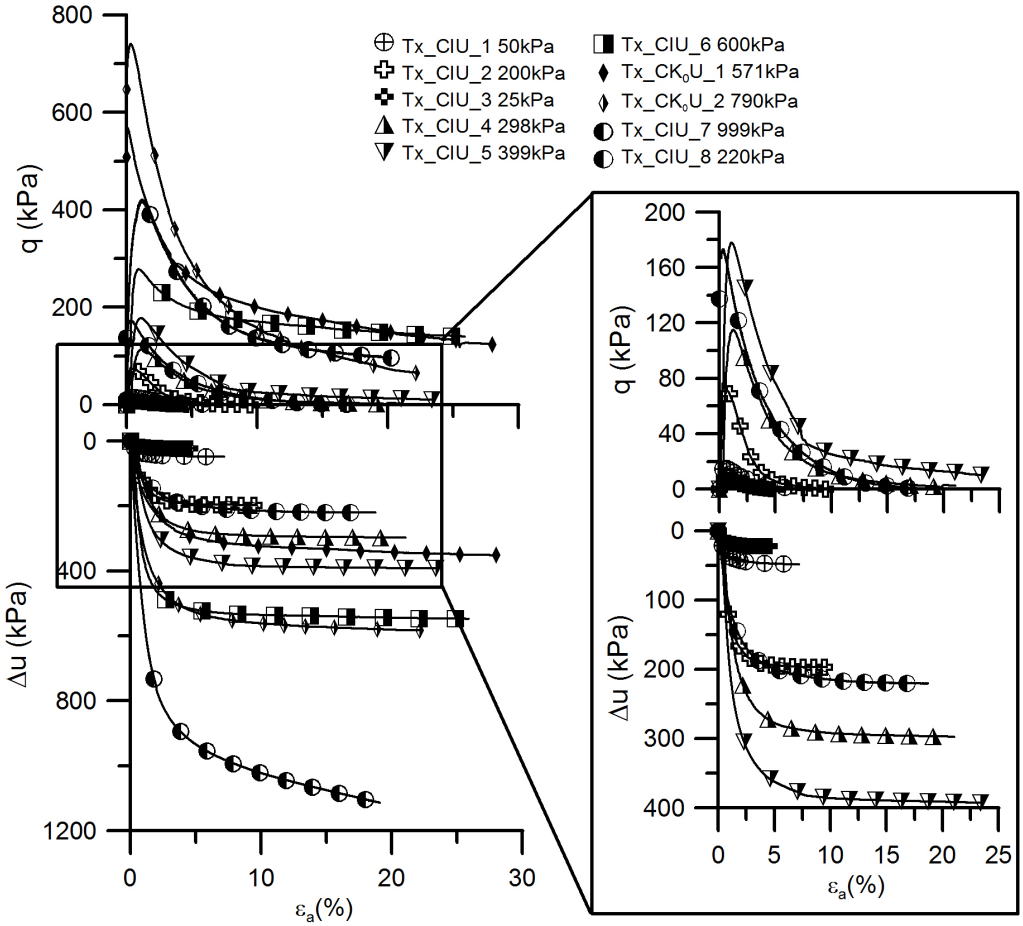


Figure 7.46: Stress-strain and strain-pore water pressure behavior of undrained triaxial tests of Mixture at low to high confining pressures

7.7.2.3 Soil Behavior Under Applied CSSM

The ultimate states attained by the compression triaxial tests allowed outlining both CSL and SSL. According to the stress-strain behavior exhibited by the undrained triaxial tests it would be expected a complete divergence between the ultimate states achieved by the triaxial tests sheared under drained or undrained conditions. Both Figures 7.47 and 7.48 clearly show this divergence between the CSL and the SSL. In fact this soil, due to it high brittleness, does not exhibit any signs of strain hardening, therefore none of the undrained triaxial tests converges with the ultimate states achieved by the drained triaxial tests.

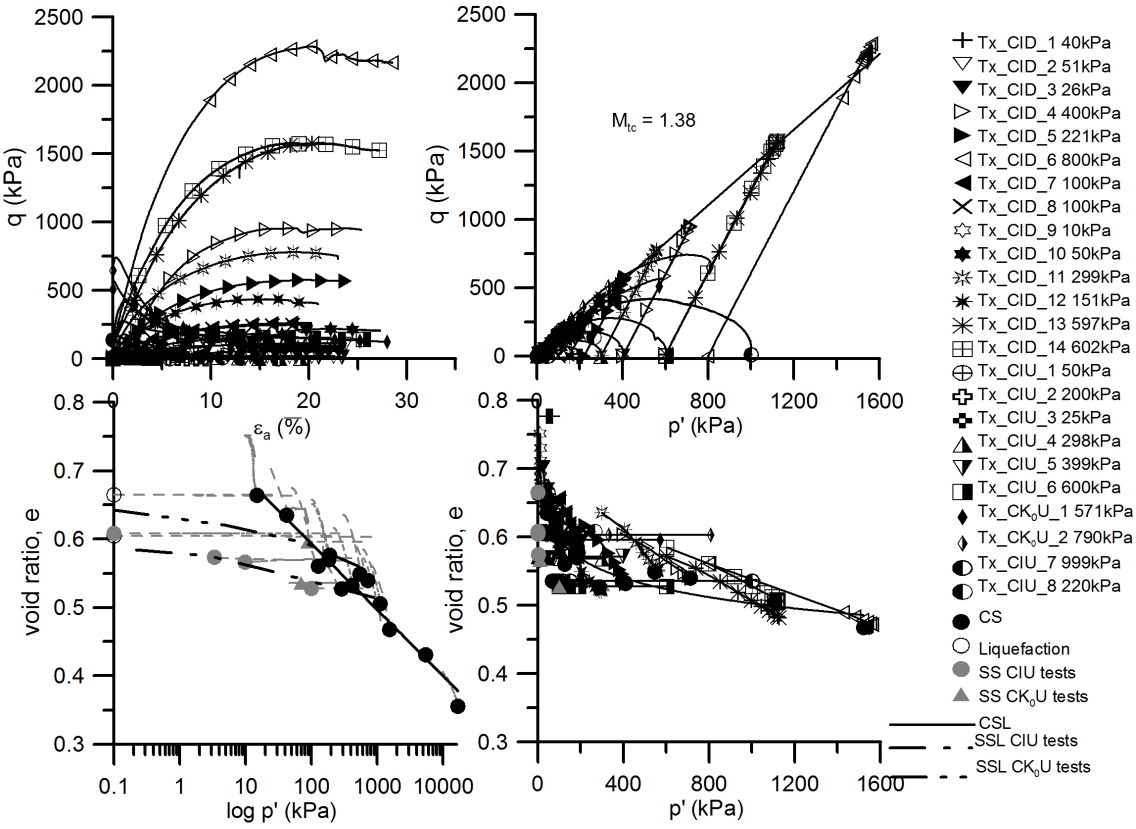


Figure 7.47: Construction of the critical state and steady state line for the Mixture

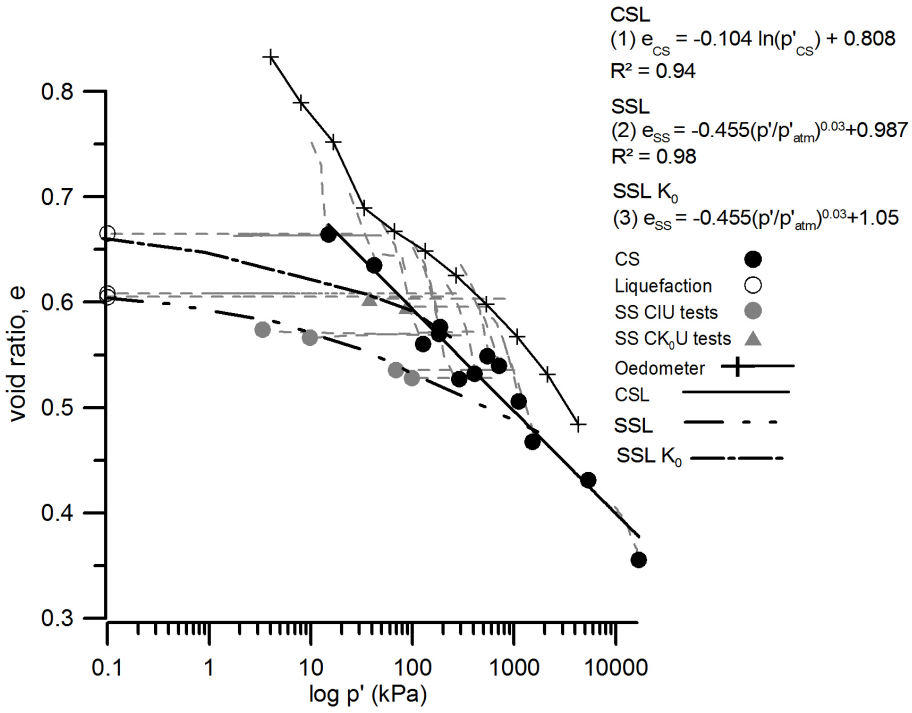


Figure 7.48: Critical state line and steady state line of the Mixture

It is also perceptible that, by observing both Figures 7.47 and 7.48, the high-pressure triaxial test seems to follow the same trend line as the low and medium confined tests, tested under undrained conditions. As explained before, this is likely to be due to the almost non occurrence of grain crushing.

During the research of this material two anisotropic consolidated specimens were also tested under undrained conditions. The effect of the induced anisotropy revealed to be very pronounced on the SSL positioning, unlike what was found for Algeria sand (Figures 7.47 and 7.48). It is obvious that the pronounced effect might be associated to the high range of void ratios covered by the CSL slope. Regardless only through brittleness index assessment major conclusions might be inferred about the effect of the induced anisotropy on the soil liquefaction potential. As can be visualized in Figure 7.47 the SSL positioning does not reflect a much higher stability of the anisotropically consolidated specimens. In fact the drop of the shear strength is also very high, but not as high as the one exhibited by the CIU tests. For example the Tx_CIU_5 and the Tx_CK$_0$U_1 tests have both similar initial void ratios and were consolidated with 400 kPa, and while the drop of the shear strength, with reference to the peak strength, was about 84% for the anisotropically consolidated specimen, the other one exhibited a shear strength drop of 95%.

Both SSL and CSL of the Mixture, are defined in Figure 7.48. The curved shaped line proposed by Li et al. (1999), $e_{ss} = e_{c0} - \lambda_s \left(\frac{p_{ss}}{p_a}\right)^{\xi}$, was adopted for both CIU and CK$_0$U tests ultimate states. Whereby, while for CIU tests values of -0.455, 0.03 and 0.987 were determined for the λ_s, ξ and e_{c0} parameters, respectively, due to the limited number of points of CK_0U tests, the SSL was assumed to be parallel to the one defined by the CIU tests, being only changed the interception value, e_{c0}, to 1.05. On the other hand, the classical definition of the CSL was adopted for the drained triaxial tests. According to the definition of the Critical State Line (CSL), $e_{cs} = \Gamma + \lambda \times \log\left(p'_{cs}\right)$, the values of the reference void ratio, Γ, and the slope, λ, determined for the Mixture, are 0.808 and -0.104, respectively.

Moreover, basing on the total set of triaxial tests, a value of 34.2^{o} for the critical friction angle, ϕ_{cv}, was found for Mixture, correspondent to a critical friction ratio, M, of 1.38.

7.7.2.4 Drained Triaxial Tests With Decreasing Mean Confining Stress And Constant Deviator Stress

The set of triaxial tests prepared to assess instability beyond the drainage boundary conditions was very limited. Among the 4 triaxial tests, led to failure by increasing pore-water pressure, only one experienced liquefaction, the $T_{x_{q=constant}}_CK_0D_1$ test (Figure 7.49). Along only one exhibited a stable behavior, the $T_{x_{q=constant}}_CK_0D_2$ and $T_{x_{q=constant}}_CK_0D_3$ tests, while the others seem to have exhibited a strain-softening behavior (Figure 7.49).

Obviously all the stress-paths move towards the zeroed condition, as BP is always increasing during the shear stage. Nevertheless it is necessary to point out that strategic points were selected before the end of the test which was approximately when the tests reached the failure envelope, unless the soil liquefied.

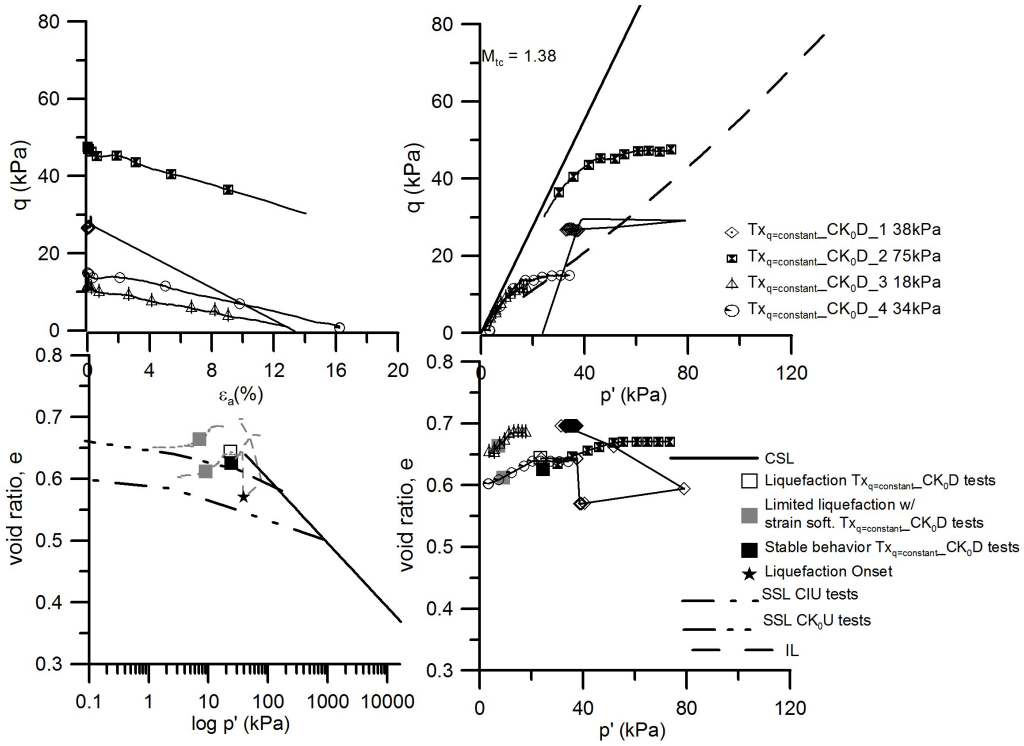


Figure 7.49: Stress-strain and stress-path of the set of triaxial tests with decreasing p' and constant q; study under applied CSSM

From Figure 7.49 it seems obvious the influence of the IL on the $Tx_{q=constant}_CK_0D_1$ test. In fact, liquefaction is only verified when the stress-path reaches the IL. However, despite the shear strength loss, the condition of p' = 0 kPa was not reached. Perhaps this is a problem associated to the TRIAX® controlling software together with the acquisition program. A possible transient condition might have occurred during which the soil actually reached zero effective stress, but due to the ability of the program to reassert the confining stresses this point was not acquired.

It is also necessary to point out that the IL, represented in Figure 7.49, was built up relying only on the isotropically consolidated specimens, and that it is also known that the induced anisotropy can definitely influence the IL positioning.

Apart the test that exhibited a stable behavior, $Tx_{q=constant}_CK_0D_2$, and the $Tx_{q=constant}_CK_0D_3$, both the other tests seem to move toward the SSL defined by the CK_0U tests, during a given time of the shear stage.

Unfortunately, all the 4 triaxial tests were prepared with very low void ratios when compared with the undrained compression triaxial tests. Thus no major conclusions can be outlined from a direct

comparison between distinct stress-paths.

Nevertheless two hypotheses can be postulated: either the initial fabric has an effect on the soil behavior at high strains, meaning that it might affect SSL positioning, or the increasing pore water pressure does not create such an unstable microstructural fabric rearrangement as it would be expected.

7.7.2.5 Drained Triaxial Tests With Constant And Decreasing Mean Confining Stress And Increasing Deviator Stress

As these soils exhibited a large divergence between the CSL and the SSL positioning, in order to investigate the fundament of its positioning a set of triaxial tests were conducted to failure with distinct stress-paths from the conventional paths. Figure 7.50 display the final results achieved by $T_{x_{p'=constant}}_CID$ and $T_{x_{p'=decreasing}}_CID$ triaxial tests. As all tests were initially isotropically consolidated a direct comparison with the T_x_CIU tests is allowed. According to Figure 7.50 apparently their ultimate states, regardless the drainage condition, fell on the same SSL defined by the T_x_CIU. The importance of such fact is of high relevance as most constitutive models predict soil liquefaction relying on the Hill condition. Figure 7.50 makes clear that the divergence between the CSL and the SSL is not associated to the prevention of the drainage conditions, rather to the loose configuration of the soil, which under non-compression loading fall into a distinct ultimate state, associated to a non-increase of the mean effective stress.

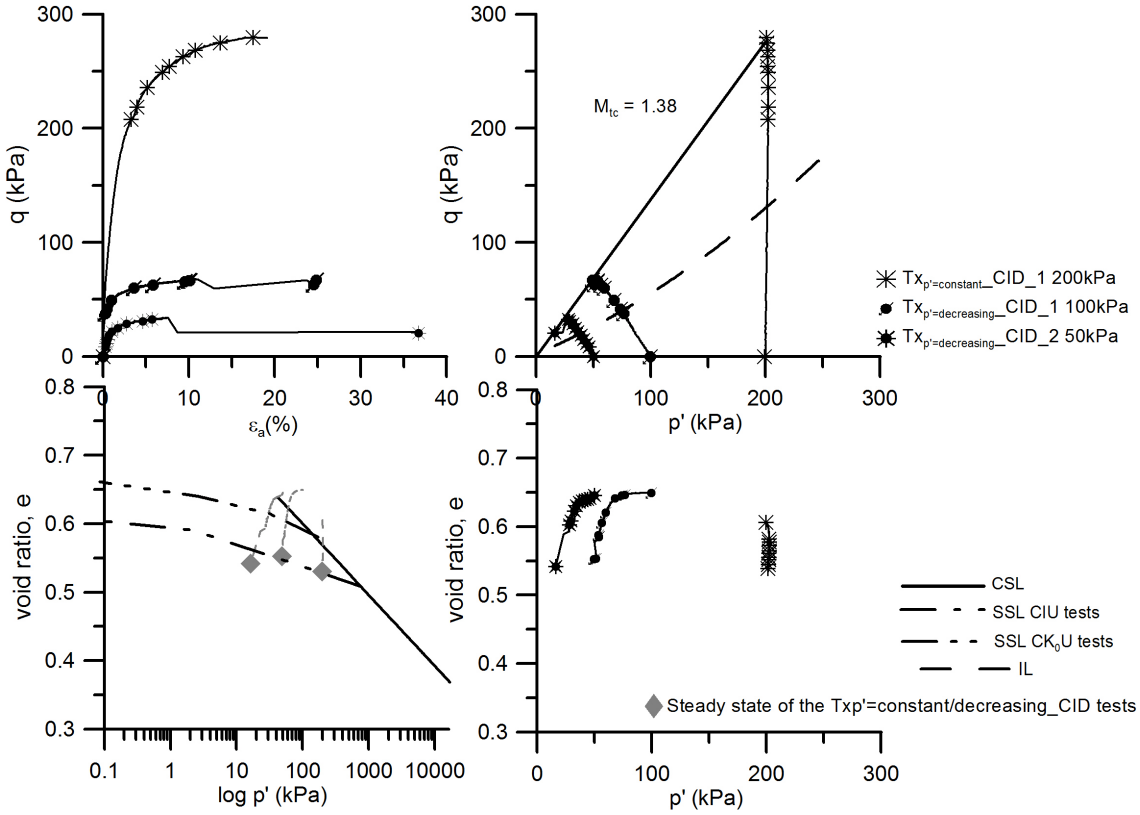


Figure 7.50: Stress-strain and stress-path of the set of triaxial tests with constant and decreasing mean confining stress and increasing deviator stress; study under applied CSSM

7.7.3 Prediction Of Liquefaction Resistance

The liquefaction potential of Mixture was assessed by correlating strength parameters with/and/or shear stiffness parameters. Before proceeding it should be refered that both the steady state parameter, ψ_{SSL} and the stress ratio p'/p'_{SSL}, represented on these frameworks were determined, basing on both SSL represented in Figure 7.48. Furthermore the ψ_{SSL}, of the $T_{x_{q=constant}}_CK_0D$ tests, were also determined with reference to the SSL defined by the CK_0U triaxial tests.

As it was expected, the steady state parameter seems to provide an accurate parameter to evaluate liquefaction susceptibility of the Mixture. From Figure 7.51 it can be observed that while for ψ_{SSL} > 0.06 the soil is potentially liquefiable (I_B = 1), for lower values and up to 0.00, the soil exhibits strain softening. As pointed out previously this soil has not exhibited a stable behavior even for high confining pressures, whereby black dots are not observed.

Comparing the left hand graph with the right hand graph it could be said that the ψ_{SSL} provides a better parameter than the stress ratio p'/p'_{SSL}. However by excluding the extreme left CK_0U tests, only two patterns become evident, the one followed by the classic triaxial tests, and the diffuse pattern followed by the $T_{x_{q=constant}}_CK_0D$ tests. No major conclusions are outlined for this last stress-path due to the dispersion of the small number of tests results.

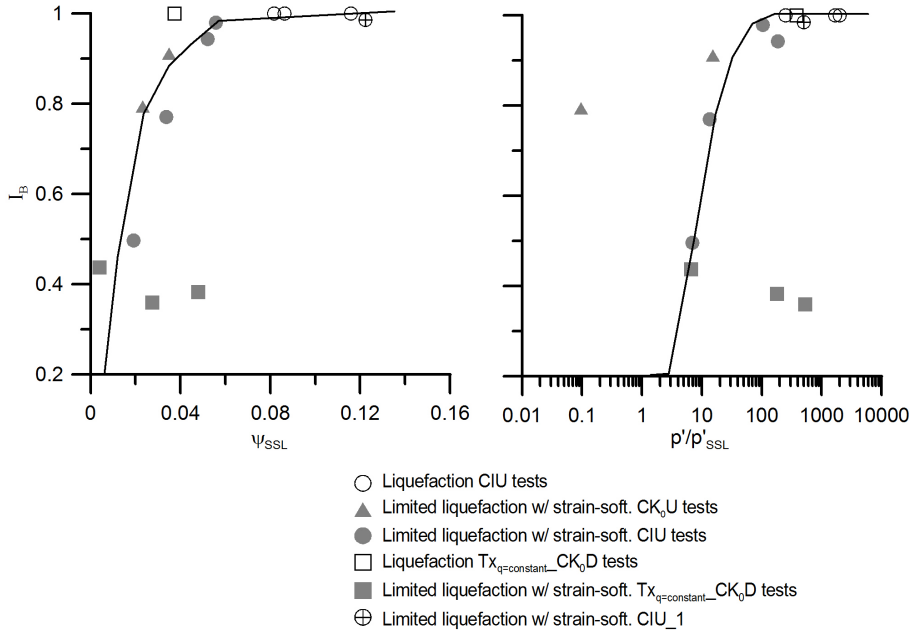


Figure 7.51: Variations of the Brittleness Index with the state parameter, ψ, and the ratio p'/p'$_{CS}$, from left to right, respectively, for the Mixture

Among the limited number of undrained compression triaxial tests, only a few triaxial tests were supplied with the measurement of shear stiffness. Hence there is a significant lack of points represented on Figure 7.52. Nevertheless the trend suggested by the circles is obvious, and a remarkable decreasing steady state parameter is observed with increasing normalized peak strength, q_1, and normalized shear wave velocity, V_{s1}. With this results it was possible to establish the limits for which the soil stops liquefying, as the first test which have not liquefied, Tx_CIU_4, initially confined with 300 kPa, provided one of the values of the shear wave velocity represented below. These limits, for isotropically consolidated specimens, are of 1.5 for the normalized peak strength, q_1, and of 135 m/s for the normalized shear waves, V_{s1} (see Figure 7.52). Yet, it seems to be reasonable not to accept these values as foresight values, as it should be reminded that the specimen confined with 1000 kPa, exhibited a peak strength of 418 kPa finishing with a minimum shear strength of 69 kPa. Thus it would be suggested, as a measure of prevention, when leading with this type of soils, to compact it to lower values than the SSL positioning. Unfortunately, as a stable behavior was not reached, within the range of confining pressures tested, the limit for which the soil is stable is unknown.

Finally, the $T_{x_{q=constant}}_CK_0D$ tests do not seem to provide a clear trend, whereby a clear limit, for which liquefaction is deemed to not take place. Regardless, the very low initial confining stress, the shear wave velocity exhibited by these tests is higher than it would be expected. This means that the shear wave velocity is clearly affected by the initial fabric of the soil, as those tests were prepared with a distinct water content from the other classic triaxial tests. This conclusion is based on its comparison with the other anisotropic consolidated specimens (represented by triangles), confined with a much higher stress. This suggests that the fabric effect may have

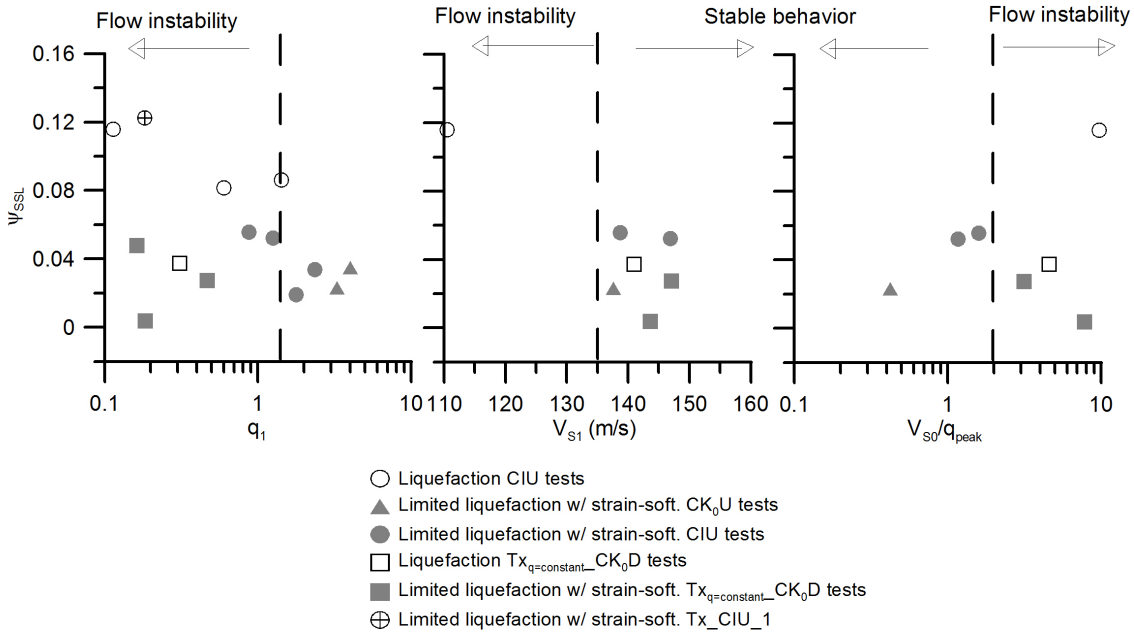


Figure 7.52: Steady state parameter expressed as a function of normalized peak shear strength (q_1) and shear stiffness for Mixture

provided a more stable microstructural fabric rearrangement. However, since the comparison has not been systematic, there is some uncertainty with the void ratios determined for this distinct moisture.

The correlation between the peak shear strength and the initial shear stiffness can be expressed as a potential function, as it is show in Figure 7.53a. On the other hand the correlation between the ratio V_{s0}/q_{peak} and the normalized peak strength, q_1, shows that soil liquefaction is limited by a ratio of, approximately, 1.5. Nevertheless, as pointed above, strain softening, associated to a large loss of shear strength, extends this limiting ratio, for a complete stable behavior, towards approximately zero.

Figure 7.54 allows a detailed analysis of IL positioning, thus of the peak strengths, on the p':q space. This graph, unlike it similarities obtained with the other materials, do not define clearly a limiting value for the p' separating liquefiable from nonliquefiable tests. Despite a diffuse pattern is found between the soils which have liquefied from those which have not liquefied. The justification for what is observed in Figure 7.54 is exclusively associated to the initial void ratio obtained for prepared specimens. For example, the two dots nearby, associated to a p' value of, approximately 250 kPa, are the peak strengths of the tests Tx_CIU_5 and of the Tx_CIU_8. These tests were consolidated with an initial confining stress of 400 kPa and 220 kPa and were prepared with an initial void ratio of 0.95 and 1, respectively. Despite having distinct final void ratios, the distance to the CSL of the initial state of the Tx_CIU_5 was very large. The specimen has reached a residual strength of 10kPa, which is not formally a liquefaction condition, but still very low strength, which can be associated to that instability (e.g. Tx_CIU_8 test).

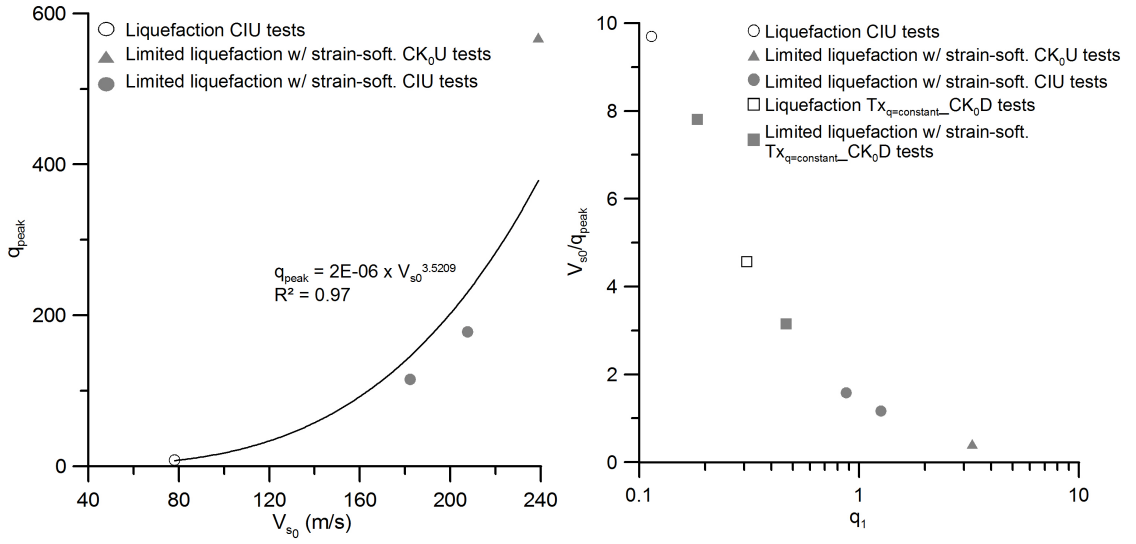
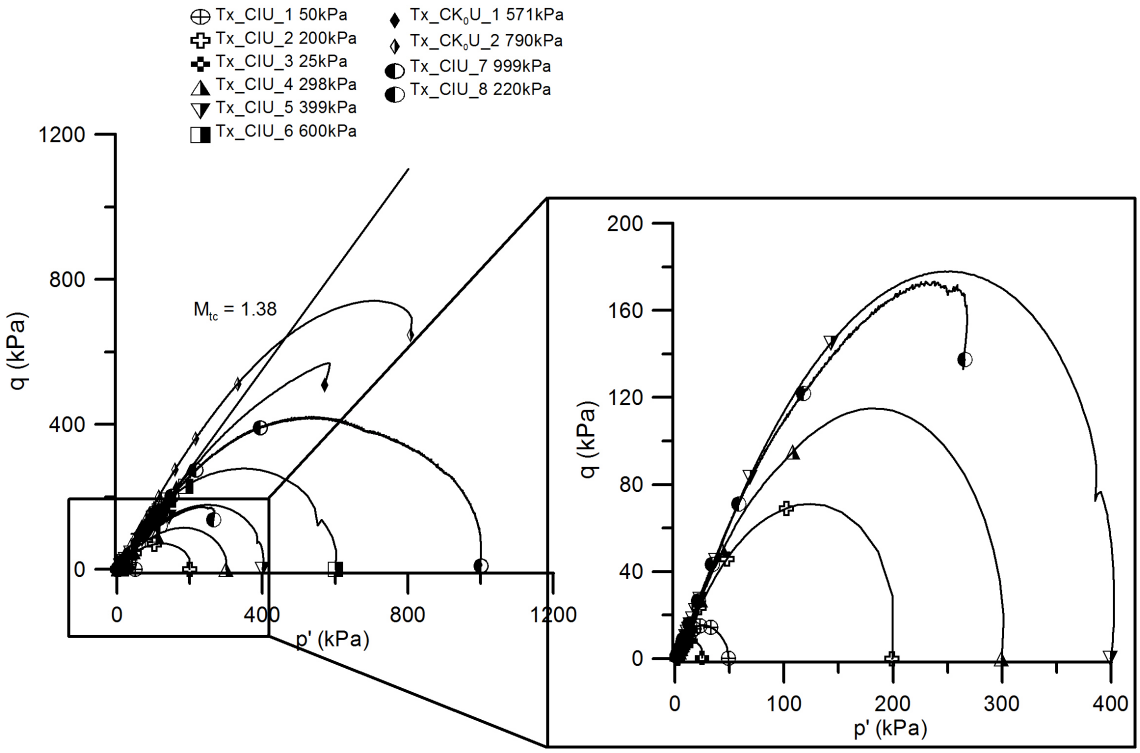
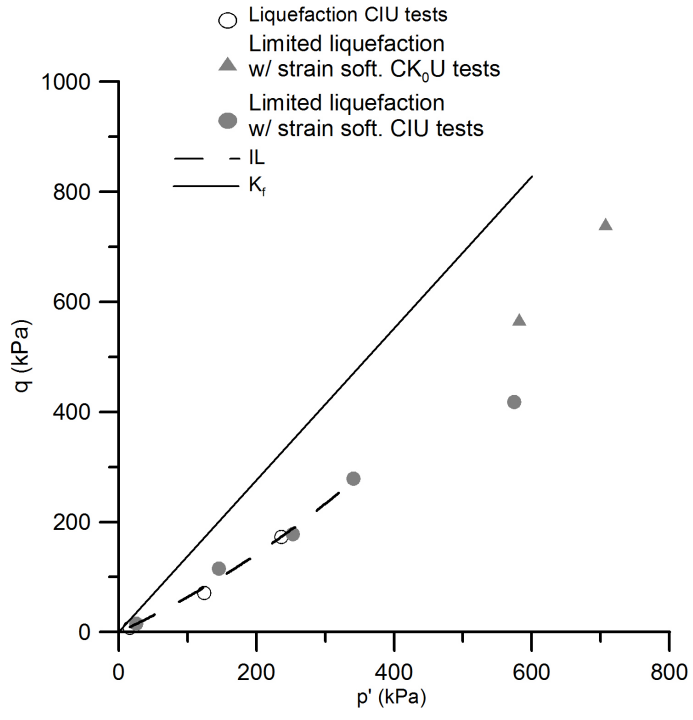


Figure 7.53: a) Peak shear strength as function of the soil stiffness; b) Correlation between the normalized peak shear strength and the ratio between shear stiffness and the peak shear strength for the Mixture

Figure 7.54 also shows an apparent increasing steepness of the IL for the anisotropically consolidated specimens, similarly to previous researches (Fourie and Tshabalala, 2005). Regardless its increasing brittleness, this cannot be considered conclusive, since it is based only on two triaxial test results. Furthermore the increasing peak strength might not be translated in a decreasing brittleness.



(a)



(b)

Figure 7.54: a) Detail of the stress-path of the triaxial tests; b) Instability Line (IL) for the Mixture

7.7.4 Partial Conclusions

A set of compression triaxial tests allowed the determination of both strength and stiffness of the Mixture. Additionally, four triaxial tests were conducted to failure by increasing the pore water pressure (BP), giving a clear indication of soil instability under other stress-path. However the distinct moisture might have resulted in a wrong interpretation due to a fabric effect. Moreover three triaxial tests were performed with decreasing and constant mean effective stresses, which allowed concluding that the divergency observed between the ultimate states of both drained and undrained compression triaxial tests might be a result of microstructural fabric rearrangment under non-compression stress-paths, instead of drainage boundary conditions.

For this mixture, three distinct ultimate states were detected. A clear bifurcation was observed between the drained and the undrained triaxial tests. Furthermore the SSL positioning was clearly influenced by the induced anisotropy created by the anisotropic consolidation.

Being most of the specimens prepared from the NCL, it is conclusive that:

- For initial confining pressure lower than 200 kPa – liquefaction takes place;
- Medium confining stresses to high confining pressures – limited liquefaction with strain softening occurs; triaxial tests under non-compression stress-paths also fall in the SSL;
- CSL was only achieved by performing drained triaxial tests.

A resume of the distinct ultimate state lines are expressed in the table below:

Table 7.13: Resume of the ultimate states for the Mixture according to the type of test

Soil behavior			Type of tests	Equation
CSL	Stable behavior		Drained triaxial tests	(1) $e_{cs} = -0.104 \log(p'_{cs}) + 0.808$
SSL	Liquefaction and strain softening	K_0=1	Undrained triaxial tests	(2) $e_{ss}=-0.455(p'_{ss}/p'_{atm})^{0.03}+0.987$
SSL	Liquefaction and strain softening	K_0~0.5	Undrained triaxial tests	(3) $e_{ss}=-0.455(p'_{ss}/p'_{atm})^{0.03}+1.05$

Once more, similarly to Osorio sand, the soil liquefaction potential was properly assessed by using the steady state parameter. This accuracy was earlier explained as being a result of the wide range of void ratios associated to the high compressibility of the soil. Therefore the ψ_{SSL}, similarly to stress ratio p'/p'_{SSL}, becomes more accurate and precise to evaluate soil liquefaction potential.

Soil stiffness (G_0 – read V_s) and the ratio stiffness-strength (V_{s0}/q_{peak}) proved to be very accurate parameters to predict soil liquefaction, apart the limited number of recorded points.

Table 7.14 provides a resume of the limiting ratios between liquefiable and nonliquefiable behavior for the Mixture. For this particular soil it was decided to define the limiting parameters for which the soil is expected to have a more stable behavior, i.e. for which it stops revealing strain softening, despite it unclearness.

Table 7.14: Limiting values between liquefaction and stable behavior for the Mixture

Parameter	Limiting value	
	Liquefaction	Strain softening
Ψ_{SSL}	Ψ_{SSL}<0.06	Ψ_{SSL}<0.0
p'/p'$_{SSL}$	<100	<2
V_{s1}	>135m/s	>?
V_{s0}/q_{peak}	<1.5	<? (almost 0)

7.8 Silt

7.8.1 Basic Characterization

Silt, an inert silty material was prepared in reference to the gold tailings. This soil, as refered on Chapter 5, was previously studied in a former work by Bedin (2010). Despite much of the present research being developed with this material, it was decided to present it at the end of this Chapter in order to precede the re-analysis of the gold tailings, which is the last material being presented.

While the study of the instability of the gold tailing was developed with the purpose of evaluating the liquefaction potential of a specific tailing dam in Brazil, the silt, an inert material, obtained by grinding Osorio sand, had the purpose of generalizing this analyses, independently of the specific mineralogy of those tailings. This material, as explained before, was prepared to reproduce a similar grain size distribution as the gold tailings.

Obviously the mineralogy of the silt, is the same as Osorio sand, being constituted predominantly by quartz (Consoli et al., 2003, 2007). The original material represented a monogranular, uniform, clean sand with sub-rounded grains. While milled the grains breakage resulted in a new material with angular, uneven edges, similar to the gold mining waste produced those tailing dams, in Brazil (Bedin, 2010).

Unfortunately and as refered on Chapter 5 a new grain size distribtution revealed both materials, silt and gold tailings, to be distinct.

A resume of the Silt basic physical characteristics, previously presented in Chapter 5, might be consulted in Table 7.15, according to tests performed at LabGeo, in FEUP.

Table 7.15: Basic physical characterization of Silt

ID	Unit Weight volume of solid particles	Unit Weight volume	Grain size distribution ASTM sieves			FC	Cu	Cc	Maximum and Minimum void ratio	
	γ_s	$\bar{\gamma}$	Nº20	Nº60	Nº200	%			e_{max}	e_{min}
	(kN/m^3)	(kN/m^3)	0.841 mm	0.250 mm	0.075 mm					
Silt	26.5	14.7	100.0	100.0	98.7	<98.7	9.6	1.47	n.v.	n.v.

7.8.2 Triaxial Tests

As previously mentioned the study of the silt was initiated in a PhD research (Bedin, 2010). The study involved the development of a set of compression triaxial tests, both under drained and undrained conditions.

In the scope of the present research, the study of Silt was complemented with some compression triaxial tests, mainly developed with the purpose of correcting the position of CSL and SSL. After the reevaluation of some procedures, together a large set of anisotropically consolidated triaxial tests led to failure by increasing pore water pressure, and a small number of extension triaxial tests completed and enclosed the investigation of this material.

As for the compression triaxial tests, it repetition resulted on a reevaluation of the previous results in order to correct the CSL positioning, when other complementary tests results were in disagreement with the first ones, resulting from the implementation of the freezing technique in LabGeo, in FEUP. In fact in the beginning of this research the initial void ratio changes were obtained by the monitoring of the internal/local strain transducers, which led to unclear volumetric strains during the percolation and the saturation stages. Therefore, and as originally proposed by Sladen and Handford (1987), the specimens were frozen at the end of the shearing stage, which allowed a proper determination of the final void ratio.

The corrections performed over the previous triaxial tests, in order to correct their volume change during the percolation and saturation stages, are detailed in Annex A. Basically the corrections implemented were based on the differences between the older and new NCL positioning as it would be incorrect to correct directly the CSL positioning.

As it will be seen, despite not being perfectly detected by Bedin (2010), the Silt also presents a clear bifurcation among the ultimate states reached by the drained and undrained triaxial tests. This divergence did not only resulted from the corrections applied over the void ratio but also due to saturation issues.

Furthermore the soil liquefaction potential is also assessed and presented by using both stiffness and strength parameters. Two kinds of instabilities are identified and compared.

7.8.2.1 Drained Triaxial Tests

The drained behavior of the silt achieved with the drained compression triaxial tests can be seen in Figure 7.55. From the stress-strain and the volumetric-strain curves a clear contractive tendency is observed. This was already expected as all silt specimens were prepared with very high void ratios.

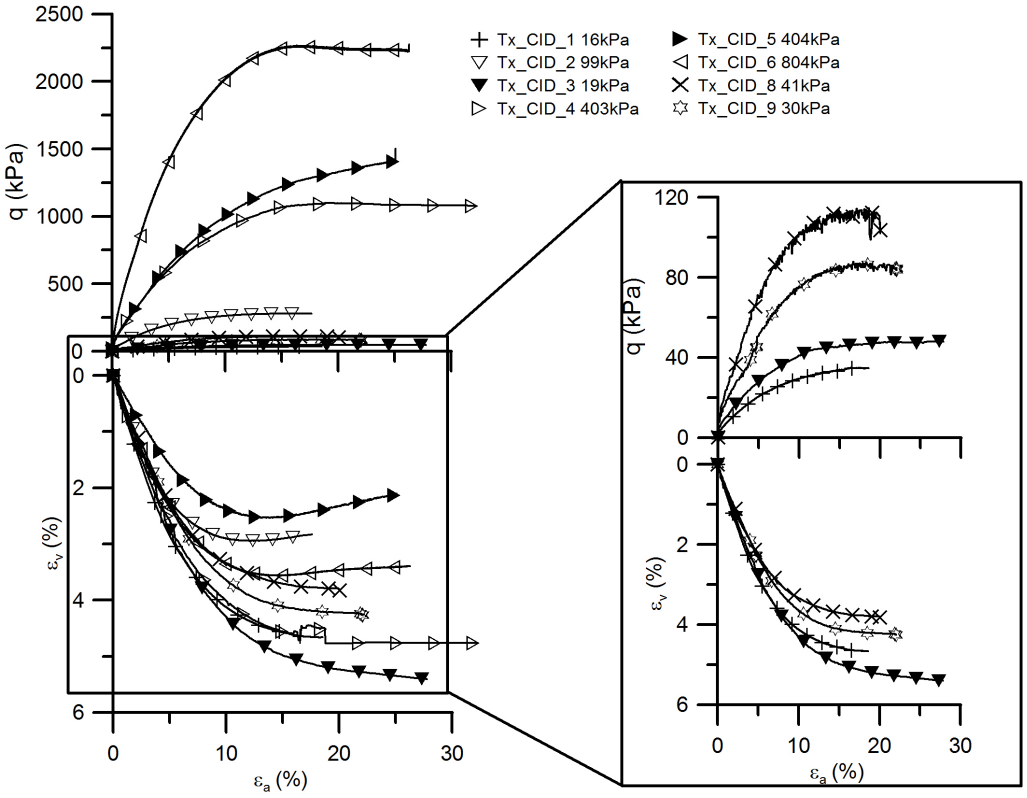


Figure 7.55: Stress-strain and volumetric-strain behavior of drained triaxial tests of Silt

It is also clear that most of the specimens exhibited a volumetric strain between 4% and 5%, meaning that most specimens were tested starting from the NCL. In fact triaxial specimens subjected to compression starting from the NCL, independently of the initial confining pressure, must exhibit a similar volume contraction, as both NCL and CSL are apparently parallel. However this was not observed in the tested sandy soils as it is much more difficult to prepare soils with the exact same

void ratio and because any minor change on the preparing void ratio will reflect on a much lower volumetric strain which is a consequence of the low gradient of both NCL and CSL. On the other hand silty and sandy-silt mixtures, which are prepared with very high void ratios, and exhibit a very high volume changes during the percolation and saturation phases, will start, most of them, from the NCL, and will exhibit a higher volumetric strain during shear due to the high gradient of both NCL and CSL.

From Figure 7.55 it can also be observed that during shear, similarly to the Mixture, the Silt has the particularity of only stabilizing, both volumetric strain and shear stress for large axial strains, of about 10% to 15%. This is significantly higher than the sandy soils specimens. This is likely to happen as the shear strength only stabilizes when the volumetric strain stops, which on sandy-silt soils, due to their large compressibility, might only occur for large axial strains. In fact it configuration prevents a quick rearrange between grains due to the large amount of small particles between the larger ones, which reflects on larger volumetric strains which only stabilizes for larger axial strains.

Figure 7.56 shows separately the behavior of the only high-pressure triaxial test performed, the Tx_CID_7. Despite no apparent grain size evolution being observed, as the volumetric strain is kept constant with axial strain, this needed to be confirmed with the re-analysis of the grading curve of the material at the end of the test. The evolution of the grain size distribution before and after the high-pressure triaxial test can be seen in Figure 7.57. Three distinct granulometric curves are ploted, the continuous line which is the original material, and two distinct curves of the material at the end of the high-pressure triaxial cell. The dotted line was obtained by the sedimentation test and the interrupted line was determined through a particle size analyzer laser equipment. Despite the first sections of the lines not being coincident, both curves display a slight increase of the smaller particles. So when comparing the two lines obtained by sedimentation it seems that the curve is left shifted, which can be explain by the finer fraction increase. In reality the test displayed a maximum shear strength located well below the failure envelope. It is believed, despite not being proved, that the uneven grains got more rounded during the shear stage, explaining both the increasing finer fraction and the lower critical friction angle, more similar to the one obtained for Osorio sand.

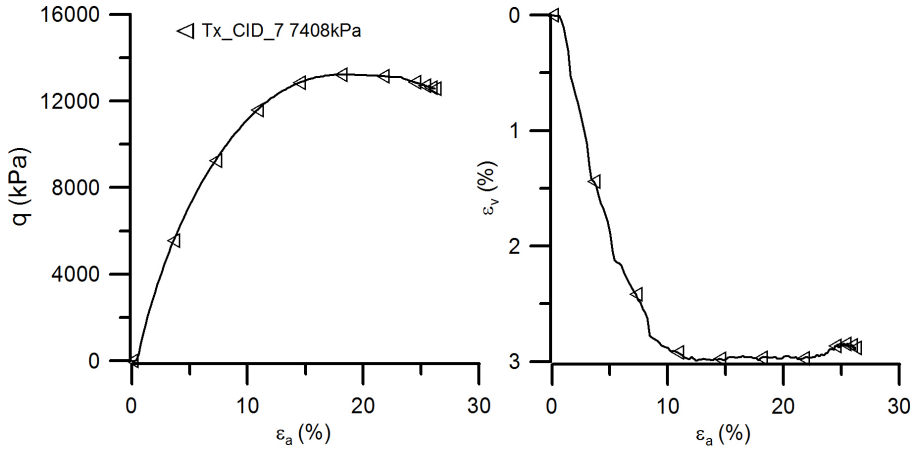


Figure 7.56: Stress-strain and strain-volumetric behavior of the high-pressure triaxial test Tx_CID_7

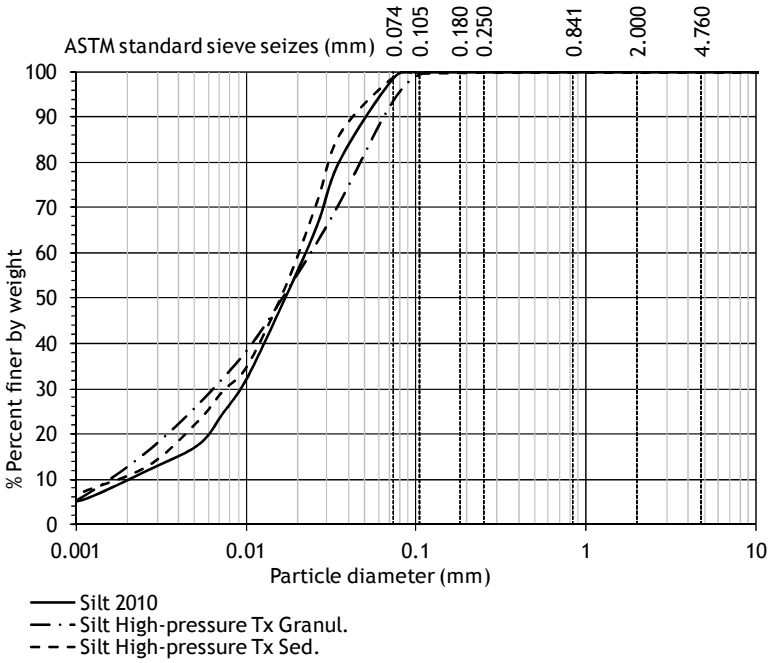


Figure 7.57: Evolution of the grain size distribution of the Tx_CID_12 high-pressure triaxial test (p'_i = 7.4 MPa)

7.8.2.2 Undrained Triaxial Tests

The undrained behavior of Silt, tested under triaxial conditions, can be seen in Figure 7.58 and Figure 7.59. Both Figures display, according to the stress-strain and the pore-pressure-strain curves, a decrease of the contractiveness tendency, which is manifested through pore pressure generation, with increasing initial confining stress. Whereby, while tests performed with low confining stresses liquefied, evolving to a strain softening behavior for medium confining stresses, for higher confining stresses a much more stable behavior, (with strain hardening),was observed . This is a typical behavior of cohesionless finer soils, and is a similar geomechanical behavior observed

previously on the Mixture.

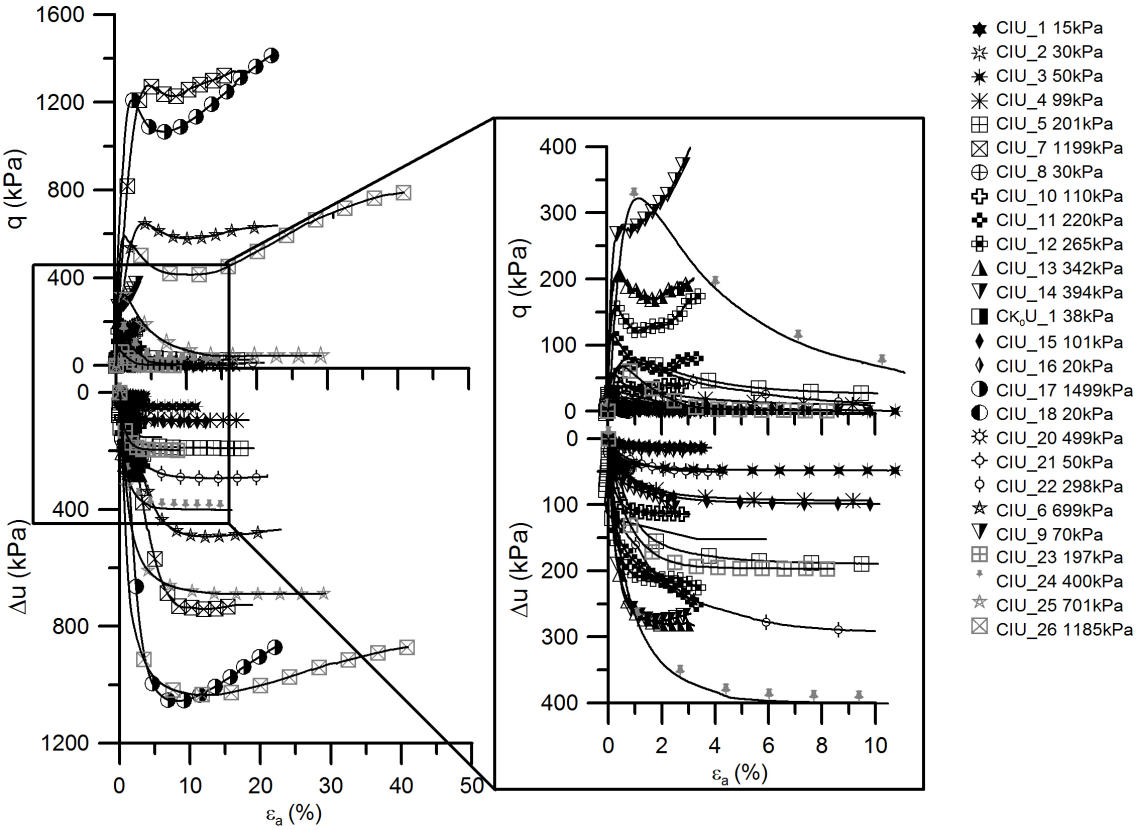


Figure 7.58: Stress-strain and strain-pore water pressure behavior of undrained triaxial tests of Silt at low to high confining pressures

All specimens were prepared with very high initial void ratios, e $\approx$ 1.2, which, after percolation and saturation, reached distinct void ratios after the consolidation stage, starting typically from the NCL. Thus, unlike what Yamamuro and Lade (1998) designated by reversal behavior, this increasing less contractiveness is a result of both increasing initial confining stress and initial densities, which is a factor similar to the monogranular sands (e.g. Algeria sand, Coimbra sand, Osorio sand).

More recently a set of additional tests under the exact same conditions as the ones prepared by Bedin (2010) were preformed and compared. Clear distinct values of shear strengths in the two tests series were observed, for specimens prepared with the same initial void ratios and confining stresses. This was attributed to and insufficient saturation degree in the previous tests. In fact the more recent tests were performed with a saturation process which includes a CO_2 percolation previous to the water percolation, ensuring a complete saturation of the specimen. As it is widely known the advantages of using CO_2 is the ability of the gas to solve in the water for much lower pressures. In Figure 7.59 the high differences associated to the degree of saturation might be observed. These differences are also more high for the high-confined triaxial tests as in the last ones a further reduction of the BP is required to achieve the required confining pressure.

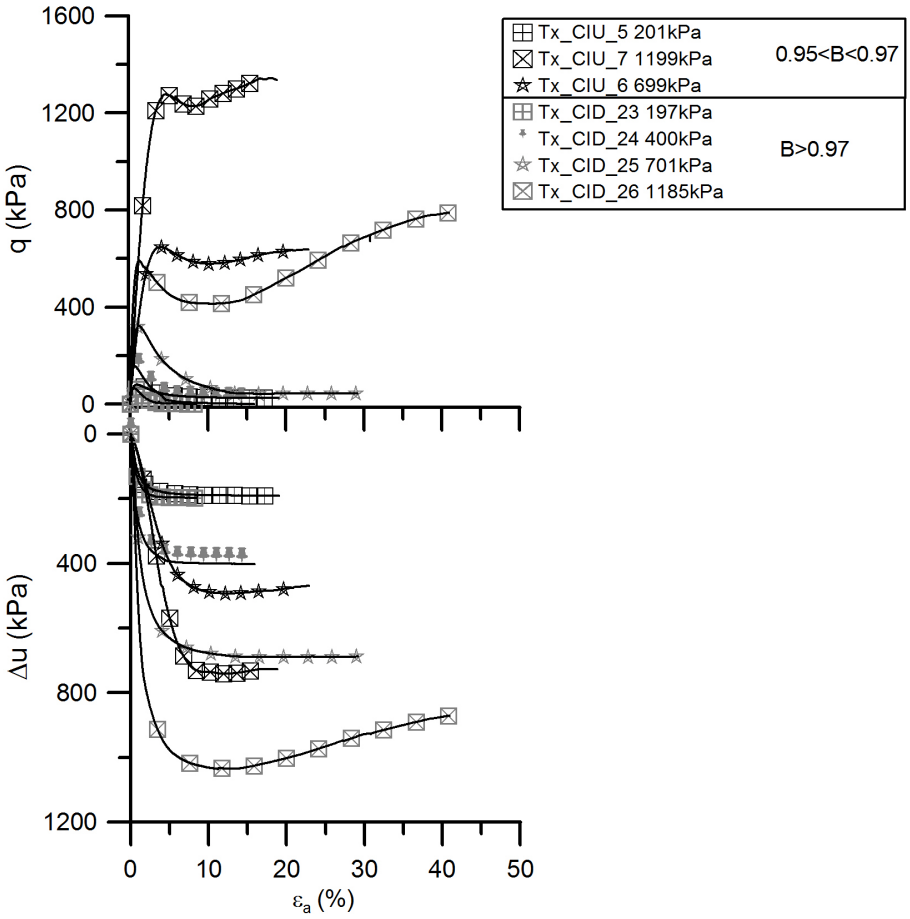


Figure 7.59: Stress-strain and strain-pore water pressure curves comparison with distinct saturation degrees

Despite not knowing the degree of saturation of the first series of tests, P wave velocities were measured in both programs. Using Yang (2002a) correlation, between the Skempton parameter, B, and the P shear wave velocities, it was concluded that most of specimens tested by Bedin (2010) had only achieved a Skempton parameter between 0.89 and 0.95 (seeB). Aware of the insufficient degree of saturation it became clear that the differences observed between the shear strengths was associated to this factor.

Analyzing carefully Figure 7.59 it becomes clear the strong effect of the saturation degree on the behavior of specimens under undrained conditions might lead to an underestimation of the pore water pressure and consequently of the peak shear strenghts, leading to erroneous liquefaction potentials.

(Note: For simplicity the symbols used were the same between similar tests.)

7.8.2.3 Soil Behavior Under Applied CSSM

Similarly to Mixture this soil exhibits a very high brittleness. Despite being both well-graded soils is obvious their higher susceptibility to static liquefaction.

Following the same justification used before, the soil ultimate states were separated according to its geomechanical behavior. Thus, while the CSL was built upon the ultimate states achieved by the drained triaxial tests and the undrained triaxial tests which exhibited strain hardening, the SSL was delineated by the ultimate states of the strain-softened undrained triaxial tests (see Figure 7.60 and 7.61).

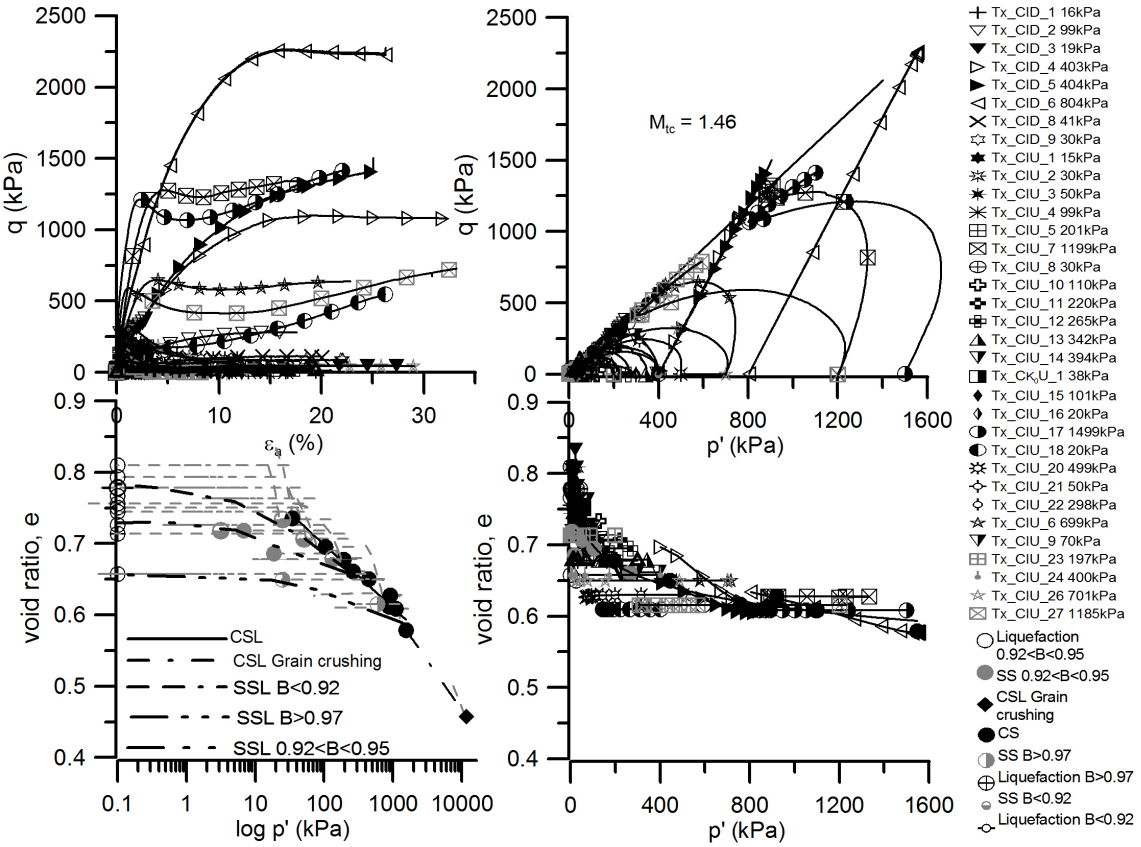


Figure 7.60: Construction of the critical state and steady state line for Silt

Unlike the Mixture, the Silt exhibited strain-hardening, for some of the triaxial tests tested under undrained conditions. Although the undrained triaxial tests which were observed to converge with the CSL did not have a guaranteed full saturation. Plus, the other ones which exhibited strain-softening were separated in distinct groups as it results in distinct SSL assocaited to distinct degrees of saturation (see Figure 7.60 and 7.61).

As for the high-pressure triaxial tests, it seems that the test achieved an ultimate state which defines a new CSL characterized by an higher gradient. After analyzing the material obtained from the high-pressure triaxial test, a minor grain crushing was observed(see Figure 7.56), which might

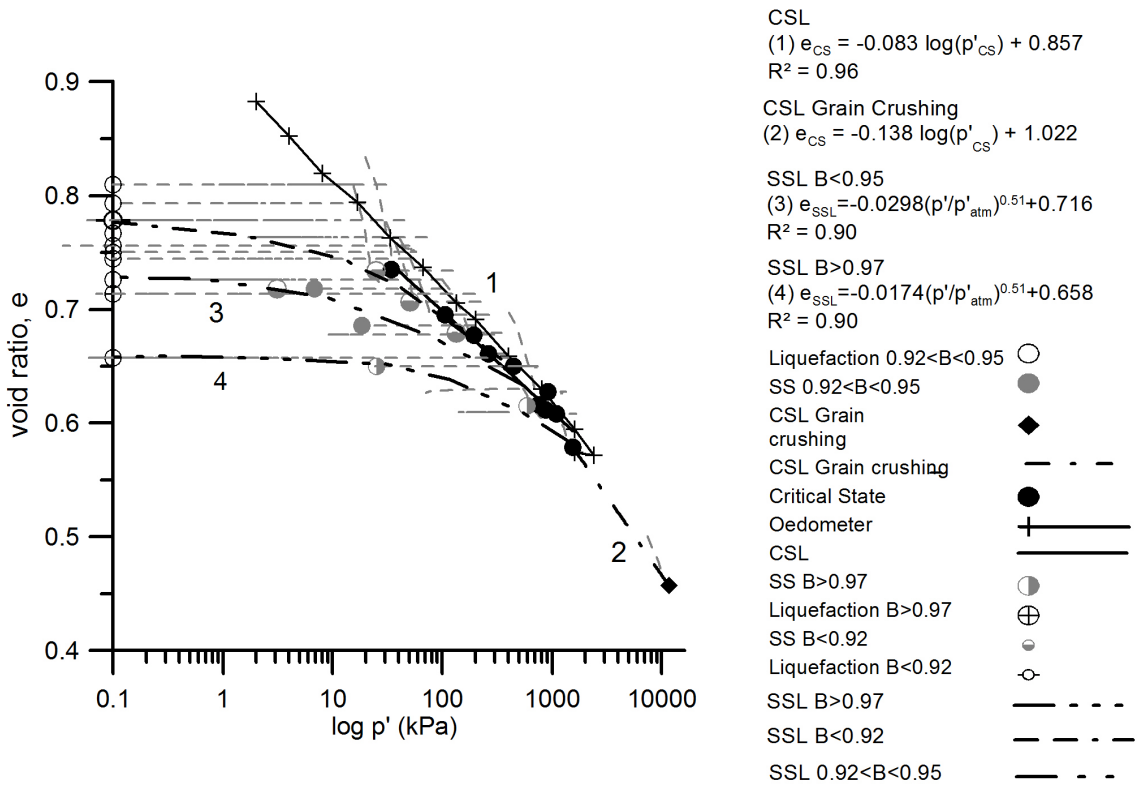


Figure 7.61: Critical state line and steady state line of Silt

explain the increasing gradient of the CSL. Therefore the particles, initially uneven, formed a minor amount of fines as a result of a partial crushing of the angular parts of the fine grains. This would also explain the much lower constant volume friction angle (not displayed in Figure 7.60), dropping from an initial value of 36° to a final value of 28.2°. As pointed out by some authors (Santamarina and Cho, 2004; Cho et al., 2006) increasing roundness decreases the volume friction angle.

The equations for SSL and CSL (with or without grain crushing), of Silt, might be consulted in Figure 7.61. Despite not being very obvious the existence of grain crushing it was decided to separate the CSL in two branches, which ideally is a unique curve shaped equation. The lower inclination, when compared with those of clean sands may be surprising, but since the soil is well-graded and fine, the particles do not tend to crush to bear the very high confining stresses and deviatoric loads.

Similarly to the other materials the SSL was determined according to the equation proposed by (Li et al., 1999). The curved equation $e_{ss} = e_{c0} - \lambda_s \left(\frac{p_{ss}}{p_a}\right)^{\xi}$, assumed the values of -0.0298, 0.51 and 0.716 for λ_s, ξ and e_{c0} respectively, for the not completly saturated isotropically consolidated specimens. While the new SSL, determined from the very well saturated specimens, (B > 0.97), adopt the values of -0.0174, 0.51 and 0.658 for the λ_s, ξ and e_{c0}, respectively.

On the other hand the CSL, following the classical definition, $e_{cs} = \Gamma + \lambda \times \ln\left(p'_{cs}\right)$, have the following values for the reference void ratio, Γ, and for the slope, λ: 0.857 and -0.083, respectively, for medium-high mean effective pressures; and for high mean effective pressures, of 1.022 and -0.138, respectively.

As stated before, the value of the critical friction angle, ϕ_{cv} is approximately 36º, which corresponds to a critical friction ratio, M, of 1.46. Plus the high pressure triaxial test led to a much lower critical friction angle, ϕ_{cv} of approximately 28.2º. Despite this drop might be theoretically explained it is convenient some test repetitions.

7.8.2.4 Extension Triaxial Tests

Silt was also studied under an extension triaxial stress-path. The material exhibited a partial liquefaction for those initially on a loose condition, and a stable behavior for those initially on denser conditions. Whereby, similarly on compression conditions, on extension conditions there is an increasing stability with increasing confining stress and decreasing void ratio, as might be seen in Figure 7.62. Due to the lack of internal instrumentation, the volumetric changes during saturation and percolation were assumed to be similar to the compression triaxial tests, as they were performed with a similar initial void ratio and were later corrected by assuming the new position of the NCL (see Annex A). Obviously it is possible the existence of a standard error on the void ratio determination, which might be the case as the initial void ratio is higher than the one determined with the oedometer (as can be seen in Figure 7.62). Nevertheless, similarly to what was observed from the compression triaxial tests, also the extension triaxial tests, when stable have an ultimate state which converges with the previously determined CSL, while those which exhibit liquefaction or strain softening fall within the SSL region.

Due to the lack of extension triaxial tests no major conclusions were achieved and the construction of tools to assess liquefaction was also compromised.

In fact among a total number of approximately 15 extension triaxial tests only few were performed till the last stage, as most of them liquefied during the anisotropic consolidation stage.

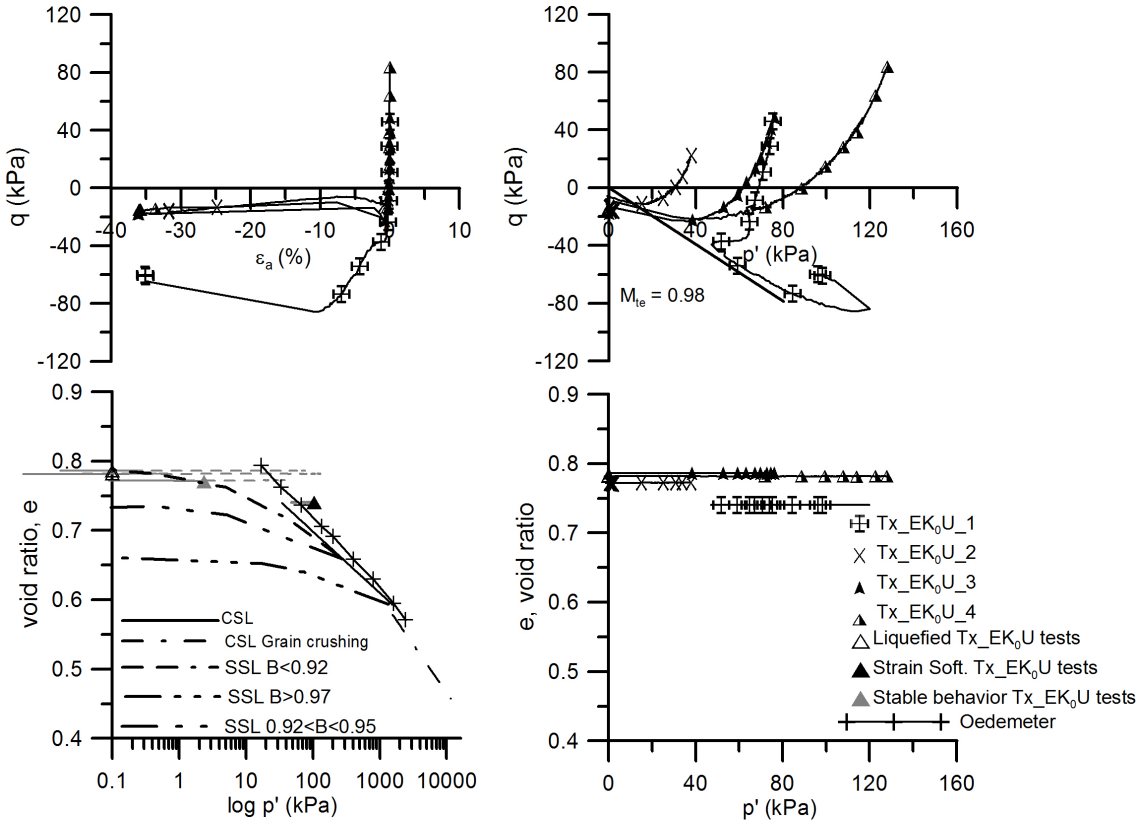


Figure 7.62: Extension triaxial tests under applied CSSM

7.8.2.5 Drained Triaxial Tests With Decreasing Mean Confining Stress And Constant Deviator Stress

Contractiveness of the silt was also assessed by leading to failure drained triaxial tests under a particular stress-path. Similarly to Osorio sand and to Mixture, one of the the stress-path chosen consisted on leading the specimens to failure by increasing the pore-water pressure. As explained before, this type of stress-path is equivalent to the occurence of rain, being responsible for many disastrous events on tailing dams. Unlike the other materials, Silt was extensively studied under this stress-path, and a wide range of initial confining stresses and K_0 stress conditions were performed in order to evaluate it influence on liquefaction onset.

(Note: Obviously, for liquefaction to take place, an anisotropic consolidation was previously applied by using dead weight.)

Before proceeding to it analyzis it should be also pointed out that, similarly to the Mixture, despite some tests exhibiting a clear shear strength loss, the condition of p' = 0 kPa was not reached for most cases. As explained before this is believed to be a problem associated to the Triax controlling software jointly with the acquisition program. Additionally, strategic points were chosen, before the end of the test, which was approximately when the tests reached the failure envelope in case

of being observed a stable behavior, and their ultimate state for those which exhibited liquefaction or strain softening.

Observing Figures 7.63 and 7.64 it is perceived that the tests with a stable behavior, represented by black squares, clearly reach the CSL. Plus the black squares with higher void ratios, $Tx_{q=constant}_CK_0D_16$ and $Tx_{q=constant}_CK_0D_17$, were tested with very low initial K_0 (0.7/0.8), which might be well below the SS strength on the compression side. Despite the SS being nearby zero for low initial confining stresses, as the tests were initially confined with 120 and 80 kPa, respectively, it is possible for them to be located below the SS point.

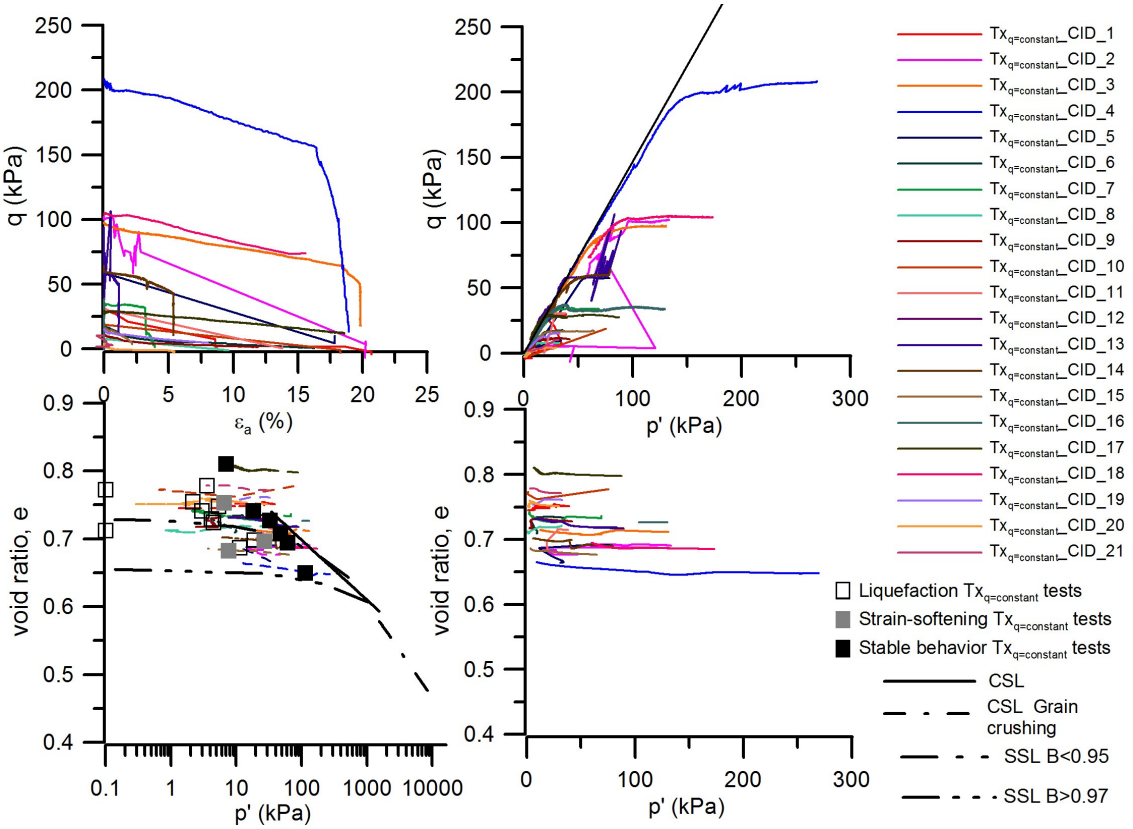


Figure 7.63: Stress-strain and stress-path of the set of triaxial tests with decreasing p' and constant q; study under applied CSSM

On the other hand the other tests, which exhibit either strain softening or complete liquefaction undergo towards the left side of the CSL, nearby the SSL, similarly to those tested under undrained compression conditions (Figure 7.63 and 7.64). Therefore it seems obvious to accept that liquefaction is not a matter of boundary condition, but a particle configuration conditioning. In fact, most of the specimens which exhibited liquefaction or limited liquefaction had very low initial void ratios, when compared with those which exhibited a stable behavior. As reported in Chapter 4 while instability due to pore water pressure increase under drained conditions is caused by an unstable microstructural fabric rearrangement, instability due to an increasing monotonic shear, under undrained conditions, is due to a contractive mechanical behavior of loose granular material

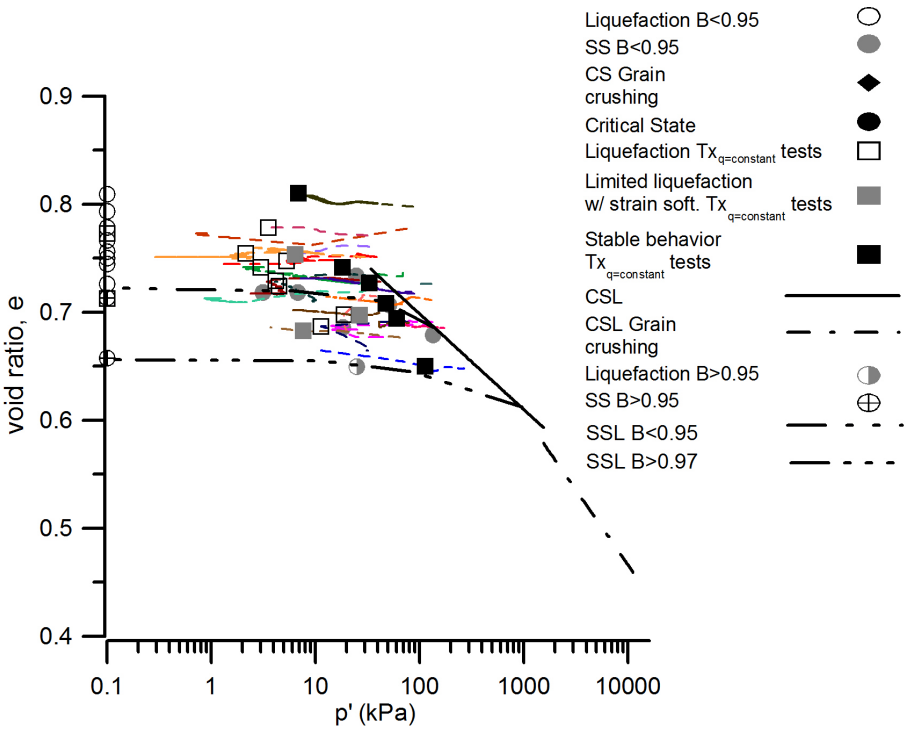


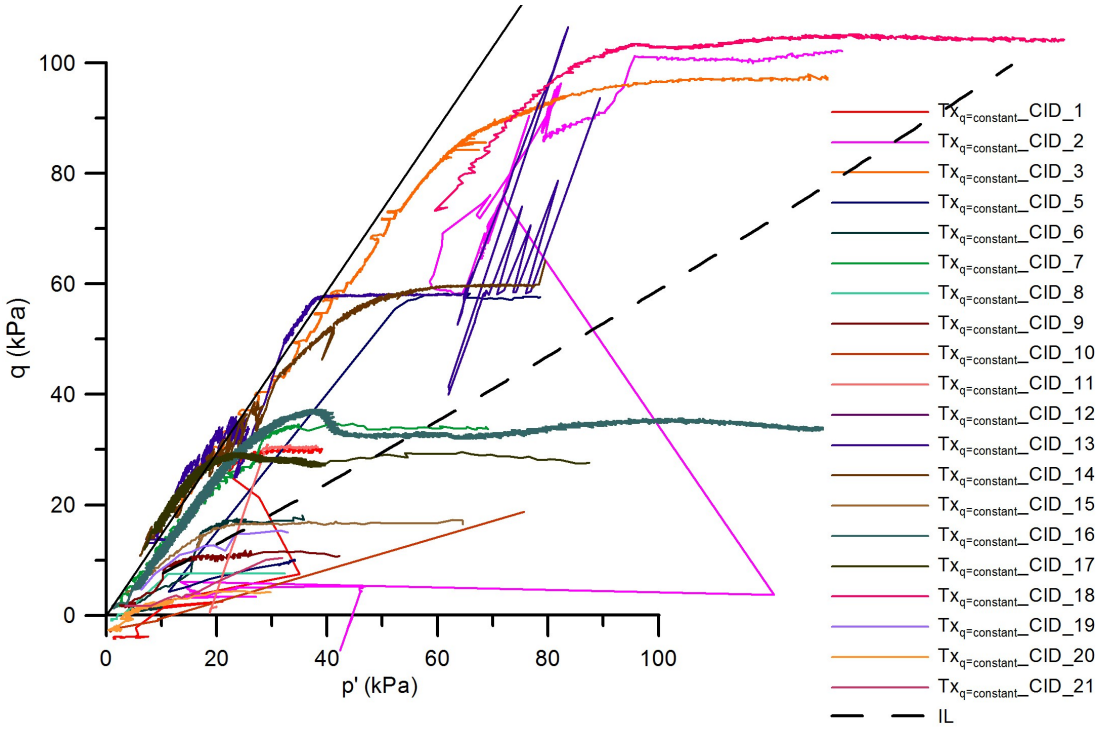
Figure 7.64: $T_{x_{q=constant}}_CK_0D$ tests ultimate state positioning on e: ln p' space

and consequent pore pressure increase (Matiotti et al., 1995). Regardless similarities, both stress-paths are found on the Instability line (IL), as it influences both drained and undrained stress-paths Chu et al. (2012). Nevertheless it should be considered that the IL positioning changes with K_0, exhibiting an increasing steepness with increasing K_0 as reported by Fourie and Tshabalala (2005). This helps justifying the fact that these tests liquefy, most of the times, after passing the IL defined by isotropically triaxial tests (Figure 7.65).

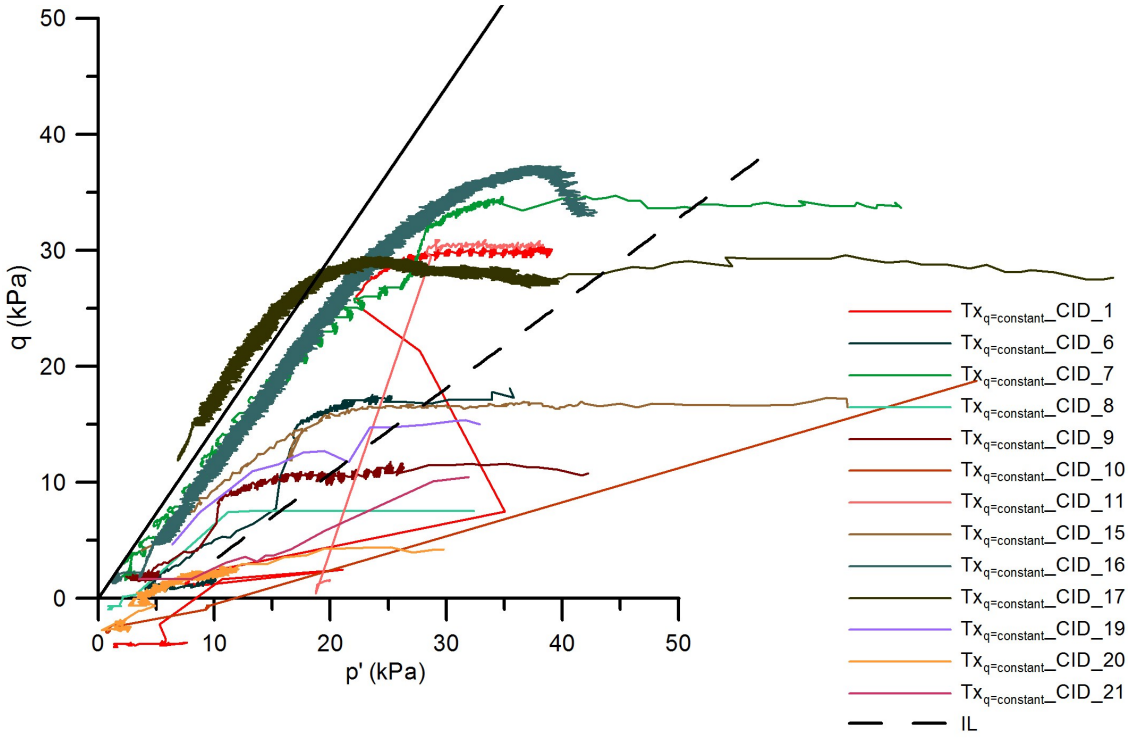
Among the data plotted on Figure 7.63, two tests were excluded from Figure 7.64, $T_{x_{q=constant}}_CK_0D_2$ and $T_{x_{q=constant}}_CK_0D_15$, due to some uncertainty on the type of behavior and on their initial state conditions. Plus it is also clear that $T_{x_{q=constant}}_CK_0D_10$ suffered instability due to a failure of the laboratory pressure system, whcih resulted in its liquefaction onset well behind the IL, which corresponds to a theoretical unperceived mechanical behavior.

Figure 7.65 helps out figuring out the tests with a stable behavior. The $T_{x_{q=constant}}_CK_0D$ number 3, 4, 12, 16, 17 and 18 tests, clearly reached the Mohr-Coulomb failure envelope without significance disturbance. On the other hand the large number of tests that liquefied after reaching the IL might also be seen, but with more detail in Figure 7.65b). Among them all there are three tests that liquefied well below the IL: $T_{x_{q=constant}}_CK_0D_8$, $T_{x_{q=constant}}_CK_0D_20$ and $T_{x_{q=constant}}_CK_0D_21$. These three triaxial tests, consolidated with no more than 40 kPa and with K_0<0.7 exhibited a behavior which cannot be explained by geomechanics whereby no conclusions were redrawn.

Conclusively, and as presented in the next sub-section, liquefaction might occur under drained



(a)



(b)

Figure 7.65: a) Stress-paths of $Tx_{q=constant}_CK_0D$ tests; b) Detail of the stress-paths of $Tx_{q=constant}_CK_0D$ tests under lower pressures

conditions and depends on the initial state conditions - which influences the ability of the particles chain to not break.

7.8.3 Prediction Of Liquefaction Resistance

7.8.3.1 Undrained Classic Triaxial Tests

For liquefaction evaluation purposes both strength and stiffness parameters were used, based on conventional correlations established for the other materials.

Most of the tests, earlier performed by Bedin (2010) and Silva (2010), exhibit a clear increasing brittleness, I_B, with increasing ψ_{SS} and increasing p'/p'$_{SSL}$ (see Figure 7.66).

The obvious tendency is well perceived by using the state parameter as, beyond most of the tests being remolded with a similar initial void ratio, the considerable curvature of the SSL allows distinct and accurate evaluations of the void ratio between the ICL and the CSL. Thus, according to Figure 7.66, the Silt liquefies for $\psi_{SSL} > 0.04$ and exhibits a stable behavior for $\psi_{SSL} < 0.02$. Nevertheless, it has to be pointed out that most of the tests represented on Figure 7.66 have not achieved a full saturation condition. Therefore, despite not being very clear, it is also observed an increasing brittleness with increasing saturation as ψ_{SSL} increases when measured with reference to the new SSL. If instead of using the SSL the state parameter was measured with reference to the CSL, the parameter would no longer be suitable to distinguish the behavior according to the degrees of saturation.

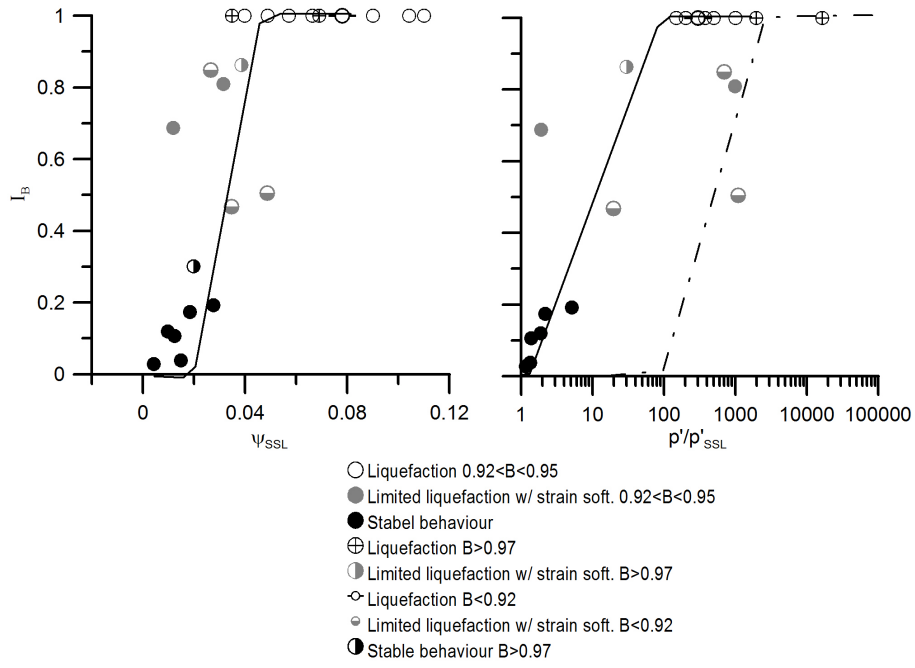


Figure 7.66: Variations of the Brittleness Index with the steady state parameter, ψ_{SSL}, and the ratio p'/p'$_{SSL}$, from left to right, respectively, for the Silt

On the other hand the use of the p'/p'_{SSL} ratio also reveals a good tendency, establishing a boundary between liquefaction, $p'/p'_{SSL} > 100$, limited liquefaction, $3 < p'/p'_{SSL} < 100$, and a stable behavior, $p'/p'_{SSL} < 3$. Moreover these differences seem to be very high then those displayed by ψ_{SSL}. However as explained the I_B, and p'/p'_{CSL} correlation have a limited interpretation due to a strong statistical correlation in the case of liquefaction or limited liquefaction, as $p'_{min} = p'_{SS}$.

As quoted before the use of shear wave velocity to assess soil liquefaction potential is prominent and reveals, despite the lack of sensibility with void ratio changes, to be a good parameter to be used. According to Figure 7.67 the steady state parameter decreases with increasing normalized shear strength, q_1, and with increasing normalized shear wave velocity, V_{s1}. This tendency reflects an increasing stability of Silt which stops liquefying for a $q_1 > 0.05$ and for a $V_{s1} > 140$ m/s. On the other hand stability is only reached for $q_1 > 1$ and $V_{s1} > 155$ m/s.

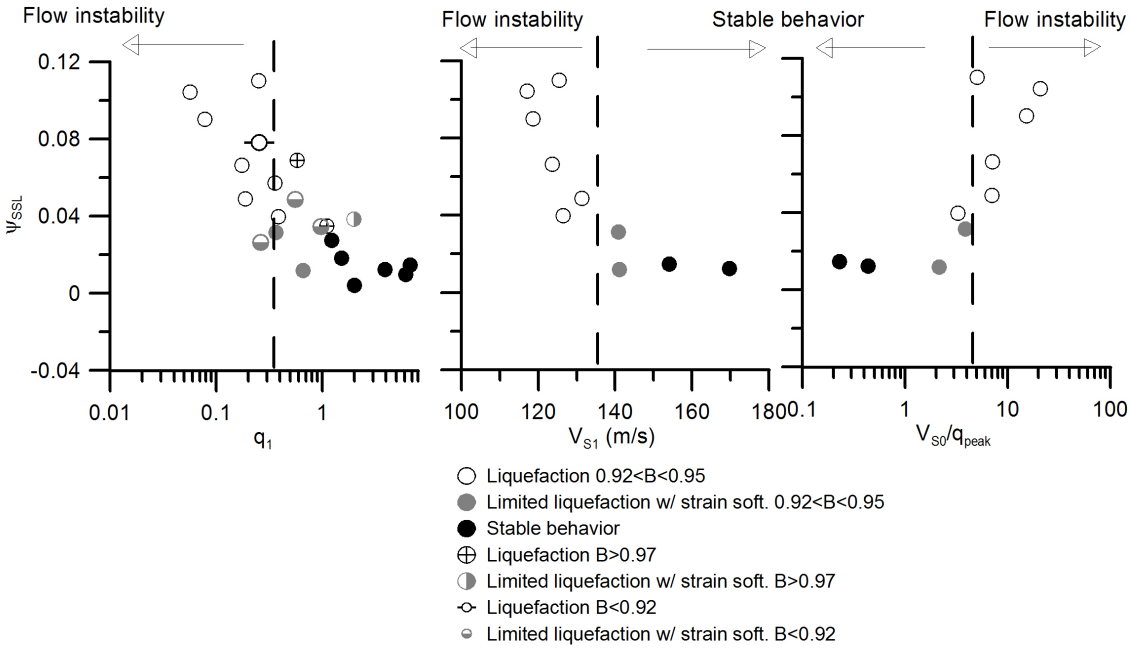


Figure 7.67: Steady state parameter expressed as a function of normalized peak shear strength (q_1) and shear stiffness for Silt

However, as explained before, these values rely on data determined from specimens not fully saturated. On the other hand, the most recent set of triaxial tests, fully saturated, had no shear waves measured as the final void ratios were thoroughly determined by freezing the specimens at the end of the test. Whereby the triaxal cells could not be equipped with bender elements. Therefore, their liquefaction potential evaluation is only feasible by using the correlation between the normalized shear strength, q_1, and the ψ_{SSL}. Despite the small number of fully saturated tests it is obvious the wider range of q_1 for which liquefaction takes place, only starting to exhibit strain softening for $q_1 > 2$. From Figure 7.67 it can be also observed an increasing liquefaction susceptibility with decreasing ψ_{SSL} and V_{s0}/q_{peak}, limiting the silt stable behavior to ratios lower than, approximately, 1 (for not fully saturated triaxial tests).

The ratio V_{s0}/q_{peak} arises from the strong correlation existent between the strength and the stiffness parameters, which can be expressed as a potential function, as displayed in Figure 7.68. Unfortunately the recent triaxial tests were not supplied with bender elements, not allowing the measurement of shear wave velocities, which in principle, would exhibit a similar value as the previous ones, but associated with much lower peak strengths, mainly for the higher confined ones. Therefore the potential curve, represented in Figure 7.68, would decrease the curvature, and the limiting ratio V_{s0}/q_{peak} would increase with an increasing saturation degree.

As explained before the relationship between the V_{s0}/q_{peak} ratio and q_1 expresses well the liquefaction susceptibility, as a consequence of both these parameters being a function of the same variables. From Figure 7.68, it is obvious liquefaction potential rises with increasing V_{s0}/q_{peak} and with decreasing q_1.

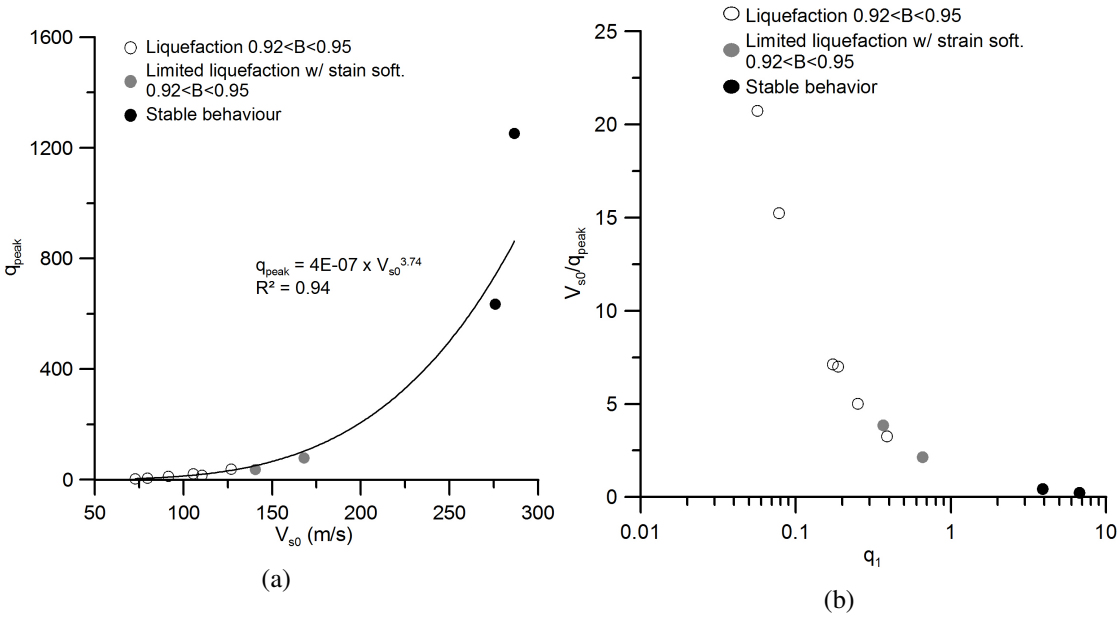


Figure 7.68: a) Peak shear strength as function of the soil stiffness; b) Correlation between the normalized peak shear strength and the ratio between shear stiffness and the peak shear strength for the Silt

Peak shear strenght of the triaxial tests can be consulted on IL positioning, which is shown in Figure 7.69 on the p':q space. The figure could not be more succinct of what was observed previously. Apparently the degree of saturation affects largely the soil behavior and the IL positioning, mainly for higher confining stresses. Expectably, an increasing steepness is observed for the less saturated specimens and with increasing confining stresses. This increasing steepness, which approaches the Mohr-Coulomb failure, is also translated on a decreasing brittleness.

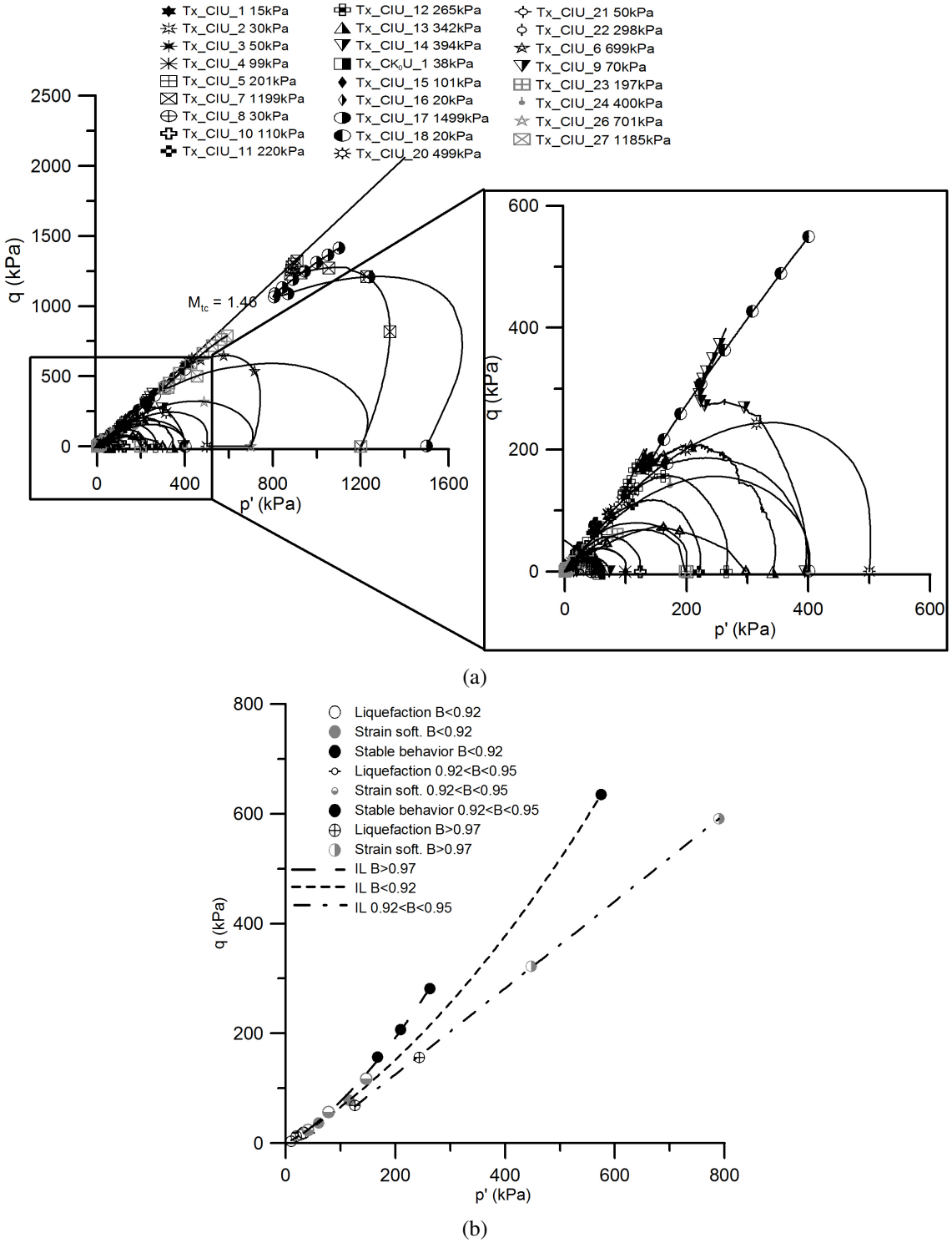


Figure 7.69: a) Detail of the stress-path of the triaxial tests; b) Instability Line (IL) for Silt

7.8.3.2 Drained Triaxial Tests With Decreasing Mean Confining Stress And Constant Deviator Stress

After studying the classic compression triaxial tests the soil liquefaction potential was also studied for the drained anisotropic triaxial tests led to failure through pore-water pressure increase.

The first framework displays, in Figure 7.70, the correlations between the brittleness index, I_B, and the steady state parameter, ψ_{SSL}, and I_B and the stress ratio p'/p'$_{SSL}$. Both frameworks are far from providing a good plotting to predict soil liquefaction potential for soils subjected to this type of stress-path. Their dispersion, which can also be observed in Figure 7.64, is probably associated to the incorrect determination of the steady state parameter. In fact, as the tests were performed with distinct K_0, it is assumed an incorrect measurement of the ψ_{SSL} as it is postulated that SSL positioning changes with K_0. Regardless, that trend needs to be confirmed with a more extensive laboratorial research.

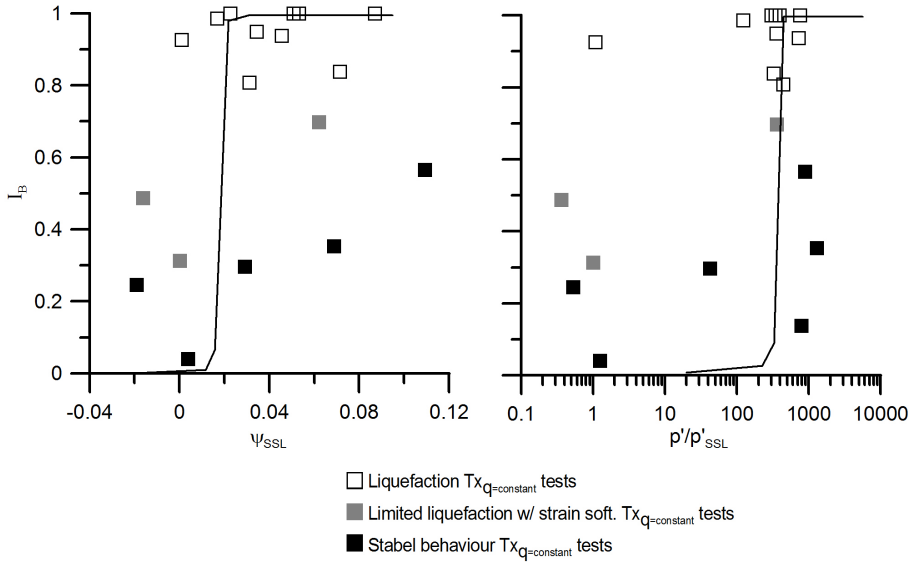


Figure 7.70: Variations of the Brittleness Index with the state parameter, ψ, and the ratio p'/p'$_{CS}$, from left to right, respectively, for the for $T_{x_{q=constant}}_CK_0D$ tests of Silt

The lack of predictability of the steady state parameter seems to be largely overcome by the shear wave velocity analysis. Despite not being obvious the existence of a tendency, both normalized shear wave velocity and the ratio V_{s0}/q seem to provide a limit boundary between the stability and liquefaction (Figure 7.71). Thus it might be inferred that the Silt is both influenced by its grain configuration clearly captured by the shear wave velocity and by the initial induced anisotropic stress, thus by K_0. By comparing this stress-path with the undrained classic one, is clear the higher stability. Thus for $V_{s1} > 135$ m/s or V_{s0} /q < 5 the soil exhibits a stable behavior under this particular stress-path.

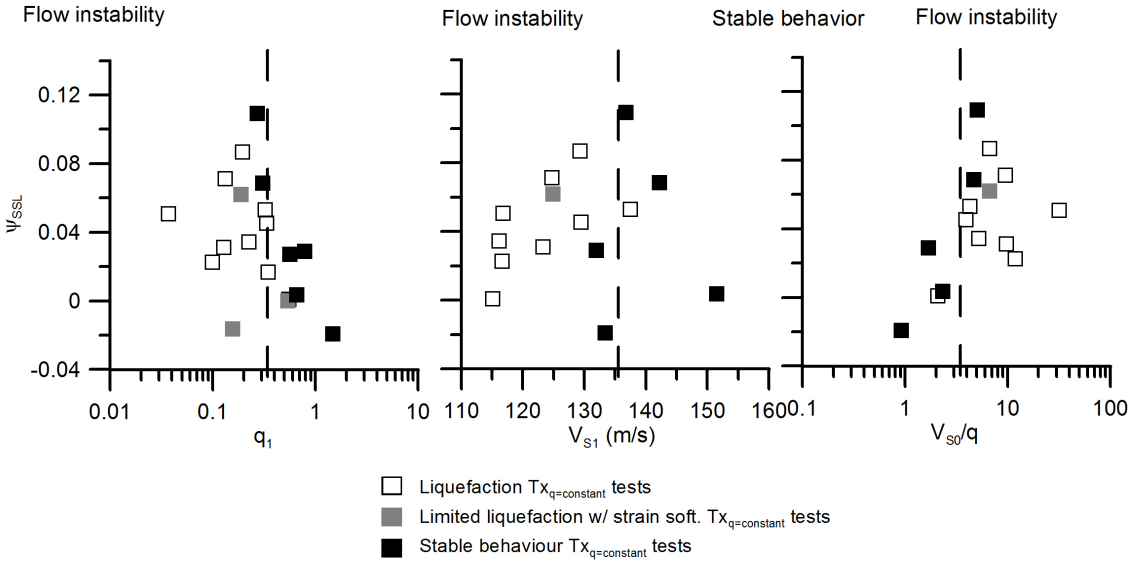


Figure 7.71: Steady state parameter expressed as a function of normalized peak shear strength (q_1) and shear stiffness for the $T_{x_{q=constant}}_CK_0D$ tests of Silt

7.8.4 Partial Conclusions

A large set of distinct triaxial tests were performed to complete those published by Bedin (2010). Beyond being performed compression triaxial tests, mainly under undrained conditions to evaluate the influence of the saturation degree on liquefaction susceptibility, it was also performed one high-pressure triaxial test and a large set of anisotropic consolidated drained triaxial tests, led to failure by pore water pressure increase (BP). This stress-path allowed investigating the main factors affecting soil liquefaction susceptibility, like the initial anisotropic stress state condition (K_0), the initial void ratio and the initial confining stress.

Similarly to Mixture, Silt exhibited three distinct ultimate states. Once more, a clear bifurcation was observed between the drained and the undrained triaxial tests. Despite this bifurcation not being so clear from the first set of tests, the second phase of tests, which guaranted a full saturation condition, allowed to perceive a clear drop of the SSL positioning on the e: lnp' space.

As most of the tests started from the NCL, excepting for the $T_{x_{q=constant}}_CK_0D$ tests, it is concluded that:

- For initial confining pressures lower than a value between 400 and 700 kPa – liquefaction takes place; since no tests were performed with an initial confining stress between 400 and 700 kPa, no further detail was obtained in this range;

- Limited liquefaction with strain softening occurs for initial confining pressure higher than a value between 400 and 700 kPa;

- CSL was achieved through the ultimate state achieved by drained triaxial tests and undrained triaxial tests whose saturation was not guaranteed; plus, some of the $T_{x_{q=constant}}_CK_0D$ also reached the CSL by the moment they reached the Mohr-Coulomb failure envelope;
- The high pressure triaxial test reached a stepper CSL probably due to the occurrence of a minor amount of grain crushing occurs; it is possible that this might also justify the lower constant volume friction angle due to a possible evolution of the grains angularity;
- Undrained extension triaxial tests also led to similar ultimate states as the compression triaxial tests; whereby while on loose conditions they deem to liquefefy, with increasing density and confining stress they evolute towards the CSL.

A resume of the distinct ultimate state lines is expressed in Table 7.16:

Table 7.16: Resume of the ultimate states for the Silt according to the type of test

Soil behavior			Type of tests	Equation
CSL	Stable behavior; Strain hardening		Drained triaxial tests and undrained triaxial tests	(1) $e_{cs} = -0.083 \log(p'_{cs}) + 0.857$
SSL	Liquefaction and strain softening	B<0.95	Undrained triaxial tests	(2) $e_{ss}=-0.0298(p'_{ss}/p'_{atm})^{0.51}+0.716$
SSL	Liquefaction and strain softening	B>0.97	Undrained triaxial tests	(2) $e_{ss}=-0.0174(p'_{ss}/p'_{atm})^{0.51}+0.658$
CSL	Grain crushing		High-pressure triaxial tests	(3) $e_{cs}=-0.138 \log(p'_{cs}) +1.022$

Silt liquefaction potential is well captured through the steady state parameter or through the stress ratio p'/p'_{SSL} while under undrained triaxial compression stress-path. However for $T_{x_{q=constant}}_CK_0D$ stress-paths both the steady state parameter and the stress ratio completely failed it prediction. This might be associated to the changing positioning of the SSL which, unlike the CSL, is not unique, depending, among other factors, of the induced anisotropy in the consolidation (thus of K_0).

On the other hand, soil stiffness (G_0 – read V_s) and the ratio stiffness-strength (V_{s0}/q_{peak}) seems being able to capture the fabric which can bear the stresses changes during any type of stress-path. Apparently the ψ_{SSL} fails due to its non-uniqueness as the soil presents distinct liquefaction susceptibilities with varying initial void ratio, initial confining stress, and initial anisotropic consolidation level.

Table 7.17 provides a resume of the limiting ratios for for either liquefaction or strain softening for occur. to occur on the silt. For this particular soil, the limiting values were determined and/or

predicted according to the stress-path and to the degree of saturation.

Table 7.17: Limiting values between liquefaction and stable behavior for the Silt

Type of test	Degree of saturation	Parameter	Limiting value	
			Liquefaction	Strain softening
Tx_CIU	B<0.95	Ψ_{SSL}	Ψ_{SSL}<0.04	Ψ_{SSL}<0.02
		p'/p'_{SSL}	<100	<3
		V_{s1}	>140m/s	>150m/s
		V_{s0}/q_{peak}	<0.5	<1
	B>0.97	Ψ_{SSL}	Ψ_{SSL}<0.04	Ψ_{SSL}<0.02
		p'/p'_{SSL}	<100	<3
		V_{s1}	>150m/s*	>150m/s*
$Tx_{q=constant}_CK_0D$	B>0.97	Ψ_{SSL}	Ψ_{SSL}<?	Ψ_{SSL}<?
		p'/p'_{SSL}	<?	<?
		V_{s1}	>135m/s	>135m/s
		V_{s0}/q_{peak}	<5	<5

* Values based on the older tests, performed over specimens with B<0.95

7.9 Silty Sand - Gold Tailings

7.9.1 Basic Characterization

The gold tailings, residual materials obtained from the process necessary to extract the gold from the rocks greenstone belt, of the Industrial Complex Mina-Usina Fazenda Brasileiro, were initially studied by Bedin (2010). Despite the data set being very extensive, including distinct stress-paths, the results were reevaluated and a consistent error in the CSL/SSL positioning was observed. Therefore, a correction procedure was required and implemented over all tests, being once more presented, in the scope of this work.

According to previous researches (Bedin, 2010; Bedin et al., 2012; Schnaid et al., 2013), gold tailings are chemically constituted by quartz (32.5%), albite (24.3%), chlorite (23.0%), and sulfides (3–6.5%). In order to achieve consistency between this and the other materials, the author decided to perform, at LabGeo, a set of basic identification with Gold tailings which might be consulted in Table 7.18.

Table 7.18: Basic physical characterization of Gold tailings

ID	Unit Weight volume of solid particles	Unit Weight volume	Grain size distribution ASTM sieves			FC	Cu	Cc	Maximum and Minimum void ratio	
	γ_s	$\bar{\gamma}$	Nº20	Nº60	Nº200	%			e_{max}	e_{min}
	(kN/m^3)	(kN/m^3)	0.841 mm	0.250 mm	0.075 mm					
Gold Tailings	29.4	15.7	100.0	99.7	70.5	<70.5	10.0	1.35	n.v.	n.v.

7.9.2 Triaxial Tests

In order to achieve the Gold tailings CSL new positioning a small set of 7 drained and undrained compression triaxial tests were carried out. The new tests were performed including the freezing technique proposed by Sladen and Handford (1987). Furthermore 2 of the 7 compression triaxial tests were performed in the high-pressure triaxial cell, also allowing the definition of the CSL positioning for higher pressures.

As has been shown, the mechanics beyond the liquefaction phenomena still remains, somehow, inexplicable. Thus a set of 6 triaxial tests sheared under drained constant and decreasing mean effective stress were performed on a Bishop-Wesley device.

7.9.2.1 Drained Triaxial Tests

All drained triaxial tests performed with Gold tailings exhibited a contractive behavior as they were prepared in loose conditions. Figure 7.72 display the stress-strain-volumetric curves of the older tests, perfomed by Bedin (2010), Tx_CID_1, Tx_CID_2, Tx_CID_3, and of the new tests, Tx_CID_4, Tx_CID_6, performed during the present research. The other two drained triaxial tests Tx_CID_5 and Tx_CID_7, as being high-pressure triaxial tests, are represented separately in Figure 7.73.

The high-pressure triaxial tests, also contractive, were subjected to grain crushing before achieving their ultimate states, at considerably high axial strains, ($\varepsilon_a > 15\%$), (see both Figures 7.73 and 7.74). While Tx_CID_7 shows a stable volumetric strain as it was continued, during shear, under undrained conditions due to a limitation of the loading cell, the other test also exhibits a constant volumetric strain indicating that grain crushing only occured before the test achieved it ultimate state. The accumulation of high plastic strains, which also occurs at lower confining stresses, is

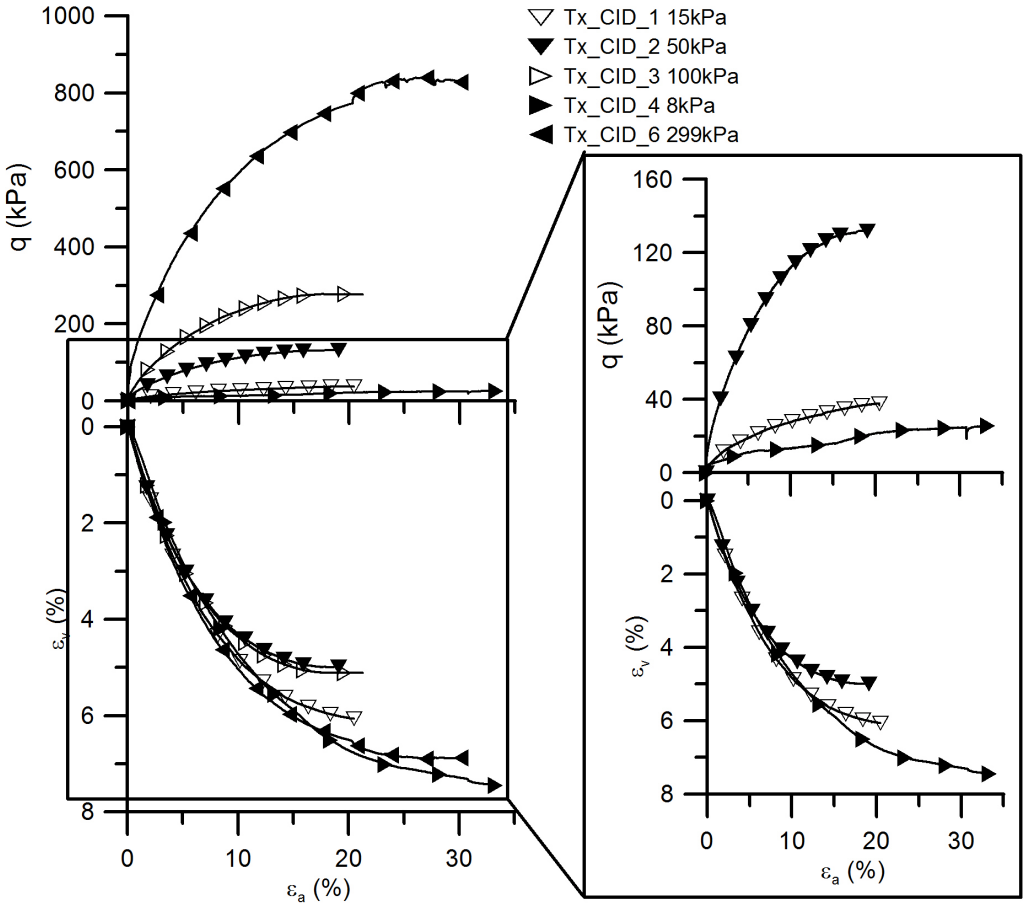


Figure 7.72: Stress-strain and volumetric-strain behavior of drained triaxial tests of Gold tailings

associated to its high compressible behavior. Therefore the material only achieves the critical state after a progressive soil rearrangement.

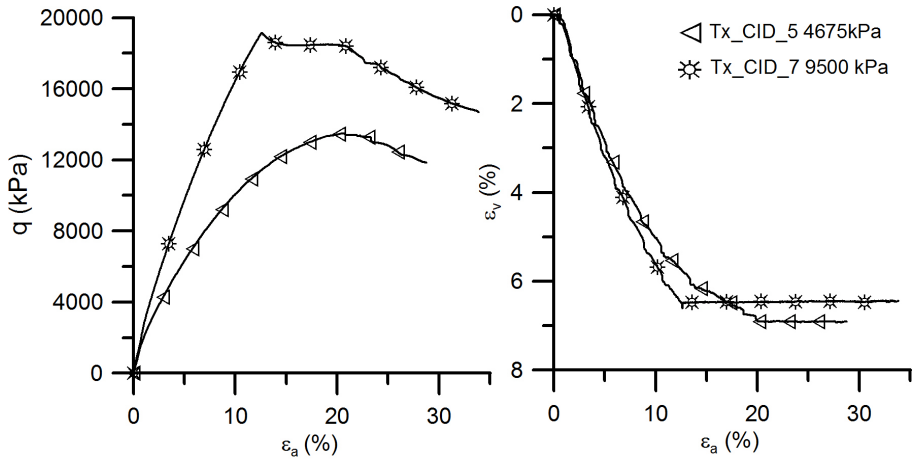


Figure 7.73: Stress-strain and strain-volumetric behavior of the high-pressure triaxial test Tx_CID_5 and Tx_CID_7

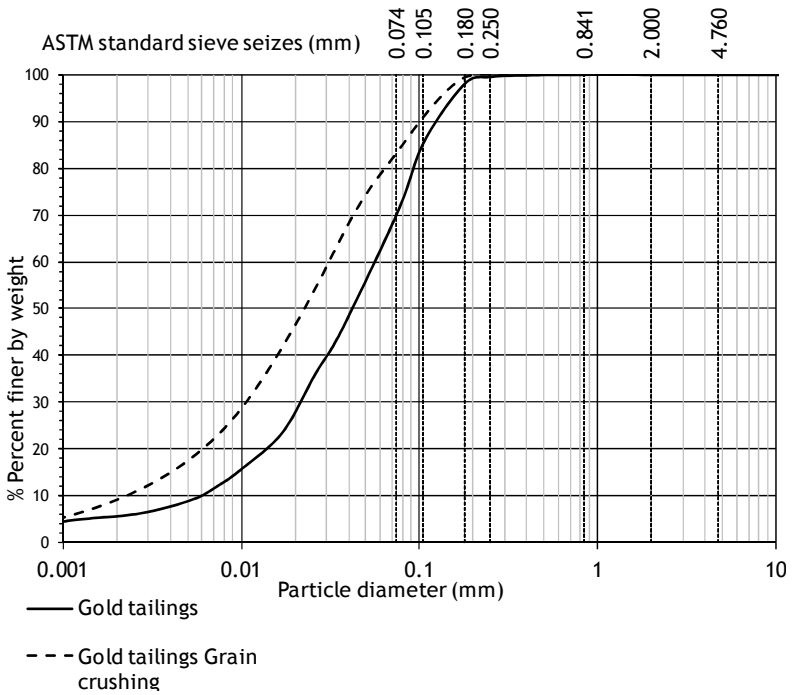


Figure 7.74: Evolution of the grain size distribution of the high-pressure triaxial tests Tx_CID_5 and Tx_CID_7 (4.7 and 9.5 MPa)

7.9.2.2 Undrained Triaxial Tests

The undrained triaxial behavior of Gold tailings might be seen in both Figures 7.75 and 7.76. Excepting the Tx_CIU_14 and Tx_CIU_16 triaxial tests the remaining ones were performed in the scope of the former research (Bedin, 2010).

Both figures display a clear evolution of the soil behavior with both increasing initial confining stresses and decreasing void ratios. Thus the soil evolves from liquefaction, for low confining stresses, passing to a strain softening behavior for medium confining stresses, reaching a stable behavior (with a minor amount of strain hardening) from medium to high confining stresses.

Despite not being extensively studied, apparently the recent tests denounced a higher brittleness associated to a higher saturation. If on one hand Tx_CIU_7 and Tx_CIU_14, confined with 100 kPa, have an almost similar behavior, on the other hand Tx_CIU_8 and Tx_CIU_16 also have a similar behavior, however while the first was confined with 200 kPa, the last one was confined with 300 kPa.

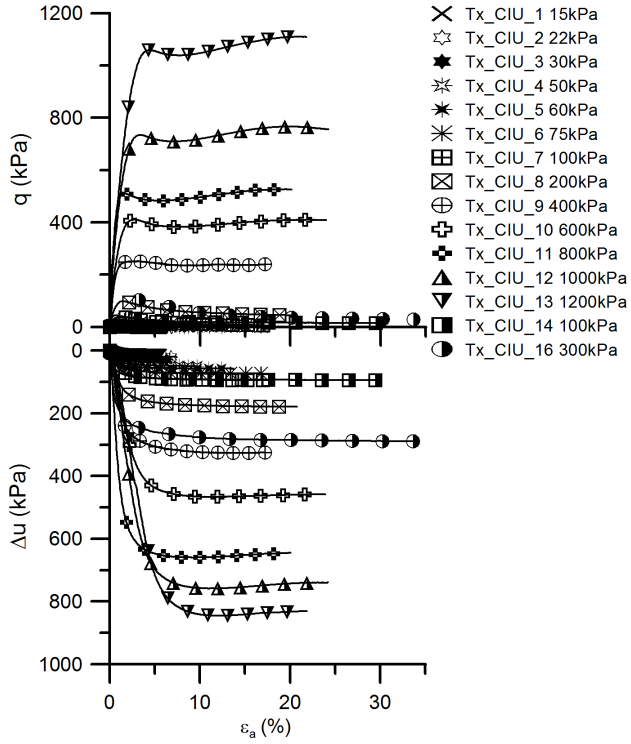


Figure 7.75: Stress-strain and strain-pore water pressure behavior of undrained triaxial tests of Gold tailings at low to high confining pressures

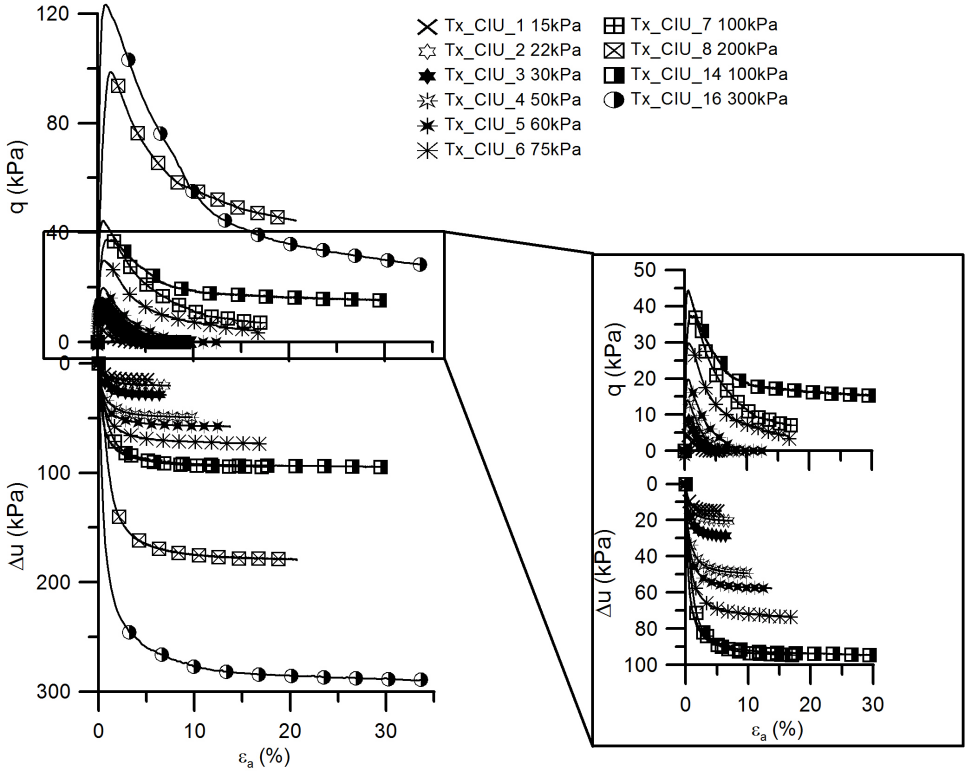


Figure 7.76: Stress-strain and strain-pore water pressure behavior of undrained triaxial tests of Gold tailings at low confining pressures

7.9.2.3 Soil Behavior Under Applied CSSM

As reported previously, CSL positioning was observed to have a standard error due to the inability of internal instrumentation to capture the changing void ratio during percolation and saturation. Therefore both old and new NCL were plotted and the error was determined by their deviation. This correction procedure can be consulted in Annex A. Whereby the old triaxial tests were corrected taking into account the new NCL positioning.

Similarly to the other materials, the ultimate states of Gold tailings reached two distinct positionings, allowing determining both CSL and SSL. While SSL was defined by the undrained triaxial tests which exhibited strain softening, the CSL was defined by the drained triaxial tests and by the medium to high confined undrained compression triaxial tests, which exhibited strain hardening (see Figures 7.77 and 7.78).

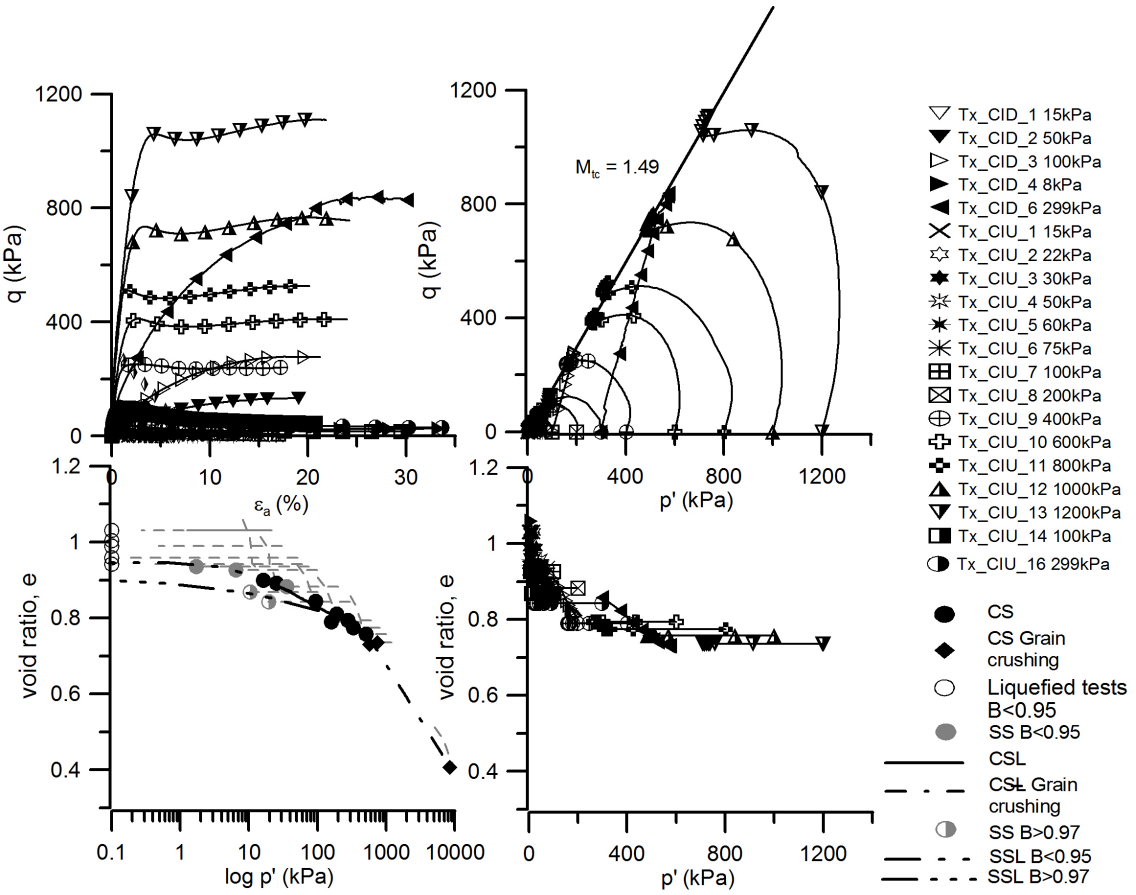


Figure 7.77: Construction of the critical state and steady state line for Gold tailings

According to the previous sub-subsections, where the undrained triaxial tests were analyzed, a distinct behavior between the old and new set of tests was already expected, as can be seen in Figure 7.78. Similarly to Silt, Gold tailings exhibit a higher brittleness with increasing degree of saturation. Therefore, it is also observed a changing positioning of SSL with the degree of

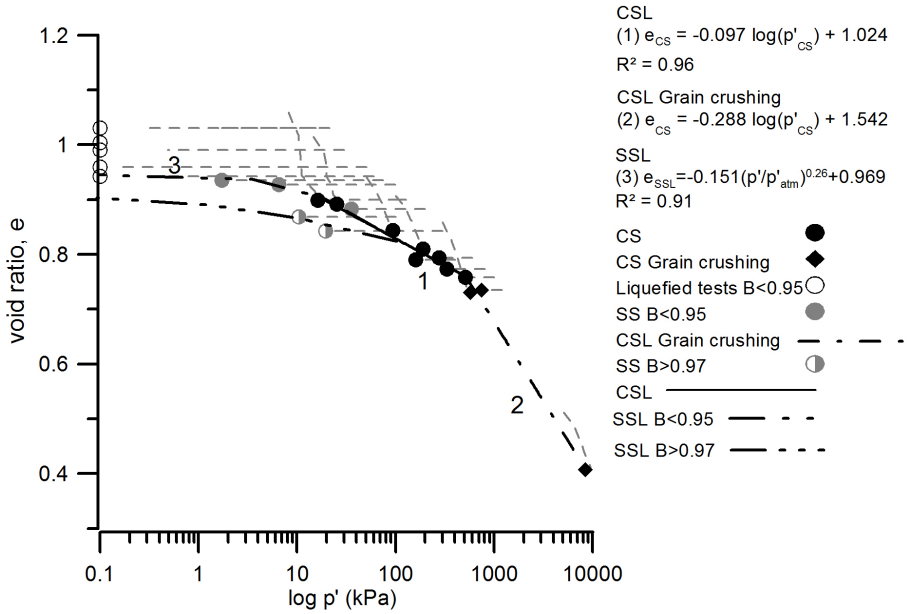


Figure 7.78: Critical state line and steady state line of Gold tailings

saturation, which are represented in both Figures 7.77 and 7.78, by two distinct SSL for two distinct Skempton parameters (B).

As for the high-pressure triaxial test it is also obvious, according to Figures 7.77 and 7.78, the occurrence of grain crushing as these tests resulted in a new, stepper CSL.

The curved shaped line proposed by Li et al. (1999), $e_{SS} = e_{c0} - \lambda_s \left(\frac{p_{SS}}{p_a}\right)^{\xi}$, was adopted to define SSL positioning, adopting the values of -0.151, 0.26 and 0.969 for the λ_s, ξ and e_{c0} parameters.

As for the CSL, the classical form was adopted: $e_{cs} = \Gamma + \lambda \times \ln\left(p'_{cs}\right)$. The new CSL positioning takes the values of 1.024 and -0.097 for the reference void ratio, Γ, and the CSL slope, λ, respectively.

According to the triaxial tests the value of the critical friction angle, ϕ_{cv}, for Gold tailings is of 36.6°, which is equivalent to a critical friction ratio, M, of 1.49. Moreover, as reported previously, the two high-pressure triaxial tests exhibit a lower critical friction ratio of 34.6° justified by the occurrence of grain crushing. This lower critical friction ratio for higher mean effective stresses is believed to be associated to a decrease in particles' angularity.

7.9.2.4 Drained Triaxial Tests With Decreasing Or Constant Mean Confining Stress

The doubts about instability on cohesionless soils, is still under research and its clarification is a key feature for constitutive modeling. Soil instability is commonly associated to the IL, which is defined by plotting the peak deviator stress of soils, exhibited during undrained monotonic

shear. Whilst in the q:p' space the soil instability is clearly defined by the existence of a clear drop of resistance after the interception of IL. In the e: lnp' space the instability has been clearly identified, along the scope of this work, by the existence of a bifurcation between the SSL and the CSL positioning. Aware of such bifurcation, it is necessary to understand the mechanics behind such behaviour. Clearness among the IL as being a boundary problem or a meta-stable (micro-mechanics) problem needs to be clarified.

Aiming to understand instability under other than compressive undrained stress-paths, Gold tailings were tested in a Bishop-Wesley cell under drained conditions, by keeping constant or decreasing the mean effective stress, p'. While liquefaction was clearly identified in the lowest confined tests, $T_{x_{p'=decreasing}}_CID_4$, and a complete stable behavior was identified on $T_{x_{p'=constant}}_CID_5$ test, a strain-softening behavior is believed to dominate the other four tests soil behavior. From Figure 7.79 the only test which suffered from liquefaction have clearly dropped on the SSL (B > 0.97) defined from the undrained compression triaxial tests. Moreover the test which exhibited strain softening, $T_{x_{p'=decreasing}}_CID_3$, also reached it ultimate sate within SSL. This clearly indicates that soil liquefaction is not only prevented by assuring an efficient drainage. Regardless, a grain configuration rules the micro-mechanical behavior.

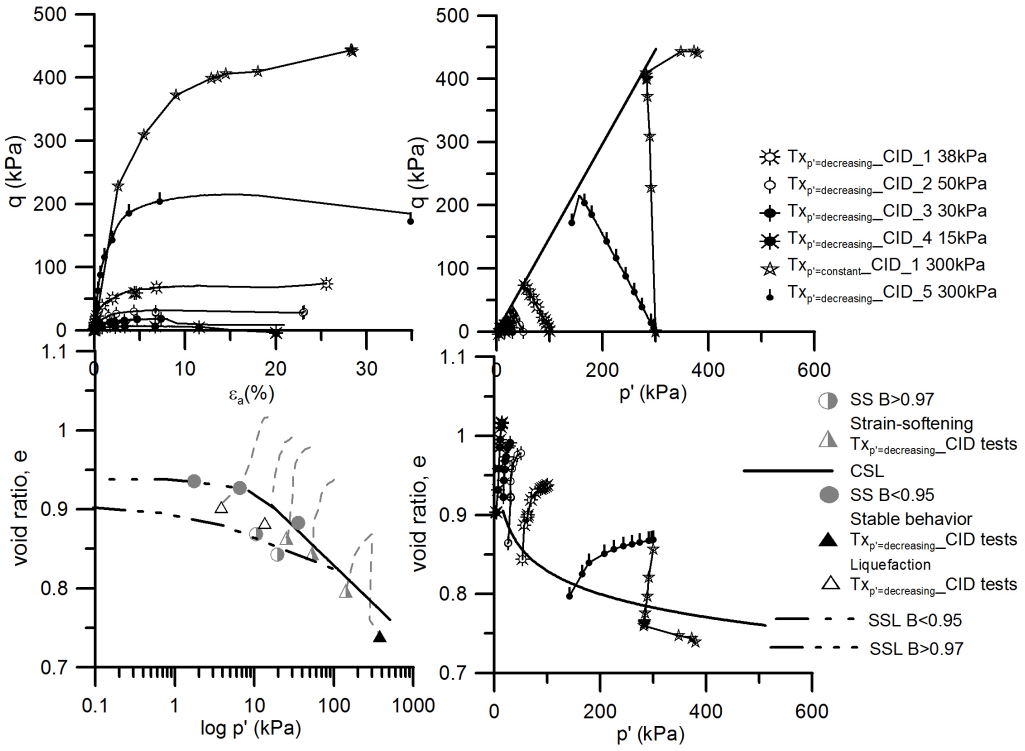


Figure 7.79: Stress-strain and stress-path of the set of triaxial tests with decreasing or constant p'; study under applied CSSM

The minor differences observed between the ultimate states achieved by those tests and the CSL and SSL positioning might be an error of the procedure adopted to measure the void ratio (see

Figure 7.79). While the compression triaxial tests were frozen, the ones performed on the Bishop-Wesley cell, which cannot be frozen, were determined through a distinct procedure. This procedure consists in carefully measuring the specimen water content, at the end of the test, through weighting capsules containing the soil. For a precise result the soil shall be immediately measured, at the end of the test, in a very precise balance. Therefore it is possible that the void ratio could be lower, but never higher than the ones predicted.

Observing Figure 7.80 is clear that $Tx_{p'=decreasing}_CID_4$ liquefaction onset occured when it reached the IL. On the other hand both the other tests exhibited a loss of shear strength far beyond the IL, but still far from the failure envelope. Observing the large volumetric strain accumulation which occured during both these tests, it is possible that such condition might led to an increasing steepness of the IL towards the failure envelope. As demonstrated by Yang (2002b) the stress ratio at peak undrained strength of loose sand approaches the failure envelope with decreasing current state parameter ψ.

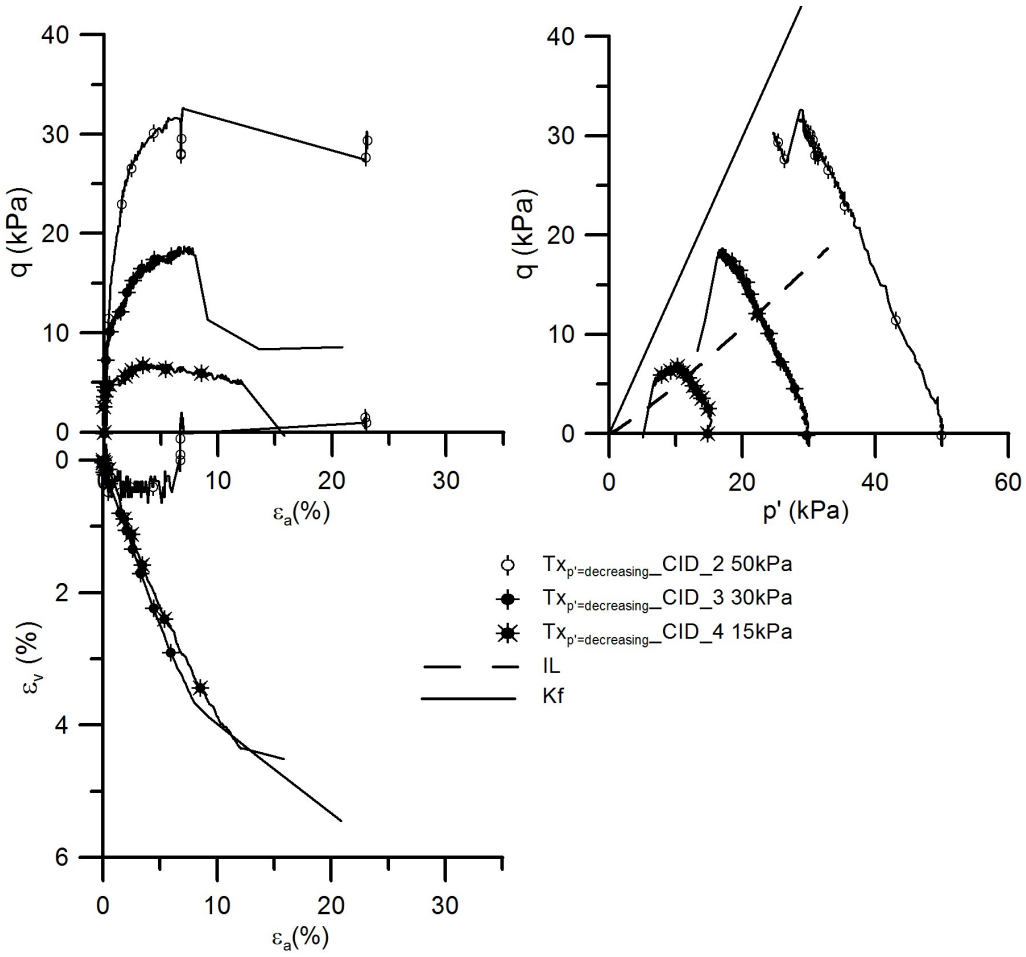


Figure 7.80: Stress-strain and stress-path of $Tx_{p'=constant}_CID_2$, $Tx_{p'=constant}_CID_3$ and $Tx_{p'=constant}_CID_4$ triaxial tests

7.9.3 Prediction Of Liquefaction Resistance

The trendline between brittleness index, I_B and the steady state parameter, ψ_{SSL}, is very accurate, and can be used to predict the behavior of Gold tailings under specific conditions. However distinct lines were found, according to the degree of saturation. Therefore it is observed that an increasing saturation of the soil is translated, as expected, in a higher brittleness which can be seen in Figure 7.81. On the other hand the other tests, carried out with a distinct drained stress-path, display a decreasing brittleness for much a higher ψ_{SSL}. The curious drop of the trendline which correlates both variables is explained by the phenomena itself. As detailed in Chapter 4, when liquefaction occurs under drained conditions is exclusively associated to an unstable microstructural fabric rearrangement. On the other hand the second type of instability, which occurs on undrained compression triaxial tests, is not only a problem associated to the loose grain configuration but also to a consequent pore pressure increase. Therefore the area between the delineated lines is exclusively associated to the extra instability generated by the pore pressure increase. The same conclusion might be redrawn from the correlation between the brittleness index and the stress ratio p'/p'$_{SSL}$, displayed in Figure 7.81.

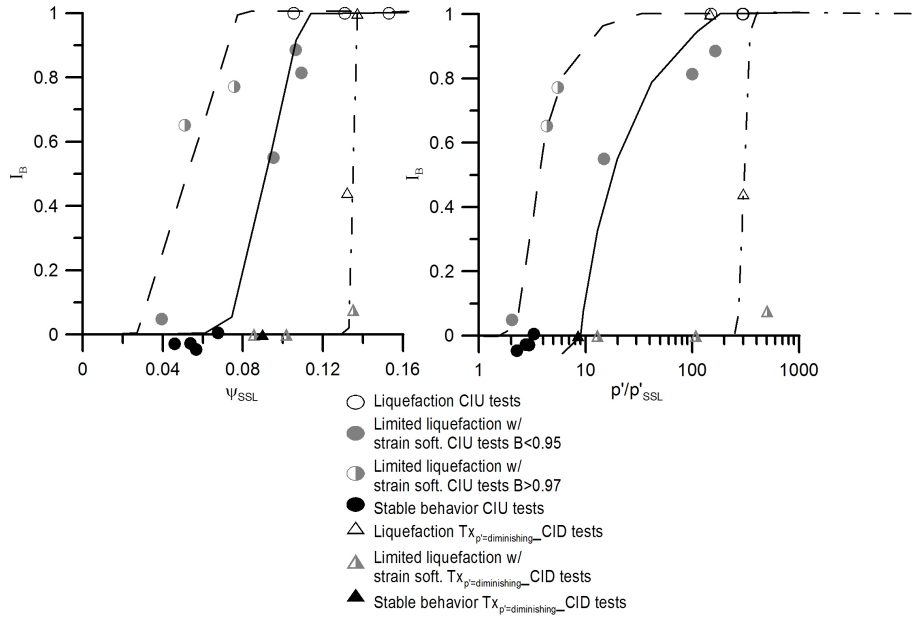


Figure 7.81: Variations of the Brittleness Index with the steady state parameter, ψ_{SSL}, and the stress ratio p'/p'$_{SSL}$, from left to right, respectively, for Gold tailings

The necessity of a framework which evaluates the soil liquefaction potential by correlating the initial state condition of the soil with reference to it ultimate state is very important for geotechnical engineering purposes as it relies on a strong theory, such as the CSSM. Notwithstanding, as explained before, the use of geophysics to evaluate soil stiffness (G_0- read V_s) has gaining importance due to its intimate correlation with the strength parameters. Figure 7.82 shows the correlation between the steady state parameter, which measures the initial state of the soil with reference to its

ultimate state, and the peak shear strength, q_1, and the normalized shear wave velocity, V_{s1}. Beyond the correlation revealing an increasing stability with increasing q_1 and increasing V_{s1} with decreasing ψ_{SSL}, it also displays a clear trendline for the distinct stress-paths. Furthermore a clear boundary exists between liquefaction ($q_1 < 0.03$, $V_{s1} < 140$ m/s, $q_1/V_{s0} > 7$), strain softening ($q_1 < 2$, $V_{s1} < 170$ m/s, $q_1/V_{s0} > 1$), and the soil stable behavior. Plus, this boundary seems to be unique for the distinct stress-paths, constituting a much more valuable parameter than the state parameter itself. A consistent result is also found when using the ratio q_1/V_{s0}, which can be observed in Figure 7.83b.

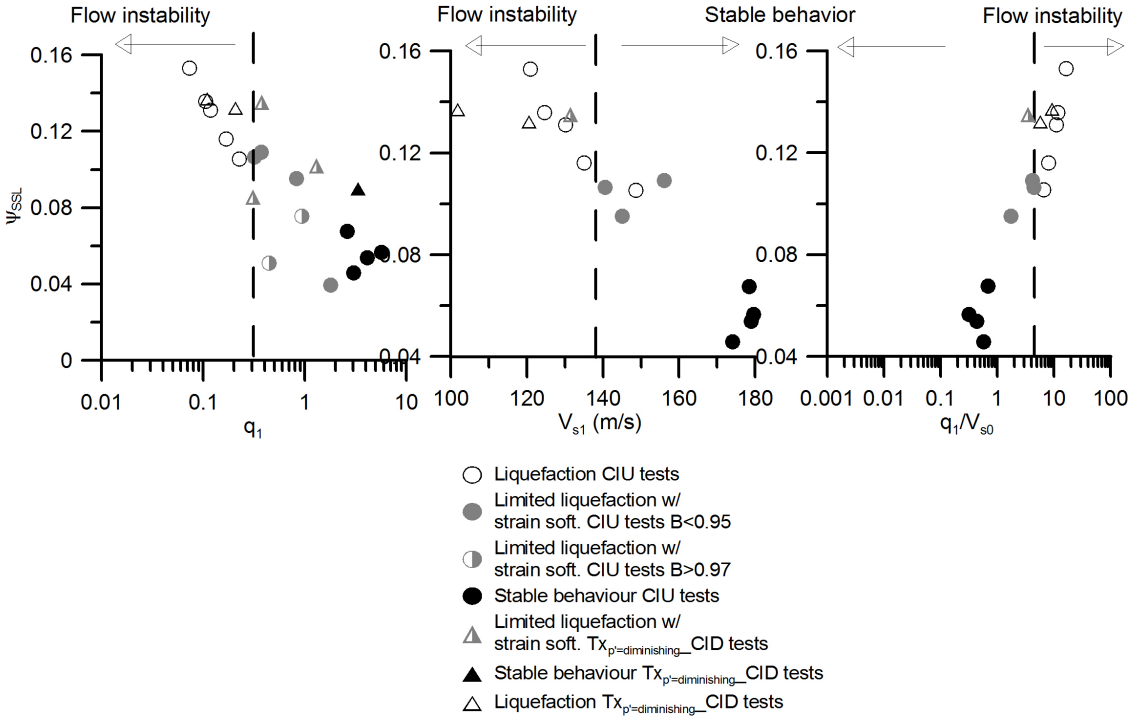


Figure 7.82: Steady state parameter expressed as a function of normalized peak shear strength (q_1) and shear stiffness for Gold tailings

The correlation between the peak shear strength and the initial shear stiffness has been greatly expressed as potential function, as can be seen in Figure 7.83a. The strong correlation between both variables might be explained in terms of energy. The energy stored on the system, which can be measured through V_s waves is spent through the accumulation of shear work and the generation of pore pressure. As the system is closed (when sheared under undrained conditions), the plastic and the elastic strains have to equalize for the system to be in equilibrium. This explanation support the high correlation observed in Figure 7.83b between the V_{s0}/q_{peak} and q_1, which by themselves also have a strong statistic correlation.

Instability line positioning on q:p' space might be used to better understand why liquefaction is featured to low mean confining pressures. As can be seen in Figure 7.84, the ratio of the peak strengths achieved under undrained conditions, $\eta = q/p'$, is about 0.5 for low confining pressures, achieving values of 1 for medium to high confining pressures, which is clearly associated to a

much stable behavior. Similarly to Silt the figure also shows a decreasing steepness with increasing degree of saturation, as a result of the increasing brittleness.

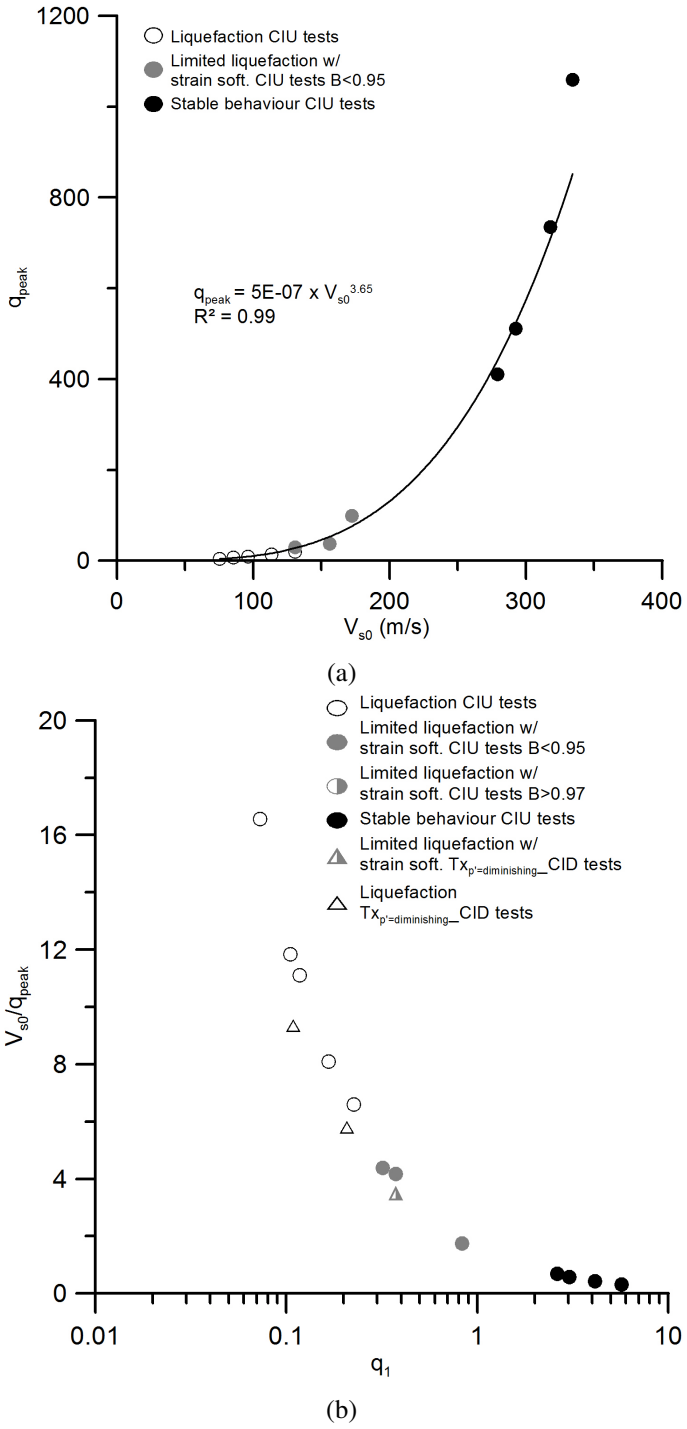
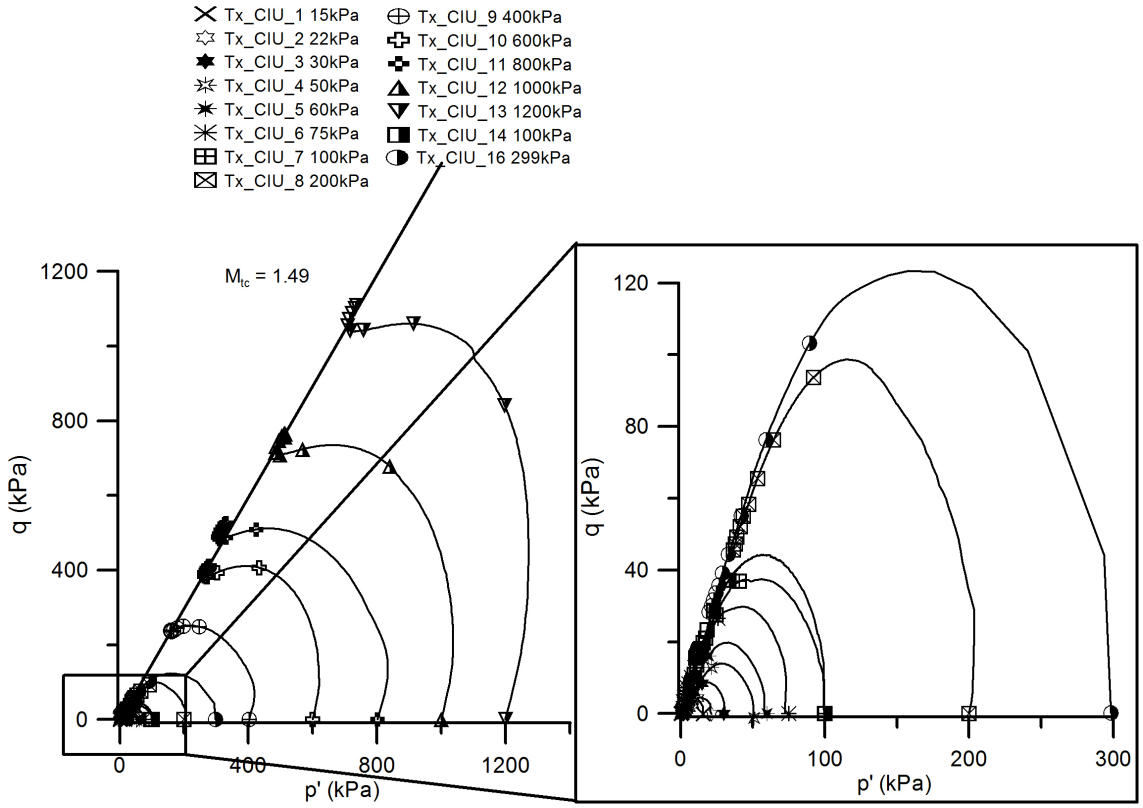
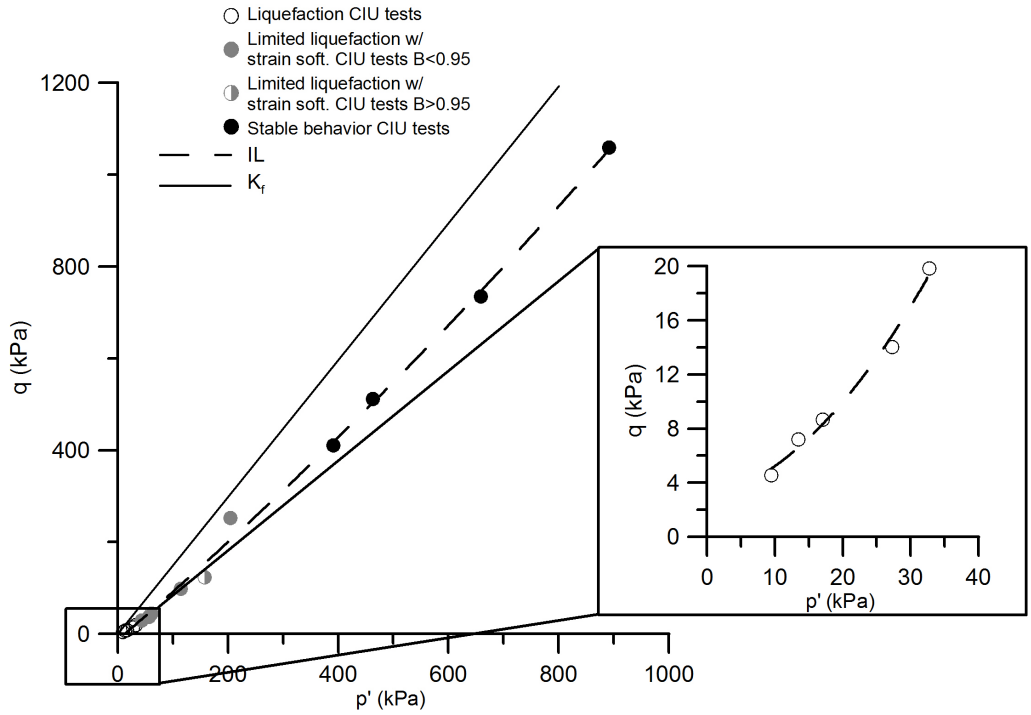


Figure 7.83: a) Peak shear strength as function of the soil stiffness; b) Correlation between the normalized peak shear strength and the ratio between shear stiffness and the peak shear strength for Gold tailings



(a)



(b)

Figure 7.84: a) Detail of the stress-path of the triaxial tests; b) Instability Line (IL) for Gold tailings

7.9.4 Partial Conclusions

The study of Gold tailings, mostly performed by Bedin (2010) was completed by introducing a correction of the CSL positioning. During it evaluation three distinct soil behavior were detected: liquefaction for low confining stresses; strain softening for low to medium confing stresses and strain hardening for medium to high confining pressures. While the strain softening allows defining the SSL positioning, the remaining one allows CSL definition. Furthermore it was also observed a SSL changing position with an increasing saturation degree.

Being most of the specimens prepared from the NCL, it is conclusive that:

- For initial confining pressure lower than 100kPa – Liquefaction takes place;
- Low confining stresses to medium confining pressures – Limited liquefaction with strain softening occurs;
- CSL was only achieved through the performance of drained triaxial tests and undrained triaxial tests which exhibited strain hardening;
- For high to very high confining pressures both drained and undrained compression triaxial tests are subjected to grain crushing, leading to a new CSL, steeper than the previous one.

A resume of the distinct ultimate state lines are expressed in Table 7.19:

Table 7.19: Resume of the ultimate states for Gold tailings according to the type of test

	Soil behavior	Type of tests	Equation
CSL	Stable behavior; Strain hardening	Drained triaxial tests and undrained triaxial tests with strain hardening	(1) $e_{cs} = -0.097 \log(p'_{cs}) + 1.024$
SSL	Liquefaction and strain softening	Undrained triaxial tests	(2) $e_{ss}=-0.151(p'_{ss}/p'_{atm})^{0.26}+0.969$
CSL Grain crushing	Stable behavior	Drained and undrained high-pressure triaxial tests	(3) $e_{cs} = -0.288 \log(p'_{cs}) + 1.542$

Among all the liquefaction assessment charts, it was observed that for Gold tailings, despite the good trends shown by the correlations between the brittleness index, I_B, and the steady state parameter, ψ_{SSL}, or the stress ratio, p'/p'_{SSL}, the better evaluation was definitly assured by the ratio q/V_{s0}.

During this research it was also concluded that the instability is not merely a boundary condition problem, regardless is associated with a meta-stable structure of the soil under loose conditions and

low confining pressures. Therefore, instability might also occur under drained non-compressive conditions as long as no large plastic strains are accumulated, which inherently would improve soil stability. This increasing plastic strain accumulation is also associated to an increasing steppeness of the IL.

The limiting values for liquefaction and strain softening to not occur under both studied stress-paths are show in Table 7.20.

Table 7.20: Limiting values between liquefaction and stable behavior for Gold tailings

Type of test	Degree of saturation	Parameter	Limiting value	
			Liquefaction	Strain softening
Tx_CIU	B<0.95	ψ_{SSL}	ψ_{SSL}<0.1	ψ_{SSL}<0.06
		p'/p'$_{SSL}$	<100	<2
		V_{s1}	>140m/s	>170m/s
		V_{s0}/q_{peak}	<7	<1
	B>0.97	ψ_{SSL}	ψ_{SSL}<0.08	ψ_{SSL}<0.02
		p'/p'$_{SSL}$	<10	<1
Tx$_{p'=diminishing}$_CID and Tx$_{p'=constant}$_CID	B>0.97	ψ_{SSL}	ψ_{SSL}<0.14	ψ_{SSL}<0.14
		p'/p'$_{SSL}$	<2	<2
		V_{s1}	>130m/s	>?
		V_{s0}/q_{peak}	<7	<1

7.10 Similarities And Differences Between Soils

After a long evaluation of each soil behavior this sub-section is exclusively dedicated to their comparisons. The importance of observing similarities and differences of soils behavior is prominent for the development of a universal framework. For example the feature which distinguishes Silt, from Mixture and from Osorio sand is the fines content. Therefore correlations such as the one proposed by Thevanayagam et al. (2002) to correct the fines content shall be tested as it suitability could spare a lot of laboratory work.

On the other hand between the three tested sands, beyond the minor changes of the grain size distribution, the feature which distinguishes the three soils is the particles shape. Thus a comparison shall be performed by correlating critical state parameters with other parameters which could explain the soil disparities and be used in their normalization.

7.10.1 Comparison Of CSL Positioning

- Osorio sand + Fines

The influence of the fines content in CSL positioning is clearly shown in Figure 7.85. Expectably the CSL moves downwards and increases it steepness when fines are added to Osorio sand. Such behavior is easily explained by the increasing contractible tendency, which under undrained conditions is compensated by a positive pore pressure generation, explaining the increasing liquefaction potential with increasing CSL steepness. It was also expected for the Mixture to have the lowest location of the CSL due to it FC being closest to the transitional fines content. On the other hand the Silt CSL moves upward, with reference to Mixture CSL, as the FC are much higher than the transitional fines content. A similar behavior was also observed by many authors while assessing the influence of fines content (Zlatovic and Ishihara, 1997; Thevanayagam et al., 2002; Naeini and Baziar, 2004; Yang et al., 2006b; Rahman and Gnanendran, 2008; Bobei et al., 2009; Carrera et al., 2011).

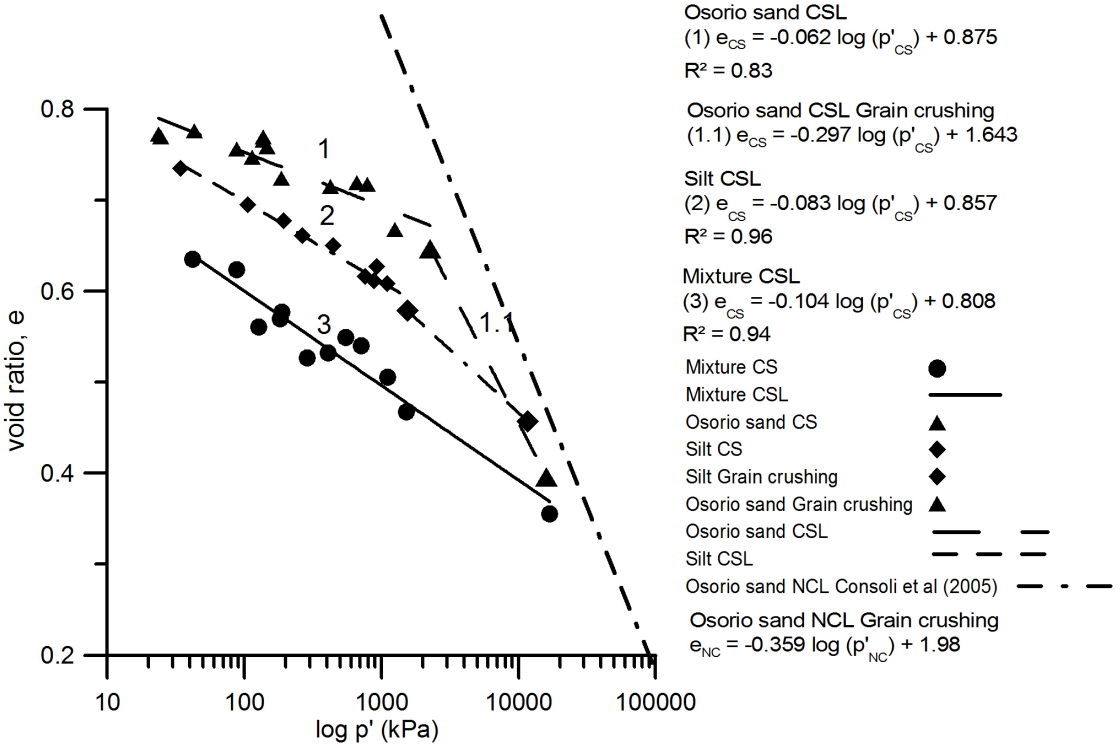


Figure 7.85: CSL varying positioning with varying fines content for Osorio sand

However the CSLs displayed in Figure 7.85 are not parallel, regardless an increasing steepness is observed for both Mixture and Silt. Similarly other authors, (Been and Jefferies, 1985; Bouckovalas et al., 2003), demonstrated that increasing fines content causes a steepening of the CSL (or SSL). This increasing steepness is explained by increasing grains angularity (Cho et al., 2006; Poulos et al., 1985), and by particle shape, which conceives an important feature to study as flatness is predominant on finer soils. Thus as the fines,

for both Silt and Mixture, were artificially obtained by grinding Osorio sand, being both angular and flat, it explains the increasing steepness of the CLSs. Moreover the CSL of the Mixture has a higher steppeness due to it highest packing capacity between bigger and smaller grains.

Aware of the CSL and SSL divergence, the equivalent intergranular and interfine void ratio, proposed by Thevanayagam et al. (2002), was tested in order to evaluate it suitability for CSL correction. According to Figure 4.38 an equivalent void ratio was determined for both Osorio sand (4% FC), Mixture (42% FC) and Silt (99% FC), basing on equations 4.7, 4.9 and 4.8, respectively. The equivalent intergranular and interfine void ratio achieved for three soils are shown in Figure 7.86b. Looking to the CSL distinct steepness's and to the equations proposed by Thevanayagam et al. (2002), it unsuitability was somehow expected. In fact the SSLs unified by Thevanayagam et al. (2002) were parallel, unlike those achieved for these materials. Therefore it is concluded, by observing the correlation between FC and the CSL parameters, shown in Figure 7.86a, that a proper parameter should be used to correct the CSL positioning.

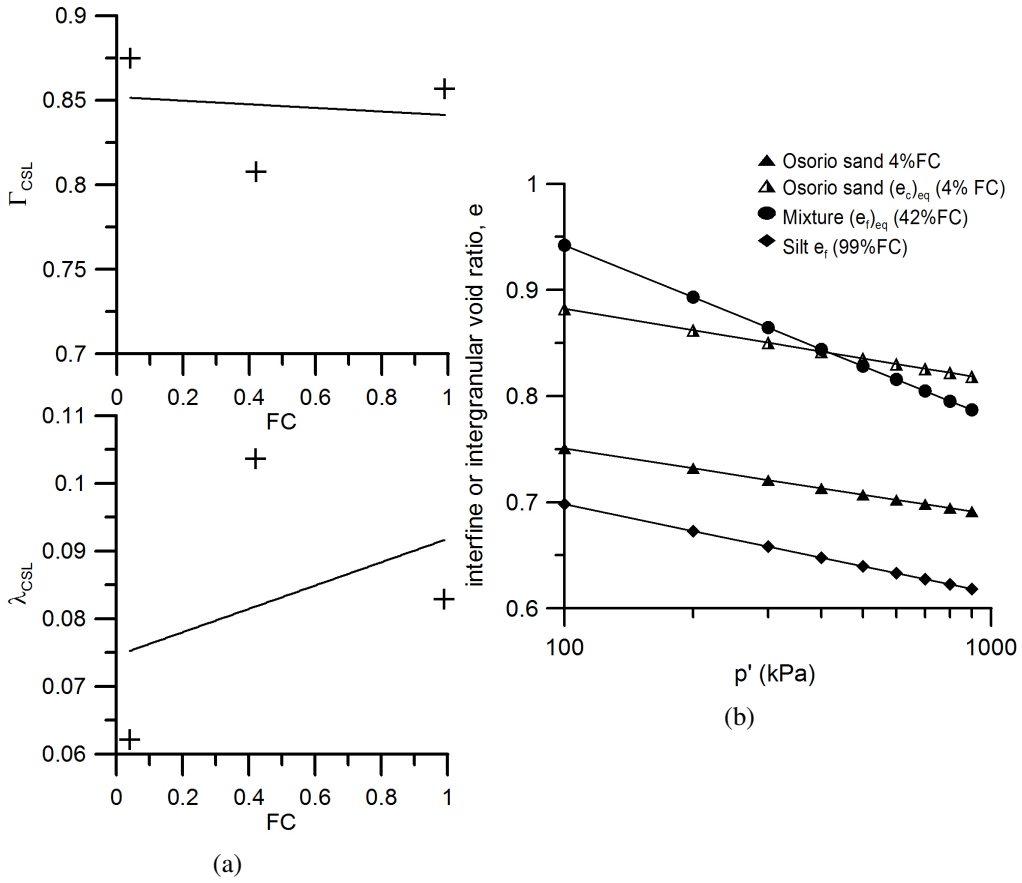


Figure 7.86: a) CSL as function of the Fines content for Osorio sand; b) CSL of Osorio sand, Mixture and Silt, corrected according to Thevanayagam et al. (2002) proposal

As liquefaction occurs under undrained conditions, it is more important to assess SSLs varying position with FC, instead of CSL. However while the classical form of the CSL is easily compared, as it only involves two parameters, SSL formula proposed by Li et al. (1999) considers three distinct parameters, λ_s, ξ and e_{c0} parameters, being it comparison impossible to be made as can be seen in Figure 7.87. Therefore a constant ξ of 0.5, which was determined by assuring a best fit to all material, was assumed for a better comparison (see Figure 7.88). Analyzing Figure 7.88 similar conclusions to the CSL varying position might be outlined. Thus the SSL positioning moves downwards with increasing fines content until the FC is equal to the transitional fines content, which can possibly be lower than the FC of the Mixture. For higher FC the SSL moves upwards, but the SSL for Silt is still located below Osorio sand SSL. Plus an increasing steepness is registered for the Mixture, which explains it highest collapsible behavior, which is associated to its highest compressibility.

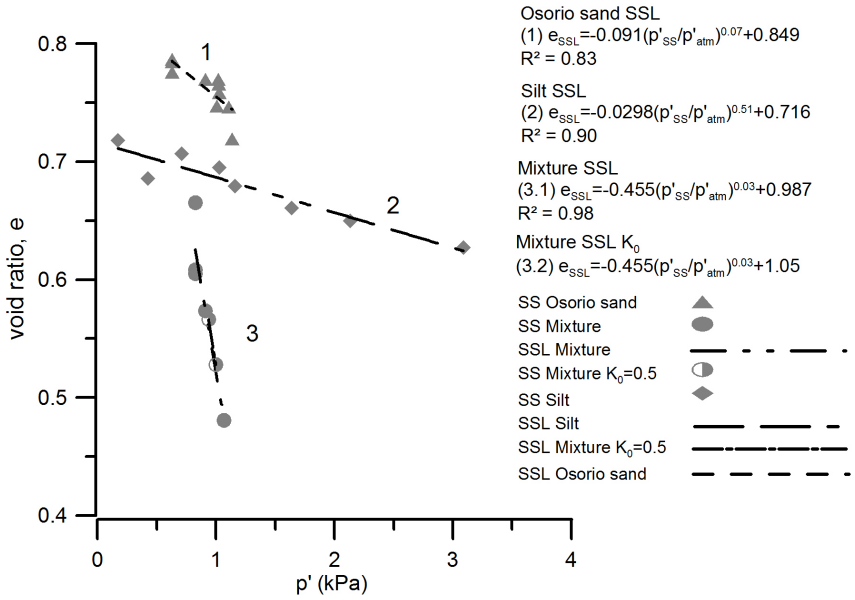


Figure 7.87: SSL varying positioning with varying fines content for Osorio sand

A wide range of parameters have been studied and correlated with CSL parameters by Santamarina and Cho (2004) and Cho et al. (2006). As quoted by Cho et al. (2006) *"The size and shape of soil particles reflect the formation history of the grains. In turn, the macroscale behavior of the soil mass results from particle level interactions which are affected by particle shape. Sphericity, roundness and smoothness characterize different scales associated to particle shape"*. Whereby, after testing a variety of parameters, Cu was found to be the one which revealed, for these materials, a better correlation with the CSL parameters. Despite Cu not being directly related with particles shape, by considering the diameters of the particles it can evaluate the soil dispersion, which is highly related with potential fabric configuration, and somehow it also considers the particle shape as the smaller particles are always platen than the granular fraction of the soil. Figure 7.89 shows the correlations achieved between the Cu and both SSL and CSL parameters achieved for Osorio sand, Silt

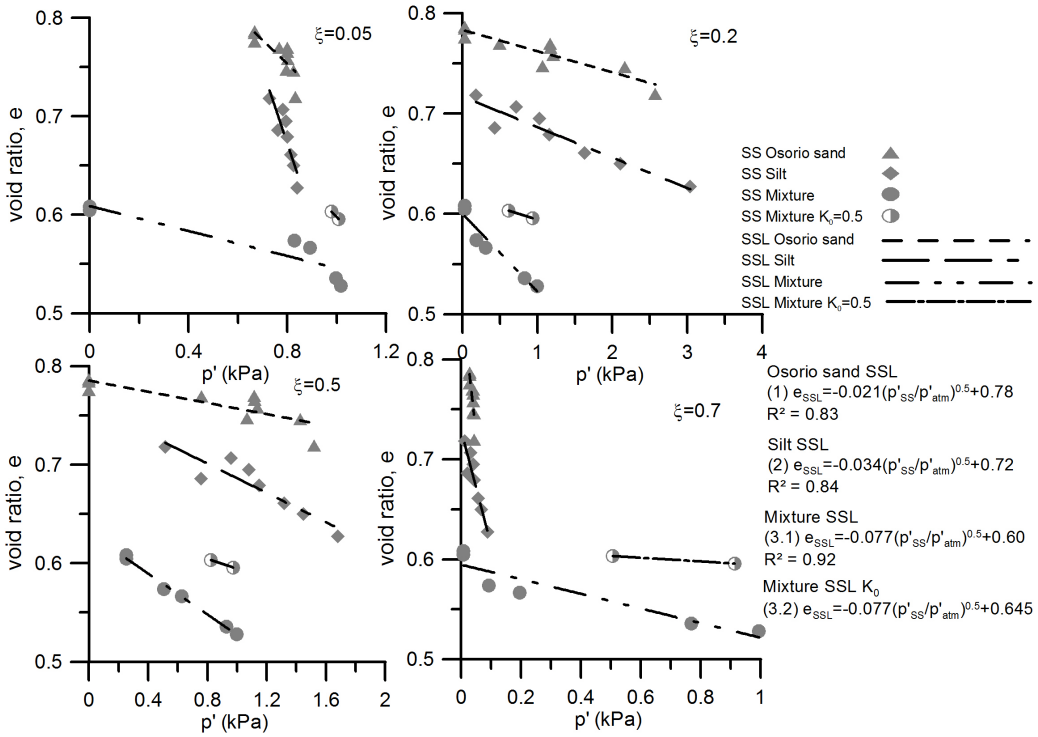


Figure 7.88: SSL varying positioning with varying fines content and varying ξ for Osorio sand and Mixture.

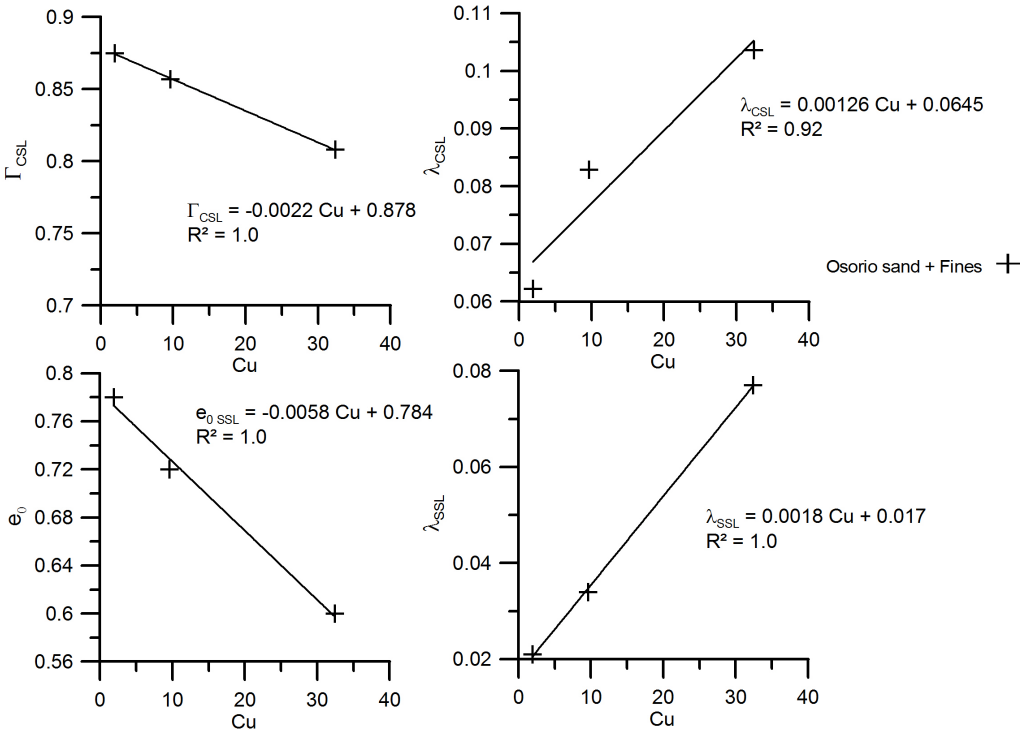


Figure 7.89: Effect of Cu on CSL and SSL positioning parameters

- Coimbra sand + Fines

While the fines used on Mixture and Silt were achieved by artificially crushing Osorio sand, the fine particles used to evaluate Coimbra sand was industrialized silica.

Due to the reduced number of tests performed with Coimbra 20 and Coimbra 40 no major conclusions were redrawn. Regardless it was possible to compare CSL positioning with increasing amount of fines (see Figure 7.90).

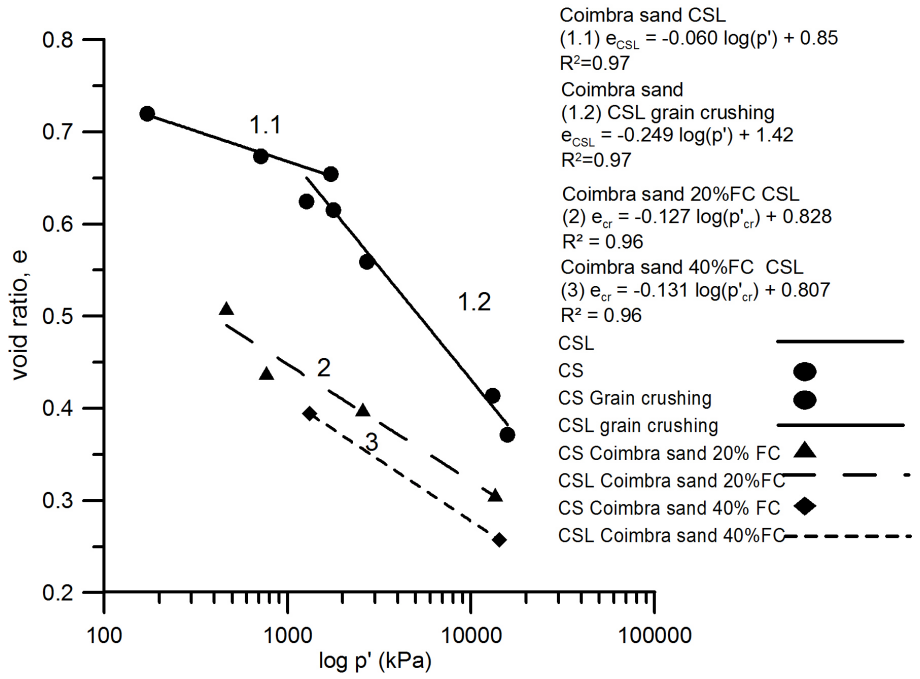


Figure 7.90: CSL varying positioning with varying fines content for Coimbra sand

Despite the CSL of Coimbra 20 and Coimbra 40 being only achieved and represented for large mean effective stresses, according to the steepness achieved for Mixture it might be inferred that even for lower confining stresses the value won't change considerably. Obviously the comparison only makes sense, excluding the CSL achieved by Coimbra sand through grain crushing. Therefore it is also concluded, similarly to Osorio sand, that CSL steepness increases with increasing fines content. Jointly CSL moves downwards due to an increasing packing capacity with increasing fines content, till a transitional fines content closer to 40% than 20%.

- All tested sands

As a minor set of tests were performed under high-pressure triaxial tests it is possible for the data to display some inaccuracy. Plus as the common range of confining stresses for engineering purposes is usually below 1000 kPa, the present study focused within this range of stresses.

As can be seen in Figure 7.91 the CSL steepness is similar for Algeria, Coimbra and Osorio sand, which can explained by their similar grain size distribution. The only differences

observed are mainly addresses to the intercept, Γ, parameter. While the Γ value is lower for Coimbra sand due to it high angularity, the lower value of Γ for Osorio sand is justified by the smaller size of the grains.

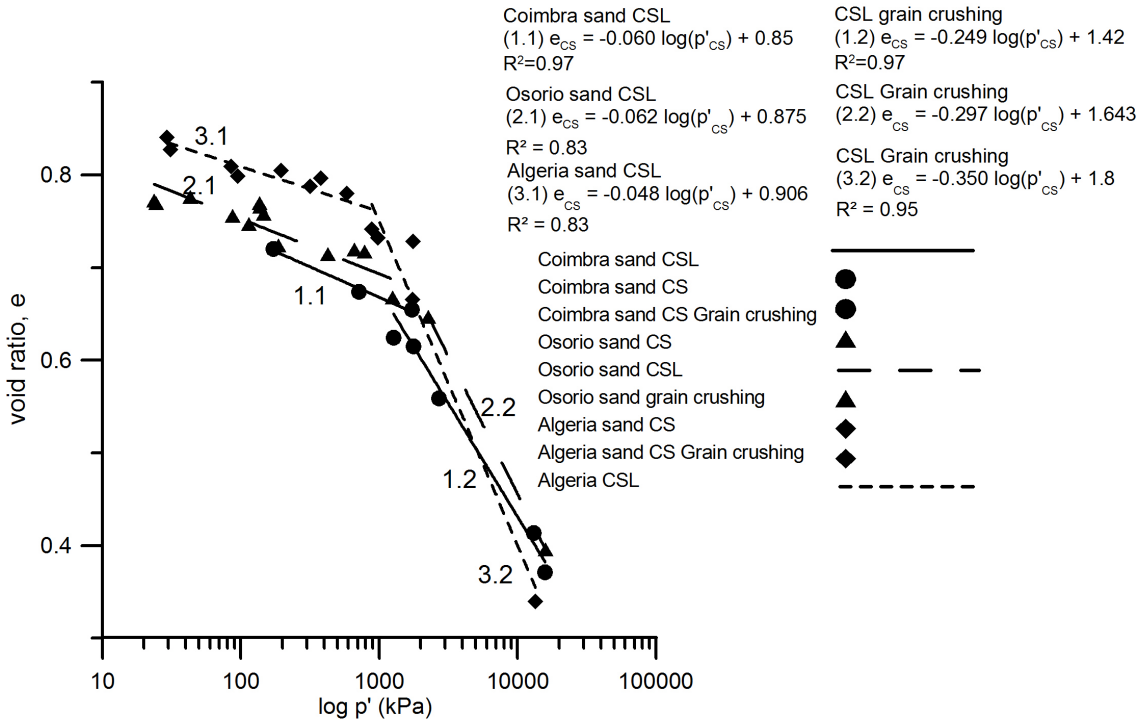


Figure 7.91: CSL varying positioning for distinct sands

The influence of both angularity and grain size reflects on both maximum and minimum attainable void ratios, which in turn affect CSL positioning, mainly the interception parameter, Γ. A good correlation, proposed by Cho et al. (2006), and displayed in Figure 7.92, can explain the variations observed in Figure 7.91.

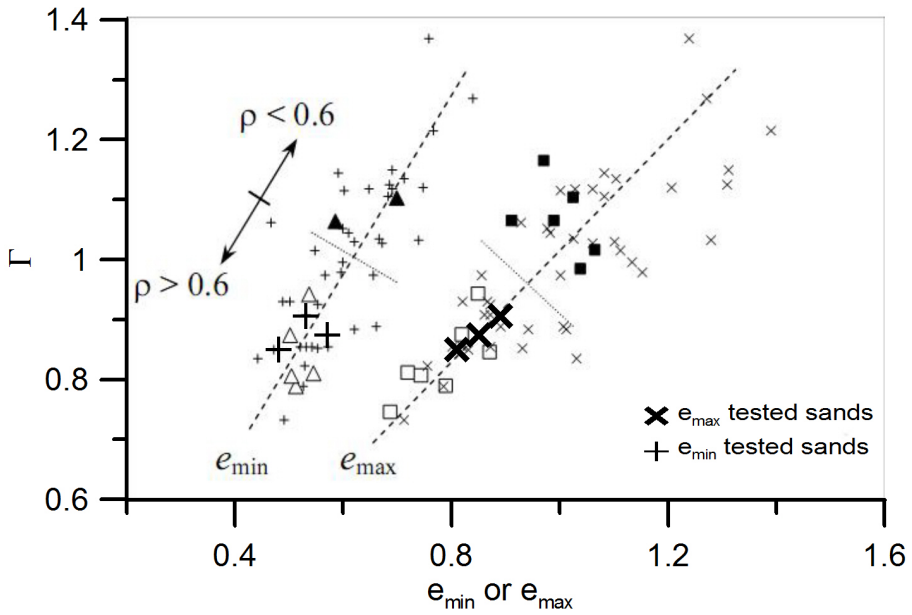


Figure 7.92: Correlations between CSL parameter, Γ, and e_{max} and e_{min}; data set compiled by Cho et al. (2006) and completed with present data

- All tested soils

  The study of soils under applied CSSM is of high relevance, allowing to determined how dilative and contractive a soil might be. Furthermore it is also very useful, as has been focused during this work, to assess the soil liquefaction potential.

  Aiming to predict soils CSL parameters two correlations were obtained for the studied materials. The strongest correlation, shown in Figure 7.93, achieved between the coefficient of uniformity, Cu, and the CSL parameters, previously presented in Figure 7.89, seems to provide a good framework, despite the disparity between the silica soils and the tailing soil. Similarly to the coefficient of uniformity also the A parameter, measured through small-strain deformations and determined according to empirical equation to estimate G_0 proposed by Hardin and Richard (1963), reflects the fabric and structure of the soil, whereby providing a good correlation with the CSL parameters (see Figure 7.94). It is important to note that despite being possible for A to assume other values for the silt and gold tailings, as the n parameter assumes other value distinct of 0.5, their comparison with the other soils would only be possible assuming a same exponent.

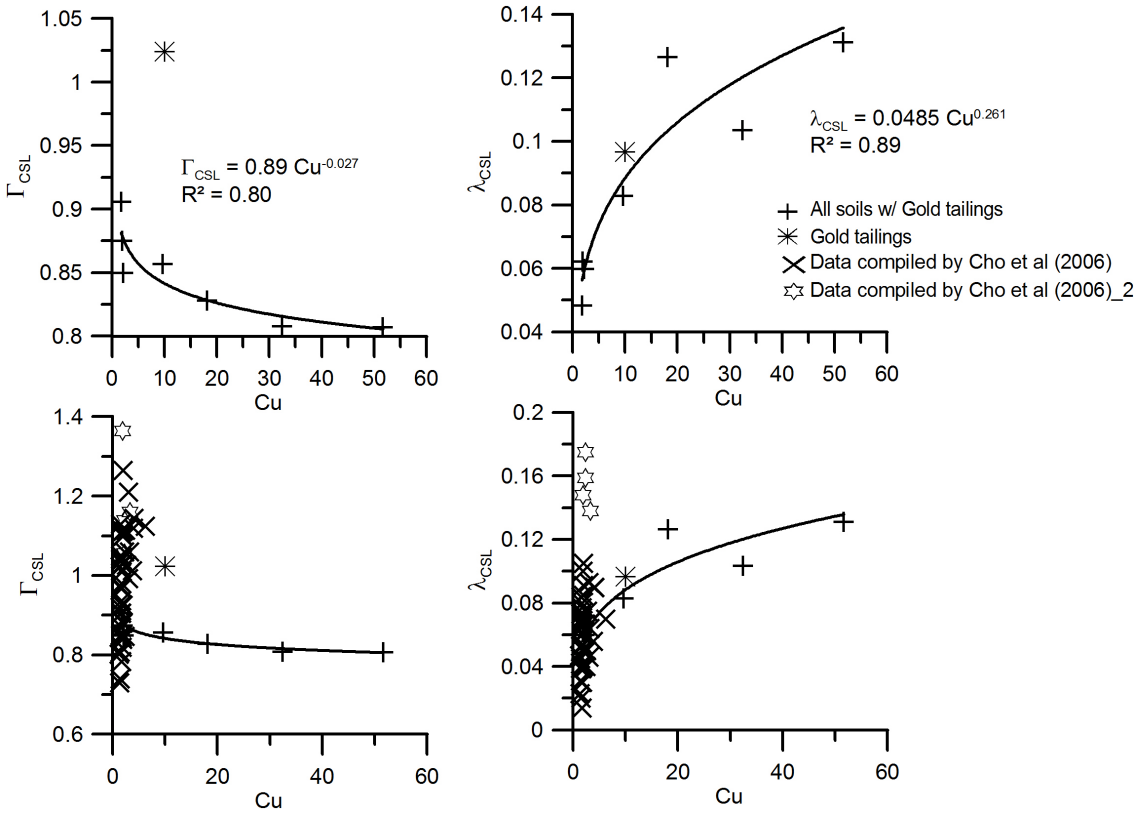


Figure 7.93: Correlations between CSL parameters, Γ and λ, and Cu

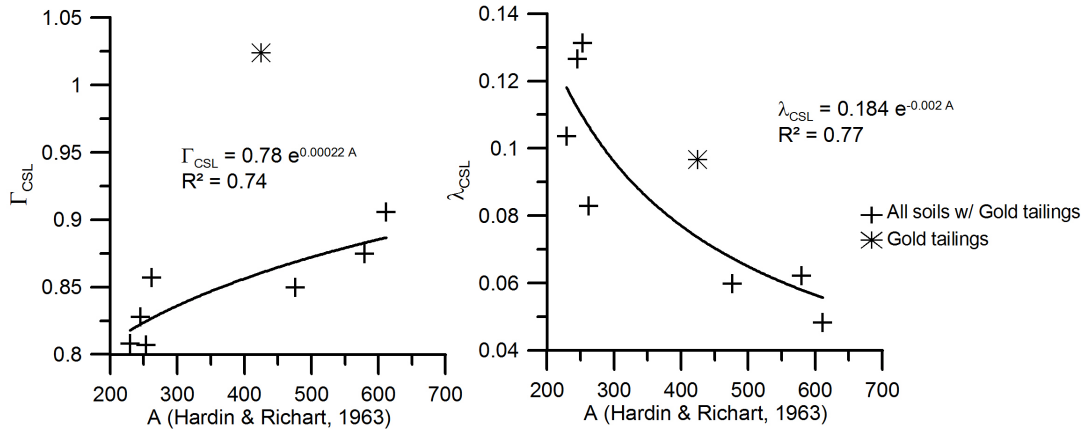


Figure 7.94: Correlations between CSL parameter, Γ and λ, and A

7.10.2 Comparison Of Residual Or Constant Volume Friction Angle, ϕ'_{cv}

Usually for a same soil an increasing fines content reduces it ultimate shear strength, thus it ϕ'_{cv}. However particle shape can surpass this tendency, as with increasing angularity the higher is the constant volume friction angle, ϕ'_{cv}, (Cho et al., 2006). This tendency was observed for both Osorio and Coimbra sand, which with increasing fines content exhibited an increasing residual friction angle (see Figure 7.95). In order to plot the data, the roundness of the soils was achieved through

a visual comparison with the framework proposed by Krumbein and Sloss (1963) which compiles particles with distinct roundness and sphericity. Nevertheless a good suitability is observed among these soils and those studied by Cho et al. (2006). Therefore it might be concluded that particles shape have a major role on constant volume friction angle.

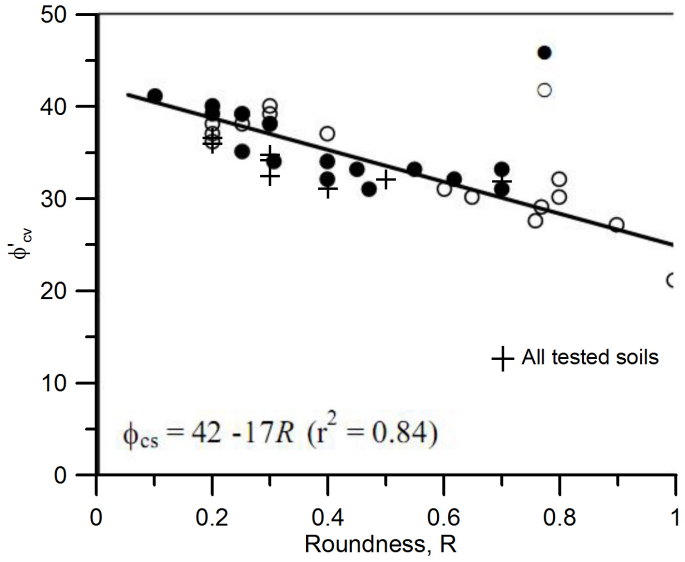


Figure 7.95: Effect of particle shape on friction angle; data set compiled by Cho et al. (2006) and completed with present data

7.10.3 Comparison Of Soil Liquefaction Potencial

Being the main focus of the present work to evaluate soil liquefaction potential a comparison between all soils is required in order to perceive the conditioning factors on the onset of liquefaction.

During this work, as the stiffness parameter, V_{s0}, revealed to be a more suitable parameter than the steady state parameter the comparison was decided to be exclusively addressed to this parameter. Furthermore this comparison was only addressed to the undrained compression triaxial tests as were the most consistent results due to the large amount of data.

Both Figures 7.96 and 7.97 display a very good correlation between the stiffness parameter, V_s, and the strength parameter, peak strength q_{peak}. From both graphs can be concluded that Coimbra sand is the soil which exhibit a higher brittleness, justified by the highly meta-stable structure created by the small contact bridges of the very angular grains. Furthermore it is also observed that both Gold tailings and Silt are more resistant to liquefaction than the other soils, yet this is not translated in a higher stability since they display a strain softening behavior within a wide range of shear wave velocities. Among the three sands, as can be seen in Figure 7.98, Argelia sand is the most stable one, which is believed to be associated to the higher roundness of its particles. Plus it was observed that both Coimbra sand and Mixture might only achieve full stability for very

high initial confining stresses, as stability was not ensured within the range of confining pressures applied on the performed triaxial tests.

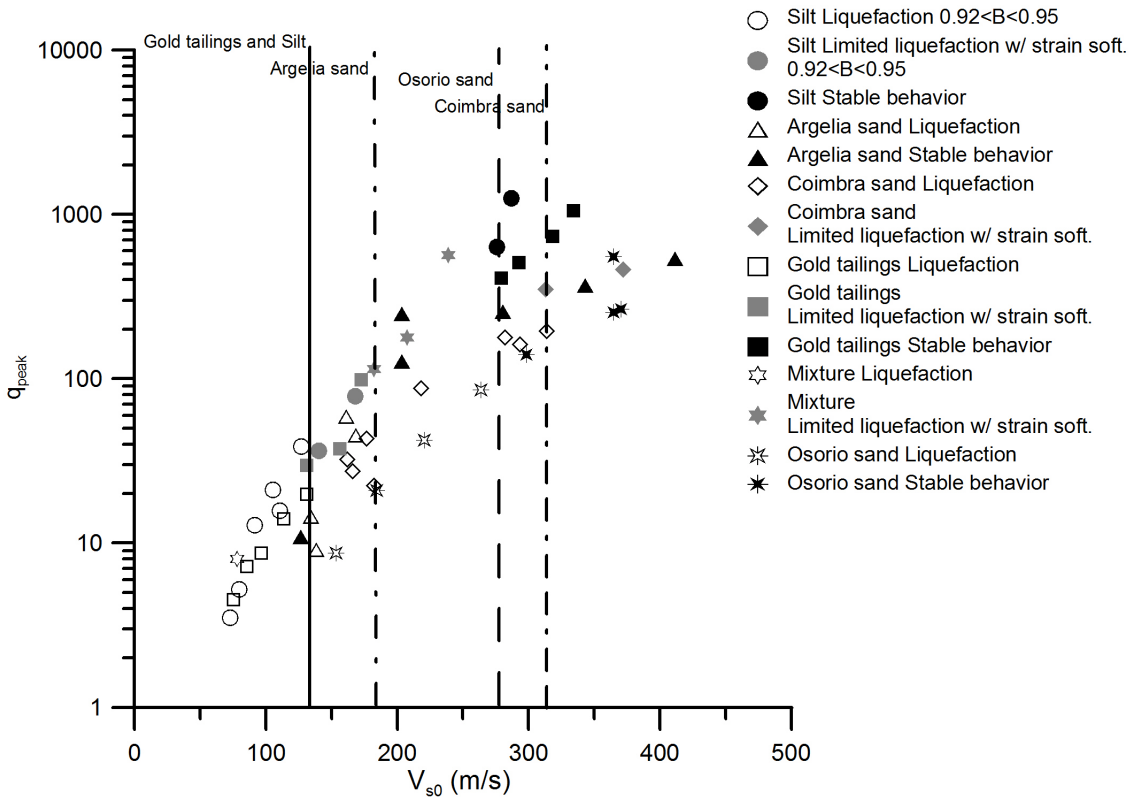


Figure 7.96: Peak shear strength as function of the soil stiffness

It is also necessary to point out that for a better comparison only the undrained isotropic triaxial compression tests were plotted. This allows for a better analysis as the only variable which distinguishes the distinct liquefaction potential is the soil by itself.

The overall conclusion which can be delineated is that, by analyzing Figure 7.97, excepting for Mixture and Coimbra sand, a stable behavior is guaranteed for ratios of V_{s0}/q_{peak} lower than 1. This does not mean that by knowing the initial stiffness of a soil, stability can be predicted. However peak shear strenght determined through in situ testing might be extrapolated to laboratory data.

Finally Figure 7.98 provides a framework to assess soil liquefaction potential, under monotonic compression loading conditions, based on the Andrus and Stokoe (1997) boundary, initially proposed for cyclic conditions. Although this chart was initially proposed for determining the cyclic resistance of sands with low fines contents, an analogy can be associated to the boundary separating liquefiable from non liquefiable tests, by zeroing the first term of equation (3.32), that represents a modified relationship between V_{s1} and CRR. It should be also pointed out that Andrus and Stokoe equation was not corrected for considering the fines content, instead it was decided to

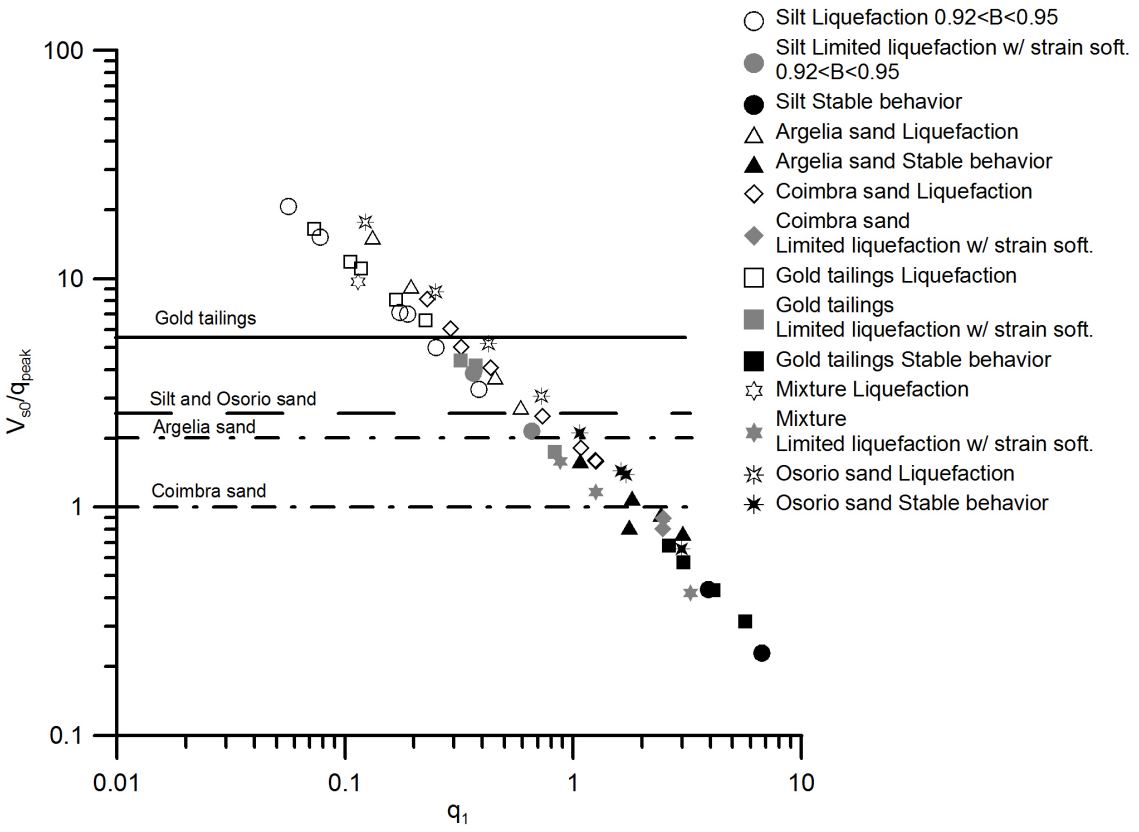


Figure 7.97: Correlation between the normalized peak shear strength and the ratio between shear stiffness and the peak shear strength

adjust both parameters b and V_{s1}^*. Therefore the main disadvantage of this framework is associated to the variability of both parameters b and V_{s1}^*, with the type of soil.

In order to surpass the dispersion of the limiting ratios with the type of soil a new framework was proposed. Aware that soil liquefaction is mainly a function of the soil compressibility, which is affected by the grain size distribution and by the shape of the grains, and a function of its unit volume weight, by eliminating the second variable (which would only differ for the Gold tailings), the limiting ratios were proposed to be a function of the coefficient of uniformity (Cu). In fact, despite not being associated to the shape of the grains, the coefficient of uniformity is directly related to soil compressibility.

Figure 7.99 displays a final framework which could be the novel mechanism to predict soil liquefaction potential for any type of soil.

While the limiting ratios of the sands and the Gold tailings were known, the limiting ratio for the Mixture was assumed to be 0.2, and the limiting ratio of the Silt was calculated basing on the shear wave velocities of the unsaturated specimens and on the peak strength exhibited by the saturated specimens, which was determined to be approximately 0.5.

Despite the previous comparisons were made basing on the boundary between liquefaction and

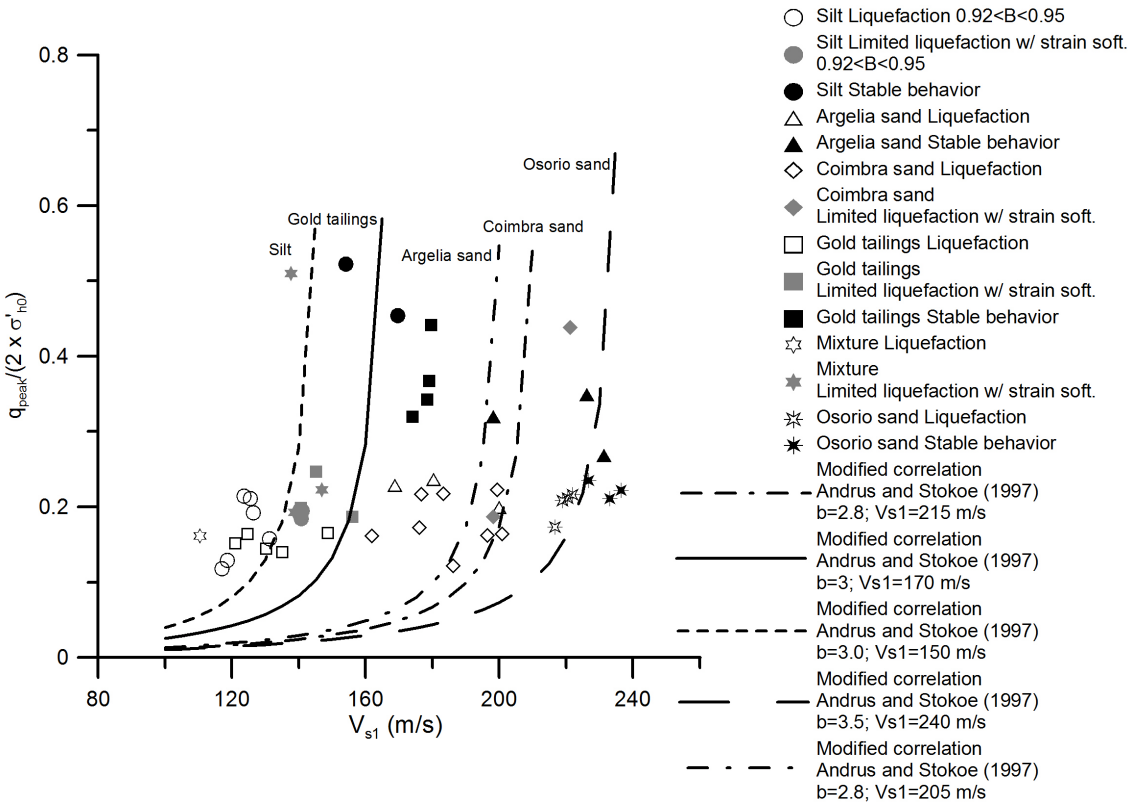


Figure 7.98: Simplified Procedure to evaluate static liquefaction

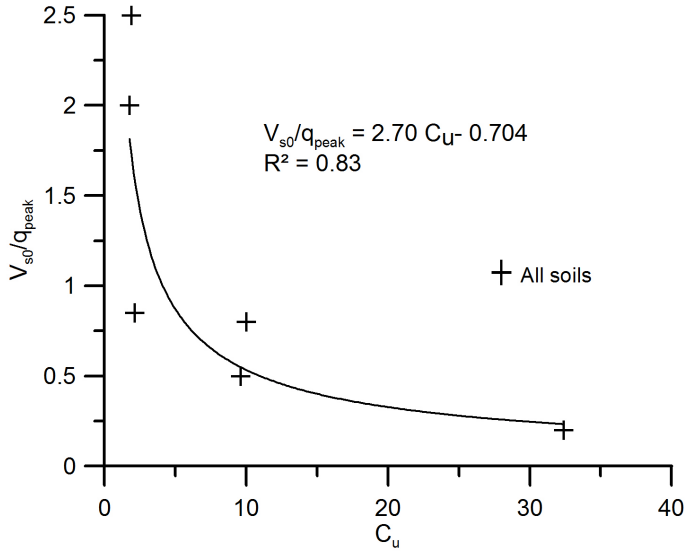


Figure 7.99: Correlation between the coefficient of uniformity and the ratio V_{s0}/q_{peak} which define the limiting boundary between a strain softening and strain hardening behavior

strain softening conditions, in order to compare all results the limit was considered to be located between the strain softening and the strain hardening behavior (as sands only exhibit liquefaction or strain hardening).

Chapter 8

Cyclic Liquefaction

8.1 Introduction

During this chapter cyclic liquefaction hazard is assessed for both Algeria and Coimbra sand. The two soils were studied on two distinct systems, cyclic Triaxial (Tx) and cyclic Direct Simple Shear (DSS) equipments. In these equipments the irregular cyclic earthquake loading (usually recorded in accelerographs, which give the acceleration histories with time) is simplified and simulated as a cyclic sinusoidal loading, reproduced with a pre-defined frequency of 0.1 Hz. Then this sinusoidal cyclic loading is converted to an equivalent field action index, the CRR (or CSR), according to the equation (3.42), proposed by Tokimatsu et al. (1991) . Hence soil liquefaction potential is evaluated by comparing it cyclic shear strength with the cyclic shear load, as previously explained in Chapters 3 and 4.

During this research, cyclic shear strength of both soils was fundamentally studied over specimens anisotropically consolidated (K_0 = 0.5), which corresponds mostly to natutal in situ confinement conditionsof recent sand deposits. Additionally, Algeria sand was also studied through the execution of isotropic cyclic Tx tests, in order to assess the influence of principal shear stress reversal.

In order to investigate the effect of principal stress rotation, both sands were also studied on a cyclic DSS device. The consequent comparison beteween the results of the Tx tests bases on the assumption of being a similar test of the undrained Simple Shear (SS) test. Similarities between constant volume cyclic DSS tests and cycli SS tests were demonstrated by some authors (Finn et al., 1978). However it is important to enhance that direct comparisons are very difficult to trace between both equipment, not being so commonly found in past literature.

Sandy soils are usually very susceptible to cyclic liquefaction hazard, and the study of both soils arose from two distinct reasons. While Algeria sand is being studied in the scope of the Bourmédes earthquake, being involved in well documented liquefaction events, the study of Coimbra sand

is mainly related to prediction purposes. As explained in Chapter 5, Coimbra was previously identified as a region with several alluvial sandy deposits susceptible to liquefaction. During this chapter both phenomena, flow liquefaction triggered under cyclic loading, and cyclic mobility are discussed and distinguished. A conclusive study is presented in order to understand the main factors involved in each one of the events.

8.2 Algeria Sand

8.2.1 Cyclic Triaxial Tests

A "universe" of 75 cyclic triaxial tests is presented in this sub-section. The cyclic Tx tests were performed over specimens of 70 mm diameter and 138 mm height, prepared by moist tamping. The large amount of tests resulted not only from the research developed during this PhD, but also includes a large group of 16 tests which begun with another doctorate study (Tahar Ghili, from USTHB in Alger) over Algeria sand, starting in 2003 and still under development. From the 75, 59 were performed over anisotropically consolidated specimens and the remaining 16 over isotropically consolidated specimens. Among the all cyclic Tx tests it was decided to exclude 7 tests which were considered outliers, as they had a clear different behavior, probably due to testing errors (including specimens'preparation). The tests excluded, which can be consulted in Table 6.11 and Table 6.12, were CTx_CK_0U_8, CTx_CK_0U_9, CTx_CK_0U_16, CTx_CK_0U_25, CTx_CK_0U_37, CTx_CK_0U_39 and CTx_CIU_10.

Four different mechanisms were detected in Algeria sand subjected to cyclic Tx tests. This study gives primacy to factors such as the initial relative density and/or void ratio, the initial confining stress and the initial static shear stress, i.e. induced anisotropy. Additionally the final results of this study are presented through frameworks correlating CSR with CRR, often expressed by stiffness or strength normalized parameters or indexes.

8.2.1.1 Cyclic Behavior of Algeria Sand

Four different mechanisms were detected while testing Algeria sand on a cyclic Tx device. As reported in Viana da Fonseca and Soares (2012) those are: deformation due to strain softening in compression with no shear stress reversal (Figure 8.1a), and with shear stress reversal (Figure 8.1b) - this being associated to the concept of flow liquefaction (when effective stress becomes zero - ru=100%); cyclic mobility with stress reversal (Figure 8.1d) and cyclic mobility without transient states of zero effective stress states (Figure 8.1c). Liquefaction associated to a complete loss of strength and/or to strain softening was only observed to occur on loose to medium-loose samples (Dr < 40%).

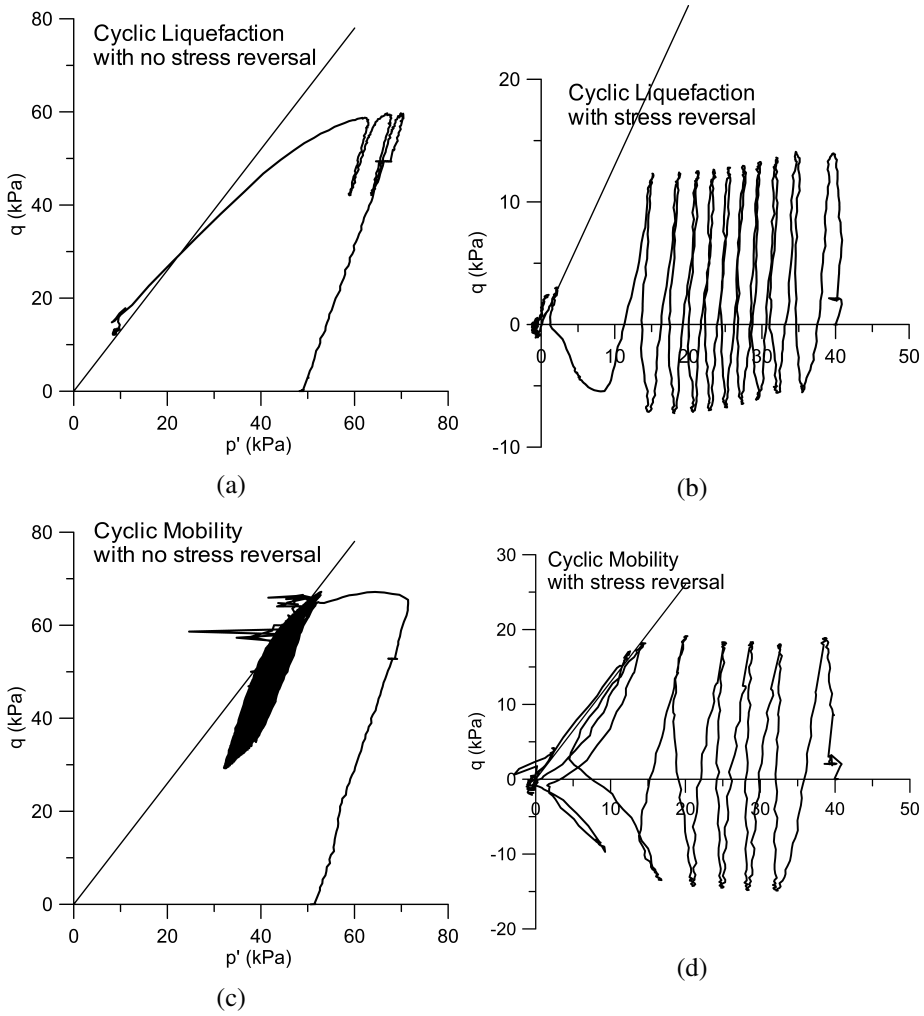


Figure 8.1: Flow liquefaction due to (a) contractive deformation in compression with no rotation of principal stresses and (b) with shear stress reversal; Cyclic mobility for (c) cyclic loading with no shear stress reversal, and d) with shear stress reversal (Viana da Fonseca and Soares, 2012)

Several features of the observed static and cyclic undrained behaviour were convergent on their fundaments, which corroborates previous observation reported by Vaid et al. (2001): *"at a given deformation in a given loading mode, the stress ratio at which strain-softening deformation is triggered in cyclic loading is essentially identical to that observed under static loading"*. Similar conclusions were also reported by Qadimi and Coop (2007). From Figure 8.1a and Figure 8.1b it can be observed that when liquefaction takes place, instability occurs, well below the failure envelope, and the soil exhibit a partial or complete loss of strength when it reaches the instability line, which is similar to what is observed under monotonic conditions.

8.2.1.2 Effect Of Relative Density On Liquefaction Resistance

Cyclic resistance curves are presented, for both isotropic and anisotropic consolidated specimens, in Figures 8.2 and 8.3. The results of both isotropic and anisotropic cyclic Tx tests prove that

cyclic resistance ratio increase with increasing relative density. This increasing resistance is more obvious for the anisotropic cyclic Tx tests, being fundamental on the separation between the two distinct soil behavior, flow liquefaction and cyclic mobility. While flow liquefaction is only observed for higher void ratios, cyclic mobility can only take place on relatively dense specimens. Therefore the phenomenon that controls the soil behavior is a matter of state condition. This succeeds for Dr values higher than 40%, liquefaction evolves from a strain softening mechanism to cyclic mobility, while dilatancy occurs.

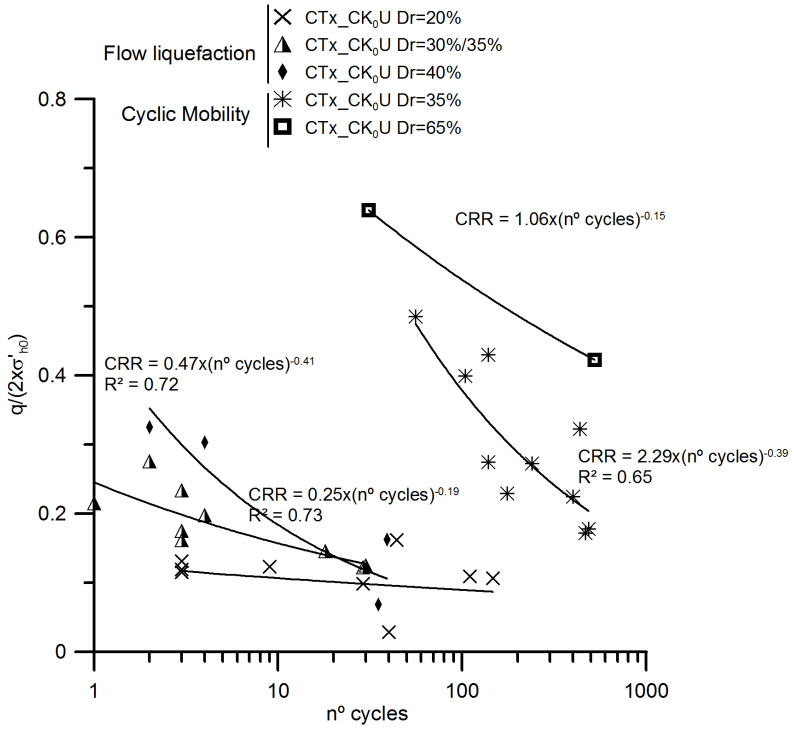


Figure 8.2: Cyclic resistance curves for Algeria sand under triaxial stress conditions for anisotropic specimens (with initial static shear stress, $\alpha = 0.33$)

It is also remarkable, how the relative density affects, in a much lower scale, the cyclic resistance of Algeria sand within each phenomenon, when compared to the differences of resistance between both phenomena. In fact, the jump of cyclic resistance, for the anisotropic consolidated specimens, between flow liquefaction and cyclic mobility can be as large as, for 15 cycles, 5 times higher (see Figure 8.2).

Furthermore it is observed that cyclic mobility only took place for a number of cycles higher than 30. This means, as it will be explained below more in detail, that for a number of cycles lower than 16, which correspond to an earthquake magnitude of 7.5, only flow liquefaction will take place, as the resistance mobilized for cyclic mobility to take place is extremely high (Figure 8.2).

As for the isotropic consolidated specimens the differences between both phenomena are not so evident, and it is possible for both flow liquefaction and cyclic mobility to take place (Figure 8.3).

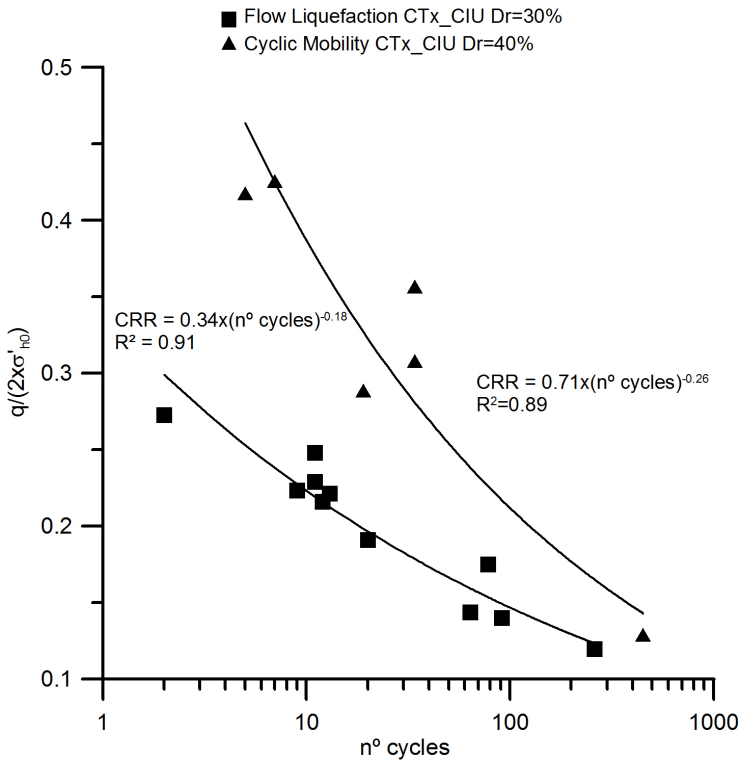


Figure 8.3: Cyclic resistance curves for Algeria sand under triaxial stress conditions for isotropic specimens (without initial static shear stress, $\alpha = 0$)

By comparing Figure 8.2 and Figure 8.3 it is also clear that the influence of the distinct factors is better assessed on the isotropic consolidated specimens, as a clearer pattern is exhibited.

The effect of the initial relative density can be also evaluated by correlating the cyclic shear strength with the relative density, for a precise number of cycles and initial confining stress. Figure 8.4 shows a data set chosen, for Algeria sand, to evaluate the effect of the initial relative density. Unfortunately due to the lack of points with the exact same number of cycles it was decided to display a unique graph, regardless the initial confining stress. The graph also shows that the initial relative density is a factor which can even surpass the effect of the initial confining stress.

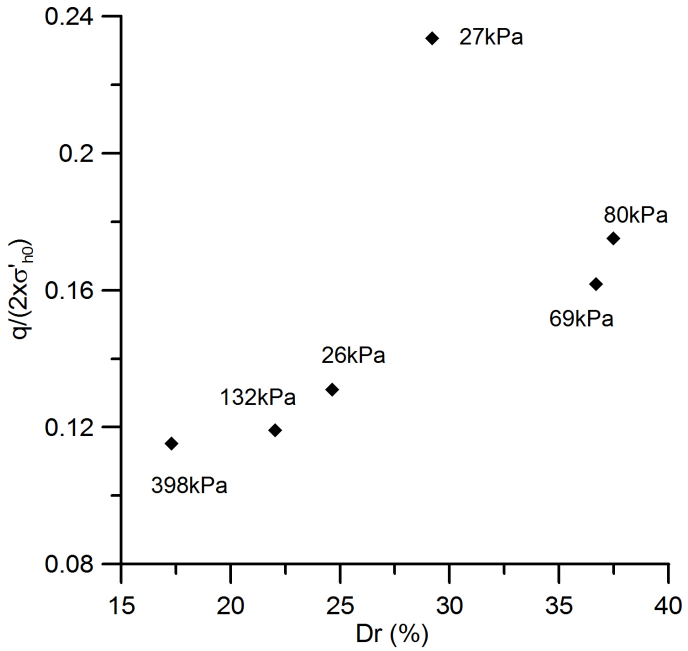


Figure 8.4: Liquefaction resistance of Algeria sand under triaxial stress conditions: effect of initial relative density for 3 cycles

8.2.1.3 Effect Of Initial Confining Stress On Cyclic Liquefaction Resistance

The effect of the initial confining stress on cyclic liquefaction resistance was a factor not much considered in the scope of this research. In fact most of the specimens were studied with very low confining pressures, between 20 and 60 kPa, in order to assess the liquefaction potential in the more superficial layers of soil, where liquefaction actually occurred during Bourmèdes earthquake (Ghili, 2003). Notwithstanding, aiming to understand the effect of the initial overburden stress, cyclic shear strength was also evaluated on specimens consolidated with 300, 600 and 800 kPa. As most of the tests liquefied for a distinct number of cycles it was decided to correlate the cyclic shear strength with the number of cycles, instead the initial confining stress. Furthermore it was also very difficult to perceive the influence of the initial confining stress as some tests liquefied for zero cycles and some of them had very high relative densities which could not be compared with the corresponding ones.

Each graph of Figure 8.5 was built for a sole same relative density, so that would be possible to compare tests. While Figure 8.5a shows the same undrained cyclic resistance regardless the initial confining stress, Figure 8.5b shows a slight increase of undrained cyclic resistance with decreasing initial confining stress. Such observation points out to the possibility of the initial confining stress having influence in specimens when they exhibit cyclic mobility, phenomena which have occurred in the set of tests displayed in Figure 8.5b. For the other set of tests, which liquefied or exhibited strain softening, the effect of the initial confining stress is not clear, thus no major conclusions were achieved.

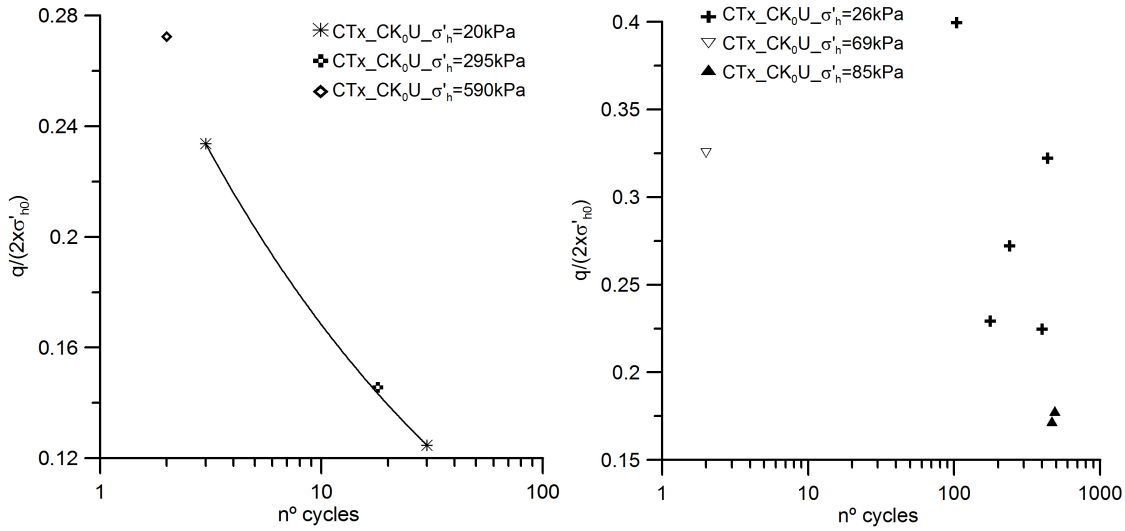


Figure 8.5: Liquefaction resistance of Algeria sand under triaxial stress conditions, effect of initial confining stress for relative densities of: a) 30%; b) 44%

As the initial confining stress seem to not affect significantly the undrained cyclic strength of Algeria sand, the graphs which are presented in the following sub-sections include all cyclic Tx tests, regardless the initial confining stress.

8.2.1.4 Effect Of Initial Static Shear On Cyclic Liquefaction Resistance

From Figures 8.6 and 8.7, and in particular from Figure 8.6 where cyclic resistance curves obtained for distinct relative densities are plotted against the number of cycles, it can be observed that anisotropic consolidated specimens (CK_0U) exhibit a higher undrained cyclic resistance than isotropic consolidated specimens (CIU) for relative densities higher than 35-40%. This increase in resistance with initial static shear, among the different stress conditions, occurs when cyclic mobility starts taking place. Thus, as can be seen, for Dr higher than approximately 40% the CRR increases with increasing initial static shear, while, for looser states, the resistance increases with decreasing α.

As highlighted by many researchers (Vaid et al., 1990; Yoshimine and Ishihara, 1998; Vaid and Sivathayalan, 2000), the range of void ratios over which contractive response manifests is much higher in extension than in compression mode. This fact explains the lower undrained cyclic strength of isotropic consolidated specimens, for relative densities higher than 40%. Similar responses were observed in monotonic and cyclic undrained tests, although some moderation has to be considered with respect to the similarity of such trends in monotonic and cyclic loading conditions.

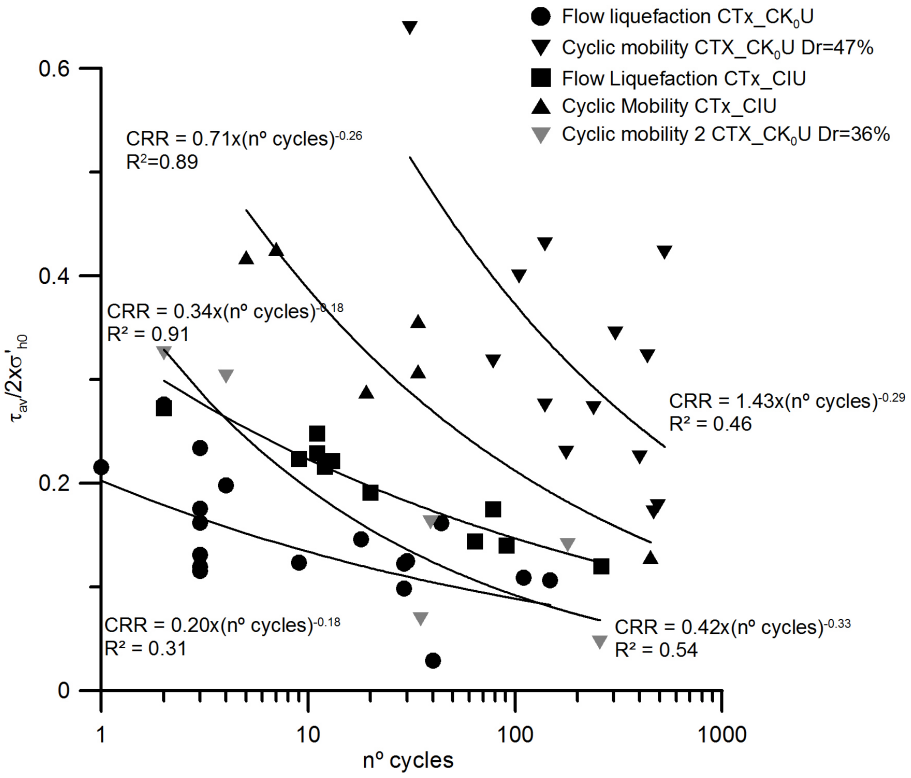


Figure 8.6: Cyclic resistance curves for Algeria sand under triaxial stress conditions for isotropic and anisotropic specimens (without initial static shear stress, $\alpha = 0$, and with initial static shear stress, $\alpha = 0.33$, respectively)

On the other hand, for relative densities lower than 35-40%, the overall dominant behaviour is flow or limited liquefaction. This explains the lower resistance exhibited by the anisotropically consolidated specimens. Vaid et al. (2001) also concluded, for Fraser River Sand, that cyclic resistance decreases with deviatoric stress if the mechanism of instability is flow liquefaction. Algeria and Fraser River sands seem to have the same behaviour, and both are in consonance with the results reported by Harder Jr and Boulanger (1997), where the contribution of initial static shear in cyclic resistance is positive for dense sand (Dr = 55%-70%) and negative for loose sand (Dr < 35%), while medium sand stands in between.

Figure 8.7 presents the CRR (or CSR) as function of the relative density. For a better interpretation of the cyclic Tx tests results, these were separated according to the type of consolidation, and according to the type of phenomena. Cyclic Tx specimens were deemed to have liquefied when a single amplitude shear strain exceeded 2.5% and/or the specimen reached a zero effective stress after 15 cycles, which represents an earthquake magnitude of 7.5 under the revised Idriss scaling factors (Idriss and Boulanger, 2004). Thus the line sketched in the Figure 8.7 is a boundary that separates the tests which liquefied or reached a 5% of total shear strain for less or equal than 15 cycles whilst specimens who required more than 15 cycles to achieve these conditions are considered to have not liquefied. To adapt the graph below to another earthquake magnitude Idriss scaling factors shall be applied.

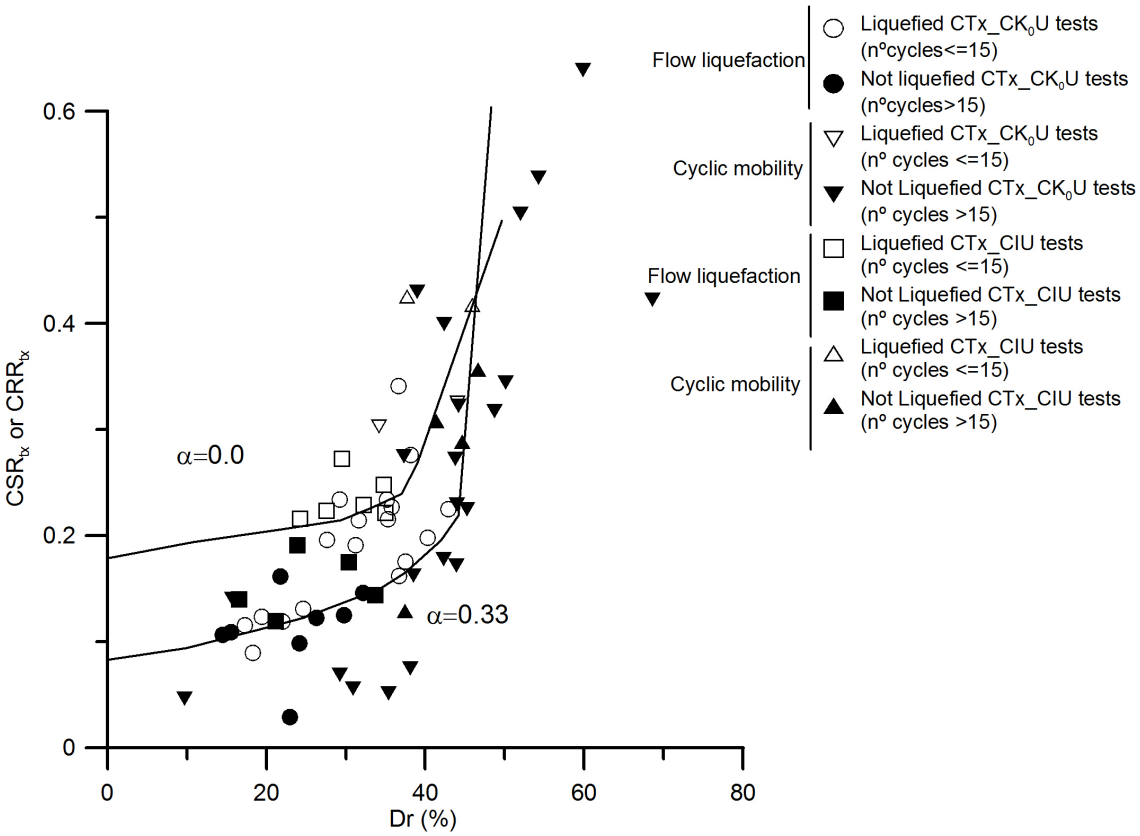


Figure 8.7: Cyclic stress ratio CSR, or Cyclic resistance ratio, CRR, versus relative density under triaxial stress conditions for Algeria Sand (Mw = 7.5)

As described previously the use of an earthquake magnitude correction factor, K_M, is a current practice of soil liquefaction evaluation and it allows establishing a boundary between cases with liquefaction from those with non-liquefaction evidences. Seed and Idriss (1982) firstly established K_M as an earthquake magnitude correction factor to a reference earthquake magnitude of 7.5. This resulted from the inability to define boundaries between liquefaction and non-liquefaction regions on CRR plots for magnitudes other than 7.5 (Youd et al., 2001). To analyze liquefaction potential of Algeria sand, a similar earthquake magnitude scaling factor was adopted for a better comprehensive analysis. This artifice not only allowed a reliable comparison of the undrained cyclic resistance of Algeria sand with previous works followed by other authors, such as Seed and Idriss, but also allowed a better comparison of the other CSR correction factors, k_σ, K_α, which take into account the overburden stress level and the pre-existing shear stress on a horizontal plane, as originally suggested by Seed (1983).

While for relative densities higher than 40% there is a clear tendency of increasing CRR with increasing Dr, for lower confining stresses this increasing CRR with increasing Dr is not so obvious. This clearness is associated to the flatten section of the boundary line which separates liquefaction from no liquefaction and associated to flow liquefaction. Similarly to monotonic Tx tests there is a delimiting region, on the e:p' space, which separates soils deeming or not to liquefy. This topic

is discussed further ahead.

Once having the results, obtained by both anisotropic and isotropic cyclic Tx tests, K_α might be obtained, as the quotient between $CRR_\alpha = 0$ (isotropic consolidated specimens, $K_0 = 1$) and $CRR_\alpha = 0.33$ (anisotropic consolidated specimens, K_0=0.5), being α the measure of the level of initial static shear stress, in order to converge the cyclic resistance curves. As most of the tests did not "liquefied" for an exact number of 15 cycles, it was decided to calculate CRR for 15 cycles basing on the curves plotted in Figure 8.2 and 8.3. Figure 8.8 display the K_α, determined for Algeria sand, plotted jointly with Seed and Harder (1990) and Vaid et al. (2001) data. Observing the graph, it is notorious the degree of conservatism between the calculated K_α and those proposed by Seed and Harder (1990). Also Vaid et al. (2001) highlighted that *"The degree of conservatism implied by the current empirical methods accounting for the effects of confining and static shear stresses on cyclic resistance seems too high, and is most pronounced for loose density states, most susceptible to liquefaction"*. Both Fraser River sand and Algeria sand seem to exhibit similar results for K_α, being less conservative for lower relative densities.

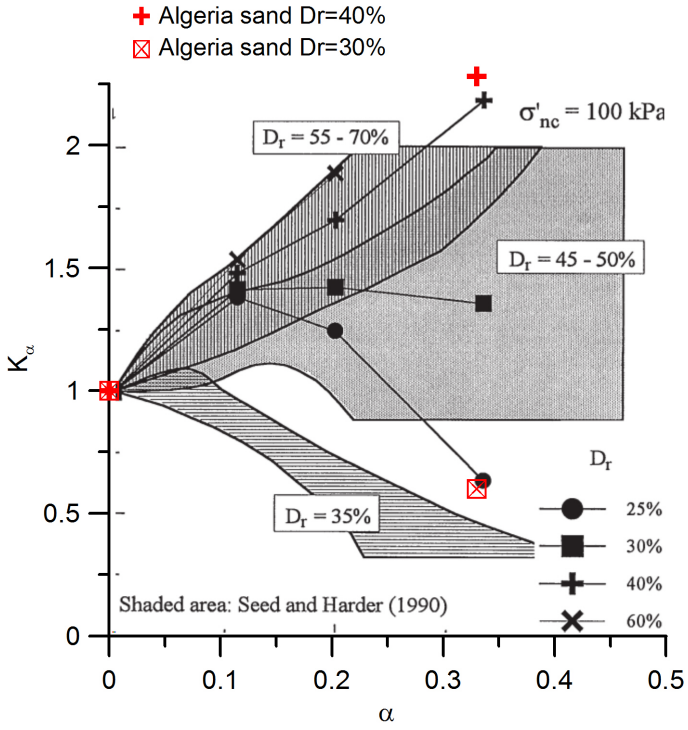


Figure 8.8: K_α versus α for Fraser River Sand at different density states at σ'_{nc} = 100 kPa (Vaid et al., 2001) complemented with results for Algerian Sand (Viana da Fonseca and Soares, 2012)

8.2.1.5 Undrained Cyclic Shear Strength Under Applied CSSM

For a clearer apprehension of the overriding cyclic behavior of Algeria sand, a comparison between those and the monotonic Tx tests was made by plotting the final results in the semi-logarithmic space e: log p' (Figure 8.9 and 8.10). All tests represented in both figures were plotted in their

final conditions, meaning after reaching 2.5% of single amplitude shear strain and or reaching a condition of zero effective stress. This means that in reality all the circles and squares liquefied, but while some took less than 16 cycles to total failure, the others needed more cycles to reach instability. On the other hand all triangles exceeded a single amplitude shear strain of 2.5% for less than 16 cycles above the lines and for more cycles below the lines.

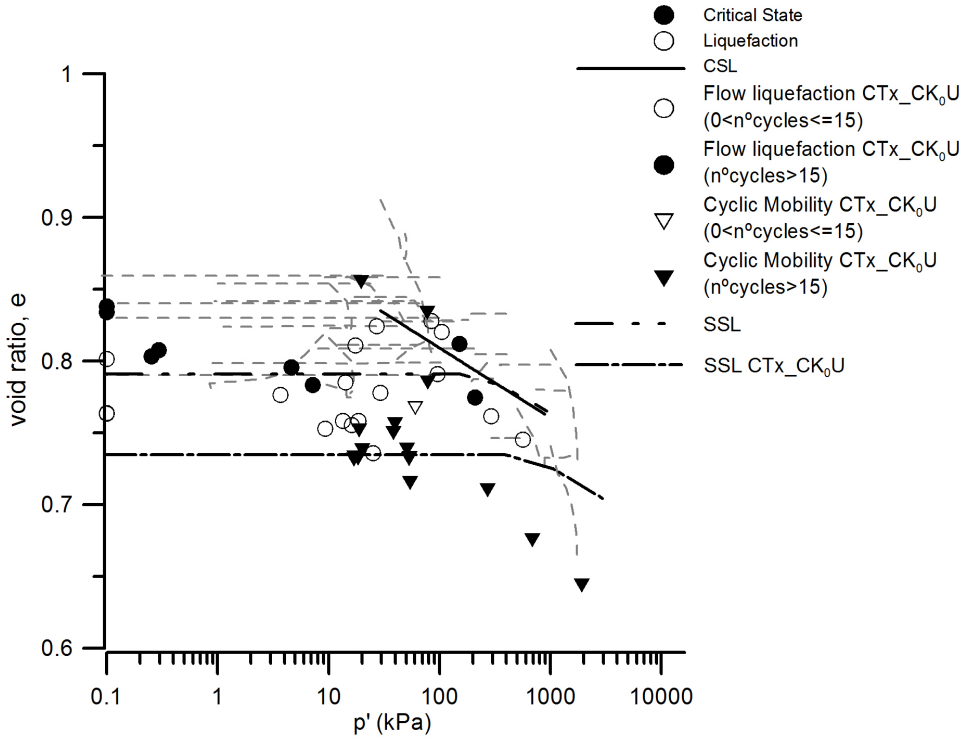


Figure 8.9: Anisotropic cyclic triaxial tests in the semi-logarithmic space e: log p' under applied CSSM

After the explanation above of what represents each set of plotted symbols it is now clear that in Figure 8.9 all circles represent tests which have liquefied (for less or more than 16 cycles), while the triangles are tests which have not exhibited any kind of instability. This means that SSL moves downwards significantly, in the semi-logarithmic space e: log p', when having by reference the SSL determined from the monotonic Tx tests results. Similarly, the isotropic Tx tests are more susceptible to liquefaction triggered under cyclic conditions, as the SSL also moves downwards (see Figure 8.10). Thus, in reality, this means that all tests, susceptible to flow liquefaction, are at the mercy of a binomial reasoning between the CSR and the number of cycles, for collapse triggering. The focus given to flow liquefaction is much higher, as it can be seen, at least for Algeria sand, for all tests above the traced lines in Figure 8.7, excepting 3 of the tests which collapsed under flow liquefaction. Thus cyclic mobility only affects a small amount of cases, as much larger CSR are required.

It is curious the down-grade suffered by what would be the SSL of the cyclic Tx tests. While

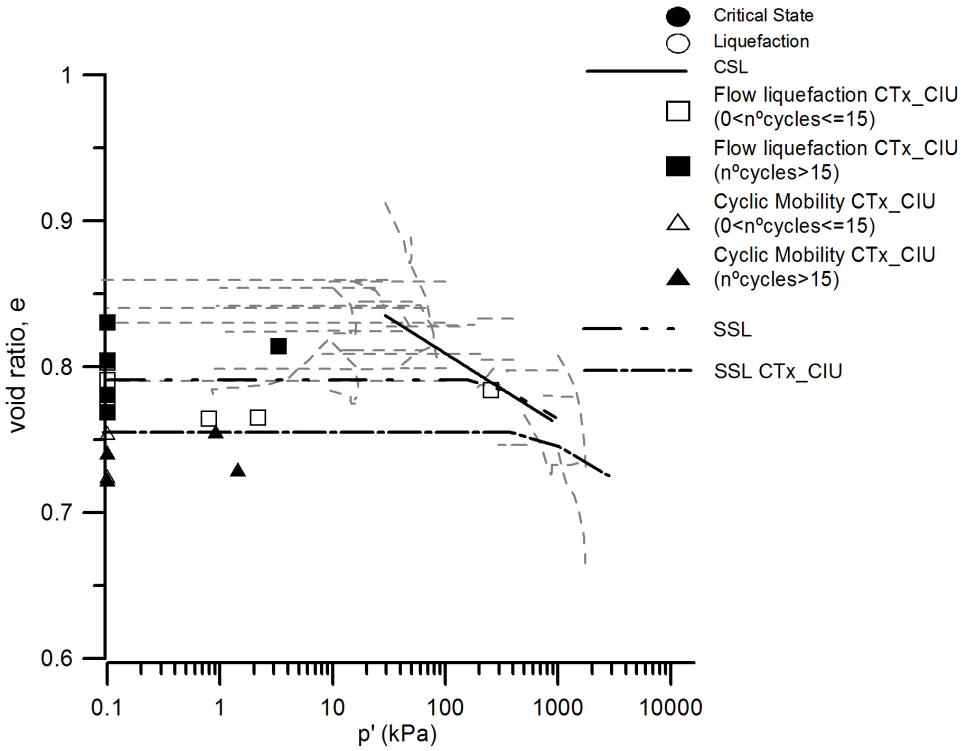


Figure 8.10: Isotropic cyclic triaxial tests in the semi-logarithmic space e: log p' under applied CSSM

it would be expected that isotropic cyclic Tx tests exhibit a lower strength when being subjected to extension, for the anisotropic ones this is kind of surprise. In fact the SSL obtained by the anisotropic Tx tests seemed to coincide with the one determined by isotropic Tx tests. Thus the reasoning behind can only be associated to the yielding surface rotation, which softens each time the specimens is unloaded. Thus for the yielding surface to shrink it is not only required for principal stress rotation to occur, but it can also takes place each time a stress rotation occurs.

8.2.1.6 Frameworks To Evaluate Algeria Cyclic Liquefaction Potential

- "Basic Berkeley Assessment chart"

  As reported before, the use of the ψ to evaluate soils shear strength is well supported on CSSM theory. The advantage of associating the CRR with the ψ, relies on the fact that both are function of density and the stress state, explaining the influence of the changing stress level for a constant void ratio. Thus when liquefaction potential is assessed through the state parameter, then no correction of the initial overburden stress is required (Jefferies and Been, 2006). Notwithstanding the use of such parameter is limited to the consideration of a unique CSL.

The State parameter, ψ, might be used to evaluate cyclic liquefaction for Algeria sand but is not considered to have a greater difference when compared to relative density, Dr. Algeria sand CSL positioning was determined in Chapter 7, jointly with SSL positioning. Basing on such facts, the use of ψ to predict cyclic liquefaction for Algeria sand is questioned. In order to understand which ψ is the most suitable, both graphs were plotted, by determining ψ with reference to the CSL and SSL, in Figures 8.11 and 8.12, respectively.

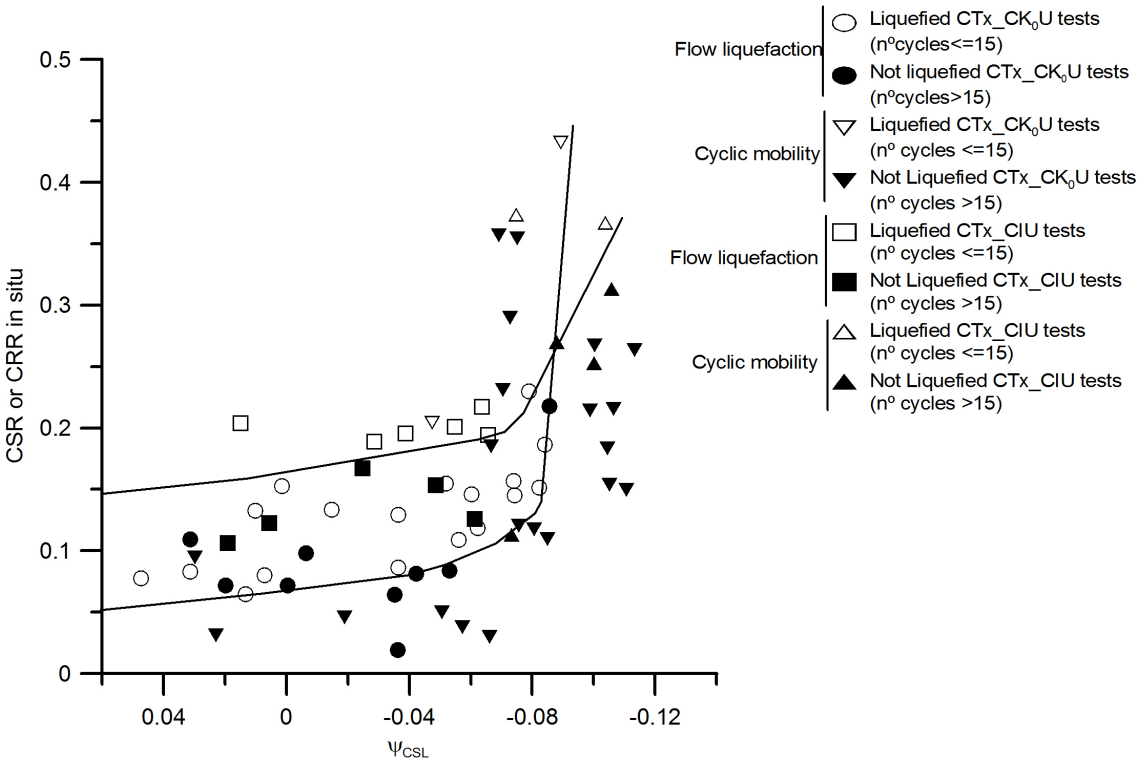


Figure 8.11: Basic Berkeley Assessment chart with reference to the CSL (Mw = 7.5); Liquefaction resistance of Algeria sand under triaxial stress conditions

Apparently both ψ_{CSL} and ψ_{SSL} seem to fit quite well, similarly to the correlation established between CRR and Dr (see Figure 8.7). Similarities between the three graphs are explained by two factors: the majority of the tests were initially confined with stresses lower than 100 kPa; the effect of the initial relative density, (i.e. void ratio), seem to surpass the effect of the initial confining stress. Therefore the differences between the isotropic and the anisotropic curves are exclusively associated with the effect of K_α.

From Figures 8.11 and 8.12, it is obvious that flow liquefaction, either by a complete loss of strength and/or strain softening, occur for ψ_{CSL} and ψ_{SSL} lower than -0.08. Thus flow liquefaction triggered by cyclic loading deems to occur below the SSL determined by the monotonic Tx tests. As explained before this is possibly associated to the stress rotation which occur during the loading and unloading stages.

It is important to highlight that the ψ_{SSL} should suit better as parameter to assess liquefaction

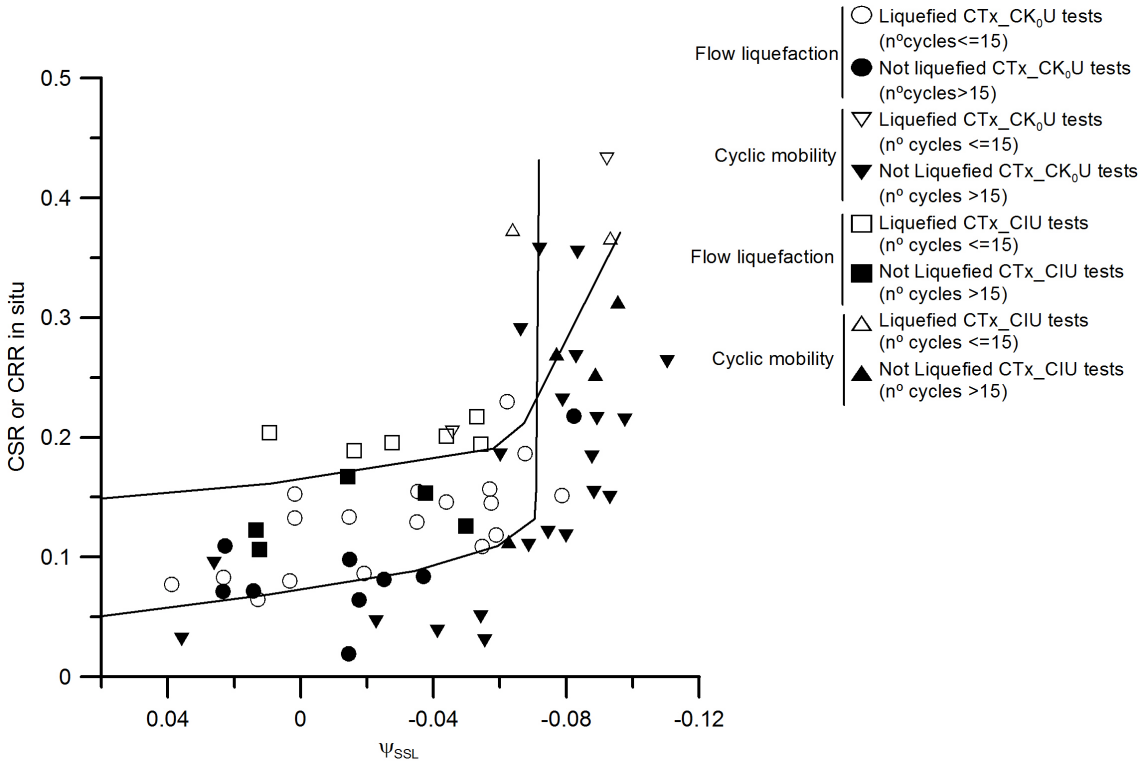


Figure 8.12: Basic Berkeley Assessment chart with reference to the SSL (Mw = 7.5); Liquefaction resistance of Algeria sand under triaxial stress conditions

resistance. This would be likely to occur as there is a limiting zone, on the e:log p' space, which separates two distinct zones, the one where soils are prone to flow liquefaction and the other, where soils will only suffer cyclic mobility. Nevertheless no major differences are observed between both parameters, ψ_{CSL} and ψ_{SSL}.

The results plotted in Figures 8.11 and 8.12 are not corrected taking into account the number of cycles for which they liquefy and the definition of CSR precedes the equation proposed by Tokimatsu et al. (1991) (i.e. $(CSR)_{tx=\sigma_{dc}/2\sigma'_{3c}}$) corrected with c_r, the correction factor between simple shear and Tx results, and 0.9 stands for the correction factor accounting for the earthquakes multidirectional shaking effect (Kramer, 1996). Thus liquefaction evaluation was made using CSRin situ.

- "Simplified Procedure", based on a stiffness parameter (G_0 – read V_s)

The "Simplified Procedure", initially proposed by Seed and Idriss (2004), later adapted by Andrus and Stokoe (1997), by evaluating the capacity of the soil to resist liquefaction through a stiffness parameter, i.e. shear wave velocity, was adapted for Algeria sand. As reported before the cyclic Tx device, available at LabGeo, is supplied with bender elements, allowing the measurement of shear wave velocities immediately before the shear stage. This data information allowed the construction of the Simplified Procedure for Algeria sand, making use of the limiting curve proposed by Andrus and Stokoe (1997), by adjusting the

curve parameters (see Figure 8.13). For Algeria sand the values of 0.01, 2.8 and 220 m/s were adopted for the parameters a, b and V_{s1}^{*} of equation (3.32).

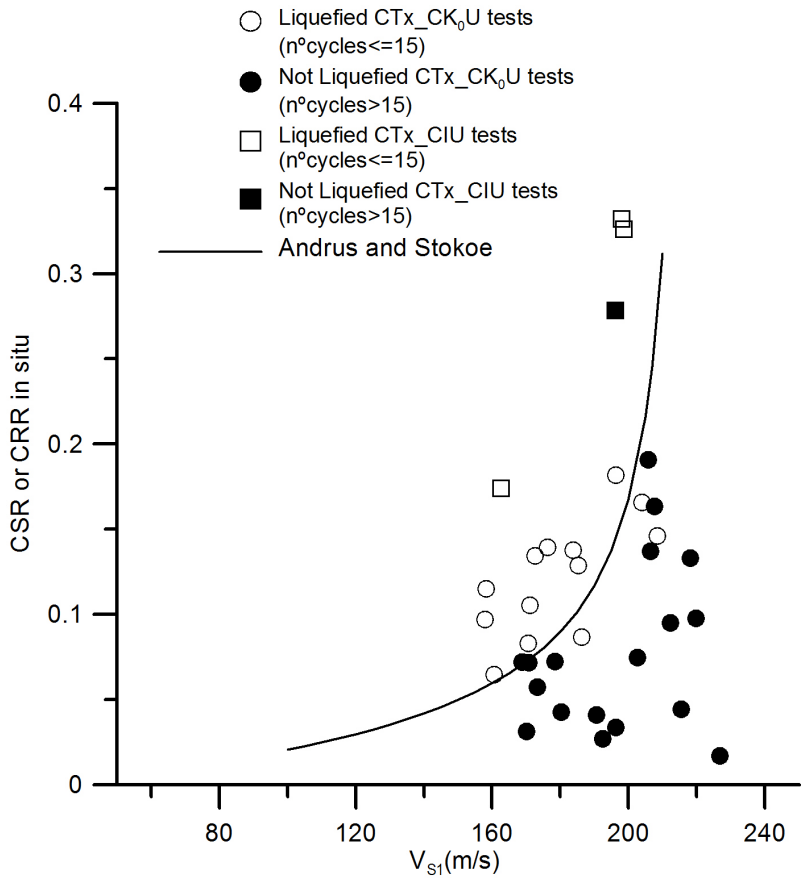


Figure 8.13: "Simplified Procedure" of Algeria sand under triaxial stress conditions

Figure 8.13 shows a quite good suitability of the limiting curve, proposed by Andrus and Stokoe (1997), to separate the tests which liquefied, i.e., which required less than 15 cycles to liquefy, from those which did not liquefied, i.e. required more than 15 cycles to liquefy.

Despite being visible the manifest aptitude of stiffness parameters to predict soil capacity to resist liquefaction, objections to it applicability are very common. One of the objections relies on the fact of the boundary curve being a unique function of the fines content. Regardless a and b parameters are function of the soil, which can be calibrated and inherently consider inherent anisotropy among other factors, etc. However it applicability is also highly contested as this framework correlates the CRR, a parameter associated to high strains, i.e. to plastic strains, with V_s, a parameter associated to low strains, i.e. to elastic strains (Youd et al., 2001). Nevertheless, as quoted previously, while working under undrained conditions the assumption is valid as the volumetric strain is zero, thus $\varepsilon_v = 0 \Leftrightarrow \varepsilon_e = -\varepsilon_p$, which led, as stated by Roy (2005) to predictable benefitting. Furthermore V_s waves were found to be a function of the accumulated dissipated energy (W), i.e. shear work, determined according to equation (3.56), during the undrained cyclic shear of each test (see Figure 8.14).

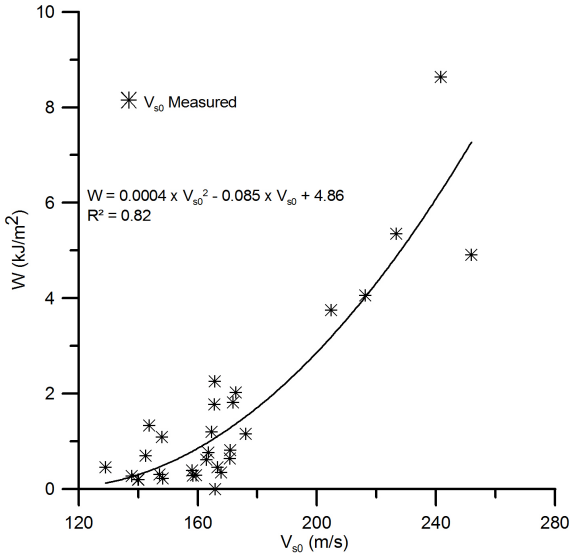


Figure 8.14: Shear work (W) as function of shear wave velocity for Algeria sand

Figure 8.14 displays a strong correlation between a parameter which measures the work required for a certain plastic strain to be achieved with the initial stiffness of the soil. This correlation fundaments and supports the use of the Simplified Procedure to ascertain soil capacity to resist liquefaction.

As shear wave velocities were only measured for 34 cyclic Tx tests V_s waves were unsuccessfully tried to be predicted by using Hardin and Drnevich (1972) popular expressions used to quantify G_0. Distinct F(e) equations proposed by Hardin and Richard (1963), Hardin (1978), Kokusho (1980) and Lo Presti (1995) were used to determine G_0 seeking the most suitable trend, by comparison with the real data. The values of the constant parameters S_{ij}, n_i and n_j of equation (3.40) were previously determined through the cyclic Tx tests. Figure 8.15 shows the overall ability of the empirical equations to predict G_0 of the cyclic Tx tests, by it comparison with the real measured values of G_0.

It is obvious, after analyzing Figure 8.15, that despite capturing the mean value of G_0, the empirical equations are not able to capture the real G_0 due to it dispersion. Aiming to understand the lack of precision behind the empirical equations, it was found that either the F(e) is not suitable or the exponent, n, which translates the type of contact between grains, is not a constant parameter, rather possibly a function of the void ratio and/or induced anisotropy. In fact, with increasing e_0 and σ'_{v0} higher the contact between grains, which might influence the type of contact, translated by the n parameter. Basing on this presupposition V_s waves were not calculated for the remaining tests as it was concluded not being able to accuratly predict the capacity of the soil to resist liquefaction.

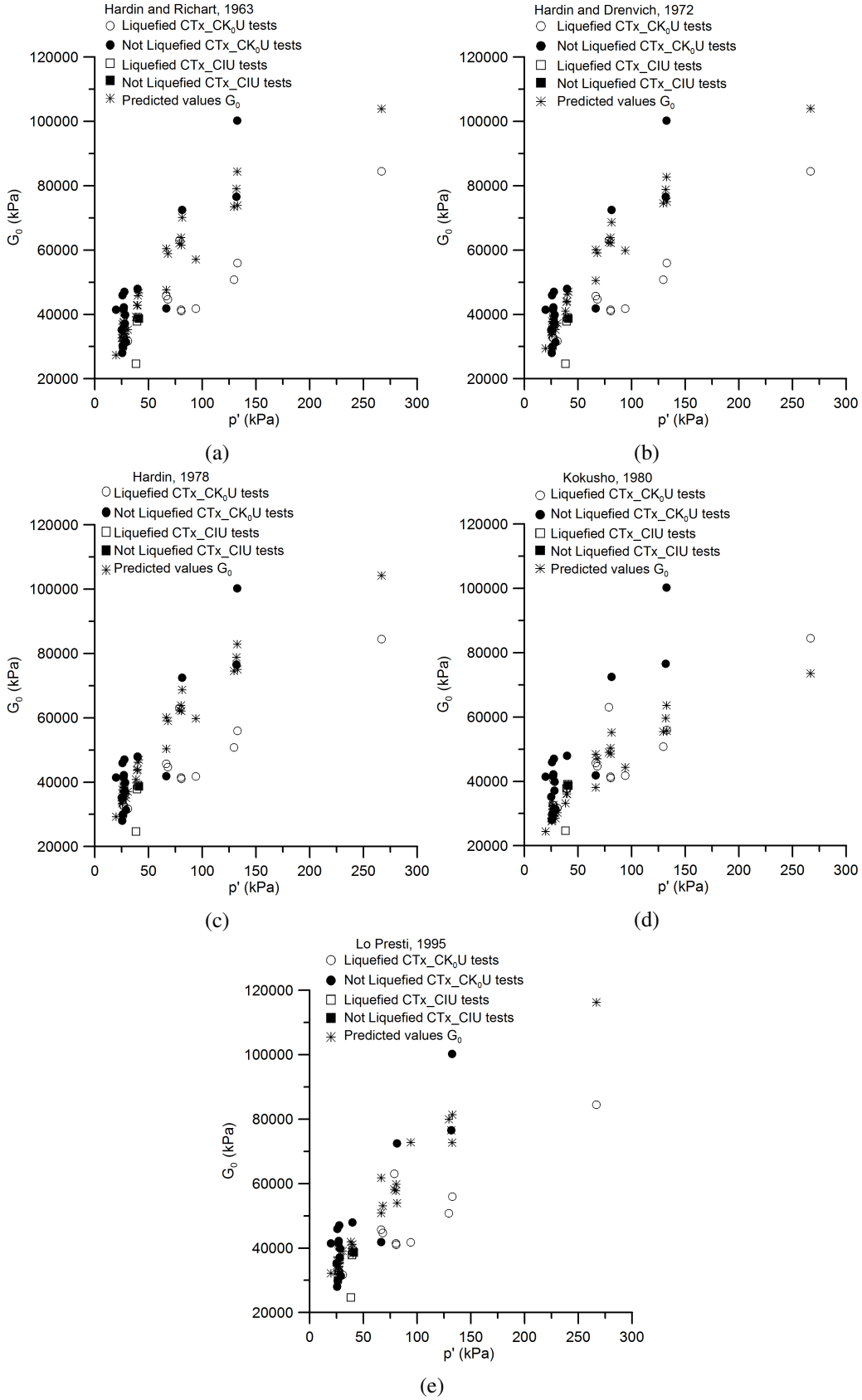


Figure 8.15: Comparison between the measured G_0, for Algeria sand, and the predicted G_0 by using the empirical equations proposed by: a) Hardin and Richard (1963); b) Hardin and Drnevich (1972); c) Hardin (1978); d) Kokusho (1980) and d) Lo Presti (1995)

8.2.2 Cyclic DSS Tests

In the scope of evaluating the effect of principal stress rotation, liquefaction susceptibility of Algeria sand was assessed through the performance of a large set of cyclic DSS tests. Several conditions of density, with initial confining stresses of 100 and 300 kPa, were evaluated.

The study involved the performance of 40 DSS tests over specimens of 72 mm diameter and 38 mm height, prepared by moist tamping.

It is important to highlight, once more, that the tests are not conventionally undrained, since there is no monitoring of pore pressures, instead DSS are constant volume tests. As discussed by Reyno et al. (2005), this is an equivalent condition in the simple shear apparatus.

The same target void ratio at three different degrees of compactness (loose, medium, dense) was pursued for all specimens; however, due to differences in the initial measurements and subsequent volume variations during consolidation, this was not totally guaranteed.

8.2.2.1 Effect Of Relative Density On Liquefaction Resistance

During this study it was observed that, like in cyclic Tx tests, Algeria sand exhibit a higher cyclic resistance at higher relative densities for all confining stresses tested. The rate of increase in cyclic resistance with relative density seems to be higher for low confining stresses, as the distance between the resistance curves increases with increasing vertical confining stress (see Figure 8.16 and 8.17).

Unlike cyclic Tx tests, as IL seems to have no influence, or at least its influence is not visible, the results achieved with the cyclic DSS device allowed grouping the tests according to the number of cycles. This was not possible for cyclic Tx tests, as the minimum variation of cycles could greatly affect the soil response, mainly within the transitory range of void ratios where the phenomena which controls the soil behavior might change (from flow liquefaction to cyclic mobility). Thus Figure 8.16 suggests this grouping to better assess relative density effect on the soil undrained cyclic strength.

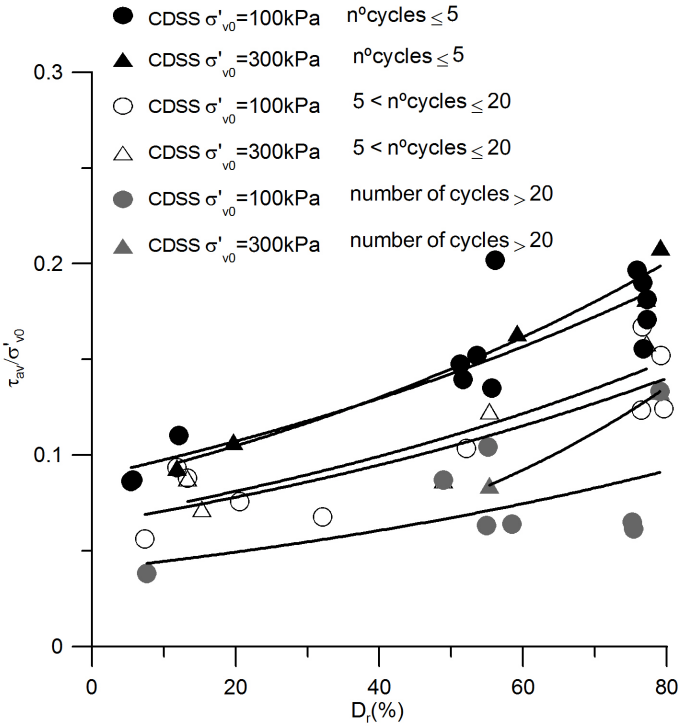


Figure 8.16: Dependence of cyclic resistance on relative density for 100 and 300 kPa of confining stress for Algeria sand under direct simple shear stress conditions

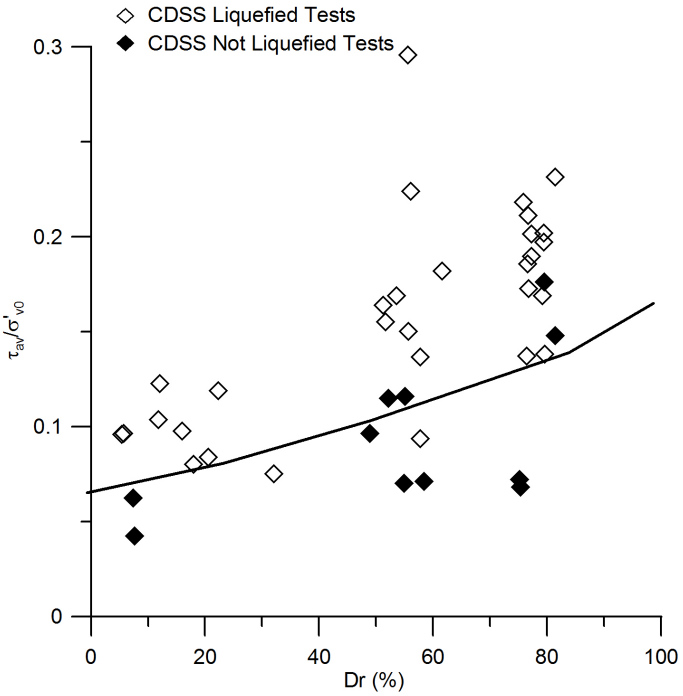


Figure 8.17: Cyclic stress ratio CSR, or Cyclic resistance ratio, CRR, versus relative density for Algeria Sand under direct simple shear stress conditions (Mw = 7.5)

8.2.2.2 Effect Of Vertical Confining Stress On Liquefaction Resistance

During this study it was observed that Algeria sand exhibit, unlike most cyclic responses observed by other authors in others sands, a less contractive tendency due to stress densification which surpasses the contractive tendency due to the increase in confining stress. Figures 8.16 to 8.18 show that Algeria sand exhibits, with increasing relative density, an increasing cyclic resistance for higher confining stresses. Figure 8.16 which correlate the CRR with the relative density (after consolidation), allow a better comparison, as the cyclic curves are located above the line for higher confining stresses, proving that for the same void ratio, soil specimens have higher cyclic resistance for higher initial confining stresses.

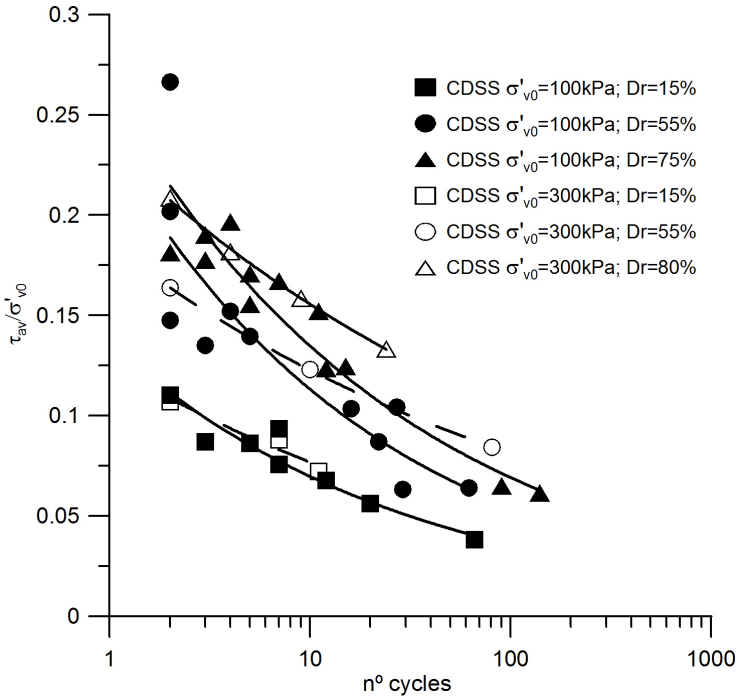


Figure 8.18: Cyclic resistance curves for Algeria sand under direct simple shear stress conditions (without initial static shear stress, $\alpha = 0$)

As explained before separation according to the number of cycles was required, as few tests have exactly the same number of cycles to trigger liquefaction.

Data for stress-strain, stress-path and excess pressure, with and without normalization, was plotted for tests with similar void ratios and number of cycles to liquefaction. Figures 8.19 corroborate what was previously concluded from Figures 8.16 and 8.18. For an almost identical initial void ratio, tests with a higher confining stress seem to be less contractive, since the normalized excess pressure is slightly higher for lower confining stresses. The relative density differences of $2 \sim 3\%$ found between the compared tests are not sufficient to explain the differences observed.

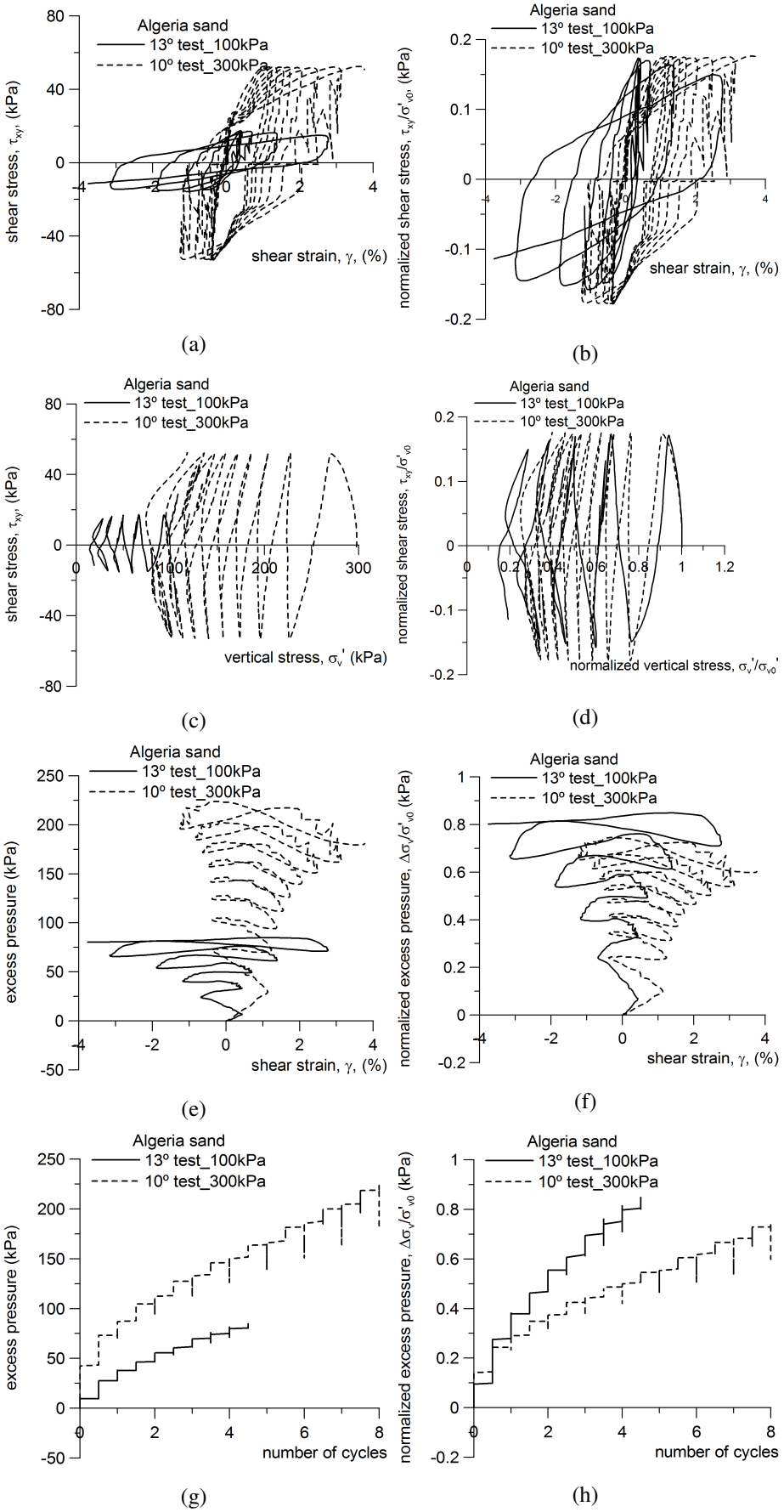


Figure 8.19: Stress-strain, stress-path, and excess pore pressure with and without normalization, from left to right respectively, for 13º test_100k Pa and 10º test_300 kPa for Algeria sand

Figures 8.19 display data for stress-strain (Figures 8.19a and 8.19b), stress-path (Figures 8.19c and 8.19d)and excess pressure (Figures 8.19e, 8.19f, 8.19g and 8.19h), with and without normalization (from left to right respectively), for two tests with similar void ratios and number of cycles to liquefaction. According to these Figures 8.19 for an almost identical initial void ratio, tests with a higher confining stress seem to be less contractive, since the normalized excess pressure is slightly higher for lower confining stresses, being most obvious in Figure 8.19h.

As these findings are not consistent with the frameworks which correct the effect of the initial confining stress, K_σ, assuming a higher contractiveness for higher confining stresses, for a same void ratio, it is postulated the existence of a second order factor that conditions this behaviour, namely rearrangement of the soils due to principal stress rotation during shearing in the simple shear apparatus.

The implication of these findings is that the K_σ values proposed by Hynes and Olsen (1999), and even those proposed more recently by Idriss and Boulanger (2004), underestimate the cyclic resistance for Algeria sand when principal stress rotation occurs (Figure 8.20). According to such findings, three hypotheses are postulated, the last one being a combination of the first two.

1st Hypothesis

Wijewickreme et al. (2005) reported an increasing CRR for loose Fraser River sand with increasing initial vertical confining stress, for specimens formed with the same energy. Despite not having exactly the same relative density, the small change in relative density that occurs when the confining stress is increased is unlikely to offset the large decrease in CRR resulting from the application of the existing correction factors, such as those in Figure 8.20. The observed behaviour was explained by the authors as a densification effect created by the sample reconstitution method. As stated by Wijewickreme et al. (2005) *"for the air-pluviated sand the gain in CRR due to stress densification exceeds the potential reduction in CRR arising from increased* $\sigma_v^{'}$*"*. Additionally, Al-Tarhouni et al. (2011) found, while studying the behavior of gold tailings, that regardless of the initial confining stress, the same number of cycles was required to induce liquefaction, for a given void ratio. Following the same assumptions, Algeria sand sample reconstitution method might have induced a densification effect which surpasses the potential reduction in CRR due to increasing $\sigma_v^{'}$.

2nd Hypothesis

It is speculated that the framework proposed by Hynes and Olsen (1999), and strongly supported by many other authors, might not be suitable for all possible stress paths. Therefore, and at least for these materials, it is believed that the increasing CRR with increasing confining stress, for the same void ratio, is related to the fact that principal stress rotations can move the stress point further inside the pre-yield zone, with yielding being only triggered on the opposite side of the yield surface (as referred from Jefferies and Been (2006)). As "*the yield surface reflects the mobilization of particle contacts at a micromechanical level*" and a "*fabric evolution during cycles*" might occur

(DeGennaro et al., 2004; Papadimitriou and Bouckovalas, 2002), it is suggested that a constant shrinkage and dilation of the yield surface dominates the cyclic undrained behavior, over any other factor. As both fabric evolution and particle contacts differ from soil to soil, due to differing grain shape and roughness, it is likely that different soils may have distinct undrained cyclic shear responses.

It should also be pointed out that for Algeria sand, cyclic resistance curves are approximately parallel to one another when varying the relative density for the same confining stress (Figure 8.18). The physical meaning of this behaviour may be associated with the intrinsic anisotropy (fabric) induced by moist tamping preparation. Plus, for Algeria sand, for the number of cycles less than 3, the resistance is higher for lower confining stresses, similar to other soils in the cited references. From these observations it can be speculated that fabric anisotropy changes with plastic strain accumulation during the test.

3rd Hypothesis

The last postulation considers K_σ unsuitability to quantify both aspects previously referred. Therefore, both factors - the adopted reconstitution technique and the test conditions, with or without principal stress rotation - will be highly controlling the yield surfaces and flow plastic rules. Therefore these aspects may jointly surpass the effect of the initial confining stress. The difference pattern of particle rearrangement induced by these two factors will be decisive in the consideration of confining stress factor in liquefaction assessment.

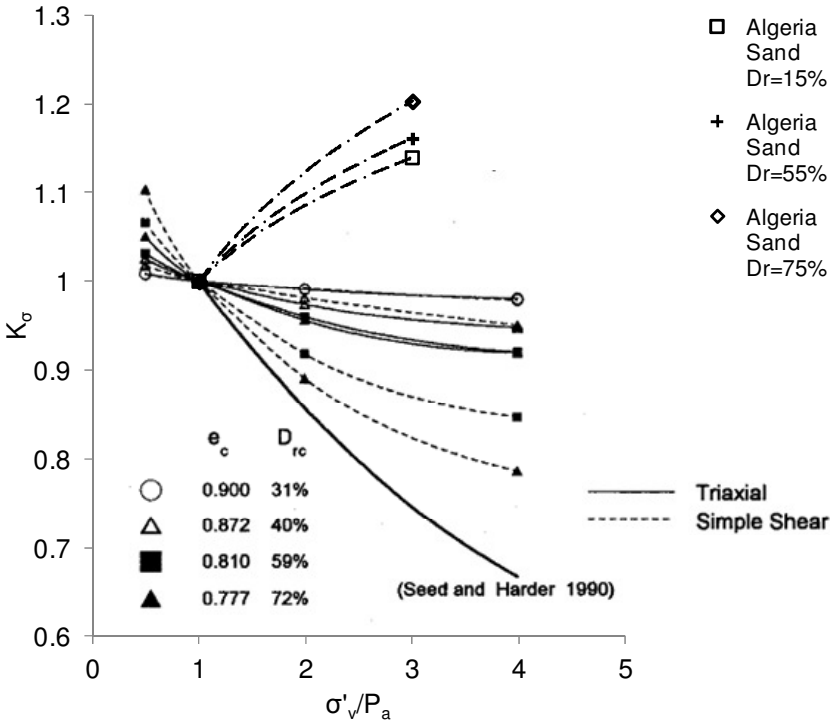


Figure 8.20: K_σ values for Fraser Delta sand and Algeria under direct simple shear and triaxial stress conditions (adapted from Vaid and Sivathayalan (1998))

8.2.2.3 Frameworks To Evaluate Algeria Cyclic Liquefaction Potential

- "Basic Berkeley Assessment chart"

To assess liquefaction potential of Algeria sand under direct simple shear stress conditions is presented the "Basic Berkeley Assessment chart" in Figure 8.21. Similarly to the Tx tests it was opted to use the steady state parameter as a reference parameter.

The existence of a boundary, separating the tests which liquefied for more or less than 16 cycles, is evident by observing Figure 8.21. Nevertheless this figure displays a lot of similarities with Figure 8.17, which correlates the liquefaction resistance of Algeria sand with the relative density Dr. Just like what happened under Tx stress conditions, the use of the state parameter is only justified when the initial confining stress has a clear effect on the liquefaction resistance. Beyond this contribution seeming to be irrelevant under direct simple shear conditions, it was also observed an increasing liquefaction resistance with increasing initial confining stress. Therefore the use of state parameter is avertable to assess cyclic liquefaction resistance of Algeria sand under cyclic DSS conditions.

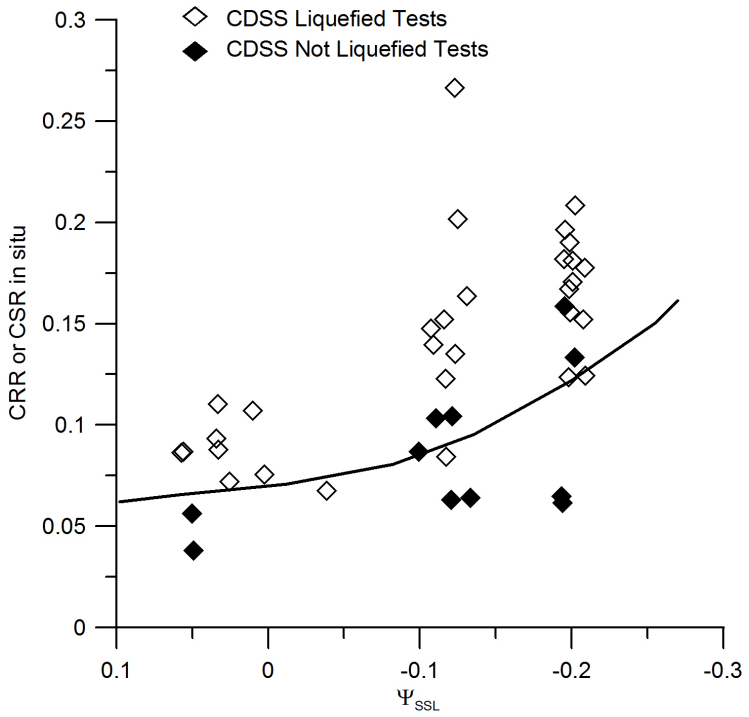


Figure 8.21: Basic Berkeley Assessment chart with reference to the CSL (Mw = 7.5); Liquefaction resistance of Algeria sand under direct simple shear stress conditions

8.2.3 Comparison Of Liquefaction Resistance Of Algeria Sand Under Simple Shear And Triaxial Stress Conditions

The differences of the undrained cyclic resistance between Tx and DSS tests are remarkable (Figure 8.22 and Figure 8.23). Despite both curves not being corrected to take into account the effect of the initial confining stress and pre-existing shear stress on a horizontal plane, it is now clear that cyclic resistance drops due to principal stress rotation. Despite the distinct overburden stresses the differences in CRR values between these different equipments/conditions, as can be seen in Figure 8.23, are too large to be assigned exclusively to the stress factor (K_σ). Plus Figure 8.22 shows that with increasing relative density, this difference in cyclic resistance becomes more pronounced.

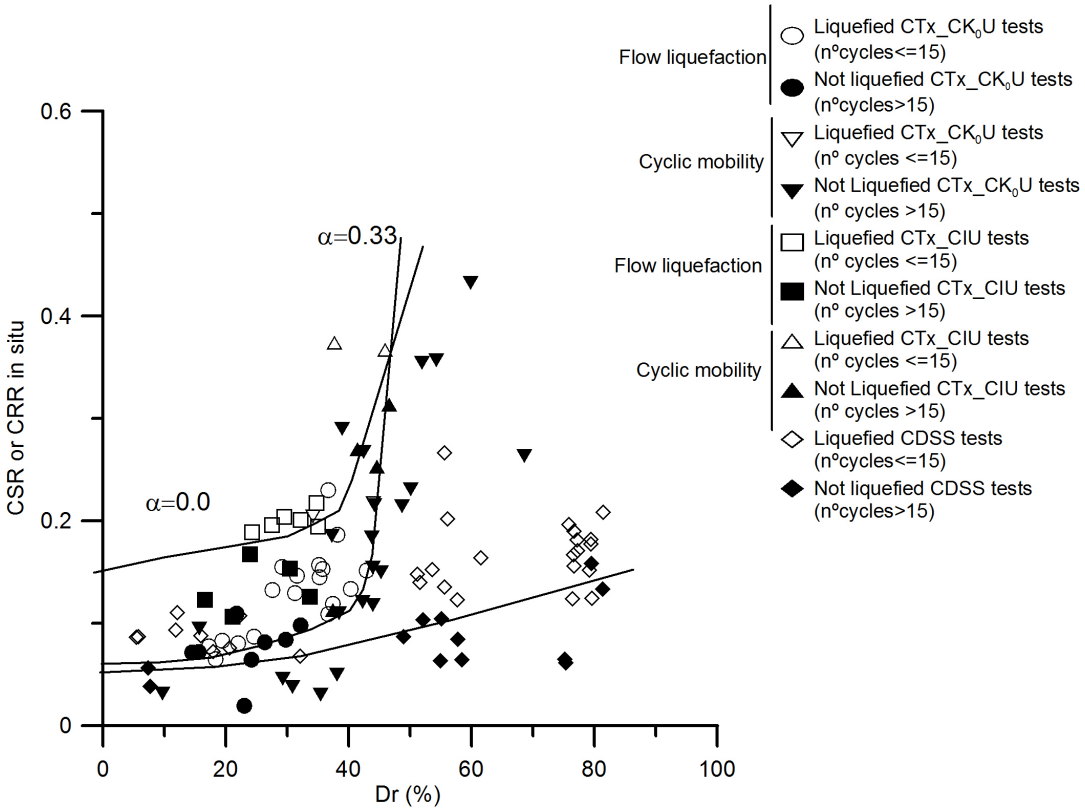


Figure 8.22: Cyclic stress ratio CSR, or Cyclic resistance ratio, CRR, versus relative density for Algeria Sand under both triaxial and direct simple shear stress conditions (Mw = 7.5)

Furthermore under cyclic stress rotation conditions it was observed an increasing liquefaction resistance with increasing initial confining stress, for a same initial density condition. Therefore, it is concluded that this change on behaviour is mostly associated to the influence of fabric, as a result of a mechanical answer to cyclic stress rotation, which surpass the effect of the initial confining stress or to a fabric evolution during the accumulation of plastic strain. This is likely to occur as by comparing the monotonic shear strength achieved by both devices they exhibit a similar brittleness (Figure 8.24).

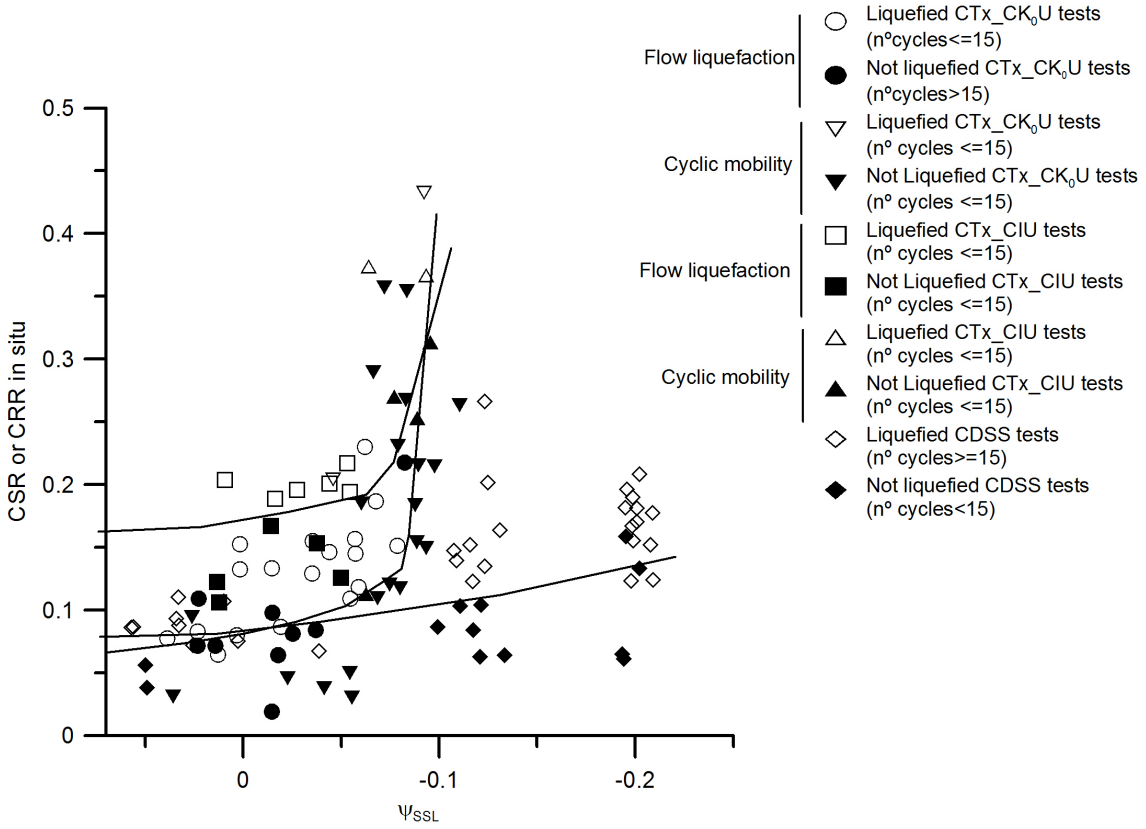


Figure 8.23: Basic Berkeley Assessment chart with reference to the SSL (Mw=7.5); Liquefaction resistance of Algeria sand under both triaxial and direct simple shear stress conditions

As indicated by Sivathayalan and Ha (2011), K_α should not be based exclusively on relative density of the sand, but on the anticipated deformation characteristics (strain softening vs strain hardening), as this direct association is not able to predict properly the changes on soil cyclic mechanical behaviour. According to these authors K_α should also take into account for inherent anisotropy.

Furthermore when comparing both cyclic Tx and DSS tests results the nonlinearity of the differences are notorious. This nonlinearity is reflected by an increasing difference with increasing relative density due to the very distinct phenomena which control the soil behaviour. While studying Fraser Delta sand Vaid and Sivathayalan (1996) also found the reduction factor c_r, used to correct Tx cyclic resistance to an equivalent simple shear, not being just a function of K_0 but also of both initial relative density and initial confining stress.

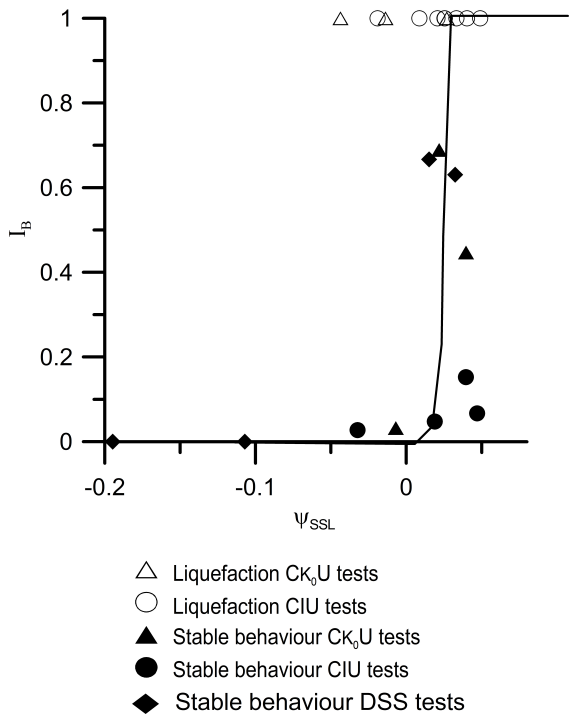


Figure 8.24: Variations of the Brittleness Index with the steady state parameter, ψ_{SSL}, of Algeria sand tested on Triaxial and DSS devices

8.3 Coimbra Sand

8.3.1 Cyclic Triaxial Tests

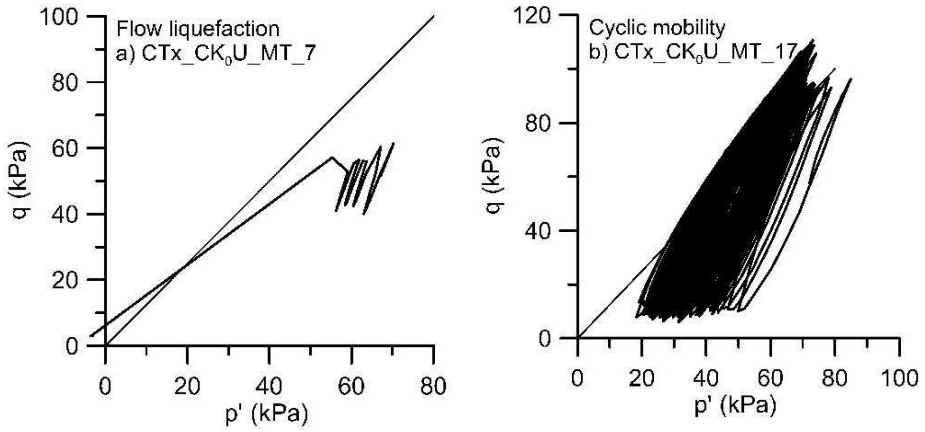
Coimbra sand cyclic liquefaction potential was assessed through the performance of 29 anisotropic cyclic Tx tests. Due to the lack of time and unavailability of equipments the number of performed tests was very small. Thus few factors were evaluated.

The cyclic Tx tests were performed with specimens of 70 mm diameter and 138 mm height, prepared by moist tamping and air pluviation. The study of two distinct reconstitution techniques aimed to assess the influence of inherent anisotropy on cyclic liquefaction potential.

The following sub-sections focus on the effect of the relative density and on the effect of the inherent anisotropy created by the sample preparation. Furthermore Coimbra sand liquefaction potential is evaluated by frameworks which correlate CSR with CRR, expressed as a stiffness or strength parameters.

8.3.1.1 Cyclic Behavior Of Coimbra Sand

As only anisotropic consolidated specimens were tested only two distinct mechanisms were detected, flow liquefaction, (Figure 8.25a) and cyclic mobility, (Figure 8.25b).



(a) (b)

Figure 8.25: Flow liquefaction due to (a) contractive deformation in compression with no rotation of principal stresses; Cyclic mobility for (c) cyclic loading with no shear stress reversal

8.3.1.2 Effect Of Relative Density On Liquefaction Resistance

Cyclic resistance curves of Coimbra sand are presented in Figures 8.26. The final results are obvious showing that Coimbra sand displays a higher resistance with increasing initial relative density. As can be observed, similarly to Algeria sand, there is a jump of the undrained cyclic resistance between loose to medium compacted specimens. This large increase of the CRR is clearly associated to the transition between flow liquefaction and cyclic mobility. This transitional behavior is clearer while represented in the semi-logarithmic space e: log p'.

Figure 8.27 also shows this increasing cyclic resistance with relative density. The increasing tendency is more pronounced for medium compacted specimens where cyclic mobility controls the overall behavior of the sand.

The points not represented in the cyclic resistance curves, in Figure 8.26, and displayed in Figure 8.27 were not plotted as they have not reached the 2.5% of single amplitude shear.

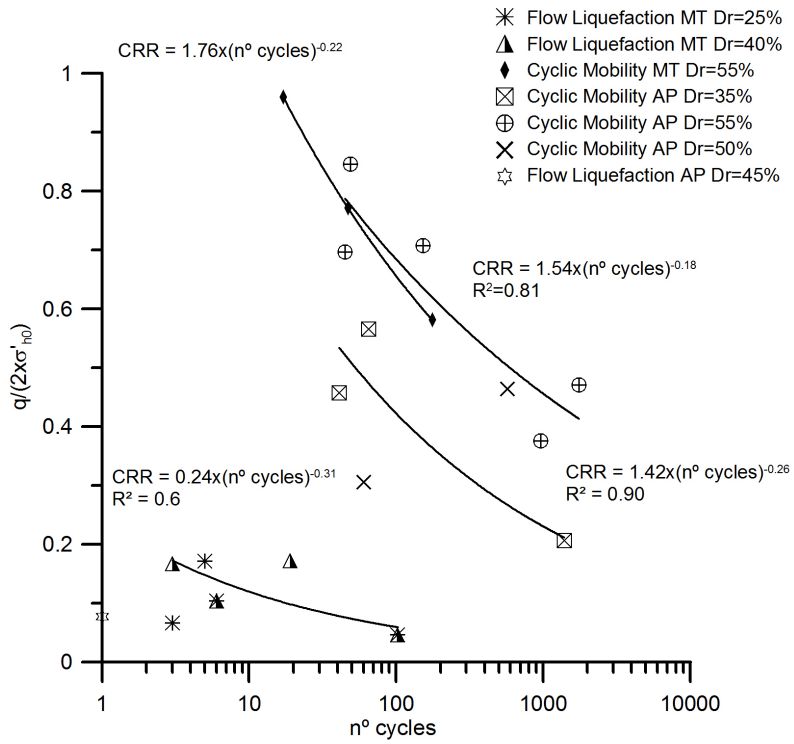


Figure 8.26: Cyclic resistance curves for Coimbra sand under triaxial stress conditions for anisotropic specimens (with initial static shear stress, $\alpha = 0.33$)

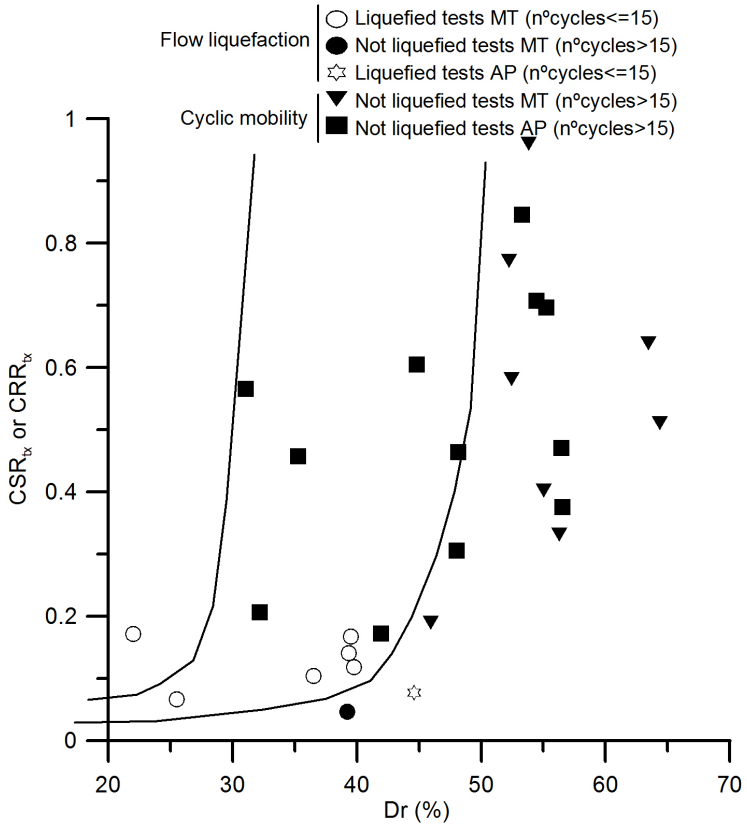


Figure 8.27: Cyclic stress ratio CSR, or Cyclic resistance ratio, CRR, versus relative density under triaxial stress conditions for Coimbra sand (Mw = 7.5)

8.3.1.3 Effect Of Sample Preparation On Liquefaction Resistance

Figure 8.26 also shows that specimens prepared by air pluviation create a fabric stiffer than those prepared by moist tamping. These differences only occur for loose to medium compacted specimens, vanishing for higher relative densities where the resistance seems to converge (see in Figure 8.26 the curves for Dr = 55%).

Notwithstanding careful shall be taken when interpreting the results obtained with air pluviated specimens as some imprecision might have resulted on an overvaluation of the cyclic strength. In fact Figure 8.26 and Figure 8.27 show a specimen which exhibited a very low resistance despite being medium compacted, when compared to similar tests. After a careful examination it was realized that the two tests, prepared by air pluviation, which exhibited a lower undrained cyclic resistance (for a number of cycles lower than 100, see Figure 8.26), were tested in the cyclic Tx device with a loading frequency of 0.1 Hz, while the other tests were performed in a stress-path device with a much lower loading frequency of about 0.033 Hz. Beyond the loading frequency should not be responsible for such differences, one of the tests performed in the cyclic Tx system, converged with the remaining tests performed on the stress-path device.

Thus it is feasible to assume the differences of the cyclic shear strength between the AP and the MT prepared specimens, for loose to medium compacted specimens, to be exclusively associated to the fabric effect, by excluding the two tests prepared by AP which exhibited a lower resistance. As reported by Mulilis et al. (1977) the influence of the depositional method, thus of inherent anisotropy and fabric on the CRR of saturated sands might be as large as a factor of 2. In this case the difference associated to the reconstitution technique, for low to medium compacted specimens is about 8 times higher for the air pluviated specimens (Figure 8.26). Notwithstanding being aware that the reason behind is associated to two distinct phenomena, i.e. the soils which exhibited lower CRR suffered flow liquefaction while those prepared by air pluviation solely suffered cyclic mobility, it should not be agreeable to compare distinct techniques associated to distinct phenomena (Chang et al., 2011).

8.3.1.4 Undrained Cyclic Shear Strength Under Applied CSSM

The clash between both cyclic and monotonic Tx tests on the semi-logarithmic space e: log p' provides a better comprehensive analysis of the state condition criteria and the respective phenomena behind each cyclic Tx test (see Figure 8.28). The cyclic Tx tests are represented in their final conditions, meaning after reaching 2.5% of single amplitude shear strain and or reaching a condition of zero effective stress.

Thus while all open symbols exhibited flow liquefaction for a number of cycles equal or lower than 15 and 2 exhibited flow liquefaction for more than 15 cycles, all the other tests achieved the 2.5% of single amplitude shear without requiring a complete or partial loss of shear strength. Similarly

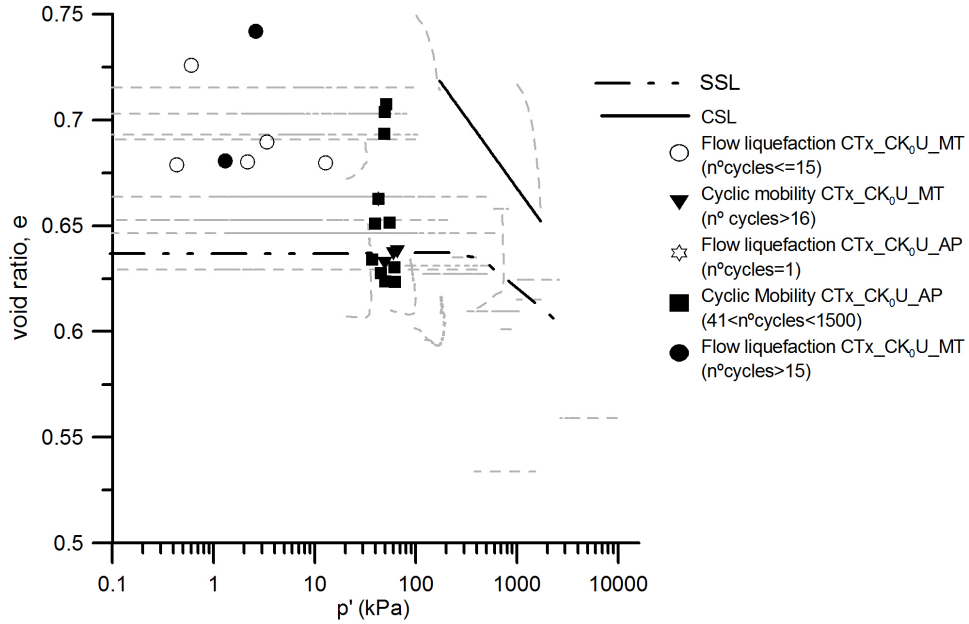


Figure 8.28: Anisotropic cyclic triaxial tests in the semi-logarithmic space e: log p' under applied CSSM

to Algeria sand it seems that it exists a boundary which separates flow liquefaction from cyclic mobility. Plus, for Coimbra sand, this boundary seems to converge with the same obtained under monotonic Tx tests.

A doubt arises for the tests prepared by air pluviation, where a unique test liquefied for a considerable low relative density, when compared with four other tests which exhibited a completely stable behavior while subjected to a higher CSR. This might be associated to the loading frequency at which was subjected. Nevertheless, even if the loading frequency has an effect on flow liquefaction triggering, as most of the specimens were tested on the stress-path device they become directly comparable. Thus, excluding this outlier, it is believed that the inherent anisotropy is responsible for the differences observed in Figures 8.27 and 8.28. Whereby for this case the SSL would upraise on the semi-logarithmic space e: log p', having the samples prepared by AP higher strength than the ones prepared by MT.

As no isotropic cyclic Tx tests were performed, nothing can be concluded about the effect of the initial static shear stress.

8.3.1.5 Frameworks To Evaluate Coimbra Cyclic Liquefaction Potential

- "Basic Berkeley Assessment chart"

  The "Basic Berkeley Assessment chart" was used to predict Coimbra sand cyclic liquefaction potential. While Figure 8.29 establishes a correlation between the cyclic resistance and the state parameter measured with reference to the CSL, Figure 8.30 correlates with the state

parameter measured with reference to the SSL presented in Chapter 7 for Coimbra sand and determined through monotonic Tx tests.

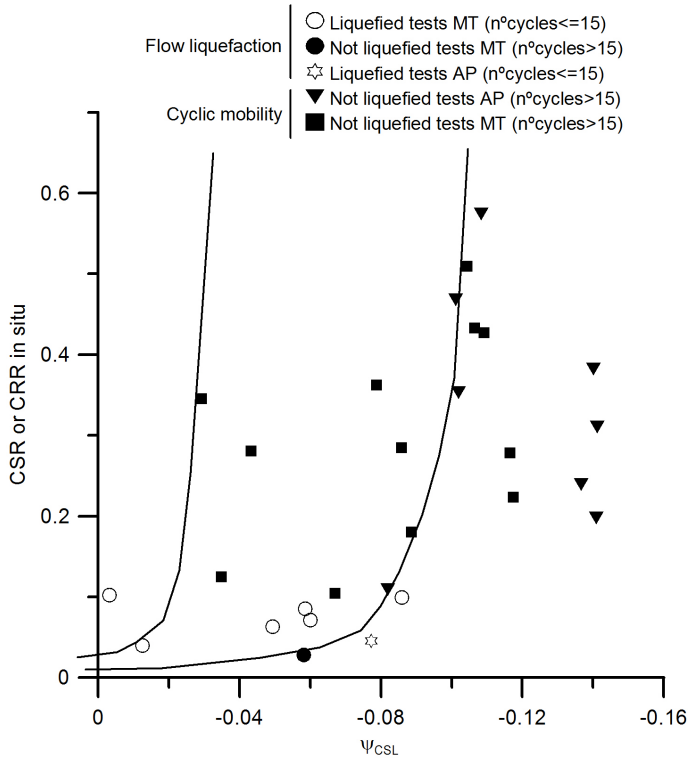


Figure 8.29: Basic Berkeley Assessment chart with reference to the CSL (Mw = 7.5); Liquefaction resistance of Coimbra sand under triaxial stress conditions

After visualizing both figures, it is clear that for the moist tamped specimens, no major differences are found between the steady state parameter measured with reference to the CSL or to the SSL. However, when looking downwards to the boundary, it is obvious that there is a better suitability provided by the ψ_{SSL}. On the other hand, the lack of suitability of the state parameter, either measured with reference to the CSL or to the SSL, to predict cyclic liquefaction potential of the air pluviated specimens is explained by Figure 8.28. As explained before there is uncertainty about the only test which liquefied for a number of cycles lower than 15. In fact, by excluding this outlier, it is obvious the higher cyclic resistance of the specimens prepared by air pluviation than those prepared by air pluvition.

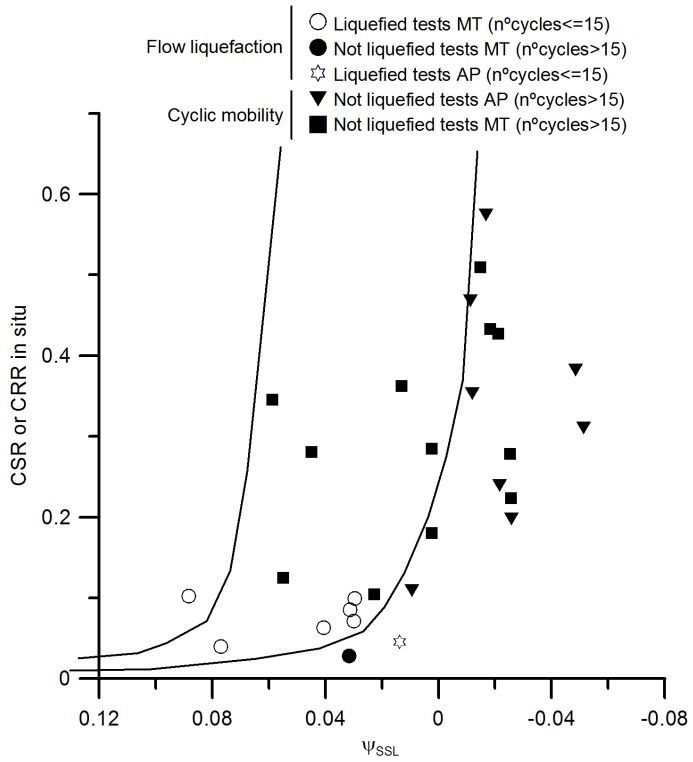


Figure 8.30: Basic Berkeley Assessment chart with reference to the SSL (Mw = 7.5); Liquefaction resistance of Coimbra sand under triaxial stress conditions

- "Simplified Procedure", based on a stiffness parameter ($G_0 - V_s$ values)

  Some cyclic Tx tests were also accompanied by the measurement of both shear and compression wave velocities. The "Simplified Procedure" was built for Coimbra sand and is represented in Figure 8.31.

  Figure 8.31 shows that despite the original values of the boundary proposed by Andrus and Stokoe (1997) not being able to capture the flow liquefaction behavior, by changing their values a better suitability was found. While the *b* parameter assumed the value of 1.8, the parameter *a* was lowered to 0, which is the same as not accounting with the first term of equation (3.32), that represents a modified relationship between V_{S1} and CSR. Therefore this suggests that flow liquefaction, triggered by cyclic loading, is, similarly to the static liquefaction, a problem of loose conditions. A similar problem was found with the anisotropic consolidated specimens of Algeria sand, where the *a* parameter was also lowered near zero.

  By comparing both air pluviated and moist tamped specimens it was clear that the air pluviated exhibited a higher undrained cyclic resistance. Similarly normalized shear wave velocity seem to corroborate this tendency, as the boundary would be left-shifted.

  Similarly to Algeria sand it was decided to display V_s waves as a function of the accumulated dissipated energy (W), i.e. shear work, to strengthen the use of the stiffness parameters as a

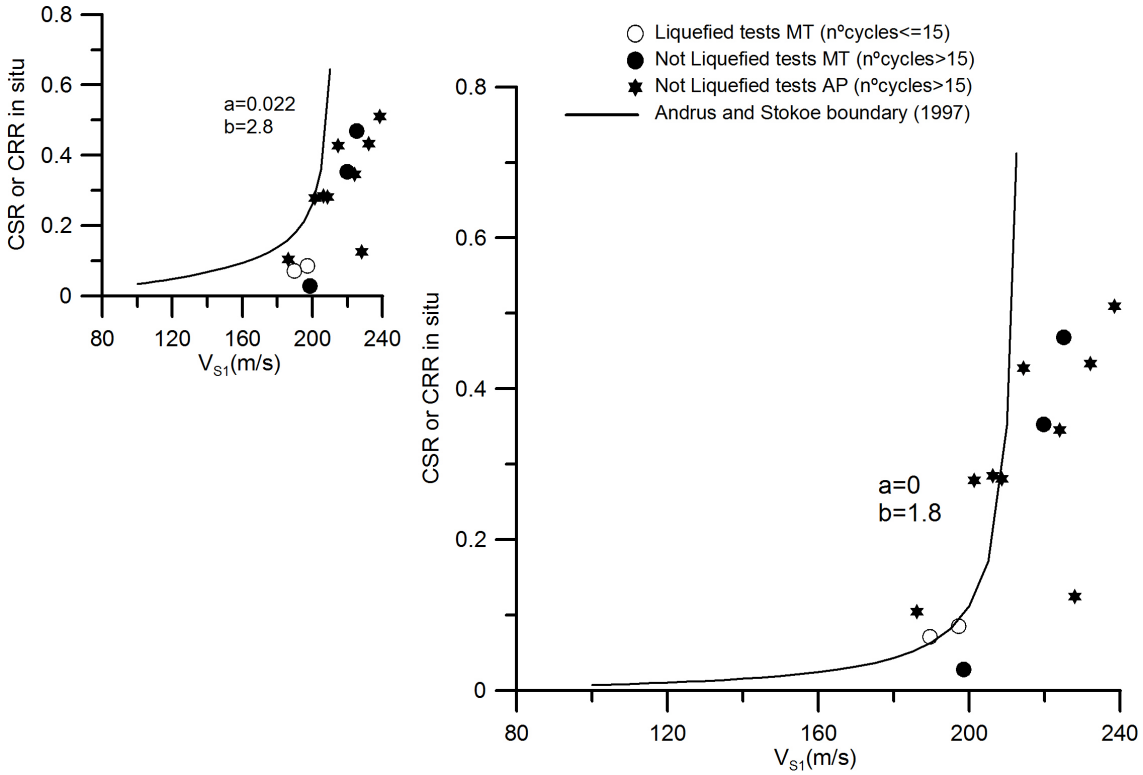


Figure 8.31: "Simplified Procedure" of Coimbra sand under triaxial stress conditions

reliable parameter to evaluate soil liquefaction potential (Figure 8.32).

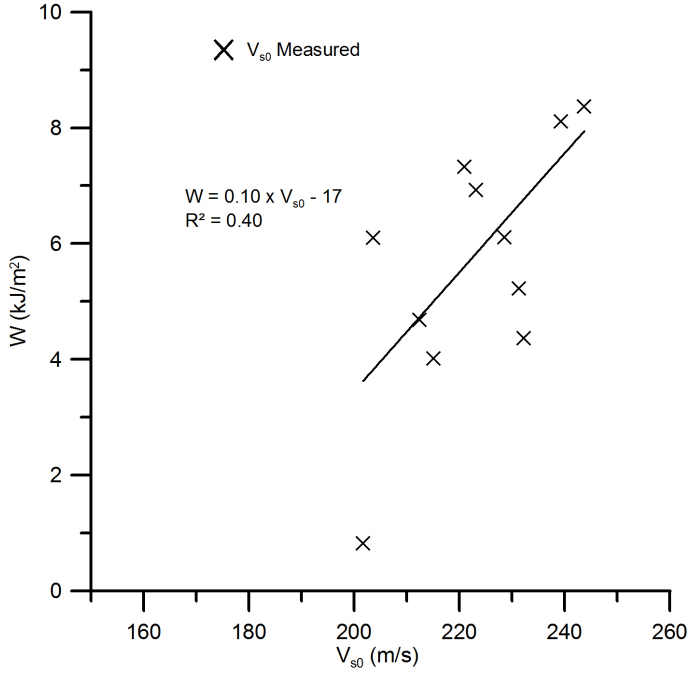


Figure 8.32: Shear work (W) as function of shear wave velocity for Algeria sand

As most tests were performed with a same initial confining stress, the correlation between

both parameters is not as obvious as the one obtained for Algeria sand. Despite a linear correlation has been chosen, which may be not the best fitting correlation law.

Aiming to predict V_s waves, G_0 was determined by comparing the real measured G_0 with the one predicted by the empirical equations initially proposed Hardin and Richard (1963), and later adapted by many other authors Hardin and Drnevich (1972); Hardin (1978); Kokusho (1980); Lo Presti (1995) (see Figure 8.33). The values of the constant parameters S_{ij}, n_i and n_j of equation (3.40) were previously determined through the monotonic Tx tests, also with measurements V_s with bender elements. Regardless, and similarly to Argelia sand, Figure 8.33 shows some disparity between the predicted G_0 and the measured data. This disparity may be high enough to justify the further inability of equation 3.40 to predict G_0 for assessing soil liquefaction potential.

Similarly to Algeria sand the lack of precision of the empirical equations might be explained either by the unsuitability of the function F(e) or of the exponent, n. Thus it is widely known one of the biggest problems associated to the use of shear wave velocity to evaluate the soil liquefaction potential is mainly due to it less sensitivity to the relative density. As quoted before, Idriss and Boulanger (2004) compared the capacity of changing response by increasing the relative density of a soil from 20% to 80%. While the SPT blow count changed by a factor of 7.1, the CPT tip resistance by a factor of about 3.3, the V_s only changed by a factor of 1.4 basing on available correlations. On the other hand the lack of accuracy of the exponent n might be justified by dependency of G_0 in each of the individual components of confining pressures (Roesler, 1979). Thus, the exponent n, usually assumed the same for both σ'_{v0} and σ'_{h0}, might be also a function of the K_0 and perhaps a function of the void ratio.

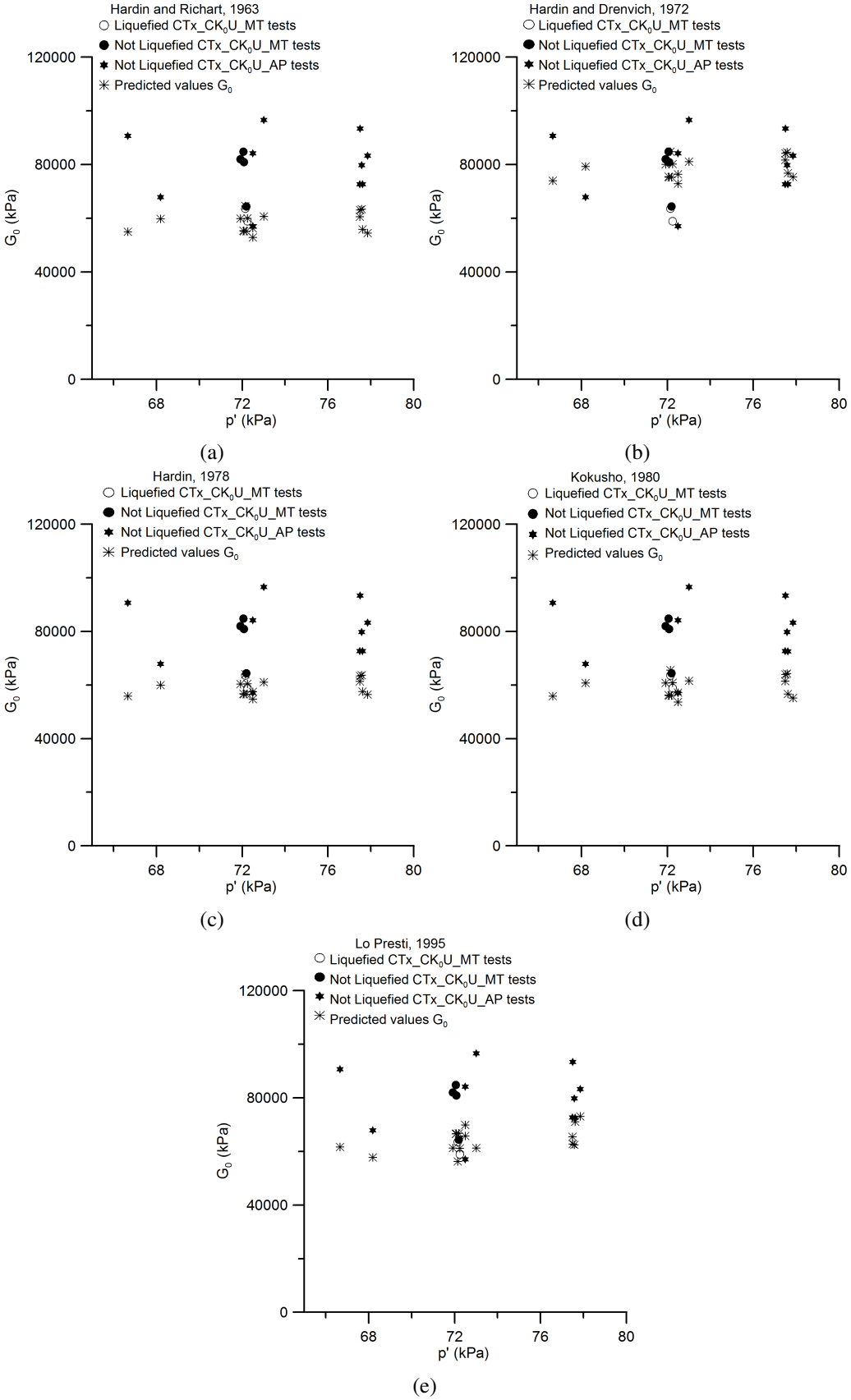


Figure 8.33: Comparison between the measured G_0, for Coimbra sand, and the predicted G_0 by using the empirical equations proposed by: a) Hardin and Richard (1963); b) Hardin and Drnevich (1972); c) Hardin (1978); d) Kokusho (1980) and d) Lo Presti (1995)

8.3.2 Cyclic DSS Tests

The study of Coimbra sand under cyclic conditions also included a set of cyclic DSS tests. These tests allowed perceiving the influence of principal stress rotation on CRR of Coimbra sand.

The tests covered initial confining stresses of 100, 300 and 500 kPa, performed over specimens prepared with distinct initial void ratios. The study involved the execution of 43 cyclic DSS tests over specimens of 72 mm diameter and 38 mm height, prepared by moist tamping. This technique, as explained before, ensures a better reproduction of a wider range of initial void ratios Ishihara (1996).

8.3.2.1 Effect Of Relative Density On Liquefaction Resistance

Figures 8.34 and 8.35 allow perceiving the effect of the initial relative density on the cyclic resistance ratio of Coimbra sand while subjected to principal stress rotation. Despite not being very pronounced it can be observed, from both graphs, that Coimbra sand exhibit an increasing CRR with increasing relative density.

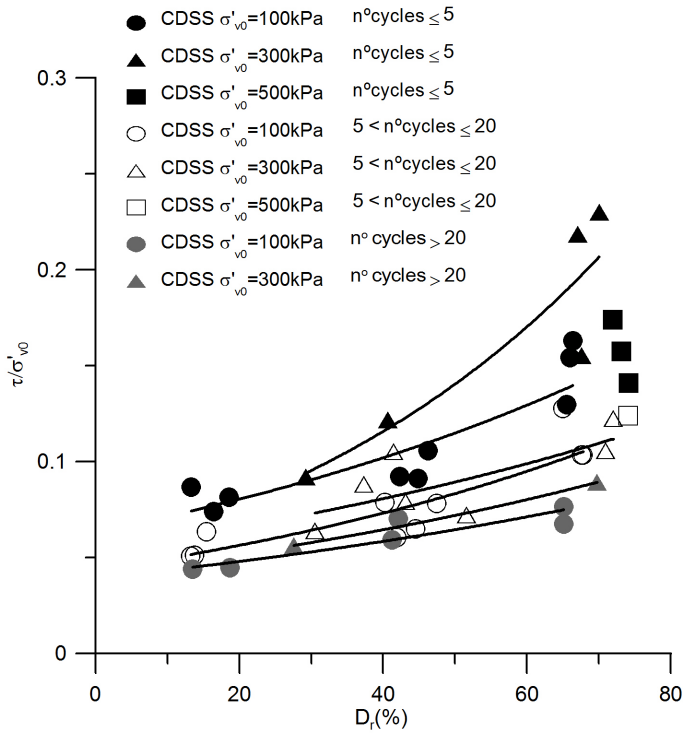


Figure 8.34: Dependence of cyclic resistance on relative density for 100, 300 and 500 kPa of confining stress for Coimbra sand

Despite exhibiting a higher CRR for higher initial confining stresses, the rate of increase in cyclic resistance with relative density seems to be higher for lower confining stresses as the resistance curves are more distant from each other (Figure 8.36).

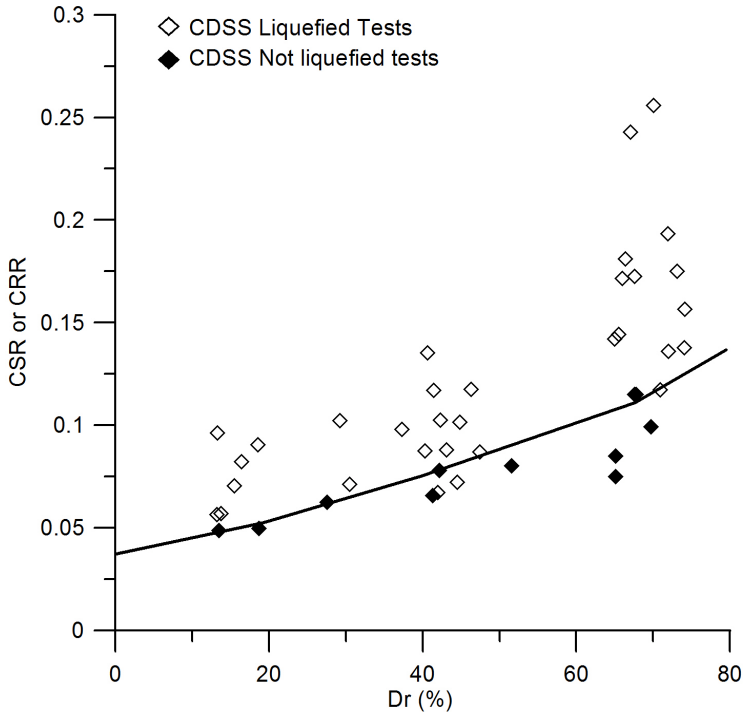


Figure 8.35: Cyclic stress ratio CSR, or Cyclic resistance ratio, CRR, versus relative density for Coimbra Sand under direct simple shear stress conditions (Mw = 7.5)

Figure 8.35 displays all cyclic DSS test results regardless their initial confining stress. A clear boundary is established for a seism magnitude of 7.5, separating the tests which exhibited liquefaction for less than 16 cycles from the ones which exhibited a higher resistance. Thus, apparently the necessity of correcting the initial confining stress is not necessary, at least for Coimbra sand under these shear stress conditions.

8.3.2.2 Effect Of Vertical Confining Stress On Liquefaction Resistance

The study of three distinct initial confining stresses allowed understanding the overall tendency of Coimbra sand. The soil, similarly to Algeria sand, exhibits a less contractive tendency due to stress densification which surpasses the contractive tendency due to the increase in confining stress (Figures 8.34 and 8.36). The sand not only exhibits a slightly higher cyclic resistance for higher confining stresses, but this less contractive behavior is also more pronounced for lower relative densities. Yet for Coimbra sand this effect seems to disappear for higher relative densities (Dr > 60%) as the undrained cyclic resistance curves seem to merge into a unique curve (Figure 8.36).

In order to strengthen the proposal of an increasing CRR with increasing confining stress, for a same initial void ratio, two distinct tests, with a same initial void ratio and a distinct confining stress, were compared. Data for stress-strain, stress-path and excess pressure, with and without normalization, are plotted, for both CDSS_7 and CDSS_12 tests, in Figure 8.37. More than the

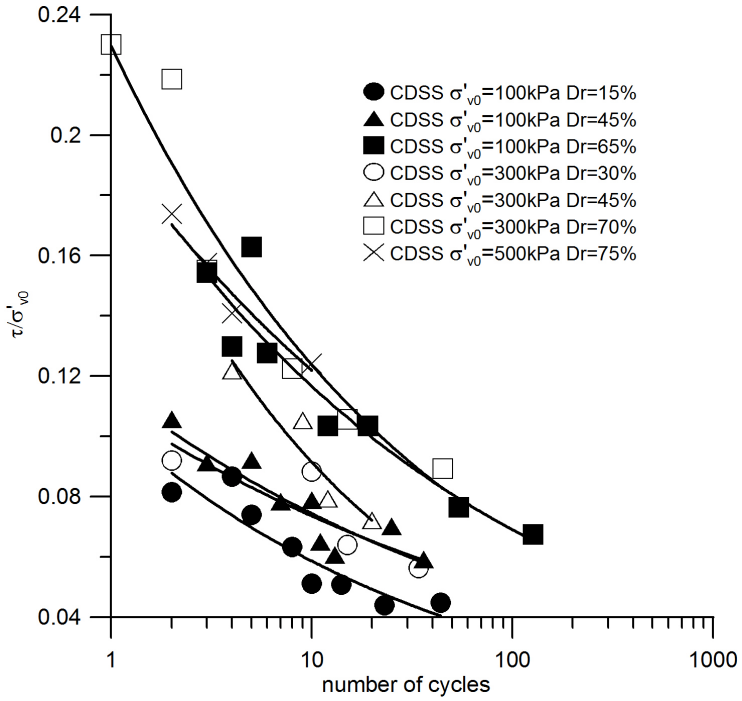


Figure 8.36: Cyclic resistance curves for Coimbra sand in DSS conditions (without initial static shear stress, $\alpha = 0$)

normalized shear stress which is almost imperceptible, the normalized excess pore pressure unexpectedly is much higher for the lower confined specimen.

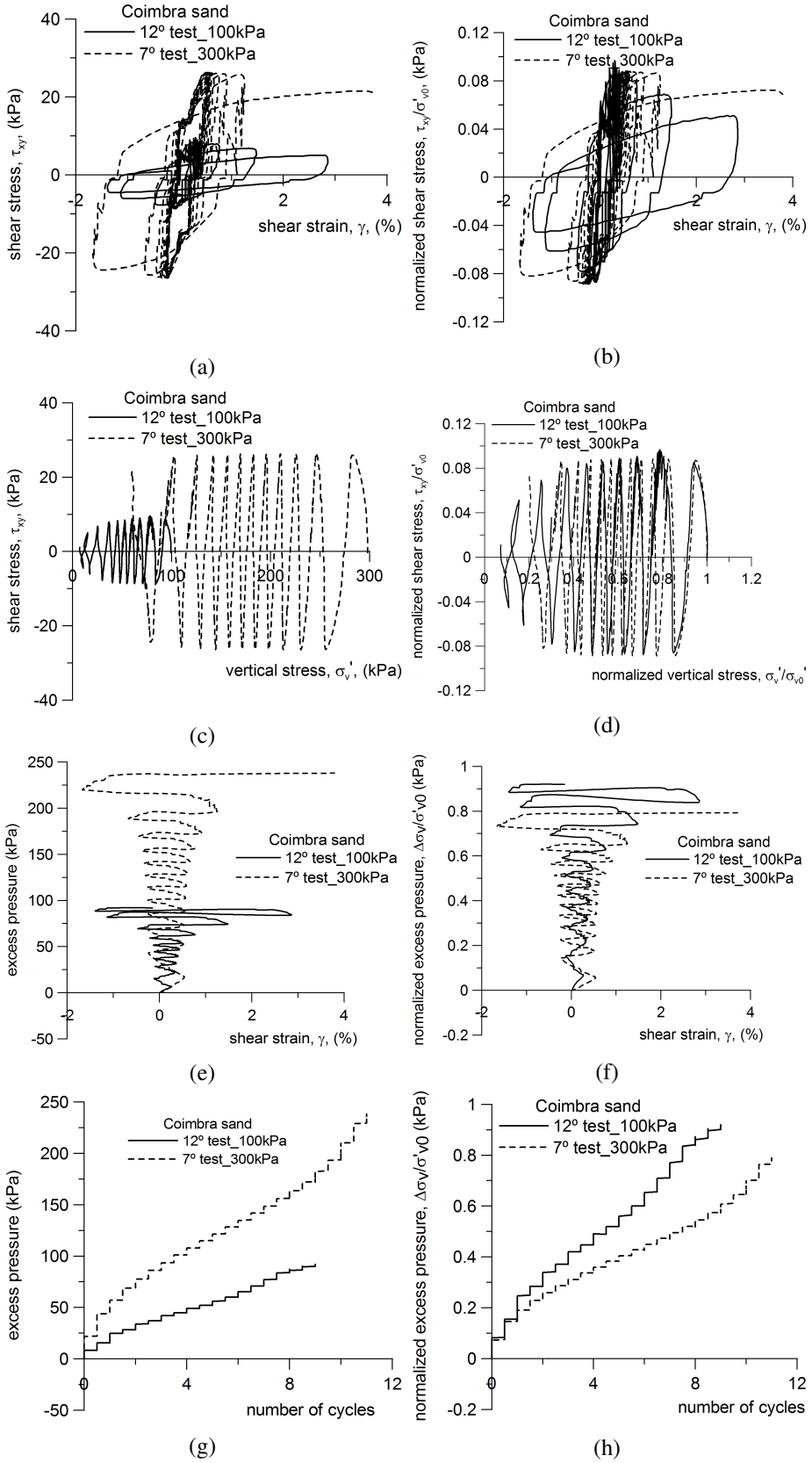


Figure 8.37: Stress-strain, stress-path, and excess pore pressure with and without normalization, from left to right respectively, for 12 test_100 kPa and 7º test_300 kPa for Coimbra sand

Once more, this sand suggests an opposite tendency, at least for the imposed shear stress conditions, to the one which is commonly featured by the overburden correction factor, K_σ (Figure 8.38). Thus it is assumed that principal stress rotation might be responsible for such event. For such conditions the curve proposed by Hynes and Olsen (1999) clearly underestimates the cyclic resistance.

From what follows it can be concluded that the effect of confining stress on cyclic resistance for cohesionless soils is not as clear as has been presented in the literature, as the contractiveness does not increase with increasing confining stress, for tests performed under cyclic DSS conditions.

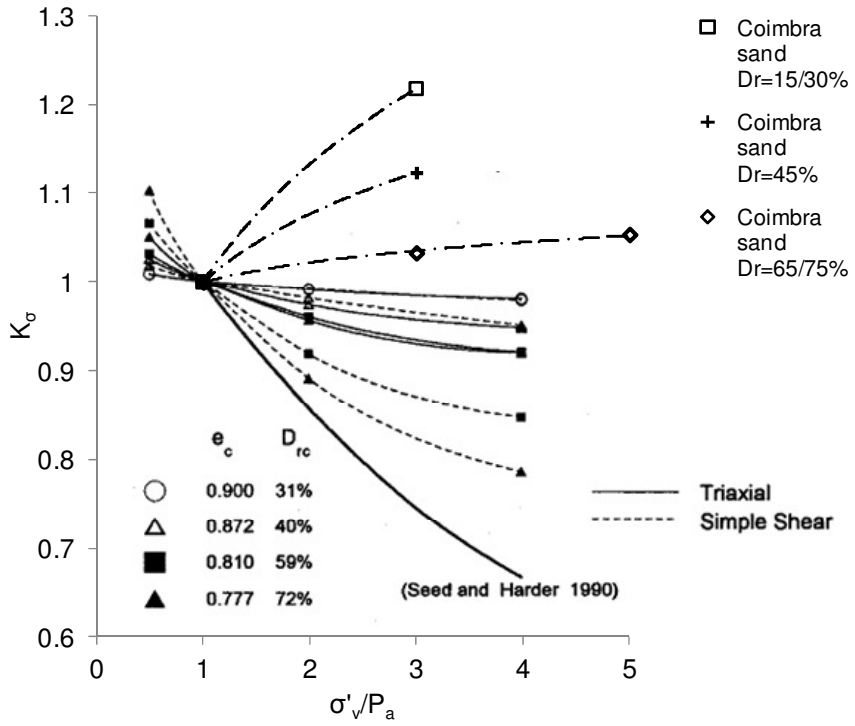


Figure 8.38: K_σ values for Fraser Delta sand and Coimbra sand under direct simple shear and triaxial stress conditions (adapted from Vaid and Sivathayalan (1998))

Such results make unclear any conclusions about the influence of the initial confining stress based on classical K_σ overburden correction factors. Thus, once again as Algeria sand, three hypotheses are postulated: i) the first one based on Wijewickreme et al. (2005) conclusions, which associate the CRR gain on the densification effect created by the sample reconstitution method, which surpasses the $\sigma_v^{'}$ effect; ii) the second associated with fabric anisotropy changes with plastic strain accumulation during the test; iii) the combination of the first and second hypothesis, as stated by Oda and Iwashita (2000) *"Rotational resistance arises not only from contractive behavior, but also from particle shape. It can be one of the dominant components to control the strength of granular media"*.

By observing Figure 8.37 it seems obvious that these differences are too big to be neglected,

despite being on the safe side. Also Vaid and Sivathayalan (1998) found the effect of increasing confining stress on the reduction in cyclic resistance to be much smaller than currently considered, varying according to the type of test device (Figure 8.38).

8.3.2.3 Frameworks To Evaluate Coimbra Cyclic Liquefaction Potential

- "Basic Berkeley Assessment chart"

  As a prominent tool to assess cyclic liquefaction potential, the "Basic Berkeley Assessment chart" was built with the cyclic DSS test results, and displayed in Figure 8.39. Once the ultimate states achieved by the monotonic Tx tests were not unique in a wide range of mean confining stresses, diverging between drained and undrained conditions, it was decided, for a logical purpose to determine the ψ with reference to the SSL.

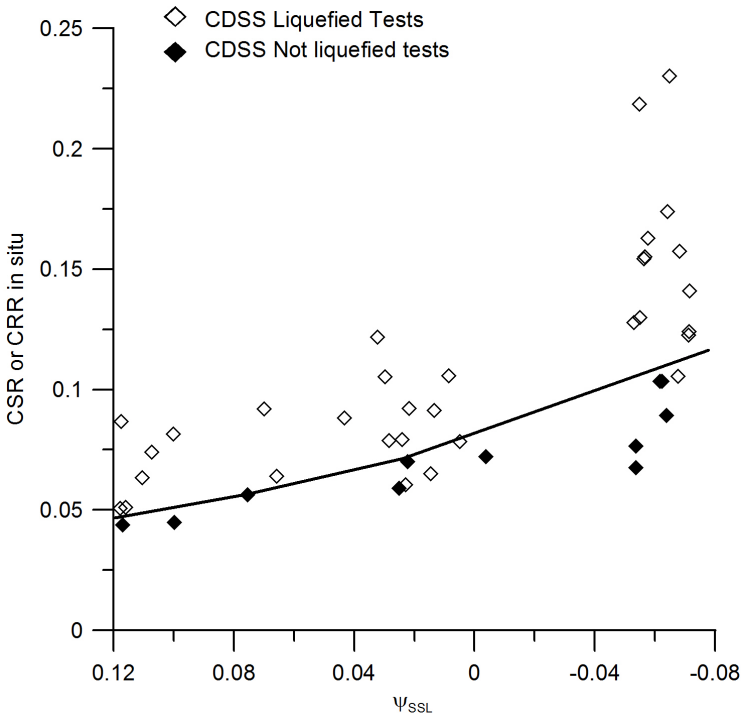


Figure 8.39: Basic Berkeley Assessment chart with reference to the CSL (Mw = 7.5); Liquefaction resistance of Coimbra sand under direct simple shear stress conditions

  As can be observed the boundary provided by the correlation between the CRR and the ψ_{SSL} seem to be quite suitable. However and after comparing Figure 8.39 with Figure 8.35 it seems that the ψ_{SSL} is useless, as the Dr seem to also provide a quite reliable parameter beyond not requiring the determination of the CSL and/or SSL. This succeeds because the initial relative density surpasses the effect of the initial vertical stress on the CRR.

8.3.3 Comparison Of Liquefaction Resistance Of Coimbra Sand Under Simple Shear And Triaxial Stress Conditions

As the differences obtained between the air pluviation technique and the moist tamping were not conclusive, only the results attained by the moist tamped tests are compared between the two equipments. Furthermore it only makes sense to compare the results obtained by the similar preparation technique, in order to avert other factors effect.

The differences achieved between the cyclic DSS and Tx are only very pronounced since cyclic mobility starts controlling the soil behavior, i.e. for Dr > 40% and $\psi_{SSL} > 0.02$, (see Figures 8.40 and 8.41). For looser conditions the soils seems to have a same CRR despite the prevailing phenomena not being comparable. As reported before, the DSS equipment is a constant volume test and not an undrained test. Whereby, while the pore-pressure generation induces the anisotropic cyclic Tx tests to incur into an instability process, the low resistance displayed by the DSS is exclusively owed to the principal stress rotation.

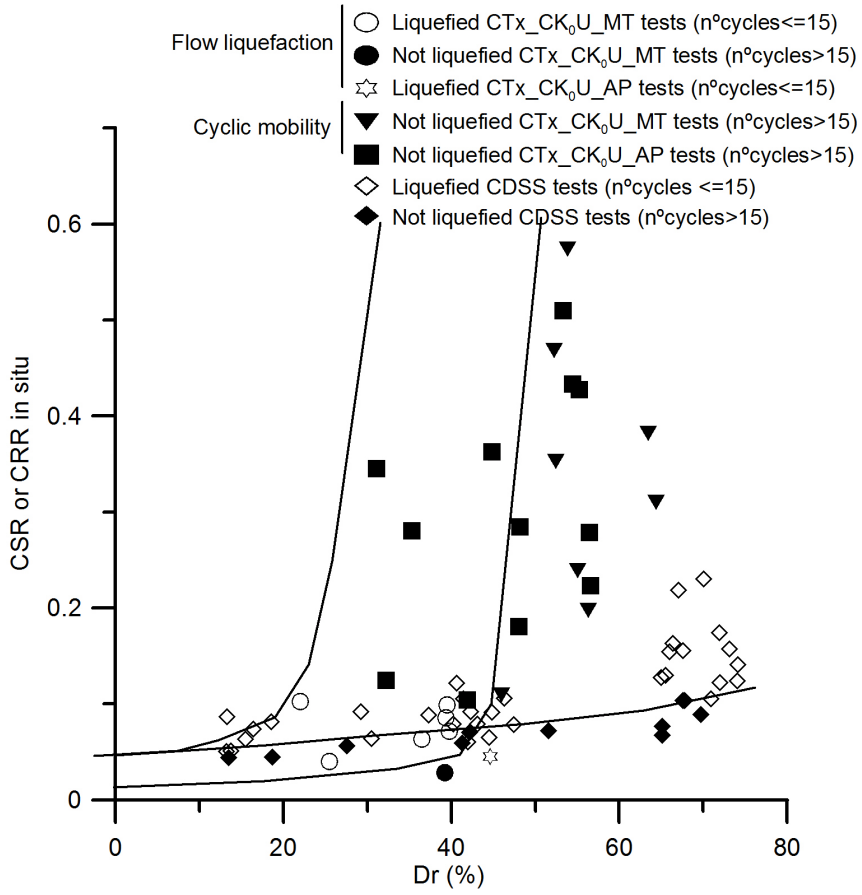


Figure 8.40: Cyclic stress ratio CSR, or Cyclic resistance ratio, CRR, versus relative density for Algeria Sand under both Tx and direct simple shear stress conditions (Mw = 7.5)

Despite the tests not being performed with a same initial confining stress, the differences cannot be directly associated to such factor. In one hand the cyclic DSS exhibits a lower CRR for lower

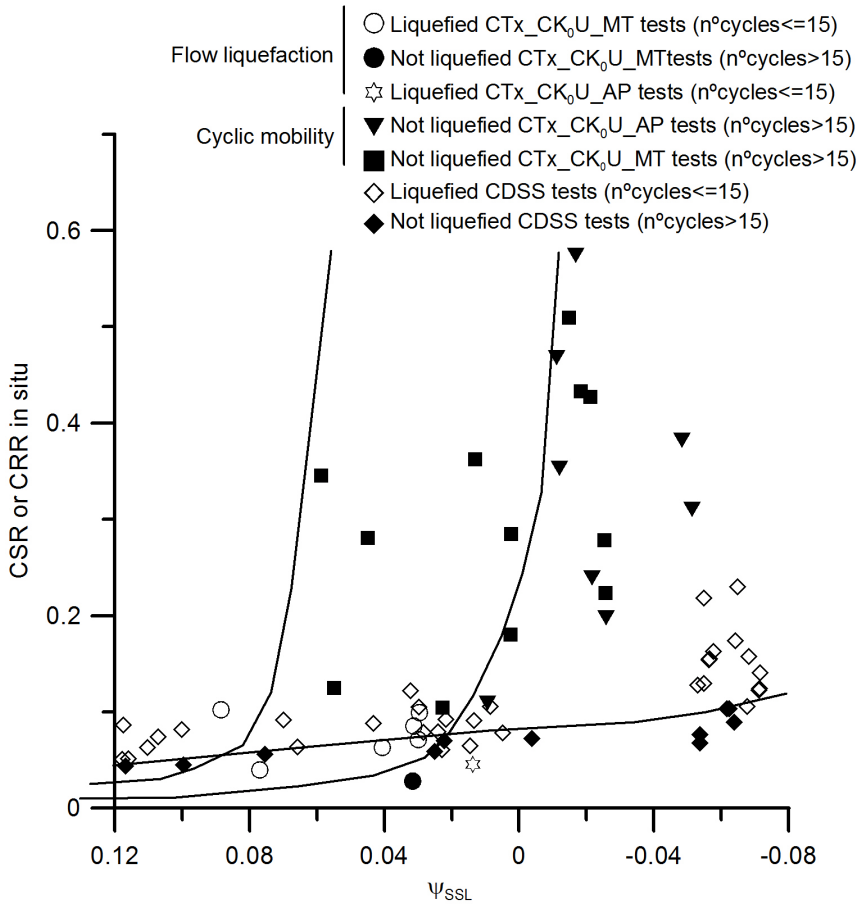


Figure 8.41: Basic Berkeley Assessment chart with reference to the SSL (Mw = 7.5); Liquefaction resistance of Algeria sand under both triaxial and direct simple shear stress conditions

confining stresses, plus the cyclic Tx tests are already known to decrease the CRR with increasing confining stress, for a same initial compaction condition. Furthermore the differences in CRR values, between these different equipments/conditions, are too large to be assigned exclusively to the stress factor (K_σ).

Once more, by comparing both Figures 8.40 and 8.41, it seems that the advantages of using the ψ_{SSL} as a prominent parameter to assess soil liquefaction potential are beyond the expected. As previously explained, if on one hand the initial confining stress affects the CRR, in opposition to the results for the cyclic DSS tests, the Tx tests were only performed with a same initial confining stress.

Plus, and similarly to Algeria sand, the differences assigned by the two equipments cannot be explained by the c_r factor, as both tests are consolidated, in a different way, under a K_0 condition, similarly to in field prevailing conditions.

Furthermore, and similarly to Algeria sand, the differences seem to prevail due to a continuously rotation of the principal stress direction. In fact if comparing the monotonic shear strength of both devices, which is not as linear as it might seem, the soil seems to exhibit a similar brittleness index

(see Figure 8.42). Therefore the differences are possibly exclusivly associated to the rotation of principal stress direction.

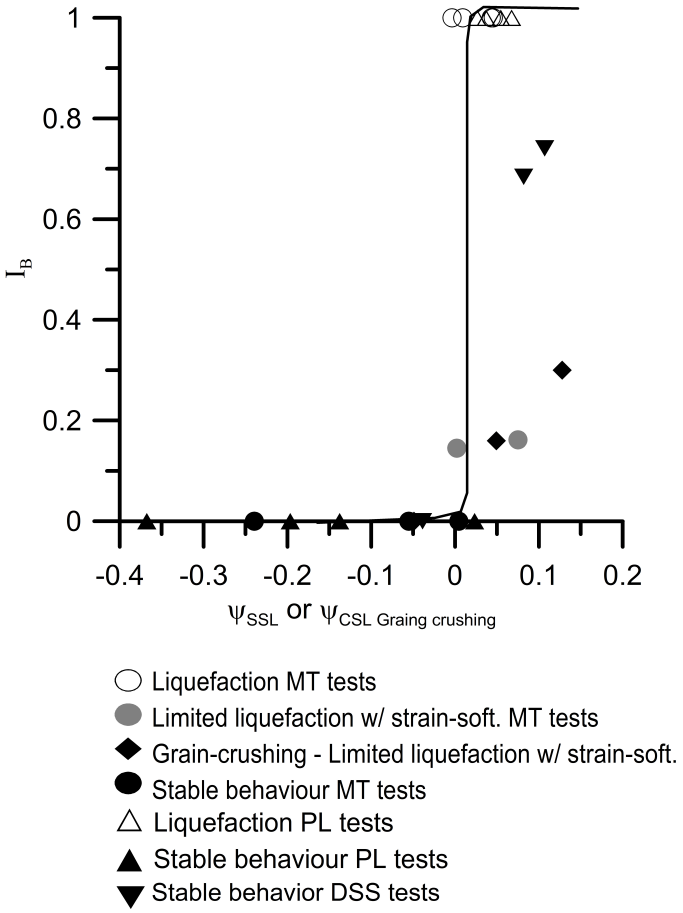


Figure 8.42: Variations of the Brittleness Index with the steady state parameter, ψ_{SSL}, of Coimbra sand tested on Triaxial and DSS devices

Chapter 9

Sanisand Model Description And Application

9.1 Introduction

Over the last chapters soil liquefaction hazard was semi-empirically evaluated through the construction of frameworks which correlate strength and deformability. The absence of an adapted constitutive model that could cope with such a complex instability guided both cyclic and static liquefaction assessment to semi-empirical frameworks based on laboratory and in situ tests databases. Nevertheless the continuous research of soil instability aims at providing, not only a proper calibration for empirical frameworks, but furthermore to contribute for a proper evolution of constitutive models.

As it is widely known, constitutive models, implemented in numerical software for engineering, might in some cases mislead soil strength, mainly in particular instability phenomena, such as soil liquefaction. Soil liquefaction has the peculiarity of exhibiting peak shear strength, as it is known and was earlier presented, followed by a significant softening, evolving to with a much lower resistance, which is not represented by conventional critical state conditions. Not only flow liquefaction, but also strain softening, are very concerning phenomena as, despite the first one results in a complete loss of strength, the second one can also result in large significant drop of stability leading to unacceptable strains. Hence it becomes essential to assess limitations and keep updating constitutive models.

In the scope of this research SANISAND model, described below, which basic principles were presented by Manzari and Dafalias (1997), was calibrated for Osorio sand and Mixture, in an attempt to evaluate its ability to reproduce the geomechanical behavior of both soils. Thus, a comparison of the experimental test results described in previous chapters and those obtained by the model was made and analyzed.

For this application of the constitutive model the program Incremental Driver (ID), developed by Niemunis (2008), was adopted. Its advantage resides on the capacity to overcome the complexity and time consuming issues very common on other numerical codes, since, as quoted by Prada (2011), "the main task of ID is to simulate the behavior of an FE program at a single integration point".

9.2 Description Of The Constitutive Model SaniSand

9.2.1 Description Of The Model

Similarly to many other constitutive models, SANISAND, a Simple ANIsotropic SAND plasticity model, is a constitutive critical state model with a bounding surface plasticity, based on the state parameter definition. This model, initially developed by Manzari and Dafalias (1997) is an elastoplastic model and has the particularity of being able to predict both softening-hardening and contractive-dilative response of sands in a wide range of initial state conditions. This has recently evolved by an adaptation made to the model, by the same authors in 2004 (Dafalias and Manzari, 2004), which included a two-surface formulation through considering specific ratios between peak strength and dilatancy controlled by the state parameter.

- Basic equations

  Despite the model being developed to ascertain a multiaxial stress-strain response of soil, in the scope of the present work the soil stress-strain response is only studied in stress conditions corresponding to triaxial test in axisymmetric conditions. Thus the principal effective stresses are σ_1 and $\sigma_2 = \sigma_3$, and ε_1 and $\varepsilon_2 = \varepsilon_3$ are the corresponding principal strains. The triaxial variables are the deviatoric stress, q, and the mean effective stress, p, the deviatoric strain, ε_q, and the volumetric strain, ε_v, defined, respectively, by equations (9.1) till (9.4):

$$q = \sigma_1 - \sigma_3 \tag{9.1}$$

$$p = \frac{\sigma_1 + 2\sigma_3}{3} \tag{9.2}$$

$$\varepsilon_q = \frac{2(\varepsilon_1 - \varepsilon_3)}{3} \tag{9.3}$$

$$\varepsilon_v = \varepsilon_1 + 2\varepsilon_3 \tag{9.4}$$

,where 1 and 3 stands for the principal maximum and minimum stress directions, axial and radial, respectively.

For practical purposes during the description of the model, a same notation of the authors will be followed, whereas the mean effective stress, usually designated by p', will be generally designated by p (which should be only applied to total stresses). However, all the calculations are in fact performed with effective stresses.

A stress ratio is also introduced:

$$\eta = \frac{q}{p} \tag{9.5}$$

Finally the elastic and plastic volumetric and deviatoric strains are given by:

$$d\varepsilon_q^e = \frac{dq}{3G} \tag{9.6}$$

$$d\varepsilon_v^e = \frac{dp}{K} \tag{9.7}$$

$$d\varepsilon_q^p = \frac{d\eta}{H} \tag{9.8}$$

$$d\varepsilon_v^e = d|d\varepsilon_q^p| \tag{9.9}$$

where G and K are the elastic and bulk incremental moduli, respectively, H is the plastic hardening modulus associated with the increment in stress ratio $d\eta$ and d is the dilatancy, not to be confused with the differential symbol, also denoted by Dafalias and Manzari (2004).

- Critical state line and state parameter

SANISAND model, as a critical state model, adopts the ultimate state condition of the soil defined, not as linear function, but as power relationship previously defined by Li et al. (1999). According to Ramos (2010) this relationship has the advantage of allowing a greater freedom in representing the critical state, since with the power exponent allows non-linear critical state lines:

$$e_c = e_{c0} - \lambda_s \left(\frac{p_c}{p_a}\right)^{\xi} \tag{9.10}$$

being e_0 the limiting value of e at $p = 0$, p_a is the atmospheric pressure λ_s and ξ are constants which depend on soil characteristics. The main advantage of the CSSM models relies on the adoption of the state parameter, $\psi = e - e_c$, which incorporates both the effects of the density and confining pressure. Furthermore the state parameter not only measures the distance between the initial and the critical state, but more importantly it controls the soil behavior until the achievement of the critical state (Yu, 1998).

- Elastic component of the model

  Before achieving the yield surface both bulk modulus and shear modulus control the soil behavior through the equations given below (9.11) and (9.12). The elastic and bulk incremental moduli, G and K, are determined, in SANISAND model, according to the empirical equations determined by Richart et al. (1970):

$$G = G_0 \frac{(2.97 - e)}{1 + e} \left(\frac{p}{p_{atm}} \right)^{1/2} \tag{9.11}$$

$$K = \frac{2G(1+\nu)}{3(1-2\nu)} \tag{9.12}$$

  where G_0 is a material constant similar to A, previously defined in Table 3.2, ν is the Poisson coefficient and p_{atm} is the atmospheric pressure for normalization (= 100 kPa).

- Yield function

  This model use a narrow open cone-type yield surface with apex at the origin obeying rotational hardening, which implies that only changes of the stress ratio can cause plastic deformations, thus $\delta \neq 0 \Rightarrow d\varepsilon_q^p \neq 0$, (Dafalias and Manzari, 2004). A more recent version of SANISAND model, proposed by Taiebat and Dafalias (2008), introduces a modified eight-curve equation which obeys rotational and isotropic hardening. Unfortunately this late version was not used during the present work, since the available code was not prepared with this version.

  According to Dafalias and Manzari (2004), for this version of the model, the yield surface, which enclosed the elastic region, is expressed as:

$$F(\eta, \alpha) = |\eta - \alpha| - m \tag{9.13}$$

  where η is the stress ratio, α is the stress ratio quantity corresponding to the rotational hardening variable of the yield surface and is called the back-stress ratio, and m a constant. Both α and m are stress ratio quantities which quantify the inclination and the size of the

yield surface, respectively. The yield surface is represented by a "wedge" in q:p space, shown by the shaded area in Figure 9.1.

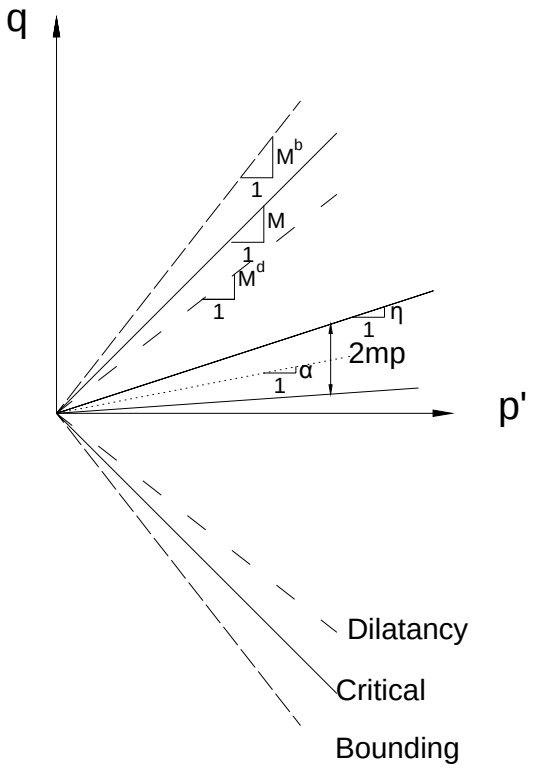


Figure 9.1: Schematic of yield surface and main ingredients plotted in effective stress space. The shaded area represents the elastic region whose inclination is dictated by α. Other important ingredients are the bounding stress ratio M_b, dilatancy stress ratio M_d and critical state ratio M (adapted from Dafalias and Manzari (2004)

The yield function is commonly represented for a homogeneous, isotropic and elastic material as:

$$F = q - Mp = 0 \tag{9.14}$$

Beyond the critical state line and the yielding surface, SANISAND constitutive model also makes use of two surfaces changing with the ψ. The bounding surface, M^b, considers the hardening-softening behavior and the dilatancy surface, M^d, conceives the dilative-contractive behavior of the soil. During shear this two surfaces move towards the critical state line (Ramos, 2010). Therefore:

$$e = e_c, \psi = 0 \text{ and } M^c = M^d = M^b \tag{9.15}$$

$$e > e_c, \psi > 0 \text{ and } M^b < M^c < M^d \tag{9.16}$$

$$e < e_c, \psi < 0 \text{ and } M^d < M^c < M^b \tag{9.17}$$

During shear, the loading increment is limited by the bounding surface, M^b, represented in Figure 9.1 as a straight dashed line, and by the dilatancy surface, M^d, represented as a straight discontinuous line in Figure 9.1:

$$M^b = Mexp\left(-\eta^b \psi\right) \tag{9.18}$$

$$M^d = Mexp\left(-\eta^d \psi\right) \tag{9.19}$$

where n^b and n^d are positive constants function of the material, (Dafalias and Manzari, 2004; Andrade et al., 2013).

It is important to note that peak strengths in loose soils are of instability type and this will be discussed on what follows.

- Plastic potential

  During shear the yielding of the soil is associated with plastic volumetric and plastic shear strain increment, $d\varepsilon_v^p$ and $d\varepsilon_q^p$, respectively. The strain increment vectors are orthogonal to the family of plastic potential functions and the ratio between both plastic strain increments is fixed by the gradient of the yield surface.

  For sands the flow rule, which specifies the direction of the plastic strain, is non-associated, i.e., the plastic potential function and the yielding surface are not the same.

  Similarly to many other models, the stress-dilatancy relation used by SANISAND model is based on the Rowe's dilatancy theory (Rowe, 1962). Being the plastic potential family curves defined by the plastic strain increments, and the plastic potential function can obviously be obtained by integrating the Rowe's stress dilatancy relation.

  According to Rowe, d is proportional to the difference of current stress ratio, η, from dilatancy stress ratio, M^d. Thus the dilatancy rate, which gives the volumetric part of the plastic flow, is defined as:

$$d = \frac{d\varepsilon_v^p}{d\varepsilon_q^p} = A_d\left(M^d - \eta\right) \tag{9.20}$$

where A_d is a function of the state variables.

A_d is a very important parameter that considers the changes of fabric during dilatancy through the fabric dilatancy internal variable z_{ij}:

$$A_d = A_0 \left(1 + \langle z_{ij} \eta_{ij} \rangle\right) \tag{9.21}$$

where A_0 is a material parameter. The MacCauley brackets, $\langle\rangle$, define that $\langle x \rangle = x$, if $x > 0$ and $\langle x \rangle = 0$, if $x \leq 0$ (Ramos, 2010). However this parameter will not be used in the present application because unload and reload cycles will not be model.

- Evolution laws

  (i) Hardening Law

  The back-stress, α, which represents the inclination of the yield surface, is governed by a kinematic hardening law (Andrade et al., 2013):

  $$d\alpha = H d\varepsilon_q^p \tag{9.22}$$

  where H is the hardening modulus.

  The stress-ratio related hardening modulus depends on the distance $b = M^b - \eta$, thus:

  $$H = h\left(M^b - \eta\right) \tag{9.23}$$

  where h is a function of the state variables. As might be assessed both hardening modulus and dilatancy are similar functions, but while the hardening modulus is function of its distance to the bounding stress, M^b, the evolution of the dilatancy is ruled by its distance to the dilatancy stress, M^d.

  The h function is a material parameter which allows the increase of the efficiency of the model by using a non-linear in reverse loading:

  $$h = \frac{G_0 h_0 \left(1 - c_h e\right)}{|\eta - \eta_{in}} \left(\frac{p}{p_{atm}}\right)^{-1/2} \tag{9.24}$$

  where h_0 and c_h are scalar parameters and η_{in} is the value of η at the initiation of a loading process (Dafalias and Manzari, 2004; Taiebat and Dafalias, 2008; Andrade et al., 2013).

  (ii) Evolution law for fabric changes

The soil dilatancy, defined by equation (9.20), also incorporates an evolution law to account the fabric changes during unload reload cycles on the dilatancy values. This is done by introducing a new parameter z which is defined as:

$$dz = -c_z \langle -d\varepsilon_v^p \rangle (sz_{max} + z) \tag{9.25}$$

where $s = \pm 1$ according to $\eta = \alpha \pm m$, and c_z and z_{max} are parameters of the material and represents the maximum value possible of the state parameter z_{ij} and its evolution. As already referred this will not be applied as the tests have not included unload/ reload cycles.

9.2.2 Flow Liquefaction Criterion

Instability systems are a very concerning issue for geotechnical design, due to their sensitivity to small perturbations. Unlike what the common constitutive models idealizes, such as the elasto-perfect plastic Mohr Coulomb model, instability may occur inside the failure surface, given by the critical volume friction angle, ϕ_{cv}. In addition to the constitutive model equations already presented, the ability of the model to predict phenomenon like liquefaction goes beyond what was presented earlier. This occurs as the mechanical stability of granular soils is dictated by the balance laws of thermodynamics, which are often broken by constitutive models, leading to non-conservative results (Ko and Masson, 1976; Zytynski et al., 1978; Einav and Puzrin, 2004; Molano, 2011).

According to the first law of thermodynamic the total energy of a system is given by:

$$\Delta U = \Delta W + \Delta Q \tag{9.26}$$

where ΔW is the incremental work and ΔQ is the energy (e.g for instance heat) which has flowed into the structure from its surrounding.

In triaxial conditions the parcel ΔW is translated as the accumulated dissipated energy due to plastic work, which is given by the following equation:

$$dW_p = \sigma_{ij} \times d\varepsilon_{ij}^p = p \times d\varepsilon_v + q \times d\varepsilon_q \tag{9.27}$$

Whereby instability can only occur under undrained conditions, when the change in volumetric strain is zero, and the second component of equation (9.27) is the only that remains.

As referred by Ramos (2010), Hill and Drucker proposed some stability postulates which also assure uniqueness in both dynamic and static loading conditions. This postulate requires that the

second increment of plastic work is greater or equal to zero. Therefore negative increments result in instability.

Negative increments often occur in granular soils after the peak strength being reached, while subjected to undrained shearing. Thus these peak strengths, which define the IL, are associated to the starting of an instability process (Hill, 1958):

$$d^2W = \frac{1}{2} dq \times d\varepsilon_q \tag{9.28}$$

$$d^2W = 0 \rightarrow q = 0 \tag{9.29}$$

Despite, as reported by Lade (1999), flow instability being a necessary condition for flow liquefaction to occur, they are not synonymous. As pointed out by Carrera (2008), not all peak points imply the liquefaction of the soil. Therefore it becomes important a proper modeling of the onset of flow liquefaction instability. SANISAND model, similarly to NORSAND, consider the triggering of flow liquefaction through a change of the hardening modulus, H (Jefferies and Been, 2006; Andrade, 2009; Been and Jefferies, 2004). Therefore, as quoted by Andrade (2009), the onset of instability is a function of the sand state (see equation 9.23). In fact, when the second-order work disappears, the general elasto-plastic formulation is characterized by a zero hardening modulus. When liquefaction occurs not only the soil becomes unstable ($d^2W = 0$), but a loss of uniqueness also succeeds. If the hardening modulus equals zero, $H = 0$, the stiffness matrix also equalize zero. This is where the importance of using a non-associated flow rule relies. An associated elasto-plastic constitutive model does not allow for the symmetric part of the compliance elasto-plastic matrix to become positive semidefinite, i.e. does not allow for the plastic part, which incorporates H, to annul (Nova, 1989; Ramos, 2010). For a better clarification of these concepts an explanation is presented below.

As explained by Andrade (2009), an elasto-plastic model has the following general formulation for triaxial conditions:

$$\begin{Bmatrix} d\varepsilon_v \\ d\varepsilon_q \end{Bmatrix} = \begin{bmatrix} \frac{1}{K} + \frac{1}{H\partial_p Q \partial_p F} & \frac{1}{H\partial_p Q \partial_q F} \\ \frac{1}{H\partial_q Q \partial_p F} & \frac{1}{3G}\frac{1}{H\partial_q Q \partial_q F} \end{bmatrix} \begin{Bmatrix} dp \\ dq \end{Bmatrix} \tag{9.30}$$

Under undrained conditions $\varepsilon_v = 0$ and the maximum increment of peak strength is zero, $dq = 0$, therefore it simplifies to the following equation:

$$\left(\frac{1}{K} + \frac{1}{H\partial_p Q \partial_p F} \right) dp = 0 \tag{9.31}$$

and since usually dp is distinct from zero, ($dp^{'} \neq 0$), the parentheses are eliminated.

Later, it was explored by Andrade (2009) that for the compliance matrix to equal zero, it is possible for critical/ limiting hardening modulus to be higher than zero, H_L (Andrade, 2009; Ramos, 2010). Regardless the model used will not consider a limiting hardening modulus.

In the scope of this work instability was only assessed for soils under loose conditions, both under monotonic shear undrained conditions and drained loading conditions. The study of shear bands on dense sands under drained loading conditions, which are also considered an instability of soil behavioral (Ramos, 2010), were not considered.

9.3 Parametrical Calibration For SANISAND Modelling

9.3.1 Model Constants

The next Table 9.1 summarizes the parameters and initial state values included in this version of SANISAND constitutive model. These model constants were determined from drained and/or undrained triaxial compression and extension tests. While the critical state parameters used were previously presented in Chapter 7, together with the elastic shear modulus G0, the rest of the parameters needed to be determined in the scope of the present chapter. Before going further is important to assign that, according to the authors' recommendations, c_h, h_0, are related to the effect of distance from the bounding surface, and similarly to z_{max} and c_z both are parameters empirically achieved by a trial-and-error procedure (Dafalias and Manzari, 2004). Similarly the m constant, the tangent of the opening angle of the yield surface at the origin, can be determined by a trial-and-error procedure and shall be as small as possible in order to have a narrow yield surface. The significance of this value is of high relevance while under cyclic loading, however in this chapter there is only the intention to cover monotonic loading conditions. Therefore only three parameters, n^d, A_0 and n^b needed to be determined.

The parameter n^d can be determined at the phase transformation state, at which $D = 0$, using the following equation:

$$n^d = \frac{1}{\psi^d} \ln\left(\frac{\alpha^d}{\alpha^c}\right) \tag{9.32}$$

where ψ^d and α^d are the values of ψ and α at the phase transformation state, measured from drained or undrained triaxial test results, and $\alpha^c = M_c - m$ (Taiebat and Dafalias, 2008). The parameter α^c might be determined by using the M determined from the extension, instead of the compression triaxial tests, if and only if working under unloading conditions. The parameter n^d was not calculated for tested materials as there were no sufficient dense tests to achieve it value. Regardless as long as considering a value higher than M^c no problems occur in modeling loose

Table 9.1: Constitutive model parameters and initial state values (adapted from Dafalias and Manzari (2004))

	Symbol	Description
Model parameters		
Elastic behavior	G_0	Elastic shear modulus – Richart et al. (1970)
	ν	Poisson coefficient
Critical state	M_c	CSL slope in p':q space
	c	CSL extension/compression
	e_0	Void ratio at p_0 on the CSL
	λ	Critical state line curvature parameter
	ξ	Critical state line exponent
Dilatancy	n^d	Factor for the stress projection on the dilatancy surface
	A_0	Dilatancy factor
Plastic modulus	n^b	Factor for the stress projection on the boundary surface
	h_0	Hardening modulus parameter
	c_h	Hardening modulus parameter
Yield surface	m	Half vertex angle of the yield surface
Fabric-dilatancy tensor	z_{max}	Maximum attainable value of z
	c_z	Control of the pace evolution of z
Model initial values		
	e_0	Initial void ratio
Principal stress components	σ_{11}	Initial vertical confining stress
	σ_{22}	Initial horizontal confining stress
	σ_{33}	Initial horizontal confining stress
Other direction stress components	σ_{12}	=0 for triaxial conditions
	σ_{13}	=0 for triaxial conditions
	σ_{23}	=0 for triaxial conditions

soils, as for $e > e_c$, $\psi > 0$, $M^b < M^c < M_d$. Therefore a trial-error procedure was also adopted to determine this constant.

The parameter A_d might be estimated, ignoring the elastic component, through drained strain-volumetric curves:

$$\frac{d\varepsilon_v}{d\varepsilon_a} \cong \frac{d\varepsilon_v^p}{d\varepsilon_v^p} = A_d \left(\alpha^d - \alpha\right) \tag{9.33}$$

where α^d is the value of α at the phase transformation state and α the current stress ratio (Dafalias and Manzari, 2007). Similarly to n^d, also n^b can be determined by evaluating the following equation at the peak stress ratio, thus at Hvorslev surface:

$$n^b = \frac{1}{\psi^b} \ln\left(\frac{\alpha^c}{\alpha^b}\right) \tag{9.34}$$

where ψ^b and α^b are the values of ψ and α at the peak stress-ratio state, measured from drained or undrained triaxial test results (Taiebat and Dafalias, 2008).

9.3.2 Calibration Of Osorio Sand

9.3.2.1 Definition Of The Parameters From Laboratory Data

As most triaxial tests performed with Osorio sand were on loose conditions, most SANISAND parameters were determined by a trial-error procedure based on the laboratory results, with exception for the critical state parameters. Even the elastic shear modulus, G_0, determined on laboratory was changed to better capture Osorio sand behavior.

Table 9.2 provides the parameters of SANISAND calibrated for the triaxial tests performed with Osorio sand.

It is important to emphasize that the Poisson coefficient shall be adopted within a range of small values, in order to reproduce the effect of an instantaneous increment impact. This low value physically means that when the soil is subjected to an instantaneous axial incremental load it results on an axial strain much larger than the radial strain.

As the triaxial tests performed with Osorio sand only incorporated a set of stress-paths with compression or constant shear stress conditions, the fabric-dilatancy tensors were not calibrated.

Table 9.2: SANISAND parameters for Osorio sand

	Symbol	Description
Model parameters		
Elastic behavior	115	Elastic shear modulus (G_0)
	0.10	Poisson ratio (ν)
Critical state	1.29	CSL slope in p':q space (M)
	0.699	CSL extension/compression (c)
	0.783	Void ratio at p_0 on the CSL (e_0)
	0.0217	Critical state line curvature parameter (λ)
	0.624	Critical state line exponent (ξ)
Dilatancy	3.5	Factor for the stress projection on the dilatancy surface (n^d)
	0.750	Dilatancy factor (A_0)
Plastic modulus	1.20	Factor for the stress projection on the boundary surface (n^b)
	6.50	Hardening modulus parameter, first scalar (h_0)
	1.14	Hardening modulus parameter, second scalar (c_h)
Yield surface	0.03	Half vertex angle of the yield surface (m)

9.3.2.2 Calibration Results

The comparison between the results achieved with the model and the tests data are presented in Figure 9.2 and in Figure 9.3.

As discussed in Chapter 7 both drained and undrained triaxial tests performed with Osorio sand achieved a unique ultimate state, thus a unique CSL. This feature allowed a good agreement with the results obtained after calibrating SANISAND.

By analyzing both figures, it can be seen that the modeling results present a good accuracy when compared with the real data tests. Nevertheless some differences are observed. These differences might be associated to the errors on the volume measurements of the specimen which, within a narrow range void ratios, can have a huge impact. As the CSL displays a low value for its slope, typical of sandy soils, these differences, however small, may result in a distinct modeling response of the soil. Excepting the errors associated with volume measurements, the biggest differences between the experimental and the model prediction are addressed to the volumetric strain. While

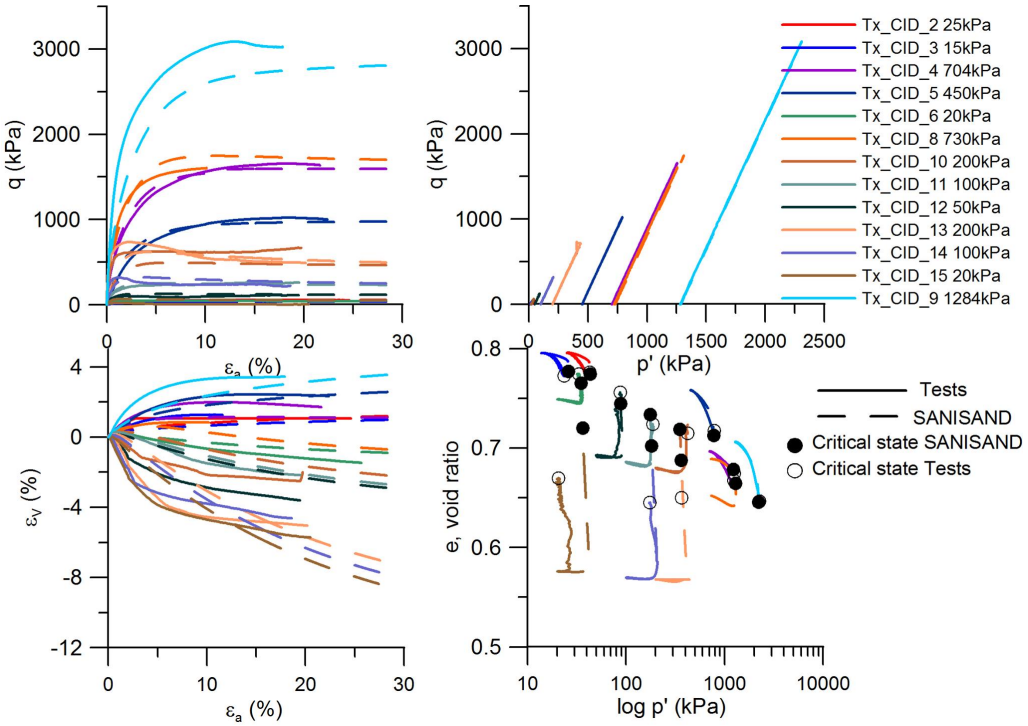


Figure 9.2: Comparison between the drained triaxial tests achieved with SANISAND and the real tests for Osorio sand

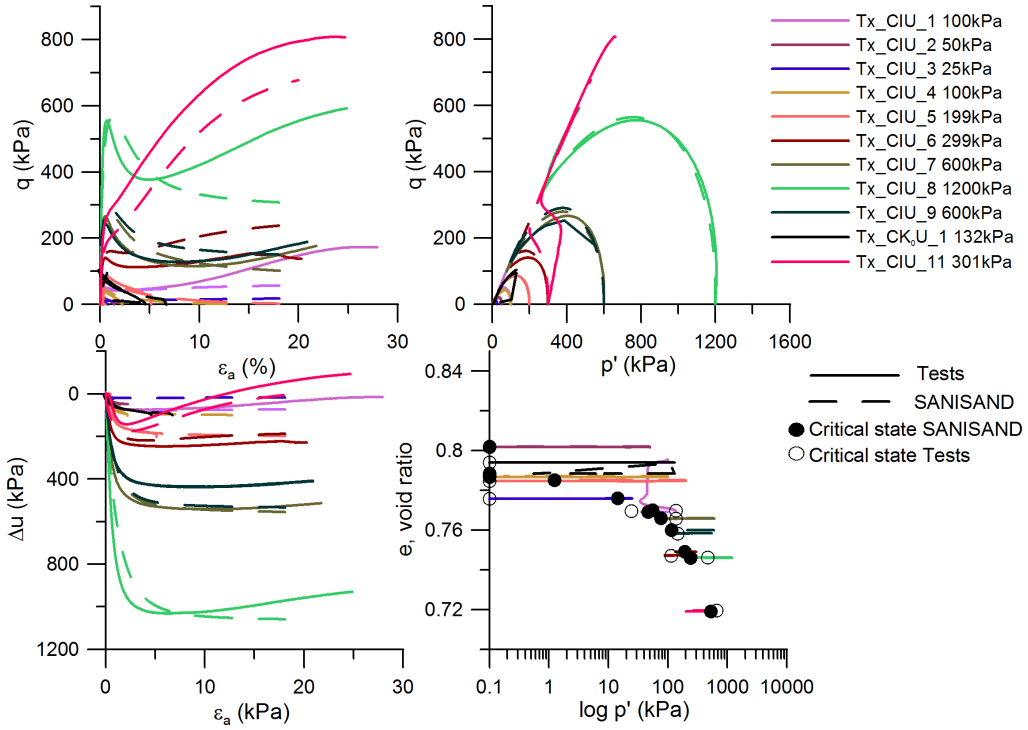


Figure 9.3: Comparison between the undrained triaxial tests achieved with SANISAND and the real tests for Osorio sand

in experimental data the majority of the volumetric strain occurs for low axial strains, on the other hand, SANISAND model data display an almost linear correlation between the volumetric strain and the axial strain. Nevertheless beyond these volumetric-strain curves being the results achieved with very dense specimens, for which the model was not properly calibrated, these were not performed at LabGeo in the scope of this research.

A detailed comparison between the tests predicted with SANISAND model and the experimental ones, mainly for the low confined triaxial tests, is displayed in Figures 9.4 and 9.5.

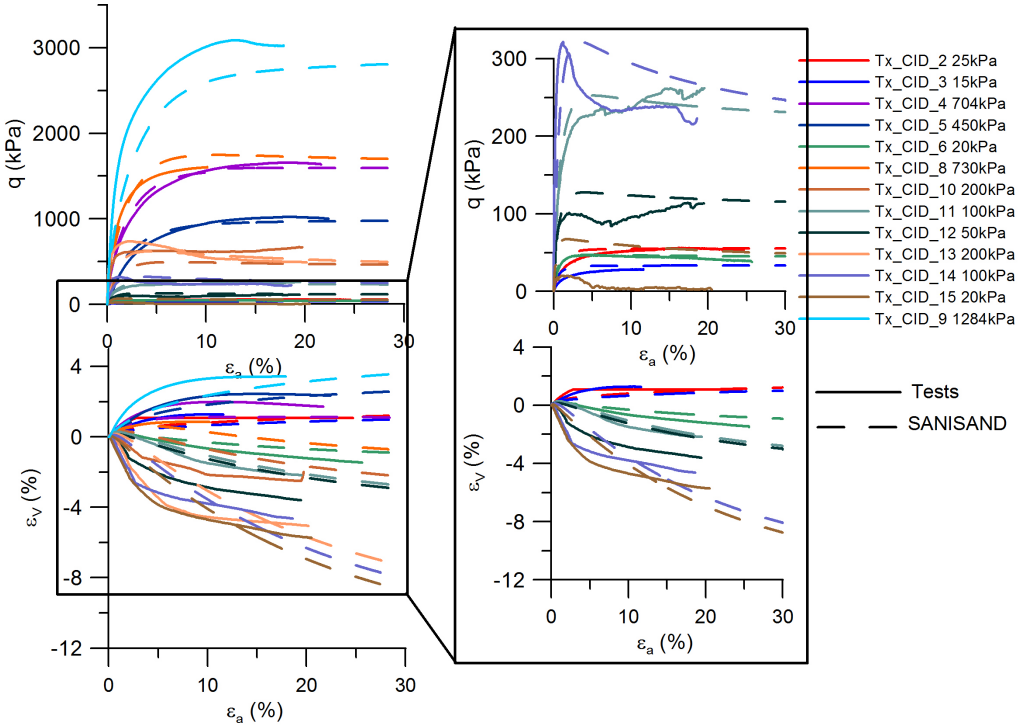


Figure 9.4: Detail of the comparison between the drained triaxial tests achieved with SANISAND and the real tests for Osorio sand

Aiming to evaluate the sensitivity of the model to the void ratio, a variation of $\pm$ 0.025 was adopted and applied. The results are clear and display large differences between each simulation which can be as high as 200% on shear strength under undrained conditions (see Figure 9.6).

This sensitivity analysis pursued to investigate the effect of laboratorial errors, mainly associated to void ratio measurement, on the model calibration. This corroborates the reasons pointed above for the differences observed between the model and the experimental data. In fact due to the reduced steepness of the CSL these errors are more likely to occur.

From the figures above it was also perceived the ability of the Hill condition to predict the onset of Osorio sand liquefaction. In order to understand this ability under distinct stress-paths the model was similarly tested for the drained triaxial tests performed with decreasing mean confining stress and constant deviator stress. Figure 9.7 shows the results achieved with the model (represented by dashed lines) which can be compared with the experimental data (represented by continuous

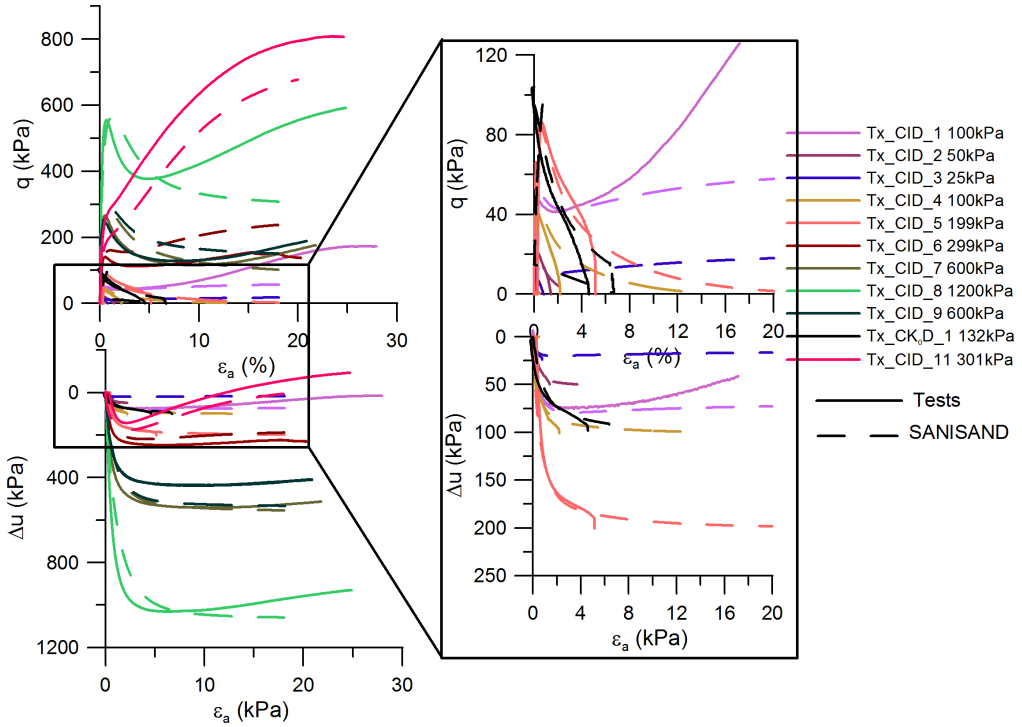


Figure 9.5: Detail of the comparison between the undrained triaxial tests achieved with SANISAND and the real tests for Osorio sand

lines). Apparently something happens after the tests achieve the failure surface; however, as it was already expected it does not predict liquefaction onset.

As explained before, the Hill condition detects the IL, i.e. the onset of flow instability, based on the postulate that the second increment of plastic work is greater or equal to zero. However as q remains constant, the increment of plastic work is in effect zero, thus the instability is not detected.

As discussed previously in Chapter 7, the IL might not be detected by this artifice as it is influenced by the soil state condition. Furthermore these types of tests also have the peculiarity of not exhibiting a large volumetric strain before reaching the IL. Whereby flow liquefaction onset occurs for the same initial state conditions. Nevertheless, instability under drained and undrained conditions are not the same as one is caused by an unstable microstructural fabric rearrangement and the second one is due to a contractive condition of the mechanical behaviour of loose granular material and consequent pore pressure increase (Matiotti et al., 1995).

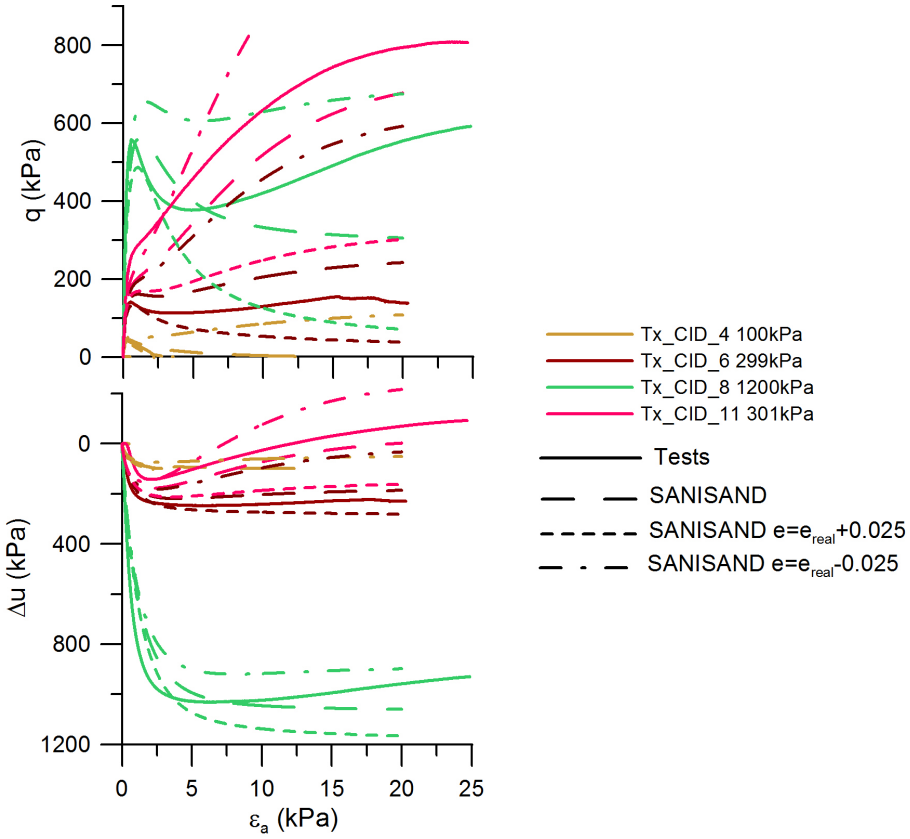


Figure 9.6: Sensitivity analysis of the void ratio for Osorio sand

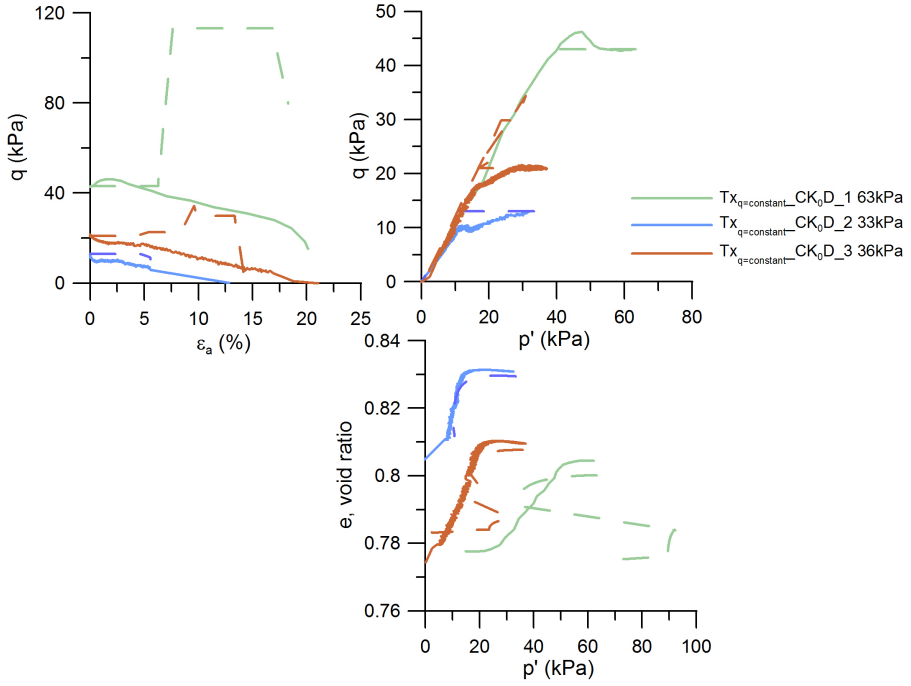


Figure 9.7: Detail of the comparison between the $T_{x_{q=constant}}_CK_0D$ tests achieved with SANISAND and the real tests for Osorio sand

9.3.3 Calibration Of Mixture

9.3.3.1 Definition Of The Parameters From Laboratory Data

Similarly to Osorio sand the only model parameters which were calibrated from the experimental data were the critical state parameters. For the same reasons pointed earlier, also the elastic shear modulus and the Poisson ratio were determined by a trial-error procedure.

Unlike Osorio sand, Mixture presented a distinct behavior under drained and undrained triaxial tests, which led to distinct ultimate states, the CSL and the SSL, respectively. Therefore, and as expected, the calibration had to be done separately for the drained and undrained triaxial tests.

The parameters achieved for both situations differ exclusively on the critical state line and on the dilatancy factor. Apart the CSL parameters a possible explanation is presented for the necessity of changing the dilatancy parameter.

Table 9.3: SANISAND parameters for Mixture

	Symbol	Description
Model parameters	Drained/ Undrained/ Undrained K_0	
Elastic behavior	60	Elastic shear modulus (G_0)
	0.05	Poisson ratio (ν)
Critical state	1.39	CSL slope in p':q space (M)
	0.524	CSL extension/compression (c)
	1.137/ 0.987/ 1.050	Void ratio at p_0 on the CSL (e_0)
	0.540/ 0.455/ 0.455	Critical state line curvature parameter (λ)
	0.0716/ 0.027/ 0.027	Critical state line exponent (ξ)
Dilatancy	6.5	Factor for the stress projection on the dilatancy surface (n^d)
	0.70/ 0.40/ 0.40	Dilatancy factor (A_0)
Plastic modulus	0.7	Factor for the stress projection on the boundary surface (n^b)
	2.00	Hardening modulus parameter, first scalar (h_0)
	1.18	Hardening modulus parameter, second scalar (c_h)
Yield surface	0.03	Half vertex angle of the yield surface (m)

9.3.3.2 Calibration Results

The comparison between the experimental data tests and the tests predicted by the model is presented in both Figures 9.8 and 9.9. A separation between the drained and the undrained triaxial tests was performed for a better analysis. Plus for simplicity the SSL nomenclature was not used, therefore all the ultimate states were addressed as critical states (either achieved by drained or undrained conditions).

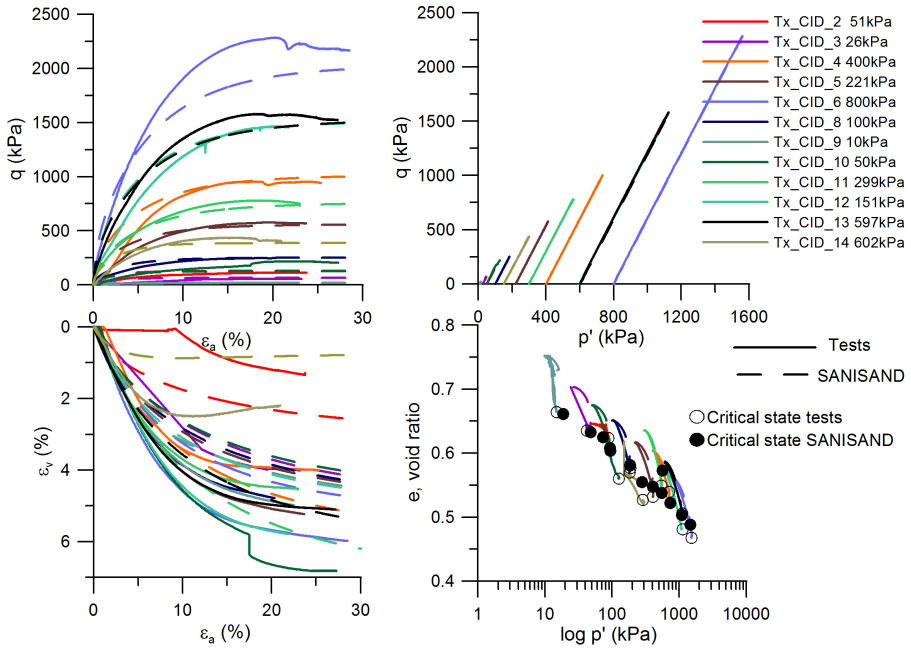


Figure 9.8: Comparison between the drained triaxial tests achieved with SANISAND and the real tests for Mixture

By comparing the results is obvious the ability of the model to capture the overall behavior of the Mixture. Besides, unlike Osorio sand, the volumetric strain-axial strain curves reproduced by the model are very similar to experimental results.

On the other hand the results of the undrained triaxial tests, after changing the CSL parameters, jointly with the A_d parameter, apparently are able, with more or less accuracy, to predict both peak and residual strengths (excepting for the Tx_CK$_0$U_2 test). Besides, in order to achieve a proper simulation, for the K$_0$-consolidated triaxial tests, the e_{c0} parameter had also to be changed according to the results presented in Table 7.13.

A detail of both Figures 9.8 and 9.9 is displayed in Figure 9.10 and 9.11.

The re-calibration of the parameters between the drained and the undrained triaxial tests was pursued as the model only incorporates a unique ultimate state line. If the critical state parameters adopted for the drained triaxial tests were used to predict the undrained triaxial tests the model would lost the ability to predict the ultimate shear strength, but not the peak strength. Figure 9.12

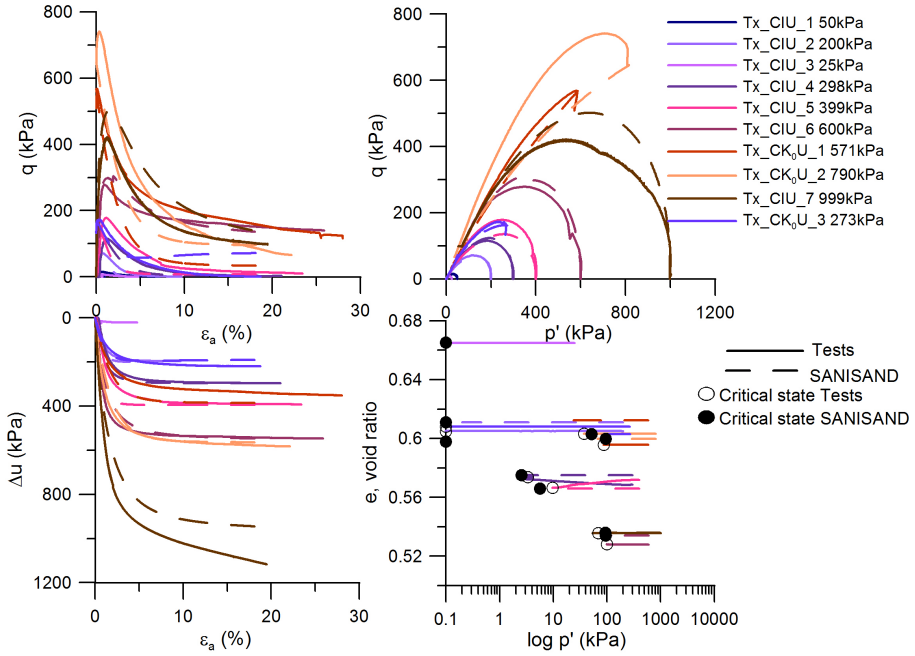


Figure 9.9: Comparison between the undrained triaxial tests achieved with SANISAND and the real tests for Mixture

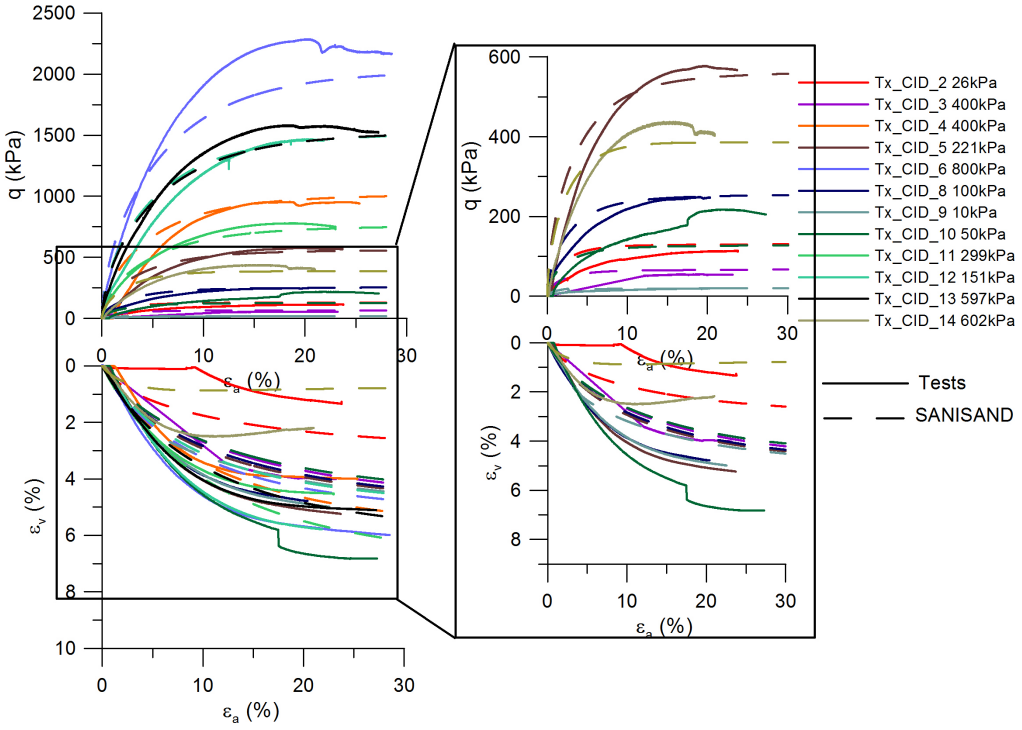


Figure 9.10: Detail of the comparison between the drained triaxial tests achieved with SANISAND and the real tests for Mixture

shows the differences between the soil behaviors reproduced with the parameters calibrated from the drained triaxial tests and with the parameters calibrated from the undrained triaxial tests.

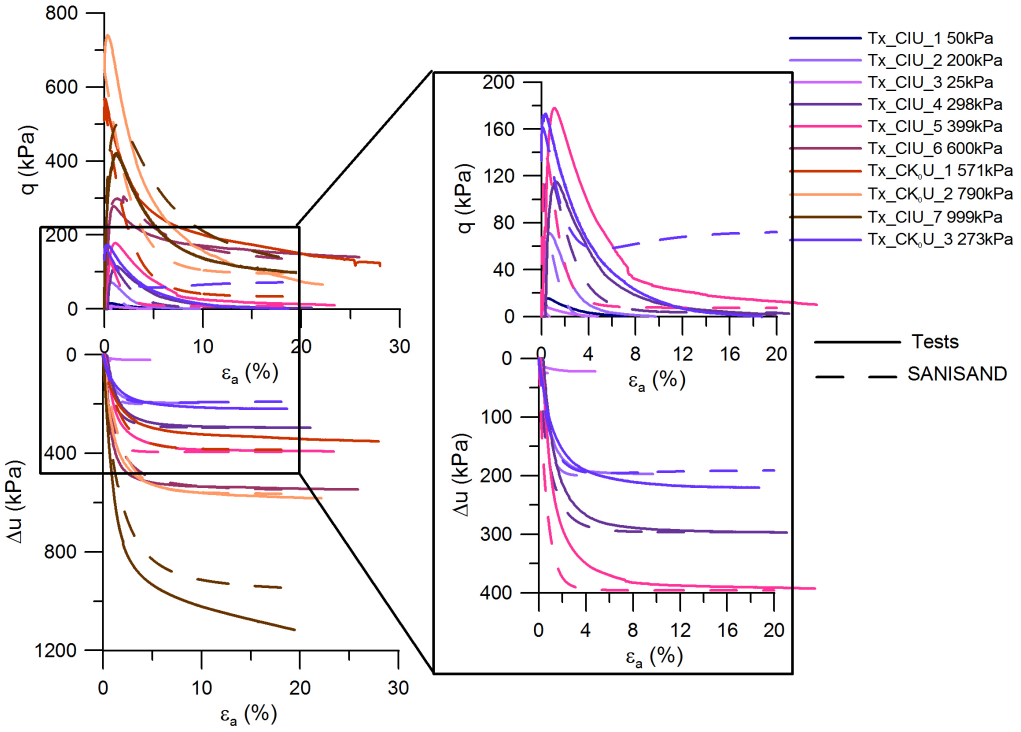


Figure 9.11: Detail of the comparison between the undrained triaxial tests achieved with SANISAND and the real tests for Mixture

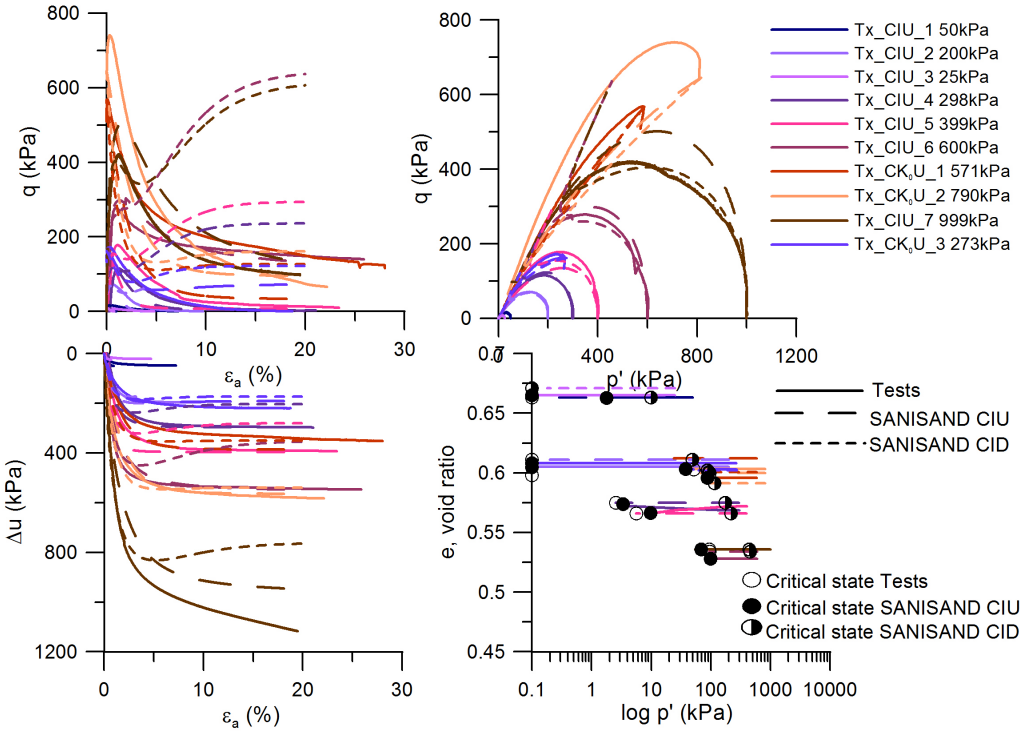


Figure 9.12: Comparison between the undrained triaxial tests achieved with SANISAND calibrated with the drained triaxial tests from those achieved with SANISAND calibrated and with the real tests for Mixture

By changing the critical state parameters, as already expected, the model stops being able to predict the minimum and ultimate strengths of the soil. Beyond the drop of strength not being as pronounced due to the proximity between the dilatancy surface and the critical state, the soil hardens towards the CSL, whereby exhibiting a much higher ultimate strength. Therefore due to the model limitation the CSL positioning has to be changed for properly modeling the soil behavior.

The necessity of also change the A_d parameter is mainly associated to the distinct behaviors observed between the drained and the undrained triaxial tests. In fact, it is believed, that the direct association between the positive pore-water pressure, under undrained conditions, and positive volumetric strain, under drained conditions, is no longer valid if the ultimate states diverge. Thus it is valid to assume that the ratio between the volumetric and the axial strain is distinct between the drained triaxial tests and what would be its effect on the undrained triaxial tests.

Similarly to Osorio sand the model was tested for the $T_{x_{q=constant}}_CK_0D$ tests. These results are more clear than those obtained earlier. However, the clear drop of shear strength before the failure surface is still not properly captured by the model (see Figure 9.13). The reasons pointed before also apply here and explain the lack of accuracy of the model in predicting this particular type of stress-path.

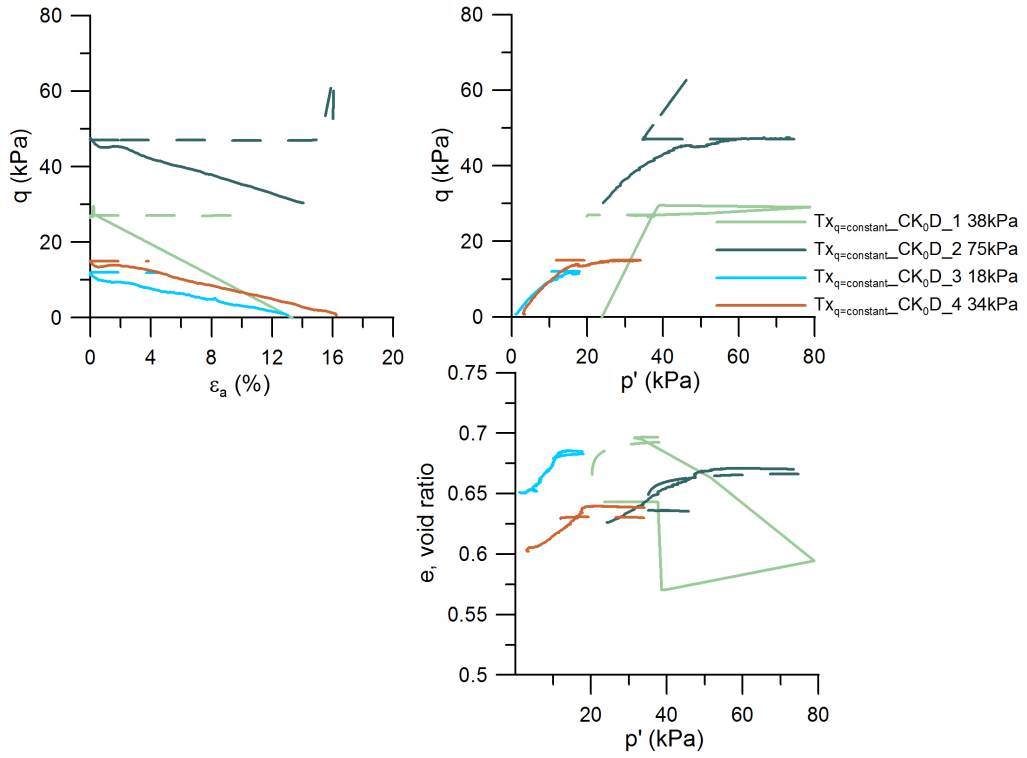


Figure 9.13: Detail of the comparison between the $T_{x_{q=constant}}_CK_0D$ tests achieved with SANISAND and the real tests for Mixture

9.4 Limitations Of The Model

The overall behavior of the model was positive as in general it captured properly the real soil behavior. Notwithstanding two major modifications are required for the model to be improved.

On one hand the model shall differentiate CSL from SSLs in order to better reproduce either the volumetric strain curves or the excess pore water pressure curves given by the real soil behavior. As observed previously the behavior of the Mixture could only be accurately predicted if two distinct curves were adopted among the drained and undrained compression triaxial tests. This SSL is the ultimate state achieved by soils which, after crossing the dilatancy surface, do not have sufficient stored energy to harden towards the CSL, which unlike the CSL is not unique (as concluded previously in Chapter 7).

On the other hand Hill condition was concluded to not being able to predict soil liquefaction under q constant stress-path. Therefore a better way which can identify the points of instability shall be considered to be further incorporated in a new version of the model.

Chapter 10

Conclusions

10.1 Conclusions

During this research six different materials were investigated under laboratory conditions. This study included the performance of a large set of both triaxial and direct simple shear tests, under both monotonic and cyclic loading conditions. Then the experimental data, focused on CSSM, was used to investigate the limitations of the current frameworks used to predict soil liquefaction, and to propose new approaches for it evaluation. Therefore a methodological investigation on the factors affecting soil liquefaction was carried out.

10.1.1 Static Liquefaction

Soil liquefaction predictability is beyond consensus. For this reason it research is continuously improving helping not only it insight but also the development of newer tools to predict soil liquefaction potential. It is in this context that this research appears, aiming to provide a minor contribution for the scientific society for further applications for design companies.

The results achieved with this research, exclusively laboratorial, allowed clarifying some concepts but mainly to understand the limitations of the actual frameworks used to predict soil liquefaction. Whereby new tools were also proposed which reliability shall be further investigated.

As most frameworks used to evaluate soil liquefaction are based on the state parameter, which measures the initial state of a soil with reference to it ultimate state, this work was developed basing on the CSL (or SSL) definition. The greatest advantage of using this parameter is the inherent connection existent between the initial relative density and the initial stress state. So not only this work allowed evaluating the state parameter reliability but it also allowed determining the most suitable parameter for soil liquefaction predictability.

According to what was observed on Chapter 7, soils initially on loose conditions and sheared on a triaxial device will liquefy for very low initial confining stresses and will strain harden towards the CSL for medium to high initial confining stresses. In between, and only for well graded soils, the soil will strain soften towards what was denominated by SSL. Therefore after crossing the CSL and when it achieves the dilatancy surface, if the soil does not have sufficient stored energy to going back to the CSL, then it will tend to a distinct ultimate state. Thus a bifurcation was observed between soils sheared under drained and non-drained conditions, which led to the SSL and CSL, respectively.

Aiming to understand this divergence, Osorio sand, Mixture and Silt were also studied under a constant deviator stress-path which was led to failure, under drained conditions, by an induced increasing pore-pressure. On first instance this allowed to understand that instability was not a phenomenon exclusively addressed to undrained conditions, but a phenomenon associated to microstructure instability, inherent to the loose rearrangement between the soil grains. Still and due to the necessity to carry out this stress-path under an initial induced anisotropic stress state condition, instability was questioned to be the same as the one carried out by the undrained compression triaxial tests. Hence a set of triaxial tests was performed, with the Mixture and the Gold tailings, on a "Bishop-Wesley" device, with a diminishing or constant mean effective stress-path, under drained conditions. The results were obvious and indicated that, despite not resulting on instability, the development of a large volumetric strain led the triaxial tests to the SSL initially defined by the undrained compression triaxial tests.

For the reason pointed above the state parameter was always measured, for soil liquefaction potential evaluation purposes, with reference to the SSL. This research also allowed concluding that SSL moves downwards with an increasing degree of saturation, with decreasing K_0, and possibly, although not conclusive, with inherent anisotropy. Thus and for practical purposes and in agreement to the presented work, when assessing soil liquefaction potential, adopting the state parameter measured with reference to the lowest SSL positioning, which is achieved with undrained compression triaxial tests carried out with completely saturated specimens (B>0.97). The reliability of the state parameter to predict soil liquefaction potential was also observed to be compromised for monogranular soils where a minimum change on the void ratio might lead to a complete stable behaviour or to liquefaction. Nevertheless it association either to the brittleness index (I_B) or to the normalized peak strength q_1 or to the normalized shear wave velocity Vs1 provides reliable tools for liquefaction assessment. Obviously the greatest disadvantage of the state parameter is the necessity of determining CSL positioning, which is a slow and expensive procedure for most companies.

Nonetheless it was shown that shear wave velocities (V_s) are an even better parameter to estimate soil liquefaction potential, discarding the necessity of determining SSL positioning. Although careful shall also be taken when considering monogranular sands, where a minimum change of the shear wave velocity correspond to a quick transition between flow liquefaction and strain

hardening. This delimiting region given by the SSL flat branch for low to medium confining stresses for clean loose monogranular sands.

Chapter 7 also allowed concluding that the ratio between the shear wave velocity and the peak strength, V_{s0}: q_{peak}, reveals to be the best parameter to be used to assess soils liquefaction potential. The association between both large and small displacement parameters which are controlled (although differently) by the void ratio, mean stresses, compressibility, and soil structure and are, therefore, different functions of the same variables, which could anticipate that as a ratio, these two measurements can be useful in predicting, not only liquefaction, but generally soil parameters (adapted from Schnaid et al. (2013)). Furthermore the delimiting ratio V_{s0}: q_{peak} between strain hardening and strain softening behaviours of the soils was found to be function of the coefficient of uniformity – Cu. The correlation achieved between both parameters seems to provide a framework which could, in the future, be used to assess soil liquefaction, regardless the soil type (as long as it is subjected to that type of stress path). It should be also highlighted that this correlation might obviously change with the degree of saturation, among other factors, as V_{s0} and Cu are kept constant while qpeak changes, being representative of lowest boundary for soil liquefaction to take place.

A final remark shall be considered about IL positioning. From this study it was observed that IL moves downwards and to the left with increasing degrees of saturation on the q:p' space and exhibits an increasing steepness with increasing K_0. Despite some authors considering the IL achieved by isotropic consolidated specimens being the lowest limiting boundary for liquefaction to take place, careful shall be taken. In fact, and as explained by other authors ((Fourie and Tshabalala, 2005)), despite the increasing steepness of the IL achieved by K_0-consolidated specimens, the brittleness index is also observed to be higher (i.e. the drop between the q_{peak} and the q_{min} was higher). Therefore studies should be reinforced in this direction.

10.1.2 Cyclic Liquefaction

Coimbra sand and Algeria sand were both picked to be evaluated under laboratory conditions. Both liquefaction susceptibility and the main factors contributing for soil liquefaction potential were investigated, such as initial void ratio (or Dr), initial effective confining stresses, initial induced anisotropy, and rotation or inversion of the principal stresses. This evaluation was exclusively achieved by performing both cyclic triaxial tests and cyclic direct simples shear tests. The final results were then used to build liquefaction assessment frameworks, assessed through parameters such as shear wave velocities and the state parameter.

According to the cyclic Tx test results it was clear, as expected, that an increasing relative density, increases the undrained cyclic resistance. On the other hand the effect of the initial confining stress was not clear and it effect shall be studied according to the phenomena which governs the soil behaviour. In fact while under cyclic mobility it might possible to distinguish this effect,

sample prepared above the cyclic SSL cannot show a clear effect of the initial confining stress. Therefore no major advantages were found on the use of the steady state parameter on cyclic liquefaction evaluation.

From the final results it was also concluded that, for Algeria sand tested under triaxial stress conditions, the contribution of initial static shear stress (K_0=0.5) is responsible for an increasing undrained cyclic resistance on medium-dense sands (Dr>35%-40%) and for a decreasing undrained cyclic resistance on loose sand (Dr<35%). This succeeds as there is transition of phenomena for this particular relative density, between flow liquefaction and cyclic mobility. Obviously this particular relative density, as explained before, seems to be a boundary, which is similar to the SSL achieved on monotonic conditions. However this boundary is located downwards with reference to the SSL achieved under monotonic conditions. The reasoning behind can only addressed to the yielding surface rotation, which softens each time the specimens are unloaded. Thus for the yield surface to shrinks is not only required for principal stress rotation to occur, but it can also takes place each time a stress rotation occurs. On the other for Coimbra sand this limiting boundary, which separates flow liquefaction from cyclic mobility, seems to be the exact same as the SSL achieved under monotonic conditions. Further explanations to the differences between the two soils should be studied having a greater attention on the sphericity of the grains.

This delimiting boundary which separates the distinct phenomena seems to also be the same as the vertical section of the curve proposed by Andrus and Stokoe (1997) for the "Simplified Procedure", used to evaluate soil liquefaction potential basing on the normalized shear wave velocity, V_{s1}. This supports the idea of being only necessary to determined, as long as no principal stress rotation occurs, the delimiting boundary for which soil actually liquefies. As explained previously in Chapter 8, the increasing steepness of the cyclic resistance curves associated to the cyclic mobility guarantee that most of the cyclic actions which are below the failure envelope of the soil will only soften 5% of axial displacement for a number of cycles higher than 15. Therefore the study of the soil anisotropically consolidated should not be so concerned with very high relative densities. On the other hand, for isotropically consolidated specimens careful shall be taken as the cyclic resistance curves associated to cyclic mobility present a lower steepness. Whereby the soil might accumulate large plastic strains for less than 15 cycles, even when the cyclic amplitude is lower than the ultimate shear strength achieved under monotonic conditions.

The main conclusions achieved for anisotropically consolidated specimens prepared with Algeria sand and tested under undrained cyclic triaxial conditions, seem to be the exact same conclusions achieved for Coimbra sand, with regards of the sample preparation. During this research distinct preparation techniques were used to test Coimbra sand cyclic resistance curves. This meant to evaluate the fabric effect on the undrained cyclic resistance of the sand. Unfortunately the results were not as clear as expected as few tests were prepared on very loose conditions. Whereby, apparently, the air pluviation technique contributes for a higher contact between particles which provides a higher resistance to flow liquefaction events. On the other hand, denser specimens seem

to exhibit a same resistance despite the sample reconstitution technique.

In order to evaluate the effect of principal stress rotation a set of cyclic DSS tests were performed. Despite the limitations of the equipment, the large data set results allowed to conclude a much higher cyclic resistance under triaxial conditions than under direct simple shear conditions, being much obvious when cyclic mobility governs the soil behaviour. The higher contractiveness observed under monotonic conditions explains the partial loss of the cyclic resistance under cyclic conditions. Still, the major contribution for this loss of resistance is associated to the continuous principal stress rotation during cyclic loading. On the other hand, if flow liquefaction dominates the soil behaviour, the resistances obtained with the DSS device are very similar with those achieved with the anisotropically consolidated specimens tested under triaxial conditions.

Despite not having sufficient data to allow a direct comparison between the cyclic DSS and triaxial tests, it was also concluded that the c_r factor which corrects the CRR between the two types of tests is not a constant and it varies with the relative density and with the initial confining stress. Therefore a comparison between triaxial and DSS tests is not linear, meaning that the cr factor is not a constant and it should be defined as a non-constant ratio.

From the cyclic DSS results device it was also perceived that the effect of confining stress on cyclic resistance for cohesionless soils is not as clear as has been presented in the literature. In fact, it seems that, at least for both sands tested in this work, contractiveness does not increase with increasing confining stress, perhaps due to fabric rearrangement during principal stress rotation. Previously Vaid et al. (2001) also pointed out that the confining stress for Fraser River sand at the loosest states, in triaxial conditions, "had little effect" on liquefaction resistance, whereby changes in K_σ are very low.

Furthermore it was also observed that although for the Algeria sand the distance between the cyclic resistance curves was greater for higher relative densities (for the number of cycles to failure higher than 3), meaning that cyclic undrained shear resistance is higher for lower confining stresses, in the case of Coimbra sand sand the distance between the lines decreases and they almost converge with increasing confining stress. Such results make unclear any conclusions about the influence of the initial confining stress based on classical K_σ overburden correction factors. The results presented in this paper support conclusions of other workers, such as Wijewickreme et al. (2005), that the CRR gain is a result of the densification effect created by the sample reconstitution and consolidation method, which surpasses the σ'_v effect. Additionally, changes in specimen fabric with plastic strain accumulation during a cyclic loading test also contribute to observed differences in cyclic response.

Regardless of the differences in the actual K_σ values and those obtained in this study (even when they are approximately unity) these differences are too big to be neglected despite being on the safe side.

As a final remark it should be highlighted that factors, such as K_σ and K_α, are far from being completely reliable. Thus an alternative method should be developed by considering a single correction factor which can incorporate the combined effects of each factors which affect soil liquefaction.

Nevertheless good results were achieved by using shear wave velocities V_{s1}, with the limitation of both parameters a, b and V^*_{s1}, from the proposed Andrus and Stokoe equation, need to be re-calibrated for each soil. Further investigations should be made on developing frameworks which relate a, b and V^*_{s1} to a soils' parameter, such as Cu.

On the other hand frameworks which rely on the state parameter despite being consistently good for each soil, beyond requiring the determination of the SSL (or CSL), the boundary which separates liquefaction from nonliquefaction also changes from soil to soil, being it applicability limited. However future developments should focus on the determination of the variables of the equation which is used as a boundary. After, these values should be correlated with a soils' parameter in order to be easily used for the evaluation of soil liquefaction potential of any other soil.

10.1.3 SANISAND Model Application

This work included a calibration of SANISAND model parameters in order to perceive it ability to predict cohesionless soils geomechanical behaviour and it ability to predict soil liquefaction potential. The overall behavior of the model was positive as in general it captured properly the real soil behavior. Notwithstanding two major modifications are required for the model to improve.

After the calibration of both Osorio sand and Mixture it was concluded that the model is not able to differentiate the ultimate state achieved by the drained and undrained compression triaxial tests, which is not, as explained before, a boundary conditions problem.

It inability of differentiating the soil behavior either under drained or undrained compression stress-paths is exclusively related with the fact that the model only incorporates a single CSL. However experimental data showed that soils tend to diverge on a CSL and on a SSL while under drained and undrained conditions, respectively. Therefore for the model to successfully predict both patterns it should differentiate CSL from SSLs.

Furthermore the model seems to also not being able to capture soil instability under stress-paths other than classic compression triaxial tests. This inability of the model to accurately predict soil instability for stress-paths other than compression ones is associated to the Hill condition. As explained previously the Hill condition can only identify liquefaction onset when the second increment of plastic work is greater or equal to zero. However this only occurs when the deviatoric stress is not constant. Therefore the model could not predict liquefaction onset under constant q stress-paths, and it improvement should pass by considering another flow liquefaction criterion.

10.1.4 Implications for design practice

The current frameworks used to assess soil liquefaction potential have been missing some important key factors affecting soil behavior.

In the case of static liquefaction, despite the current design codes not including frameworks and procedures on how to evaluate liquefaction potential, studies have been progressing, mainly associated to CSSM theory. However it is important to highlight that the use of the state parameter to predict soil liquefaction potential shall be made in a judgmental manner. This is mainly due to, as reported previously, the existence of a set of SSLs. Therefore the measurement of state parameter shall always be made, in order to be conservative, with reference to the ultimate states achieved by fully saturated isotropic compression triaxial tests. Nonetheless it assessment should be always, if not only, complemented with Vs waves measurement, but by having previous charts as a reference.

On the other hand, the evaluation of cyclic liquefaction shall consider, according to the in situ conditions, the type of laboratory test to better assess the soil behavior. Beyond being shown that the c_r factor, which corrects the CRR among different equipments, is not only a function of the K_0, it seems that on what concerns to principal stress rotation both "Simplified Procedure" and "Basic Berkeley School assessment charts" are far from being accurate.

10.2 Future Developments

While semi-empirical procedures prevail for assessing soil liquefaction potential there is still much work to be done.

Under monotonic loading conditions futures researches should consider the study of the anisotropic consolidated specimens to ascertain if, despite the increasing IL steepness, there is in fact a higher brittleness associated. This study should assess both SSL positioning and brittleness in order to evaluate if an increasing brittleness is either associated to a lower or to a higher void ratio when compared to those isotropically consolidated. Then if lower void ratios might lead to a stable behaviour than those achieved by isotropically consolidated specimens, then the limit boundary shall be always considered as the one achieved with the last ones.

Future investigations should be carried out focusing on the framework presented on this work, which correlates the ratio V_{s0}: q_{peak} with Cu, in order to perceive it reliability for further applications. It should also consider the K_0-consolidation effect, to perceive if an increasing brittleness would also result, in this type of framework, in a lower boundary, as both V_{s0} and qpeak change with induced anisotropy.

While flow liquefaction seems to be more straightforward, cyclic liquefaction is still a problem of major concern, mainly when principal stress rotation occurs. As the correction factors reveal to mislead a correct interpretation of the soil behaviour, the author suggests, in order to surpass this difficulty, the study of soil liquefaction potential by using stiffness parameters such as shear wave velocity. According to the present study this parameter reveals to be highly accurate and practical. The use of bender elements in others directions other than vertical results can be used in to normalize the effect created by soil fabric or even of particle shapes. By eliminating these effects it becomes more feasible to investigate the real effect of cyclic loading direction, enabling a proper study of the effect remaining factors.

As for the constitutive model it is suggested the implementation of a unique CSL and a set of SSLs. Jointly it should be also modified in order to conceive the possibility of the soil to, when reaching a minimum amount of stored energy, and after reaching the dilatancy surface, to fall in the respective SSL. Therefore all soils which exhibit a strain softening behaviour shall fall on the SSL. The author believes this minimum amount of stored energy to be accurately identified by the critical hardening modulus, H_L, previously presented Andrade (2009) and Andrade et al. (2013). Nevertheless an evolution of the Hill condition shall be considered as it was confirmed it inability to predict liquefaction onset of cohesionless soils under distinct stress-paths (e.g. q constant stress-paths).

Further studies shall also consider the effect of the degree of saturation on SSL positioning to be further incorporated on the constitutive model.

References

Standard practice for determining the normalized penetration resistance of sands for evaluation of liquefaction potential. Standard d6066 – 11, American Standards for Testing and Materials (ASTM).

Geotechnical design d part 3: Design assisted by fieldtesting. Eurocode 7 ENV: 1997 - 3, Brussels: European Committee for Standardization, 1997.

Design of structures for earthquake resistance – part 5: Foundations, retaining structures and geotechnical aspects. Eurocode 8, Brussels: European Committee for Standardization, 2005.

http://www.energyandresources.vic.gov.au/, 2014. Organization: Department of State Development, Business and Innovation, Victoria, Australia.

Abreu, E. Study of the general conditions of liquefaction on coimbra sand under both monotonic and cyclic triaxial tests. Msc in civil engineering, Faculty of Engineering of the University of Porto, Porto, Portugal, 2012.

Al-Tarhouni, M., P. Simms, and S. Sivathayalan. Cyclic behaviour of reconstituted and desiccated – rewet thickened gold tailings in simple shear. *Can. Geotech. J.*, 48:1044–1060, 2011.

Alarcon-Guzman, A., A. Leonards, and J. L. Chameau. Undrained monotonic and cyclic strength of sands. *J. Geotech. Eng.*, 114:1089–1109, 1988.

Allen, N.F., F.E.Jr. Richart, and R.D. Woods. Fluid wave propagation in saturated and nearly saturated sands. *J. of Geotech. Eng.*, 106(GT3):235–254, 1980.

Ambraseys, N. N. Engineering seismology: Part i. *Earthquake Engineering and Structural Dynamics*, 17(1):1–105, 1988.

Andrade, J. E., A. M. Ramos, and A. Lizcano. Criterion for flow liquefaction instability. *Acta Geotechnica*, 8(5):525–535, 2013.

Andrade, J.E. A predictive framework for liquefaction instability. *Gèotechnique*, 59(8):673–682, 2009.

Andrus, R. D. and K. H.II. Stokoe. Liquefaction resistance of soils from shear-wave velocity. *J. Geotech. Geoenviron. Eng.*, 126(11):1015–1025, 2000.

Andrus, R. D. and K.H.II. Stokoe. Liquefaction resistance based on shear wave velocity. Technical report, National Center for Earthquake Engineering Research (NCEER), 1997.

Andrus, R. D., K. H. II. Stokoe, and C. Hsein Juang. Guide for shear-wave-based liquefaction potential evaluation. *Earthquake Spectra*, 20(2):285–308, 2004.

APNC, Autoridade Nacional de Protecção Civil. Estudo do risco sísmico e de tsunamis do algarve. Technical report, Direcção Nacional de Planeamento de Emergência / Núcleo de Riscos e Alerta, 2010. Portuguese.

Atkinson, J. *An introduction to the mechanics of soils and foundations: through critical state soil mechanics*. McGraw-Hill Book Company (UK) Ltd, 1993.

Atkinson, J. *The Mechanics of Soils and Foundations, Second Edition*. Spon text. Taylor & Francis, 2007.

Azam, S. and Q. Li. Tailings dam failures: a review of the last one hundred years. *Geotechnical News*, 28(4):50–54, 2010.

Barrera, Sergio, Luis Valenzuela, and Jose Campaña. Sand tailings dams: design, construction and operation. Proceedings Tailings and Mine Waste, 2011.

Baziar, M. H., Y. Jafarian, H. Shahnazari, V. Movahed, and M. Amin Tutunchian. Prediction of strain energy-based liquefaction resistance of sand–silt mixtures: An evolutionary approach. *Computers & Geosciences*, 37(11):1883–1893, 2011.

Bedin, J. *Study of the geomechanical behavior of tailings*. Phd thesis in civil engineering, Universidade Federal do Rio Grande do Sul, Rio Grande do Sul, Brazil, 2010. Portuguese.

Bedin, J., F. Schnaid, A. FonsecaViana da , and L. Costa-Filho. Gold tailings liquefaction using critical state soil mechanics concepts. *Géotechnique*, 62(3):263–267, 2012.

Been, K. and M. Jefferies. Stress dilatancy in very loose sand. *Can. Geotech. J.*, 41(5):972–989, 2004.

Been, K. and M. G. Jefferies. A state parameter for sands. *Géotechnique*, 35(2):99–112, 1985.

Been, K. and M. G. Jefferies. Answer to discussion of "a state parameter for sands". *Geotéchnique*, 36(1):127–132, 1986.

Been, K., M. G. Jefferies, and J. Hachey. The critical state of sands. *Géotechnique*, 41(3):365–381, 1991.

Belloti, R., J. Jamiolkowski, D. C. F. Lo Presti, and D. A. O'Neill. *Anisotropy of small strain stiffness of Ticino sand*, volume 46. Geotechnique, 1996.

Bendimerad, F. M., Sarah K. N., and G. Marjorie. The boumerdes, algeria, earthquake may 21, 2003: Eeri learning from earthquakes reconnaissance report. Technical report, Earthquake Engineering Research Institute, 2003.

Bishop, A.W. Progressive failure with special reference to the mechanism causing it. panel discussion. volume 2, pages 142–150, Oslo, Norway, 1976. Proc. of the Geotech. Conf., Norwegian Geotechnical Institute, Oslo.

Bjerrum, L. and A. Landva. Direct simple-shear tests on a norwegian quick clay. *Géotechnique*, 16(1):1–20, 1966.

Blewett, J., I. J. Blewett, and P. K. Woodward. Phase and amplitude responses associated with the measurement of shear-wave velocity in sand by bender elements. *Can. Geotech. J.*, 37: 1348–1357, 2000.

Bobei, D., S. R. Lo, D. Wanatowski, C. T. Gnanendran, and M. Rahman. A modified state parameter for characterizing static liquefaction of sand with fines. *Can. Geotech. J.*, 46(3):281–295, 2009.

Bolt, B.A. Nuclear explosions and earthquakes, 1976.

Bolton, M. D. Strength and dilatancy of sands. *Géotechnique*, 36(1):65–78, 1986.

Bouckovalas, G. D., K. I. Andrianopoulos, and A. G. Papadimitriou. A critical state interpretation for the cyclic liquefaction resistance of silty sands. *Soil Dynamics and Earthquake Eng.*, 23(2): 115–125, 2003.

Bouhadad, Y., A. Nour, A. Slimani, N. Laouami, and D. Belhai. The boumerdes (algeria) earthquake of may 21, 2003 (mw = 6.8): Ground deformation and intensity. *Journal of Seismology*, 8:497–506, 2004.

Boulanger, R. and I. Idriss. Evaluating the potential for liquefaction or cyclic failure of silts and clays. Technical report, Depart. of Civil and Environ. Eng. College of Eng., University of California, 2004.

Boulanger, R.W. Relating k_α to relative state parameter index. *J. of Geotech. and Geoenviron. Eng., ASCE*, 129(8):770–773, 2003.

Bray, J. and R. Sancio. Assessment of the liquefaction susceptibility of fine-grained soils. *J. of Geotech. and Geoenviron. Eng.*, 132(9):1165–1177, 2006.

Burton, S. and G. Scobie. Soil improvement for liquefaction mitigation using nanoparticles. http://liquefactionmitigation.weebly.com/problem-statement.html. Publisher: The University of Edinburgh, Edinburgh.

Cabral, J., C. Moniz, J. Batló, P. Figueiredo, J. Carvalho, L. Matias, P. Teves-Costa, R. Dias, and N. Simão. The 1909 benavente (portugal) earthquake: search for the source. *Natural hazards*, 69(2):1211–1227, 2013.

Carrera, A. *Mechanical behaviour of Stava tailings*. Phd thesis in civil engineering, Politecnico di Torino, Torino, Italy, 2008.

Carrera, A., M. R. Coop, and R. Lancellotta. The influence of grading on the mechanical behaviour of stava tailings. *Géotechnique*, 61(11):935–946, 2011.

Casagrande, A. Characteristic of cohesionless soils affecting the stability of slope and earth fill. *J. of the Boston society of Civil Eng.*, pages 13–32, January 1936.

Casagrande, A. Liquefaction and cyclic deformation of sands — a critical review. volume 5, pages 79–133, Buenos Aires, Argentina, 1975. In Proc. of the 5th Pan-American Conf. on Soil Mech. and Foundation Eng.

Casagrande, A. Liquefaction and cyclic mobility of sands: a critical review. *Harvard Soil Mechanics*, 88, 1976.

Castro, G. Liquefaction of sand. 1969. Harvard University.

Castro, G. and S. J. Poulos. Factors affecting liquefaction and cyclic mobility. *J. of the Geotech. Eng. Div., ASCE*, 103(6):501–506, 1977.

Castro, G., J. L. Enos, J. W. France, and S. J. Poulos. Liquefaction induced by cyclic loading. Technical Report NSF/CEE-82018, National Science Foundation, 1982.

Castro, G., S. J. Poulos, and F. D. Leathers. A reexamination of the slide of the lower san fernando dam. *J. of Geotech. Eng., ASTM*, 111(9):1093–1107, 1985.

Cetin, K. O., R. B. Seed, R. E. S. Moss, K. Tokimatsu, L. F. Jr. Harder, and R. E. Kayen. Field case histories for spt-based in situ liquefaction potential evaluation. Technical report, Geotech. Eng., Depart. of Civil Eng., University of California, Berkeley, 2000.

Chang, C. S. and Zhen-Yu Yin. Micromechanical modeling for behavior of silty sand with influence of fine content. *Int. J. of Solids and Structures*, 48(19):2655–2667, 2011.

Chang, N., G. Heymann, and C. R. I. Clayton. The effect of fabric on the behaviour of gold tailings. *Géotechnique*, 61(3):187–197, 2011.

Chester, D.K. The 1755 lisbon earthquake. *Progress in Physical Geography*, 25(3):363–383, 2001.

Chiaro, G., J. Koseki, and T. Sato. Effects of initial static shear on liquefaction and large deformation properties of loose saturated toyoura sand in undrained cyclic torsional shear tests. *Soils and Foundations*, 52(3):498–510, 2012.

Cho, G., J. Dodds, and J. C. Santamarina. Particle shape effects on packing density, stiffness, and strength: natural and crushed sands. *J. of Geotech. and Geoenviron. Eng.*, 132(5):591–602, 2006.

Chu, J. and W. K. Leong. Effect of fines on instability behaviour of loose sand. *Geotechnique*, 52 (10):751–755, 2002.

Chu, J., S. Leroueil, and W. Leong. Unstable behaviour of sand and its implication for slope instability. *Can. Geotech. J.*, 40:873–885, 2003.

Chu, J., W. K. Leong, W. L. Loke, and D. Wanatowski. Instability of loose sand under drained conditions. *J. of Geotech. and Geoenviron. Eng.*, 138(2):207–216, 2012.

Consoli, N.C., M. Vendruscolo, and P. Prietto. Behavior of plate load tests on soil layers improved with cement and fiber. *Journal of Geotechnical and Geoenviron. Engineering*, 129(1):96–101, 2003.

Consoli, N.C., K.S. Heineck, M.R. Copp, A. FonsecaViana da , and C. Ferreira. Coal bottom ash as geomaterial: influence of particle morphology on the behavior of granular materials. *Soils and Foundations*, 47(2):361–373, 2007.

Consoli, N.C., C.A. Ruver, V. Girardello, L. Festugato, and A. Thome. Effect of polypropylene fibers on the uplift behavior of model footings embedded in sand. *Geosynthetics International*, 19(1):79–84, 2012.

Coop, M. R. and J. H. Atkinson. The mechanics of cemented carbonate sands. *Géotechnique*, 43 (1):53–67, 1993.

Coop, M. R. and I. K. Lee. The behaviour of granular soils at elevated stresses. *Predictive soil mechanics*, pages 186–199, 1993.

Coop, M. R., K. K. Sorensen, T. Bodas Freitas, and G. Georgoutsos. Particle breakage during shearing of a carbonate sand. *Géotechnique*, 54(3):157–163, 2004.

Coop, M.R. On the mechanics of reconstituted and natural sands. In *Deformation characteristics of geomaterials*, volume 2, pages 29–58. eformation characteristics of geomaterials. Recent investigations and prospects, 2003.

Costa, C. Development of a monitoring system for control of triaxial tests of soils. Msc in eletronic engineering, Faculty of Engineering of the University of Porto, Porto, Portugal, 2008.

Cresswell, A. and W. Powrie. Triaxial tests on an unbonded locked sand. *Géotechnique*, 54(2): 107–115, 2004.

Dafalias, Y., A. Papadimitriou, and X. Li. Sand plasticity model accounting for inherent fabric anisotropy. *J. Eng. Mech.*, 130(11):1319–1333, 2004.

Dafalias, Y. F. and M. T. Manzari. Simple plasticity sand model accounting for fabric change effects. *J. Eng. Mech.*, 130(6):622–634, 2004.

Dave, D. Remembering the aberfan disaster – 45 years ago today. http://blogs.agu.org/landslideblog/2011/10/21/remembering-the-aberfan-disaster-45-years-ago-today/, 2011.

Davies, M., E. McRoberts, and T. Martin. Static liquefaction of tailings – fundamentals and case histories. page 233–255. Proceedings of the Joint ASDSO/USSD Specialty Conference, 2002.

De Alba, P., C. K. Chan, and H. B. Seed. Sand liquefaction in large scale simple shear tests. *J. of the Geotech. Eng. Div., ASCE*, 102(GT9):909–927, 1976.

DeGennaro, V., J. Canou, J. C. Dupla, and N. Benahmed. Influence of loading path on the undrained behaviour of médium loose sand. *Can. Geotech. J.*, 41:166–180, 2004.

Degg, M. and J. Doornkamp. *Earthquake hazard atlas: 7. Iberia (Portugal and Spain) including the Azores, Balearics, Canary and Madeira Islands*. London: London Insurance and Reinsurance Market Association, 1994.

Degg, M. R. Some implications of the 1985 mexican earthquake for hazard assessment. *Geohazards*, pages 105–114, 1992.

Di Prisco, C., R. Matiotti, and R. Nova. Theoretical investigation of the undrained stability of shallow submerged slopes. *Géotechnique*, 45(3):479–496, 1995.

Dobry, R. Personal communication to r.d. andrus in andrus and stokoe in "liquefaction resistance based on shear wave velocity". 1996.

Dyvik, R., S. Berre, T. dan Lacasse, and B. Raadim. Comparison of truly undrained and constant volume direct simple shear tests. *Géotechnique*, 37(1):3–10, 1987.

Einav, I. and A. M. Puzrin. Pressure-dependent elasticity and energy conservation in elastoplastic models for soils. *J. of Geotech. and Geoenviron. Eng., ASCE*, 130(1):81–92, 2004.

Elliott, A. Liquefaction in new zealand. http://blogs.agu.org/tremblingearth/2011/03/04/liquefaction-in-new-zealand/, 2011.

Ferreira, C. *The use of seismic wave velocities in the measurement of stiffness of a residual soil*. Phd thesis in civil engineering, Faculty of Enginnering of the University of Porto, Porto, Portugal, 2008.

Festugato, L. Analysis of the mechanical behavior of fibre-reinforced soil under distinct aspects. Msc in civil engineering, Universidade Federal do Rio Grande do Sul, Rio Grande do Sul, Brazil, 2008.

Figueroa, J. L., A. S. Saada, L. Liang, and N. M. Dahisaria. Evaluation of soil liquefaction by energy principles. *J. of Geotech. Eng., ASCE*, 120(9):1554–1569, 1994.

Finn, W. D. L. and Y. P. Vaid. Liquefaction potential from drained constant volume cyclic simple shear tests. volume 6, pages 7–12. Proc. of the 6th World Conf. on Earthquake Engineering, 1977.

Finn, W. D. L., Y. P. Vaid, and Bhatia S. K. Constant volume cyclic simple shear testing. volume 2, pages 839–851. Proceedings of 2nd International Conference on Microzonation for Safer Construction, November 1978.

Finn, W.D.L., J. Pickering, and P.L. Bransby. Sand liquefaction in triaxial and simple shear tests. *J. of the Soil Mech. and Found. Div., ASCE*, (SM4):639–659, 1971.

Finno, R. J. and A. L. Rechenmacher. Effects of consolida- tion history on critical state of sand. *J. of Geotech. and Geoenviron. Eng., ASCE*, 129(4):350–360, 2003.

Fonseca, M. The use of seismic wave velocities in the measurement of stiffness of a residual soil. Msc in civil engineering, Faculty of Enginnering of the University of Porto, Porto, Portugal, 2009.

Earth. Eng., Nat. Inf. Serv.for . Damage due to liquefaction. http://nisee.berkeley.edu/bertero/html/damage_due_to_liquefaction.html. Publisher: University of California, Berkeley.

Fourie, A. and L. Tshabalala. Initiation of static liquefaction and the role of k_0 consolidation. *Can. Geotech. J.*, 42:892–906, 2005.

Ghili, M. T. Liquefaction du sable 'les dunes'. pages 8–11. ISSMGE, Congrès Régional Africain Mécanique des Sols, 2003.

Ghiona, V. and D. Porcino. Liquefaction resistance of undisturbed and reconstituted samples of a natural coarse sand from undrained cyclic triaxial tests. *J. of Geotech. and Geoenviron. Eng.*, 132(2):194–202, 2006.

Ghionna, V. N. and D. Porcino. Liquefaction resistance of undisturbed and reconstituted samples of a natural coarse sand from undrained cyclic triaxial tests. *J. of Geotech. and Geoenviron. Eng., ASCE*, 132(2):194–202, 2006.

Goddard, J. D. Nonlinear elasticity and pressure-dependent wave speeds in granular media. A 430, pages 105–131. Proc. Skempton Conf, March 1990.

Graham, J. and G. T. Houlsby. Anisotropic elasticity of a natural clay. *Géotechnique*, 33(2): 165–180, 1983.

Harder, L. F. Jr. and H. B. Seed. Determination of penetration resistance for coarse-grained soils using the becker hammer drill. Technical report, University of California, Berkeley, 1986.

Harder Jr, L. F. and R. Boulanger. Application of k and k correction factors. In *Technical Report NCEER*, volume 97, pages 167–90. US National Center for Earthquake Engineering Research (NCEER), 1997.

Hardin, B. O. The nature of stress-strain behavior of soils. volume 1, pages 3–90. Proc. of the Earthquake Eng. and Soils Dynamics Conf., ASCE, 1978.

Hardin, B. O. and G. E. Blandford. Elasticity of articulate materials. *J. of Geotech. Eng., ASCE*, 115(6):788–805, 1989.

Hardin, B. O. and V. P. Drnevich. Shear modulus and damping in soils: Design equations and curves. *J. of Soil Mech. and Foundations Div., ASCE*, 98(7):667–692, 1972.

Hardin, B.O. and W.L. Black. Closure to: Vibration modulus of normally consolidated clays. *J. of Soil Mech. and Foundation Div., ASCE*, 95(6):1531–1537, 1969.

Hardin, B.O. and F.E. Richard. Elastic wave velocities in granular soils. *J. of Mech. and Foundation Div. ASCE*, 89:33–65, 1963.

Hareb, H. and T. Doanh. Probing into the strain induced anisotropy of hostun rf loose sand. *Granular Matter*, 14(5):589–605, 2012.

Heymann, G., C. Clayton, and N. Chang. The effect of fabric on the behaviour of gold tailings. *Géotechnique*, 61(3):187–197, 2011.

Hill, R. A general theory of uniqueness and stability in elastic-plastic solids. *J. of the Mech. and Physics of Solids*, 6(3):236–249, 1958.

Hird, C. C. and F. A. K. Hassona. Some factors affecting the liquefaction and flow of saturated sands in laboratory tests. *Eng. Geol.*, 28(1-2):149–170, 1990.

Hoque, E. and F. Tatsuoka. Anisotropy in elastic deformation of granular materials. *Soils and foundation*, 38(1):163–179, 1998.

Houlsby, G. How the dilatancy of soils affects their behavior. volume 4. Proc. of the 10th European Conf. on Soil Mech. and Foundation Eng., May 1991.

Huang, A. and W. Chang. Geotechnical and geophysical site characterization oriented to seismic analysis. January 2011.

Huang, Y.-T., A.-B. Huang, Y.-Ch. Kuo, and M.-D. Tsai. A laboratory study on the undrained strength of a silty sand from central western taiwan. *Soil Dynamics and Earthquake Eng.*, 24 (9):733–743, 2004.

Hyde, , T. Higuchi, and K. Yasuhara. Liquefaction, cyclic mobility, and failure of silt. *J. of Geotech. and Geoenviron. Eng.*, 132(6):716–735, 2006.

Hynes, M. E. and R. S. Olsen. Influence of confining stress on liquefaction resistance. pages 145–152. Proc. Int. Workshop on Phys. and Mech. of Soil Liquefaction, Balkema, 1999.

Idriss, I. and R. Boulanger. Soil liquefaction during earthquakes. Technical report, Earthquake Engineering Research Institute (EERI), 2008.

Idriss, I. M. An update to the seed-idriss simplified procedure for evaluating liquefaction potential. Proc. of the TRB Workshop on New Approaches to Liquefaction, Federal Highway Administration, January .

Idriss, I. M. and R. W. Boulanger. Estimating k_α for use in evaluating cyclic resistance of sloping ground. Number Report MCEER-03-0003, pages 449–468. Proc. 8th US-Japan Workshop on Earthquake Resistant Design of Lifeline Facilities and Countermeasures against Liquefaction, December 2003.

Idriss, I. M. and R. W. Boulanger. Semi-empirical procedures for evaluating liquefaction potential during earthquakes. pages 32–56, 2004.

Igwe, O., K. Sassa, and F. W. Wang. The influence of grading on the shear behavior of loose sands in stress-controlled ring shear tests. *Landslides*, 4(1):43–51, 2007.

Ishibashi, I. and O. Capar. Liquefaction resistance and its relation to wave velocities. pages 550–557. Proc. of the Twelfith Int. Offshore and Polar Eng. Conf., May 2002.

Ishihara, K. Liquefaction and flow failure during earthquakes. *Geotéchnique*, 43(3):351–115, 1993.

Ishihara, K. *Soil behavior in earthquake geotechnics*. Oxford Univ. Press, New York, 1996.

Ishihara, K. Liquefaction of subsurface soils during earthquakes. *Journal of Disaster Research*, 1 (2):245–261, 2006.

Ishihara, K., F. Tatsuoka, and S. Yasua. Undrained deformation and liquefaction of sands under cyclic stresses. *Soils and Foundations*, 15(1):29–44, 1975.

Ishihara, K. et al. Recent studies on liquefaction resistance of sand – effect of saturation. 4th Int. Conf. on Recent Advances in Geotech. Earthquake Eng. and Soil Dynamics, March 2001.

Iwasaki, T. and F. Tatsuoka. Effects of grain size and grading on dynamic shear moduli of sands. *Soils and Foundations*, 17(3):19–35, 1977.

J., Wang. *The Stress-Strain and Strength Characteristics of Portaway Sand*. Phd thesis, University of Nottingham, Nottingham, UK, 2005.

Jaky, J. The coefficient of earth pressure at rest. *Journal of the Society of Hungarian Architects and Engineers*, pages 335–358, 1944.

Jefferies, M. and K. Been. *Soil Liquefaction: A Critical State Approach*. Taylor & Francis, 2006.

Jefferies, M. and D. Shuttle. Understanding liquefaction through applied mechanics. 5th International Conference on Earthquake Geotechnical Engineering, January 2011.

Johansson, J. Where does liquefaction commonly occur? http://www.ce.washington.edu/~liquefaction/html/where/where1.html, 2000a. Organization: University of Washington.

Johansson, J. Why does liquefaction occur? http://www.ce.washington.edu/~liquefaction/html/why/why1.html, 2000b. Organization: Department of Civil Engineering, University of Washington.

Jorge, C.R.R. Zonation of liquefaction potential. application in portugal. Msc in geology engineering, New University of Lisbon, Lisbon, Portugal, 1994.

Kavazanjian, Jr. E., N. Matosovic, T.H. Hamou, and P.J Sabatini. Geotechnical engineering circular no. 3, geotechnical earthquake engineering for highways, volume ii – design examples. *FHWA*, (FHWA-SA-97-077):163, 1997.

Kayen, R. E., J. K. Mitchell, R. B. Seed, and S. N. Nishio. Soil liquefaction in the east bay during the earthquake. http://walrus.wr.usgs.gov/geotech/soil/index.html#FIG8, 1989.

Kayen, R. E., J. K. Mitchell, R. B. Seed, A. Lodge, S. Nishio, and R. Coutinho. Evaluation of spt-, cpt-, and shear wave-based methods for liquefaction potential assessment using loma prieta data. volume 1, pages 177–204. 4th Japan-U.S. Workshop on Earthquake Resistant Design of Lifeline Facilities and Countermeasures for Soil Liquefaction, 1992.

Ko, H. Y. and R. Masson. Nonlinear characterization and analysis of sand. pages 294–305. 2nd Int. Conf. on Numerical Methods in Geomechanics, 1976.

Kokusho, T. Cyclic triaxial test of dynamic soil properties for wide strain range. *Soils and Foundations*, 20(2):45–60, 1980.

Konrad, J. Minimum undrained strength of two sands. *J. Geotech. Eng.*, 116(6):932–947, 1998.

Kramer, S. L. and H. B. Seed. Initiation of soil liquefaction under static loading conditions. *J. of Geotech. Eng., ASCE*, 114(4):412–430, 1988.

Kramer, S.L. *Geotechnical earthquake engineering*. Prentice Hall International Series in Civil Engineering And. Prentice Hall, 1996.

Krumbein, W. C. and L. L. Sloss. *Stratigraphy and sedimentation*. Freeman and Company, 2nd edition, 1963.

Kumruzzaman, Md. and J. Yin. Influences of principal stress direction and intermediate principal stress on the stress–strain–strength behaviour of completely decomposed granite. *Can. Geotech. J.*, 47:164–179, 2010.

Kuribayashi, E. and F. Tatsuoka. Brief review of liquefaction during earthquakes in japan. *Soils and Foundations*, 15(4):81–92, 1975.

Lade, P. and J. Yamamuro. Evaluation of static liquefaction potential of silty sand slopes. *Can. Geotech. J.*, 48(2):247–264, 2011.

Lade, P., R. Nelson, and Y. Ito. Instability of granular materials with nonassociated flow. *J. Eng. Mech.*, 114(12):2173–2191, 1988.

Lade, P. V. and J. A. Yamamuro. Stability of granular materials in post peak softening regime. *J. of Eng. Mech.*, 119(1):128–144, 1993.

Lade, P. V. and J. A. Yamamuro. Effects of nonplastic fines on static liquefaction of sands. *Can. Geotech. J.*, 34:918–928, 1997.

Lade, P. V., J. A. Yamamuro, and P. A. Bopp. Significance of particle crushing in granular materials. *J. of Geotech. Eng., ASCE*, 122(4):309–316, 1996.

Lade, P. V., J. A. Yamamuro, and C. D. Liggio. Effects of fines content on void ratio, compressibility, and static liquefaction of silty sand. *Geomechanics and Eng.*, 1(1):1–15, 2009.

Lade, P.V. Static instability and liquefaction of loose fine sandy slopes. *J. Geotech. Eng.*, 118: 51–71, 1992.

Lade, P.V. *Instability of granular materials*. Balkema, 1999.

Lade, P.V. and J.A. Yamamuro. Undrained sand behavior in axisymmetric tests at high pressures. *J. of Geotech. Eng., ASCE*, 122(2):120–129, 1996.

Lambe, T. W. and R. V. Whitman. *Soil Mechanics*. John Wiley and Sons, 1979.

Lee, K. L. and J. A. Fitton. Factors affecting the cyclic loading strength of soil. *Vibration Effects of Earthquakes on Soils and Foundation, ASTM*, STP 450:71–95, 1968.

Lee, K. L. and J. A. Fitton. Factors affecting the cyclic loading strength of soil. *Vibration Effects of Earthquakes on Soils and Foundations*, 450:71–95, 1969.

Lee, K. L. and H. B. Seed. Drained strength characteristics of sand. *J. of the Soil Mech. and Foundation Eng. Div., ASCE*, 93(SM6):117–141, 1967.

Lee, W. F., K. Ishihara, C. H. Chen, and B. L. Chu. Liquefaction induced ground failures caused by strong ground motion. 5th Int. Conf. on Earthquake Eng., January 2011.

Leroueil, J., Chu and D. Wanatowski. Slope instability due to pore water pressure increase. pages 81–90. Proceedings of the 1st Italian Workshop on Landslides (1st IWL), 2009.

Leroueil, S. Natural slopes and cuts: movement and failure mechanisms. *Géotechnique*, 51(3): 197.243, 2001.

Li, Bo and Xiangwu Zeng. Effects of fabric anisotropy on elastic shear modulus of granular soils. *Earthquake Eng. and Eng. Vibration*, 13(2):269–278, 2014.

Li, X. S. and Y. F. Dafalias. Dilatancy for cohesionless soils. *Géotechnique*, 50(4):449–460, 2000.

Li, X. S., Y. F. Defalias, and Z. L. Wang. State-dependent dilatancy in critical-state constitutive modelling of sand. *Can. Geotech. J.*, 36(4):599–611, 1999.

Liang, L., J. L. Figueroa, and A. S. Saada. Liquefaction under random loading: unit energy approach. *J. of Geotech. Eng., ASCE*, 121(11):776–781, 1995.

Liao, S. S. C. and R. V. Whitman. Overburden correction factors for spt in sand. *J. Geotech. Eng.*, 112(3):373–377, 1986.

Liu, N. and J. K. Mitchell. Influence of nonplastic fines on shear wave velocity-based assessment of liquefaction. *J. of Geotech. and Geoenviron. Eng., ASCE*, 132(8):1091–1097, 2006.

Lo Presti, D. C. F. General report: Measurement of shear deformation of geomaterials in the laboratory. volume 2, pages 1067–1088. Proc. Int. Symp. on Pre-failure Deformation of Geomaterials, Balkema, 1995.

Manual, CDSS. *Cyclic Direct Simple Shear User's Manual*, 1982-2010.

Manzari, M. T. and Yannis Y. F. Dafalias. A critical state two-surface plasticity model for sands. *Geotechnique*, 47(2):255–272, 1997.

Marchetti, S. Detection of liquefiable sand layers by means of quasi-static penetration tests. volume 2, pages 689–695. 2nd European Symp. on Penetration Testing, 1982.

Marchetti, S. Liquefaction using the dmt's parameter kd to estimate liquefaction resistance crr and settlements in sand. *J. of Geotech. Eng. ASCE*, 2014.

Marques, F. Analasysis of the liquefaction potential of sands with fines. influence of non-plastic fines on the resistance of coimbra sand to liquefaction: Laboratory research and numerical modeling. Msc in civil engineering, Instituto Superior Técnico de Lisboa, Lisbon, Portugal, 2011.

Matiotti, R., C. Priscodi , and R. Nova. Experimental observations on static liquefaction of loose sand. *Earthquake Geotech. Eng.*, pages 817–822, 1995.

Mattioti, R., C. Priscodi , and R. Nova. Experimental observations on static liquefaction of loose sand. *Earthquake Geotechnical Engineering*, pages 817–822, 1995.

McDowell, G. R. and M. D. Bolton. On the micromechanics of crushable aggregates. *Géotechnique*, 48(5):667–680, 1998.

Mendes, M.B. Geotechnical behavior of a tailing dam subjected to an upsetram heightening method. Msc in geotechnical engineering, University of São Paulo, São Paulo, Brazil, 2007.

Mendes-Victor, L., C. S. Oliveira, I. Pais, and P. Teves-Costa. Earthquake damage scenarios in lisbon for disaster preparedness. *Issues in urban earthquake risk*, pages 265–289, 1994.

Mezcua, J., J. Rueda, and J. M. Martínez Solares. *Seismicity of the Ibero-Maghrebian region*. Madrid: Instituto Geográfico Nacional, 1991.

Midorikawa, S. and K. Wakamatsu. Intensity of earthquake ground motion at liquefied sites. *Soils and Foundations*, 28(2):73–84, 1988.

Mill, Retsch Ball. Planetary ball mill pm 100. http://www.retsch.com/products/milling/ball-mills/planetary-ball-mill-pm-100/function-features/.

Mitchell, J. K. *Fundamentals of Soil Behavior*. John Wiley and Sons, Inc., 1st edition, 1976.

Molano, N. *Development of a family of constitutive models for geotechnical applications*. Phd thesis in civil engineering, Universitat Politècnica de Catalunya, 2011.

Monaco, P. and S. Marchetti. Evaluating liquefaction potential by seismic dilatometer (sdmt) accounting for aging/ stress history. 4th Int. Conf. on Earthquake Geotech. Eng., June 2007.

Monaco, P., S. Marchetti, G. Totani, and M. Calabrese. Sand liquefiability assessment by flat dilatometer test. page 2693–2697. 16th Int. Conf. Soils Mech. Geotech. Eng., 2005.

Mooney, M. A., R. J. Finno, and M. G. Viggiani. A unique critical state for sand? *J. of Geotech. Eng. Div., ASCE*, 112(10):941–958, 1998.

Morgenstern, N. Geotechnics and mine waste management – update. Seminar Proceedings, Safe Tailings Dam Constructions, September 2001.

Morris, D. V. A note on earthquake-induced liquefaction. *Géotechnique*, 33(4):451–454, 1983.

Moss, R. and J. Schneider. Linking cyclic stress and cyclic strain based methods for assessment of cyclic liquefaction triggering in sands. *Géotechnique Letters*, 1(6):458–482, 2011.

Moss, R., R. Seed, and R. Olsen. Normalizing the cpt for overburden stress. *J. of Geotech. and Geoenviron. Eng.*, 132(3):378–387, 2006.

Muir Wood, D. Critical states and soil modelling. volume 22-24, pages 51–72. In Proceedings of the 4th International Symposium on Deformation Characteristics of Geomaterials, IOS Press, 2008.

Mulilis, J. P., H. B. Seed, C. K. Chan, and J. K. Mitchell. Effect of sample preparations on sand liquefaction. *J. of Geotech. Eng. Div., ASCE*, 103(GT2):91–10, 1977.

Naeini, S. A. and M. H. Baziar. Effect of fines content on steady-state strength of mixed and layered samples of a sand. *Soil Dynamics and Earthquake Eng.*, 24(3):181–187, 2004.

Negussey, D. and M. S. Islam. Uniqueness of steady state and liquefaction potential. *Can. Geotech. J.*, 31(1):132–139, 1994.

Negussey, D. and W. Wijewckreme. Constant-volume friction angle of granular materials. *Canadian Geotechnical Journal*, 25:50–55, 1988.

Nicholson, P. G., R. B. Seed, and H. A. Anwar. Elimination of membrane compliance in undrained triaxial testing. i measurement and evaluation. *Can. Geotech. J.*, 30:727–738, 1993.

Niemunis, A. *Incremental Driver User's manual*. IBF, Karlsruhe, Germany, 2008.

Noce, T. E. and T. L. Holzer. Subsurface exploration with the cone penetration testing truck. http://pubs.usgs.gov/fs/old.2003/fs028-03/, 2003. Organization: U.S. Geological Survey.

Nougier-Lehon, C., E. Vincens, and B. Cambou. Structural changes in granular materials: the case of irregular polygonal particles. *Int. J. of Solids and Structures*, 42(24-25):6356–6375, 2005.

Nouguier-Lehon, C., E. Vincens, and B. Cambou. Structural changes in granular materials: the case of irregular polygonal particles. *Int. J. of Solids and Structures*, 42(24):6356–6375, 2005.

Nova, R. Liquefaction, stability, bifurcations of soil via strain hardening plasticity, 1989.

NRC, . *Liquefaction of Soils During Earthquakes*. National Academy Press, 1985.

O., Igwe, H. Fukuoka, and K. Sassa. The fffect of relative density and confining stress on shear properties of sands with varying grading. *Geotech. Geol. Eng.*, 30(5):1207–1229, 2012.

Oda, M. and K. Iwashita. Study on couple stress and shear band development in granular media based on numerical simulation analyses. *Int. J. of Eng. Science*, 38:1713–1740, 2000.

Okur, V. and S. Umu. Energy approach to unsaturated cyclic strength of sand. *Bulletin of Earthquake Engineering*, 11(2):503–519, 2012.

Oliveira, M. Study of flow liquefaction induced instability on silty-sand soils under laboratorial conditions. Msc in civil engineering, Faculty of Enginnering of the University of Porto, Porto, Portugal, 2014.

Olson, S. and B. Mattson. Mode of shear effects on yield and liquefied strength ratios. *Can. Geotech. J.*, 45(4):574–587, 2008.

Papadimitriou, A. G. and G. D. Bouckovalas. Plasticity model for sand under small and large cyclic strains: a multiaxial formulation. *Soil Dynamics and Earthquake Eng.*, 22:191–204, 2002.

Park, S., P. Byrne, and D. Wijewickreme. A swinging plane model for soil liquefaction analysis. pages 845–850. 6th Int. Conf. on Soil Mech. and Geotech. Eng., 2005.

Peacock, W.H. and H.B. Seed. Sand liquefaction under cyclic loading simple shear conditions. *J. Soil Mech. and Found. Div.*, 99(12):1170–1184, 1968.

Pestana, J. M. and A. J. Whittle. Shear and interface strength of clay at very low effective stress. *Geotéchnique*, 45(4):611–631, 1995.

Petcher, A. A life in a year – 21st may, hillmorton county junior and infants school. https://aipetcher.wordpress.com/tag/lindsay-petcher/, 2010.

Pinheiro, A. Laboratorial evaluation of the state conditions which might lead to soil liquefaction of dune sands during the earthquake of 2003 in "bourmedes". Msc in civil engineering, Faculty of Enginnering of the University of Porto, Porto, Portugal, 2009.

Porcino, D., V. Marciano, A. Santini, and N. Moraci. Effect of initial fabric on cyclic and monotonic undrained shear strength of gioia tauro sand. volume 1020, pages 448–455. 2008 Seismic Engineering Conference Commemorating the 1908 Messina and Reggio Calabria Earthquake; Adolfo Santini and Nicola Moraci. AIP Conference Proceedings, 2008.

Poulos, J. The steady state of deformation. *J. of Geotech. Eng. Div., ASCE*, 107(GT5):553–562, 1981.

Poulos, S. J., G. Castro, and J. France. Liquefaction evaluation procedure. *J. of Geotech. Eng., ASCE*, 111(6):772–792, 1985.

Prada, L. F. *Paraelastic description of small-strain soil behaviour*. Phd thesis in civil engineering, Universidad de los Andes, Bogotá, Colombia, 2011.

Qadimi, A. and M.R. Coop. The undrained cyclic behaviour of a carbonate sand. *Gèotechnique*, 57(9):739–750, 2007.

Rahman, Md. M., S. R. Lo, and C. T. Gnanendran. On equivalent granular void ratio and steady state behaviour of loose sand with fines. *Can. Geotech. J.*, 45(10):1439–1456, 2008.

Rahman, S. R., Lo and C. T. Gnanendran. On equivalent granular void ratio and steady state behaviour of loose sand with fines. *Can. Geotech. J.*, 45(10):1439–1456, 2008.

Ramos, A. M. C. *Instabilites in sands*. Phd thesis, Faculty of Engineering of Universidad de Los Andes, Bogotá, Colombia, 2010.

Rauch, A. F. Personal comunication to youd and idriss and publisehd in "liquefaction resistance of soils: summary report from the 1996 nceer and 1998 nceer/msf workshops on evaluation of liquefaction resistance of soils". 1998.

Rauch, A.F. *EPOLLS: An empirical method for predicting surface displacements due to liquefaction induced lateral spreading in earthquakes*. Phd thesis in civil engineering, Faculty of the Virginia Polytechnic Institute and State University, Blacksburg, VA, USA, 1997.

Reyno, A. R., D. W. Airey, and H. A. Taiebat. Influence of height and boundary conditions in simple shear tests. pages 1101–1107. Proc of Frontiers in Offshore Geotechnics, 2005.

Reynolds, O. On the dilation of media composed of rigid particles in contact with experimental illustrations. *Philosophical Magazine*, 20(127):469–481, 1885.

Richart, F. E., J. R. Hall, and R. D. Woods. *Vibrations of soils and foundations*. Prentice-Hall, 1970.

Rico, M., G. Benito, A.R. Salgueiro, A. Díez-Herrero, and H. G. Pereira. Reported tailings dam failures: a review of the european incidents in the worldwide context. *Journal of Hazardous Materials*, 152(2):846–852, 2008.

Riemer, M. F. and R. B. Seed. Factors affecting apparent position of steady-state line. *J. of Geotech. and Geoenviron. Eng., ASCE*, 123(3):281–288, 1997.

Rios Silva, S. *A general framework for the geomechanical caracterisation of artificially cemented soil*. Phd thesis in civil engineering, Faculty of Enginnering of the University of Porto, Porto, Portugal, 2011.

Robertson, P. K. and C. E. Wride. Cyclic liquefaction and its evaluation based on spt and cpt. Technical Report Technical Report No. NCEER-97-0022, Nat. Center for Earthquake Eng. Research, State University of New York, Buffalo, 1997.

Robertson, P. K., D. J. Woeller, and W. D. L. Finn. Seismic cone penetration test for evaluating liquefaction potential under cyclic loading. *Can. Geotech. J.*, 29(4):686–695, 1992.

Robertson, P.K. Performance based earthquake design using the cpt. pages 3–20. Proceedings of IS-Tokyo, Taylor & Francis Group, 2009.

Robertson, P.K. Mitchell lecture. interpretation of in-situ tests - some insight. volume 1, pages 3–24. 4th Int. Conf. on Site Characterization ISC-4, 2012.

Rocha, J. Assessment of soil liquefaction conditions under triaxial conditions basing on critical state and evaluation of the risk basing on stress waves of a dune sand. Msc in civil engineering, Faculty of Enginnering of the University of Porto, Porto, Portugal, 2010.

Roesler, S. K. Anisotropic shear modulus due to stress anisotropy. *J. Geotech. Eng. Div., ASCE*, 105(7):871–880, 1979.

Roscoe, K. H. The influence of strains in soil mechanics. *Géotechnique*, 20(2):129–170, 1970.

Roscoe, K. H., A. N. Schofield, and M. A. Wroth. On the yielding of soils. *Geotechnique*, 8: 22–53, 1958.

Rowe, P. The stress-dilatancy relation for static equilibrium of an assembly of particles in contact. volume 269, pages 500–527. Proceedings of the Royal Society of London, 1962.

Roy, D. Liquefaction susceptibility and shear wave velocity. volume 2, pages 435–438. 16th Int. Conf. on Soil Mechanics and Geotech. Eng., September 2005.

Saada, A. S. Hollow cylinder torsional devices: Their advantages and limitations. volume STP 977, pages 766–795. Sympo. on Advanced Triaxial Testing of Soil and Rock, ASTM, 1988.

Sadrekarimi, A. and S. Olsen. Yield strength ratios, critical strength ratios and brittleness of sandy soils from laboratory tests. *Can. Geotech. J.*, 48:493–510, 2011.

Sadrekarimi, A. and S. Olson. Effect of sample-preparation method on critical-state behavior of sands. *Geotech. Testing Journal*, 35(4):1–15, 2013.

Salgado, F. Atas do seminário "Área metropolitana de lisboa - ambiente urbano e riscos", 2012.

Santamarina, J. and G. Cho. Soil behaviour : The role of particle shape. pages 1–14. Proceedings Skempton Conference, 2004.

Santos, J., R. Gomes, F. Lourenço, J.and Marques, P. Coelho, P. A. L. F. Fonseca, R. J. N. Azeiteiro, L. A. Santos, V. D. Marques, A. FonsecaViana da , M. Soares, and É. Abreu. Coimbra sand round robin tests to evaluate liquefaction resistance. 15th World Conf. on Earthquake Eng., 2012.

Santos, L. Behaviour of coimbra sand under monotonic loading. Msc in civil engineering, FCTUC. University of Coimbra, Coimbra, Portugal, 2009.

Sasitharan, S., P. K. Robertson, D. . Sego, and N. R. Morgenstern. Collapse behavior of sand. *Can. Geotech. J.*, 30:569–577, 1993.

Schnaid, F. Geocharacterization and engineering properties of natural soils by in situ tests. volume 1, page 3–45, Rotterdam, Netherlands, 2005. Proc. 16th Int. Conf. on Soil Mechanics and Geotechnical Engineering, Balkema.

Schnaid, F. and H. S. Yu. Theoretical interpretation of the seismic cone test in granular soils. *Géotechnique*, 57(3):265–272, 2007.

Schnaid, F., B. M. Lehane, and M. Fahey. In situ test characterisation on geomaterials. page 49–74, Porto, Portugal, 2004. Proc. 2nd Int. Conf. on Site Characterization.

Schnaid, F., J. Bedin, A. FonsecaViana da , and L. Costa-Filho. Stiffness and strength governing the static liquefaction of tailings. *J. Geotech. Geoenviron. Eng.*, 139(12):2136–2144, 2013.

Seed, H. B. Soil liquefaction and cyclic mobility evaluation for level ground during earthquake. *J. of Geotech. Eng. ASCE*, 105(2):201–225, 1979.

Seed, H. B. Earthquake-resistant design of earth dams. Number 41–64. Proc. Symp. Seismic Des. of Earth Dams and Caverns, ASCE, 1983.

Seed, H. B. and I. M. Idriss. Simplified procedure for evaluating liquefaction potential. *J. Geotech. Engrg. Div.*, 97(9):1249–1273, 2004.

Seed, H. B. and K. L. Lee. Liquefaction of saturated sands during cyclic loading. *J. of Soil Mech. and Foundation Div., ASCE*, 92(6):105–134, 1966.

Seed, H. B. and W. H. Peacock. Test procedures for measuring soil liquefaction characteristics. *J. of the Soil Mech. and Foundations Div.*, 97:1099–1119, 1971.

Seed, H. B., I. M. Idriss, and I. Arango. Evaluation of liquefaction potential using field performance data. *J. of Geotech. Eng. ASCE*, 109(3):458–482, 1983.

Seed, H. B., K. Tokimatsu, L. Harder, and R. Chung. Influence of spt procedures in soil liquefaction resistance evaluations. *J. of Geotech. Eng. ASCE*, 111(12):1425–1445, 1985.

Seed, H.B. and I.M. Idriss. *Ground motions and soil liquefaction during earthquakes*. Earthquake Engineering Research Institute Monograph, 1982.

Seed, R. B., K. O. Cetin, R. E. S. Moss, A. Kammerer, J. Pestana, J. Wu, and M. Riemer. Recent advances in soil liquefaction engineering and seismic site response evaluation. 4th Int. Conf. and Symp. on Recent Advances in Geotech. Earthquake Eng. and Soil Dynamics, March 2001. Paper SPL-2.

Seed, R. B., K. O. Cetin, R. E. S. Moss, A. Kammerer, J. Wu, J. Pestana, M. Riemer, R. B. Sancio, J. D. Bray, R. E. Kayen, and A. Francis. Recent advances in soil liquefaction engineering: A unified and consistent framework. Proc., 26th Annual Los Angeles Geotechnical Spring Seminar, 2003.

Seed, R.B. and Jr. Harder, L.F. Spt-based analysis of cyclic pore pressure generation and undrained residual strength. In *Proceedings of the H.B. Seed Memorial Symposium*, volume 2, pages 351–376. Bi-Tech Publishing Ltd., 1990.

Silva, J. Definition of liquefaction risk assessment frameworks based on shear wave velocities for silty tailings from triaxial tests with bender elements. Msc in civil engineering, Faculty of Enginnering of the University of Porto, Porto, Portugal, 2010.

Silver, M.L., F. Tatsuoka, A. Phukunnhaphan, and A. Avramidis. Cyclic undrained strength of sand by triaxial test and simple shear test. volume 3, pages 281–288. Proc. of the 7th World Conf. on Earthquake Engineering, 1980.

Sivathayalan, S. Static, cyclic and post liquefaction simple shear response of rands. Msc, Department of Civil Engineering, Faculty of Enginnering of the University of British Columbia, Vancouver, Canada, 1994.

Sivathayalan, S. and D. Ha. Effect of static shear stress on the cyclic resistance of sands on simple shear loading. *Can. Geotech. J.*, 48(10):1471–1484, 2011.

Sivathayalan, S. and Y. P. Vaid. Influence of generalized initial state and principal stress rotation on the undrained response of sands. *Can. Geotech. J.*, 39:63–76, 2002.

Skempton, A. W. Residual strength of clays in landslides, folded strata and the laboratory. *Géotechnique*, 35(1):3–18, 1985.

Skopek, P., N. R. Morgenstern, P. K. Robertson, and D. C. Sego. Collapse of dry sand. *Can. Geotech. J.*, 31(6):1008–1014, 1994.

Sladen, J. A. and G. Handford. A potential systematic error in laboratory testing of very loose sands. *Can. Geotech. J.*, 24(3):462–466, 1987.

Sladen, J. A., R. D. D'Hollander, and J. Krahn. The liquefaction of sands, a collapse surface approach. *Can. Geotech. J.*, 22:564–578, 1985.

Somasundaram, S. Cyclic loading response of fraser river sand for validation of numerical models simulating centrifuge tests. Msc in civil engineering, Univertisy of British Columbia, Vancouver, CA, 2004.

Standard, . Geotechnical investigation and testing - laboratory testing of soil - part 4: Determination of particle size distribution. Technical report, Brussels: Comité Européen de Normalisation, 2004a.

Standard, . Geotechnical investigation and testing – laboratory testing of soil – part 9: Consolidated triaxial compression on water saturated soil. Technical report, Brussels: Comité Européen de Normalisation, 2004b.

Stark, T.D. and S.M. Olson. Liquefaction resistance using cpt and field case histories. *J. of Geotech. Eng., ASCE*, 121(12):856–869, 1995.

Stokoe, K. H. II., S. H. H. Lee, and D. P. Knox. Shear moduli measurements under the triaxial stresses. pages 166–185. Proc. of Advances in the art of testing soil under cyclic conditions, ASCE, 1985.

Stokoe, K. H. II., J. M. Roesset, J. G. Bierschwale, and M. Aouad. Liquefaction potential of sands from shear wave velocity. volume 3, pages 213–218. 9th World Conf. on Earthquake Engineering, 1988.

Stokoe, K. H. II, S. H. Joh, and R. D. Woods. Some contributions of in situ geophysical measurements to solving geotechnical engineering problems. volume 1, pages 97–132, Porto, Portugal, 2004. Proceedings of ISC-2: Geotechnical and Geophysical Site Characterization.

Suzuki, Y., K. Tokimatsu, K. Koyamada, Y. Taya, and Y. Kubota. Field correlation of soil liquefaction based on cpt data. volume 2, page 583–588. International Symposium on Cone Penetration Testing, CPT'95, 1995.

Sykora, D. W. Creation of a data base of seismic shear wave velocities for correlation analysis, 1987.

Taiebat, M. and Y. F. Dafalias. Sanisand: Simple anisotropic sand plasticity model. *Int. J. for Numerical and Analytical Methods in Geomech.*, 32(8):915–948, 2008.

Tanaka, H. and M. Tanaka. Characterization of sandy soils using cpt and dmt. *Soils and Foundations*, 38(3):55–65, 1998.

Tatsuoka, F., K. Ochi, S. Fuji, and M. Okamoto. Cyclic undrained triaxial and torsional shear strength of sands for different preparation methods. *Soils Foundations*, 263:23–41, 1986a.

Tatsuoka, F., S. Toki, S. Miura, H. Kato, M. Okamoto, S.-I. Yamada, S. Yasuda, and F. Tanizawa. Some factors affecting cyclic undrained triaxial strength of sand. *Soils and Foundations*, 26(3): 99–116, 1986b.

Terzaghi, K. and R. B. Peck. *Soil mechanics in engineering practice*. J. Wiley & Sons, New York, 1948.

Teves-Costa, Paula and Josep Batlló. The 23 april 1909 benavente earthquake (portugal): macroseismic field revision. *Journal of Seismology*, 15(1):59–70, 2011.

Thevanayagam, S. and S. Mohan. Intergranular state variables and stress-strain behaviour of silty sands. *Géotechnique*, 50(1):1–23, 2000.

Thevanayagam, T., Shenthan, S. Mohan, and J. Liang. Undrained fragility of clean sands, silty sands, and sandy silts. *Journal of Geotechnical and Geoenviron. Engineering*, 128(10):849–859, 2002.

Tokimatsu, K. and Y. Yoshimi. Empirical correlation of soil liquefaction based on spt n-value and fines content. *Soils and Foundations*, 23(4):56–74, 1983.

Tokimatsu, K., S. Kuwayama, and S. Tamura. Liquefaction potential evaluation based on rayleigh wave investigation and its comparison with field behavior. volume 1, pages 357–364. 2nd Int. Conf. on Recent Advances in Geotechnical Earthquake Engineering and Soil Dynamics, University of Missouri-Rolla, 1991.

Tosatti, G. editor. A review of scientific contributions on the stava valley disaster (eastern italian alps), 2003.

Towhata, I. *Geotechnical earthquake engineering*. Springer, 2008.

Tsuchida, H. Prediction and countermeasure against the liquefaction in sand deposits. Seminar in the Port and Harbor Research Institute, 1970. in Japanese.

Tsukamoto, Y., K. Ishihara, and T. Nonaka. Undrained deformation and strength characteristics of soils from reclaimed deposits in kobe. *Soils Foundations (special issue)*, (2):47–55, 1998.

Tsukamoto, Y., K. Ishihara, and S. Nakayama. Evaluation of undrained flow of anisotropically consolidated sands. ISRM International Symposium, International Society for Rock Mechanics, November 2000.

U.S.Department, of the Interior and Survey U.S.Geological. Historic earthquakes. http://earthquake.usgs.gov/earthquakes/world/events/1964_06_16.php.

Usmani, , G. V. Ramana, and K. G. Sharma. Experimental evaluation of shear-strength behavior of delhi silt under static loading conditions. *J. of Materials in Civil Eng.*, 23(5):533–541, 2011.

Uthayakumar, M. and Y.P. Vaid. Static liquefaction of sands under multiaxial loading. *Can. Geotech. J.*, 35:273–283, 1998.

Vaid, Y. P. and J. C. Chern. Cyclic and monotonic undrained response of saturated sands. pages 120–147. Proceedings of the ASCE Convention on: In advances in the art of testing soils under cyclic loading conditions, 1985.

Vaid, Y. P. and A. Eliadorani. Instability and liquefaction of granular soils under undrained and partially drained states. *Can. Geotech. J.*, 35(6):1053–1062, 1998.

Vaid, Y. P. and S. Sivathayalan. Static and cyclic liquefaction potential of fraser delta sand in simple shear and triaxial tests. *Can. Geotech. J.*, 33:281–289, 1996.

Vaid, Y. P. and S. Sivathayalan. Fundamental factors affecting susceptibility of sands. *Can. Geotech. J.*, 37:592–606, 2000.

Vaid, Y. P. and J. Thomas. Liquefaction and post liquefaction behavior of sand. *J. of Geotech. Eng., ASCE*, 121(2):163–173, 1995.

Vaid, Y. P., E. K. F. Chung, and R. Kuerbis. Stress path and steady state. *Can. Geotech. J.*, 27: 1–7, 1990.

Vaid, Y. P., J. D. Stedman, and S. Sivathayalan. Confining stress and static shear effects in cyclic liquefaction. *Can. Geotech. J.*, 38:580–591, 2001.

Vaid, Y.P. and S. Sivathayalan. Fundamental factors affecting liquefaction susceptibility of sand. page 105–120. In Proceedings of the International Workshop on the Physics and Mechanics of Soil Liquefaction, John Hopkins University, 1998.

Vaz, T. Contribution for the study of the movements triggered by seismic events in portugal continental. Msc, University of Lisbon, Lisbon, Portugal, 2010. Master on physical geography and urban planning.

Ventouras, K. and M. R. Coop. On the behaviour of thanet sand: an example of an uncemented natural sand. *Géotechnique*, 59(9):727–738, 2009.

Verdugo, R. and K. Ishihara. The steady state of sandy soils. *Soils and Foundations*, 36(2):81 – 91, 1996.

Fonseca, A.Viana da . *Geomechanics in residual soils from Porto granite. Criteria for the design of shallow foundations*. Phd thesis in civil engineering, Faculty of Engineering of University of Porto, Porto, Portugal, 1996.

Fonseca, A.Viana da and M. Soares. Effect of principal stress rotation on cyclic liquefaction. Second Int. Conf. on Performance-Based Design in Earthquake Geotech. Eng., 2012.

Fonseca, A.Viana da , M. R. Coop, M. Fahey, and N. C. Consoli. The interpretation of conventional and non-conventional laboratory tests for changeling geotechnical problems. Seoul, Korea, November 2011a. Int. Symp. on Deformation Characteristics on Deformation of Geomaterials.

Fonseca, A.Viana da , J. Rocha, and G. Tahar. Liquefaction assessment charts on state and waves' velocities from static and cyclic triaxial tests on "les dunes" sands from algier. 5th Int. Conf. on Earthquake Geotech. Eng., January 2011b.

Vieira Faria, N., A. FonsecaViana da , and C. Ferrreira. Processo de saturación de ensayos triaxiales. volume 104, pages 31–42. Geotechnical Portuguese Society, 2006.

Vilhar, G., V. Jovicic, and M. R. Coop. The role of particle breakage in the mechanics of a non-plastic silty sand. *Soils and Foundations*, 53(1):91–104, 2013.

Wakamatsu, K. *History of soil liquefaction in Japan and assessment of liquefaction potential based on geomorphology*. Phd thesis, Waseda University Tokyo, Tokyo, Japan, 1993.

Wan, R. and P. Guo. Effect of microstructure on undrained behaviour of sands. *Can. Geotech. J.*, 38(1):16–28, 2001.

Wang, J.-H., K. Moran, and C. D. P. Baxter. Correlation between cyclic resistance ratios of intact and reconstituted offshore saturated sands and silts with the same shear wave velocity. *J. of Geotech. and Geoenviron. Eng., ASCE*, 132(12):1574–1580, 2006.

Wang, W. Some findings in soil liquefaction. *Chinese J. of Geotech. Eng.*, 2(3):55–63, 1980.

Wang, Z.L., Dafalias Y.F., X.S. Li, and F. I. Makdisi. State pressure index for modeling sand behavior. *J. Geotech. Geoenviron. Eng.*, 128(6):511–519, 2002.

Wijewickreme, D. and Y. P. Vaid. The stress-strain and strength characteristics of portaway sand. *Can. Geotech. J.*, 30:953–964, 1993.

Wijewickreme, D. and Y. P. Vaid. Experimental observations on the response of loose sand under simultaneous increase in stress ratio and rotation of principal stresses. *Can. Geotech. J.*, 45(5): 597–610, 2008.

Wijewickreme, D., S. Sriskandakumar, and P. Byrne. Cyclic loading response of loose air-pluviated fraser river sand for validation of numerical models simulating centrifuge tests. *Can. Geotech. J.*, 42:550–561, 2005.

Wood, F. M., J. A. Yamamuro, and P. V. Lade. Effect of depositional method on the undrained response of silty sand. *Can. Geotech. J.*, 45(11):1525–1537, 2008.

Woodfor, K. Understanding the christchurch earthquake: building damage. http://keithwoodford.wordpress.com/2011/02/27/understanding-the-christchurch-earthquake-building-damage/, 2011.

Wroth, C.P. Twenty forth rankine lecture: The interpretation of in situ soils test. *Geotéchnique*, 34(4):449–489, 1984.

Yamada, S., T. Takamori, and K. Sato. Effects on reliquefaction resistance produced by changes in anisotropy during liquefaction. *Soils and foundations*, 50(1):9–25, 2010.

Yamada, S., R. Orense, and M. Cubrinovski. Earthquake news "geotechnical damage due to the 2011 christchurch, new zealand". *ISSMGE Bulletin*, 5(2):27–45, 2011.

Yamamuro, J. A. and P. V. Lade. Static liquefaction of very loose sands. *Can. Geotech. J.*, 34(6): 905–917, 1997.

Yamamuro, J. A. and P. V. Lade. Steady-state concepts and static liquefaction of silty sands. *J. of Geotech. and Geoenviron. Eng., ASCE*, 124(9):868–877, 1998.

Yamamuro, J. A., F. M. Wood, and P. V. Lade. Effect of depositional method on the microstructure of silty sand. *Can. Geotech. J.*, 45(11):1538–1555, 2008.

Yamamuro, J.A. and K.M. Covert. Monotonic and cyclic liquefaction of very loose sands with high silt content. *J. of Geo. and Geoenvir. Engrg*, 127(4):314–324, 2001.

Yan, W.M. and J. Dong. Effect of particle grading on the response of an idealized granular assemblage. *Int. J. of Geomechanics*, 11(4):276–285, 2011.

Yang, J. Liquefaction resistance of sand in relation to p-wave velocity. *Géotechnique*, 52(4): 295–298, 2002a.

Yang, J. Non-uniqueness of flow liquefaction line for loose sand. *Géotechnique*, 52(10):757–760, 2002b.

Yang, J. Liquefaction resistance of sand in relation to p-wave velocity. *Géotechnique*, 52(4): 295–298, 2002c.

Yang, J. Discussion: Non-uniqueness of flow liquefaction line for loose sand. *Géotechnique*, 54 (1):66–68, 2004.

Yang, J. and T. Sato. On the variation of poisson's ratio in shallow soil layers. pages 786–787, Kobe, Japan, 1998. 53rd Nat. Conf. of Japan Society of Civil Engineers.

Yang, J. and T. Sato. Liquefaction resistance of sand in relation to p-wave velocity. *Geotecnhique*, 51(2):161–165, 2001.

Yang, J. and H. Y. Sze. Cyclic behavior and resistance of saturated sand under non-symmetrical loading conditions. *Géotechnique*, 61(1):59–73, 2011.

Yang, S. L., R. Sandven, and L. Grande. Instability of sand–silt mixtures. *Soil Dynamics and Earthquake Eng.*, 26(2-4):183–190, 2006a.

Yang, S. L., R Sandven, and L. Grande. Steady-state lines of sand – silt mixtures. *Can. Geotech. J.*, 43:1213–1219, 2006b.

Yoshimine, M. and K. Ishihara. Flow potential of sand during liquefaction. *Soils and Foundations*, 38(3):189–198, 1998.

Yoshimine, M., P. K. Robertson, and C. E. Wride. Undrained shear strength of clean sands to trigger flow liquefaction. *Can. Geotech. J.*, 36(5):891–906, 1999.

Youd, T., I. Idriss, R. Andrus, I. Arango, G. Castro, J. Christian, R. Dobry, W. Finn, L. Harder, M. Hynes, K. Ishihara, J. Koester, S. Liao, W. Marcuson, G. Martin, J. Mitchell, Y. Moriwaki, M. Power, P. Robertson, R. Seed, and K.H.II. Stokoe. Liquefaction resistance of soils: Summary report from the 1996 nceer and 1998 nceer/nsf workshops on evaluation of liquefaction resistance of soils. *J. of Geotech. and Geoenviron. Eng.*, 127(10):817–833, 2001.

Yu, H. The first james k. mitchell lecture in situ soil testing: from mechanics to interpretation. *Geomechanics and Geoengineering*, 1(3):165–195, 2006.

Yu, H. S. Casm: A unified state parameter model for clay and sand. *Int. J. for Numerical and Analytical Methods in Geomech.*, 22(8):621–653, 1998.

Yu, P. and F. E. Richard. Stress ratio effects on shear moduli of dry sands. *J. Geotech. Eng., ASCE*, 110(3):331–345, 1984.

Zhou, Y. and Y. Chen. Laboratory investigation on assessing liquefaction resistance of sandy soils by shear wave velocity. *J. of Geotech. and Geoenviron. Eng., ASCE*, 133(8):959–972, 2007.

Zhou, Y.-G., Y.-M. Chen, and Y. Shamoto. Verification of the soil-type specific correlation between liquefaction resistance and shear-wave velocity of sand by dynamic centrifuge test. *J. of Geotech. and Geoenviron. Eng., ASCE*, 136(1):165–177, 2009.

Zlatovic, S. and K. Ishihara. Normalized behavior of very loose non-plastic soils: effects of fabric. *Soils and Foundations*, 37(4):47–56, 1997.

Zytynski, M., M. F. Randolph, R. Nova, and C. P. Wroth. On modelling the unloading-reloading behaviour of soils. *Int. J. for Numerical and Analytical Methods in Geomech.*, 2:87–93, 1978.

Appendix A

Initial Stiffness, Peak Strengths, Critical And Steady State Parameters

Due to the large data set of laboratory tests all the intermediate calculated values were indexed to the Annex. In this section of the thesis the principal intermediate values of each test stage are provided.

The procedure of calculus used for each test was followed according to Chapter 6. Plus some extra calculations were required in order to correct the void ratio of some triaxial tests.

The following tables provide a resume of each test stage, giving the volumetric strain after percolation and saturation and after consolidation, and the principle values achieved from the shear stage such as the shear strength, the mean effective stress associated to the shear strength, and the ultimate state strengths, which allows for CSL to be outlined. Plus tables also display shear waves velocities and for the cyclic triaxial and direct simple shear tests the number of cycles required for reaching the liquefaction condition.

In these tables an extra column follows up each test stage, marking those which void ratio was corrected. The symbols attributed to each correction are following explained:

- The symbol * represents those tests which void ratio was corrected after the percolation and saturation stages. A linear regression was adopted basing on measurements provided by other triaxial tests performed with exact same material;
- The double symbol (**) was adopted for those tests which volumetric strain was not acquired or measured (for various reasons). Therefore the void ratio of these tests was determined basing on the NCL definition or basing on a similar test. On the other hand the symbol ****** represents those tests which volumetric strain during consolidation was determined basing on the internal instrumentation measurements;

- The ultimate tests performed in the scope of the present research were most of all frozen at the end of the shear stage, being represented by ***. This technique revealed to be very accurate and due to the differences observed between these and those which void ratio was determined by using internal instrumentation, a correction was adopted and represented by **. This correction considers a new NCL, determined basing oh the freezing technique and an old NCL, determined with the internal instrumentation. The differences were implemented after the consolidation stage, meaning that the differences are exclusively attributed to the inaccuracy of the internal instrumentation on capturing the volumetric strain during the percolation and saturation stages, where the specimen is not fully saturated;

- During the shear stage some acquisition problems demanded the implementation of the hyperbolic model in order to predict the missing values. Those which the hyperbolic model was required are represented by ****.

- Finally the symbol ***** represents those triaxial tests which void ratio was carefully determined at the end of the shear stage by collecting the soil from the specimen. Then the soil was placed on capsules and weighted on a high precision balance. The procedure adopted to calculate the void ratio is similar to the freezing technique with exception that not all the soil is collected; therefore the void ratio is determined basing on the water content but the final volume of the specimen bases on the initial dry soil weight.

The graphs which follow the tables are properly identified and were used to correct the triaxial tests which are marked with the symbol * or with **. As explained previously the triaxial tests marked with * were corrected basing on the linear regressions given by Figures A.1, A.2, A.3, A.4 and A.6, while those marked with ** were corrected basing on linear regressions given by Figures A.5, A.7 and A.8. Obviously each table and each graph are addressed to each soil for which the correction was used.

Table A.1: List of the triaxial tests performed with Algeria sand completed with initial state values, strength and stiffness parameters

		After modelling	Percolation + Saturation			Consolidation						Shear				Values used for
	Test ID	e_0	ε_v (%)	e_{i-1}		ε_v (%)	e_i	p'_i kPa	K_0	V_s m/s	ε_v (%)	ef	p'_f kPa	q_f kPa	p'_{qpeak} kPa	q_{peak} kPa		used for
ALGERIA SAND	Tx_CID_1	0.882	0.44	0.873		5.67	0.767	500	1.0	n.v.	1.45	0.741	883.7	1151.2				CSL
	Tx_CID_2	0.862	0.15	0.859		0.00	0.859	14	1.0	n.v.	0.98	0.841	29.0	41.4				CSL
	Tx_CID_3	0.862	0.37	0.855		2.52	0.808	1006	1.0	n.v.	4.39	0.729	1756.5	2267.6				CSL Grain crushing
	Tx_CID_4	0.541	0.16	0.539		0.21	0.535	100	1.0	n.v.	-5.94	0.627	180.5	226.4				Too dense to reach the CSL
	Tx_CID_5	0.612	0.24	0.609		0.04	0.608	31	1.0	n.v.	-6.87	0.718	56.1	73.5				Too dense to reach the CSL
	Tx_CID_6	0.783	-0.04	0.784		0.00	0.784	10	1.0	n.v.	0.29	0.779	16.2	21.1				Other reasons
	Tx_CID_7	0.790	0.29	0.785		2.48	0.741	1000	1.0	n.v.	4.33	0.666	1740.5	2227.8				CSL Grain crushing
	Tx_CID_8	0.832	0.87	0.816		0.00	0.816	10	1.0	92	1.74	0.785	15.5	17.3				Other reasons
	Tx_CID_9	0.862	0.45	0.853	*	0.00	0.853	10	1.0	n.v.	1.51	0.825	13.3	11.9				Other reasons
	Tx_CID_10	0.950	1.62	0.918	*	0.35	0.912	29	1.0	n.v.	1.24	0.889	49.2	55.4				Other reasons
	Tx_CID_11	0.952	1.63	0.920	*	0.87	0.868	50	1.0	n.v.	3.17	0.809	84.2	103.3		***		CSL
	Tx_CID_12	0.540	0.09	0.539		4.04	0.485	7433	1.0	n.v.	9.82	0.340	13449.7	18243.5		****		CSL Grain crushing
	Tx_CIU_1	0.804	0.00	0.804	*	0.30	0.799	50	1.0	n.v.		0.799	95.0	108.9	40.1	41.5		CSL
	Tx_CIU_2	0.873	0.82	0.857	*	1.32	0.833	402	1.0	n.v.		0.833	225.8	261.3	264.1	229.4		Other reasons
	Tx_CIU_3	0.908	1.23	0.884	*	1.37	0.858	99	1.0	n.v.		0.858	0.1	0.0	80.1	58.5		
	Tx_CIU_4	0.866	0.84	0.851	*	0.32	0.845	50	0.9	n.v.		0.845	30.0	36.3	35.0	31.9		Other reasons
	Tx_CIU_5	0.866	0.84	0.851	*	0.49	0.842	48	1.0	n.v.		0.842	0.1	0.0	34.0	20.5		
	Tx_CIU_6	0.866	0.84	0.851	*	2.27	0.809	200	1.0	n.v.	(**)	0.809	0.1	0.0	147.0	94.8		
	Tx_CK$_0$U_1	0.882	1.39	0.856		0.84	0.840	68	0.5	161		0.840	0.1	0.0	67.8	59.0		
	Tx_CK$_0$U_2	0.865	1.06	0.845		0.93	0.828	134	0.5	203		0.828	30.9	39.7	137.1	127.6		CSL
	Tx_CK$_0$U_3	0.840	0.69	0.827		1.57	0.788	267	0.5	203		0.788	316.5	404.7	237.9	248.9		CSL
	Tx_CK$_0$U_4	0.840	0.60	0.829	*	0.09	0.829	50	0.6	156		0.829	200.1	254.7	39.5	39.0		Other reasons
	Tx_CK$_0$U_5	0.833	0.64	0.821		0.78	0.798	76	0.5	n.v.		0.798	0.1	0.0	73.2	49.7		
	Tx_CIU_7	0.814	0.61	0.803		0.71	0.790	100	1.0	n.v.		0.790	0.1	0.0	63.8	52.5		
	Tx_CIU_8	0.868	0.75	0.854		0.00	0.854	23	1.0	138		0.854	0.1	0.0	17.6	9.1		
	Tx_CIU_9	0.852	0.18	0.848		1.29	0.824	220	0.9	n.v.		0.824	0.1	0.0	42.6	39.4		
	Tx_CIU_10	0.871	0.51	0.861		0.10	0.859	31	1.0	134		0.859	0.1	0.0	22.0	14.5		
	Tx_CIU_11	0.866	1.04	0.846		0.89	0.830	99	1.0	168		0.830	0.1	0.0	70.3	45.3		
	Tx_CIU_12	0.841	0.40	0.834		1.60	0.805	400	1.0	280		0.805	194.7	257.8	248.2	255.9		CSL
	Tx_CIU_13	0.867	0.85	0.851	*	2.92	0.797	1001	1.0	411		0.797	376.5	495.6	540.4	536.9		CSL
	Tx_CIU_14	0.809	-0.12	0.811		0.00	0.811	15	1.0	127		0.811	63.0	85.8	13.2	10.9		Other reasons
	Tx_CK$_0$U_6	0.871	0.89	0.854	*	2.55	0.779	1451	0.4	n.v.		0.780	585.4	749.2	1451.1	1354.2		CSL
	Tx_CIU_15	0.783	0.33	0.777		1.72	0.746	529	1.0	343		0.746	512.6	645.7	369.4	369.0		Other reasons
	Tx_CIU_16	0.799	0.17	0.796		3.47	0.734	1503	1.0	415		0.732	976.6	1236.7	1197.5	1136.2		CSL Grain crushing
	Tx_CK$_0$U_7	0.833	0.16	0.830	*	0.00	0.780	13	0.4	n.v.		0.780	0.1	0.0	13.4	10.8		

Table A.2: List of the triaxial tests performed with Coimbra sand completed with initial state values, strength and stiffness parameters

	After modelling	Percolation + Saturation				Consolidation						Shear				Values used for
Test ID	e_0	ε_v (%)	e_{i1}		ε_v (%)	e_i	p'_i kPa	K_0	V_s m/s		ε_v (%)	ef	p'_f kPa	q_f kPa	p'_{qpeak} kPa	q_{peak} kPa	used for
Tx_CID_MT_1	0.617	0.67	0.606		-0.05	0.607	20	1.0	153		-2.69	n.v.	n.v.	n.v.			Too dense to reach the CSL
Tx_CID_MT_2	0.672	-0.10	0.674		0.11	0.672	20	1.0	n.v.		-1.15	0.691	30.8	33.7			Other reasons
Tx_CID_MT_3	0.607	-0.51	0.615	*	0.30	0.610	50	1.0	n.v.		-1.50	0.634	87.9	105.5			Too dense to reach the CSL
Tx_CID_MT_4	0.789	1.40	0.764		0.81	0.750	101	1.0	182		1.99	0.715	172.0	214.1			CSL
Tx_CID_MT_5	0.621	-0.34	0.627		0.95	0.611	400	1.0	305		-3.59	0.669	712.0	934.1		****	CSL
Tx_CID_MT_6	0.766	0.17	0.763	*	2.60	0.717	1002	1.0	n.v.		3.59	0.655	1720.9	2157.0			CSL
Tx_CID_MT_7	0.670	-0.12	0.672	*	6.26	0.564	8010	1.0	n.v.		10.08	0.406	13111.7	15348.6			CSL Grain crushing
Tx_CID_MT_8	0.645	-0.27	0.649	*	5.48	0.559	9500	1.0	n.v.		14.62	0.371	15819.5	18984.1		****	CSL Grain crushing
Tx_CIU_MT_1	0.718	0.16	0.715	*	1.29	0.693	100	1.0	177			0.693	0.1	0.0	57.7	43.4	
Tx_CIU_MT_2	0.710	0.12	0.708	*	1.04	0.691	100	1.0	162			0.691	0.1	0.0	65.2	32.2	
Tx_CIU_MT_3	0.685	0.03	0.685	*	1.91	0.653	201	1.0	218			0.653	0.1	0.0	121.4	87.3	
Tx_CIU_MT_4	0.661	-0.17	0.664	*	1.75	0.635	400	1.0	313			0.635	243.3	299.8	282.1	350.7	SSL
Tx_CIU_MT_5	0.499	-3.71	0.554		1.32	0.534	400	1.0	285			0.534	1418.6	1762.7	no peak	no peak	Other reasons
Tx_CIU_MT_6	0.659	-0.37	0.665		2.16	0.629	400	1.0	282			0.629	0.1	0.0	241.1	178.0	
Tx_CIU_MT_7	0.641	-0.30	0.646	*	2.71	0.601	900	1.0	377			0.601	845.6	1035.7	no peak	no peak	SSL
Tx_CIU_MT_8	0.641	-0.30	0.645	*	1.85	0.615	1100	1.0	n.v.			0.615	1772.0	2269.0	no peak	no peak	CSL Grain crushing
Tx_CIU_MT_9	0.691	0.01	0.691	*	7.79	0.559	9500	1.0	n.v.			0.559	2713.8	3066.7	4286.0	4381.3	CSL Grain crushing
Tx_CIU_MT_10	0.716	0.15	0.713	*	3.21	0.658	698	1.0	363			0.658	n.v.	n.v.	no peak	no peak	
Tx_CIU_MT_11	0.690	-0.02	0.687	*	2.43	0.641	1242	1.0	372	**		0.641	356.0	435.4	471.8	463.5	SSL
Tx_CIU_MT_12	0.670	0.00	0.672	*	2.83	0.624	2505	1.0	n.v.	**		0.624	1268.4	1525.2	1842.6	1611.4	CSL Grain crushing
Tx_CID_PL_1	0.656	-0.20	0.660	*	7.71	0.526	5091	1.0	n.v.			n.v.	n.v.	n.v.	0	0	
Tx_CID_PL_2	0.620	-0.43	0.627	*	0.70	0.602	202	1.0	n.v.			0.617	179.3	217.7	0	0	Too dense to reach the CSL
Tx_CIU_PL_1	0.638	-0.32	0.643	*	0.08	0.631	50	1.0	206			0.631	520.1	691.8	no peak	no peak	SSL
Tx_CIU_PL_2	0.655	-0.21	0.659	*	2.95	0.610	509	1.0	306			0.610	1046.1	1299.1	no peak	no peak	SSL
Tx_CIU_PL_3	0.651	-0.24	0.654	*	1.64	0.627	251	1.0	246			0.627	501.2	615.5	no peak	no peak	SSL
Tx_CIU_PL_4	0.626	-0.39	0.632	*	0.24	0.620	896	1.0	341			0.620	876.2	1154.3	no peak	no peak	SSL
Tx_CIU_PL_5	0.739	0.18	0.734	*	1.08	0.715	92	1.0	182			0.715	0.1	0	64.0	22.4	
Tx_CIU_PL_6	0.718	0.17	0.716	*	0.74	0.703	79	1.0	166			0.703	0.1	0	56.3	27.4	
Tx_CIU_PL_7	0.724	0.20	0.721	*	3.32	0.664	498	1.0	293			0.664	0.1	0	327.9	161.5	
Tx_CIU_PL_8	0.753	0.36	0.747	*	5.76	0.647	596	1.0	314			0.647	0.1	0	394.3	195.2	

COIMBRA SAND

Table A.3: List of the triaxial tests performed with Osorio sand completed with initial state values, strength and stiffness parameters

		After modelling	Percolation + Saturation			Consolidation							Shear				Values used for
	Test ID	e_0	ε_v (%)	e_{-1}		e_i	p'_i kPa	K_0	V_s m/s		ε_v (%)	e_f	p'_f kPa	q_f kPa	p'_{qpeak} kPa	q_{peak} kPa	used for
OSORIO SAND	Tx_CID_1	0.869	3.130	0.810		2.080	0.803	41	1.0	n.v.		n.v	n.v.	80.8	88.5			
	Tx_CID_2	0.861	3.208	0.801		0.299	0.796	25	1.0	n.v.		1.07	0.776	42.7	52.8			CSL
	Tx_CID_3	0.815	0.869	0.799		0.221	0.795	15	1.0	109		1.27	0.773	23.3	27.8			CSL
	Tx_CID_4	0.783	2.844	0.733		2.077	0.697	704	1.0	366		1.71	0.668	1247.0	1636.1			CSL
	Tx_CID_5	0.852	2.910	0.798		2.193	0.758	450	1.0	333		2.33	0.717	784.0	1001.2			CSL
	Tx_CID_6	0.749	-0.635	0.760		0.643	0.749	20	1.0	126		-1.46	0.774	33.6	39.1			Too dense to reach the CSL
	Tx_CID_7	0.717	?	0.696		7.201	0.582	9330	1.0	n.v.		11.98	0.495	15895.9	19649.5		****	CSL Grain crushing
	Tx_CID_8	0.737	0.404	0.731		2.795	0.682	730	1.0	n.v.		0.54	0.675	1253.7	1601.4			Other reasons
	Tx_CID_9	0.785	1.474	0.756		2.762	0.706	1284	1.0	391		3.45	0.647	2213.4	2802.2			CSL Grain crushing
	Tx_CID_10	0.748	n.v.	n.v.		n.v.	0.680	200	1.0	n.v.	**	-2.01	0.715	423.7	669.5			CSL
	Tx_CID_11	0.752	n.v.	n.v.		n.v.	0.686	100	1.0	n.v.	**	-2.17	0.724	186.7	261.6			CSL
	Tx_CID_12	0.756	n.v.	n.v.		n.v.	0.693	50	1.0	n.v.	**	-3.60	0.756	87.3	113.4			CSL
	Tx_CID_13	0.634	n.v.	n.v.		n.v.	0.568	200	1.0	n.v.	**	-5.05	0.650	365.2	496.1			Too dense to reach the CSL
	Tx_CID_14	0.633	n.v.	n.v.		n.v.	0.570	100	1.0	n.v.	**	-4.62	0.645	173.8	223.0			Too dense to reach the CSL
	Tx_CID_15	0.637	n.v.	n.v.		n.v.	0.576	20	1.0	n.v.	**	-5.72	0.669	20.6	3.2			Too dense to reach the CSL
	Tx_CIU_1	0.830	1.828	0.796		1.536	0.769	100	1.0	244			0.770	137.0	172.1	63.9	47.0	CSL
	Tx_CIU_2	0.864	2.019	0.826		1.338	0.802	50	1.0	184			0.802	0.1	0.0	35.8	21.0	
	Tx_CIU_3	0.857	3.771	0.787		0.641	0.776	25	1.0	153			0.776	0.1	0.0	17.7	8.7	
	Tx_CIU_4	0.834	1.908	0.799		0.711	0.787	100	1.0	221			0.787	0.1	0.0	63.0	42.5	
	Tx_CIU_5	0.873	3.604	0.805		1.134	0.785	199	1.0	264			0.785	0.1	0.0	127.8	86.3	
	Tx_CIU_6	0.863	4.830	0.773		1.345	0.749	299	1.0	298			0.747	114.1	137.5	193.0	140.7	CSL
	Tx_CIU_7	0.867	2.584	0.819		2.935	0.766	600	1.0	370			0.766	137.5	176.1	403.2	266.3	CSL
	Tx_CIU_8	0.830	1.676	0.799	*	2.936	0.746	1200	1.0	365			0.746	467.9	591.8	773.7	555.3	Other reasons
	Tx_CIU_9	0.850	2.648	0.801	*	2.372	0.758	600	1.0	365			0.758	146.5	189.2	386.0	253.4	CSL
	Tx_CIU_10	0.834	1.886	0.800	*	1.676	0.770	600	1.0	336			0.770	24.5	25.0	?	?	CSL
	Tx_CIU_11	0.848	1.619	0.818		1.312	0.794	132	0.5	n.v.			0.794	0.1	0.0	130.9	104.1	
	Tx_CIU_12	0.744	1.328	0.721		0.105	0.719	301	1.0	n.v.	******		0.719	661.6	806.8	no peak	no peak	CSL
	$TX_{q=constant}_CK_0D_1$	0.914	4.971	0.819		0.777	0.804	63	0.5	209			0.778	14.9	15.3	15.3	42.8	
	$TX_{q=constant}_CK_0D_2$	0.902	3.412	0.837		0.317	0.831	33	0.7	172			0.805	0.1	0.0	0.0	13.0	
	$TX_{q=constant}_CK_0D_3$	0.848	1.896	0.813		0.163	0.810	36	0.6	175			0.780	5.4	5.4	5.4	21.1	

Table A.4: List of the triaxial tests performed with Mixture completed with initial state values, strength and stiffness parameters

		After modelling	Percolation + Saturation			Consolidation							Shear				Values used for
	Test ID	e_0	ε_v (%)	e_{sl}	ε_v (%)	e_f	p'_i kPa	K_0	V_s m/s		ε_v (%)	e_f	p'_i kPa	q_f kPa	p'_{qpeak} kPa	q_{peak} kPa	used for
MIXTURE	Tx_CID_1	0.897			1.441	0.777	40	1.0	n.v.	**	n.v.	0.777	67.3	86.0			
	Tx_CID_2	0.932			1.527	0.646	51	1.0	n.v.	**	1.34	0.623	87.4	111.3		****	
	Tx_CID_3	0.946			0.836	0.703	26	1.0	75	**	4.01	0.635	40.8	53.4			CSL
	Tx_CID_4	0.911			4.267	0.604	400	1.0	n.v.	**	4.00	0.540	711.7	939.9			CSL
	Tx_CID_5	0.832		*	4.099	0.617	221	1.0	174	**	5.24	0.532	407.5	566.5			CSL
	Tx_CID_6	1.014		*	6.906	0.561	800	1.0	261	**	5.98	0.468	1518.7	2164.3			CSL
	Tx_CID_7	0.892			2.987	0.658	100	1.0	126	**	4.88	0.577	186.0	259.7			CSL
	Tx_CID_8	0.945			2.964	0.651	100	1.0	133	**	4.79	0.570	181.8	246.5			CSL
	Tx_CID_9	0.889			0.000	0.752	10	1.0	53	**	4.99	0.664	14.9	19.9			CSL
	Tx_CID_10	0.937			0.710	0.675	50	1.0	n.v.	**	6.83	0.560	124.8	213.7			
	Tx_CID_11	0.905	9.902	0.717	4.836	0.636	299	1.0	n.v.		4.54	0.549	544.7	731.7		***	CSL
	Tx_CID_12	0.834	8.964	0.669	3.065	0.618	151	1.0	n.v.		2.19	0.527	287.4	403.4		***	CSL
	Tx_CID_13	0.903	7.929	0.752	7.465	0.572	597	1.0	n.v.		5.78	0.481	1123.3	1568.5		***	
	Tx_CID_14	0.932	13.639	0.657	4.576	0.587	602	1.0	n.v.		5.10903	0.506	1107.1	1526.3		***	CSL
	Tx_CID_15	0.481			5.912	0.406	9397	1.0	n.v.		3.303461	0.356	16864.6	22481.5		***	CSL
	Tx_CID_16	0.571	2.684	0.533	5.660	0.450	3024	1.0	n.v.		1.34	0.431	5395.4	7117.2		***	CSL
	Tx_CIU_1	0.800			1.459	0.663	50	1.0	n.v.	**		0.663	1.8	0.2	25.5	15.3	
	Tx_CIU_2	0.942			2.415	0.611	200	1.0	n.v.	**		0.605	0.1	0.0	124.0	71.2	
	Tx_CIU_3	1.042		*	1.425	0.671	25	1.0	78	**		0.665	0.1	0.0	16.4	8.0	
	Tx_CIU_4	0.991			5.766	0.575	298	1.0	182	**		0.574	3.4	2.4	145.6	115.0	SSL
	Tx_CIU_5	0.954		*	6.252	0.578	399	1.0	208	**		0.566	9.7	10.1	252.9	178.0	SSL
	Tx_CIU_6	0.937			4.619	0.534	600	1.0	n.v.	**		0.528	99.2	140.2	340.9	278.4	SSL
	Tx_CIU_7	0.953		*	8.392	0.541	571	0.4	239	**		0.596	87.8	117.1	582.0	568.5	SSL K_0
	Tx_CIU_8	0.978	13.536	0.711	6.278	0.603	790	0.5	n.v.			0.603	37.8	65.6	707.5	741.4	***	SSL K_0
	Tx_CIU_9	0.880	12.963	0.639	6.714	0.536	999	1.0	n.v.			0.536	68.7	96.1	574.7	418.5	***	SSL
	Tx_CIU_10	1.001	15.228	0.701	5.791	0.608	220	1.0	n.v.			0.608	0.1	0.0	236.1	173.2	***	
	$Tx_{q=constant}_CK_0D_1$	0.821	3.888	0.750	3.064	0.697	38	0.5	122		3.08	0.645	23.4	0.0	37.7	26.6	
	$Tx_{q=constant}_CK_0D_2$	0.801	3.074	0.746	4.325	0.670	75	0.6	149		2.64	0.626	23.6	29.8	74.8	47.4	
	$Tx_{q=constant}_CK_0D_3$	0.788	3.748	0.721	2.100	0.685	18	0.5	n.v.		1.99	0.664	6.8	6.9	17.8	11.5	
	$Tx_{q=constant}_CK_0D_4$	0.653	0.042	0.652	1.276	0.631	34	0.7	117		2.21	0.612	8.5	8.1	34.1	15.0	
	$Tx_{p'=constant}_CID_1$	0.840	9.981	0.658	3.246	0.606	200	1.0	n.v.		4.71	0.530	197.0	182.0		*****	
	$Tx_{p'=diminishing}_CID_1$	0.872	9.552	0.695	2.775	0.650	101	1.0	n.v.		5.90	0.552	48.6	64.7		*****	
	$Tx_{p'=diminishing}_CID_2$	0.868	9.301	0.694	2.935	0.646	50	1.0	n.v.		6.32	0.542	16.1	20.5		*****	

Table A.5: List of the triaxial tests performed with Silt – part 1 completed with initial state values, strength and stiffness parameters

		After modelling	Percolation + Saturation		Consolidation							Shear					Values used for
	Test ID	e_0	ε_v (%)	e_{-1}	ε_v (%)	e_i	p'_i kPa	K_0	V_s m/s		ε_v (%)	e_f	p'_f kPa	q_f kPa	p'_{qpeak} kPa	q_{peak} kPa		used for
SILT	Tx_CID_1	1.255			0.896	0.809	16	1.0	76	**	4.66	0.724	26.0	34.6				Other reasons
	Tx_CID_2	1.255			5.060	0.726	99	1.0	128	**	2.83	0.677	192.8	278.9				CSL
	Tx_CID_3	1.285			1.025	0.834	19	1.0	n.v.	**	5.40	0.735	34.2	47.9				CSL
	Tx_CID_4	1.282			4.844	0.697	403	1.0	206	**	4.76	0.616	759.8	1078.6				CSL
	Tx_CID_5	1.203			n.v.	0.647	404	1.0	n.v.	**	2.12	0.612	877.6	1410.0				CSL
	Tx_CID_6	1.195			2.826	0.634	804	1.0	n.v.	**	3.40	0.579	1548.6	2228.3				CSL
	Tx_CID_7	0.602	0.762	0.604	6.444	0.501	7408	1.0	n.v.		2.88	0.457	11600.6	12572.7				CSL Grain crushing
	Tx_CID_8	1.033			1.473	0.763	41	1.0	107	(**)	3.82	0.695	73.5	102.3				CSL
	Tx_CID_9	1.112			1.329	0.777	30	1.0	n.v.	(**)	4.25	0.701	57.5	84.0				CSL
	Tx_CIU_1	1.255			0.848	0.810	15	1.0	73	**		0.810	0.1	0.0	10.3	3.5		
	Tx_CIU_2	1.244			2.430	0.767	30	1.0	91	**		0.767	0.1	0.0	19.3	12.8		
	Tx_CIU_3	1.244			3.564	0.744	50	1.0	110	**		0.744	0.1	0.0	27.6	15.8		
	Tx_CIU_4	1.244			4.894	0.718	99	1.0	140	**		0.718	6.8	7.0	59.7	36.5		SSL B<0.95
	Tx_CIU_5	1.244			6.546	0.686	201	1.0	168	**		0.686	18.5	24.5	115.2	78.3		SSL B<0.95
	Tx_CIU_6	1.212			6.946	0.649	699	1.0	276	**		0.650	443.4	637.5	575.2	635.0		CSL
	Tx_CIU_7	1.212			8.132	0.626	1199	1.0	287	**		0.627	920.4	1337.0	1097.2	1252.8		CSL
	Tx_CIU_8	1.213			0.293	0.778	30	1.0	n.v.	**		0.778	0.1	0.0	32.8	18.9		
	Tx_CIU_9	1.208			2.119	0.718	70	1.0	n.v.	**		0.718	3.1	3.6	40.4	24.1		SSL B<0.95
	Tx_CIU_10	1.218			2.841	0.734	110	1.0	n.v.	**		0.734	24.7	43.2	77.7	56.8		SSL B<0.95
	Tx_CIU_11	1.218			4.243	0.707	220	1.0	n.v.	**		0.707	50.9	80.7	146.7	117.8		SSL B<0.95
	Tx_CIU_12	1.214			4.643	0.695	265	1.0	n.v.	**		0.695	105.5	146.3	167.3	157.2		CSL
	Tx_CIU_13	1.218			5.681	0.679	342	1.0	n.v.	**		0.679	134.2	200.5	209.6	206.8		SSL B<0.95
	Tx_CIU_14	1.211			6.241	0.661	394	1.0	n.v.	**		0.661	264.8	398.1	262.8	281.9		CSL
	Tx_CK$_0$U_1	1.127			2.684	0.755	38	0.5	n.v.	(**)		0.755	0.1	0.0	34.7	31.0		
	Tx_CIU_15	1.274				0.726	101	1.0	127	**/(**)		0.726	0.1	0.0	58.1	38.8		
	Tx_CIU_16	1.303			* 0.677	0.793	20	1.0	80	**		0.793	0.1	0.0	14.7	5.2		
	Tx_CIU_17	1.224			11.787	0.608	1499	1.0	n.v.	(**)		0.608	1094.6	1396.4	1272.3	1210.7		CSL
	Tx_CIU_18	1.224			0.794	0.844	20	1.0	n.v.	**		n.v.	n.v.	n.v.	0	0	***	not completly undrained
	Tx_CIU_19	1.004	16.058	0.672	4.521	0.600	401	1.0	n.v.			0.610	400.7	549.8	210.9	185.2	***	not completly undrained
	Tx_CIU_20	1.006	15.227	0.700	4.273	0.630	499	1.0	n.v.			0.626	72.1	95.0	349.6	244.2	***	not completly undrained
	Tx_CIU_21	1.278			3.039	0.756	50	1.0	105	**		0.756	0.1	0.0	32.9	21.1		
	Tx_CIU_22	1.144			3.996	0.678	298	1.0	204	**		0.678	16.0	10.5	173.1	66.9		Other reasons
	Tx_CIU_23	1.043	13.903	0.781	3.952	0.713	197	1.0	n.v.			0.713	0.1	0.0	125.7	68.7	***	
	Tx_CIU_24	1.098	16.904	0.746	5.342	0.658	400	1.0	n.v.			0.657	0.1	0.0	243.5	156.3	***	
	Tx_CIU_25	1.125	18.300	0.736	5.235	0.650	701	1.0	n.v.			0.650	25.0	44.2	447.9	322.1	***	SSL B>0.97
	Tx_CIU_26	1.127	18.273	0.741	7.661	0.617	1185	1.0	n.v.			0.615	592.6	788.8	789.6	591.1	***	CSL

Table A.6: List of the triaxial tests performed with Silt – part 2 completed with initial state values, strength and stiffness parameters

		After modelling	Percolation + Saturation				Consolidation							Shear				Values used for
	Test ID	e_0	ε_v (%)	e_{-1}		ε_v (%)	e_i	p'_i kPa	K_0	V_s m/s		ε_v (%)	e_f	p'_f kPa	q_f kPa	p'_{qpeak} kPa	q_{peak} kPa	used for
SILT	Tx_EK$_0$U_1	1.127			*	0.426	0.800	77	0.6	n.v.	**		0.740	104.0	-36.7	60.4	-38.0	
	Tx_EK$_0$U_2	1.073			*	0.785	0.772	46	0.4	n.v.	**		0.771	2.3	-16.2	17.0	-11.4	
	Tx_EK$_0$U_3	1.076			*	1.366	0.786	76	0.6	n.v.	**		0.786	0.1	-17.7	39.3	-22.8	
	Tx_EK$_0$U_4	1.192			*	2.094	0.782	128	0.5	n.v.	**		0.782	-0.2	-15.1	51.4	-21.7	
	Tx$_{q=constant}$_CK$_0$D_1	1.251			*	3.583	0.751	39	0.5	n.v.	**	0.19	0.748	5.3	0.0	39.2	28.1	
	Tx$_{q=constant}$_CK$_0$D_2	1.189			*	3.623	0.691	133	0.5	120	**	0.19	0.688	13.4	6.1	133.3	102.1	
	Tx$_{q=constant}$_CK$_0$D_3	1.256				3.971	0.711	131	0.5	146	**	0.19	0.708	47.4	64.7	130.9	92.0	
	Tx$_{q=constant}$_CK$_0$D_4	1.205				3.563	0.648	269	0.5	155	**	-0.10	0.650	112.5	157.2	269.0	208.3	
	Tx$_{q=constant}$_CK$_0$D_5	1.191			*	3.706	0.691	79	0.5	189	**	0.24	0.687	11.3	4.2	78.7	57.4	
	Tx$_{q=constant}$_CK$_0$D_6	1.191			*	1.488	0.733	35	0.6	127	**	0.24	0.729	4.2	0.9	35.2	18.6	
	Tx$_{q=constant}$_CK$_0$D_7	1.194			*	1.472	0.737	72	0.7	96	**	-0.28	0.742	3.0	2.0	72.1	32.9	
	Tx$_{q=constant}$_CK$_0$D_8	1.178			*	1.421	0.722	35	0.8	127	**	0.53	0.713	0.1	0.0	34.6	7.9	
	Tx$_{q=constant}$_CK$_0$D_9	1.246			*	1.278	0.728	44	0.8	93	**	0.23	0.724	4.5	2.1	44.0	10.8	
	Tx$_{q=constant}$_CK$_0$D_10	1.249			*	2.147	0.778	76	0.8	104	**	0.26	0.773	0.1	0.0	75.7	18.8	
	Tx$_{q=constant}$_CK$_0$D_11	1.176			*	1.660	0.715	39	0.5	125	**	0.98	0.698	18.7	0.4	38.9	30.4	
	Tx$_{q=constant}$_CK$_0$D_12	1.232			*	6.930	0.717	79	0.5	n.v.	**	0.56	0.727	32.9	50.4	78.6	58.4	
	Tx$_{q=constant}$_CK$_0$D_13	1.176			*	2.961	0.690	79	0.5	n.v.	**	-0.41	0.697	26.6	38.1	78.8	55.5	
	Tx$_{q=constant}$_CK$_0$D_14	1.212				0.353	0.677	64	0.8	n.v.	**	-0.38	0.683	7.7	7.4	63.9	14.4	
	Tx$_{q=constant}$_CK$_0$D_15	1.249				2.587	0.706	117	0.7	n.v.	**	-0.20	0.708	14.6	7.8	116.6	49.5	
	Tx$_{q=constant}$_CK$_0$D_16	1.266				1.668	0.751	130	0.8	144	**	0.54	0.742	18.2	21.8	130.1	33.8	
	Tx$_{q=constant}$_CK$_0$D_17	1.261				0.957	0.798	89	0.7	158	**	-0.70	0.810	6.9	12.0	89.3	27.6	
	Tx$_{q=constant}$_CK$_0$D_18	1.241				3.501	0.685	136	0.6	139	**	-0.53	0.694	60.5	73.7	135.9	76.8	
	Tx$_{q=constant}$_CK$_0$D_19	1.211			*	1.107	0.761	36	0.7	177	**	0.41	0.754	6.4	4.7	35.9	15.5	
	Tx$_{q=constant}$_CK$_0$D_20	1.195			*	0.744	0.751	30	0.9	103	**	-0.21	0.755	2.1	0.0	30.2	2.8	
	Tx$_{q=constant}$_CK$_0$D_21	1.158			*	1.357	0.771	32	0.7	88	**	-0.40	0.778	3.5	1.7	32.3	10.4	

Table A.7: List of the triaxial tests performed with Gold tailings completed with initial state values, strength and stiffness parameters

		After modelling	Percolation + Saturation		Consolidation							Shear				Values used for
	Test ID	e_0	ε_v (%)	e_{i-1}	ε_v (%)	e_i	p'_i kPa	K_0	V_s m/s		ε_v (%)	e_i	p'_i kPa	q_i kPa	p'_{qpeak} kPa	q_{peak} kPa		used for
GOLD TAILINGS	Tx_CID_1	1.333			0.81	1.014	15	1.0	78	**	6.07	0.892	25.3	37.0				CSL
	Tx_CID_2	1.336			3.83	0.940	50	1.0	115	**	4.99	0.843	93.6	132.0				CSL
	Tx_CID_3	1.336			5.04	0.907	100	1.0	141	**	5.11	0.810	190.7	276.5				CSL
	Tx_CID_4	1.184	5.91	1.059	0.00	1.059	8	1.0	n.v.		7.78	0.899	16.3	25.4			***	CSL
	Tx_CID_5	0.880	9.19	0.710	13.11	0.512	4675	1.0	n.v.		6.91	0.407	8442.9	11845.8			***	CSL Grain crushing
	Tx_CID_6	1.239	11.17	0.994	7.31	0.859	299	1.0	n.v.		6.88	0.731	570.1	826.9			***	CSL Grain crushing
	Tx_CID_7	0.851	8.31	0.697	16.18	0.461	9500	1.0	n.v.		6.43	0.367	11222.5	14728.7			***	CSL Grain crushing
	Tx_CIU_1	1.350			0.82	1.031	15	1.0	75	**		1.031	0.1	0.0	9.5	4.5		
	Tx_CIU_2	1.350			1.89	1.004	22	1.0	85	**		1.004	0.1	0.0	13.5	7.2		
	Tx_CIU_3	1.350			2.37	0.990	30	1.0	96	**		0.990	0.1	0.0	17.1	8.7		
	Tx_CIU_4	1.350			3.56	0.959	50	1.0	114	**		0.959	0.1	0.0	27.3	14.0		
	Tx_CIU_5	1.350			4.26	0.943	60	1.0	131	**		0.943	0.1	0.0	32.7	19.8		
	Tx_CIU_6	1.350			4.48	0.936	75	1.0	131	**		0.936	1.7	3.4	43.9	29.8		SSL B<0.95
	Tx_CIU_7	1.350			4.74	0.927	100	1.0	156	**		0.927	6.5	6.9	56.5	37.4		SSL B<0.95
	Tx_CIU_8	1.350			6.47	0.883	200	1.0	173	**		0.883	35.6	44.4	114.2	98.7		SSL B<0.95
	Tx_CIU_9	1.197			6.05	0.790	400	1.0	n.v.	**		0.790	159.3	240.5	204.5	252.9		CSL
	Tx_CIU_10	1.350			11.06	0.794	600	1.0	279	**		0.794	277.5	408.7	391.1	410.7		CSL
	Tx_CIU_11	1.350			11.97	0.774	800	1.0	293	**		0.774	331.9	526.3	463.2	511.4		CSL
	Tx_CIU_12	1.350			12.70	0.758	1000	1.0	318	**		0.758	512.0	755.4	658.7	734.7		CSL
	Tx_CIU_13	1.350			13.76	0.735	1200	1.0	334	**		0.735	740.2	1109.1	891.5	1059.3		CSL Grain crushing
	Tx_CIU_14	1.247	13.20	0.954	4.56	0.869	100	1.0	n.v.			0.869	10.4	15.4	60.7	44.3	***	SSL B>0.97
	Tx_CIU_15	1.334	14.19	1.006	5.41	0.903	100	1.0	n.v.			n.v.	n.v.	n.v.	n.v.	n.v.	***	
	Tx_CIU_16	1.267	11.64	1.003	8.70	0.843	299	1.0	n.v.			0.843	19.5	28.2	157.9	123.4	***	SSL B>0.97
	$Tx_{p'\text{-diminishing}}$_CID_1	1.314	11.80	1.041	5.30	0.938	38	0.5	n.v.		4.84	0.844	53.2	75.0			*****	
	$Tx_{p'\text{-diminishing}}$_CID_2	1.282	10.37	1.050	3.61	0.978	50	1.0	111		5.78	0.864	25.3	29.1			*****	
	$Tx_{p'\text{-diminishing}}$_CID_3	1.333	13.10	1.030	1.96	0.991	30	1.0	89		7.54	0.883	13.4	8.6			*****	
	$Tx_{p'\text{-diminishing}}$_CID_4	1.283	11.72	1.020	0.23	1.015	15	1.0	63		5.65	0.903	3.8	0.0			*****	
	$Tx_{r'\text{-constant}}$_CID_1	1.305	0.86	1.288	23.22	0.857	300	1.0	n.v.		6.31	0.740	379.1	441.1			*****	
	$Tx_{p'\text{-diminishing}}$_CID_5	1.256	9.43	1.047	9.52	0.869	300	1.0	n.v.		3.85	0.797	141.2	171.4			*****	

Table A.8: List of the cyclic triaxial tests performed with Algeria sand – part 1 completed with initial state values, strength and stiffness parameters

	After modelling	Percolation + Saturation					Consolidation					Cycles to liquefy		Type of liquefaction
	Test ID	e_0	ε_v (%)	e_{i+1}		ε_v (%)	e_i	p'_i kPa	K_0	$\tau/(2\sigma'_{n0})$	V_s m/s			
ALGERIA SAND	CTx_CK$_0$U_1	0.851	0.535	0.841	*	0.937	0.824	94	0.6	0.09	206		0	Flow liquefaction
	CTx_CK$_0$U_2	0.837	0.432	0.829	*	1.009	0.811	133	0.5	0.12	n.v.		3	Flow liquefaction
	CTx_CK$_0$U_3	0.858	0.585	0.847	*	1.440	0.820	267	0.5	0.12	242		9	Flow liquefaction - Strain soft.
	CTx_CK$_0$U_4	0.863	0.628	0.852	*	0.739	0.838	67	0.5	0.11	171		147	Flow liquefaction
	CTx_CK$_0$U_5	0.884	0.803	0.869	*	1.166	0.834	132	0.5	0.14	201		179	Cyclic mobility
	CTx_CK$_0$U_6	0.853	0.549	0.843	*	0.479	0.834	31	0.5	0.11	131		110	Flow liquefaction
	CTx_CK$_0$U_7	0.865	0.642	0.853	*	0.228	0.855	34	0.5	0.05	144		256	Cyclic mobility
	CTx_CK$_0$U_8	0.847	0.505	0.838	*	0.951	0.849	133	0.5	0.06	196	**	9	Flow liquefaction - Strain soft.
	CTx_CK$_0$U_9	0.846	0.492	0.836	*	1.074	0.817	130	0.5	0.06	186	**	2	Flow liquefaction
	CTx_CIU_1	0.845	0.488	0.836	*	1.195	0.814	202	1.0	0.12	n.v.	**	260	Flow liquefaction
	CTx_CIU_2	0.852	0.542	0.842	*	0.318	0.830	48	0.9	0.14	n.v.	**	91	Flow liquefaction - Strain soft.
	CTx_CK$_0$U_2	0.760	0.000	0.760	*	0.386	0.753	132	0.5	0.07	257	**	>590	Did not reached the CSL
	CTx_CK$_0$U_13	0.764	0.015	0.763	*	0.029	0.763	40	0.3	0.05	178	**	>606	Did not reached the CSL
	CTx_CK$_0$U_14	0.805	0.227	0.801	*	0.874	0.785	132	0.5	0.07	227	**	35	Cyclic mobility
	CTx_CK$_0$U_15	0.803	0.215	0.799	*	0.039	0.799	31	0.5	0.05	146	**	13	Flow liquefaction - Strain soft.
	CTx_CK$_0$U_16	0.813	0.272	0.808	*	0.029	0.807	20	0.5	0.03	168		40	Flow liquefaction
	CTx_CK$_0$U_17	0.784	0.075	0.783	*	0.164	0.779	28	0.5	0.06	158		n.v.	Did not reached the CSL
	CTx_CK$_0$U_18	0.793	0.155	0.790	*	0.274	0.785	27	0.5	0.23	148		3	Flow liquefaction - Strain soft.
	CTx_CK$_0$U_19	0.819	0.397	0.811	*	0.459	0.803	25	0.5	0.10	138		29	Flow liquefaction - Strain soft.
	CTx_CK$_0$U_20	0.804	0.258	0.799	*	0.203	0.796	26	0.5	0.12	142		29	Flow liquefaction - Strain soft.
	CTx_CK$_0$U_21	0.833	0.531	0.823	*	0.408	0.816	29	0.5	0.07	146		n.v.	Did not reached the CSL
	CTx_CK$_0$U_22	0.817	0.380	0.810	*	0.464	0.802	26	0.5	0.13	148		3	Flow liquefaction
	CTx_CK$_0$U_23	0.791	0.136	0.788	*	0.283	0.783	28	0.5	0.12	164		30	Flow liquefaction - Strain soft.
	CTx_CK$_0$U_24	0.791	0.136	0.788	*	0.342	0.782	25	0.5	0.46	154		950	Flow liquefaction - Strain soft.
	CTx_CK$_0$U_25	0.762	0.007	0.762	*	0.189	0.758	27	0.5	0.34	n.v.		0	Flow liquefaction - Strain soft.
	CTx_CK$_0$U_26	0.771	0.048	0.761	*	0.360	0.764	26	0.5	0.23	173		0	Flow liquefaction
	CTx_CK$_0$U_27	0.761	0.004	0.761	*	0.456	0.753	27	0.5	0.28	163		2	Flow liquefaction - Strain soft.
	CTx_CK$_0$U_28	0.751	-0.034	0.752	*	0.796	0.738	82	0.5	0.18	n.v.		488	Cyclic mobility
	CTx_CK$_0$U_29	0.745	-0.058	0.746	*	0.795	0.732	86	0.5	0.17	n.v.		467	Cyclic mobility
	CTx_CK$_0$U_30	0.724	-0.124	0.727	*	0.654	0.715	81	0.5	0.32	216		78	Cyclic mobility
	CTx_CK$_0$U_31	0.724	0.093	0.779	*	0.654	0.767	79	0.5	0.30	205		4	Cyclic mobility
	CTx_CK$_0$U_32	0.775	0.066	0.774	*	0.883	0.758	80	0.5	0.16	166		3	Flow liquefaction
	CTx_CK$_0$U_33	0.748	-0.048	0.749	*	0.726	0.736	67	0.5	0.22	173		0	Flow liquefaction - Strain soft.
	CTx_CK$_0$U_34	0.772	0.054	0.771	*	0.900	0.756	68	0.5	0.18	172		3	Flow liquefaction - Strain soft.
	CTx_CK$_0$U_35	0.749	-0.042	0.750	*	0.806	0.736	66	0.5	0.08	n.v.		0	Flow liquefaction - Strain soft.
	CTx_CK$_0$U_36	0.795	0.167	0.792	*	0.782	0.778	80	0.5	0.19	166		0	Flow liquefaction - Strain soft.
	CTx_CK$_0$U_37	0.771	0.046	0.770	*	0.374	0.763	26	0.5	0.22	147		1	Flow liquefaction
	CTx_CK$_0$U_38	0.757	-0.014	0.757	*	0.282	0.752	28	0.5	0.16	176		39	Cyclic mobility
	CTx_CK$_0$U_39	0.729	0.039	0.768	*	0.193	0.728	26	0.5	0.22	173		400	Did not reached the CSL
	CTx_CK$_0$U_40	0.782	0.100	0.780	*	0.207	0.776	28	0.5	0.21	167		0	Flow liquefaction - Strain soft.

Table A.9: List of the cyclic triaxial tests performed with Algeria sand – part 2 completed with initial state values, strength and stiffness parameters

		After modelling	Percolation + Saturation				Consolidation					Cycles to liquefy	Type of liquefaction
	Test ID	e_0	ε_v (%)	e_{i-1}		ε_v (%)	e_i	p'_i kPa	K_0	$\tau/(2x\sigma'_{in0})$	V_s m/s		
ALGERIA SAND	CTx_CK$_0$U_41	0.734	-0.094	0.736	*	0.223	0.732	27	0.5	0.23	165	176	Cyclic mobility
	CTx_CK$_0$U_42	0.735	-0.093	0.736	*	0.205	0.733	27	0.5	0.27	166	239	Cyclic mobility
	CTx_CK$_0$U_43	0.733	-0.098	0.735	*	0.193	0.732	26	0.5	0.32	n.v.	436	Cyclic mobility
	CTx_CK$_0$U_44	0.739	-0.079	0.741	*	0.158	0.738	26	0.5	0.40	n.v.	104	Cyclic mobility
	CTx_CK$_0$U_45	0.781	0.093	0.779	*	0.181	0.776	27	0.5	0.49	144	56	Cyclic mobility
	CTx_CK$_0$U_46	0.742	-0.069	0.743	*	0.648	0.732	69	0.5	0.33	n.v.	2	Cyclic mobility
	CTx_CK$_0$U_47	0.758	-0.009	0.758	*	0.451	0.750	54	0.5	0.43	153	139	Cyclic mobility
	CTx_CK$_0$U_48	0.760	0.023	0.756	*	0.227	0.756	54	0.5	0.27	n.v.	139	Cyclic mobility
	CTx_CK$_0$U_49	0.709	-0.163	0.712	*	1.000	0.704	439	0.6	0.50	n.v.	1000	Cyclic mobility
	CTx_CK$_0$U_50	0.693	0.302	0.688	*	0.090	0.695	868	0.5	0.54	n.v.	>1000	Cyclic mobility
	CTx_CK$_0$U_51	0.703	-0.176	0.706	*	1.806	0.675	866	0.5	0.64	n.v.	31	Cyclic mobility
	CTx_CK$_0$U_52	0.682	-0.210	0.685	*	0.691	0.644	1225	0.4	0.42	n.v.	526	Cyclic mobility
	CTx_CK$_0$U_53	0.857	0.577	0.846	*	4.613	0.762	1064	0.5	0.23	n.v.	0	Flow liquefaction - Strain soft.
	CTx_CK$_0$U_54	0.816	0.290	0.811	*	3.642	0.745	1066	0.5	0.20	n.v.	4	Flow liquefaction - Strain soft.
	CTx_CK$_0$U_55	0.844	0.480	0.835	*	2.425	0.791	398	0.5	0.20	n.v.	0	Flow liquefaction - Strain soft.
	CTx_CK$_0$U_56	0.802	0.206	0.798	*	1.318	0.774	396	0.5	0.15	n.v.	18	Flow liquefaction - Strain soft.
	CTx_CK$_0$U_57	0.913	1.075	0.893	*	3.437	0.828	398	0.5	0.12	n.v.	3	Flow liquefaction - Strain soft.
	CTx_CK$_0$U_58	0.869	0.676	0.856	*	2.414	0.812	399	0.5	0.16	n.v.	44	Flow liquefaction - Strain soft.
	CTx_CK$_0$U_59	0.744	-0.063	0.745	*	2.005	0.710	401	0.5	0.34	n.v.	305	Cyclic mobility
	CTx_CIU_3	0.761	0.005	0.761	*	0.311	0.756	40	0.9	0.13	n.v.	451	Cyclic mobility
	CTx_CIU_4	0.778	0.079	0.776	*	0.413	0.769	38	0.9	0.14	n.v.	64	Flow liquefaction - Strain soft.
	CTx_CIU_5	0.790	0.143	0.788	*	0.385	0.781	39	0.9	0.17	n.v.	78	Flow liquefaction - Strain soft.
	CTx_CIU_6	0.787	0.125	0.785	*	0.578	0.774	40	1.0	0.23	n.v.	11	Flow liquefaction - Strain soft.
	CTx_CIU_7	0.770	0.042	0.769	*	0.218	0.765	40	0.9	0.25	n.v.	11	Flow liquefaction - Strain soft.
	CTx_CIU_8	0.819	0.307	0.813	*	0.486	0.804	40	0.9	0.19	n.v.	20	Flow liquefaction - Strain soft.
	CTx_CIU_9	0.772	0.050	0.771	*	0.357	0.764	38	1.0	0.22	n.v.	13	Flow liquefaction - Strain soft.
	CTx_CIU_10	0.733	-0.098	0.735	*	0.300	0.730	38	0.9	0.29	n.v.	19	Cyclic mobility
	CTx_CIU_11	0.744	-0.060	0.746	*	0.236	0.741	39	0.9	0.31	n.v.	34	Cyclic mobility
	CTx_CIU_12	0.793	0.155	0.790	*	0.190	0.786	40	1.0	0.32	n.v.	19	Cyclic mobility
	CTx_CIU_13	0.728	-0.114	0.730	*	0.290	0.725	40	1.0	0.42	159	5	Cyclic mobility
	CTx_CIU_14	0.759	-0.006	0.759	*	0.235	0.755	39	1.0	0.43	158	7	Cyclic mobility
	CTx_CIU_15	0.721	-0.133	0.724	*	0.060	0.723	41	1.0	0.36	158	34	Cyclic mobility
	CTx_CIU_16	0.806	0.228	0.802	*	0.578	0.791	38	0.9	0.22	129	9	Flow liquefaction - Strain soft.
	CTx_CIU_17	0.820	0.319	0.815	*	0.645	0.803	35	0.9	0.22	n.v.	12	Flow liquefaction - Strain soft.
	CTx_CIU_18	0.848	0.513	0.839	*	2.982	0.784	690	0.7	0.27	n.v.	2	Flow liquefaction - Strain soft.

Table A.10: List of the cyclic triaxial tests performed with Coimbra sand completed with initial state values, strength and stiffness parameters

	Test ID	After modelling	Percolation + Saturation				Consolidation		$\tau/(2x\sigma'_{h0})$	Freq	V_s	Cycles to liquefy	Type of liquefaction
		e_0	ε_v (%)	e_{i-1}		ε_v (%)	e_i	p'_i kPa	K_0		Hz	m/s	
COIMBRA SAND	CTx_CK_0U_MT_1	0.680	0.282	0.675	*	0.185	0.680	26	0.5	0.2	0.1	n.v.	3	Flow liquefaction - Strain soft.
	CTx_CK_0U_MT_2	0.628	-0.187	0.632	*	0.119	0.628	26	0.5	0.4	0.1	n.v.	>109	Cyclic mobility
	CTx_CK_0U_MT_3	0.624	-0.226	0.628	*	0.098	0.624	26	0.5	0.3	0.1	n.v.	>109	Cyclic mobility
	CTx_CK_0U_MT_4	0.658	0.088	0.657	*	0.372	0.658	68	0.4	0.2	0.1	n.v.	>109	Cyclic mobility
	CTx_CK_0U_MT_5	0.601	-0.441	0.608	*	0.085	0.601	67	0.5	0.6	0.1	n.v.	>1232	Cyclic mobility
	CTx_CK_0U_MT_6	0.742	0.852	0.727	*	0.494	0.742	65	0.5	0.2	0.1	n.v.	19	Flow liquefaction
	CTx_CK_0U_MT_7	0.737	0.812	0.723	*	0.781	0.737	67	0.5	0.2	0.1	n.v.	5	Flow liquefaction
	CTx_CK_0U_MT_8	0.709	0.551	0.700	*	0.596	0.690	72	0.5	0.1	3.3×10^{-2}	n.v.	6	Flow liquefaction
	CTx_CK_0U_MT_9	0.756	1.172	0.756	*	1.355	0.726	73	0.5	0.1	3.3×10^{-2}	n.v.	3	Flow liquefaction
	CTx_CK_0U_MT_10	0.601	-0.441	0.608	*	0.253	0.598	72	0.5	0.5	3.3×10^{-2}	222	0	Cyclic mobility
	CTx_CK_0U_MT_11	0.642	-0.066	0.643	*	0.356	0.637	72	0.5	0.6	3.3×10^{-2}	223	176	Cyclic mobility
	CTx_CK_0U_MT_12	0.643	-0.057	0.644	*	0.359	0.638	72	0.5	0.8	3.3×10^{-2}	229	47	Cyclic mobility
	CTx_CK_0U_MT_13	0.639	-0.090	0.640	*	0.499	0.632	67	0.5	1.0	3.3×10^{-2}	n.v.	17	Cyclic mobility
	CTx_CK_0U_MT_14	0.698	0.454	0.691	*	0.622	0.680	72	0.5	0.1	3.3×10^{-2}	200	0	Flow liquefaction
	CTx_CK_0U_MT_15	0.701	0.474	0.693	*	0.819	0.679	72	0.5	0.1	3.3×10^{-2}	193	0	Flow liquefaction
	CTx_CK_0U_MT_16	0.700	0.465	0.692	*	0.665	0.681	72	0.5	0.0	3.3×10^{-2}	202	102	Flow liquefaction
	CTx_CK_0U_PL_1	0.682	0.308	0.677	*	0.335	0.672	72	0.5	0.2	3.3×10^{-2}	189	>720	Cyclic mobility
	CTx_CK_0U_PL_2	0.722	0.673	0.711	*	0.405	0.704	72	0.5	0.2	3.3×10^{-2}	232	1393	Cyclic mobility
	CTx_CK_0U_PL_3	0.708	0.543	0.699	*	0.307	0.694	78	0.5	0.5	3.3×10^{-2}	215	41	Cyclic mobility
	CTx_CK_0U_PL_4	0.623	-0.238	0.627	*	0.206	0.623	66	0.5	0.4	0.1	n.v.	965	Cyclic mobility
	CTx_CK_0U_PL_5	0.672	0.214	0.669	*	0.348	0.663	68	0.5	0.1	0.1	n.v.	1	?
	CTx_CK_0U_PL_6	0.659	0.095	0.658	*	0.370	0.651	69	0.5	0.3	0.1	n.v.	60	Cyclic mobility
	CTx_CK_0U_PL_7	0.727	0.713	0.714	*	0.402	0.708	78	0.5	0.6	3.3×10^{-2}	231	65	Cyclic mobility
	CTx_CK_0U_PL_8	0.630	-0.169	0.633	*	0.169	0.630	78	0.5	0.7	3.3×10^{-2}	239	152	Cyclic mobility
	CTx_CK_0U_PL_9	0.656	0.066	0.655	*	0.237	0.651	77	0.5	0.5	3.3×10^{-2}	212	569	Cyclic mobility
	CTx_CK_0U_PL_10	0.629	-0.184	0.632	*	0.252	0.628	78	0.5	0.7	3.3×10^{-2}	221	45	Cyclic mobility
	CTx_CK_0U_PL_11	0.633	-0.144	0.636	*	0.085	0.634	73	0.5	0.8	3.3×10^{-2}	244	49	Cyclic mobility
	CTx_CK_0U_PL_12	0.671	0.203	0.668	*	0.335	0.662	67	0.5	0.6	3.3×10^{-2}	238	>1407	Cyclic mobility
	CTx_CK_0U_PL_13	0.623	-0.235	0.627	*	0.204	0.624	68	0.5	0.5	3.3×10^{-2}	204	1754	Cyclic mobility

Table A.11: List of the direct simple shear tests performed with Algeria sand

		After modelling	Consolidation			Shear		
	Test ID	e_0	e_i	σ'_{vi}	τ/σ'_{v0}	Condition of liquefaction		
				kPa		(nº cycles **≤15)**	σ'_v**=0**	γ_s**=3.75%**
ALGERIA SAND	CDSS_2_100	0.638	0.605	100	0.20	3		
	CDSS_3_100	0.924	0.847	100	0.12	2	x	x
	CDSS_4_100	0.900	0.848	100	0.10	7	x	x
	CDSS_5_100	0.900	0.816	100	0.08	7	x	x
	CDSS_6_100	0.690	0.690	100	0.30	2		x
	CDSS_7_100	0.735	0.689	100	0.22	2		x
	CDSS_8_100	0.735	0.698	100	0.17	4		x
	CDSS_10_100	0.734	0.690	100	0.15	3		x
	CDSS_11_100	0.835	0.775	100	0.08	12	x	x
	CDSS_12_100	0.648	0.606	100	0.17	11		x
	CDSS_13_100	0.650	0.615	100	0.17	5		x
	CDSS_14_100	0.652	0.604	100	0.14	15	x	
	CDSS_15_100	0.647	0.616	100	0.14	12	x	
	CDSS_16_100	0.741	0.693	100	0.07	29	x	
	CDSS_17_100	0.718	0.680	100	0.07	62	x	
	CDSS_18_100	0.649	0.613	100	0.19	5		x
	CDSS_19_100	0.651	0.615	100	0.19	7		x
	CDSS_20_100	0.646	0.613	100	0.20	2		x
	CDSS_21_100	0.646	0.618	100	0.22	4		x
	CDSS_22_100	0.646	0.615	100	0.21	3		x
	CDSS_23_100	0.646	0.619	100	0.07	140		x
	CDSS_24_100	0.654	0.620	100	0.07	90		x
	CDSS_26_100	0.933	0.863	100	0.04	66	x	
	CDSS_27_100	0.938	0.864	100	0.06	20	x	
	CDSS_28_100	0.936	0.869	100	0.10	3	x	x
	CDSS_29_100	0.940	0.871	100	0.10	5	x	x
	CDSS_30_100	0.745	0.706	100	0.16	2		x
	CDSS_31_100	0.739	0.705	100	0.16	5		x
	CDSS_32_100	0.739	0.703	100	0.11	16		x
	CDSS_33_100	0.744	0.714	100	0.10	22	x	x
	CDSS_34_100	0.733	0.692	100	0.12	27	x	
	CDSS_1_300	0.924	0.810	300	0.12	2		x
	CDSS_2_300	0.924	0.833	300	0.10	7		x
	CDSS_3_300	0.924	0.826	300	0.08	11		x
	CDSS_4_300	0.733	0.669	300	0.18	2		x
	CDSS_5_300	0.733	0.683	300	0.14	10		x
	CDSS_6_300	0.733	0.683	300	0.09	2		x
	CDSS_7_300	0.646	0.598	300	0.23	4		x
	CDSS_8_300	0.646	0.605	300	0.20	81		x
	CDSS_9_300	0.646	0.598	300	0.15	24		x
	CDSS_10_300	0.646	0.605	300	0.18	9		x
					τ'_{peak}	τ'_{min}	$\tau'_{critical}$	
					kPa	kPa	kPa	
	DSS_1	0.939	0.829	100	5.7	1.9	2.2	
	DSS_2	0.646	0.619	100	no peak	no minimum	72.6	
	DSS_3	0.758	0.699	200	no peak	no minimum	61.6	
	DSS_4	0.922	0.832	300	23.3	8.6	8.6	

Table A.12: List of the direct simple shear tests performed with Coimbra sand

	Test ID	After modelling e_0	Consolidation e_i	σ'_{vi} kPa	τ/σ'_{v0}	Shear Condition of liquefaction (nº cycles ≤15)	σ'_v=0	γ_s=3.75%
COIMBRA SAND	CDSS_1_100	0.632	0.591	100	0.18	5		x
	CDSS_2_100	0.628	0.592	100	0.17	3		x
	CDSS_3_100	0.623	0.595	100	0.08	127	x	
	CDSS_4_100	0.630	0.595	100	0.09	54	x	
	CDSS_5_100	0.630	0.586	100	0.12	19	x	
	CDSS_6_100	0.623	0.587	100	0.12	12	x	
	CDSS_8_100	0.628	0.596	100	0.14	6		x
	CDSS_9_100	0.634	0.594	100	0.14	4		x
	CDSS_10_100	0.722	0.670	100	0.10	5	x	
	CDSS_11_100	0.730	0.662	100	0.10	3	x	
	CDSS_12_100	0.725	0.677	100	0.09	10	x	
	CDSS_13_100	0.719	0.654	100	0.09	7	x	x
	CDSS_14_100	0.719	0.671	100	0.08	25	x	
	CDSS_15_100	0.729	0.663	100	0.07	11	x	
	CDSS_16_100	0.734	0.672	100	0.07	13	x	
	CDSS_17_100	0.724	0.674	100	0.07	36	x	
	CDSS_18_100	0.827	0.756	100	0.08	5	x	
	CDSS_19_100	0.836	0.765	100	0.06	10	x	
	CDSS_22_100	0.840	0.759	100	0.07	8	x	
	CDSS_23_100	0.840	0.766	100	0.06	14	x	
	CDSS_24_100	0.841	0.766	100	0.05	23	x	
	CDSS_25_100	0.836	0.748	100	0.05	44	x	
	CDSS_26_100	0.838	0.749	100	0.09	2	x	x
	CDSS_27_100	0.841	0.766	100	0.10	4	x	x
	CDSS_28_100	0.719	0.657	100	0.12	2	x	x
	CDSS_1_300	0.837	0.714	300	0.10	2		x
	CDSS_2_300	0.834	0.709	300	0.07	15		x
	CDSS_3_300	0.839	0.719	300	0.06	34		x
	CDSS_4_300	0.731	0.676	300	0.14	4		x
	CDSS_5_300	0.729	0.673	300	0.12	9		x
	CDSS_6_300	0.757	0.687	300	0.10	10		x
	CDSS_7_300	0.728	0.668	300	0.09	12		x
	CDSS_8_300	0.629	0.579	300	0.26	1		x
	CDSS_9_300	0.636	0.589	300	0.24	2		x
	CDSS_10_300	0.639	0.587	300	0.17	3		x
	CDSS_11_300	0.632	0.572	300	0.14	8		x
	CDSS_12_300	0.636	0.576	300	0.12	15		x
	CDSS_13_300	0.635	0.580	300	0.10	45		x
	CDSS_14_300	0.730	0.640	300	0.08	20		x
	CDSS_1_500	0.634	0.573	500	0.19	2		x
	CDSS_2_500	0.632	0.569	500	0.18	3		x
	CDSS_3_500	0.635	0.565	500	0.16	4		x
	CDSS_4_500	0.630	0.566	500	0.14	10		x
					τ'_{peak} kPa	τ'_{min} kPa	$\tau'_{critical}$ kPa	
	DSS_1	0.840	0.755	100	5.4	1.4	1.9	
	DSS_2	0.635	0.610	100	no peak	no minimum	41.9	
	DSS_3	0.836	0.725	300	20.0	6.3	6.4	

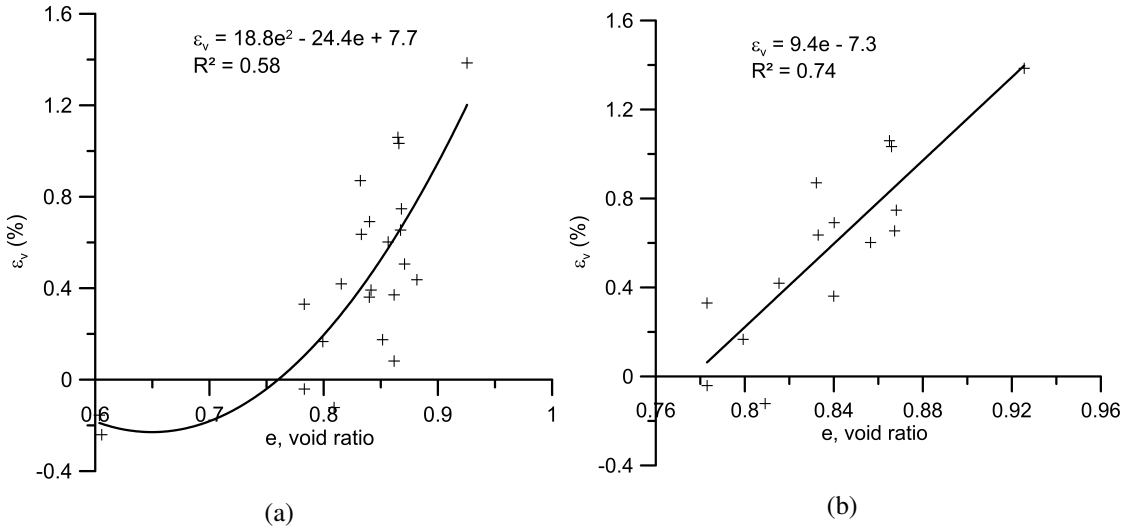


Figure A.1: Volumetric strain as function of the initial modelling void ratio for Algeria sand; Linear regression model used on triaxial tests marked with * on table A.1, A.9 and A.10

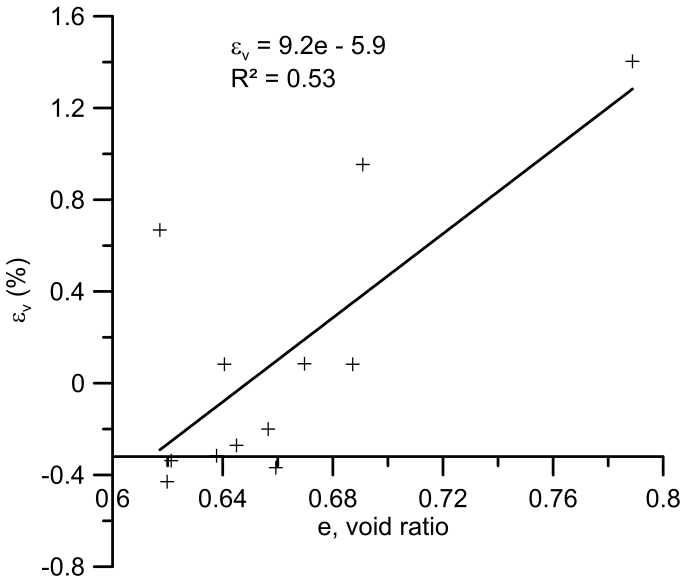


Figure A.2: Volumetric strain as function of the initial modelling void ratio for Coimbra sand; Linear regression model used on triaxial tests marked with * on table A.2 and A.11

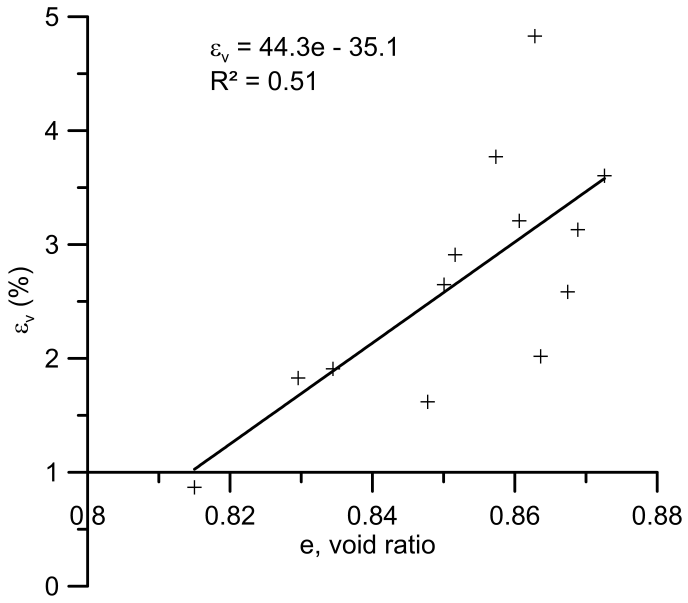


Figure A.3: Volumetric strain as function of the initial modelling void ratio for Osorio sand; Linear regression model used on triaxial tests marked with * on table A.3

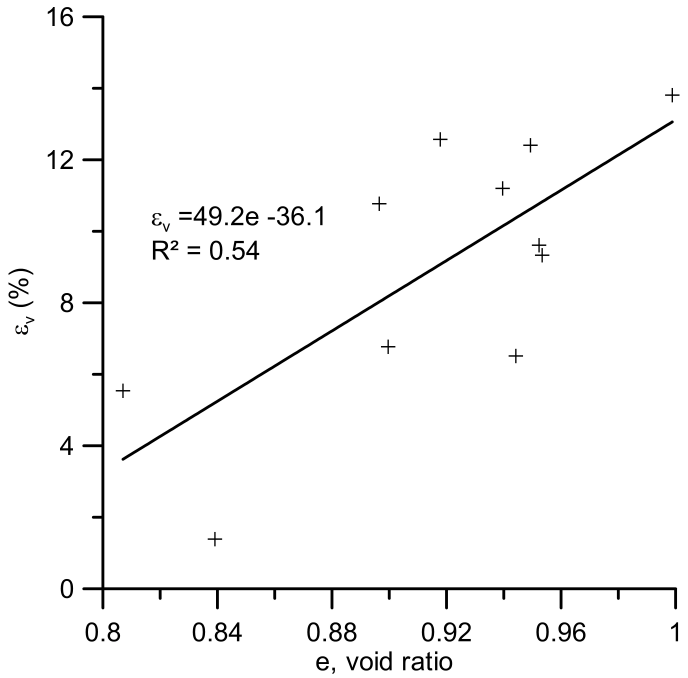


Figure A.4: Volumetric strain as function of the initial modelling void ratio for Mixture; Linear regression model used on triaxial tests marked with * on table A.4

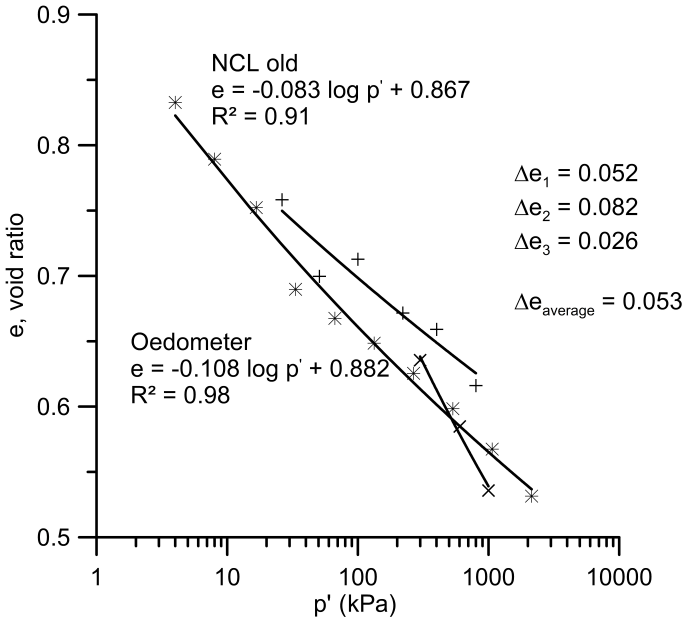


Figure A.5: Normal consolidation lines of Mixture determined with internal instrumentation (NCL old) and by using the freezing technique (NCL new); Corrections used on triaxial tests marked with ** on table A.4

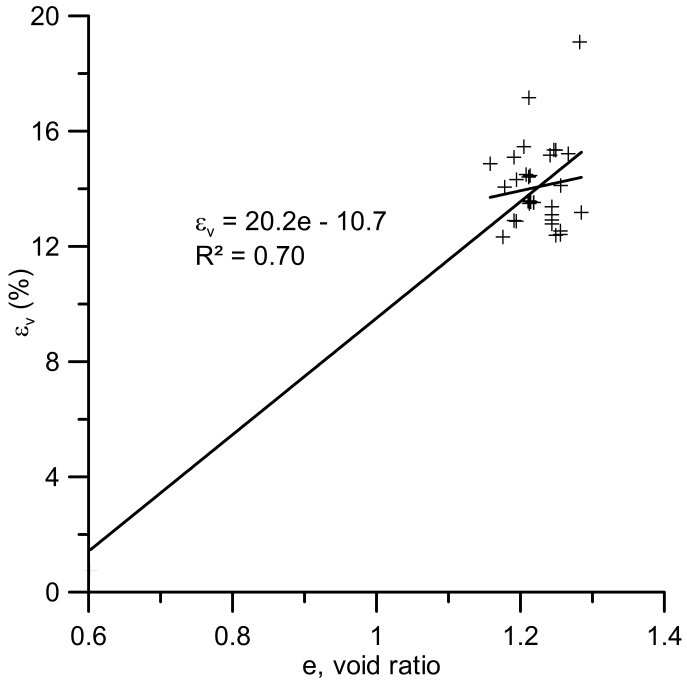


Figure A.6: Volumetric strain as function of the initial modelling void ratio for Silt; Linear regression model used on triaxial tests marked with * on table A.5 and A.6

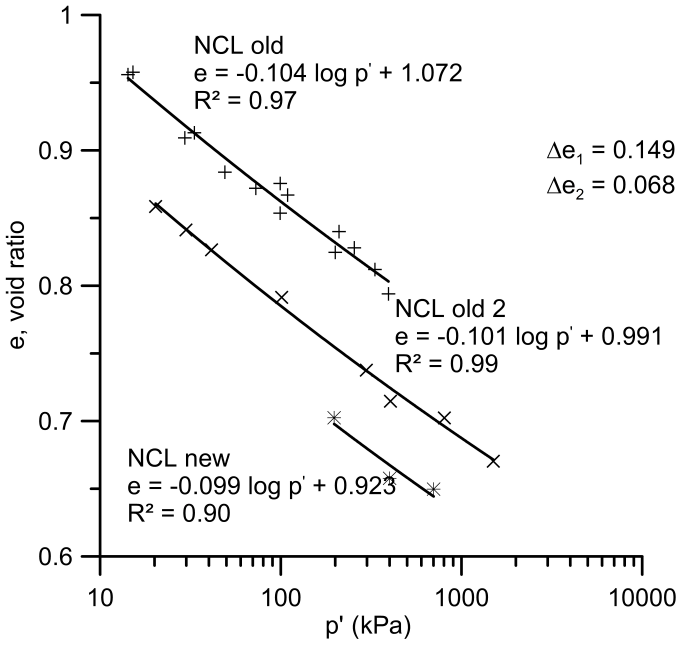


Figure A.7: Normal consolidation lines of Silt determined with internal instrumentation (NCL old) and by using the freezing technique (NCL new); Corrections used on triaxial tests marked with ** on table A.5 and A.6

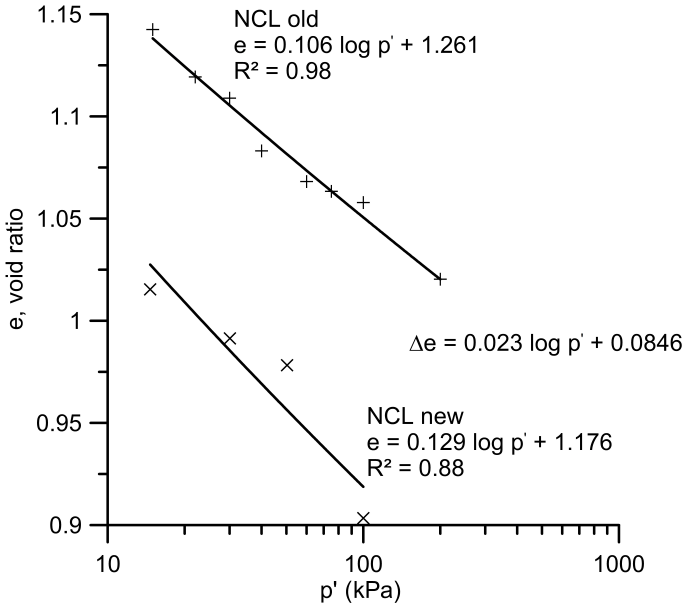


Figure A.8: Normal consolidation lines of Gold tailings determined with internal instrumentation (NCL old) and by using the freezing technique (NCL new); Corrections used on triaxial tests marked with ** on table A.7

Appendix B

Degree of Saturation of Undrained Triaxial Tests Performed with Silt and Gold Tailings

The influence of the degree of saturation on both peak and residual strengths, thus on soils' brittleness is notorious. In the scope of this research soil saturation was determined either by the measurement of the Skempton parameter, B, which shall be at least 0.97, or through the measurement of P waves' velocities, which shall be around the same value of the propagation of the compression wave' on water, i.e. 1500 m/s.

While the new triaxial tests were performed by ensuring a B parameter of at least of 0.97 and, when possible a V_p of 1500 m/s, the saturation degree of the earlier triaxial tests performed by Bedin (2010), with the Silt and the Gold tailings, were reassessed through the data available.

The information referent to the degree of saturation of the undrained triaxial tests can be found on Table B.1 for both Silt and Gold tailings. For a better perception and analysis both data were plotted in Figures B.1, which can be compared with the framework developed by Yang (2002a).

Note: The assessment of the degree of saturation was only performed for these two materials as they were both executed by two distinct researchers and dispersion of values was observed

Table B.1: Saturation degree of undrained triaxial tests performed with Silt and Gold tailings

	Test ID	e_i	p'_i kPa	Range of saturation degree	V_p (m/s)	B Skempton
SILT	Tx_CIU_8	0.778	30	B<0.92	780	0.85
	Tx_CIU_9	0.718	70		780	0.85
	Tx_CIU_10	0.734	110		750	0.83
	Tx_CIU_11	0.707	220		750	0.83
	Tx_CIU_13	0.679	342		750	0.83
	Tx_CIU_1	0.81	15	0.92<B<0.95	853	0.87
	Tx_CIU_2	0.767	30		860	0.87
	Tx_CIU_3	0.744	50		875	0.88
	Tx_CK_0U_1	0.755	38		1350	0.95
	Tx_CIU_15	0.726	101		907	0.89
	Tx_CIU_16	0.793	20		748	0.83
	Tx_CIU_21	0.76	50		744	0.83
	Tx_CIU_4	0.718	99		871	0.88
	Tx_CIU_5	0.686	201		884	0.88
	Tx_CIU_23	0.702	197	B>0.97	1700	0.98
	Tx_CIU_24	0.658	400		1700	0.98
	Tx_CIU_25	0.65	701		1900	0.99
	Tx_CIU_26	0.617	1185		1900	0.99
Gold tailings	Tx_CIU_1	1.031	15	B<0.95	864	0.87
	Tx_CIU_2	1.004	22		871	0.88
	Tx_CIU_3	0.990	30		929	0.89
	Tx_CIU_4	0.959	50		829	0.86
	Tx_CIU_5	0.943	60		928	0.89
	Tx_CIU_6	0.936	75		913	0.88
	Tx_CIU_7	0.927	100		898	0.88
	Tx_CIU_8	0.883	200		918	0.89
	Tx_CIU_14	0.869	100	B>0.97	1700	0.98
	Tx_CIU_16	0.843	299		1700	0.98

Red values estimated basing on Yang (2002a) correlation between P-wave velocities and B

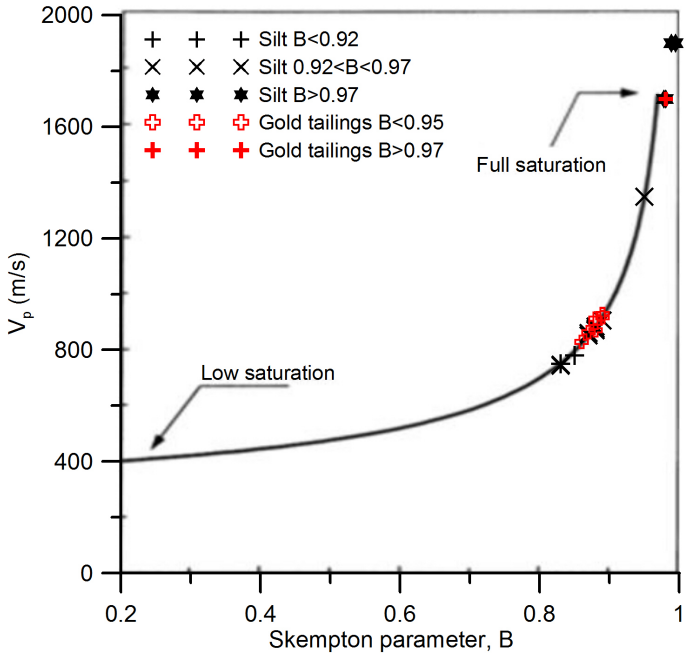


Figure B.1: Relation between P-wave velocity and B for Silt and Gold tailings, adapted from Yang (2002a)